



## **State-of-the-Art Reactor Consequence Analyses Project**

### **Uncertainty Analysis of the Unmitigated Short-Term Station Blackout of the Surry Power Station**

**Draft Report**

## AVAILABILITY NOTICE

### Availability of Reference Materials Cited in NRC Publications

#### NRC Reference Material:

As of November 1999, you may electronically access NUREG-series publications and other NRC records at NRC's Public Electronic Reading Room at <http://www.nrc.gov/reading-rm.html>.

Publicly released records include, to name a few, NUREG-series publications; *Federal Register* notices; applicant, licensee, and vendor documents and correspondence; NRC correspondence and internal memoranda; bulletins and information notices; inspection and investigative reports; licensee event reports; and Commission papers and their attachments.

NRC publications in the NUREG series, NRC regulations, and *Title 10, Energy*, in the Code of *Federal Regulations* may also be purchased from one of these two sources.

1. The Superintendent of Documents  
U.S. Government Printing Office  
Mail Stop SSOP  
Washington, DC 20402-0001  
Internet: [bookstore.gpo.gov](http://bookstore.gpo.gov)  
Telephone: 202-512-1800  
Fax: 202-512-2250
2. The National Technical Information Service.  
Springfield, VA 22161-0002  
[www.ntis.gov](http://www.ntis.gov)  
1-800-553-6847 or, locally, 703-605-6000

A single copy of each NRC draft report for comment is available free, to the extent of supply, upon written request as follows:

Address: U.S. Nuclear Regulatory Commission  
Office of Administration  
Publications Branch  
Washington, DC 20555-0001  
E-mail: [DISTRIBUTION.SERVICES@nrc.gov](mailto:DISTRIBUTION.SERVICES@nrc.gov)  
Facsimile: 301-415-2289

Some publications in the NUREG series that are posted at NRC's Web site address:

<http://www.nrc.gov/reading-rm/doc-collections/nuregs> are updated periodically and may differ from the last printed version. Although references to material found on a Web site bear the date the material was accessed, the material available on the date cited may subsequently be removed from the site.

#### Non-NRC Reference Material:

Documents available from public and special technical libraries include all open literature items, such as books, journal articles, and transactions, *Federal Register* notices, Federal and State legislation, and congressional reports. Such documents as theses, dissertations, foreign reports and translations, and non-NRC conference proceedings may be purchased from their sponsoring organization.

Copies of industry codes and standards used in a substantive manner in the NRC regulatory process are maintained at:

The NRC Technical Library  
Two White Flint North  
11545 Rockville Pike  
Rockville, MD 20852-2738

These standards are available in the library for reference use by the public. Codes and standards are usually copyrighted and may be purchased from the originating organization or, if they are American National Standards, from:

American National Standards Institute  
11 West 42<sup>nd</sup> Street  
New York, NY 10036-8002  
[www.ansi.org](http://www.ansi.org)  
212-642-4900

Legally binding regulatory requirements are stated only in laws; NRC regulations; licenses, including technical specifications; or orders, not in NUREG-series publications. The views expressed in contractor-prepared publications in this series are not necessarily those of the NRC.

The NUREG series comprises (1) technical and administrative reports and books prepared by the staff (NUREG-XXXX) or agency contractors (NUREG/CR-XXXX), (2) proceedings of conferences (NUREG/CP-XXXX), (3) reports resulting from international agreements (NUREG/IA-XXXX), (4) brochures (NUREG/BR-XXXX), and (5) compilations of legal decisions and orders of the Commission and Atomic and Safety Licensing Boards and of Directors' decisions under Section 2.206 of NRC's regulations (NUREG-0750).

**DISCLAIMER:** This report was prepared as an account of work sponsored by an agency of the U.S. Government. Neither the U.S. Government nor any agency thereof, nor any employee, makes any warranty, expressed or implied, or assumes any legal liability or responsibility for any third party's use, or the results of such use, of any information, apparatus, product, or process disclosed in this publication, or represents that its use by such third party would not infringe privately owned rights.



# **State-of-the-Art Reactor Consequence Analysis Project**

## **Uncertainty Analysis of the Unmitigated Short-Term Station Blackout of the Surry Power Station**

**Draft Report**

Manuscript Completed:  
Date Published:

Prepared by: K. Ross\*, N. Bixler\*, S. Weber\*, C. Sallaberry\*, and J. Jones\*

\*Sandia National Laboratories  
Albuquerque, NM 87185  
Operated by Sandia Corporation  
for the U.S. Department of Energy

Prepared for  
Division of Systems Analysis  
U.S. Nuclear Regulatory Commission  
Washington, DC 20555-0001  
T. Ghosh, U.S. Nuclear Regulatory Commission Technical Lead

NRC Job Code

**Office of Nuclear Regulatory Research**

Sandia National Laboratories is a multi-program laboratory managed and operated by Sandia Corporation, a wholly owned subsidiary of Lockheed Martin Corporation, for the U.S. Department of Energy's National Nuclear Security Administration under contract DE-AC04-94AL85000.



## **ABSTRACT**

The State of the Art Reactor Consequence Analyses (SOARCA) project published best estimate analyses for select accident scenarios at the Peach Bottom Atomic Power Station and Surry Power Station in 2013. This work was followed by a first of a kind integrated uncertainty analysis (UA) performed on the SOARCA unmitigated long term station blackout (LTSBO) scenario for Peach Bottom. The approach developed for the Peach Bottom UA was implemented in this Surry Power Station UA. The Surry UA also included additional knowledge gained since the original Surry best estimate calculation. The project included an integrated Monte Carlo analysis using the MELCOR and MACCS codes as applied to the Surry SOARCA unmitigated short term station blackout (STSBO) scenario. Regression analyses and separate sensitivity analyses were conducted to understand the contributions of individual uncertain inputs to the uncertainty in analysis results. Single realizations were analyzed to investigate individual parameter effects, typically associated with the extreme bounds, and to confirm phenomenological explanations of variations in system behavior and results. Consistent with the Peach Bottom UA, rank regression, quadratic regression, recursive partitioning, and multivariate adoptive regression splines (MARS) techniques were used to identify the importance of the input parameters with regard to the uncertainty of the results. The analysis provides insights into the sensitivity of the best estimate results to selected model inputs. Like the Peach Bottom UA, the analyses herein corroborate the conclusions of the original SOARCA study and further extend the body of knowledge on severe reactor accidents.



# TABLE OF CONTENTS

<u>Section</u>	<u>Page</u>
ABSTRACT.....	III
TABLE OF CONTENTS.....	V
LIST OF FIGURES.....	VIII
LIST OF TABLES.....	XV
EXECUTIVE SUMMARY.....	XIX
ACKNOWLEDGMENTS.....	XXXIII
ABBREVIATIONS AND ACRONYMS.....	XXXV
1. INTRODUCTION.....	1-1
1.1 Background on SOARCA.....	1-2
1.2 Objectives.....	1-3
1.3 Scope.....	1-4
1.4 Methodology.....	1-4
2. UNCERTAINTY ANALYSIS APPROACH.....	2-1
2.1 Accident Scenario.....	2-1
2.2 Selection of Uncertain MELCOR Parameters.....	2-2
2.2.1 MELCOR Parameters Considered but not Included.....	2-6
2.3 Selection of Uncertain MACCS Parameters.....	2-6
2.3.1 MACCS Parameters Considered but not Included.....	2-8
3. DESCRIPTION OF CODES AND REGRESSION ANALYSIS.....	3-1
3.1 Severe Accident Analysis Codes.....	3-1
3.1.1 MELCOR.....	3-2
3.1.3 MACCS.....	3-6
3.2 Uncertainty Quantification and Propagation.....	3-7
3.2.1 Introduction.....	3-7
3.2.2 Uncertainty Type.....	3-7
3.2.3 Uncertainty Characterization.....	3-8
3.2.4 Uncertainty Propagation for Source Term and Consequence Analysis..	3-9
3.3 Analyzing Uncertainty Results.....	3-10
3.3.1 Uncertainty Analysis.....	3-10
3.3.2 Regression Analysis.....	3-10

3.3.3	Stability Analysis.....	3-16
4.	UNCERTAIN INPUT PARAMETERS AND DISTRIBUTIONS .....	4-1
4.1	Source Term Model Uncertainty (MELCOR Inputs) .....	4-1
4.1.1	Sequence .....	4-4
4.1.2	In-vessel Accident Progression .....	4-30
4.1.3	Ex-vessel Accident Progression .....	4-47
4.1.4	Containment Behavior .....	4-52
4.1.5	Chemical Form (CHEMFORM I2).....	4-59
4.1.6	Aerosol Deposition.....	4-63
4.2	Consequence Model Uncertainty (MACCS Inputs) .....	4-65
4.2.1	Wet Deposition Model (CWASH1).....	4-68
4.2.2	Dry Deposition Velocities (VDEPOS) .....	4-70
4.2.3	Shielding Factors (GSHFAC and PROTIN).....	4-74
4.2.4	Early Health Effects (EFFACA, EFFACB, EFFTHR).....	4-80
4.2.5	Latent Health Effects (DDREFA, CFRISK, Long-Term Inhalation Dose Coefficients).....	4-85
4.2.6	Dispersion (CYSIGA, CZSIGA) .....	4-91
4.2.7	Emergency Response (Evacuation and Relocation) .....	4-95
4.2.8	Weather .....	4-110
4.2.9	MACCS Correlated Parameters .....	4-113
4.3	Quality Assurance Review of Input Parameters .....	4-115
4.3.1	MELCOR QA Review .....	4-115
4.3.2	MACCS QA Review.....	4-117
5.	UPDATED MELCOR BASE CASE .....	5-1
5.1	Source Term Model (MELCOR) .....	5-1
5.1.1	Updated Best Estimate Run .....	5-1
6.	SOARCA MODEL PARAMETER UNCERTAINTY AND SENSITIVITY ANALYSES.....	6-1
6.1	Source Term Parameter Uncertainty Analysis .....	6-1
6.1.1	Iodine Release Fraction to Environment.....	6-3
6.1.2	Cesium Release Fraction to Environment .....	6-18
6.1.3	Hydrogen Production .....	6-33
6.1.4	Time of Release.....	6-44
6.1.5	Steam Generator Tube Rupture .....	6-51
6.1.6	Analysis of Select MELCOR Individual Realizations .....	6-66
6.1.7	MELCOR Analysis Extended to 72 Hours .....	6-82
6.1.8	MELCOR Sensitivity Analyses.....	6-96

6.2	Offsite Consequences .....	6-117
6.2.1	Latent Cancer Fatality Risk.....	6-118
6.2.2	Early Fatalities .....	6-127
6.2.3	Regression Analysis .....	6-127
6.2.4	Analysis of Single Realizations.....	6-156
6.2.5	Sensitivity Results for Phase Durations and Dose Projection Period .....	6-158
6.2.6	Evaluation of Multiple Tube Ruptures.....	6-159
6.2.7	Summary of Consequence Results .....	6-160
7.	SUMMARY OF RESULTS AND CONCLUSIONS .....	7-1
8.	REFERENCES.....	8-1
APPENDIX A:	MELCOR MODEL AND CODE ENHANCEMENTS .....	A-I
APPENDIX B:	GLOSSARY OF UNCERTAINTY ANALYSIS TERMS	

## LIST OF FIGURES

<u>Figure</u>		<u>Page</u>
Figure ES-1	Cesium release fractions over 48 hours with mean, median, 5 <sup>th</sup> and 95 <sup>th</sup> percentiles.....	xxii
Figure 2-1	Parameter storyboard used to capture key information for each parameter investigated.....	2-5
Figure 3-1	Diagram of the code information flow.....	3-1
Figure 3-2	MELCOR Uncertainty Application.....	3-2
Figure 3-3	Comparison of the NUREG/CR 7110 Volume 2 and the UA steam generator nodalizations.....	3-4
Figure 3-4	Typical representation of stability analysis for MACCS results showing confidence intervals around the mean of each subset for latent-cancer fatality risk at 0 to 10 miles.....	3-18
Figure 4-1	Possible transitions in the 3-SV pressurizer pressure relief system considering both FTO and FTC valve conditions.....	4-5
Figure 4-2	Mean CDF for number of cycles at which any SV of a 3-SV system fails open compared to the mean CDF for number of cycles at which all 3 valves fail.....	4-6
Figure 4-3	CDF of the beta distribution ( $\alpha = 17.5$ , $\beta = 756.5$ ) developed to characterize the epistemic uncertainty associated with the probability that an individual SV fails to close conditional on a demand to close.....	4-9
Figure 4-4	CDFs characterizing uncertainty in the number of demands at which an individual SV fails to close conditional on a specific value of p.....	4-9
Figure 4-5	CDF of the beta distribution ( $\alpha = 0.5$ , $\beta = 773.5$ ) developed to characterize the epistemic uncertainty associated with an individual safety valve failing to open.....	4-11
Figure 4-6	CDFs characterizing uncertainty in the number of demands at which an individual SV fails to open conditional on a specific value of p.....	4-11
Figure 4-7	CDF of SV FTCW valve cycle per-demand failure probability.....	4-14
Figure 4-8	Mean, 5 <sup>th</sup> , 50 <sup>th</sup> , and 95 <sup>th</sup> percentile CDFs of SV FTCW as a function of valve cycles.....	4-14
Figure 4-9	CDF for the temperature for SV thermal FTC after one valve cycle at a specified temperature.....	4-21
Figure 4-10	CDF for the SV thermal FTC open area fraction.....	4-23
Figure 4-11	CFD predictions indicating expanded mixing region [44].....	4-26
Figure 4-12	CDF of normalized hottest tube temperature.....	4-27
Figure 4-13	CDF of tube thickness distribution.....	4-30
Figure 4-14	Schematic of zirconium melt breakthrough.....	4-31
Figure 4-15	Depiction of the fuel rod degradation.....	4-31
Figure 4-16	Qualitative oxygen concentration in the $\alpha$ -ZrO region.....	4-32
Figure 4-17	Zircaloy melt breakout temperature cumulative distributions.....	4-34
Figure 4-18	CDF of molten pool drainage rate.....	4-36
Figure 4-19	CDF for radial debris liquid relocation time constant.....	4-38
Figure 4-20	CDF for radial debris solid relocation time constant.....	4-39
Figure 4-21	BOC, MOC, and EOC decay power.....	4-41
Figure 4-22	BOC and MOC decay power relative to EOC decay power.....	4-43
Figure 4-23	BOC decay heat uncertainty.....	4-43
Figure 4-24	MOC decay heat uncertainty.....	4-44

Figure 4-25	EOC decay heat uncertainty .....	4-44
Figure 4-26	Combined BOC, MOC, and EOC decay heat uncertainties .....	4-44
Figure 4-27	CDF of effective temperature of the eutectic reaction temperature .....	4-47
Figure 4-28	Uncertainty distribution for ignition propagation direction .....	4-48
Figure 4-29	Decontamination factor per steam generator stage versus particle size and associated confidence bounds .....	4-49
Figure 4-30	Decontamination factor from the separator and dryer versus particle size .....	4-50
Figure 4-31	PDF for number of stages traversed after SGTR .....	4-51
Figure 4-32	CDF of Containment Design Leakage .....	4-53
Figure 4-33	Range of containment design leakage .....	4-53
Figure 4-34	Containment functional failure leakage .....	4-56
Figure 4-35	CDF for containment overpressure ratio for liner plate yield .....	4-57
Figure 4-36	PDF of heat transfer coefficients and mass transfer multipliers .....	4-58
Figure 4-37	CDF of heat transfer coefficients and mass transfer multipliers .....	4-59
Figure 4-38	French measured fission gas release to the fuel/cladding gap .....	4-60
Figure 4-39	CDF for the gaseous iodine percentage at EOC .....	4-61
Figure 4-40	PDF for the fraction of cesium as cesium molybdate .....	4-63
Figure 4-41	Dynamic shape factor compared to number of spheres within a chain .....	4-64
Figure 4-42	CDF of the dynamic shape factor .....	4-65
Figure 4-43	CDF of the linear coefficient CWASH1 .....	4-70
Figure 4-44	CDF of dry deposition velocities for mass median diameters representing MACCS aerosol bins .....	4-73
Figure 4-45	Cumulative distribution functions of GSHFAC for normal activity, sheltering, and evacuation based on expert elicitation data .....	4-76
Figure 4-46	Cumulative distribution function of GSDE .....	4-77
Figure 4-47	CDF of GSHFAC accounting for uncertainty in GSDE .....	4-77
Figure 4-48	CDFs of PROTIN for normal activity, sheltering, and evacuation .....	4-80
Figure 4-49	CDFs of EFFACA for specified health effects .....	4-83
Figure 4-50	CDFs of EFFACB for specified health effects .....	4-84
Figure 4-51	CDFs of EFFTHR for specified health effects .....	4-85
Figure 4-52	Normalized PDFs for DDREFA for breast and other cancers .....	4-86
Figure 4-53	CDFs of DDREFA for breast and other cancer types .....	4-87
Figure 4-54	CDF for CFRISK for each of the organs included in the analysis .....	4-88
Figure 4-55	Cs-137 lifetime inhalation dose coefficient distributions for organs included in the consequence analysis .....	4-90
Figure 4-56	Pu-241 long-term inhalation dose coefficient distributions for organs included in the consequence analysis .....	4-91
Figure 4-57	CDFs of CYSIGA for individual stability classes .....	4-94
Figure 4-58	CDFs of CZSIGA for individual stability classes .....	4-95
Figure 4-59	General response timeline representing MACCS activities .....	4-97
Figure 4-60	CDF of DLTEVA for each cohort .....	4-101
Figure 4-61	CDFs of ESPEED for each cohort .....	4-104
Figure 4-62	CDF of TIMHOT .....	4-106
Figure 4-63	CDF of TIMNRM .....	4-107
Figure 4-64	CDF of DOSHOT .....	4-108
Figure 4-65	CDF of DOSNRM .....	4-109
Figure 4-66	Illustration of four consecutive plume segments, where the tail of one segment aligns in distance traveled, but not in direction, with the head of the next segment .....	4-113
Figure 4-67	Illustration of four consecutive plume segments with tails that do not align .....	4-113
Figure 4-68	SV1 temperature and open fraction for thermal failure sensitivity .....	4-116

Figure 5-1	RCS primary press (Base Case).....	5-5
Figure 5-2	RCS secondary press (Base Case).....	5-5
Figure 5-3	RCS primary level (Base Case).....	5-6
Figure 5-4	RCP seal leakage (Base Case).....	5-6
Figure 5-5	SG level referenced to top of tube sheet (Base Case).....	5-7
Figure 5-6	In-Vessel hydrogen production (Base Case).....	5-8
Figure 5-7	Core mass relocated to the reactor cavity (Base Case).....	5-8
Figure 5-8	Containment pressure (Base Case).....	5-9
Figure 5-9	Energy produced by deflagrations in containment (Base Case).....	5-10
Figure 5-10	Containment dome temperature (Base Case).....	5-10
Figure 5-11	Noncondensable gas generation from core-concrete interaction, kg (Base Case).....	5-11
Figure 5-12	Noncondensable gas generation from core-concrete interaction, kg-mol (Base Case).....	5-11
Figure 5-13	Containment dome partial pressures (Base Case).....	5-12
Figure 5-14	Containment leakage rate (Base Case).....	5-12
Figure 5-15	SG tube creep damage accumulation (Base Case).....	5-13
Figure 5-16	Iodine distribution (as I <sub>2</sub> and CsI, Base Case).....	5-14
Figure 5-17	Iodine distribution (log, as I <sub>2</sub> and CsI, Base Case).....	5-14
Figure 5-18	Cs distribution (as CsOH, CsI, and Cs <sub>2</sub> MoO <sub>4</sub> , Base Case).....	5-15
Figure 5-19	Cs distribution (log, as CsOH, CsI, and Cs <sub>2</sub> MoO <sub>4</sub> , Base Case).....	5-16
Figure 5-20	Fuel temperature (Base Case).....	5-16
Figure 5-21	Concrete ablation and cavity water depth (Base Case).....	5-17
Figure 6-1	Iodine release fractions over 48 hours with mean, median, 5 <sup>th</sup> and 95 <sup>th</sup> percentiles.....	6-5
Figure 6-2	Cumulative probabilities for the fraction of iodine release for selected time intervals.....	6-5
Figure 6-3	Comparison of iodine release fraction in the original SOARCA STSBO to the calculated values of all successful realizations.....	6-7
Figure 6-4	Comparison of containment failure models used for the original SOARCA STSBO and the UA realizations.....	6-7
Figure 6-5	Scatterplot of iodine release fraction versus integrated decay energy representing time at cycle input values.....	6-10
Figure 6-6	Scatterplot of iodine release fraction versus containment failure input values...6-11	11
Figure 6-7	Scatterplot of iodine release fraction versus containment leakage input values6-12	12
Figure 6-8	Scatterplot of iodine release fraction versus Chemform I <sub>2</sub> input values ( <i>higher gaseous iodine leads to greater release to environment</i> ).....	6-13
Figure 6-9	Scatterplot of iodine release fraction versus decay heat deviations.....	6-14
Figure 6-10	Scatterplot of iodine release fraction versus dynamic shape factor input values.....	6-15
Figure 6-11	Containment pressure over 48 hours with mean, median, 5 <sup>th</sup> and 95 <sup>th</sup> percentiles, and the original SOARCA result.....	6-17
Figure 6-12	Comparison of cesium and iodine environmental release fractions at 48 hours6-19	19
Figure 6-13	Cesium release fractions over 48 hours with mean, median, 5 <sup>th</sup> and 95 <sup>th</sup> percentiles.....	6-20
Figure 6-14	Cumulative probabilities for the fraction of cesium release for selected time intervals.....	6-21

Figure 6-15	Comparison of cesium release fraction in the original SOARCA STSBO to the calculated values of all successful realizations .....6-22
Figure 6-16	Comparison of containment failure models used for the Surry SOARCA STSBO and the Surry uncertainty analysis .....6-23
Figure 6-17	Scatterplot of cesium release fraction versus containment leakage input values .....6-25
Figure 6-18	Scatterplot of cesium release fraction versus integrated decay energy representing time at cycle input values .....6-26
Figure 6-19	Scatterplot of cesium release fraction versus dynamic shape factor input values .....6-27
Figure 6-20	Scatterplot of cesium release fraction versus containment failure input values .6-28
Figure 6-21	Scatterplot of cesium release fraction versus decay heat deviation .....6-29
Figure 6-22	Scatterplot of cesium release fraction versus Chemform Cs input values .....6-30
Figure 6-23	Containment pressure over 48 hours with mean, median, 5 <sup>th</sup> and 95 <sup>th</sup> percentiles, and the original SOARCA result .....6-32
Figure 6-24	Total Hydrogen production over 48 hours with mean, median, 5 <sup>th</sup> and 95 <sup>th</sup> percentiles .....6-34
Figure 6-25	Cumulative probabilities for the quantity of hydrogen produced for selected time intervals .....6-34
Figure 6-26	Comparison of hydrogen production in the original SOARCA STSBO to the calculated values of all successful realizations .....6-35
Figure 6-27	Scatterplot of in-vessel hydrogen production versus SV 48 hour post-calculated open fraction .....6-37
Figure 6-28	Scatterplot of in-vessel hydrogen production versus eutectic melt temperature input values .....6-38
Figure 6-29	Scatterplot of in-vessel hydrogen production versus integrated decay energy representing time at cycle input values .....6-39
Figure 6-30	Scatterplot of in-vessel hydrogen production versus SV status values .....6-40
Figure 6-31	Scatterplot of in-vessel hydrogen production versus Zircaloy breakout temperature input values .....6-41
Figure 6-32	Scatterplot of in-vessel hydrogen production versus SV cycles to failure values .....6-42
Figure 6-33	Select realizations demonstrating the timing differences for the onset of Hydrogen productions .....6-44
Figure 6-34	Scatterplot of timing of release versus design leakage flow path length input values .....6-47
Figure 6-35	Scatterplot of timing of release versus integrated decay energy representing time at cycle input values .....6-48
Figure 6-36	Scatterplot of timing of release versus tube thickness input values .....6-49
Figure 6-37	Scatterplot of timing of release versus SV open fraction input values .....6-50
Figure 6-38	Cesium and iodine environmental release fractions from original SOARCA SGTR sensitivities .....6-53
Figure 6-39	Scatterplot of cesium and iodine release fractions versus SV open fractions .....6-58
Figure 6-40	Primary and secondary pressure for realization 1151 .....6-58
Figure 6-41	Primary and secondary pressure for realization 119 .....6-59
Figure 6-42	Scatterplot of cesium and iodine release fractions versus steam generator tube thickness input values .....6-60
Figure 6-43	Scatterplot of cesium release fraction versus SGTR location input values for all SGTRs .....6-61

Figure 6-44	Scatterplot of cesium release fraction versus SGTR location input values for SGTRs with a SV open fraction of 0.0 .....	6-61
Figure 6-45	Maximum fuel and hottest tube temperature, and creep damage fraction for realizations 356 (blue) and 441 (red) .....	6-62
Figure 6-46	Pressure, temperature and creep fractions for RLz 243 .....	6-64
Figure 6-47	Pressure, temperature and creep fractions for RLz 751 with stuck open pressurizer SV .....	6-65
Figure 6-48	RLZ 9 Cs distribution .....	6-71
Figure 6-49	RLZ 9 containment pressure .....	6-72
Figure 6-50	RLZ 9 containment leakage rate .....	6-72
Figure 6-51	RLZs 9 and 48 integral fission product decay power .....	6-73
Figure 6-52	RLZs 9 and 48 containment pressure .....	6-74
Figure 6-53	RLZs 9 and 48 containment temperature .....	6-74
Figure 6-54	RLZs 9 and 48 containment leakage rate .....	6-75
Figure 6-55	RLZ 50 I release to the environment .....	6-76
Figure 6-56	RLZs 50 and 66 containment leakage rate .....	6-77
Figure 6-57	Containment leak rate and burn energy in RLZ 48 .....	6-79
Figure 6-58	In-vessel H <sub>2</sub> production versus actual number of cycles of the RCS primary-side 3-safety valve system .....	6-81
Figure 6-59	Base case containment pressure .....	6-83
Figure 6-60	Base case leakage rate .....	6-84
Figure 6-61	Base case iodine release fractions .....	6-84
Figure 6-62	Realization 965 containment pressure .....	6-85
Figure 6-63	Realization 243 containment pressure .....	6-86
Figure 6-64	Realization 243 cesium release fractions .....	6-86
Figure 6-65	Realization 14 containment pressure .....	6-87
Figure 6-66	Realization 14 cesium release fractions .....	6-88
Figure 6-67	Realization 32 cesium release fractions .....	6-89
Figure 6-68	Realization 32 iodine release fractions .....	6-89
Figure 6-69	Realization 19 containment pressure .....	6-90
Figure 6-70	Realization 19 leakage rate .....	6-91
Figure 6-71	Realization 19 iodine release fractions .....	6-91
Figure 6-72	Realization 53 containment pressure .....	6-92
Figure 6-73	Realization 53 cesium release fractions .....	6-93
Figure 6-74	Realization 53 concrete ablation .....	6-93
Figure 6-75	Realization 1017 containment pressure .....	6-94
Figure 6-76	Realization 9 cesium release fractions .....	6-95
Figure 6-77	Realization 9 containment pressure .....	6-95
Figure 6-78	PDF of number of tubes simultaneously failing upon an SGTR .....	6-98
Figure 6-79	Iodine environmental release fraction with number of tubes color-coded .....	6-99
Figure 6-80	Cesium environmental release fraction with number of tubes color-coded .....	6-100
Figure 6-81	Scatterplots of iodine and cesium release fractions versus number of failed tubes input values .....	6-101
Figure 6-82	Scatterplots of iodine and cesium release fractions versus secondary SV open fraction input values .....	6-101
Figure 6-83	Scatterplots of iodine and cesium release fractions versus SGTR location input values .....	6-102
Figure 6-84	Scatterplots of iodine and cesium release fractions versus primary SV open fraction input values .....	6-103
Figure 6-85	Pressure, temperature and creep fractions for RLz 29 .....	6-104
Figure 6-86	Pressure, temperature and creep fractions for RLz 62 .....	6-105

Figure 6-87	MCCI debris surface and ablation depth.....	6-106
Figure 6-88	MCCI non-condensable gas contribution and sum total .....	6-107
Figure 6-89	Containment pressure response .....	6-107
Figure 6-90	Containment temperature response.....	6-108
Figure 6-91	Energy transfer from the cavity to containment atmosphere.....	6-109
Figure 6-92	Environmental release fraction of cesium and iodine.....	6-110
Figure 6-93	MCCI debris surface and ablation depth for varied rebar .....	6-111
Figure 6-94	MCCI NCG contribution for varied rebar .....	6-111
Figure 6-95	Containment pressure response for varied rebar.....	6-112
Figure 6-96	Containment temperature response for varied rebar .....	6-113
Figure 6-97	Energy transfer from the cavity to containment atmosphere for varied rebar ....	6-114
Figure 6-98	Environmental release fraction of cesium and iodine for varied rebar .....	6-114
Figure 6-99	Comparison of primary pressures for select values of pump seal leakage..	6-117
Figure 6-100	Complementary cumulative distribution functions of mean, population-weighted LCF risk (based on LNT dose response) conditional on an STSBO occurring for five circular areas centered on the Surry site.....	6-120
Figure 6-101	Complementary cumulative distribution function of mean, population-weighted LCF risk (based on LNT dose response) conditional on an STSBO occurring for five annular areas centered on the Surry site .....	6-120
Figure 6-102	Complementary cumulative distribution functions of fraction of the population-weighted LCF risk (based on LNT dose response) from the emergency phase for residents within five annular areas centered on the Surry site .....	6-121
Figure 6-103	Complementary cumulative distribution function of mean, population-weighted LCF risk (based on US background dose truncation) conditional on an STSBO accident for five circular areas centered on the Surry site .....	6-123
Figure 6-104	Complementary cumulative distribution function of mean, population-weighted LCF risk (based on US background dose truncation) conditional on an STSBO accident for five annular areas centered on the Surry site.....	6-124
Figure 6-105	Complementary cumulative distribution function of mean, population-weighted LCF risk (based on HPS dose truncation) conditional on an STSBO accident for five circular areas centered on the Surry site.....	6-126
Figure 6-106	Complementary cumulative distribution function of mean, population-weighted LCF risk (based on HPS dose truncation) conditional on an STSBO accident for five annular areas centered on the Surry site .....	6-126
Figure 6-107	Scatter plot of mean, individual, LCF risk within a 50-mile circular area for all realizations, versus steam generator tube thickness, TUBTHICK, conditional on an STSBO accident.....	6-131
Figure 6-108	Scatter plot of mean, individual, LCF risk within a 50-mile circular area for all realizations, versus safety valve open area fraction, SVOAFRAC, conditional on an STSBO accident.....	6-131
Figure 6-109	Scatter plot of mean, individual, LCF risk within a 50-mile circular area for all realizations, versus time in the fuel cycle, CYCLE, conditional on an STSBO accident.....	6-132
Figure 6-110	Scatter plot of mean, individual, LCF risk within a 50-mile circular area for all realizations, versus groundshine shielding factor, GSHFAC.2, conditional on an STSBO accident.....	6-132
Figure 6-111	Scatter plot of mean, individual, LCF risk within a 50-mile circular area for all realizations, versus containment leakage path length, conditional on an STSBO accident.....	6-133

Figure 6-112	Scatter plot of mean, individual, LCF risk within a 50-mile circular area for realizations involving SGTR, conditional on an STSBO accident, versus steam generator tube thickness, TUBTHICK.....6-137
Figure 6-113	Scatter plot of mean, individual, LCF risk within a 50-mile circular area for realizations involving SGTR, conditional on an STSBO accident, versus aerosol deposition velocity, VDEPOS.1 .....6-138
Figure 6-114	Scatter plot of mean, individual, LCF risk within a 50-mile circular area for realizations with SGTR, conditional on an STSBO accident, versus groundshine shielding factor for emergency phase sheltering, GSHFAC.3.....6-138
Figure 6-115	Scatter plot of mean, individual, LCF risk within a 50-mile circular area for realizations with SGTR, conditional on an STSBO accident, versus groundshine shielding factor for normal activity during the emergency phase, GSHFAC.2 ...6-139
Figure 6-116	Scatter plot of mean, individual, LCF risk within a 50-mile circular area for realizations involving SGTR, conditional on an STSBO accident, versus cancer fatality risk factor for the residual organ, CFRISK.8 .....6-139
Figure 6-117	Scatter plot of mean, individual, LCF risk within a 50-mile circular area for realizations involving SGTR, conditional on an STSBO accident, versus containment leak path length, DLEAK .....6-140
Figure 6-118	Scatter plot of mean, individual, LCF risk within a 50-mile circular area for realizations involving SGTR, conditional on an STSBO accident, versus I-134 inhalation dose coefficient for the lungs, I.134_ICH.9 .....6-140
Figure 6-119	Scatter plot of mean, individual, LCF risk (based on LNT) within a 50-mile circular area for realizations that do not involve SGTR, conditional on an STSBO accident, versus time during the fuel cycle, CYCLE .....6-143
Figure 6-120	Scatter plot of mean, individual, LCF risk (based on LNT) within a 50-mile circular area for realizations that do not involve SGTR, conditional on an STSBO accident, versus groundshine shielding factor for normal activity during the emergency phase, GSHFAC.2.....6-144
Figure 6-121	Scatter plot of mean, individual, LCF risk (based on LNT) within a 50-mile circular area for realizations that do not involve SGTR, conditional on an STSBO accident, versus containment leak path length, DLEAK .....6-144
Figure 6-122	Scatter plot of mean, individual, LCF risk (based on LNT) within a 50-mile circular area for realizations that do not involve SGTR, conditional on an STSBO accident, versus residual cancer fatality risk factor, CFRISK.8 .....6-145
Figure 6-123	Complementary cumulative distribution function of mean, population-weighted LCF risk (based on LNT dose response) within two annular areas centered on the Surry site for three single realizations and for the base Surry uncertainty analysis results from Figure 6-100 .....6-157
Figure 6-124	Complementary cumulative distribution function of mean, population-weighted LCF risk (based on LNT dose response) within two annular areas centered on the Surry site for four sensitivity cases and for the Large Source Term case shown in Figure 6-122.....6-159
Figure 6-125	Complementary cumulative distribution function of mean, population-weighted LCF risk (based on LNT dose response) within three distance intervals centered on the Surry site for the SGT UA and the Surry UA.....6-160

## LIST OF TABLES

<u>Table</u>		<u>Page</u>
Table ES-1	MELCOR regression analyses completed. ....	xxiii
Table ES-2	Mean, individual LCF risks using LNT dose response, conditional on STSBO occurring (per event). ....	xxvi
Table ES-3	Mean, individual, LCF risk (LNT dose response) regression results within a 10-mile circular area for all realizations. ....	xxvii
Table 2-1	Surry MELCOR model uncertain parameters. ....	2-4
Table 2-2	Surry MACCS model uncertain parameters. ....	2-7
Table 4-1	MELCOR sampled parameters. ....	4-2
Table 4-2	SV failure data and associated epistemic uncertainty distributions for probability of occurrence on demand for FTO and FTC. ....	4-5
Table 4-3	RCP seal leak probabilities at operating pressure. ....	4-24
Table 4-4	Zircaloy melt breakthrough temperature estimates from S/Q simulations of two ZrO <sub>2</sub> failure modes. ....	4-33
Table 4-5	Radionuclide core inventory and class definition. ....	4-41
Table 4-6	VERCORS test results for collapse temperature. ....	4-46
Table 4-7	Uncertain MACCS parameters applied in the analysis. ....	4-67
Table 4-8	Dry deposition velocities. ....	4-73
Table 4-9	Groundshine shielding factor distribution parameters. A value of unity represents full groundshine for a person standing on an infinite flat plane with uniform concentration; a value of zero represents complete shielding. ....	4-78
Table 4-10	Inhalation protection factor distribution parameters. A value of unity represents direct inhalation from a passing plume; a value of zero represents complete protection. ....	4-80
Table 4-11	Radionuclides treated as having uncertain inhalation dose coefficients. ....	4-90
Table 4-12	Log-triangular values for dispersion parameter CYSIGA for each stability class. ....	4-93
Table 4-13	Log-triangular values for dispersion parameter CZSIGA for each stability class. ....	4-95
Table 4-14	MACCS uncertain parameters – evacuation delay. ....	4-101
Table 4-15	MACCS uncertain parameters – evacuation speeds. ....	4-104
Table 4-16	Rain bins and wind speed and stability class bins. ....	4-111
Table 4-17	MACCS correlated parameters. ....	4-114
Table 5-1	Values used for or associated with UA uncertain parameters in the base calculation. ....	5-1
Table 5-2	Key event timing in the base UA calculation. ....	5-3
Table 6-1	MELCOR regression analyses completed. ....	6-2
Table 6-2	Post-calculated regression parameters. ....	6-2
Table 6-3	Regression analysis of iodine release fraction. ....	6-9
Table 6-4	Regression analysis of cesium release fraction. ....	6-24
Table 6-5	Regression analysis of hydrogen production. ....	6-36
Table 6-6	Regression analysis of release timing for non-SGTRs. ....	6-46
Table 6-7	Regression analysis of release timing for all realizations. ....	6-46
Table 6-8	Regression analysis of iodine release fraction for SGTRs. ....	6-55
Table 6-9	Regression analysis of cesium release fraction for SGTRs. ....	6-56
Table 6-10	Select individual realization uncertain parameter values. ....	6-68

Table 6-11	Select individual realization timing of key events, key occurrences/attributes, Cs and I releases and in-vessel H <sub>2</sub> production.....6-69
Table 6-12	Select individual realization timing of key events, key occurrences/attributes, Cs and I releases and in-vessel H <sub>2</sub> production.....6-70
Table 6-13	Comparison of boiler-side aerosol deposition in a steam generator in the event of an SGTR high or low in the tube bundle. ....6-78
Table 6-14	Cs release via containment leakage and containment bypass in RLZs 495 and 562. ....6-78
Table 6-15	72 hour individual cases.....6-82
Table 6-16	Sensitivity on concrete type and rebar file names.....6-106
Table 6-17	MACCS regression analyses completed by spatial intervals and dose threshold. ....6-118
Table 6-18	Mean, individual LCF risk using LNT dose response, conditional on an STSBO occurring for five circular areas centered on Surry site. ....6-119
Table 6-19	Mean, individual LCF risk using LNT dose response, conditional on an STSBO occurring for four annular areas centered on Surry site. ....6-119
Table 6-20	Mean, individual LCF risk using US annual background dose truncation, conditional on an STSBO accident for five circular areas centered on the Surry site.....6-122
Table 6-21	Mean, individual LCF risk using US annual background dose truncation, conditional on an STSBO accident for four annular areas centered on the Surry site.....6-123
Table 6-22	Mean, individual LCF risk using HPS dose truncation, conditional on an STSBO accident occurring for five circular areas centered on the Surry site. ....6-125
Table 6-23	Mean, individual LCF risk using HPS dose truncation, conditional on an STSBO accident occurring for four annular areas centered on the Surry site. ....6-125
Table 6-24	Mean, individual, LCF risk regression results within a 10-mile circular area for all realizations based on LNT.....6-128
Table 6-25	Mean, individual, LCF risk regression results within a 10- to 20-mile annular area for all realizations based on LNT. ....6-129
Table 6-26	Mean, individual, LCF risk regression results within a 50-mile circular area for all realizations based on LNT.....6-129
Table 6-27	Mean, individual, LCF risk regression results within a 10-mile circular area for realizations with SGTR based on LNT. ....6-135
Table 6-28	Mean, individual, LCF risk regression results within a 10- to 20-mile annular area for realizations with SGTR based on LNT.....6-136
Table 6-29	Mean, individual, LCF risk regression results within a 50-mile circular area for realizations with SGTR based on LNT.....6-136
Table 6-30	Mean, individual, LCF risk (based on LNT) regression results within a 10-mile circular area for realizations that do not involve SGTR.....6-141
Table 6-31	Mean, individual, LCF risk (based on LNT) regression results within a 10- to 20-mile annular area for realizations that do not involve SGTR.....6-142
Table 6-32	Mean, individual, LCF risk (based on LNT) regression results within a 50-mile circular area for realizations that do not involve SGTR.....6-142
Table 6-33	Mean, individual, LCF risk regression results within a 10-mile circular area for all realizations (US background dose-response model).....6-146
Table 6-34	Mean, individual, LCF risk regression results within a 10- to 20-mile annular area for all realizations (US background dose-response model). ....6-147
Table 6-35	Mean, individual, LCF risk regression results within a 50-mile circular area for all realizations (US background dose-response model).....6-147

Table 6-36	Mean, individual, LCF risk regression results within a 10-mile circular area for all realizations (HPS dose-response model). ....6-148
Table 6-37	Mean, individual, LCF risk regression results within a 10- to 20-mile annular area for all realizations (HPS dose-response model). ....6-148
Table 6-38	Mean, individual, LCF risk regression results within a 50-mile circular area for all realizations (HPS dose-response model). ....6-149
Table 6-39	Mean, individual, LCF risk regression results within a 10-mile circular area for realizations with SGTR (US background dose-response model). ....6-150
Table 6-40	Mean, individual, LCF risk regression results within a 10- to 20-mile annular area for realizations with SGTR (US background dose-response model). ..6-150
Table 6-41	Mean, individual, LCF risk regression results within a 50-mile circular area for realizations with SGTR (US background dose-response model). ....6-151
Table 6-42	Mean, individual, LCF risk regression results within a 10-mile circular area for realizations with SGTR (HPS dose-response model). ....6-151
Table 6-43	Mean, individual, LCF risk regression results within a 10- to 20-mile annular area for realizations with SGTR (HPS dose-response model). ....6-152
Table 6-44	Mean, individual, LCF risk regression results within a 50-mile circular area for realizations with SGTR (HPS dose-response model). ....6-152
Table 6-45	Mean, individual, LCF risk regression results within a 10-mile circular area for realizations without SGTR (US background dose-response model). ....6-153
Table 6-46	Mean, individual, LCF risk regression results within a 10- to 20-mile annular area for realizations without SGTR (US background dose-response model). ...6-154
Table 6-47	Mean, individual, LCF risk regression results within a 50-mile circular area for realizations without SGTR (US background dose-response model). ....6-154
Table 6-48	Mean, individual, LCF risk regression results within a 10-mile circular area for realizations without SGTR (HPS dose-response model). ....6-155
Table 6-49	Mean, individual, LCF risk regression results within a 10- to 20-mile annular area for realizations without SGTR (HPS dose-response model). ....6-155
Table 6-50	Mean, individual, LCF risk regression results within a 50-mile circular area for realizations without SGTR (HPS dose-response model). ....6-156



## EXECUTIVE SUMMARY

The evaluation of accident phenomena and the offsite consequences of severe reactor accidents has been the subject of considerable research by the NRC over the last several decades. As a result of this research, capability exists to conduct more detailed, integrated, and realistic analyses of severe accidents at nuclear power reactors. A desire to leverage this capability to address conservative aspects of previous reactor accident analyses was a major motivating factor in the State of the Art Reactor Consequence Analyses (SOARCA) project. Through the application of modern analysis tools and techniques, the SOARCA project [1] developed a body of knowledge regarding the realistic outcomes of severe reactor accidents with best estimate analyses of selected accident scenarios at the Peach Bottom Atomic Power Station (Peach Bottom) and the Surry Power Station (Surry). The SOARCA project continued with an integrated uncertainty analysis (UA) of the unmitigated long term station blackout (LTSBO) at Peach Bottom [2] and the Surry integrated UA presented herein.

The SOARCA project [1] analyzed selected scenarios, first assuming the events proceeded without the 10 CFR 50.54(hh) mitigation measures (unmitigated), and then assuming that the 10 CFR 50.54(hh) mitigation measures were successful (mitigated). While these analyses have generally met the SOARCA project objectives, certain additional severe accident consequence analyses were warranted to expand upon the body of knowledge developed in SOARCA and to support and inform other NRC activities including the Site Level 3 Probabilistic Risk Assessment (PRA) project and Fukushima lessons learned. These additional analyses are discussed in SECY-12-0092, "State-of-the-Art Reactor Consequence Analyses – Recommendation for Limited Additional Analysis," [4], where staff recommended performing a UA for a severe accident scenario at Surry, the insights from which would inform the Site Level 3 PRA. The Commission's Staff Requirements Memorandum on SECY-12-0092 further noted that the ongoing SOARCA studies should support post-Fukushima activities including Tier 3 items [4].

In 2013, an integrated UA was completed on the unmitigated LTSBO for Peach Bottom [2]. The Peach Bottom study provided a quantitative analysis of the robustness of the deterministic calculation, and in the process, demonstrated the feasibility of producing integrated uncertainty results. The ability to implement an integrated UA permitted consideration of epistemic uncertainty in parameters, and to some degree aleatory uncertainty, across accident progression, release, and consequence modeling domains. The uncertainty aspect included sampling severe accident model parameters over defined distributions and performing regression analyses to identify the importance of the input parameters with regard to the uncertainty of the results. The Peach Bottom UA results are informative, but were conducted for the unmitigated LTSBO for a boiling water reactor (BWR). As with the Surry UA presented herein, the application of the results must be tempered with an understanding of the reactor type, accident scenario for which results were produced, and site specific characteristics.

The Surry UA followed the approach developed for the Peach Bottom UA. Lessons learned from the Peach Bottom UA and feedback from the NRC's Advisory Committee on Reactor Safeguards (ACRS) on the Peach Bottom UA were considered, as well as additional knowledge gained since the Surry best estimate calculation [3]. One of the original objectives of the Surry UA was to quantify the robustness of the Surry best estimate unmitigated short term station blackout (STSBO) analysis [3]. However, since the completion of the Surry SOARCA study [3], there have been many enhancements and updates to the state of the art in modeling severe accidents applied in that study. Changes to the severe accident and consequence codes reduce the benefit of the initial objective of directly quantifying the robustness of the original

analysis. Nonetheless, this UA provided a comparison of the results of the Surry best estimate analysis [3] with the current, more advanced, severe accident modeling systems applied in an uncertain framework. Additional objectives included:

- Determining whether the Surry UA results corroborate the general conclusions and insights from the original SOARCA best estimate study.
- Developing insights into the overall sensitivity of results to uncertainty in selected modeling inputs.
- Identifying the most influential input parameters contributing to accident progression and offsite consequences through application of an uncertainty analysis methodology.
- Informing the NRC's Site Level 3 PRA and post-Fukushima activities including Tier 3 items.

Figures of merit were selected to support the analysis and investigation of results. The source term (MELCOR) figures of merit were the environmental release fractions of cesium and iodine, in-vessel hydrogen production, and release timing. The consequence (MACCS) figures of merit were latent-cancer fatality (LCF) risk and early fatality risk at specified distances.

The Surry SOARCA unmitigated STSBO was selected as the accident scenario in part because of the importance of station blackout scenarios and in part because accident progression occurs relatively quickly under the postulated conditions. The relatively quick accident progression provides a basis to assess the effect of offsite response parameters while the release is potentially underway. Of the scenarios selected for Surry in the SOARCA best estimate study, the unmitigated STSBO with induced SGTR was also one of the two scenarios with the highest conditional individual LCF risk [1].

To meet the objective of developing insights into the overall sensitivity of SOARCA results to uncertainty in selected modeling inputs, a reasonable number of modeling inputs important to the figures of merit being assessed were chosen (See Section 4.1 and 4.2 for detailed parameter descriptions; the project scope did not include model uncertainty). Many parameters are basic input, such as core inventory, material properties, sizes and lengths of piping, weather files, etc. Selecting parameters was an iterative process to identify those expected to influence the results.

As developed, most of the parameters characterized epistemic uncertainty and a few characterized aleatory uncertainty. Often the mode (most likely value) of the distribution corresponded to the best estimate value used in the original analysis. In an effort to represent a state of the art study, when additional or new knowledge was available, the information was considered, and this resulted in the mode of some parameters being different than the SOARCA best estimate value [3]. Section 5 documents the MELCOR updated "best-estimate" values for some of the parameters.

MELCOR, MeIMACCS, and the MELCOR Accident Consequence Code System (MACCS) are the three primary codes used in the integrated analysis. These codes are continually enhanced, updated, and maintained as part of the NRC research program making it difficult to perform a direct comparison of the Surry UA results with the Surry NUREG/CR 7110 Volume 2 results. A comparison of the MELCOR 1.8.6 model of Surry and the MELCOR 2.1 model was conducted

and is presented in Appendix A. With the improvements in the Surry model and in the current state of knowledge since the original SOARCA modeling, it was determined that additional selected model enhancements should be added to advance the analysis to improve areas where enhancements would benefit the analysis. A baseline MELCOR calculation (base case) was then performed of the Surry unmitigated STSBO scenario. A few insights from the base case calculation include:

- An over-cycling fail to close (FTC) of the lowest set-point safety valve (SV) on the pressurizer occurred.
- A hot leg nozzle rupture occurred.
- Energetic hydrogen deflagrations occurred in containment.
- Containment design pressure and the pressure associated with liner yield were both exceeded.
- Releases to the environment of iodine and cesium at 48 hours were small, 0.073 percent and 0.029 percent of the inventory at scram, respectively, both well below the original SOARCA source term [1].

After completion of the updated base case, a high performance computing cluster was used to execute a Monte Carlo simulation with 1200 MELCOR runs, of which 1003 successfully completed the 48 hour analysis time<sup>12</sup>. Each MELCOR run was identified with a unique realization number. In the 1003 successful calculations (i.e., realizations):

- A steam generator tube rupture (SGTR) occurred in 104 realizations (10% of realizations), and a hot leg nozzle rupture occurred in 930 realizations;
- In every realization that an SGTR occurred, a hot leg nozzle rupture also occurred;
- A failure of one or more reactor coolant system (RCS) secondary side safety valves to close occurred in 954 realizations (95% of realizations), and an SV on the RCS primary side (on the pressurizer) failed to close in 686 realizations (68% of realizations);
- The steel containment liner yielded and tore in 742 realizations (74% of realizations); and
- Containment rebar yielded (and the concrete fractured) in 72 realizations (7% of realizations).

The uncertainty analyses produced sets of time-dependent results (e.g., horsetail plots) which were used in the analysis. Figure ES-1, shows the horsetails for Cs release over the 48 hour analysis period. A wide spread is observed between the calculated mean, median, and 95<sup>th</sup> percentile curves. The 95<sup>th</sup> percentile falls in the SGTR realizations (those in the upper portion of Figure ES-1), the median in the non-SGTR realizations, while the mean is in between where

---

<sup>1</sup> MELCOR runs typically fail due to convergence or timestep errors, most commonly in the COR package.

<sup>2</sup> 48 hours was the run time for the batch calculations. A set of realizations was further analyzed to 72 hours and is documented as a sensitivity study in this report.

no actual realizations exist. There is a significant time difference between the mean and median, with the median releasing much later in time. This is due to how the mean and median are calculated. Because the SGTR releases are about two orders of magnitude higher than the other runs, they disproportionately influence the mean, which is not representative of any specific realization. Meanwhile, the median takes the middle realization at each time, and is representative of a non-SGTR at all times although not necessarily the same realization at all times. The calculated 5th percentile curve has an associated initial release time that is much later than the calculated median curve, and the 5th percentile remains under 0.01 percent at 48 hours. The figure shows all four calculated curves are relatively steady by 20 hours, but the median and 5th percentile start increasing again around 40 hours, primarily due to containment liner failure, and in a few cases, rebar failure, both of which are driven more by pressure increase of steam in containment due to decay heat, rather than creation of additional non-condensable gases. The 95th percentile has no observable late increase, because it represents an SGTR (containment bypass). The mean is primarily influenced by the SGTR realizations and also does not exhibit a late increase.

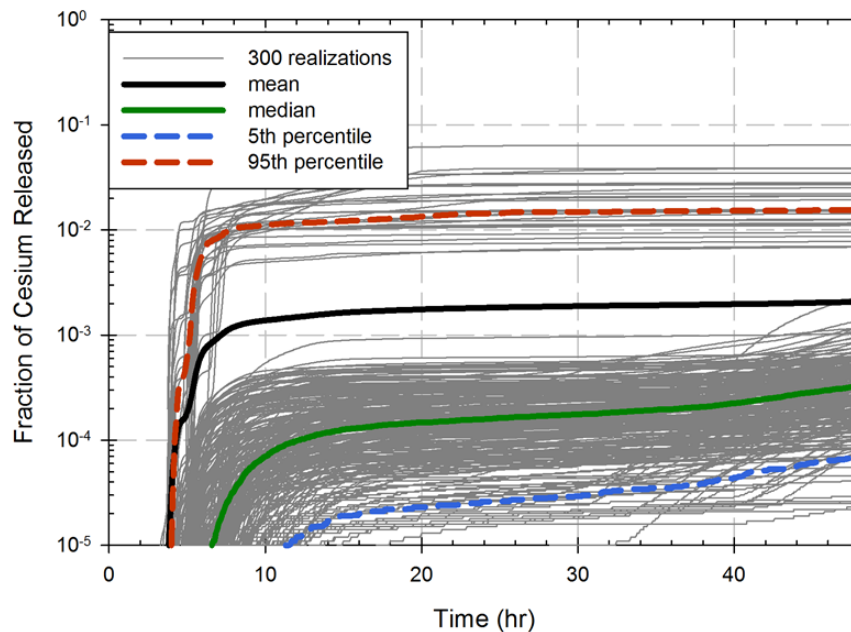


**Figure ES-1 Cesium release fractions over 48 hours with mean, median, 5<sup>th</sup> and 95<sup>th</sup> percentiles**

Additional insights related to accident progression were obtained through investigation of selected single realizations to identify phenomena affecting the Cs and I releases to the environment and in-vessel hydrogen production. Key phenomena identified in the MELCOR single realization analysis include:

- Containment building rebar yielding and resulting concrete fracture,
- Importance in the timing of the pressure relief tank (PRT) dryout – if the PRT fails early, there was no problem, but if it failed late, (near containment failure) it was very important,

- The number of successful cycles experienced by the system of 3 parallel SVs serving the primary-side of the RCS, and
- Chemisorption of Cs from CsOH into the stainless steel of reactor pressure vessel (RPV) internals.

There were 104 SGTRs observed in the results, corresponding to a tube rupture in about 10 percent of the realizations. Even though only 10 percent of realizations had SGTRs, with the exception of in-vessel hydrogen production, these SGTR realizations dominated the regression<sup>3</sup> results. Therefore, regression analyses listed in Table ES-1, were performed on the full set of realizations, the set of realizations that experienced an SGTR, and the set that did not experience an SGTR, to gain an understanding of influential parameters for non-SGTR STSBO scenarios.

**Table ES-1 MELCOR regression analyses completed.**

Output Parameter												
Data set used based on occurrence of SGTR												
Cycle	Cs frac			I frac			H2 Prod			Release Timing		
	SGTR	Non-SGTR	Both	SGTR	Non-SGTR	Both	SGTR	Non-SGTR	Both	SGTR	Non-SGTR	Both
All	✓	✓	✓	✓	✓	✓	✓	✓	✓		✓	✓
BOC		✓	✓		✓	✓		✓	✓			
MOC		✓	✓		✓	✓		✓	✓			
EOC		✓	✓		✓	✓		✓	✓			

For the full set of realizations and the non-SGTR set, regression analyses were performed for beginning of cycle (BOC), middle of cycle (MOC), and end of cycle (EOC) to understand the extent to which time at cycle (e.g., burnup) influenced non-SGTR realizations and whether any parameters would have raised importance with time at cycle kept constant. This was accomplished by including an uncertain parameter named CYCLE, which identifies the point during the fuel cycle (BOC, MOC, and EOC) at which the accident occurs. This sampled parameter directly affects the MELCOR source term calculation through decay heat, and it directly affects the MACCS consequence analysis through fission product inventory. Of all the sampled parameters, CYCLE is the only one that has such a dual status. Because fission product inventories in the fuel increase with burnup, this parameter can have a significant influence on risk. The inventories of shorter lived isotopes increase with burnup only until secular equilibrium is established; however, the inventories of longer lived isotopes, like Cs-137, can nearly double from BOC to EOC. Because the longer lived isotopes have a significant effect on LCF risk, especially in the long-term phase, this parameter is significant to the predicted results. The correlation between CYCLE and predicted risk is positive, (i.e., greater burnup relates to increased risk).

The regression analysis were performed for results obtained at the end of the 48 hour analysis period, and it should be recognized that results could be different if results were evaluated at an

<sup>3</sup> Regression analyses are used to determine which inputs, amongst those that are uncertain, are driving the output uncertainty.

earlier or later time in the calculation. Results from each regression technique for the individual contribution of a parameter and the conjoint influence<sup>4</sup> of a parameter on the results are provided. Overall influence of a parameter is reported as an average of the influence suggested by the four regression techniques.

Almost all of the MELCOR realizations showed the iodine and cesium environmental release fractions were significantly lower than their respective Surry SOARCA calculation [3], except for a few non-SGTR realizations where cesium was equal or greater. The lower release fractions were driven primarily by slower containment pressurization, caused by a number of factors including sampling of time at cycle which impacts the total decay heat, and a modification to the containment failure model that incorporates a more realistic yield-before-rupture model.

As seen in Figure ES-1, there is a large split between SGTR and non-SGTR runs, where SGTR runs had one to two orders of magnitude higher release fractions. This is different than the original SOARCA analysis, primarily caused by a new model for secondary decontamination factors and a variation of the time between the SGTR and hot leg creep. The most influential parameters contributing to cesium and iodine environmental release fractions for non-SGTR (the majority of releases) are time at cycle (e.g., burnup), nominal leakage, the containment failure curve, and dynamic shape factor. The first three influence containment pressurization rates and determine the open area from the containment to the environment, while dynamic shape factor influences agglomeration and deposition rates for aerosols before release. The time at cycle parameter is specific to Surry and very well understood, while nominal leakage and the dynamic shape factor are based on technical specifications and well understood experimental results, respectively. There is slightly lower confidence in the containment failure curve (CFC) model, based on difficulties scaling from the 1/6<sup>th</sup> scale tests from which the model was created, but the yield-before-rupture behavior was confirmed as more realistic by structural experts. Important for iodine release fractions but not cesium was the fraction of gaseous iodine, because it does not deposit on structures but remains airborne. Thus, it is released in much higher percentages than aerosolized CsI. The two parameters that determine the amount of gaseous iodine, time at cycle and chemical form of iodine (ChemformI2), are both identified as significant main contributors by the regression analyses. For BOC analyses, design leakage becomes the most important parameter contributing to iodine and cesium release because containment liner yield is never reached and leakage is the only release path to the environment.

The calculated mean and median of the in-vessel hydrogen production distribution at 48 hours were similar in magnitude to the Surry SOARCA calculation [3]. Regression results for hydrogen generation uncertainty were essentially the same with and without an SGTR, because this is an in-vessel effect. The most important parameters early in hydrogen production were those related to primary system depressurization, impacting steam generation and flow, followed by time at cycle. The magnitude of the total hydrogen generation within 48 hours was driven by effective fuel melt temperature and the time at cycle, both of which determine the amount of time the fuel remains in place before relocation, which suppresses the oxidation process. There were no significant differences in regression results for the time at cycle independent analyses.

For release timing, the metric evaluated was release of 1 percent of noble gas to the environment. It was observed that 18 percent of non-SGTR realizations do not release 1 percent of noble gases by 48 hours. Investigation of the release timing identified a large timing

---

<sup>4</sup> Conjoint influence is the influence of two or more input parameters acting together, which may have synergistic effects that would not be uncovered by studying the influence of each parameter separately and individually.

difference between SGTR and non-SGTR realizations, with non-SGTR realizations meeting the environmental release timing metric about 20 to 40 hours later, if they meet the criteria at all. In the original SOARCA analysis the timing difference was about 25 hours, at the lower end of this range. Since almost all noble gases enter containment quickly after core damage, this may indicate that the flow area to the environment for SGTRs is larger than design leakage. This was tested through one-off calculations and results show that flow rates to environment through the secondary side (combination of MSIV leakage and a stuck open secondary SV) are approximately three orders of magnitude greater than nominal leakage, regardless of any uncertainty sampling. However, since only 10 percent of runs have SGTRs, and because the majority of realizations do not reach rebar failure, design leakage is the highest contributor to release timing uncertainty in regression results for all realizations and for non-SGTR realizations.

The two parameters that show the highest importance in determining whether an SGTR occurs are TUBTHICK, which represents the initial tube thickness of the most damaged steam generator tube in the hottest region, and SVOAFRAC, which represents the fraction of the full open area of a primary or secondary safety relief valve at the time it fails. Both of these parameters have physical bounds, providing high confidence in their uncertainty ranges. The TUBTHICK parameter directly affects the initial damage state (and effective stress multiplier for creep) of one of the steam generator tubes. The SVOAFRAC parameter influences the depressurization of the RCS after SV failure to close, and thus controls the pressure differential across the damaged steam generator tube. Testing of SGTR realizations, through one-off calculations showed that a pressure differential of 1000 psi or more was needed during core damage to induce the SGTR. The magnitude of releases for an SGTR is primarily driven by the time between the SGTR and hot leg creep rupture, because before hot leg rupture, the SGTR is the primary transport path for radionuclides released from the fuel. The average time difference in these realizations was 28 minutes.

Containment pressure was generally observed to increase from 48 to 72 hours, unless the rebar yield point was reached. This was further investigated by selecting a subset of the single realizations and extending the runs to 72 hours. In the cases where rebar yield was reached, the pressure levels off (to a plateau) and then gradually begins to decrease as the leakage more than compensates for steam generation and heating of the atmosphere. There are marked increases in cesium and iodine environmental release at the point of liner yield, with some increases of an order of magnitude from 48 to 72 hours. Such increases did not occur with rebar yield only. There appear to be no realizations that could ablate through all available concrete by 72 hours, nor are there any BOC realizations that will reach liner yield by 72 hours.

The MACCS results were generated for linear no-threshold (LNT) and two linear with-threshold models (called dose truncation here), referred to as US background and Health Physics Society (HPS) truncation models. The dose truncations (thresholds) are described as: (1) annual dose truncation based on average background plus medical radiation, which is 620 mrem/yr and (2) dose truncation based on the HPS position statement, which states that “the Health Physics Society recommends against quantitative estimation of health risks below an individual dose of 5 rem in one year or a lifetime dose of 10 rem above that received from natural sources.”

Like the original SOARCA study, the Surry UA demonstrates that early fatality risks are negligible, essentially zero. LCF risks are even lower than those evaluated in the original SOARCA study. Table ES-2 shows that the mean LCF risks from this uncertainty analysis, conditional on the occurrence of a STSBO scenario, are below  $3 \times 10^{-5}$ , within 10 miles of the site and the risk diminishes at longer distances. This mean value includes the 10 percent of the

realizations with induced SGTRs. For comparison, these values are about a factor of three lower than the SOARCA unmitigated STSBO risks (excluding occurrence of SGTRs) at the same distance ranges (cf., Table 7-4 in [3]). Furthermore, even the 95<sup>th</sup> percentile LCF risks from this UA are about a factor of two lower than the mean risks for the unmitigated SOARCA STSBO with induced SGTR (cf., Table 7-6 in [3]). This is a meaningful comparison because the top 10 percentile results from this UA represent SGTR realizations; thus, the 95<sup>th</sup> percentile is approximately the median result for the subset of SGTR realizations.

**Table ES-2 Mean, individual LCF risks using LNT dose response, conditional on Surry unmitigated STSBO occurring (per event) at different radial distances.**

	0-10 miles	10-20 miles	0-50 miles
UA Mean	2.8E-05	1.1E-05	5.3E-06
UA Median	6.3E-06	1.8E-06	8.9E-07
UA 5 <sup>th</sup> percentile	6.9E-07	2.2E-07	1.0E-07
UA 95 <sup>th</sup> percentile	1.7E-04	7.2E-05	3.5E-05
SOARCA estimate, STSBO	9.4E-05	N/A	1.5E-05
SOARCA estimate, STSBO with SGTR	3.2E-04	N/A	6.5E-05

Table ES-3 provides the regression results for the LNT dose-response for the complete set of regression runs (SGTR and non-SGTR). The top two parameters, TUBTHICK and SVOAFRAC, have an important influence on magnitude and timing of the release and directly influence the evaluation of LCF risk. Both parameters have large values for individual (main) and conjoint contributions. The large conjoint contributions and the lack of significant conjoint influence for the other parameters indicate that the two parameters work together to affect source term. Both parameters are negatively correlated with risk, which indicates that the magnitude of the source term increases as SGT thickness and the open area fraction of a stuck-open safety valve decrease. This combination of parameters makes a SGTR more likely to occur. Additional parameters that significantly increase consequences are time during cycle (fuel burnup, CYCLE), groundshine shielding factor (GSHFAC.2)<sup>5</sup>, a parameter controlling leakage from containment (DLEAK), and the cancer fatality risk factor for residual cancers (CFRISK.8)<sup>6</sup>, which is the largest single cancer type that contributes to cancer risk.

---

<sup>5</sup> GSHFAC.2 represents the groundshine shielding factor for normal activity. Numbers 1, 2, and 3 are used to represent evacuation, normal activity, and sheltering conditions for GSHFAC.

<sup>6</sup> CFRISK.8 represents residual cancer risk, which accounts for all cancers that are not explicitly modeled. Residual cancers are based on doses to the pancreas, which is a surrogate organ to represent generic soft tissues.

**Table ES-3 Mean, individual, LCF risk (LNT dose response) regression results within a 10-mile circular area for all realizations.**

	Rank Regression		Quadratic		Recursive Partitioning		MARS		Main Contr.*	Conjoint Contr. *
Final R <sup>2</sup>	0.54		0.60		0.86		0.74			
Input	R <sup>2</sup> contr.	SRRC	S <sub>i</sub>	T <sub>i</sub>	S <sub>i</sub>	T <sub>i</sub>	S <sub>i</sub>	T <sub>i</sub>		
TUBTHICK	0.04	-0.20	0.33	0.53	0.30	0.86	0.35	0.80	0.189	0.309
SVOAFRAC	0.03	-0.18	0.23	0.40	0.09	0.55	0.11	0.45	0.082	0.250
CYCLE	0.18	0.44	0.01	0.02	0.01	0.01	0.02	0.02	0.050	0.005
GSHFAC.2	0.13	0.35	0.02	0.05	0.00	0.00	0.01	0.03	0.038	0.011
DLEAK	0.08	0.26	0.01	0.04	0.01	0.01	0.00	0.01	0.022	0.010
CFRISK.8	0.02	0.15	0.02	0.05	0.00	0.06	0.02	0.08	0.011	0.037
SV_STATUS	---	---	0.04	0.04	---	---	---	---	0.006	0.000
DDREFA.8	0.01	-0.12	0.00	0.02	0.00	0.05	0.00	0.03	0.004	0.025
CYSIGA.1	0.02	-0.13	---	---	---	---	---	---	0.004	0.000
TUBETEMP	---	---	0.02	0.02	0.00	0.00	0.01	0.03	0.004	0.006
DEV_DEC_HEAT	0.01	-0.09	0.00	0.03	0.00	0.03	0.01	0.02	0.004	0.015
VDEPOS.1	0.01	0.09	0.01	0.01	0.00	0.04	---	---	0.003	0.011
CFRISK.7	0.01	0.09	---	---	---	---	---	---	0.002	0.000
CFC	0.01	-0.09	---	---	---	---	0.00	0.01	0.002	0.001
CFRISK.6	0.01	0.07	---	---	---	---	0.00	0.02	0.002	0.003
PROTIN.2	---	---	---	---	0.01	0.09	---	---	0.001	0.023
CHEMFORMCS	0.01	-0.06	---	---	---	---	---	---	0.001	0.000
SGTRLOC	0.00	0.06	0.00	0.01	---	---	---	---	0.001	0.002
CFRISK.2	---	---	0.00	0.03	---	---	---	---	0.001	0.005
LA.140_IJH.9	---	---	0.00	0.04	0.00	0.03	0.00	0.01	0.000	0.018
PARTSHAPE	---	---	0.00	0.01	0.00	0.01	---	---	0.000	0.004
CHEMFORMI2	---	---	---	---	0.00	0.02	0.00	0.01	0.000	0.009

\* highlighted if main contribution larger than 0.02 or conjoint contribution larger than 0.1

All consequence results are presented as conditional risks, which are the risks conditional on the accident occurring. The emergency phase used in this analysis is the first seven days following the beginning of release to the environment. The long-term phase immediately follows the emergency phase and lasts for 50 years. Results for the LNT dose-response show the large majority of the LCF risk is from the long-term phase at all five distance intervals evaluated, even for the realizations with SGTR. The mean values of the fraction of risk from the emergency phase are 1 percent within 10 miles and about 15 percent at distances beyond 10 miles. Only a handful of realizations have emergency-phase contributions to risk that exceed those from the long-term phase.

The results for the distance from 0 to 10 miles have a very different character than those for the other distance ranges, because evacuation is very effective in reducing risk during the emergency phase for the population living within the emergency planning zone (EPZ). Most of the overall risk within 10 miles is to the 0.5 percent of the public that is assumed to not evacuate; however, some of the risk is to the slowly evacuating cohorts for the realizations with relatively early releases, mainly the realizations with SGTR.

A set of sensitivity analyses was also completed with this project. Some of the sensitivities were performed to support parameter development and more detailed sensitivities were performed to better understand the contributions of individual uncertain inputs to the uncertainty in analysis results. The following MELCOR sensitivity analyses were performed to provide targeted insights into the results of the analysis.

### **Sensitivity analysis on concrete type**

The Surry SOARCA analyses [1][3] used limestone aggregate in the calculation, which was the aggregate identified in the reference Modular Accident Analysis Program (MAAP) file. However, during the investigations into this UA, it was discovered that Surry actually has a basaltic aggregate. A sensitivity analysis was conducted to understand the effects of the different concrete types. The basaltic concrete produced a more vigorous molten core-concrete interaction (MCCI) than the limestone concrete; however, the limestone concrete showed approximately 30 percent greater release of non-condensable gases (NCGs). There was little difference in containment pressure and temperature between the calculations even though the mass of gas generated by core concrete interaction varied by approximately 30 percent. The key observation was that most pressure in containment is attributable to the partial pressure of steam. The partial pressures of NCGs generated by MCCI do not contribute much to the overall pressure. The environmental release fraction from limestone concrete for cesium and iodine was found to be greater (~25% and ~50%, respectively) than from basaltic concrete at the end of the 48 hour simulation. This was attributed to the increased containment pressurization in the limestone concrete analysis which reached liner yield (i.e., functional failure of containment) at approximately 36.5 hours, compared to the basaltic concrete analysis which reached liner yield at approximately 41 hours.

### **Sensitivity analysis on rebar mass**

The Surry SOARCA analyses [1][3] used a value of 17 percent by mass of rebar in containment. This sensitivity analysis was developed after discussions with the Level 3 PRA team revealed their analysis used a lower percent of rebar. This sensitivity considered two extremes for rebar including zero percent and 30% (approximately double the base case) rebar by mass within the concrete. Although zero percent would never be expected, analyzing zero percent supported quantification of the effect of the rebar. The results showed hydrogen deflagrations have a strong correlation between the amount of rebar within the concrete and the length of the deflagration.

### **Joint sensitivity analysis on number of steam generator tubes ruptured**

A joint sensitivity analysis was conducted with sampling performed on number of tubes, primary and secondary SV open fraction, and SGTR location to determine the effect of more than one SG tube failing on cesium and iodine environmental release fractions. Releases for one tube were slightly higher than the SGTR realizations observed in the full UA. There were step increases in release fractions for the failure of two and three tubes, but no significant difference from three to five tubes. This indicates that when three or more tubes fail, flow to environment is limited by main steam isolation valve (MSIV) leakage and the stuck open secondary SV, and not by the flow through the SG tubes. Another key result is that releases from one tube increase more gradually while three to five tubes has more of a quick puff release. The number of tubes parameter dominated results, with none of the other three sampled parameters having a significant additional impact. A large factor in the total release fractions is the time of hot leg creep relative to the SGTR. This timing is primarily due to depressurization rate, based on the number of tubes failing and exacerbated by the primary SV open fraction. Out of 97 Monte Carlo realizations in this joint sensitivity, one had sampled five tubes failing and had no hot leg creep within the 48 hour simulation time leading to the highest release fractions.

### **MACCS sensitivity analyses**

Four MACCS sensitivity analyses were conducted using one of the larger source terms from MELCOR. The sensitivities evaluated emergency phase durations of 15 and 30 days, intermediate phase duration of 6 months, and a 4-day dose projection period for the emergency phase. The results were all essentially the same with one exception, the risks for the 0- to 10-

mile distance interval was noticeably larger for the case when the intermediate phase is 6 months than when there was no intermediate phase. The increase in risk for the 0- to 10-mile interval indicates that less decontamination occurs when the intermediate phase is included and that more individuals receive a larger dose when they return home than receive a smaller dose. This can occur when the 6 months of decay and weathering provided by the intermediate phase brings the dose levels below the habitability threshold without the need to decontaminate. However, these dose levels can be higher than they would have been if decontamination were performed because the MACCS decontamination modeling reduces dose levels by pre-defined fixed factors of 3, or 15 if a reduction factor of 3 is insufficient to restore habitability.

The habitability criteria applied in these sensitivity analyses is considered to be an important uncertain parameter, but was not included with this Surry UA because a detailed sensitivity analysis was performed with the Peach Bottom UA [2]. The Peach Bottom analysis showed, as would be expected, that when the dose truncation models were used, the LCF risks within the EPZ were orders of magnitude lower when the habitability criteria was below the dose truncation level. Beyond the EPZ, the habitability criteria showed a smaller effect on the overall LCF risk when a dose truncation model was applied.

### **Summary**

As described above, this Surry UA modeled distributions for parameter values that historically were modeled with fixed values and applied multiple regression techniques to support an understanding of the results. Such an analysis produces substantial information which is described in detail in this document. A summary of important insights is provided below:

- SGTRs occurred in about 10 percent of the Monte Carlo realizations and had release fractions one to two orders of magnitude larger.
- SGTRs always included both a thermal and pressure element.
- In the number of SG tubes joint sensitivity analysis, one realization with 5 tubes failing had no hot leg creep leading to the highest release fractions.
- In most of the Monte Carlo realizations, iodine and cesium environmental release fractions were higher early in the transient than the Surry SOARCA calculation [3], but all were significantly lower at 48 hours, except that cesium was equal in a few realizations.
- Lower release fractions at 48 hours were primarily driven by time at cycle sampling, higher nominal containment leakage and changes to the containment failure model (gradually degrading containment versus sudden catastrophic failure). All of these lead to slower containment pressurization and the leak-before-break failure modeling prevents large amounts of revaporization.
- The LCF risk was observed lower than the Surry SOARCA calculation and is attributable to the lower source terms from the UA (again due to more realistic containment degradation modeling).
- The consequence analysis showed that the mean population-weighted LCF risk distribution is much narrower when only uncertain consequence parameters are considered than when both source-term and consequence parameters are considered in the analysis. It appears the results are more heavily influenced by uncertainties in

source term than by uncertain consequence parameters, just as they were for the Peach Bottom uncertainty analysis [2]. This is true when a single dose-response model (LNT) is used, but uncertainties in risks created by uncertainties in dose-response model are large and most likely would have altered this conclusion if dose response had been included as part of the integrated uncertainty analysis.

The most influential input parameters were identified with respect to the figures of merit.

- For early hydrogen production primary system depressurization followed by time at cycle, were most important, but the total magnitude of hydrogen was most influenced by the effective fuel melt temperature.
- For non-SGTR realizations (90% of the realizations), the most important parameters were time at cycle, design leakage, the containment failure curve, and the dynamic shape factor. For iodine, the amount that was assumed to be gaseous was very important, determined by time at cycle and chemical form of iodine.
- Primary SV open fraction and tube thickness were the main determinants regarding whether an SGTR occurred, and secondary SV open fraction had the highest importance in Cs and I release fractions for SGTR releases.
- For LCF risk, TUBTHICK and SVOAFRAC are the most influential parameters. These two parameters largely determine whether the accident progresses toward an SGTR. Thus, they have an important influence on magnitude and timing of the release and directly influence LCF risk.
- In addition to TUBTHICK and SVOAFRAC, three other parameters have a significant effect on LCF risk. These are time at cycle (fuel burnup), groundshine shielding factor, and design leakage from the containment. Time at cycle affects both the amount of decay heat in MELCOR and fission product inventory in MACCS. Both of these increase LCF risk as time at cycle increases. Decay heat quickly approaches steady state early in the fuel cycle while some influential fission products, like Cs-137, increase approximately linearly during the fuel cycle. Groundshine shielding factor directly influences dose through the groundshine pathway, which is the dominant dose pathway during the long-term phase. Finally, design leakage influences the release of radioactivity through the containment, which is especially important when a SGTR does not occur.
- The most important parameter in the Peach Bottom UA, dry deposition velocity, is not shown to be very important in the Surry UA. This may be because the distribution for dry deposition velocity was made narrower in the Surry UA or it may be because some other parameters are relatively more important, e.g., the parameters that influence the occurrence of SGTR. The rationale for the narrower distribution is that the one used in the Peach Bottom UA reflects variations from one weather instance to another, not variations in the best value to use for an entire year of weather data.

The project informed the Level 3 PRA by including staff in Surry parameter development meetings, presenting Level 3 PRA staff early Surry UA results, and interacting with Level 3 PRA staff on key issues of interest. In addition, like the Peach Bottom UA [2] did, the results of this Surry UA corroborate the conclusions from the SOARCA project [1]:

- Latent cancer and early fatality risks from severe nuclear accident scenarios modeled are smaller than those projected in NUREG/CR-2239.
- The delay in releases calculated provides more time for emergency response actions (such as evacuating or sheltering).
- “Essentially zero” absolute early fatality risk is projected.



## ACKNOWLEDGMENTS

Numerous NRC and Sandia National Laboratories (Sandia) managers and technical experts contributed to the production of this uncertainty analysis. The NRC manager, Pat Santiago and project manager, Jonathan Barr, provided the leadership to ensure this project met the objectives of the program and ensured sufficient resources were available. Tina Ghosh served as the NRC technical lead interacting directly with the Sandia team. Additional NRC staff provided technical insights supporting key elements of the document through parameter reviews, review of the analysis, and review of the integrated document. Sandia technical staff, including Doug Osborn, Matt Denmen, Aubrey Eckert, Dusty Brooks, and Jeff Cardoni, performed research in developing technical bases for parameters, enhanced the state of the MELCOR model, and advanced the regression techniques used in the analysis. Special acknowledgment is made for the support provided by dycoda, Inc., with Mr. KC Wagner supporting model development and analysis of results and Jon Helton for his support with the complex mathematics applied in the parameter development.



## ABBREVIATIONS AND ACRONYMS

AC	alternating current
ACRS	Advisory Committee on Reactor Safeguards
ANS	American Nuclear Society
ARP	Automatic Rapid Processing
ARTIST	Aerosol Trapping in a Steam Generator
atm	atmosphere
BEIR	Biological Effects of Ionizing Radiation
BOC	beginning of cycle
BWR	boiling water reactor
CCDF	complementary cumulative distribution function
CDF	cumulative distribution function
CEA	Atomic Energy and Alternative Energies Commission
CFC	containment fragility curve
CFRISK	cancer fatality risk
CRAC	Calculation of Reactor Accident Consequences
CV	control valve
DC	direct current
DCF	dose conversion factor
DDREFA	dose and dose rate effectiveness factor
DEGB	double-ended guillotine break
DF	decontamination factor
EAS	emergency alert system
ECCS	emergency core cooling systems
ECST	emergency condensate storage tank
EOC	end of cycle
EPA	Environmental Protection Agency
EPRI	Electric Power Research Institute
EPZ	emergency planning zone
ETE	evacuation time estimate
FGR	Federal Guidance Report
FP	flow path
FPT	fission product tests
FTC	failure to close
FTO	failure to open
gpm	gallons per minute
GSDE	ground shine deposited energy
Gy	gray
HPS	Health Physics Society
HTC	heat transfer coefficient
IPE	individual plant examination
LCF	latent cancer fatality
LET	linear energy transfer
LEU	low enriched uranium
LHS	Latin hypercube sampling
LNT	linear no threshold
LTSBO	long-term station blackout
LWR	light water reactor
m	meter

MAAP	Modular Accident Analysis Program
MACCS	MELCOR Accident Consequence Code System
MARS	Multivariate Adaptive Regression Splines
MCCI	molten core concrete interactions
MOC	middle of cycle
mph	miles per hour
MSIV	main steam isolation valve
MSL	main steam line
mSv	millisievert
NCG	non-condensable gas
Nu	Nusselt number
ORO	offsite response organization
PAG	protective action guide
PAR	protective action recommendation
PDF	probability density function
PRA	probabilistic risk assessment
PRT	pressure relief tank
PRY	per reactor year
PSV	pressurizer safety valve
PWR	pressurized water reactor
RCP	reactor coolant pump
RCS	reactor coolant system
RLZ	realization
ROP	reactor oversight program
RPV	reactor pressure vessel
RRC	rank regression coefficient
SAE	Site Area Emergency
SBO	station blackout
scfh	standard cubic feet per hour
SG	steam generator
SGTR	steam generator tube rupture
SME	subject matter expert
SNL	Sandia National Laboratories
SOARCA	State of the Art Reactor Consequence Analyses
SPAR	standardized plant analysis risk
SRRC	standardized rank regression coefficient
SRS	simple random sampling
SRV	safety relief valve
SSE	sum of square error
STSBO	short-term station blackout
SV	safety valve
SVV	code safety valve
TAF	top of active fuel
TDAFW	turbine driven auxiliary feedwater
TF	tabular function
UA	uncertainty analysis
USBGR	U.S. background

# 1. INTRODUCTION

The evaluation of accident phenomena and the offsite consequences of severe reactor accidents has been the subject of considerable research by the NRC over the last several decades. As a result of this research, capability exists to conduct more detailed, integrated, and realistic analyses of severe accidents at nuclear power reactors. A desire to leverage this capability to perform more realistic analyses to address conservative aspects of previous reactor accident analyses was a major motivating factor in the State of the Art Reactor Consequence Analyses (SOARCA) project. Objectives of SOARCA included: (1) evaluating the potential benefits of post-9/11 mitigation improvements, (2) updating the quantification of offsite consequences found in earlier NRC publications, such as the 1982 Siting Study, and (3) enabling the NRC to better communicate severe accident related aspects of nuclear safety to stakeholders, including federal, state, and local authorities, licensees, and the general public. Through the application of modern analysis tools and techniques, the SOARCA project [1] developed a body of knowledge regarding the realistic outcomes of severe reactor accidents of selected accident scenarios at the Peach Bottom Atomic Power Station (Peach Bottom) and the Surry Power Station (Surry). The SOARCA project continued with an integrated uncertainty analysis (UA) of the unmitigated long term station blackout (LTSBO) at Peach Bottom [2] and the Surry integrated UA of the unmitigated short term station blackout (STSBO) presented herein.

The SOARCA project [1] analyzed selected scenarios, first assuming the events proceeded without the 10 CFR 50.54(hh) mitigation measures (unmitigated), and then assuming that the 10 CFR 50.54(hh) mitigation is successful (mitigated). While these analyses have generally met the SOARCA project objectives, certain additional severe accident consequence analyses are warranted to expand upon the body of knowledge developed in SOARCA and to support and inform other agency activities including the Site Level 3 Probabilistic Risk Assessment (PRA) and Fukushima lessons learned projects. These additional analyses are discussed in SECY-12-0092, "State-of-the-Art Reactor Consequence Analyses – Recommendation for Limited Additional Analysis", dated July 5, 2012 [4], where staff recommended performing a UA for a severe accident scenario at Surry, the insights from which would inform the Site Level 3 PRA. The Commission's Staff Requirements Memorandum on SECY-12-0092 further noted that the ongoing SOARCA studies should support post-Fukushima activities including Tier 3 items [4].

MELCOR and the MELCOR Accident Consequence Code System (MACCS) are the NRC developed codes for analysis of severe accidents and their consequences. These codes were used in all of the SOARCA calculations. The SOARCA analyses show that successful implementation of existing mitigation measures can prevent reactor core damage or delay or reduce offsite releases of radioactive material [1]. All SOARCA scenarios [1], even when unmitigated, progress more slowly and release much less radioactive material than in earlier studies (e.g., NUREG/CR-2239, "Technical Guidance for Siting Criteria Development," commonly referred to as the 1982 Siting Study) [5]. The SOARCA analyses show that emergency response programs, implemented as planned and practiced, would reduce the scenario-specific risk of health consequences among the public during a severe reactor accident at the plants evaluated [1]. As a result, the calculated risks of public health consequences from severe accidents modeled in SOARCA are very small.

In 2013, an integrated UA was completed on the unmitigated LTSBO for Peach Bottom [1]. The Peach Bottom UA study provided a quantitative analysis of the robustness of the deterministic calculation, and in the process, demonstrated the feasibility of producing integrated uncertainty

results. The Peach Bottom UA results are informative; however, the analysis was conducted for the unmitigated LTSBO scenario for a boiling water reactor (BWR). As with the Surry UA presented herein, the application of the results must be tempered with the understanding of the reactor type, scenario for which results were produced, and site specific characteristics. This UA of the unmitigated STSBO at the Surry Power Station continues the SOARCA work.

The Surry UA followed the approach developed for the Peach Bottom UA. The unmitigated STSBO was selected as the accident scenario for the Surry UA, in part because of the importance of station blackout scenarios and because accident progression occurs relatively quickly under the postulated conditions, which provides opportunity to assess the offsite response parameters while the release is potentially underway. The unmitigated LTSBO had been analyzed in the Peach Bottom UA [2], which showed that battery life is important in delaying the start of releases. For the Surry UA, the short term variant on the station blackout (SBO) was selected to investigate a potentially earlier release and greater consequences. Of the scenarios selected for Surry in the SOARCA best estimate study, the unmitigated STSBO with induced SGTR was also one of the two scenarios with the highest conditional individual LCF risk [1]. As an unmitigated scenario, a few operator actions were considered to be attempted, but were not successful as described in Section 2.1. Lessons learned from the Peach Bottom UA and feedback from the NRC's Advisory Committee on Reactor Safeguards (ACRS) on the Peach Bottom UA were included, as well as additional knowledge gained since the publication of NUREG/CR 7110 Volume 2 [3] (also referred to as the original SOARCA or Surry SOARCA throughout this study).

Epistemic uncertainty was explored by randomly sampling distributions for selected parameters. In NUREG/CR 7110 Volume 2, the only uncertainty considered was that associated with weather conditions at the time of the accident. The reported offsite consequence values represented the mean value (arithmetic average) of a large number of aleatory weather trials. This best practice approach [6] to weather uncertainty was also applied for Surry.

A distribution was developed for each varied parameter with the intent of representing the degree of belief in the expected range. Often the mode (most likely value) of the distribution corresponded to the best estimate value used in the original analysis. Each of the probability distributions were applied in the respective MELCOR and MACCS models (e.g., the specific Surry model). For MELCOR, this often required enhancing the model to accept the distributions. When final runs were ready to be executed, the most current MELCOR and MACCS codes (the actual codes) available at the time were used. These changes to the codes made it very difficult to make a direct comparison of results to understand the precise robustness of the original SOARCA calculation; particularly for MELCOR, because MELCOR 1.8.6, used in the original SOARCA study, is no longer maintained. The MELCOR model progression and a comparison of the MELCOR 1.8.6 and 2.1 results are presented in Appendix A.

## **1.1 Background on SOARCA**

The NRC, the nuclear power industry, and the international nuclear energy research community have devoted considerable research over the last several decades to examining severe reactor accident phenomena and offsite consequences. These updated analyses incorporated the wealth of accumulated research and used more detailed, integrated, and best estimate modeling than past analyses. An insight gained from security assessments was that the NRC needed updated analyses of severe reactor accidents to reflect realistic estimates of the more

likely outcomes, considering the current state of plant design and operation and the advances in understanding of severe accident behavior [1].

The NRC initiated the SOARCA project to develop best estimates of the offsite radiological health consequences for potential severe reactor accidents for Peach Bottom and Surry. Peach Bottom is a U.S. operating reactor using the General Electric boiling-water reactor (BWR) design with a Mark I containment. Surry is a U.S. operating reactor using the Westinghouse pressurized-water reactor (PWR) design with a large, dry (subatmospheric) containment [1].

Preparations for SOARCA [1] included extensive cooperation from the licensees to develop high-fidelity plant system models, define operator actions including the most recently developed mitigation actions at the time, and develop models for simulation of site-specific and scenario-specific emergency response. In addition to input for model development, licensees provided information on accident scenarios from their PRAs. Through tabletop exercises of the selected scenarios with senior reactor operators, PRA analysts, and other licensee staff, licensees provided input on the timing and nature of the operator actions to mitigate the selected scenarios. The licensee input for each scenario was used to develop assumed timelines of operator actions and equipment configurations for implementing available mitigation measures which include mitigation measures beyond those routinely credited in current PRA models. A human reliability analysis was not performed for SOARCA, but instead tabletop exercises, plant walkdowns, simulator runs and other inputs from licensee staff were employed to ensure that operator actions and their timings were correctly modeled [1].

Updated and benchmarked standardized plant analysis risk (SPAR) models and available plant-specific external events information were used in the SOARCA scenario selection process [1]. Scenarios common to both Peach Bottom and Surry included the STSBO and LTSBO. Both types of SBOs involve a loss of all alternating current (AC) power. The STSBO also involves the loss of turbine-driven systems through loss of direct current (DC) control power or loss of the condensate storage tank and therefore proceeds to core damage more rapidly (hence “short term”). The STSBO has a lower core damage frequency than the LTSBO, since it requires a more severe initiating event and more extensive system failures. SOARCA [1] assumed that an SBO is initiated by a seismic event, since this is the most extreme case in terms of both the timing and amount of equipment that fails. SBO scenarios are commonly identified as important contributors in PRA because of the common cause of failure for both reactor safety systems and containment safety systems.

## **1.2 Objectives**

The overall objective of the SOARCA project was to develop a body of knowledge regarding realistic outcomes of severe reactor accidents. The SOARCA uncertainty analyses further expand this body of knowledge. The objectives of the Surry UA include:

1. Evaluate the robustness of the NUREG/CR 7110 Volume 2 SOARCA Surry deterministic results.
2. Determine whether the Surry UA results corroborate the general conclusions and insights from the original SOARCA best estimate study.
3. Develop insights into the overall sensitivity of SOARCA results to uncertainty in selected modeling inputs.

4. Identify the most influential input parameters contributing to accident progression and offsite consequences through application of an uncertainty analysis methodology.
5. Inform the NRC's Site Level 3 PRA and post-Fukushima activities including Tier 3 items.

With regard to informing the Level 3 PRA, this was accomplished by including NRC Level 3 PRA staff in Surry UA meetings, beginning early in the project. This continued through parameter development and as early results became available.

### **1.3 Scope**

The scope of the Surry UA was to produce a state of the art UA that achieves the objective of evaluating the robustness of the best estimate analysis and provides insights into the overall uncertainty of the best estimate results and conclusions. This required:

- Developing distributions for selected parameters;
- Implementing MELCOR model enhancements to accommodate the distributions;
- Implementing additional enhancements to improve selected features of the MELCOR model;
- Performing the severe accident and consequence analyses;
- Performing regression analysis;
- Conducting sensitivity analyses and investigating single realizations; and
- Examining results to identify parameter importance and severe accident insights.

To achieve the scope within a reasonable level of effort, project limitations were necessary. Each sampled parameter in MELCOR and MACCS required extensive research, and in some cases model enhancements; therefore, a reasonable number of parameters was selected. The scope of this project does not include model uncertainty or completeness uncertainty.

### **1.4 Methodology**

A methodology for the integrated investigation of uncertainties in MELCOR accident progression and MACCS offsite consequence analyses was applied in the Peach Bottom UA [2]. The methodology for the Surry UA generally followed the same approach. Similar to Peach Bottom, the accident scenario was selected, followed by identification of parameters of interest to be varied in the analyses, specific to a PWR reactor type. A minor departure from Peach Bottom was that some sensitivity analyses and 'one-off' calculations<sup>7</sup> were performed earlier in the process to help inform some of the parameter distributions. This approach was suggested during the ACRS review of the Peach Bottom study. The Surry study applied the same tools as the Peach Bottom UA, and expanded and enhanced selected project activities based on lessons learned and on the continuing advancement of the state of knowledge and understanding relevant to severe accident analyses.

---

<sup>7</sup> MELCOR analysts run periodic analyses to view the effects on model performance or results of a specific parameter.

The Surry team conducted a lessons learned meeting to identify the processes and applications that worked well for the Peach Bottom UA [2] and those that could have worked better. The lessons learned, a few of which are described below, are addressed throughout the report.

- Better parameter documentation. For Surry, a storyboard approach was implemented to justify and defend the parameter distributions early in the effort. A 'storyboard' was simply a specified format for each author to document key parameter information.
- The results of the sensitivity analyses could have been useful in informing the selection of parameters for investigation. For Surry, some sensitivity analyses were completed early.
- MACCS output volume was very high causing post processing to take longer than planned. The amount of data to be post processed overwhelmed the capabilities of MACCS. This problem was addressed on an ad hoc basis for Peach Bottom. For Surry, the code was modified to resolve the issue.
- Quality assurance (QA) of the Peach Bottom model inputs was implemented but was not systematic or documented. For Surry, a systematic and rigorous QA of the MELCOR and MACCS inputs and model enhancements was performed, including legacy values when appropriate (e.g., dose coefficients).



## 2. UNCERTAINTY ANALYSIS APPROACH

The approach implemented for the Surry UA generally followed that applied with the Peach Bottom UA. The major activities included:

- Selecting the accident scenario;
- Selecting parameters and developing distributions;
- Model modifications and enhancements;
- Analysis; and
- Investigation of results.

To meet the objective of developing insights into the overall sensitivity of SOARCA results to uncertainty in selected modeling inputs, modeling inputs important to the figures of merit being assessed, were identified. The MELCOR figures of merit are environmental release fraction of cesium and iodine, in-vessel hydrogen production, and release timing. The MACCS figures of merit are latent-cancer fatality (LCF) risk and early fatality risk at specified distances. The accident scenarios and parameter selection process are described below. The code modifications, analysis, and investigation of results are described in subsequent sections.

### 2.1 Accident Scenario

The Surry SOARCA unmitigated STSBO was selected as the accident scenario in part because of the importance of station blackout scenario and because accident progression occurs relatively quickly under the postulated conditions. The relatively quick accident progression provides an opportunity to assess the offsite response parameters while the release is potentially underway. (Of the scenarios selected for Surry in the SOARCA best estimate study, the unmitigated STSBO with induced SGTR was also one of the two scenarios with the highest conditional individual LCF risk [1].) This scenario, as described in the Surry SOARCA document [3], is initiated by an earthquake (0.5–1.0g peak ground acceleration) and has an estimated frequency of  $1 \times 10^{-6}$  to  $2 \times 10^{-6}$  per reactor year (prr). System failures were specified in the Surry SOARCA calculation [3] based on the type of event. The seismic event causes a loss of onsite power and failure of onsite emergency AC power resulting in an SBO where neither onsite nor offsite AC power are recoverable. All systems dependent on AC power are unavailable, including all active emergency core cooling systems (ECCSs) and the containment engineered safety systems (e.g., the containment sprays and fan coolers). The reactor coolant system (RCS) and containment are undamaged, and the containment is isolated. No instrumentation is available. Significant auxiliary structural damage outside containment is judged to have occurred, including structural failure of the turbine building and loss of access to the condenser blow down valves [3]. Additionally, this seismic event causes a failure of the emergency condensate storage tank (ECST), which is the source of water for the turbine driven auxiliary feedwater (TDAFW) system making this an STSBO rather than an LTSBO. The available systems include the passive ECCS accumulators, as well as unused mitigative equipment including portable power supplies, portable air bottles, and portable high-pressure (Kerr) and low-pressure (Godwin) diesel driven pumps. Containment spray and firewater piping is assumed to remain intact, but these systems were not active in the unmitigated analysis.

Although mitigative actions would be recommended and attempted throughout an emergency, the unmitigated STSBO in this analysis assumes no mitigative actions are successful. The mitigated response, analyzed in SOARCA [3], included successful implementation of mitigative actions which are intended to prevent the accident from progressing, termination of core

damage if it begins, maintenance of the integrity of the containment as long as possible, and minimization of the effects of offsite releases. As described in NUREG/CR 7110 Volume 2 [3], an expected national level response to a severe nuclear power plant accident provides a basis for truncating the release no later than 48 hours after the accident begins. Past studies, including NUREG-1150, typically truncated releases after 24 hours [10]. Consistent with SOARCA analyses [1] and the Peach Bottom UA, the MELCOR analyses here stopped at 48 hours. (A sensitivity analysis extending some of the MELCOR realizations to 72 hours is documented in section 6.1.7.)

## **2.2 Selection of Uncertain MELCOR Parameters**

MELCOR uses thousands of parameters in the evaluation of the equations and algorithms embedded in its constituent models. Many parameters are basic well-known input, such as core inventory, material properties, sizes and lengths of piping, etc. There are many parameters for which the base values were established through comparison to experiments. Some parameters were established long ago by subject matter experts (SMEs) and are assumed reasonable for the present application.

The extensive investigation into parameters for the Peach Bottom UA was leveraged for Surry. The Peach Bottom parameters were used as the starting point in the review because they were initially chosen by collective expert judgment, due to their proposed impact on key portions of accident progression, such as in-vessel melting. Although some of these parameters did not show importance in the Peach Bottom results, the parameters were maintained for further investigation because they could be important for a different reactor type and different scenario. The parameters were kept at this stage primarily because in the Peach Bottom analysis, the overwhelming importance of a handful of parameters in determining whether the accident progressed to main steam line (MSL) rupture, which in turn was a large determinant of release magnitude, could mask parameters that are important for other scenarios and reactor types. Peach Bottom parameters specific only to BWRs were removed from consideration, such as parameters related to drywell refueling dome leakage.

The chosen set of parameters is not an exhaustive list of all parameters important for MELCOR analyses. There are many alternative parameters that could represent the phenomenology of interest, and a practical subset was chosen to capture important aspects of modeling without introducing unnecessary complications, such as the need to extensively specify correlations.

Developing the parameter list was a multi-step iterative process. An initial parameter list was prepared and reviewed jointly by Sandia and NRC technical staff very early in the project. This meeting included a brainstorming session where additional parameters were discussed and added to the list. The next step was more comprehensive where the team conducted a parameter review from a systems approach with detailed consideration of the following:

- Sequence issues,
- In-vessel accident progression,
- Ex-vessel accident progression,
- Containment behavior,
- Chemical form, and
- Aerosol deposition.

During these reviews, the project analysts described the phenomenology and characteristics of each system and discussed why the parameters should be considered candidates for analysis. After the systems review, the candidate parameter list was updated. At this point, identification of parameters through expert judgment had been completed and the parameter list was fairly complete.

Next, a phenomenological based review was conducted of the MELCOR Reference Manual [8] rather than a mechanistic review of parameters in the MELCOR User's Guide [9], because a review of the User's Guide, which contains thousands of parameters and inputs, was not practical. The Reference Manual chapters together with brief notes from the review meeting are listed below.

- Burn Package Reference Manual
  - Sample hydrogen lower flammability limit based on variability in direction of flame propagation
  - Sample the maximum steam concentration supportive of a hydrogen burn based on the variability in direction of flame propagation
- Cavity Package Reference Manual
  - Consider addressing uncertainty in the amounts of gasses generated by molten core-concrete interaction by sampling the proportions of common sand and aggregate in the concrete.
- Condenser Package Reference Manual
  - Not applicable. The Surry units do not have isolation condensers or a passive containment cooling system.
- Core Package Reference Manual
  - Consider varying core blockage user input
- Control Volume Hydrodynamics-Flow Path Packages Reference Manual
  - No related parameters identified as potentially significant.
- Decay Heat Package Reference Manual
  - Address variation in decay heat dependent on where the core is in its lifecycle when the accident occurs.
- Fan Cooler Package Reference Manual
  - This is an SBO scenario, and without AC power the fan coolers would not be operating.
- Fuel Dispersal Package Reference Manual
  - This parameter is only important if the analysis shows a high pressure ejection. After the initial set of MELCOR uncertainty runs were complete, the results were reviewed and confirmed the fuel dispersal package parameters did not require investigation.
- Heat Structures Package Manual
  - Condensation was identified as a potential parameter. The effect of the presence of non-condensable gas on condensation rate.

- Material Properties Package Manual
  - Eutectic temperatures for zircaloy oxide and uranium oxide
- Non-condensable Gas and Water Package Reference Manual
  - No uncertainty modeling suggested here.
- Passive Autocatalytic Hydrogen Recombiner Package Manual
  - Not applicable because there are no passive autocatalytic hydrogen recombiners at US reactors.
- Radionuclide Package Reference Manual
  - Model uncertainty in dynamic shape factor
  - CHEMFORM
- Containment Sprays Package Reference Manual
  - Not applicable. Containment sprays are not available in the SBO scenario.

After review of the reference manual, the list of parameters was finalized and is presented in Table 2-1.

**Table 2-1 Surry MELCOR model uncertain parameters.**

<b>MELCOR</b>
<b><i>Sequence</i></b>
Primary safety valve (SV) stochastic failure to close
Primary SV stochastic failure to open
Primary SV failure to close due to passing water
Secondary SV stochastic failure to close
Primary and Secondary SV open area fraction
Primary SV thermal seizure criterion
Reactor coolant pump seal leakage
Normalized temperature of hottest steam generator (SG) tube
Steam generator tube thickness
<b><i>In-Vessel Accident Progression</i></b>
Zircaloy melt breakout temperature (SC1131(2))
Molten clad drainage rate (SC1141(2))
Radial molten debris relocation time constant (RDMTC)
Radial solid debris relocation time constant (RDSTC)
Time at cycle <sup>1</sup>
Decay heat
Effective temperature at which the eutectic formed from zircaloy oxide and uranium oxide melts
<b><i>Ex-Vessel Accident Progression</i></b>
Hydrogen ignition criteria (H <sub>2</sub> LFL)
<b><i>Containment Behavior</i></b>

<b>MELCOR</b>
Containment design leakage rate
Containment fragility curve (CFC)
Containment convection heat transfer coefficient
<b><i>Chemical Forms of Iodine and Cesium</i></b>
CHEMFORM iodine fraction
CHEMFORM cesium fraction
<b><i>Aerosol Transport and Deposition</i></b>
Dynamic shape factor
Secondary side decontamination factor (ARTIST)

<sup>1</sup> This parameter is developed in the Decay Heat section and is not itemized separately.

The team reviewed the transcripts from the Peach Bottom ACRS meetings to gain an understanding of the level of detail considered defensible for the technical bases. A frequent ACRS comment was for the technical team to clearly identify the point of departure from a known technical basis, at which use of professional judgment begins. Such judgment was often required in the development of parameters and has been identified, where applicable, in this project. Another area of interest in the ACRS review was the level of detail of the technical justification for the uncertainties assigned to each parameter and the rationale for the type of distribution used to characterize the uncertainty.

To facilitate development of parameter justification and rationale, a storyboard process was implemented. Figure 2-1 illustrates the form that was created to identify the parameter, responsible owner, technical justification for uncertainty, type of distribution, and rationale for the distribution. The intent was to capture, in a concise format, specific information regarding each parameter from which the detailed technical bases could ultimately be developed.

<b>Parameter Name:</b>	Type of Distribution:
Technical justification for the uncertainties:	
Rationale for type of distribution:	
Were similar or related parameters considered and rejected.	
Graphic: (plot of the distribution)	

**Figure 2-1 Parameter storyboard used to capture key information for each parameter investigated**

The storyboards were reviewed internally where analysts explained and defended each parameter. The team challenged the technical leads to explain the basis and defend the appropriateness of supporting data. This approach often resulted in the need for additional research to support the rationale. When significant changes were required to a storyboard, the parameter was again reviewed internally. Once a set of storyboards was ready, Sandia coordinated a joint review meeting with NRC staff SMEs to review and critique the parameter distributions and rationale.

The state of knowledge is not fully developed for some of the parameters investigated, which is evident in the MELCOR Code Manual where two parameters are identified as “order-of-magnitude parameters” [7]. However, the team believed that including some of these less understood parameters was important to establish an understanding of the potential effects, even though the technical bases for the parameter bounds may not have been as technically sound as the more mature parameters. The bounds for these parameters were established with values judged reasonable by the team.

### **2.2.1 MELCOR Parameters Considered but not Included**

The process described above included multiple review steps, each of which provided an opportunity to add parameters or justify why further consideration of a parameter was not needed. The parameters below represent some of those that were considered but not included in the analysis.

#### **SV reseal pressure**

SV reseal pressure (the pressure at which an SV closes, lower than the opening condition) was considered, but was omitted from further investigation based on insights from the Peach Bottom UA [2] and because SV dynamics are well represented in the Surry analysis. The Peach Bottom UA identified that the SV Setpoint Drift will produce analogous results to the distributions considered for SV stochastic failure to close (FTC) [1]. A delay in the SV stochastic FTC or failure to open (FTO) will be representative of those sequences within the Surry analysis that have long SV cycle periods prior to stochastic failure. These long SV cycle periods will produce sequence results similar to what would be expected from uncertainty in the SV reseal pressure.

#### **Concrete properties**

The molten core-concrete interaction (MCCI) is an important phenomenon in ex-vessel accident progression where uncertainty is expected. Varying CORCON parameters was considered. The team considered the potential for varying the aggregate quantity of the concrete mix, which could affect gas generation. A sensitivity analysis on concrete aggregate was already planned and this would be expected to provide the desired insights, including on ablation temperature.

#### **Reactor Pressure Vessel (RPV) drain line off the lower head**

Review of plant drawings found no evidence that a reactor pressure vessel (RPV) drain line off the lower head exists at Surry. The parameter was removed from further consideration.

#### **Secondary Decontamination Factor**

The Aerosol Trapping in a Steam Generator facility (ARTIST) built at the Paul Scherrer Institute (PSI) in Switzerland hosted a series of tests to try to determine the amount of decontamination that occurs within a steam generator following a steam generator tube rupture (SGTR) [7]. An alternative to implementing the ARTIST approach was reviewed and would have included turning on normal MELCOR models for aerosol capture and settling on the secondary side. For this to be a reasonable alternative, significant effort would have to be made to model all possible deposition structures on the secondary side, and there is uncertainty regarding whether such an approach would produce a more physical result due to MELCOR limitations (i.e., lack of a particle bounce model). Because of this, the total secondary decontamination factor (DF) (ARTIST approach) was selected.

### **2.3 Selection of Uncertain MACCS Parameters**

There are also potentially thousands of parameter values that could be varied in MACCS. Therefore, an early effort was to select a reasonable number of parameters important to the figures of merit being assessed. The figures of merit for MACCS are LCF risk and early fatality risk at specified distances. The project team again began with a review of the MACCS parameters in the Peach Bottom UA [2]. There was no compelling reason to remove any of the parameters from consideration. Furthermore, the plant type and accident scenario differences could show a different priority of importance of the Peach Bottom parameters when applied in the Surry analysis. Therefore, the full list of MACCS parameters used in the Peach Bottom UA was the starting point.

A complete review of MACCS parameters identified in Appendix D, "Glossary of Input File Variables," of NUREG/CR-6613, "Code Manual for MACCS2," was conducted [76]. The following parameter sets were included in the analysis. Each set consists of multiple individual parameters.

- Deposition,
- Dispersion,
- Shielding,
- Early Health Effects,
- Latent Health Effects, and
- Emergency Response.

Both epistemic and aleatory uncertainty exists for many MACCS parameters, and the combined effect adds complexity when developing the distributions. Furthermore, for some MACCS parameters, compromise values were necessary when a large number of different situations (e.g., weather trials and time of day) exist, but only one input value may be assigned. The specified values selected were deemed the most appropriate to use for these situations. As a result, the epistemic uncertainty distributions for these parameters attempt to characterize the uncertainty of the most appropriate values.

Aleatory uncertainty in weather is treated in MACCS. Weather conditions that would apply in the case of a potential accident at some time in the future cannot be known in advance. MACCS accounts for weather variability by analyzing a statistically significant set of weather trials, and the modeled results are ensemble averages of weather that represent the full spectrum of meteorological conditions. This sampling strategy was chosen to represent the statistical variations of the weather and is consistent with MACCS best practices [6].

The MACCS parameters varied in the analysis are listed in Table 2-2.

**Table 2-2 Surry MACCS model uncertain parameters.**

Epistemic Uncertainty
<b>Deposition</b>
Wet Deposition Coefficient (CWASH1)
Dry Deposition Velocities (VDEPOS)
<b>Shielding Factors</b>
Groundshine Shielding Factors (GSHFAC)
Inhalation Protection Factors (PROTIN)
<b>Early Health Effects</b>

<b>Epistemic Uncertainty</b>
Early Health Effects LD <sub>50</sub> Parameter (EFFACA)
Early Health Effects Exponential Parameter (EFFACB)
Early Health Effects Threshold Dose (EFFTHR)
<b>Latent Health Effects</b>
Dose and Dose Rate Effectiveness Factor (DDREFA)
Lifetime Cancer Fatality Risk Factors (CFRISK)
Long Term Inhalation Dose Coefficients
<b>Dispersion</b>
Crosswind Dispersion Linear Coefficient (CYSIGA)
Vertical Dispersion Linear Coefficient (CZSIGA)
<b>Emergency Response</b>
Evacuation Delay (DLTEVA)
Evacuation Speed (ESPEED)
Hotspot Relocation Time (TIMHOT)
Normal Relocation Time (TIMNRM)
Hotspot Relocation Dose (DOSHOT)
Normal Relocation Dose (DOSNRM)
<b>Aleatory Uncertainty</b>
Weather Trials

The storyboard process described in Section 2.2 was also implemented for MACCS parameters.

### 2.3.1 MACCS Parameters Considered but not Included

The parameters described below represent some of those that were considered but not included in the analysis.

#### Risk of Early Injury

Parameters to estimate the risk of an early injury, specifically pneumonitis, were made uncertain in the Peach Bottom UA. However, early injuries were not reported in the Peach Bottom study, so there was little value to treating this uncertainty. Early injuries are not commonly reported because they are not life threatening and are of relatively less concern than fatalities. Therefore, for the Surry UA, the parameters for early injuries were set to the values used in the original SOARCA study [3].

#### Ingestion Pathway

The ingestion pathway was not treated in the SOARCA analyses because uncontaminated food and water supplies are abundant within the United States, and it is unlikely that the public would eat radioactively contaminated food [3].

#### Habitability

The habitability criteria is considered to be an important uncertain parameter, but was not included with Surry because a detailed sensitivity analysis was performed with the Peach Bottom UA [2]. The Peach Bottom analysis showed, as would be expected, that when the dose truncation models were used, the LCF risks within the emergency planning zone (EPZ) were orders of magnitude lower when the habitability criteria was below the dose truncation level.

Beyond the EPZ, the habitability criteria showed a smaller effect on the overall LCF risk when a dose truncation model was applied.

### **Non-Evacuees**

Evacuation research has documented that some residents refuse to evacuate [81][88]. MACCS does not have a capability to reapportion population fractions in an uncertain application. It was determined the code modifications to support varying population fractions could not be completed during the course of this project.

### **Wet Deposition**

The wet deposition model parameters include CWASH1 and CWASH2. CWASH1 was selected to vary because there is considerable research and data available to support development of the distribution. The same is not true for CWASH2. Although this would be a reasonable parameter to evaluate, it was not considered because there are insufficient data to support development of a defensible distribution. Furthermore, CWASH1 captures the effect of wet deposition sufficiently, such that it was not necessary to evaluate CWASH2 as an exploratory parameter.

### **Cloudshine Shielding Factor**

The cloudshine shielding protection factor (CSFACT) was included in the Peach Bottom uncertainty analysis. However, in the storyboard process for Surry, it was discovered that there was an error in the reference from which the cloudshine distribution was taken. There was no other source found to inform an accurate distribution for this parameter. Since this was not identified as an important parameter in the Peach Bottom UA and the team lacked a basis for specifying a distribution for this parameter, a single point estimate was used.



### 3. DESCRIPTION OF CODES AND REGRESSION ANALYSIS

The NRC severe accident codes were applied in this UA, and regression analyses were conducted on the results. The codes and techniques applied in this study were the same as those used in the Peach Bottom UA [2]. Some updates have been implemented in the codes and in the regression approach and these are described below.

#### 3.1 Severe Accident Analysis Codes

MELCOR, MeIMACCS, and MACCS are the three primary codes used in the integrated analysis. These codes are continually enhanced, updated, and maintained as part of the NRC research program. Version control numbers are assigned to each code throughout this process. The codes were designed for outputs from one code to become inputs for the next code to support deterministic analyses. The codes have been integrated for use in analyzing uncertainty in the same manner as implemented for the Peach Bottom UA [2], as illustrated in Figure 3-1. The full Surry UA analysis also uses the MELCOR uncertainty engine and an external macro that creates RN inventories for time at cycle and CHEMFORM sampling. A brief description of each code is presented below and a detailed description of the MELCOR code is presented in Appendix A.

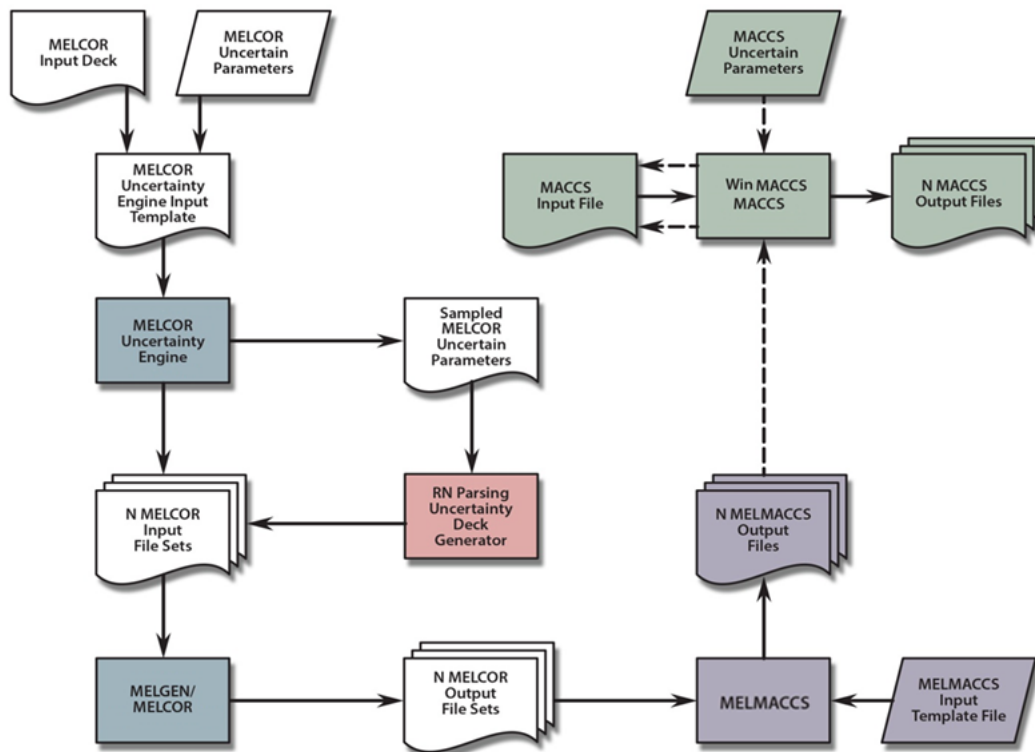


Figure 3-1 Diagram of the code information flow

The MELCOR uncertainty engine implements two processes, illustrated in the vertical path on the left of Figure 3-1. The engine creates a base set of 'N MELCOR input file sets' with all the common .gen files that are created 'N' number of times for 'N' number of uncertainty file folders.

It also creates uncertainty inputs specific to each MELCOR run. Based on some of those input specifics (time at cycle), the RN parsing is created. All of these data are then fed into the 'N' number of uncertainty file folders which make each of the file folders unique

### 3.1.1 MELCOR

MELCOR is a fully integrated, engineering level computer code that models the progression of severe accidents in light water reactor nuclear power plants [7]. A broad spectrum of severe accident phenomena in both boiling and pressurized water reactors is treated in MELCOR in a unified framework. This includes thermal-hydraulic response in the reactor coolant system, reactor cavity, containment, and confinement buildings; core heatup, degradation, and relocation; core-concrete attack; hydrogen production, transport, and combustion; and fission product release and transport behavior. An illustration of applying MELCOR in an uncertain framework is provided in Figure 3-2.

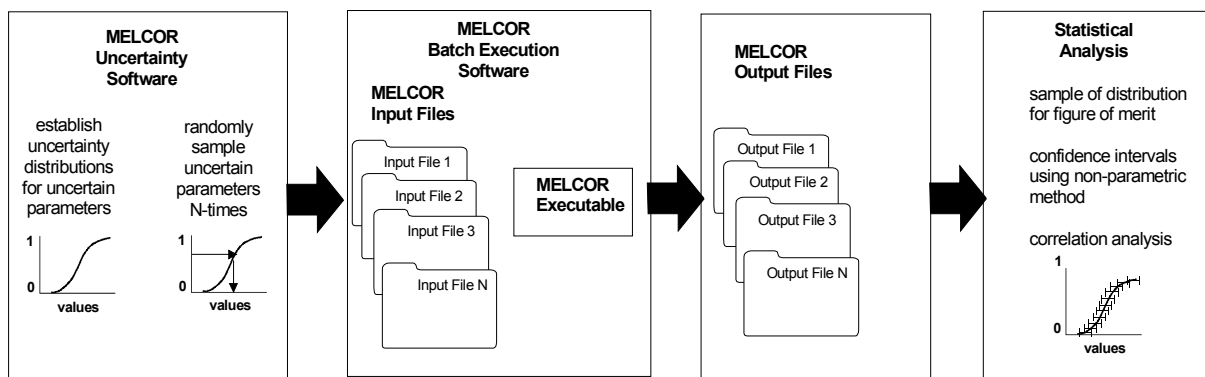


**Figure 3-2 MELCOR Uncertainty Application**

The MELCOR SOARCA Surry analysis in NUREG/CR 7110 Volume 2 was performed with MELCOR 1.8.6 YV3780 [3] circa 2007. A code modernization effort initiated in early 2000 resulted in conversion of the source code from Fortran 77 (MELCOR 1.8.6) to Fortran 95 (MELCOR 2.1). MELCOR 2.1 is currently the main computational tool for accident analysis, and the early versions of the code are no longer maintained. Therefore, it was decided to use the most current version of the code (MELCOR 2.1 IVF6717).

Since direct comparison of the MELCOR runs is not straightforward due to the code upgrade, the team decided that additional enhancements to the model should be added to maintain a state of art approach and errors identified in the original model should be corrected. Since 2007, the STSBO model used in NUREG/CR 7110 Volume 2 has continued to be advanced to support other non-SOARCA activities. Therefore, the first MELCOR activity for the Surry UA was to reconcile the SOARCA STSBO model with the most recent Surry model. Once this was complete, the model was converted to MELCOR 2.1. A limited set of additional enhancements were then implemented to improve areas of the model known to be weak or under represented. These are described in detail in Appendix A and selected items are listed below:

- Added MCCI modeling input to take advantage of the most recent code modifications to improve predictions;
- Improved the steam generator nodalization (illustrated in Figure 3-3);

- Included hot tube modeling in the SGTR logic;
- Added igniter logic to H<sub>2</sub>/CO burn modeling;
- RCS hot leg nozzle creep rupture input was modified to:
  - Reflect that both the carbon and the stainless steels of the nozzle need to fail for the pipe to rupture and that the carbon steel will fail first;
  - Consider whether the carbon steel of the nozzle has failed when determining the stress on the nozzle (realizing that the stress would increase markedly when the carbon steel failed);
  - Reflect that the nozzles are clad (on the inside) with 1/8" stainless steel and that the wall thickness of the nozzles is 2 1/2" inclusive of cladding; and
- Identified the appropriate heat structure nodes to be examined for temperature dependencies in the creep failure logic; and
- Implemented the Surry core inventory, as described in Appendix A.

During the model enhancements and parameter research, several errors in the Surry SOARCA model [3] were identified and corrected. These errors include:

- Errant vapor pressure coefficients for control rod materials silver, indium, and cadmium were corrected.
- The constituency of the aggregate in the concrete used for the Surry containment was corrected from limestone (used in the SOARCA study [3]) to a basalt-based aggregate. The SOARCA study [3] modeled a limestone-based aggregate, because this was identified in the Surry Modular Accident Analysis Program (MAAP) model input, and was assumed correct. However, during research related to the UA, the team identified that the individual plant examination (IPE) model had specified a basalt-based aggregate. Sandia obtained copies of the concrete test results from the University of Virginia which confirmed that basaltic based aggregate was used.
- The hot leg nozzle was modeled in the original Surry analysis as stainless steel, but was found to be Inconel.
- Errant particle density function was corrected.
- Steam drains were not isolating.

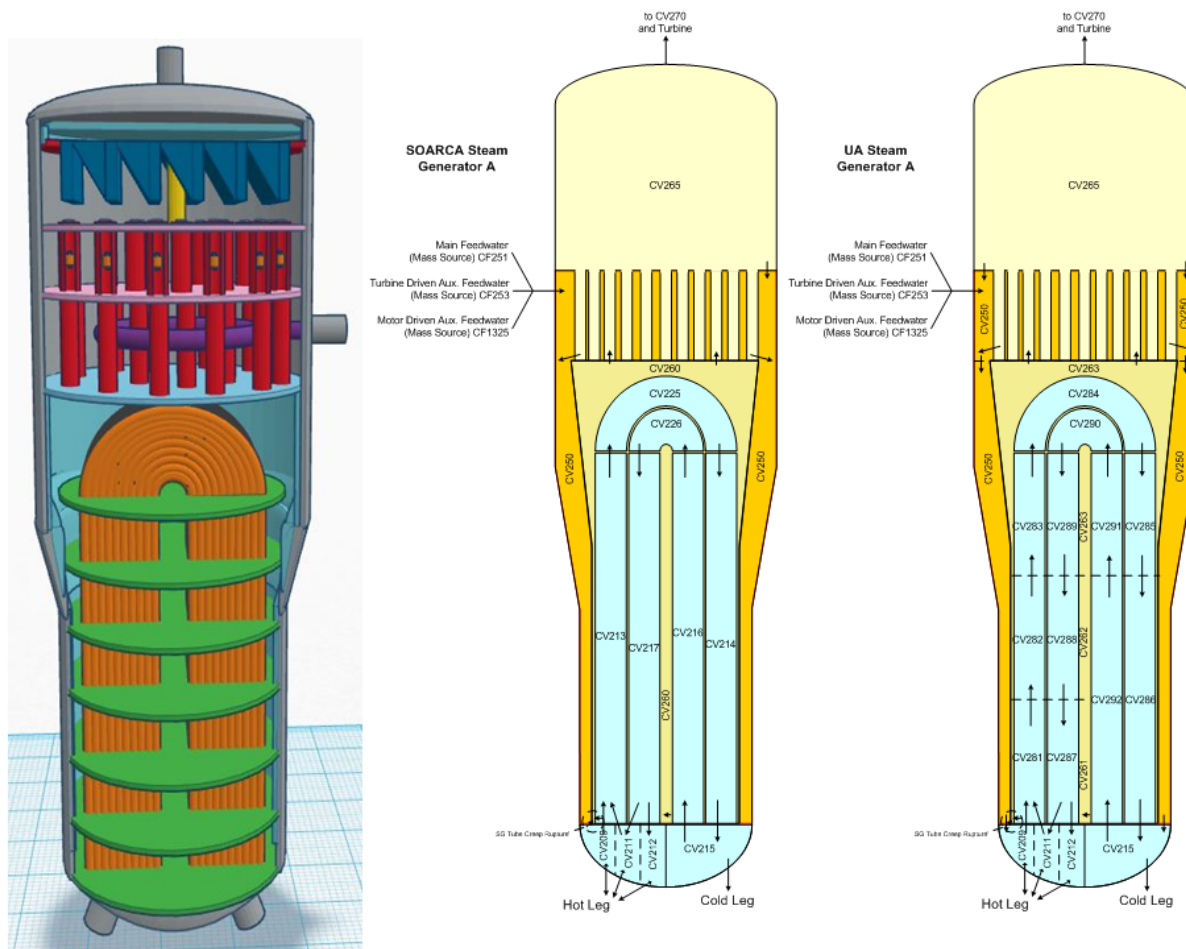


**Figure 3-3 Comparison of the NUREG/CR 7110 Volume 2 and the UA steam generator nodalizations**

A comparison of the results from the direct conversion of the MELCOR 1.8.6 model to the MELCOR 2.1 model is described in detail in Appendix A. There is a very good comparison of the thermal-hydraulic response prior to the hot leg creep rupture. After the hot leg creep rupture failure, the MELCOR 2.1 accident progression proceeds more slowly than the original MELCOR 1.8.6 calculation. The timing to core plate and lower core plate is 28 and 57 minutes slower, respectively. The failure of the lower head occurs 50 minutes later. A slightly higher fraction of volatile radionuclides were released from the fuel to the containment following the accumulator discharge in the MELCOR 1.8.6 calculation. Following the vessel failure, the core debris relocates to the reactor cavity. As a result of higher heating from the ex-vessel debris in the MELCOR 1.8.6 calculation, the containment pressurized slightly faster and had a slightly larger leakage rate. The net effects of the lower in-vessel retention and higher containment leakage were slightly higher releases of volatile radionuclides to the environment. The only exception was the Molybdenum, which was due to differences in the ex-vessel core-concrete interaction heat balance.

## MeIMACCS

MACCS requires isotopic breakdowns of the RN classes present in the MELCOR source term output and obtains these breakdowns from a pre-processing program called MeIMACCS, which takes as input masses and activities for nuclides separated by ORIGEN-S output libraries (i.e. light elements, actinides, and fission products) and reactor model type. MELMACCS requires both nuclide mass and activity because it does not contain nuclear decay data, such as decay constant. The nuclide masses were historically used to linearly scale the activities for each nuclide by comparing the appropriate MELCOR class mass (in the MELCOR plot file) to the class mass in MeIMACCS, which is calculated by summing the applicable user-specified nuclide masses. This process allowed for rough usage of inconsistent source terms and nuclide inventories, if desired. However, the SNL process for automatic generation of consistent MELCOR and MACCS inventories directly from ORIGEN-S output supersedes the need for the scaling algorithm. Thus, for the Surry UA, class masses in MELCOR and MACCS are completely consistent.

The isotopic inventories for beginning of cycle (BOC), middle of cycle (MOC), and end of cycle (EOC) calculated using ORIGEN S are implemented in MeIMACCS for the consequence analyses in the Surry UA. Consequently, three MeIMACCS inventories are used in the Surry UA. The time at cycle was a simple random sample selection with a uniform distribution within the MELCOR uncertainty inputs.

MeIMACCS Version 1.7.7 SVN-2575 was used in this analysis. Implementation of MeIMACCS required additional inputs that are not direct outputs from MELCOR [6], including:

- the radionuclide classes to include,
- high, medium, or low burnup fuel and the type of reactor (PWR or BWR),
- time of accident initiation in the MELCOR time frame,
- grade (ground height) relative to the MELCOR coordinate system,
- building height and initial plume width and height for building wake calculations,
- parameters and choices used to estimate deposition velocities,
- mass-fraction thresholds for paths and plume segments to be considered, and
- time intervals for plume segments.

Version 1.5.1 was used in NUREG/CR-7110 Volume 2. A discussion of MeIMACCS improvements from Version 1.5.1 to Version 1.7.0 is provided in Appendix C of NUREG/CR-7155 [1]. Major changes to MeIMACCS from Version 1.7.0 to Version 1.7.7, important to the Surry UA, are described below.

The major change from Version 1.7.0 to 1.7.1 was the ability to read MELCOR plot files (.ptf) in Windows 7. Important changes from Version 1.7.1 to 1.7.2 included:

- The ability to edit and add radionuclide inventories (e.g., Surry BOC, MOC, and EOC inventories),
- The ability to read MELCOR 2.1 plot files (.ptf or .plt),
- The ability to leverage a computers dynamic memory for reading MELCOR plot files into MeIMACCS,
- The addition of the user having to define the risk dominant plume segment (MAXRIS),

- An adjustment to the algorithm that chooses time of first mass release to start at the MELCOR time step just prior to the release to ensure all mass is captured, and
- An adjustment to the algorithm calculating gas density (PLMDEN) adjusting the lower bound of the integral to the time corresponding to the first nonzero temperature.

The only change from Version 1.7.2 to Version 1.7.3 was the change in 'MELCOR height associated with ground level' from 0 to 1000 meters to -1000 meters to 1000 meters. There were no major changes from Version 1.7.3 to Version 1.7.4 that affect the Surry UA. Major changes from Version 1.7.4 to Version 1.7.5 include:

- Added the core inventory scale factor (CORSCA),
- Allowed the manual adjustment of the plume release height for each release path,
- Changed the upper bound for surface roughness from 0.2 meters to 1.0 meters, and
- Changed the model setting lines in the MelMACCS output file to comment lines.

There were no major changes from Version 1.7.5 to Version 1.7.7 that affect the Surry UA.

### **3.1.2 MACCS**

MACCS uses a Gaussian plume dispersion model and incorporates plume depletion, exposure pathway assessment, emergency response, and dose analysis. The MACCS Best Practices document [6] describes the code in detail and identifies the best practice approach for implementation of the model. The MACCS application for the Surry UA was consistent with the best practices document except that some point-estimates for input were modified based on the new distributions.

MACCS Version 2.5.0.0 was used in the Surry SOARCA study [3]. Version 3.10.0.0 SVN-2560 was used in this Surry UA. MACCS code changes made between Version 2.5.0.0 and Version 2.5.0.9 are described in software quality assurance documentation [11]. Changes between MACCS Version 2.5.0.9 and Version 3.6.2 used in the Peach Bottom UA are described in Section 3 of NUREG/CR-7155 [2]. Important changes from Version 3.6.2 to Version 3.10.0.0 are described below. Most of these would not cause a difference in the results calculated.

- Provide file locations on MACCS cyclical files (e.g., MelMACCS source term files) to provide enhanced traceability between inputs and results;
- Increased maximum plume segments (MAXNP) allowed from 200 to 500;
- Addition of simple random sampling as an uncertainty analysis input variable option;
- Lower plume density limit consistent with the MACCS User Manual;
- Change to a FORTRAN compiler compatible with the Windows 7 operating system;
- Correction of the NRC Regulatory Guide 1.145 plume meander model [10]. This feature was not used in the original SOARCA and was therefore not used in this UA. It likely would have had a minimal impact on the predicted doses because this model only affects the plume dimensions at relatively short distances [6];

- The allowable upper limit of the early phase (ENDEMP) was increased to 40 days to allow modeling of prolonged releases;
- The addition of a new dose-projection period for the emergency phase (DPPEMP) and intermediate phase (DPP\_INTERPHAS); and
- The relocation times calculated in CHRONC for health effect risks were corrected to take into account multiple cohorts (evacuation and non-evacuation cohorts) within the same grid space.

## **3.2 Uncertainty Quantification and Propagation**

### **3.2.1 Introduction**

The inclusion of uncertainty is an inherent part of any risk analysis of complex systems. The approach chosen for this Surry analysis is consistent with the methodologies used for the Peach Bottom analysis [2], with minor changes implemented based on the lessons learned.

### **3.2.2 Uncertainty Type**

When analyzing a complex system, it is useful to classify the uncertainty under consideration into aleatory uncertainty and epistemic uncertainty [20]. Aleatory (or stochastic) uncertainty refers to the (apparent) inherent randomness in the properties or behavior of the system. For example, the weather conditions at the time of a reactor accident are inherently random. Another example is the variability in the possible future environmental conditions to which a system component could be exposed. Alternative designations for aleatory uncertainty include variability, stochastic, irreducible, and type A.

Epistemic (or subjective) uncertainty derives from the lack of knowledge about a known, but usually fixed, quantity (or at least a quantity that has a fixed representative value in the context of the analysis). For example, the pressure at which a given reactor containment would fail for a specified set of pressurization conditions is fixed but not precisely known. This type of uncertainty is usually reducible by increasing the knowledge about the parameter or model under consideration<sup>8</sup>. The use of a probabilistic framework to characterize lack of knowledge uncertainty is not necessarily the best approach. Over several decades, multiple mathematical structures were developed to better represent this uncertainty type [21]. However, these methods are computationally intensive and lack the clarity of a simple probabilistic approach. Therefore, in this study, epistemic uncertainty is represented by the classical probabilistic approach. Alternative designations for epistemic uncertainty include state of knowledge, subjective, reducible and type B.

The main reason to separate aleatory and epistemic uncertainty is that it brings more insight to decision making [22][23]. Estimates can be made regarding which part of the uncertainty is irreducible, which part can be reduced with further study, and the relative and cumulative effects

---

<sup>8</sup> Epistemic uncertainty includes parameter, model, and completeness uncertainty. See NRC's Regulatory Guide 1.174, "An Approach for Using Probabilistic Risk Assessment in Risk-Informed Decisions on Plant-Specific Changes to the Licensing Basis," for a more complete discussion [14]. The scope of this project does not include model or completeness uncertainty.

of both types of uncertainty. Regression analyses are used to determine which inputs, amongst those that are uncertain, are driving the output uncertainty, i.e., where to focus future work.

The analysis of complex systems typically requires answering the following four questions:

1. What can happen?
2. How likely it is to happen?
3. What are the consequences if it happens?
4. What is the confidence level in the answers to the first three questions?

The first three questions are referred to as the Kaplan-Garrick ordered triplet [12]. The separation of uncertainty with respect to aleatory and epistemic classifications allows for the definition of a formal mathematical framework in which aleatory uncertainty is used to answer the first two questions (as they deal with randomness in future events and the conditions at the time of the event that may affect the consequences). For this study, STSBO is assumed and the first question relates to the amounts of release of hydrogen, iodine, and cesium that are possible within that scenario. The second question pertains to the likelihoods of the possible release amounts. The third question is answered by the models, which estimate (deterministically) the consequence, given a fixed set of inputs. The consequences are the health effects associated with the release amounts. Epistemic uncertainty answers the fourth question (as confidence increases with the state of knowledge that directly depends on epistemic uncertainty), which is investigated with sensitivity and stability analyses.

While it is desirable to keep a separation between epistemic and aleatory uncertainty, this is not always possible in practice. First, the separation requires a simulation to include two embedded loops (see section 3.2.4). If high accuracy is necessary for both loops, the number of realizations may quickly become prohibitive. Second, while the definitions of aleatory and epistemic uncertainties are unambiguous, the characterization may be much more complex. It is not uncommon to find both an aleatory and an epistemic component in the uncertainty associated with a given input. Finally, some software does not allow for such separation.

When the separation of aleatory and epistemic uncertainty is not feasible, the analysis of the results can still provide a great deal of insight. In this UA, when such a separation is not practical, all uncertainty is represented as epistemic. This decision is driven by the fact that regression analysis (see section 3.3.2) may be applied to epistemically uncertain inputs. Note that it is still possible, once the regression analysis is performed, to separate the inputs into two groups in order to partly estimate how much of the total uncertainty is considered random and how much derives from a lack of knowledge.

### **3.2.3 Uncertainty Characterization**

Each input that is considered uncertain in this analysis has its uncertainty represented with a probability distribution assigned to potential values of that input. The process through which the parameters are selected, and how the associated uncertainty is represented (via a probability distribution) is a crucial part of any probabilistic analysis, as the results will be strongly affected by the choices. The methodology developed to build the uncertainty distributions can be summarized as follows:

- Data and information was gathered and categorized based on relevance and reliability. For instance, observations and measurements were given more credit than expert

judgment by itself. In the same spirit, data associated with the same mechanism or from Surry were considered more representative than proxies.

- Depending on the amount of data available, an appropriate selection of distribution representation was selected. The choice varied from simple distribution fitting when enough observations were available, to Bayesian updating, and to judgment when limited data was available.
- Consequent effort was made to document the rationale and assumptions to demonstrate the depth of the technical basis because the results are interpreted conditionally upon those assumptions.

### **3.2.4 Uncertainty Propagation for Source Term and Consequence Analysis**

Monte Carlo methods were developed in the late 1940's [25] as an answer to a specific problem: how can a function of a large number of inputs be estimated numerically? The problem of dimensionality quickly led to an impractical number of runs. The Monte Carlo technique consists of covering the input space by randomly sampling a value in that input space. A dense coverage insures that the approximation of the function is close enough to reality so that the appropriate conclusion can be reached. Demonstrations showed that the Monte Carlo approach will converge to the true solution as the sample size increases. The Monte Carlo method is the core of any sampling based approach, notably when the input space represents uncertainty with respect to the system. The original Monte Carlo method is characterized by sampling randomly in each direction, and is sometimes called Simple Random Sampling (SRS).

Latin hypercube sampling (LHS), developed in the 1970's [26] [28] improves the Monte Carlo technique by stratifying each distribution in order to insure a dense coverage in each direction of the input space. LHS reduces the variance in each estimate without introducing a bias. One limitation of LHS is that the stratification requires the sample size under consideration to be known at the beginning of the analysis. This limits the feasibility of LHS when the sufficient sample size is unknown ahead of time or when realizations fail to converge (i.e. MELCOR realizations do not run to completion), resulting in a reduction of the pre-defined sample size and a change in the input space stratification.

These limitations of the LHS application resulted in the decision to use SRS in the present context. MELCOR is a complex code that requires a change in the time-stepping or discretization for some realizations to reach convergence. Some of these refinements are so demanding that they are computationally impractical. The Peach Bottom UA [2] showed that rejecting some of the realizations due to a lack of convergence did not invalidate the coverage of the input space and did not bias the results toward a specific region. Such an analysis is once again necessary considering that it is not practical to have convergence for all realizations. However, the cost of the removal of these non-convergent realizations is that the required pre-specified sample size for LHS to insure complete stratification of the input space is reduced post-sampling, resulting in incomplete stratification. Also, because the sample locations are dependent, an additional set of simulations cannot be used to replace the failed realizations. Thus, the use of LHS is not recommended and the SRS technique was used. MACCS is not affected by the same problem and each realization leads to a convergent result. Nevertheless, in order to maintain a consistent approach (and mainly in order to use bootstrapping to support stability analysis as will be explained in section 3.3.3) the SRS technique was also used for the MACCS analysis.

The traditional method utilized to distinguish between aleatory and epistemic uncertainty is to use an inner loop for aleatory uncertainty and an outer loop for epistemic. The order of the loops could be reversed in theory, but a preference towards an inner aleatory loop and an outer epistemic loop is derived from what each uncertainty type represents. Aleatory uncertainty in the context of risk analysis is typically represented as a summary statistic (e.g., mean or median) or a distribution. For a given epistemic set (i.e., for a specific set of input parameter values in the outer loop), risk can be represented conditionally on the assumption that one would have perfect knowledge about the value of the parameter. Epistemic uncertainty is then represented as a distribution on the representative value (e.g., distribution of mean or median of aleatory outcomes) or a set of distributions showing confidence in the results given the current state of knowledge. The MACCS code was developed with this strategy in mind, and thus distinguishes between random inputs (mostly weather conditions) and epistemically uncertain inputs. This distinction is preserved and the outputs of interest (individual LCF risk and individual early fatality risk at various locations or areas) are estimated as expected values over aleatory uncertainty.

The MELCOR uncertainty engine considers only one loop and does not allow the separation between aleatory and epistemic uncertainty. The choice is to consider all uncertainties as potentially reducible and therefore epistemic. The distinction between epistemic and aleatory uncertainty can then be partially assessed at the regression analysis level.

### **3.3 Analyzing Uncertainty Results**

In the last step of a probabilistic approach, results are statistically analyzed (via uncertainty analysis) and the influence of input parameter uncertainty over the variance of each output under consideration is assessed (via regression analysis). Such analyses help to draw insights with respect to the results. Many techniques have been developed to perform such analyses, several of which are presented in Storlie et al. [22].

#### **3.3.1 Uncertainty Analysis**

Uncertainty analysis usually refers to the determination of the uncertainty in the output of interest that derives from the uncertainty in the inputs. Its main purpose is to assess the extent of uncertainty in the results of interest given the uncertainty in the overall system. When a sampling-based approach is used to propagate uncertainty, a sample is generated for each output under consideration. Uncertainty analysis thus corresponds to a statistical analysis of the results of interest.

Graphical representations, such as probability density functions (PDF) and cumulative or complementary cumulative distribution functions (CDF and CCDF), are usually used to visualize the extent of the uncertainty under consideration. Statistical measures such as moments (mean, standard deviations) and percentiles (e.g., median, 5<sup>th</sup> and 95<sup>th</sup> percentile) are used to summarize the distributions.

#### **3.3.2 Regression Analysis**

The purpose of the regression analysis was to determine the contributions of individual uncertain inputs to the uncertainty of the analysis results. Several techniques can be used to estimate the influence of each uncertain input on the output uncertainty. Some methods are

qualitative while some are more quantitative and can assess the importance of each input relative to the others with respect to uncertainty [18].

The four regression techniques applied in the Peach Bottom UA [2] were also applied in this analysis to assess quantitatively the importance of uncertain inputs. The results of these four regressions are presented showing the influence of the uncertainty of each input parameter according to each of the techniques. The conclusions of these techniques are supported by the qualitative graphical representations of the relations using scatterplots.

Rank regression, quadratic regression, recursive partitioning, and multivariate adaptive regression splines (MARS) were the four regression techniques used in this analysis to estimate the importance of the input parameters on the uncertainty of the outputs. The use of a set of regressions, instead of a single technique, was demonstrated to be beneficial in the Peach Bottom analysis [2] and was motivated by the fact that there is no universal regression approach capable of capturing all possible relationships from a given sample. Some regression techniques (such as linear regression) have the advantage of being robust (in the sense that they will not overfit the model and lead to artificial  $R^2$  values) but are unable to capture complex relationships (nonlinear and non-monotonic influences, conjoint influences). Other techniques are more flexible, but may still include some assumptions on the nature of the relationship. Furthermore, such techniques can be less robust and might give importance to spurious relations. In particular, techniques considering conjoint influence can examine so many possibilities that they identify a combination that appears to drive the uncertainty of the output of interest when this is not the case in reality.

Using a suite of regression techniques allows for better coverage of potential relations between input uncertainty and output uncertainty, while also increasing the confidence that an influence is not spurious if it is captured by multiple regressions. The results of each regression were studied by professionals experienced in the physical phenomenon under simulation to confirm that the regression results were expected in the physical sense based on the variation of the related input values. Although the use of multiple regression techniques leads to a more complex interpretation of the results, it was considered a necessary step since the application of a single regression technique could lead to a misinterpretation and erroneous conclusions. A short description of each selected technique follows, and more detailed descriptions of the techniques can be found in [18][19] and[22].

### **Rank regression**

The rank regression technique uses a rank transformation over the input and output variables under consideration. The smallest value of a variable is given a rank of one, the next a rank of two, and so on up to the largest value having a rank of  $n$  (i.e. sample size). A stepwise linear regression is then applied to the rank-transformed data. The model is linear and additive and is shown in the following form:

$$Y = a_0 + a_1X_1 + a_2X_2 + \cdots + a_nX_n + \varepsilon = a_0 + \sum_{i=1}^n a_iX_i + \varepsilon$$

Eq. 3-1

where  $\varepsilon$  represents (for this regression and the subsequent ones) the difference between  $Y$  and the regression estimate  $\hat{Y}$  for  $Y$ .

The stepwise approach starts with trying to find the best fit with only one parameter by testing all possible input parameters. It then builds up from this initial fit by selecting the best fit with two parameters, conditional upon keeping the first parameter, and so on. A stopping criterion is set via a generalized cross validation approach. Rank regression is effective in capturing monotonic relationships between inputs and outputs. The non-parametric aspect makes it less sensitive to outliers. This technique is limited to additive models where no conjoint influences are considered and may perform poorly on non-monotonic relationships.

Three metrics are included for each input variable used to display rank regression results. Two are based on the coefficient of determination, noted conventionally  $R^2$ , which represents the amount of variance explained by the regression model. The coefficient of determination is a normalized value which varies between 0 (no variance explained) and 1 (all the variance explained).

- $R^2_{inc}$  gives the cumulative coefficient of determination of the rank regression model when the  $i^{\text{th}}$  variable has been added (that includes all variables up to the  $i^{\text{th}}$  for the model).
- $R^2_{cont}$  gives the incremental gain in  $R^2$  when the  $i^{\text{th}}$  variable has been added compared to the model with  $(i - 1)$  variables. It is a good indicator of the contribution of this specific variable in explaining the variance of the output in consideration.
- The rank regression coefficient (RRC) is an indication of the strength of the influence. An absolute value close to zero means that the parameter has a small influence, while an absolute value close to one indicates a very strong influence. The RRC also indicates the positive or negative direction of the influence of this input variable on the considered output. A negative sign represents negative influence in which high values of the input lead to low values of the output and low values of the input lead to high values of the output. A positive sign represents positive influence where high values of input lead to high values of the output and low values of the input lead to low values of the output. For notational consistency with results obtained in traditional linear regression, results obtained in rank regressions are often presented with standardized rank regression coefficients (SRRCs). However, when there are no ties in the data, RRCs and SRRCs are equal.

### ***Quadratic regression, recursive partitioning, and MARS techniques***

The three additional regression techniques (i.e., quadratic regression, recursive partitioning and MARS) are treated differently, as their models do not allow for a direct estimate of the contribution to each individual input to the variance of the output. For each of these models a coefficient of determination ( $R^2$ ) is estimated for the entire regression technique and can be used as an indicator of how the regression performed. Once the regression model is available, it can be used to generate a large number of realizations via a variance decomposition technique known as the Sobol' decomposition. The Sobol' decomposition is a technique that can estimate the contribution of each input and their potential interactions (i.e., conjoint influence) via an integral decomposition of variance [17]. However, this technique requires a large number of realizations (tens of thousands) to be accurate (within a few percentages) and cannot usually be applied directly to a computationally demanding model. The regression techniques described below lead to analytical models that can quickly be run a large number of times (over the course of seconds to minutes). Once the Sobol' decomposition is applied, the importance of each variable (according to its uncertainty) can be assessed given the regression model. The answer is thus strongly dependent on the quality of the regression model and caution should be applied

when the  $R^2$  value is relatively low. In some situations, a regression technique may overfit and lead to an artificially high  $R^2$ . In such case, scatterplots can be used to confirm whether there is indeed a relation or not.

The Sobol' decomposition leads to different measures of effect than those used in stepwise linear regression. The two metrics selected for this analysis are described below:

- $S_i$  represents the first order sensitivity index and characterizes how much of the variance of the selected output is explained by the input parameter under consideration by itself (i.e., without conjoint influence). This index therefore estimates the same quantity as  $R^2_{\text{cont}}$  for the rank regression technique and it is acceptable to compare these two quantities.
- The second measure, labeled  $T_i$ , characterizes how much of the variance of the selected output is explained by the input parameter alone plus its interaction with the other uncertain parameters (i.e., conjoint influence). It has no analogue in the rank regression model as the additive model does not capture conjoint influences. The difference between  $T_i$  and  $S_i$  provides an estimate of the conjoint influence for a single input on the output considered.

### ***Quadratic regression***

Quadratic regression techniques apply the same approach as linear regression, including individual input variables, the square of these variables, and second order multiplicative interaction terms. The prediction model is of the form:

$$Y = a_0 + \sum_{i=1}^n a_i X_i + \sum_{i=1}^n b_i X_i^2 + \sum_{i=1}^n \sum_{j=i+1}^n c_i X_i X_j + \varepsilon$$

Eq. 3-2

Quadratic regression is not solely additive, as it can capture second order interactions. It can also capture the parabolic influence measured by the square of variables in the regression model. However, a complex relationship between variables and the output, like asymptotic behavior, may still be hard to capture with this technique and the method remains parametric, making it sensitive to outliers. Similar to traditional regression and rank regression, quadratic regression can be performed in a stepwise manner. As mentioned above, quadratic regression, like recursive partitioning and MARS, may overfit the data and lead to an artificially high  $R^2$  value.

### ***Recursive partitioning***

Recursive partitioning regression, also known as a regression tree, is a regression method that captures conjoint influences. A regression tree splits the data into subgroups in which the values are relatively homogeneous. The regression function is constructed using the sample mean of each subgroup. This approach results in a piecewise constant function over the input space under consideration. The predictive model is:

$$Y = \sum_{s=1}^{nP} (d_s I_s(X_i))_{i=1, \dots, n} + \varepsilon$$

Eq. 3-3

Recursive partitioning is well adapted to the present study as it strives to capture the effect of thresholds (e.g., a low value for one parameter and a high value for another parameter, or when a certain parameter reaches a threshold value). MELCOR includes many such threshold conditions to initiate some events or processes. One of the drawbacks of this regression is that it considers so many potential relations that it tends to overfit by capturing spurious correlations. Consequently, checking the relations only found by this regression using scatterplots is recommended and was performed.

### ***Multivariate Adaptive Regression Splines (MARS)***

MARS is a combination of (linear) spline regression, stepwise model fitting and recursive partitioning. A regression with a single input starts with a mean-only model and adds basis functions in a stepwise manner while adding the overall linear trend first. A second model using linear regression via least squares is fit to the data. This model is then added to the basis functions in a way that reduces the sum of squared error (SSE) between the observations and predictions. A fourth basis function is then added to minimize the SSE again. This process is repeated until  $M$  (set by default at 200) basis functions have been added.

At this point, the MARS procedure will try to simplify the model using stepwise deletion of basis functions while keeping the y-intercept and linear trend. The  $M - 2$  candidate leading to the smallest increase of SSE will be selected. This deletion will be applied until regressed to the original linear model.

Stepwise addition and deletion leads to the creation of two different  $M - 2$  models. The “best” model is chosen using a generalized cross validation score which corresponds to a SSE normalized by the number of basis functions considered. With multiple inputs, the basis functions will consider main effects and multiple-way interactions. The options used for this analysis consider only two-way interactions to avoid the exponential cost of considering more interactions.

MARS usually leads to similar results as linear regression with a greater accuracy, and with the inclusion of non-monotonic effects and conjoint influences. However, it performs poorly with discrete inputs due to the use of splines<sup>9</sup>.

### ***Ranking the variables according to the four regression techniques***

A consequence of the use of multiple regressions is that the ranking of the inputs amongst themselves is not obvious when the different regressions disagree. A qualitative approach has been used in the past [1] based on the physics considered in the problem and expert knowledge, but such an approach introduces some subjectivity and is hard to document. A more quantitative approach for the current analysis was implemented, along with the continued

---

<sup>9</sup> A spline is a numeric function that is piecewise-defined by polynomial functions.

understanding that such a quantitative ranking is an indicator and should be supported by expert opinion based on the physics of the problem.

Two effects of the uncertainty in the input on the output of consideration are estimated in the present study. The individual or “main” effect represents the influence of the uncertain input by itself and is estimated with  $R_{cont}^2$  in the stepwise regression and  $S_i$  for the other three regression techniques. Then the effect of the uncertain input from its interaction with other variables, which is ignored by the stepwise regression as it is an additive regression, is estimated with  $T_i - S_i$  for the other three regressions.

The first effect of the uncertainty in the input was considered the most important, and a decision was made to rank the variables according to this main effect. Stepwise regression provides an estimate of the main effect for each variable directly. For the other regressions techniques, the real effect has to be adjusted by the goodness of fit of the model (i.e. the  $R^2$  value from the regression model). In order to accomplish this, each  $S_i$  value is multiplied by the  $R^2$  value of the regression model. Finally, if a variable is not included in a given regression, it is supposed that its main effect is null and the corresponding value is set to 0. This weighted average is represented by:

$$\text{Main influence} = \frac{R_{cont}^2 + \sum_{j=1}^3 R_j^2 \cdot S_{i,j}}{4} \quad \text{Eq. 3-4}$$

where  $R_{cont}^2$  is from rank regression, j is the index of the three non-linear regression techniques, and  $R_j^2$  is the final  $R^2$  for each non-linear technique.

The conjoint influence is captured by estimating  $T_i - S_i$  for each of the last three regressions, adjusted using the  $R^2$  value as a weight. An average is taken again, represented by:

$$\text{Conjoint influence} = \frac{\sum_{j=1}^3 R_j^2 \cdot (T_{i,j} - S_{i,j})}{3} \quad \text{Eq. 3-5}$$

If the average value is greater than 0.1 (meaning 10 percent of the regression is explained via conjoint influence with this input), the  $T_i$  are emphasized to draw attention to a potential important conjoint influence. As the first order indices (i.e.,  $S_i$ ) and total order indices (i.e.,  $T_i$ ) are estimated numerically using a Sobol’ decomposition, they are approximations. If no conjoint influence is present, it may happen that  $T_i$  is estimated slightly lower than  $S_i$ . In such situations the value of  $(T_i - S_i)$  was set to 0. These two metrics, main contribution and conjoint contribution, are added to the summary tables for the four regression results, as an indicator of the importance of the input uncertainty to the output uncertainty. This represents a best estimate of the input uncertainty influence on the uncertainty of the output considered.

The first four major columns in the regression tables presented in the analysis sections are labeled with the regression technique used to create the results. The last two columns contain average values of the main contribution of the parameter on the result metric and the conjoint influence of the parameter on the result metric. For ease of reading the regression tables which are presented with the results, highlighting is applied in the main contribution and conjoint contribution columns to identify the best estimate importance of each input parameter, based on the overall analysis. The cutoff for main contribution effect was set at 0.02, and the cutoff for

conjoint effect was set at 0.1. The reason for a difference in the contribution effects is that conjoint contribution influence looks at a larger range of possible interactions (for instance, with 20 inputs variables, the main contribution looks at 20 potential relations while conjoint influence of 2 inputs looks at 190 potential relations) and is more likely to identify spurious correlations. Therefore, an approach that concentrates on the larger contribution was considered appropriate. The threshold values of 0.02 and 0.1 were selected based on the knowledge acquired during Peach Bottom UA [2] and the regressions tables for the present analysis, such that important parameters would be acknowledged and negligible influence would not be highlighted.

### ***Testing for potential over-fitting***

Recursive partitioning has a tendency to be more permissive and therefore to overfit. In other words, the regression technique may lead to an artificially high  $R^2$ . This may also happen during the application of quadratic regression and MARS. When a single regression technique identifies a strong relation, it is necessary to check for the validity of the relation found. An approach aimed at checking a relation's validity created a random output for each realization and used this to check on the result of the regression technique. Two uniform random variables were generated (one continuous and one discrete). The four regression techniques were then used with the same inputs to regress these random outputs. The results can infer whether the selected regression technique can be trusted or not. Testing completed for this project has shown that recursive partitioning can usually lead to an  $R^2$  of around 0.6 to 0.7 all the time, with mostly conjoint influence captured (no high  $S_i$  values, only high  $T_i$  values). As a result, for any set of regressions leading to only  $T_i$  influence, the results of the regression were minimized in the discussion of the results.

### ***Scatterplots***

The use of scatterplots is a qualitative yet powerful technique that completes the suite of regression techniques applied in this analysis. Scatterplots display a set of points, one per realization, whose coordinates correspond to the value of one selected input for the x-axis and of the output considered on the y-axis. It confirms graphically that the relation estimated by any of the regression techniques is indeed present and not spurious.

### **3.3.3 Stability Analysis**

As with any numerical method, Monte Carlo techniques will lead to different levels of accuracy, depending notably on the sample size. The purpose of stability analysis is to assess this level of accuracy and determine if the sample size is big enough or if more realizations may be required. The notion of stability is hard to capture quantitatively, as it is inherently qualitative and often includes subjective judgments. While it can be expressed with a formal approach (for instance, it is not desirable for the confidence interval to be larger than a certain fraction of the standard deviation or a standard error), the ultimate criteria is whether there is enough confidence that the conclusion will not be affected by the accuracy of the Monte Carlo technique used. In order to address this, a decision was made to represent stability as a confidence interval around the statistics of interest and rely on the judgment of professionals to conclude whether such an interval is acceptable within the context of this analysis instead of selecting an arbitrary cut-off.

The method selected to estimate these confidence intervals is a classical percentile bootstrap. This method requires the generation of a new sample of the same size (with replacement) from the original output sample. The operation is then repeated a large number of times (1000

iterations was used) to generate a set of possible output distributions. This leads to a distribution for each statistic (mean and quantiles in the present analysis). A 95 percent confidence interval using percentile bootstrap is obtained by looking at the location of the 2.5 percentile for the lower bound and 97.5 percentile for the upper bound for each of the statistics. A more complete description of the bootstrap technique can be found in [29].

To establish the stability of the statistical results reported in the analysis sections, the data from MACCS and MELCOR were partitioned into subsets by randomly sampling without replacement so that each subset represents the original distribution of the output parameter, but with a smaller sample size. Then 95% confidence intervals were generated for the mean and 95<sup>th</sup> percentile of each subset using classical percentile bootstrapping, where each subset was sampled with replacement to generate 1000 new samples.

A typical representation of the stability analysis for MELCOR and MACCS results is provided in Figure 3-4, showing confidence intervals around the mean of each subset for LCF risk at 0 to 10 miles. Each color in the plot represents a different partitioning of 1000 data points, with the dotted line indicating the mean calculated from the complete data set. Each line represents a 95 percent confidence interval around the mean for that set in the partition. Thus, when the sample size is 100 and the data is partitioned into 10 sets, the portion of the output space covered by the collection of confidence intervals is larger than the portion covered by the confidence intervals for sample size 500 or 1000, as expected. Since each confidence interval contains the overall mean from all of the data, and the confidence intervals for sample size 500 and 1000 cover a similar portion of the output space, the statistical results are stable with the sample size used in this study (and could be decreased to 500 in future studies). The samples used sufficiently represent the true distributions of the output parameters. Though only one plot from this analysis is included, similar plots were generated for the means and 95<sup>th</sup> percentiles for LCF risk at 0 to 10 miles, at 10 to 20 miles, at 0 to 50 miles, and for fraction of cesium released, fraction of iodine released, and hydrogen production. All of these plots similarly support the stability of the statistical results for both MELCOR and MACCS.

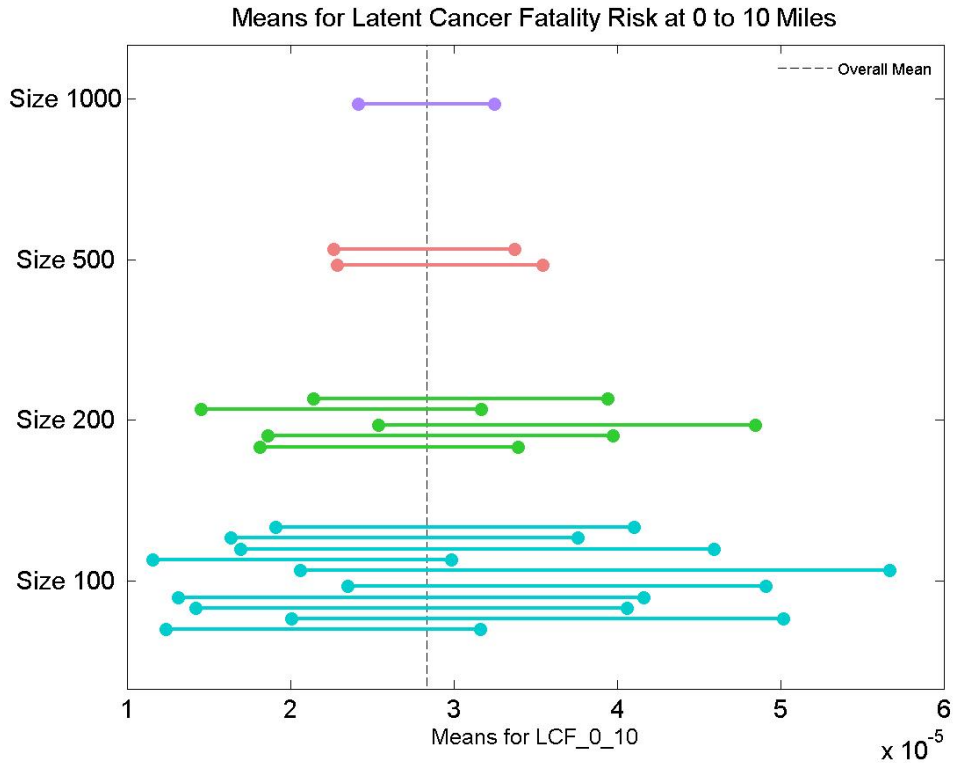


**Figure 3-4 Typical representation of stability analysis for MACCS results showing confidence intervals around the mean of each subset for latent-cancer fatality risk at 0 to 10 miles**

One advantage of the SRS technique is that it is easy to increase the sample size, as any new realization can be added to the existing set. Furthermore, a subset of the sample is a valid sample of the original distribution, which is one of the required assumptions for the use of the bootstrap technique. This property of SRS can also be used to determine an optimal sample size that will lead to an appropriate stable estimate of one output of interest (within the context of this analysis). Any output data can be split into  $n$  groups of samples of size  $\frac{M}{n}$  (where  $M$  represents the initial sample size). Each sample can then be used to assess the quantity (or quantities) of interest. The operation can be repeated a large number of times by creating different combinations of values within each sample. This technique is equivalent to a bootstrap with the exception that each sample has a size representing a fraction of the initial sample size. With such an approach, confidence intervals can be generated for different sample sizes and compared. Since the sample size controls the accuracy of the Monte Carlo techniques (much as grid size controls the spatial accuracy of any numerical method) this approach can be used to estimate when a sample size is big enough to lead to adequate stable results for the selected output of interest (e.g., statistics). Furthermore, if the desired accuracy is not met using the initial sample size, such technique can be used to extrapolate a potential sample size that should meet the corresponding criterion.

***Regression analysis of failed realizations***

A certain number of MELCOR calculations fail to converge within a reasonable computational time for various reasons. An analysis is thus completed to determine whether there is a

correlation between failed runs and having the realization set in a particular area of the input space. Such a situation would indicate that a particular value for one input (or combination of values for several inputs) would lead to failure, biasing the conclusion that could be drawn by only analyzing the successful runs. In order to detect a potential relation between input uncertainty and failure, a regression analysis (using the four regressions techniques described in section 3.3.2) was performed, using an indicator function set to 0 when the realization failed to run to completion and 1 when it ran up to the end as the output of interest.

Two additional regression analyses were performed. Two dependent variables were defined; one was a continuous and uniformly distributed random variable between 0 and 1, and the other was discrete, generated by rounding the continuous random variable to the nearest integer. Then, the same regression techniques that were applied in the analysis of failed runs were used with either the continuous or discrete random variable as the dependent variable, rather than the failed run indicator variable. Similar regression results for all three regressions indicated that the instance of realization failure is random with respect to the input space, showing that the completed realizations are representative and there is not a significant relationship between input values and realization completion.



## **4. UNCERTAIN INPUT PARAMETERS AND DISTRIBUTIONS**

### **4.1 Source Term Model Uncertainty (MELCOR Inputs)**

As discussed in Section 2.2, the MELCOR uncertain parameters were selected to cover the following issues of severe accident phenomenological areas:

- Sequence,
- In-vessel accident progression,
- Ex-vessel accident progression,
- Containment behavior,
- Chemical forms of iodine and cesium, and
- Aerosol transport and deposition.

Table 4-1 lists the distributions and bounds related to each MELCOR parameter sampled in this analysis. The sampling approach for many of the parameters is quite complex and is described in the following sections along with the rationale for each distribution, and justification for the upper and lower bounds. The basis for defining many distributions is strong where known physical or chemical phenomena are well understood. For some parameters, the technical basis for establishing the distribution was less defensible. In such cases, these distributions were considered exploratory and intended to inform the severe accident community on the effect of applying a distribution to these parameters. The bounds for exploratory parameters were generally based on professional judgment, and in some cases were based on sensitivity analyses conducted early in the course of this project.

Correlation of the MELCOR parameters was considered, but ultimately no correlations were implemented. It was originally planned to correlate Zircaloy breakout temperature, eutectic temperature, and the time at temperature model; sampling on the time at temperature was removed from consideration, and the sampling for breakout temperature and eutectic temperature were 85 percent exclusionary, thus it was decided no correlation was necessary. Correlation of radial relocation times for molten and solid debris was considered, but instead distributions were created that were 100 percent exclusionary (upper bound for one is lower bound for the other). Lastly, SV parameters were effectively correlated by sampling according to a single model, and gaseous iodine sampling was dependent on time at cycle but not through the uncertainty engine. There were no other MELCOR parameters where correlation was determined necessary.

**Table 4-1 MELCOR sampled parameters.**

Uncertain Parameter	Distribution type	Distribution Parameters		Lower Bound	Upper Bound
<b>Sequence Related Parameters</b>					
Primary SV stochastic FTC (-) (Section 4.1.1.1.1)	Beta <sup>1</sup>	$\alpha: 17.5$ $\beta: 756.5$		0	1
Primary SV stochastic FTO (-) (Section 4.1.1.1.2)	Beta <sup>1</sup>	$\alpha: 0.5$ $\beta: 773.5$		0	1
Primary SV FTC due to passing water (-) (Section 4.1.1.1.3)	Beta <sup>1</sup>	$\alpha: 0.5$ $\beta: 4.5$		0	1
Secondary SV stochastic FTC (-) (Section 4.1.1.1.4)	Beta <sup>1</sup>	$\alpha: 17.5$ $\beta: 756.5$		0	1
Primary SV thermal failure to close (K) (Section 4.1.1.2.1)	Beta	$\alpha: 5$ $\beta: 10.7615$		811	1422
SV open area fraction (-) (Section 4.1.1.3.1)	Uniform	-		0.01	1
Reactor coolant pump seal leakage (RCPSL) (gpm/RCP) (Section 4.1.1.4)	Discrete	Bin (gpm)	Prob.	-	-
		21	0.79		
		76	0.01		
		182	0.1975		
		480	0.0025		
Normalized temperature of hottest SG tube (-) (Section 4.1.1.5)	Beta	$\alpha: 43.7$ $\beta: 54.9$		0	1
SG tube thickness (mm) (Section 4.1.1.6)	Triangular	Mode: 0.791		0.312	1.27
<b>In-Vessel Accident Progression</b>					
Zircaloy melt breakout temperature (SC1131(2)) (K) (Section 4.1.2.1)	Scaled Beta <sup>5</sup>	$\alpha: 3.83$ $\beta: 3$		2100	2540
Molten clad drainage rate (SC1141(2)) (kg/m-s) (Section 4.1.2.2)	Log triangular	Mode: 0.2		0.1	2
Radial molten debris relocation time constant (RDMTC) (s) (Section 4.1.2.3)	Uniform	-		10	100
Radial solid debris relocation time constant (RDSTC) (s) (Section 4.1.2.4)	Uniform	-		100	1000
Time at Cycle <sup>2</sup> (-) (Section 4.1.2.5)	Discrete	Bin	Prob.	-	-
		BOC	0.33		
		MOC	0.33		
		EOC	0.33		
Decay Heat <sup>3</sup> (-) (Section 4.1.2.5)	Uniform	-		1	500
Effective temperature at which the eutectic formed from UO <sub>2</sub> and ZrO <sub>2</sub> melts (K) (Section 4.1.2.6)	Normal	Mean: 2479 $\sigma: 83$		-	-

Uncertain Parameter	Distribution type	Distribution Parameters		Lower Bound	Upper Bound
<b>Ex-Vessel Accident Progression</b>					
Hydrogen ignition criteria (H2 LFL) (%) (Section 4.1.3.1)	Discrete	Bin	Prob.	-	-
		4%	0.33		
		6%	0.33		
		9%	0.33		
Secondary side rupture location and decontamination factor (ARTIST) (-) (Section 4.1.3.2)	Discrete	Bin	Prob.	-	-
		1	0.02		
		2	0.03		
		3	0.05		
		4	0.08		
		5	0.14		
		6	0.25		
7	0.43				
<b>Containment Behavior</b>					
Containment design leakage rate (DLEAK) (% Vol/day) (Section 4.1.4.1)	Discrete	Bin	Prob.	-	-
		0.1	0.1		
		0.2	0.1		
		0.3	0.1		
		0.4	0.1		
		0.5	0.1		
		0.6	0.1		
		0.7	0.1		
		0.8	0.1		
		0.9	0.1		
1.0	0.1				
Containment fragility curve (CFC) (Section 4.1.4.2)	Scaled Beta <sup>5</sup>	$\alpha: 5.6$ $\beta: 6.3$		1.09	2.03
Containment convection heat transfer coefficient (Section 4.1.4.3)	Triangular	Mode: 1.4		1.0	2.0
<b>Chemical Forms of Iodine and Cesium</b>					
CHEMFORM iodine <sup>4</sup> (Section 4.1.5.1)	Truncated-Lognormal	$\mu: -9.94$ $\sigma: 0.28$		0.0	-1.0
CHEMFORM cesium (Section 4.1.5.2)	Beta	$\alpha: 9$ $\beta: 3$		0.0	1.0
<b>Aerosol Transport and Deposition</b>					
Dynamic Shape Factor (Section 4.1.6.1)	Scaled Beta <sup>5</sup>	$\alpha: 1$ $\beta: 5$		1.0	5.0

<sup>1</sup> The sampling scheme is more complicated than a simple Beta. The probability of failure conditional on demand is described by the given beta, but then is updated based on a distribution.

<sup>2</sup> This parameter is developed in the Decay Heat section and is not described separately.

<sup>3</sup> This parameter is used along with the Time at Cycle parameter to pick a specific decay heat table from pre-created files to be used as the MELCOR input.

<sup>4</sup> This is a simplification. This lognormal is sampled externally, and then the burn-up at each time at cycle is used to pre-create gaseous iodine fractions which are manually input.

<sup>5</sup> A Beta distribution by definition has bounds of 0 and 1. Any Beta with other bounds can be referred to as a Scaled Beta.

### 4.1.1 Sequence

The timing of SV failure was found to be the most influential uncertain parameter of all the uncertain parameters considered in the Peach Bottom UA [2]. With this insight from the Peach Bottom analysis, failure probabilities of safety valves (SVs) on the pressurizer and MSLs were included as uncertain in the Surry UA. Failure to open (FTO) due to over-cycling and failure to close (FTC) due to over-cycling, passing water or overheating, were considered for the SVs on the pressurizer. FTC due to over-cycling was considered for the lowest set-point SV serving each steam generator. FTC due to overheating of the MSL SVs was not considered because the valves are only exposed to design temperatures. FTO due to over-cycling of these valves was not considered because of the multiple SVs on each line and the small probability associated with FTO. If one of these valves were to fail to open, the function of pressure relief would simply move on to the next valve. As this is a STSBO scenario PORVs are not available on either the pressurizer or MSLs.

#### 4.1.1.1 Primary SV Stochastic Failure

In the Surry best estimate analysis [3], SV stochastic failure was modeled for the lowest-set-point SV and only for an FTC failure mode. The mean probability of failure per demand was taken and used as the number of SV demands at which failure occurred. See the probability distribution and cumulative distribution functions for the negative binomial distribution below:

$$f(n|p) = P(N = n|p) = p(1 - p)^{n-1}, 0 \leq p \leq 1, n \sim [1, 2, 3 \dots]$$

Eq. 4-1

$$F(n|p) = P(N \leq n|p) = 1 - (1 - p)^{n+1}, 0 \leq p \leq 1, n \sim [1, 2, 3 \dots]$$

Eq. 4-2

Where  $p$  is the probability of a failed state for the SV per demand, and  $n$  is the number of valve cycles the SV experiences.

Once the distributions were defined, the SOARCA study used the mean of the number of SV demands at which failure occurred to define the number of cycles at which FTC occurs [3]. This approach did not include the FTO failure mode. The approach was justified by assuming that redundancy in the SVs would ensure a FTC state would be reached before an all valves FTO end state occurred. The Peach Bottom UA also assumed only FTC. The sampling conducted to support the Peach Bottom UA was on the beta distribution for the FTC probability per demand and then taking the mean of the number of SV demands at which failure occurred instead of sampling directly from the distribution in Eq. 4-1 and Eq. 4-2. The Surry UA is expanding upon the Peach Bottom UA approach by sampling from both the FTC and FTO uncertainty distributions.

The Surry pressurizer has three SVs with differing set-points. The set-points serve automatic valve operation such that when pressure rises in the primary system to a set-point, the associated valve opens and steam is released to the Pressurizer Relief Tank (PRT). Once the system reduces to 96 percent of the set-point, the valve reseats. This is considered one "cycle" of the SV. Every opening and closing of the SV has a failure probability associated with the state transition.

The FTO and FTC distributions were obtained from data in Appendix A.2.42 of NUREG/CR-7037 [30]. Only valve responses to actual scram events were considered, i.e., data from valve

testing reported in NUREG/CR-7037 was not considered. The testing data was not considered because the failure rates in the testing differed largely from the failure rates associated with actual scram events suggesting that something was not prototypic in the testing. The data is typically only for failures in a single SV cycle, so there may be some limitation in extrapolating to repeated cycles during a severe accident, but this is the best data available. Bayesian updating was conducted on the failure and testing counts for the SV FTO and FTC failure modes with a Jefferys uninformed beta distribution ( $\alpha = 0.5, \beta = 0.5$ ) as the 'prior,' which roughly corresponds to half a failure observed in a full trial. The Jefferys uninformed beta distribution is commonly used in Bayesian analysis with limited data because of invariance to transformation in the Fisher Information matrix, which describes the amount of information entropy within a distribution [37]. The failure information and the sampling distributions are presented in Table 4-2.

**Table 4-2 SV failure data and associated epistemic uncertainty distributions for probability of occurrence on demand for FTO and FTC.**

Mode	# Failures	# Tests	Distribution*
FTO	0	773	$\beta(\alpha = 0.5, \beta = 773.5)$
FTC	17	773	$\beta(\alpha = 17.5, \beta = 756.5)$

\*Development of indicated distributions described in Sections 4.1.1.1.1 and 4.1.1.1.2.

The possible states of a 3-valve RCS primary pressure relief system are presented in Figure 4-1 and the probability of being in a given state as a function of cycles can be seen in Figure 4-2. As FTOs occur, the system transitions from cycling on the lowest set-point valve (State 1), to cycling on the middle set-point valve (State 2), to cycling on the highest set-point valve (State 3). If an FTC doesn't occur at some point in the transition process such that a failed open state of the system develops (State 4), a failed closed state develops where pressure relief is no longer available (State 5).

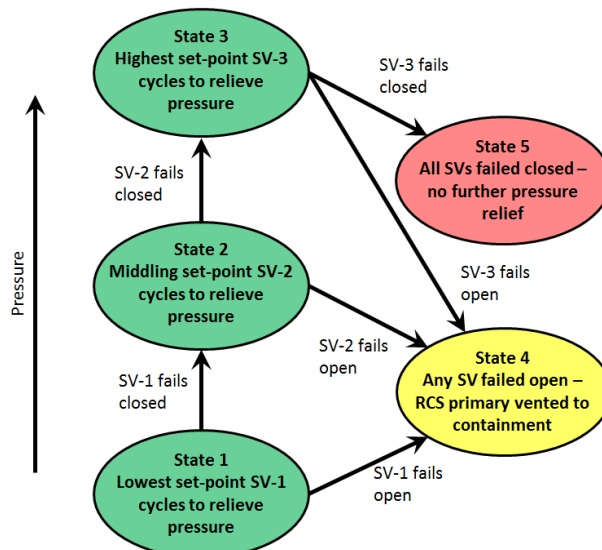


**Figure 4-1 Possible transitions in the 3-SV pressurizer pressure relief system considering both FTO and FTC valve conditions**

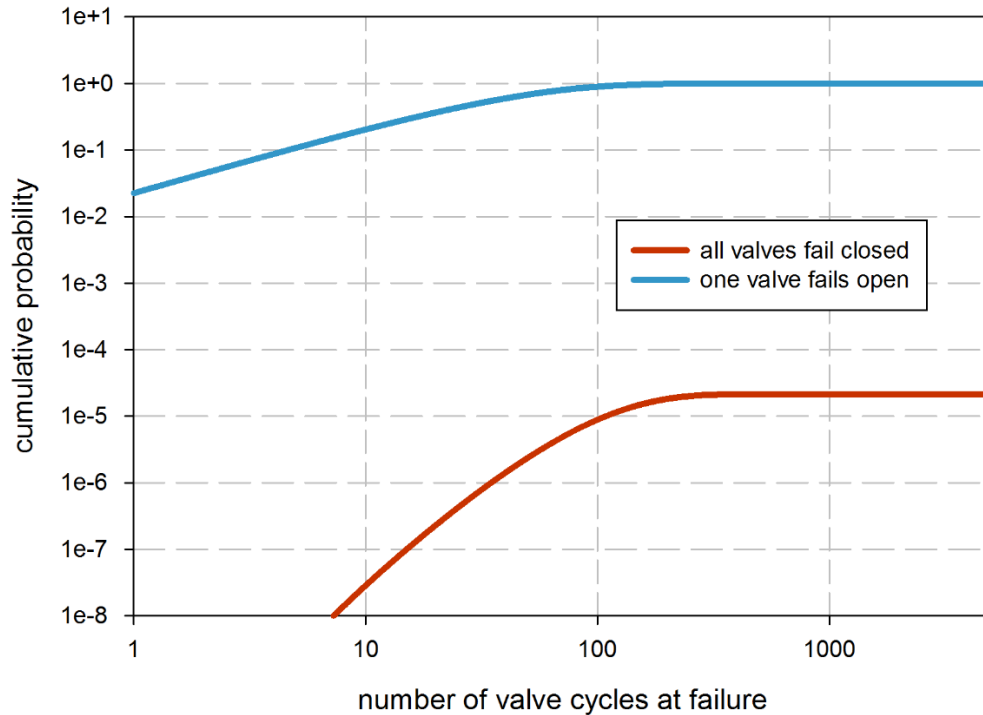


**Figure 4-2 Mean CDF for number of cycles at which any SV of a 3-SV system fails open compared to the mean CDF for number of cycles at which all 3 valves fail**

Figure 4-2 shows the mean SV FTC and FTO distributions associated with the transitions outlined in Figure 4-1. The probability of one valve failing open versus the probability of all 3 valves failing closed is illustrated in the curves. The plot is truncated at 1,000 cycles based on professional judgment that an SV would likely not cycle more than a few hundred times prior to failure. It is noted that a very low possibility that all 3 valves would fail to open was identified, but was never sampled in the 1200 created uncertain realizations. However, failure to open was observed for the lowest set-point SV, and a sensitivity was conducted for all 3 failed closed.

#### 4.1.1.1.1 Primary SV Stochastic Failure to Close (SVLAMFTC)

The probability that a pressurizer SV fails to close conditional on a demand to close is represented in the analysis by SVLAMFTC (e.g., failure of an SV to close is based on a per demand failure probability). The uncertainty is represented by a beta distribution ( $\alpha: 2.5; \beta: 3132.5$ ) with a lower bound of 0 and an upper bound of 1 to model the epistemic uncertainty of the per demand probability of a FTC. The sampling scheme is more complicated, as described below. Failure to close of a pressurizer SV due to excessive cycling would cause the RCS to depressurize. The MELCOR model is configured to open an SV at a specified pressure. An SV closes when pressure drops below 96 percent of its lift pressure.

#### Rationale for Distribution

The epistemic uncertainty distribution for  $p = \text{SVLAMFTC}$  is based on use of Bayes theorem to update the FTC data in Table 4-2 for pressurizer SVs (i.e.,  $n = 17$  FTCs in  $N = 773$  demands). As used in this context, Bayes theorem has the form

$$\pi_2(p | E) = \frac{\pi_1(p)L(E | p)}{\int_0^1 \pi_1(p)L(E | p)dp},$$

Eq. 4-3

where 1)  $E$  is the available evidence supporting possible values for  $p$  (i.e.,  $n = 17$  FTCs in  $N = 773$  demands), 2)  $\pi_1(p)$  is the density function defining the prior distribution for  $p$  (i.e., the distribution for  $p$  prior to evidence  $E$ ), 3)  $L(E|p)$  is the likelihood function (i.e., the probability of observing evidence  $E$  for a given probability  $p$ ), 4) the integral in the denominator is a normalizing term, and 5)  $\pi_2(p | E)$  is the density function defining the posterior distribution for  $p$  (i.e., the distribution for  $p$  after evidence  $E$  is taken into account) (see Sect. 9.3, [39] for details on Bayes theorem).

The prior density function  $\pi_1(p)$  is assumed to correspond to a beta distribution with parameters  $\alpha_1 = 0.5$  and  $\beta_1 = 0.5$ . Specifically,

$$\pi_1(p) = \frac{\Gamma(\alpha_1 + \beta_1)}{\Gamma(\alpha_1)\Gamma(\beta_1)} p^{\alpha_1-1}(1-p)^{\beta_1-1}$$

Eq. 4-4

where  $\Gamma(\alpha_1)$ ,  $\Gamma(\beta_1)$ , and  $\Gamma(\alpha_1+\beta_1)$  are gamma functions. This choice used for  $\pi_1(p)$  corresponds to what is known as Jefferys uninformed beta distribution prior, which is a prior often used in Bayesian analyses when there is limited prior information to support the Bayesian updating indicated in Eq. 4-3 (See Sect. 6.3.2.3.2, [40]). The likelihood function  $L(E|p)$  is based on the assumption that there is a single failure probability  $p$  that applies to all SV demands to close. Specifically,

$$L(E | p) = \frac{N!}{n!(N-n)!} p^n (1-p)^{N-n}$$

Eq. 4-5

with  $N = 773$  and  $n = 17$  is the probability of 17 FTCs in 773 demands to close if the per demand probability of FTC is  $p$  (i.e.,  $L(E|p)$  corresponds to a binomial probability distribution with parameter  $p$ ).

As indicated in Eq. 4-3, the prior density function  $\pi_1(p)$  defined in Eq. 4-4 and the likelihood function  $L(E|p)$  defined in Eq. 4-5 together define the posterior density function  $\pi_2(p | E)$ . A known, computationally convenient form for  $\pi_2(p | E)$  is not immediately obvious from Eq. 4-3. However, it can be shown that  $\pi_2(p | E)$  corresponds to a beta distribution with parameters  $\alpha_2$  and  $\beta_2$  defined by

$$\alpha_2 = \alpha_1 + n \text{ and } \beta_2 = \beta_1 + N - n$$

Eq. 4-6

when  $\pi_1(p)$  corresponds to a beta distribution with parameters  $\alpha_1$  and  $\beta_1$  as indicated in Eq. 4-4 and  $L(E|p)$  corresponds to a binomial distribution with parameter  $p$  as indicated in Eq. 4-5 (Table 9.1, [39]). As a result, the assumed epistemic uncertainty distribution for  $p = SVLAMFTC$  is a beta distribution with parameters  $\alpha$  and  $\beta$  defined by

$$\alpha = 0.5 + n = 0.5 + 17 = 17.5 \text{ and } \beta = 0.5 + N - n = 0.5 + 773 - 17 = 756.5$$

Eq. 4-7

In NUREG/CR-6823, it is recommended that uncertainties associated with the probability of failure on demand be characterized by a beta distribution with the Jefferys non-informative prior distribution [beta (1/2,1/2)] to prevent weak data from biasing the uncertainty in the overall estimate [40]. With regard to the SOARCA best estimate calculation, per-demand FTC probability value was cited as  $P_d = 2.7 \times 10^{-3}$  per-demand based on information provided from the site [3], and the SV FTC was assumed to occur when the CDF value equaled 0.5 (the median of the distribution). This corresponded to a FTC after 256 valve cycles. The Surry report then explains that future PWR calculations should adopt the 'expected value' (calculated as  $1/P_d$ ) as the recommended base case value [3], which was suggested in comments from the SOARCA Peer Review Panel.

The CDF for the beta distribution ( $\alpha=17.5$ ,  $\beta=756.5$ ) developed to characterize the epistemic uncertainty in  $p = SVLAMFTC$  is shown in Figure 4-3. As illustrated in Figure 4-4, each potential value for  $p = SVLAMFTC$  on the abscissa in Figure 4-3 defines a CDF for the number of demands to close at which a pressurizer SV experiences an FTC. In contrast to the CDF in Figure 4-3 that characterizes the epistemic uncertainty in  $p = SVLAMFTC$ , the individual CDFs in Figure 4-4 are characterizing the aleatory uncertainty in the number of demands at which a pressurizer SV experiences an FTC conditional on a specific value for  $p = SVLAMFTC$  (i.e.,  $p = p_{0.05}$ ,  $p_{0.5}$ ,  $p_{0.95}$  or  $\bar{p}$ , where (i)  $p_{0.05} = 1.46 \times 10^{-2}$ ,  $p_{0.5} = 2.22 \times 10^{-2}$  and  $p_{0.95} = 3.20 \times 10^{-2}$  are the 0.05, 0.5 and 0.95 quantile values for  $p = SVLAMFTC$  and (ii)  $\bar{p} = 2.26 \times 10^{-2}$  is the expected value for  $p = SVLAMFTC$ ). This yields a new best-estimate cycles to failure of 45, a significant departure from the original SOARCA analysis. In addition, Figure 4-4 also shows the expected CDF over possible values for  $p = SVLAMFTC$  defined by the points

$$\begin{aligned} \left[ n, \overline{prob}(\tilde{n} \leq n) \right] &= \left[ n, \int_0^1 prob(\tilde{n} \leq n | p) d(p) dp \right] \\ &= \left[ n, \int_0^1 [1 - (1-p)^n] d(p) dp \right] \end{aligned}$$

Eq. 4-8

for  $n = 0, 1, 2, \dots$ , where (i)  $prob(\tilde{n} \leq n | p)$  is the probability that FTC will occur in less than or equal to  $n$  demands to close conditional on probability  $p$  and (ii)  $d(p)$  is the density function for  $p$  (i.e., the density function corresponding to the CDF in Figure 4-3). The red dot along the x-axis shows the value used in the Surry SOARCA analysis [3].

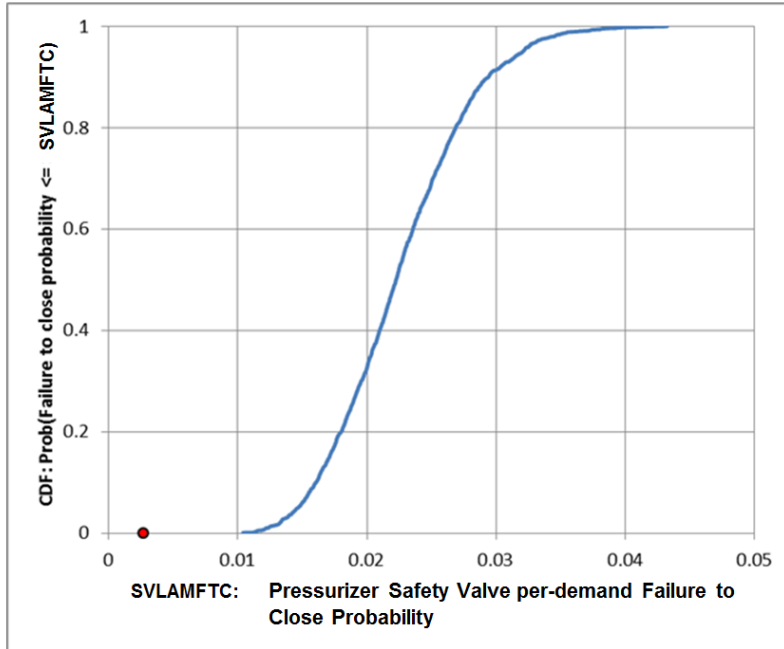


**Figure 4-3** CDF of the beta distribution ( $\alpha = 17.5, \beta = 756.5$ ) developed to characterize the epistemic uncertainty associated with the probability that an individual SV fails to close conditional on a demand to close

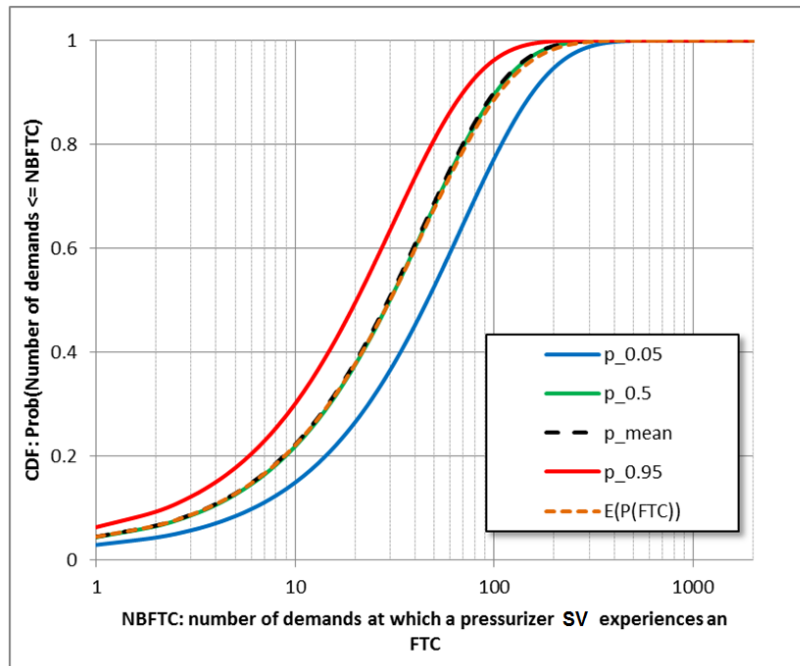


**Figure 4-4** CDFs characterizing uncertainty in the number of demands at which an individual SV fails to close conditional on a specific value of  $p$

#### 4.1.1.1.2 Primary SV Stochastic Failure to Open (SVLAMFTO)

The probability that a pressurizer SV stochastically fails to open conditional on a demand to open is represented in the analysis by SVLAMFTO (e.g., the SV FTO is based on a per demand failure probability). Uncertainty was represented by a beta distribution ( $\alpha: 10.5; \beta: 3132.5$ ) with a lower bound of 0 and an upper bound of 1.

As described above, an SV in the MELCOR model opens at a prescribed pressure and closes when pressure drops below 96 percent of the opening pressure. Logic to open and close a valve was structured such that a failure to open will occur after a certain number of cycles and a failure to close will occur after a different number of cycles. The number of cycles to failure was predetermined uniquely for each of the three valves via a Monte Carlo sampling of the epistemic FTC and FTO uncertainty distributions (modeled as beta distributions) associated with normal SV operation, a single SV FTC, and all SVs FTO.

#### Rationale for Distribution

The epistemic uncertainty distribution for  $p = \text{SVLAMFTO}$  is based on use of Bayes theorem to update the FTO data in Table 4-2 for pressurizer SVs (i.e.,  $n = 0$  FTOs in  $N = 776$  demands to open) in exactly the same manner as described in Eq. 4-3 to Eq. 4-7 for  $p = \text{SVLAMFTC}$ . Specifically, the Bayesian updating procedure described in Eq. 4-3 to Eq. 4-7 for  $p = \text{SVLAMFTC}$  results in a beta epistemic uncertainty distribution for  $p = \text{SVLAMFTC}$  with parameters  $\alpha$  and  $\beta$  defined by

$$\alpha = 0.5 + n = 0.5 + 0 = 0.5 \text{ and } \beta = 0.5 + N - n = 0.5 + 773 = 773.5$$

Eq. 4-9

The only difference between the Bayesian updating procedures for  $p = \text{SVLAMFTC}$  and  $p = \text{SVLAMFTO}$  is that (i) the updating for  $p = \text{SVLAMFTC}$  is performed with  $n = 17$  and  $N = 773$  and (ii) the updating for  $p = \text{SVLAMFTO}$  is performed with  $n = 0$  and  $N = 773$ . The CDF in Figure 4-5 was also developed from the failure data in Table 4-2 and the same updating procedures.

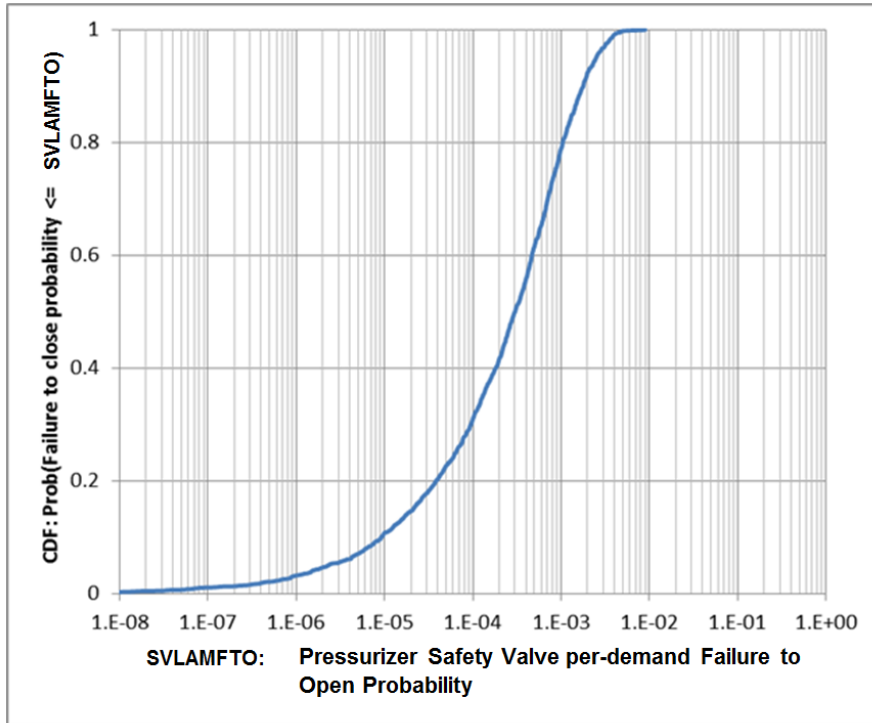


Figure 4-5 CDF of the beta distribution ( $\alpha = 0.5$ ,  $\beta = 773.5$ ) developed to characterize the epistemic uncertainty associated with an individual safety valve failing to open

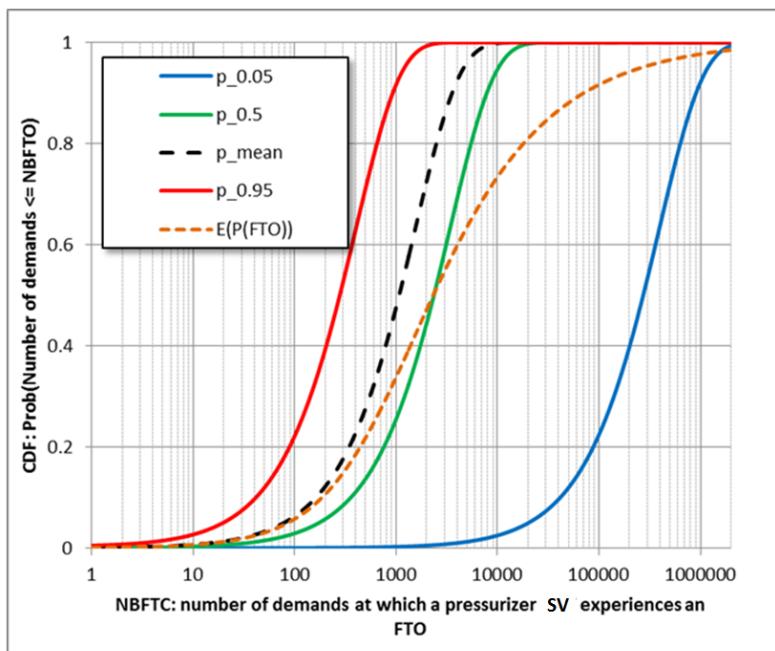


Figure 4-6 CDFs characterizing uncertainty in the number of demands at which an individual SV fails to open conditional on a specific value of  $p$

#### 4.1.1.1.3 Primary SV Failure to Close Due to Passing Water (SVWTR)

The probability that a pressurizer SV stochastically fails to close after a cycle of passing water conditional on a demand to close is represented in the analysis by SVWTR. This approach, described below, considers the potential for the RCS to depressurize by the failing open of a pressurizer SV due to excessive cycling while passing liquid. Uncertainty is represented by a beta distribution ( $\alpha: 0.5; \beta: 4.5$ ) with a lower bound of 0 and an upper bound of 1. This failure mode was not considered in SOARCA.

NUREG-1570 [31] and selected Electric Power Research Institute (EPRI) reports [36] state from the observed damage to an SV passing water, there is a 'possibility' that an SV 'could' fail from passing water. To derive a failure model, EPRI reviewed failure rate data used in IPEs, results from a series of EPRI-sponsored tests conducted on seven pressurizer safety valves (PSVs) in the early 1980s, and reviewed limited operating experience reported in NRC information notices and license event reports. EPRI assessed the PSV failure rates per demand to be  $2.7 \times 10^{-2}$  for steam cycles and  $1.1 \times 10^{-1}$  for liquid cycles. In the aggregate, the EPRI model indicates that the PSV will fail to reclose during the boil-down phase at a total likelihood of 0.69 to 0.98 (for PSVs with dead bands of 15 and 5 percent, respectively) [31]. In NUREG-1570, NRC staff noted that the failure rates derived by EPRI were based on the assumption that the limited valve damage observed in the EPRI-sponsored tests led to the valves failure to reclose. NRC staff also noted there was insufficient evidence to conclude that the instances of valve damage observed in the tests constitute a failure to reclose. Specifically, the test documentation did not indicate that the valves failed to reclose in any of the tests, or that the observed damage would prevent continued operation of the valves. Staff concluded that the fraction of sequences involving early power operated relief valve/safety valve failure (about 14 percent, according to the plant damage state information for Surry) provided a reasonable basis for the scoping assessment.

The failure mode, where an SV fails to close due to an excessive number of cycles when it passed liquid, is based on a per-demand probability. If an SV lifts when water level is within 1.45 inches of the top of the pressurizer, the valve cycle is counted as one where the valve passed liquid. 1.45 inches is the diameter of the piping in the MELCOR model leading to an SV.

#### Rationale for Distribution

The epistemic uncertainty in SV FTCW per-demand failure probability is described by the beta distribution in Figure 4-7 with parameters  $\alpha = 0.5$  and  $\beta = 4.5$  and employs the methodology provided in NUREG/CR-6928. The epistemic uncertainty distribution for  $p = \text{SVWTR}$  is based on two assumptions. First, based on analyst judgment, it was decided that FTCW would not occur for the first 10 demands involving passing water, where "passing water" is assumed to mean a release in which the void fraction is less than 0.5. Second, after the first 10 events involving passing water, the epistemic uncertainty in  $p = \text{SVWTR}$  is assumed, based on analyst judgment, to be characterized by a beta distribution with parameters  $\alpha = 0.5$  and  $\beta = 4.5$  as developed and presented in Section A.2.42 and Table 5.1 of NUREG-1570.

The CDF for the beta distribution ( $\alpha = 0.5, \beta = 4.5$ ) developed to characterize the epistemic uncertainty in  $p = \text{SVWTR}$  is shown in Figure 4-7. As illustrated in Figure 4-8, each potential value for  $p = \text{SVWTR}$  on the abscissa in Figure 4-7 defines a CDF for the number of demands to open at which a pressurizer SV experiences an FTCW; these CDFs also include the assumed zero probability of FTCW for the first 10 demands to close when passing water. In contrast to the CDF in Figure 4-7 that characterizes the epistemic uncertainty in  $p = \text{SVWTR}$ , the individual CDFs in Figure 4-8 are characterizing the aleatory uncertainty in the number of

demands at which a pressurizer SV experiences an FTCW conditional on a specific value for  $p = \text{SVWTR}$ . In addition, Figure 4-8 also shows the expected CDF over possible values for  $p = \text{SVWTR}$  defined by the points for  $n = 0, 1, 2, \dots$ ,

$$\begin{aligned} \left[ n, \overline{\text{prob}}(\tilde{n} \leq n) \right] &= \left[ n, \int_0^1 \text{prob}(\tilde{n} \leq n | p) d(p) dp \right] \\ &= \left[ n, \int_0^1 [1 - (1-p)^n] d(p) dp \right] \end{aligned}$$

Eq. 4-10

Where: (i)  $\text{prob}(\tilde{n} \leq n | p)$  is the probability that FTCW will occur in less than or equal to  $n$  demands to close conditional on probability  $p$  and (ii)  $d(p)$  is the density function for  $p$  (i.e., the density function corresponding to the CDF in Figure 4-7).

An analysis of industry-average data for SV FTCW performance is documented in NUREG/CR-6928 [38], but is not based on any observed failures for either SVs or code safety valves (SVVs). Instead SV FTCW is an average of the 95<sup>th</sup> percentiles of the NUREG/CR-6928 FTC data entries. NUREG/CR-6928 computed an estimated per-demand failure probability described in Table 5-1 (SV FTCW) with a mean value of  $Pd = 1.00 \times 10^{-1}$  per-demand with 5<sup>th</sup> and 95<sup>th</sup> percentile values of  $4.62 \times 10^{-4}$  and  $6.02 \times 10^{-1}$  per-demand, respectively.

Since failure of a SV caused by passing water has never been observed and the likelihood of a SV failing after a single cycle of water passing through is negligible, a piecewise failure probability is created. The team's engineering judgment assumes there is no failure for the first ten valve cycles in which the SV passes water. Thus, for the first ten cycles, it is assumed that the per-demand failure probability is zero. Figure 4-8 shows as examples the mean, 5<sup>th</sup>, 50<sup>th</sup>, and 95<sup>th</sup> percentile piecewise CDFs created with the negative binomial sampling methodology using the distribution from Figure 4-7 and assuming that the first ten valve cycles passing liquid do not cause a failure to close. This yields a unique number of cycles to failure for each MELCOR realization.

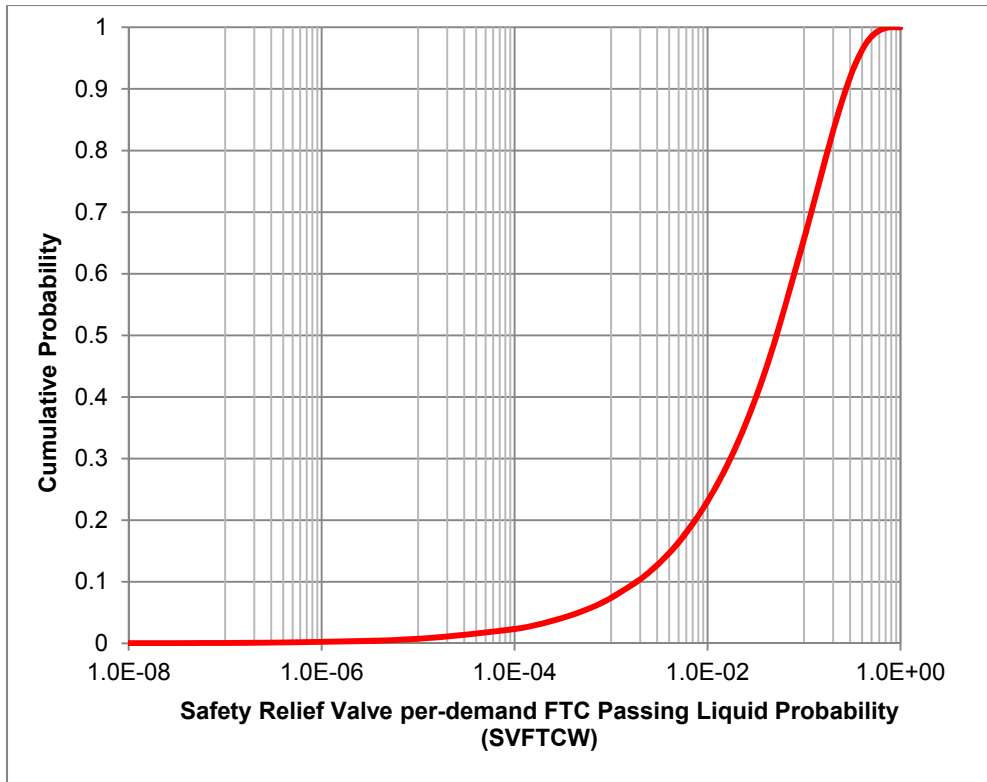


Figure 4-7 CDF of SV FTCW valve cycle per-demand failure probability

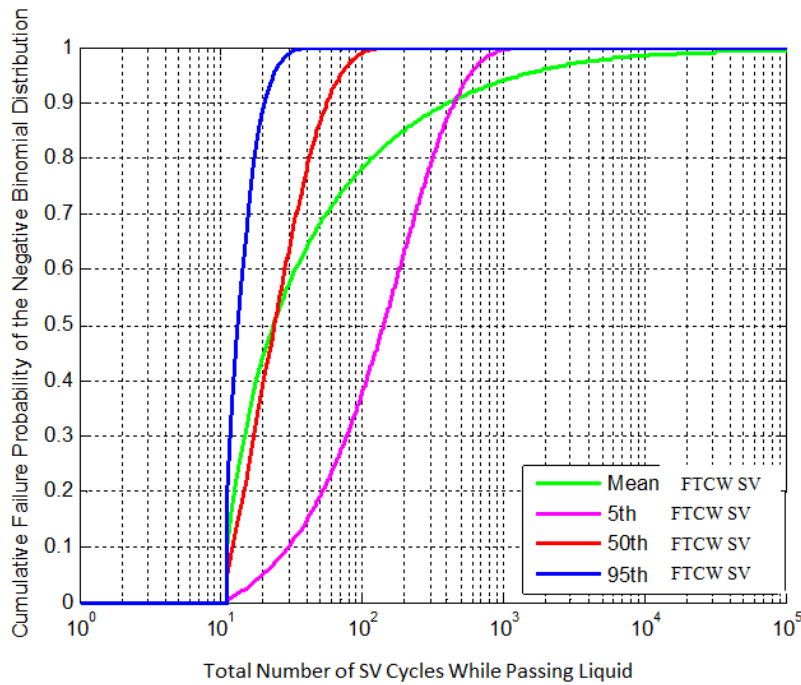


Figure 4-8 Mean, 5<sup>th</sup>, 50<sup>th</sup>, and 95<sup>th</sup> percentile CDFs of SV FTCW as a function of valve cycles

#### 4.1.1.1.4 Secondary SV Stochastic Failure to Close (SVLAMFTC-SG)

The probability that a secondary SV fails to close conditional on a demand to close is represented in the analysis by SVLAMFTC-SG (e.g., failure of an SV to close is based on a per demand failure probability). This parameter is identified as SG\_B\_SV\_cycl in the regression tables in Section 6.1. Appendix A.2.42 of NUREG/CR-7037 [30], points out that RCS primary side SVs and RCS secondary side SVs do not differ physically and includes instances of successful and failed operation without regard to whether a valve was mounted off a pressurizer or off a main steam line. The sampling described above for the failure of a primary side SV to close was therefore adopted identically in the sampling for the failure of a secondary side SV to close. The failure of the lowest-set-point SV of the 5 SVs mounted off each of the 3 main steam lines was so sampled. The sampling was done individually such that for each realization there was a distinct number of cycles after which a failure to close would result in the case of each of the lowest set-point SV on all 3 steam lines.

#### 4.1.1.1.5 Implementation of Stochastic SV Failure

The mathematical approach for the four epistemically uncertain probabilities for SV failure described above was incorporated into the Surry MELCOR calculations as presented below. To simplify the equations below, parameter descriptions are defined by  $p_{fc}$ ,  $p_{fo}$ ,  $p_{fcl}$ ,  $p_{fcsg}$ , where:

$p_{fc}$  = SVLAMFTC (Primary SV Stochastic Failure to Close): Probability (unitless) that a pressurizer SV will fail to close conditional on a demand to close.

$p_{fo}$  = SVLAMFTO (Primary SV Stochastic Failure to Open): Probability (unitless) that a pressurizer SV will fail to open conditional on a demand to open.

$p_{fcl}$  = SVWTR (Primary SV Failure to Close Due to Passing Water): Probability (unitless) that a pressurizer SV will fail to close conditional on a demand to close when discharging liquid after the 10<sup>th</sup> discharge of liquid.

$p_{fcsg}$  = SVLAMFTC-SG (Secondary SV Stochastic Failure to Close): Probability (unitless) that a steam generator SV will fail to close conditional on a demand to close.

The above variables and their associated distributions define the epistemic uncertainty in distributions that characterize the aleatory uncertainty in the number of demands that can be placed on an SV before it fails to perform a specified demand. Specifically, if  $p$  is the probability that an SV will fail conditional on a demand to operate, then the CDF for the demand  $N$  on which the SV fails to perform appropriately is

$$prob(N \leq n | p) = 1 - (1 - p)^n,$$

Eq. 4-11

where  $prob(N \leq n | p)$  is the probability that the demand (i.e., demand  $N$ ) on which the SV fails to perform its intended operation satisfies the inequality  $N \leq n$ . As discussed in conjunction with Eq. 4-13,  $p = p_{fc} + p_{fo}$  is used in Eq. 4-11 instead of separate use of  $p = p_{fc}$  and  $p = p_{fo}$  as a

way to incorporate the fact that  $p_{fc}$  and  $p_{fo}$  together define a “competing risk” problem in which an SV has the potential to fail by one of two mutually exclusive failure modes (i.e., FTC and FTO).

The analysis uses a sampling based approach to incorporate the effects of  $nV = 23$  epistemically uncertain variables, of which four are  $p_{fc}$ ,  $p_{fo}$ ,  $p_{fcl}$  and  $p_{fcsg}$ . Specifically, a sample

$$\begin{aligned} \mathbf{x}_i &= [x_{1i}, x_{2i}, \dots, x_{nV,i}], i = 1, 2, \dots, nE \\ &= [x_{1i}, \dots, p_{fc,i}, p_{fo,i}, p_{fcl,i}, p_{fcsg,i}, \dots, x_{nV,i}] \end{aligned}$$

Eq. 4-12

of size  $nE$  (e.g.,  $nE = 1003$  successful realizations) is used to propagate the effects of the indicated epistemically uncertain variables through MELCOR. However, a conceptual and computational challenge exists with respect to the propagation of the effects of the failure-on-demand probabilities  $p_{fc,i}$ ,  $p_{fo,i}$ ,  $p_{fcl,i}$  and  $p_{fcsg,i}$  because these probabilities are not single scalar quantities that must be propagated through MELCOR but rather, in effect, are designators for distributions of the form indicated in Eq. 4-11 that characterize aleatory uncertainty in the per demand failure of SVs.

A full incorporation of the aleatory uncertainty characterized by  $p_{fc,i}$ ,  $p_{fo,i}$ ,  $p_{fcl,i}$  and  $p_{fcsg,i}$  would require the generation and subsequent propagation through MELCOR of samples (e.g., random or stratified) of size  $nA$  from the distributions  $prob(N \leq n | p_i)$ ,  $p_i = p_{fc,i}$ ,  $p_{fo,i}$ ,  $p_{fcl,i}$  and  $p_{fcsg,i}$ , as defined in Eq. 4-11. As an example, the number of required MELCOR calculations would be 15,000 for  $nE = 300$  and  $nA = 50$ , which is not practical with the current state of modeling.

The use of  $p_{fc,i}$  and  $p_{fo,i}$  to obtain failure values (i.e., number of demands at SV failure and status of SV at failure) for the three pressurizer SVs at Surry is described below. Due to the approximate equality  $1 \cong 1 - p_{fo,i}$ ,

$$p_{f,i} = p_{fo,i} + (1 - p_{fo,i})p_{fc,i} \cong p_{fc,i} + p_{fo,i}$$

Eq. 4-13

is a reasonable approximation to the probability that a SV will fail conditional on a demand to operate. Given the reasonableness of the approximation in Eq. 4-13, the distribution

$$prob(N \leq n | p_{f,i}) = 1 - (1 - p_{f,i})^n$$

Eq. 4-14

is independently sampled 3 times to obtain the numbers  $N_{1i}$ ,  $N_{2i}$  and  $N_{3i}$  of demands at which SVs 1, 2 and 3, respectively, fail. In addition, it is necessary to determine the failure status (i.e., FTC or FTO) of each SV. Specifically, the probabilities

$$\frac{P_{fc,i}}{P_{fc,i} + P_{fo,i}} \quad \text{and} \quad \frac{P_{fo,i}}{P_{fc,i} + P_{fo,i}}$$

Eq. 4-15

for FTC and FTO, respectively, conditional on SV failure are used to sample the type of failure that occurred for each SV failure. As a result of this sampling, each potential SV failure has an associated status value defined by

$$s = \begin{cases} ftc & \text{for a "failure to close" failure} \\ fto & \text{for a "failure to open" failure} \end{cases}$$

Eq. 4-16

The results of the indicated sampling are 'status values' at failure  $s_{1i}$ ,  $s_{2i}$  and  $s_{3i}$  for the 3 SVs. Specifically, a single sampled vector

$$sv_i = [N_{1i} \cdot s_{1i} \cdot N_{2i} \cdot s_{2i} \cdot N_{3i} \cdot s_{3i}]$$

Eq. 4-17

of SV properties is generated for the sampled values  $p_{fc,i}$  and  $p_{fo,i}$  as indicated in conjunction with Eq. 4-13 to Eq. 4-16.

The use of  $p_{fcl,i}$  to obtain failure values due to passing liquid (i.e., number of demands at FTC) for the 3 pressurizer SVs is similar to the use of  $p_{f,i}$  to obtain  $N_{1i}$ ,  $N_{2i}$  and  $N_{3i}$  for the 3 SVs. Specifically, the distribution

$$prob(N \leq n | p_{fcl,i}) = 1 - (1 - p_{fcl,i})^n$$

Eq. 4-18

is independently sampled 3 times to obtain the numbers  $INL_{1i}$ ,  $INL_{2i}$  and  $INL_{3i}$  of demands after an initial 10 liquid discharges at which SVs 1, 2 and 3, respectively, fail due to passing liquid. In turn, the actual number of liquid discharges at which SV  $j$  fails is given by

$$NL_{ji} = 10 + INL_{ji}$$

Eq. 4-19

for  $j=1, 2, 3$ . In summary, a single sampled vector

$$svl_i = [NL_{1i} \cdot NL_{2i} \cdot NL_{3i}]$$

Eq. 4-20

of SV demands at failure due to passing liquid is generated for each sampled value  $p_{fcl,i}$  as indicated in conjunction with Eq. 4-18 and Eq. 4-19.

The use of  $p_{fcsg,i}$  to obtain failure values (i.e., number of demands at FTC) for the lowest set-point SV on each MSL is identical to obtain  $N_{1i}$ ,  $N_{2i}$  and  $N_{3i}$  for the 3 pressurizer SVs. Specifically, the distribution

$$prob(N \leq n | p_{fcsg,i}) = 1 - (1 - p_{fcsg,i})^n$$

Eq. 4-21

is independently sampled 3 times to obtain the numbers  $NSG_{Ai}$ ,  $NSG_{Bi}$ , and  $NSG_{Ci}$  of demands after which the lowest set-point SV on MSL A, MSL B, and MSL C, respectively, fail to close due to repeated cycling. Specifically, a single sampled vector

$$sg_i = [NSG_{Ai} \cdot NSG_{Bi} \cdot NSG_{Ci}]$$

Eq. 4-22

of SG SV demands at failure is generated for each sampled value  $p_{fcsg,i}$ .

Once the vectors  $sv_i$ ,  $svl_i$ , and  $sg_i$  have been generated, they in effect replace  $p_{fc,i}$ ,  $p_{fo,i}$ ,  $p_{fcl,i}$  and  $p_{fcsg,i}$  in the sample indicated in Eq. 4-12. Specifically, the sample in Eq. 4-12 now becomes

$$\begin{aligned} x_i &= [x_{1i}, \dots, sv_i \cdot svl_i \cdot sg_i, \dots, x_{nVi}], i = 1, 2, \dots, nE \\ &= [x_{1i}, \dots, N_{1i} \cdot s_{1i} \cdot N_{2i} \cdot s_{2i} \cdot N_{3i} \cdot s_{3i} \cdot NL_{1i}, NL_{2i}, NL_{3i}, NSG_{Ai}, NSG_{Bi}, NSG_{Ci}, x_{nVi}] \end{aligned}$$

Eq. 4-23

which is the sample that is actually propagated through the MELCOR calculations. Due to this replacement, the individual identities and effects of  $p_{fc,i}$ ,  $p_{fo,i}$ ,  $p_{fcl,i}$  and  $p_{fcsg,i}$  are effectively lost in the resultant MELCOR calculations.

As shown above, the algorithm that led to the sample in Eq. 4-23 is easy to describe; however, exactly what has been done at a conceptual level is not easy to formally describe. In a broad sense, a probability space is being introduced with elementary events of the form

$$\begin{aligned} \mathbf{s} &= [sv, svl, sg] \\ &= [N_1 \cdot s_1 \cdot N_2 \cdot s_2 \cdot N_3 \cdot s_3 \cdot NL_1, NL_2, NL_3, NSG_A, NSG_B, NSG_C] \end{aligned}$$

Eq. 4-24

and the sample space  $\Sigma$  corresponding to all possible values for  $\mathbf{s}$ . The sample space  $\Sigma$  is easy to define as each demand value (i.e.,  $N_1, N_2, N_3, NL_1, NL_2, NL_3, NSG_A, NSG_B, NSG_C$ ) is a positive integer and each failure condition (i.e.,  $s_1, s_2, s_3$ ) can have only one of two possible values. However, definition of the probability measure  $p_S$  for the elements (i.e., events) contained in the set and the corresponding density function  $d_{\mathbf{s}}(\mathbf{s})$  defined on  $\Sigma$  is difficult due to the epistemic uncertainty distributions for  $p_f = p_{fc} + p_{fo}, p_{fcl}$  and  $p_{fcsg}$  and the aleatory uncertainty distributions for  $\mathbf{sv}, \mathbf{svl}$  and  $\mathbf{sg}$  that are conditional on specific values for  $p_f = p_{fc} + p_{fo}, p_{fcl}$  and  $p_{fcsg}$ .

The assumed inherent variability associated with the elements of  $\mathbf{s}$  is aleatory uncertainty. However, as indicated above, the distribution that characterizes this uncertainty is actually based on a comingling of both aleatory uncertainty and epistemic uncertainty. Given that one value for  $\mathbf{s}$  is included in each sample element for propagation through MELCOR as indicated in Eq. 4-23, the distribution for  $\mathbf{s}$  is, in effect, being treated as if it is characterizing epistemic uncertainty. More broadly, for these variables, the MELCOR analysis for Surry is not making a distinction between distributions that characterize aleatory uncertainty and distributions that characterize epistemic uncertainty. Rather, all distributions are being sampled once for each sample element as is done in the propagation of epistemic uncertainty. In contrast, a more complex situation exists when a distinction is maintained between the effects and implications of aleatory uncertainty and the effects and implications of epistemic uncertainty. Specifically, maintaining a distinction between aleatory uncertainty and epistemic uncertainty requires a “two loop” analysis, with the outer loop over epistemic uncertainty and the inner loop over aleatory uncertainty conditional on specific realizations of epistemic uncertainty (e.g., as will be done in the MACCS analyses for Surry).

#### 4.1.1.2 SV Thermal Failure

An SV will exhibit a FTC if the SV temperature reaches a sampled high temperature limit which allows the valve components to heat up to possible damage conditions. It is anticipated that heat up and thermal expansion of the SV would occur primarily during periods of gas flow (open cycles), although penetration (conduction) of heat transferred to inner surfaces would occur at all times (valve open or closed). The pressurizer SV thermal FTC is analyzed along with the pressurizer SV thermal FTC open area fraction.

##### 4.1.1.2.1 Primary SV Thermal Failure to Close (SVFAILT)

The temperature at which a pressurizer SV will experience thermal FTC is represented by SVFAILT. Uncertainty of SVFAILT is represented by a beta distribution ( $\alpha: 5; \beta: 10.7615$ ) with a lower bound of 811 K and an upper bound of 1422 K. Uncertainty related to the FTC due to thermal load exists for Crosby SVs [90]. The Crosby SV design is a spring loaded valve that ‘pops’ open to relieve RPV pressure, and then gradually closes as internal pressure decreases. The variable valve stem position (or valve open fraction) allows RCS pressure to be maintained close to a target value until RCS pressure reduces below a minimum setpoint when the valve closes.

The effect of high temperature to valve seizure causes softening or reduction of strength in stainless steel at temperatures greater than ~1000 °F (811 K) and a suggested maximum temperature that could be experienced by the SV is about 1600 °F (1144 K) [90].

EPRI performed an SV thermal analysis in early 2000 [99]. The conclusion from this analysis is the spring rate decreases with increasing temperature, which in turn decreases the valve lift pressure. A correlation for the percent change of the spring rate as a function of temperature is given:  $1.6879 - 0.02409 * T$ , where T is in °F. Although the test was conducted for spring temperatures from 50 to about 350 °F, an extreme extension of the correlation suggests significant change of spring rate (> 35%) at T > 1600 °F (1144 K) the maximum SV temperature given above.

The MELCOR model is setup to cause the SVs to open at predetermined pressures with specified flow rates. The SVs will close when pressure drops below 96 percent of their opening pressure. This model sets the SVs to FTC based on a per-demand failure probability.

### **Rationale for Distribution**

A beta distribution was created for SVFAILT based on failure information, which is similar to the methodology in NUREG/CR-7155 for SV FTC due to thermal failure. Failure by thermal expansion is not likely to occur until temperatures exceed 1000 K [3]. A mean of 900 K was recommended for failure by material deformation. The EPRI study describes that significant change in spring rate would occur by 1144 K. These references are in general agreement with temperatures near 1000 K for failure.

An initial criterion for high-temperature valve failure was based on manufacturers' information describing the strength of stainless steel, published by the Stainless Steel Information Center<sup>10</sup>. Softening or loss of strength of stainless steel (300 series) was described to start to occur at 'about 1000 °F' (811 K). This provides the lower bound for the distribution. The median temperature used in this distribution is 1000 K, also used in the Surry SOARCA analysis [3], which agrees with the failure temperatures given above. Given that material deformation would be expected at the hot working temperature of 304 stainless steel, between 1149-1260°C [100], a physical upper bound limit for plastic deformation is based on the lower end of this temperature range, 1422 K.

The parameters of the beta distribution (alpha=5, beta=10.7615) were set to provide the majority of sampling close to the median value of 1,000 K, which is supported by the range of failure temperature data previously described. The distribution is shaped such that the suggested maximum temperature of 1144K is calculated at the 97<sup>th</sup> percentile. However the distribution still allows for limited sampling up to the physical upper limit of 1422 K. Once the temperature of a heat structure representing the SV reaches the determined temperature limit shown in Figure 4-9, the SV will fail to close on the next cycle. The Surry SOARCA value is shown in Figure 4-9 at the 0.5 CDF.

---

<sup>10</sup> [www.ssina.com/composition/temperature.html](http://www.ssina.com/composition/temperature.html)

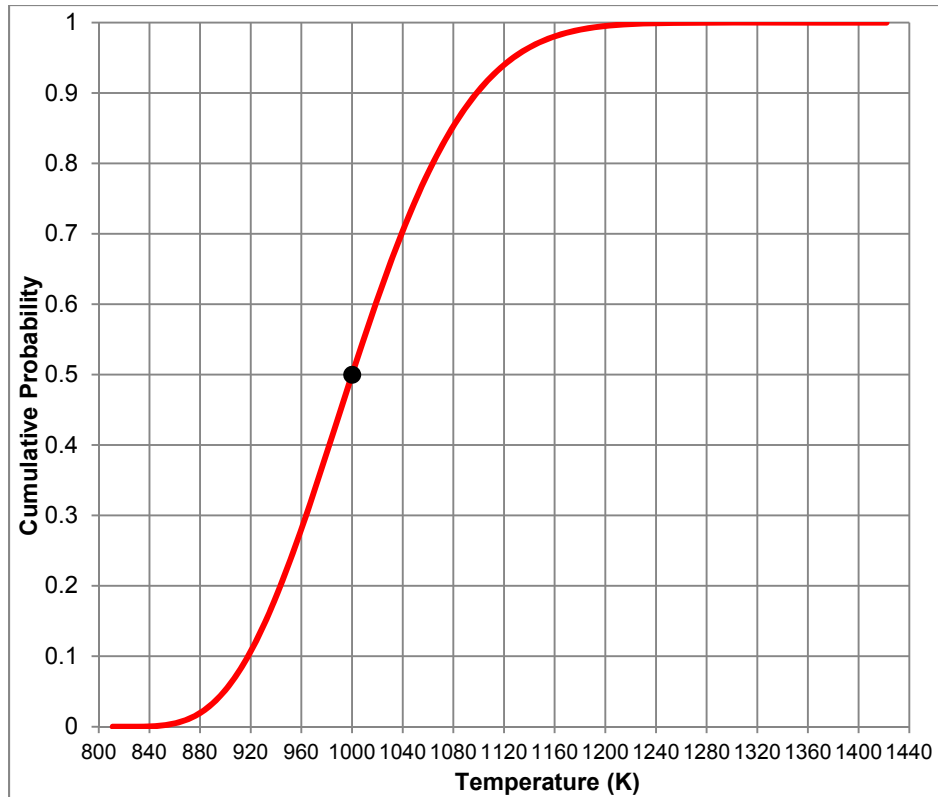


**Figure 4-9 CDF for the temperature for SV thermal FTC after one valve cycle at a specified temperature**

### 4.1.1.3 SV Open Fraction

#### 4.1.1.3.1 SV Open Area Fraction (SVOAFRAC)

Uncertainty in the partially open position that an SV would assume given a stochastic or overheating FTC is addressed through the sampled variable SVOAFRAC. This variable is the fraction of the fully open flow area of an SV that remains open to flow (normally choked) given a stochastic or overheating failure of the valve to fully reseal. It was applied to the failed operation of the SVs atop the pressurizer and on the main steam lines (MSLs) in the MELCOR model. The application of SVOAFRAC varied somewhat between different SVs in the model.

The application of SVOAFRAC to the pressurizer safety valves differed depending upon whether a valve failed to close stochastically or from overheating. If failed from overheating, the uncertainty was modeled as a purely epistemic uncertainty and the sampled value of SVOAFRAC was applied identically to any SV that failed from overheating. If failed stochastically, the sampled value of SVOAFRAC was applied identically in the case of SV 1 and in the case of SV 3 but in the case of SV 2, the compliment of SVOAFRAC (i.e., 1 minus SVOAFRAC) was applied. This was done to prevent the unlikely physical situation where all 3 valves fail stochastically (where an epistemic correlation should not be applicable) in a nearly closed condition.

In applying SVOAFRAC given a stochastic failure of an SV on the MSLs to close, the intention was to set the open area fraction of a failed lowest set-point valve on MSLs A or C to the

compliment of the sampled value of SVOAFRAC. Then, so as not to affect all 3 steam generators with identical SV failure position, open area fraction for the lowest set-point SV on MSL B given an FTC was set to SVOAFRAC. Logic errors in the MELCOR model, however, allowed valves on MSLs A and C to fail only in the fully closed position. Open area fraction in the case of the lowest set-point SV on MSL B was accomplished per intention. Overheating failures of MSL SVs were not considered.

A uniform distribution was assumed in the sampling of SVOAFRAC given no known information on the likelihood of any particular area fraction being greater than another. Some considerations relative to mechanisms that might be at work as a valve overheats to failure are discussed below, but they are not suggestive of particular open area fractions being more likely. A lower bound of 0.01 was imposed in the sampling of SVOAFRAC realizing that stuck valves in the fully closed position are addressed in the UA by the failure-to-open (FTO) mode of SV failure.

In considering the implications of the variability in SV open fraction given an FTC, it is pertinent that in the MELCOR calculations:

- No SV overheating failures occurred
- Leakage past the MSIVs depressurized the steam generators before the onset of core damage whether or not a MSL SV fails to close.

#### **Rationale for Distribution**

As mentioned above, there is no known information on the likelihood of any particular open flow area fraction being more likely than another for an SV to present following an FTC. With respect to an overheating failure, there may be related considerations such as the temperature of 811 K being associated with the softening of stainless steel. Possibly above this temperature forces developed at the extremes of valve movement could cause material deformation and valve seizure at fully open or fully closed (yet leaky) positions. Or maybe differential thermal expansion of close-tolerance parts could seize a valve most likely while passing hot gas in a fully open position. Yet such seizure could relieve if the valve cooled allowing its normal function to possibly return. Possibly thermal softening of an SV's return spring could keep a valve from completely reseating. None of these considerations, however, seems quantifiable with respect to likelihood. Consequently, a uniform distribution between 0.01 and 1.0 was selected as best representative of the uncertainty associated with open fraction following an overheating failure of a SV. The distribution is shown in Figure 4-10 with the black dot representing the original Surry SOARCA value.

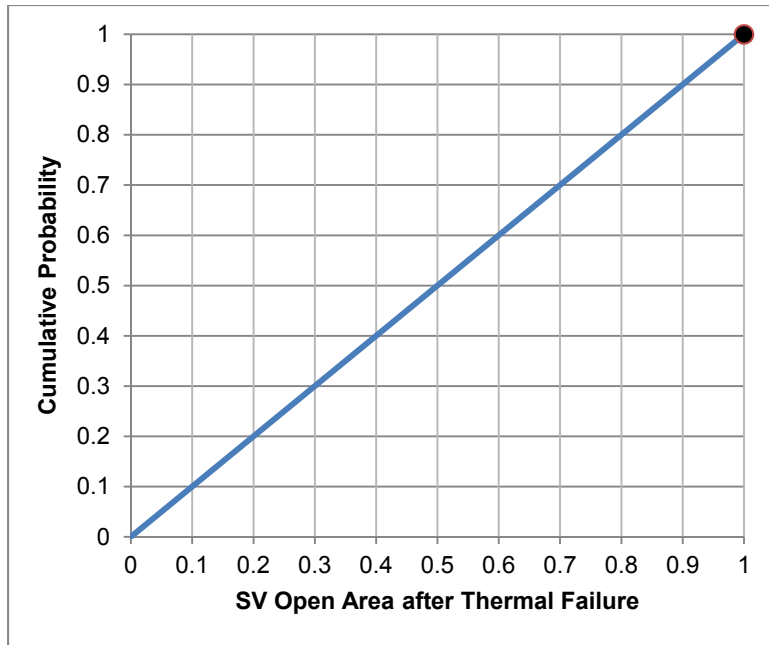


**Figure 4-10 CDF for the SV thermal FTC open area fraction**

#### **4.1.1.4 Reactor Coolant Pump Seal Leakage (RCPSL)**

The reactor coolant pump seal leakage rates upon loss of seal cooling system are represented by RCPSL. Specifically, the potential for above nominal leakage 13 minutes into the accident transient is sampled. A discrete distribution is used to represent uncertainty with probabilities for each of 4 different leakage rates. The uncertainty in the flow rate of reactor coolant pump (RCP) seal leakage can change the evolution of an accident scenario by precluding failure of the SVs. As observed in the Surry SOARCA STSBO analysis [3], when the RCP seal leak rate increases above 21 gpm, the primary depressurizes at a sufficient rate that there is no longer a demand on the SVs.

Under normal operating conditions, cooling water is supplied to the RCP seals at a higher pressure than the primary. As a result, the water keeps the RCP seals cool while preventing any primary coolant from flowing up the RCP shaft and contaminating areas outside the primary boundary. When a loss of AC power occurs, the RCP seal cooling system no longer supplies cooling water and as a result, primary coolant begins leaking along the RCP shaft through the mechanical seals at a 21 gpm per RCP flow rate for pressures near operating pressure (based on calculation from a Westinghouse Owners Group model [40]). In the uncertainty analysis, RCP seal leakage begins at 21 gpm per pump for all sequences [41]. As the primary system heats up, the mechanical seals begin to thermally degrade, resulting in higher leak rates estimated at 76 gpm, 182 gpm, or 480 gpm per RCP as described in NUREG-1953, Table 13 [43]. The leakage rates described with this parameter are related to steady state primary system pressure; as the pressure changes the model will adjust the leakage accordingly. Both the 21 gpm per RCP and 182 gpm per RCP leak rates were used in the SOARCA analysis [3].

## Rationale for Distribution

In this Surry UA, the four discrete leak rates assumed in NUREG-1953, Table 13, occurring at 13 minutes [43] are sampled. The probability of occurrence for each leak rate is also taken directly from Table 13 and is based on work done by the Westinghouse Owners Group [42]. A summary of the leak rates, times of occurrence, and probabilities are given in Table 4-3. While there will be a very limited number of realizations with leakage of 76 or 480 gpm per RCP there is no technical justification to adjust these probabilities.

**Table 4-3 RCP seal leak probabilities at operating pressure.**

Time = 0 min	Time ≥ 13 min	Probability
21 gpm/RCP	21 gpm/RCP	0.79
21 gpm/RCP	76 gpm/RCP	0.01
21 gpm/RCP	182 gpm/RCP	0.1975
21 gpm/RCP	480 gpm/RCP	0.0025

### 4.1.1.5 Normalized Temperature of the Hottest Steam Generator Tube

The normalized SG tube temperature is represented by this parameter, which along with the MELCOR-calculated hot leg and cold tube temperatures is used to determine the time-dependent hottest tube temperature applied to the single tube model. The uncertainty of the normalized temperature is represented with a beta distribution that has parameters of  $\alpha=43.7$  and  $\beta=54.9$ . The lower and upper bounds were established at the normalized limits of 0.0 and 1.0, but are effectively reduced by the distribution parameters.

The NRC and industry have been studying SG tube ruptures for decades because of their importance in maintaining the RCS pressure boundary [31][32]. In particular, a tube failure during a severe accident has the potential for radioactive release to the environment that bypasses containment. At high temperature conditions during a severe accident, natural circulation flow patterns are established where high temperature gases from the core circulate into the hot leg and SG. The effectiveness of the high temperature gases to heat the SG tubes is an important factor in determining their failure. The NRC and industry performed 1/7<sup>th</sup> scale experimental tests to characterize the natural circulation flows between the vessel and the steam generator [33][34]. The tests were studied using computational fluid dynamics techniques [44]. The computational fluid dynamic techniques were subsequently scaled to full plant geometry and severe accident conditions. In NUREG-1922 [46], modeling parameters were developed to characterize the natural circulation for lumped parameter codes. Specific recommendations were developed for (a) the hot leg discharge coefficient, (b) the SG mixing fraction, (c) the ratio of the hot leg flow to the SG recirculation flow, (d) the percentage of tubes involved in up-flow versus the circulatory return flow ratio, (e) the bounding normalized temperature of the hottest tube, and (f) the hot and cold stream flow split into the surge line. The computational fluid dynamics calculations included sensitivity studies to provide an estimate of the variation in these parameters under a variety of conditions and assumptions [46]. The following conclusions were drawn from the NUREG-1922 sensitivity studies.

- a. the hot leg discharge coefficient remained relatively constant with maximum variations of less than 8 percent,

- b. the SG mixing fraction was found to vary by only a few percent over the range of conditions considered,
- c. the recirculation ratio is not sensitive to the secondary side temperature,
- d. the hot tube fraction was difficult to predict with confidence because some of the tubes change direction. However, the hottest tube region was not significantly affected by changes in the overall size and shape of the hot tube region,
- e. the normalized temperature of the hottest tube is a significant parameter because it refers to the portion of the tube bundle where the thermal loading is most severe. The sensitivity of this parameter to changes in the modeling parameters was significant.
- f. the tube bundle heat-transfer rate was found to impact the recirculation ratio in previous work. However, the reasonable variations around best estimate heat transfer conditions are well characterized by a recirculation ratio of 2.4.

Based on these conclusions, the normalized temperature ( $T_n$ ) of the single hottest tube was selected as the most significant parameter for use in this uncertainty study. The observed variation of  $T_n$  in the computational fluid dynamics calculations is partly due to variations in the recirculation ratio and the SG mixing fraction. Hence, the variability in  $T_n$  is somewhat representative of the variability in the mixing and recirculation ratio parameters. The normalized temperature is defined below as:

$$T_n = \frac{T_{ht} - T_{ct}}{T_h - T_{ct}}$$

Eq. 4-25

Where:

- $T_n$  Normalized hot tube temperature
- $T_{ht}$  Hottest tube temperature
- $T_h$  Hot leg hot stream temperature
- $T_{ct}$  Cold tube temperature

An example temperature distribution is shown in Figure 4-11 where  $T_h$  is the red portion of the flow directly off the vessel and  $T_{ct}$  is the dark blue return to the SG inlet plenum. Both  $T_h$  and  $T_{ct}$  are calculated internally by MELCOR. By sampling the normalized hot tube temperature  $T_n$ , the temperature of the hottest tube can be automatically calculated. This time-dependent temperature is imposed on a single-tube model, and was a MELCOR model enhancement implemented for this project. It is assumed the hottest tube is where an SGTR would occur if conditions are reached. Therefore, sampling this parameter is, in effect, sampling on the temperature that is used in the creep rupture equations.

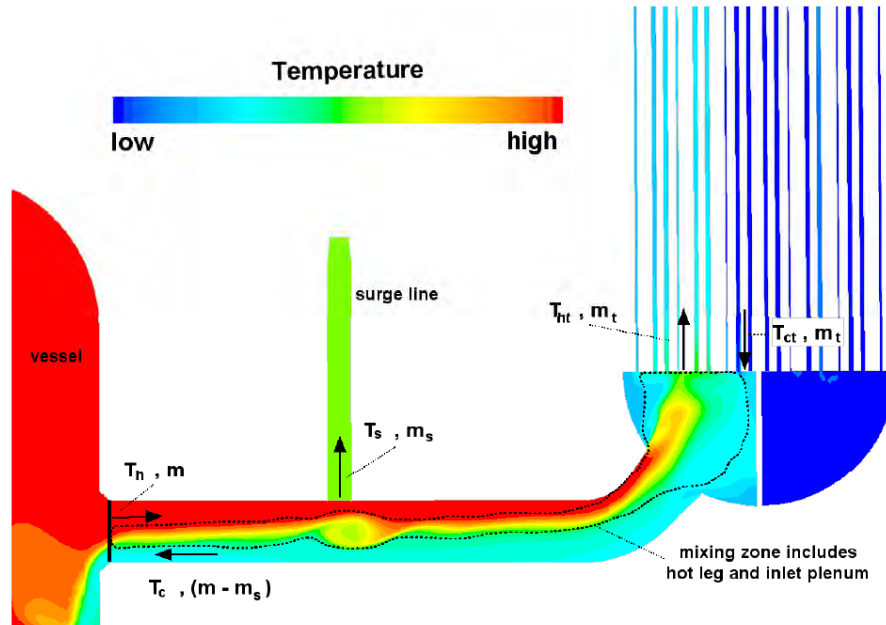


Figure 4-11 CFD predictions indicating expanded mixing region [46]

### Rationale for Distribution

Two methodologies were applied in NUREG-1922 [46] to evaluate the hottest tube temperatures, and the CDF created is based on data from both methodologies. First, the normalized temperature range was divided into 20 subranges (0.0-0.05 up to 0.95-1.0) and the fraction of tubes within each range was obtained for each of the 140 data sets in the base case prediction. The data from the normalized temperature groupings ranged from 0.0 to 0.7. The data in the upper three ranges (i.e., 0.55-0.6, 0.6-0.65, and 0.65-0.7) represented less than a single tube in the computational fluid dynamics model and were considered insignificant. At the peak normalized temperature results representing more than a single tube, an average of 0.6 percent of the tubes fall into the temperature range from 0.5-0.55. This represented two tubes in the computational fluid dynamics model, analogous to 18 tubes in a full-scale steam generator that has 3,388 tubes. However, the location of the two tubes in this range varied with time.

With the second methodology, the hottest tubes were considered individually. A mass-weighted, average normalized temperature was determined for each tube in the model. The single hottest tube over the 140 data sets was described with a normal distribution with a mean of 0.43 and standard deviation of 0.1. Next, the data was broken down into seven groups containing 20 data sets each, which yielded 7 averaged normalized temperature predictions ranging from 0.38 to 0.51. The author notes that these predictions may slightly under predict the prototypical hottest temperature, due to the enlarged size of the tubes (i.e., the computational fluid dynamics model uses one tube to represent nine prototypical tubes) but the impact is expected to be small.

The CDF for this Surry UA was created using data from both methodologies, recognizing the uncertainty in computational fluid dynamics and the identified conservatism (i.e., one computational fluid dynamics tube corresponds to 9 tubes). A 90 percent confidence, based on analyst judgment, was applied to the seven averaged normalized temperatures recommended

for use by NUREG-1922. This means that the seven points were ordered by increasing temperature and equally spaced (since they represent equally considered data sets) from 0.0 to 0.9 on the CDF. Three higher data points were also included in the distribution, but were only weighted with a 10 percent confidence (i.e. defining the CDF from 0.9 to 1.0). This was done because the original computational fluid dynamics data set that reported the peak temperature at any tube had three data sets with higher normalized tube temperatures than the specific tube method, but very low reliability. Instead of being equally spaced, the maximum tube data was also weighted by relative frequency of occurrence (e.g., the data in the 0.6-0.65 interval only occurred 0.16 percent of the time).

Because the original seven data points were from a normal distribution, and additional points were only added at higher normal temperatures and not symmetrically, the new discrete CDF could not be fit with a normal distribution for sampling. Instead, the 10 discrete points comprising the new CDF were fit with a beta distribution, presented in Figure 4-12 that has parameters of  $\alpha=43.7$  and  $\beta=54.9$ . The lower and upper bounds were taken to be the physical limits of 0.0 and 1.0, although almost all samples will be in the 0.3-0.6 range.

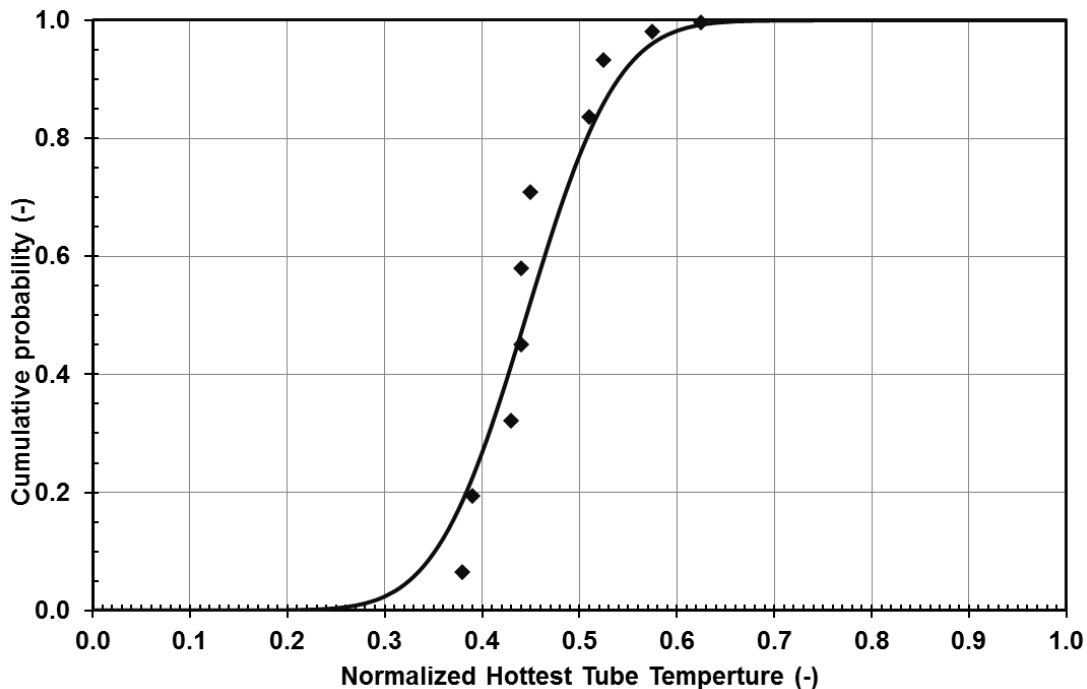


**Figure 4-12 CDF of normalized hottest tube temperature**

Since the calculation for the hottest tube temperature is dependent on the hot stream and cold tube temperatures, it is also affected by other parameters that influence the natural circulation and countercurrent flow in the steam generator. For example, RCP seal leakage can depressurize the primary system loops, reducing the amount of recirculation.

#### 4.1.1.6 Steam Generator Tube Thickness

The SG tube thickness is sampled to represent the most degraded section of tube in the hottest region. For ease of viewing, the distribution is created as the total thickness, but within MELCOR it must be input as the outer diameter. It is converted accordingly and thus the

regression results use the OD, not the thickness. A triangular distribution is used to represent uncertainty with a mode of 0.791 mm, a lower bound of 0.312 mm and an upper bound of 1.27 mm. These bounds are defined based on physical limits.

In the SOARCA analysis [3], an SGTR induced by creep rupture was only predicted after prescribing a stuck-open secondary SV in the model and lowering the stress criterion on the tube [3]. This approach was necessary due to limitations in the MELCOR input SG model. For the Surry UA, model enhancements have been implemented including implementing a single steam generator tube model, which is run concurrently with the full steam generator model. This enhancement allows a temperature multiplier to the single tube, reflective of actual temperature gradients within a steam generator, while all other boundary conditions match the full steam generator. Since creep is partially dependent on temperature, the model enhancement increases the likelihood that a creep-induced SGTR will be predicted during some of the uncertainty realizations. Since a bypass release path has such a strong influence on the total environmental releases, it was important to sample additional uncertainty associated with the likelihood of an SGTR occurring.

Creep rupture depends on temperature and stress. Temperature variation is determined using the single tube temperature multiplier. Traditionally in SGTR modeling, a direct multiplier is applied to the stress on the SG tubes; however, the Surry UA team identified this as a potential area for improvement. The calculation for circumferential or hoop stress ( $\sigma_{\theta}$ ), as modeled in MELCOR, includes differential pressure (P), tube radius (r), and tube wall thickness (t) according to the equation:

$$\sigma_{\theta} = \frac{Pr}{t}$$

Eq. 4-26

Differential pressure across the tube (i.e., difference between inside and outside pressures) is influenced by accident conditions on the primary side and by the failure of the secondary SV or leakage past the main steam valve, both of which can lead to a depressurization of the secondary side. Tube radius can change if a tube balloons, however this would not occur until after there is already a small rupture. Thus, tube thickness is the parameter to sample that is directly related to the stress calculation. Since thickness is in the hoop stress equation, varying thickness is essentially the same as applying a stress multiplier, but the bounds for thickness can be physically determined.

Examination of SG tubes during outages has revealed thinning, which can be caused by corrosion, vibrational fretting and wearing, or a combination thereof. By 1996, over 50 percent of the PWR units worldwide reported some occurrence of tube fretting and wear [47] (pg. 38). Fretting at the Ginna reactor caused by foreign objects in the steam generator removed 84 percent of one tube's wall thickness over 100 mm of length, causing a "fish mouth" bursting of the tube [47] (pg. 55). Additionally, outside diameter pitting and corrosion wastage can also lead to localized tube thinning. Pitting is generally thought to reduce thickness at 10 percent throughwall depth/cycle but can be as high as 50 percent [47], (pg. 58).

The theoretical lower limit for the wall thickness is the thickness at which the yield strength of the material (Inconel 600) would be exceeded at steady state pressure and the design radius. It follows that if there are no spontaneous SGTRs during steady state operation, the current hoop stress must be lower than the yield strength. A representative yield strength of 45,000 psi for Inconel 600 is provided from the materials industry. The steady state pressures at Surry are 2210 psia on the primary side of the tubes and 784 psia on the secondary side, giving a

differential pressure of 1426 psi. From the Surry input deck, a single tube radius is 9.845 mm. This yields failure thickness of 0.312 mm under steady state condition according to Eq. 4-26. As the design thickness is 1.27 mm, this represents a throughwall reduction of 75 percent or a maximum multiplier to the stress calculation of 4.

### **Rationale for Distribution**

The upper bound of 1.27 mm is established as the design thickness. The lower bound is established as 0.312 mm through application of the hoop stress equation. For the triangular distribution, the symmetric midpoint is 0.791 mm. The CDF is presented in Figure 4-13.

A uniform distribution for thickness is not appropriate, because the majority of plants have observed flaws; therefore, a full-wall thickness should be weighted less than a damaged state. Furthermore, because high damage tubes are often plugged or sheathed (i.e., removed from service) during inspections, the lower bound of the distribution should also be weighted less.

Historically, tubes have been removed from service when they were discovered to be at 60 percent of the original wall thickness. However, the probability of detection of such tubes is not high [49], (pg. 30 and 33). At Surry, 60 percent of the original tube thickness would correspond to 0.762 mm. A report on SCDAP/RELAP modeling of an SGTR identifies a stress multiplier of 3 as a conservative upper bound [32], (pg. 6). For the Surry UA, a stress multiplier of 3 would give a thickness range of 0.423-1.27 mm with a midpoint of 0.8465 mm. Additionally, a 50 percent throughwall reduction from pitting, as described above would give a thickness of 0.635 mm. This range of values does not provide a consensus on a most likely value, but the data group around the distribution midpoint. Therefore, the midpoint (0.791 mm) was selected as the mode of the triangular distribution between 0.312 and 1.27 mm.

It can be assumed that some, but not all, tubes are in a damaged state. Therefore, the distribution represents the thickness of the most damaged tube in the steam generator. It is recognized the most damaged tube may not fall into the hottest plume section where this effective stress multiplier is applied. However in the present analysis, it is conservatively assumed that the most damaged tube is in the hottest plume region. The conservative assumption could cause excessive numbers of SGTRs to occur, which is not a realistic outcome; therefore, early sensitivity analyses were performed to determine whether this approach would cause a large number of SGTRs to occur. This was not the case, thus the approach was maintained for the final analysis.

There was also an option to include a set of correlations into MELCOR to calculate a direct stress multiplier based on tube cracking [48]. There is a strong basis for this method, and it has been employed during NRC research in the past. However, the use of these correlations would introduce a new set of multiple uncertain parameters and would be much more difficult to incorporate into the MELCOR model, and was therefore not included.

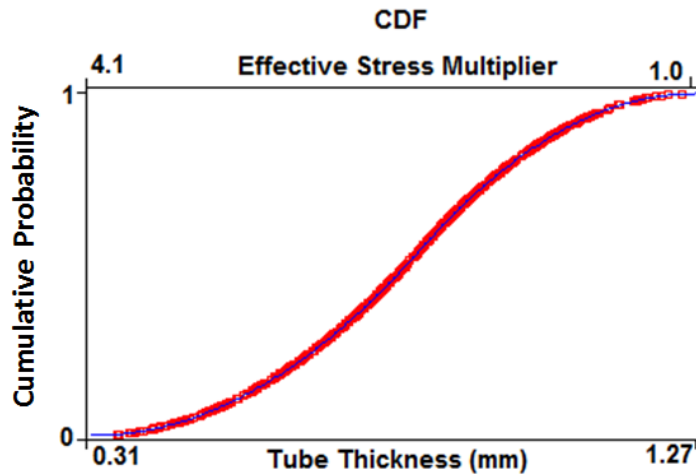


**Figure 4-13 CDF of tube thickness distribution**

## **4.1.2 In-vessel Accident Progression**

### **4.1.2.1 Zircaloy Melt Breakout Temperature (SC1131(2))**

The Zircaloy melt breakout temperature and its associated distribution characterize the uncertain properties that determine the temperature at which the  $ZrO_2$  shell releases underlying molten Zircaloy, which can occur for two reasons, both captured by this parameter. First, the outer oxide shell can crack due to physical stresses from the extreme environment, and second the molten Zircaloy can chemically reduce the oxide, leading to localized failures. The oxide shells have a high melting temperature relative to that of unoxidized cladding and, as shown in the Phebus experiments [50], can maintain fuel geometry as Zircaloy interior to the shell melts and drains away. Uncertainty is represented by a beta distribution ( $\alpha: 3.83; \beta: 3$ ) with a lower bound of 2100 K and an upper bound of 2540 K.

As modeled in MELCOR, once the temperature reaches 1173 K, the fuel rod cladding ruptures and releases fission products from the fuel-cladding gap. As the temperature increases (starting as low as 1100 K) the steam oxidizes the cladding; thus forming a  $ZrO_2$  shell. After 2100 K, the zirconium that does not fully oxidize forms an  $\alpha$ -phase  $ZrO$  fluid which is held up by the  $ZrO_2$  shell. The  $ZrO$  also migrates through the fuel pellet cracks and forms a  $(U,Zr)O_{2-x}$  mixture through slow dissolution of the irradiated  $UO_2$  fuel. The thickness of the  $ZrO_2$  is primarily a function of:

- Steam supply of oxygen to the  $\alpha$ - $ZrO$ , thus increasing the  $ZrO_2$  shell thickness.
- Oxygenation of the  $\alpha$ - $ZrO$  from the  $ZrO_2$  shell, thus decreasing the shell thickness (does not occur below 2273 K [53]).
- Rod temperatures, which heavily influence reaction rates (i.e., a higher temperature yields faster reactions).

It is noted that the  $\alpha$ - $ZrO$  can also extract oxygen from the  $UO_2$  pellet. Schematic representations of the zirconium melt breakthrough process can be seen in Figure 4-14 and

Figure 4-15. An approximation of the oxygen content in the  $\alpha$ -ZrO can be seen in Figure 4-16. When zirconium-melt breaks through the  $ZrO_2$  shell, it also removes some dissolved uranium and fission products and stops the heat generation from the zirconium oxidation reaction. This dissolution process is simulated in SOARCA by assuming 0.2 kg of  $UO_2$  (via COR\_CMT) is dissolved for every 1 kg of Zr melt generated by the candling process.

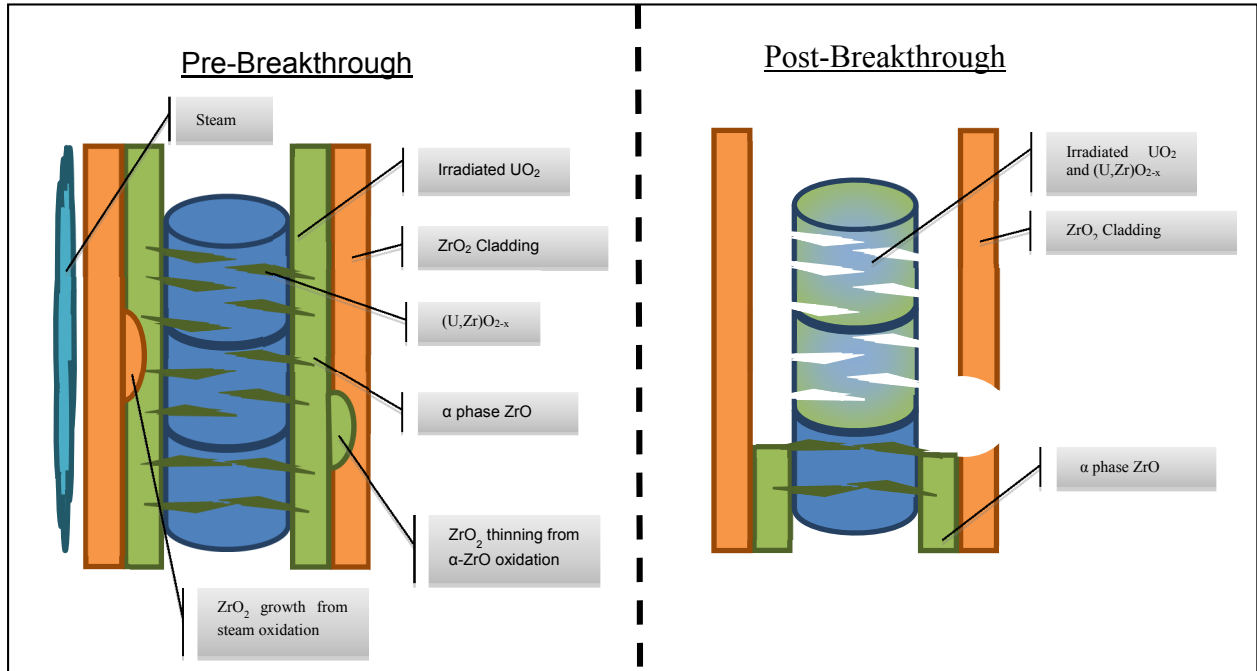


**Figure 4-14 Schematic of zirconium melt breakthrough**

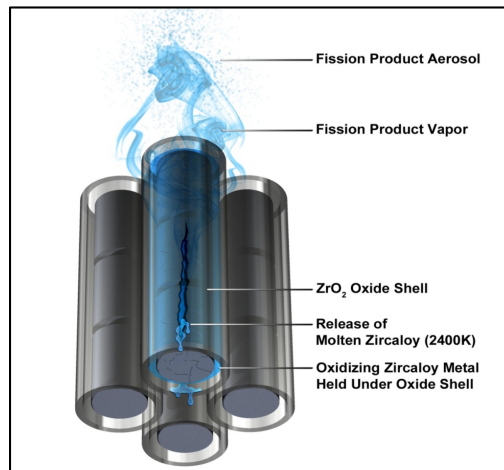


**Figure 4-15 Depiction of the fuel rod degradation**

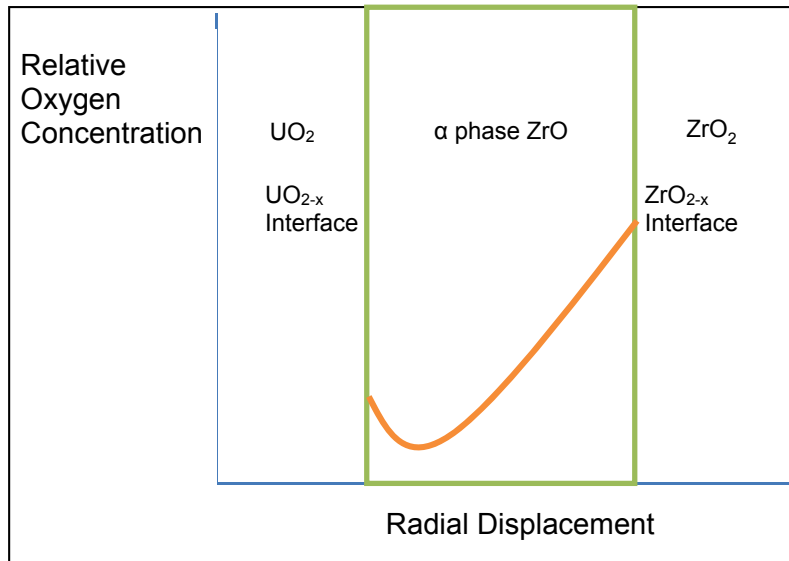


**Figure 4-16 Qualitative oxygen concentration in the  $\alpha$ -ZrO region**

It has been shown, using structural models of the oxide shell, that high temperature failure (a.k.a. Flowering) of the  $ZrO_2$  shell can occur through two primary failure modes. The first occurs when the oxide shell grows too thick under intermediate rate temperature ramps:

$$\left\{ \sim 3 \frac{K}{s} < \frac{dT}{dt} < \sim 6 \frac{K}{s} \right\}$$

Eq. 4-27

where  $K$  is temperature in Kelvin,  $s$  is time in seconds,  $T$  is temperature, and  $t$  is time. This results in the surface stress exceeding the flexural limits. The stress causes cracks in the  $ZrO_2$  shell, which are filled with melt. The melt then oxidizes, causing more cracks. Eventually, the oxide shell expands to the point where the incompressible melt applies enough internal pressure to rupture the oxide shell.<sup>11</sup> Simulations with the code S/Q [53] have been conducted. The second failure mode occurs when the oxide shell erodes and is too thin under rapid temperature ramps to contain the melt:

$$\left\{ \frac{dT}{dt} > \sim 6 \frac{K}{s} \right\}$$

Eq. 4-28

This thinning of the oxide shell is caused by internal erosion from the melt.

The last possibility of failure that is beyond flowering occurs when the oxide shell completely oxidizes the melt. This is predicted to occur under extremely slow temperature ramps:

---

<sup>11</sup> Small variations in pellet diameter can dramatically change the predicted failure temperature.

$$\left\{ \frac{dT}{dt} < \sim 3 \frac{K}{s} \right\}$$

Eq. 4-29

It is noted that the CORA experiments suggest that the temperature ramps allowing for complete oxidation of the melt are closer to 0.3K/s [98].

The breakout temperature initiates the downward drainage of molten Zircaloy on a ring and axial level basis in the MELCOR simulation and can act in terminating or decreasing oxidation reaction rates in the originating core cell. Previous SNL studies [51][52], determined that at the "breakout temperature" oxidizing molten Zircaloy is relocated to cooler regions at a time when the oxidation rate is at its peak value. Fuel temperatures are increasing rapidly (~10K/s) at this time, hydrogen generation rate is locally at a maximum, and fission product release rates are large. The relocation of the oxidizing melt has the effect of terminating the intense local fuel heating, since the chemical heating source has relocated to a cooler region of the vessel. This should affect release rate for volatile fission products and total localized releases of low-volatile species.

### Rationale for Distribution

This distribution for Zircaloy melt breakout temperature is created by Bayesian updating the Peach Bottom Zircaloy Melt Breakout Temperature (prior distribution) with the S/Q simulation results [53] provided in Table 4-4. A binomial likelihood function was used to update a scaled version of the prior distribution and then rescale the posterior distribution to the appropriate range.

**Table 4-4 Zircaloy melt breakthrough temperature estimates from S/Q simulations of two ZrO<sub>2</sub> failure modes.**

Failure Mode	Temperature	Assigned Weight
#1-Surface stress exceeds the flexural limits.	2393 K	0.5
#1-Surface stress exceeds the flexural limits.	2223 K	0.5
#2-Oxide shell erodes and is too thin.	2372 K	1

The prior distribution was defined as a triangular distribution. The lower bound value is the Zircaloy melting temperature of 2100 K. The value of 2100 K also corresponds to fragile outer oxide shells that are incapable of retaining molten Zircaloy. The upper value of 2540 K was selected in the original hydrogen uncertainty study based on fuel rod failure in 15 minutes using the time at temperature model (precluding failure by Zircaloy breakout), which in turn is based on qualitative consideration of the alpha-Zr(O) phase diagram and observations/analyses of the Phebus experiments [50]. The mode is 2400K, which was the value used in the SOARCA analysis [3] and is the default MELCOR value because it allows for holdup by Zircaloy oxide but not by steel oxide. The selection of a triangular distribution suggests that a most probable value for the uncertain parameter is recommended (mode), with decreasing likelihood for values away from the most probable. The CDF is presented in Figure 4-17.

Two simulations were conducted for failure mode #1 to show variability due to pellet diameter uncertainties that result because individual pellets have differential thermal expansions during

reactor operation. During the updating process, the two failure modes were assigned equal weight, and the two variability simulation results were assigned equal weight. To ensure that the weights are additive in the product likelihood function, the updating equation shown in Eq. 4-30 was used.

$$\pi(Temp|E) = \frac{1}{c} \pi(Temp) \prod_{i=1}^N \{L(E^i|Temp)\}^{w^i}$$

Eq. 4-30

In Eq. 4-30,  $\pi(Temp)$  represents the state of knowledge of the values for the Zircaloy melt breakout temperature (SC1131(2)) without simulation estimates,  $\pi(Temp|E)$  represents the state of knowledge for SC1131(2) given the estimates in Table 4-4,  $L(E^i|Temp)$  is the likelihood that if the actual value for SC1131(2) was Temp, the  $i^{th}$  evidence ( $E^i$ ) would be observed,  $w^i$  is the weight of the  $i^{th}$  evidence as defined in Table 4-4, and  $c$  is a normalization constant. The likelihood function was assumed to be proportional to the binomial function if the evidence was transformed to fall within 0 to 1, given zero represented the lower bound of the distribution (2100K) and one represents the upper bound of the distribution (2540K).

Because the MELCOR uncertainty engine cannot sample from user specified distributions, a maximum likelihood estimate fit (beta distribution) of the posterior distribution was sampled. The shape parameters of that distribution are  $\alpha = 3.83$  and  $\beta = 3.0$  with upper and lower bounds set the same as the prior triangular distribution [2100.0, 2540.0].

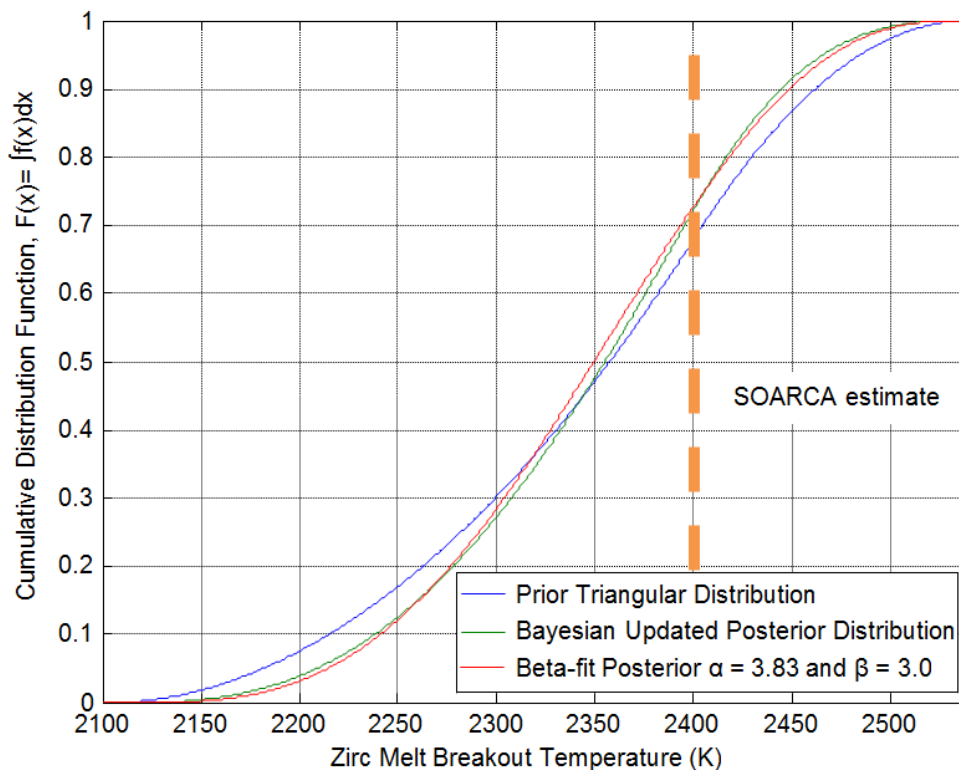


Figure 4-17 Zircaloy melt breakout temperature cumulative distributions

The Zircaloy melt breakout temperature showed importance in the Peach Bottom UA [2]. Intuitively, it is suspected that molten Zircaloy breakout must occur before  $ZrO_2$  and  $UO_2$  eutectic reactions (and other chemical reactions) cause local fuel failure, which is supported by experimental observations of fuel oxidation and failure. The the temperature at which the eutectic formed from  $UO_2$  and  $ZrO_2$  melts is another uncertain parameter in this Surry UA and correlation between the two was considered. However, it was calculated, that with the distributions for the two parameters, Zircaloy breakout would occur before fuel failure by eutectic reactions in 85 percent of the sampled realizations. By not correlating the two parameters, the sequence of events that is intuitively expected and experimentally supported, will occur the majority of the time, but some samples will allow for the exploration of the alternative scenario.

#### 4.1.2.2 Molten Clad Drainage Rate (SC1141(2))

MELCOR uses sensitivity coefficients SC1141(1) and SC1141(2) to control the candling model when molten material has just been released after holdup by an oxide shell or by a flow blockage (crust) [9]. The sensitivity coefficient (SC1141(2)) is defined as the maximum melt flow rate per unit width after breakthrough (with units of kg/m-s), and is described herein as the molten clad drainage rate. The molten clad drainage rate is an uncertain input in MELCOR that influences the in-vessel accident progression. A log triangular distribution was implemented with a mode of 0.2 kg/m-s, a lower bound of 0.1 kg/m-s and an upper bound of 2 kg/m-s.

In MELCOR, when molten material has just been released after holdup by a flow blockage or oxide crust, the assumption built into the candling model of constant generation of melt over the timestep is no longer valid. Behavior of the model related to the amounts of mass refrozen in lower core cells would thus be highly dependent on the size of the current timestep. Therefore, for those situations involving the sudden release of a large mass of molten material built up over perhaps several previous timesteps, application of the candling model is modified slightly. In order to eliminate dependencies on molten pool mass and timestep size, SC1141(1) is a constant timestep used for the breach of an oxide shell, while SC1141(2) is the maximum flow rate (per unit surface width) of the molten pool after breakthrough of a flow blockage, which is used to calculate a timestep according to:

$$\Delta t_{contact} = \max \left[ \Delta t, \frac{M_m \Delta z}{\Gamma_{max} A_s} \right]$$

Eq. 4-31

Where  $\Delta t_{contact}$  is the timestep used after failure of a flow blockage holding up a molten pool,  $\Delta t$  is the nominal MELCOR timestep,  $\Gamma_{max}$  is the maximum flow rate,  $M_m$  is the mass of molten material,  $\Delta z$  is axial cell height and  $A_s$  is the surface area available for flow.

In other words, a large molten pool is allowed to discharge at a maximum rate of  $\Gamma_{max}$ , (SC1141(2)), and the amount refreezing onto structures below (candling) will be a linear function of the total mass of the pool. This effect can be visualized as the melt pool moving axially down a fuel rod in the open space between 4 closest fuel rods in the square assembly lattice.

The release timestep and the maximum melt flow rate affect subsequent code calculations for heat transfer, refreezing, core degradation kinetics, and overall in-vessel accident progression.

## Rationale for Distribution

A log triangular distribution is used for SC1141(2) with a mode of 0.2 kg/m-s and 0.1 and 2.0 kg/m-s respectively for the lower and upper bounds. The mode of 0.2 kg/m-s is the current MELCOR best practice [54] and was used in the SOARCA analysis [3]. It was determined by observing video of the CORA-13 experiment showing movement of molten material following the breakthrough of a flow blockage and calculating the flow rate. There is no citable technical basis to inform the bounds of the distribution, making the uncertainty of this parameter exploratory. For an exploratory study, an approximate order of magnitude uncertainty range was desired to allow investigation of a large amount of uncertainty. Had the regression results indicated high importance for this parameter, the distribution would have been revisited.

The selection of a log-triangular distribution suggests that a most probable value for the uncertain parameter is recommended (mode), with decreasing likelihood for values away from the most probable. A triangular distribution would give too much weight to sampling near the bounds. Since the parameter represents the maximum possible flow rate, it is more beneficial to sample larger values, since some smaller values may occur naturally during the MELCOR runs. Additionally, the historical default value for MELCOR was 1 kg/m-s and it is beneficial to analyze some runs at and above this value. Because of these two reasons and the desire to have an approximate order of magnitude range, an upper limit of 2.0 kg/m-s and lower limit of 0.1 kg/m-s were selected. This selection gives approximately 10 percent of samples above the previous default of 1 kg/m-s, while keeping the majority of samples near the mode. The CDF is presented in Figure 4-18.

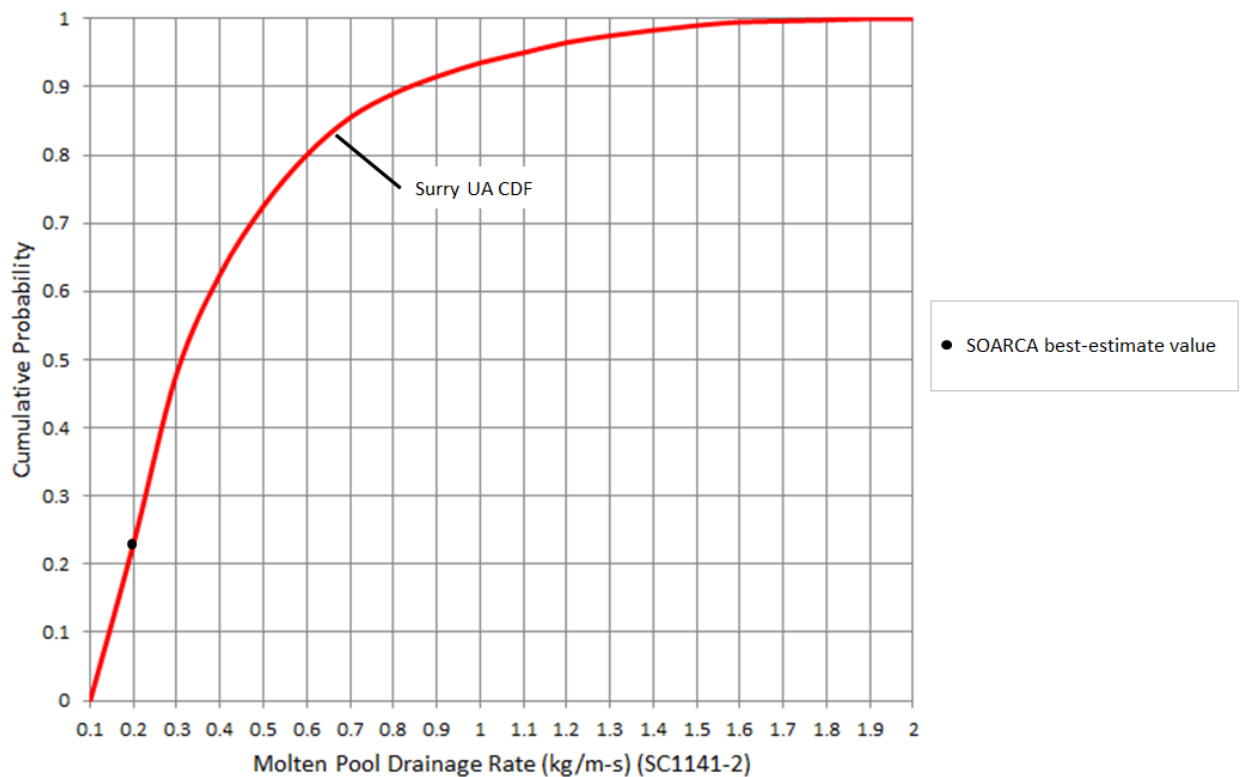


Figure 4-18 CDF of molten pool drainage rate

The corresponding timestep size following rupture through an oxide shell is not considered. Although it is also an uncertain parameter that affects subsequent code calculations, only the variation of the maximum molten pool flow rate after breach of a blockage is considered in the Surry UA. The maximum molten pool drainage rate parameter is a carryover from the Peach Bottom UA.

#### **4.1.2.3 Radial Molten Debris Relocation Time Constant (RDMTC)**

The radial molten debris relocation time constant (RDMTC) controls the relocation of molten material from ring to ring, meaning it determines the amount of molten material that can be moved within a single timestep. It is used as a surrogate for the broad uncertainty of debris relocation rate into water in the lower head. This is one of a few MELCOR parameters, which could be modified to influence large scale movement, but since there is no stronger technical justification for uncertainty in those other parameters, RDMTC was chosen. These parameters also influence axial debris relocation. Slower relocation rates improve the ability of the debris to cool, whereas faster relocation rates conversely decrease the potential ability. RDMTC is sampled to characterize the uncertainty associated with the time constant used to calculate the radial relocation of molten debris. A uniform distribution was chosen with a lower bound of 10 seconds and an upper bound of 100 seconds. Had the regression results indicated high importance for this parameter, the distribution would have been revisited.

Although many experiments exist to inform axial fuel relocation, there is a decided lack of data available to inform radial relocation. The main reason for this is because the test facilities, such as Phebus and CORA, were too small in scale to observe the effects of radial relocation. The MELCOR default for the radial relocation time constant (60 s), which was used for SOARCA [3], is described as “an order-of-magnitude value based on engineering judgment and the recommendations of code users” in the MELCOR Reference Manual [8]. Therefore, to better understand the importance of this parameter, it was judged reasonable to use an order of magnitude range as the uncertainty range. Given the broad range and lack of defensible data for the distribution, this is an exploratory parameter, with the values used assumed to bound reasonable behavior of leveling of partly molten two-phase or fully molten debris.

#### **Rationale for Distribution**

A uniform distribution was chosen since, although there is a MELCOR default which was used for SOARCA, there is no reason to believe the default is the central tendency of a distribution as would be indicated by using it as the mode of something like a triangular or log-triangular distribution. However, some credit is given to the MELCOR Reference Manual [8], particularly in the choice of seconds as the base time unit and the use of “order-of-magnitude value”. Therefore the upper and lower bounds of the uniform distribution are set to encompass a single order of magnitude range in the chosen units. The lower bound is 10 seconds and the upper bound is 100 seconds. The bounds of the distribution are set such that RDMTC will never be greater than RDSTC (Section 4.1.2.4). The CDF is presented in Figure 4-19.

With regard to how MELCOR moves debris, the Core chapter of the MELCOR Reference Manual [8] explains that the code loops over all adjacent pairs of radial rings between which relocation is possible and compares the calculated liquid levels in the adjacent rings. If unequal, then the volume of molten material that would balance the levels is calculated. The actual volume relocated during a timestep depends on the volume of molten material, the timestep, and the relocation rate time constant. If the stratified molten pool model is active, leveling is performed for each component. Relocation is always directed inward preferentially. Once

molten pools are relocated, solid debris is also leveled and can displace a molten pool, which will then backfill. In the lower head, volume of debris spreading is limited to represent a crust of refrozen material on the vessel surface.

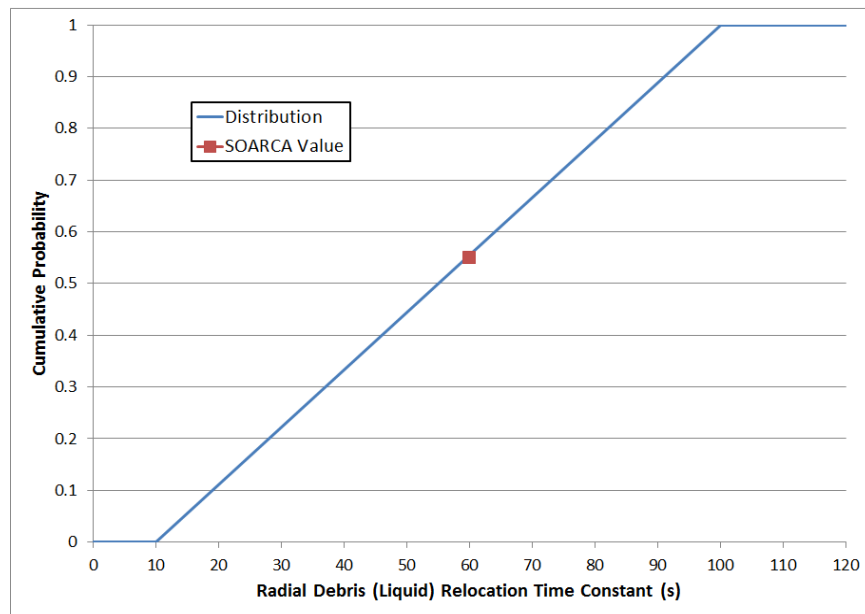


**Figure 4-19 CDF for radial debris liquid relocation time constant**

#### 4.1.2.4 Radial Solid Debris Relocation Time Constant (RDSTC)

The radial solid debris relocation time constant (RDSTC) controls the relocation of solid material from ring to ring, meaning it determines the amount of solid material that can be moved within a single timestep. It is used as a surrogate for the broad uncertainty of debris relocation rate into water in the lower head. This is one of a few MELCOR parameters, which could be modified to influence large scale movement, but since there is no stronger technical justification for uncertainty in those other parameters, RDSTC was chosen. These parameters also influence axial debris relocation. RDSTC is sampled to characterize the uncertainty associated with the time constant used to calculate the radial relocation of solid debris. A uniform distribution was chosen with a lower bound of 100 seconds and an upper bound of 1,000 seconds.

Although many experiments exist to inform axial fuel relocation, there is a decided lack of data available to inform radial debris relocation. The main reason for this is because the test facilities, such as Phebus and CORA, were too small in scale to really observe the effects of radial relocation. The MELCOR default for radial relocation (360 s), which was used for SOARCA, was chosen as “an order-of-magnitude value based on engineering judgment and the recommendations of code users” [7]. Therefore, to determine the importance of this parameter, it was decided to use an order of magnitude range as the uncertainty range. Thus, the inclusion of this parameter is really to “see what happens” when it is varied. Professional judgment is that the values used bound reasonable behavior of leveling of solid debris. Had the regression results indicated high importance for this parameter, the distribution would have been revisited.

## Rationale for Distribution

A uniform distribution was chosen since, although there is a MELCOR default which was used for SOARCA, there is no reason to believe the default is the central tendency of a distribution as would be indicated by using it as the mode of something like a triangular or log-triangular distribution. However, some credit is given to the reference manual, particularly in the choice of seconds as the unit and the use of “order-of-magnitude value”. Therefore, the upper and lower bounds of the uniform distribution are set to encompass a single order of magnitude range in the chosen units. The lower bound is 100 seconds and the upper bound is 1000 seconds. The bounds of the distribution are set such that RDSTC will never be less than the Radial Molten Debris Relocation Time Constant (RDMTC). The CDF is presented in Figure 4-20.

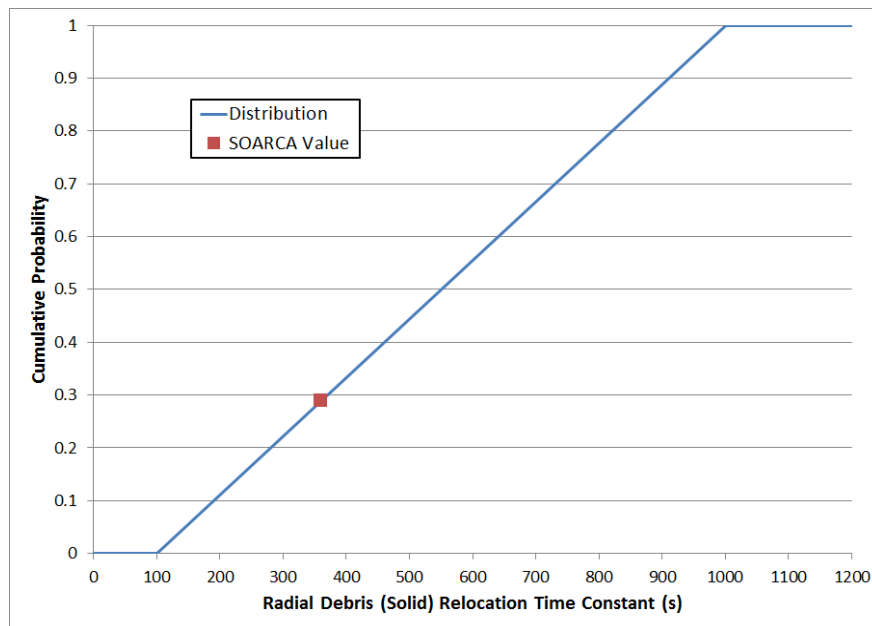


**Figure 4-20 CDF for radial debris solid relocation time constant**

### 4.1.2.5 Decay Heat

Decay heat is influenced by two parameters in this analysis. First, the time at cycle is varied between beginning, middle, and end of cycle (BOC, MOC, and EOC). This determines the radionuclide inventory which is the source of decay heat, thus there are baseline decay heat curves for each time at cycle. Second, for each uncertain realization, variation from the base decay heat curve is sampled. The uncertainty of the time at cycle is represented as a discrete distribution with equal probabilities for BOC, MOC, and EOC at 0.33 each. Tables of decay heat variation from the base curves are pre-created, and these tables are sampled with a unitless uniform distribution with a lower bound of 1 and upper bound of 500. In the regression results, this parameter is represented by a percent deviation of integrated energy at 48 hours compared to the baseline energy.

The radionuclide inventory and decay power generated in the fuel are the principal safety problems of any severe accident that assumes successful reactor shutdown. In sampling the uncertainty associated with this, a two-pronged approach is used. First, a pointer variable is

used to sample time-at-cycle, which dictates the use of a particular pre-created radionuclide inventory and base decay power curve. Second, the uncertainty in the base decay power curve is sampled using the methodology described below.

For a particular reactor design, operation history, and core loading, modern codes (i.e., burnup/depletion codes) such as ORIGEN-S [94], can calculate radionuclide inventories and decay power for a particular point in time with relatively low uncertainty; at least relative to typical uncertainties in other severe accident boundary conditions. Past severe accident research has observed considerable variation in accident progression and releases attributable to relatively minor changes in decay power [95][96], i.e. a “cliff-edge” effect like lower head failure can potentially be mitigated by water in the lower plenum with a smaller amount of decay heat. Furthermore, in conjunction with significant additional uncertainties associated with variability in reactor operation (e.g. time of scram in the cycle), the associated variation in the decay power and radionuclide inventory input for MELCOR and MACCS can have a first-order impact on key severe accident signatures such as H<sub>2</sub>/CO generation, radionuclide release fractions and environmental source terms, and event timing.

For a given set of reactor conditions, the uncertainty in the decay power soon after shutdown may vary from 1 to 10 percent from the base decay heat curve according to the “Decay Heat Power in Light Water Reactor” standard (ANS-5.1-2005), which considers the decay heat of fission products, U-239, and Np-239 for light water reactors (LWRs) that predominantly involve fission of U-235, U-238, and plutonium isotopes; uncertainties vary with time after shutdown, among other factors. The uncertainty is based on one standard deviation of a normal distribution. An ORIGEN-S calculation with modern cross-section data is more aligned with the ‘best estimate’ approach of SOARCA, and the uncertainties inherent to the code’s computational methods and approximations are likely less than that of the American Nuclear Society (ANS) standard. Nonetheless, the ANS standard provides for readily available quantification of uncertainty in the decay power after shutdown, which would otherwise require random sampling and analysis of uncertain ORIGEN-S inputs (namely nuclear data).

Uncertainty in decay heat is treated using a combined approach with ORIGEN-S and the ANS standard. ORIGEN-S is used to calculate consistent decay heat and inventory information for a few sets of reactor conditions (i.e. the time of scram in the last operating cycle), while uncertainty within each decay heat curve will be derived from ANS-5.1-2005. The uncertainties derived from the ANS standard principally reflect the uncertainties in nuclear decay data for short-lived nuclides. From the ORIGEN-S calculations, fractional fission powers of important actinides (U-235, U-238, Pu-239, Pu-241) over the previous cycle can be extracted. Using these nuclide specific fission power levels, the time-dependent uncertainties in percentage of total decay heat power can be calculated using the methods described in Section 3 of ANS-5.1-2005.

Surry reactor operating data from cycles 18, 19, and 20 are used as input for ORIGEN-S and Automatic Rapid Processing (ARP) for burnup-dependent cross sections, which are supplied via the TRITON sequence within the SCALE6.1.3 code package, along with state of the art ENDF/B-VII.1 nuclear data [93]. Three sets of decay heat and inventory information are generated for BOC, MOC, and EOC for cycle 20 at Surry. The uncertainties, informed by ANS-5.1-2005 [56], are then applied to ORIGEN-S generated decay heat curves. Hence, two quantities are sampled for an integrated approach to the decay heat and inventory uncertain parameter: a uniform-discrete distribution over the three predetermined times of shutdown in cycle 20 (BOC, MOC, EOC), which varies both decay heat and inventory, along with an unbiased simple random sampling of pre-created decay heat curves, which are informed by ANS-5.1-2005 [56]. The baseline BOC, MOC, and EOC decay power curves are shown in

Figure 4-21 with respect to the time considered for the STSBO scenario. Decay heat variability is applied to these base curves. Table 4-5 shows the differences in radionuclide core inventory according to MELCOR RN class definition for BOC, MOC, EOC, and what was used for SOARCA. Additionally, Table 4-5 shows total mass of specific radionuclide classes that are distributed within the MELCOR model (e.g., Cesium is distributed amongst Cs, CsI, and Cs<sub>2</sub>MoO<sub>4</sub> RN classes).

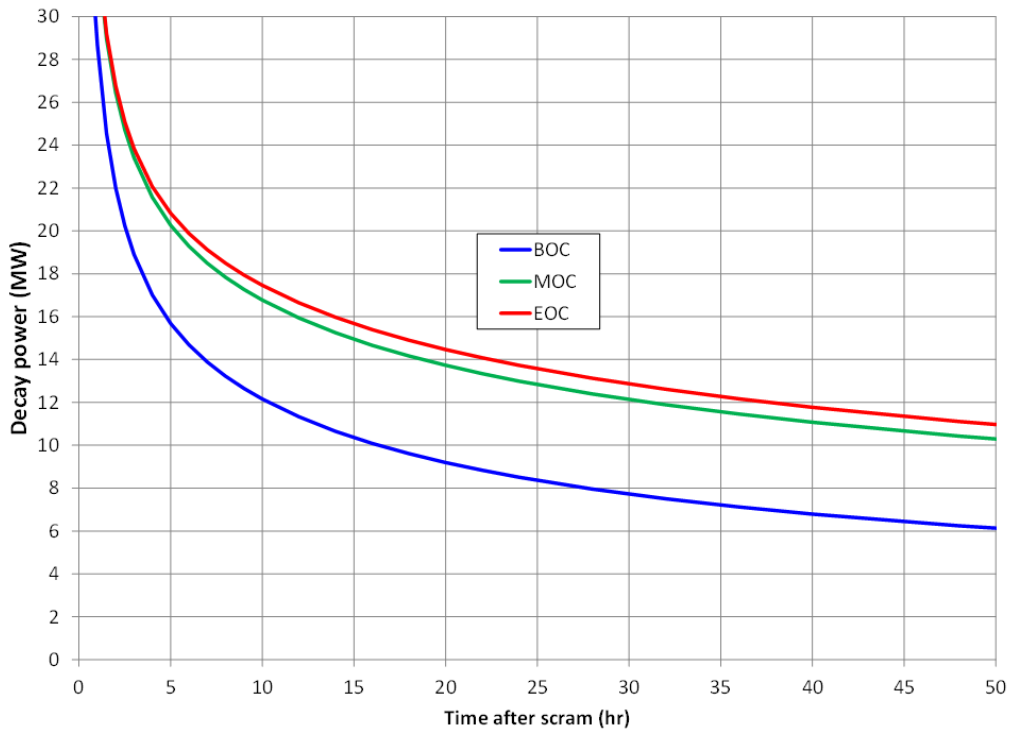


**Figure 4-21 BOC, MOC, and EOC decay power**

**Table 4-5 Radionuclide core inventory and class definition.**

RN Class #	Class (representative)	BOC (kg)	MOC (kg)	EOC (kg)	SOARCA (kg)
1	Noble Gases (Xe)	223.30	309.16	442.28	448.1
2	Alkali Metals (Cs)	5.99	8.20	11.54	11.7
3	Alkaline Earths (Ba)	94.43	132.12	184.86	187.6
4	Halogens (I)	all in Csl	all in Csl	all in Csl	all in Csl
5	Chalcogens (Te)	20.94	28.88	41.57	40.9
6	Platinoids (Ru)	148.45	205.11	308.71	309.5
7	Early Transition Elements (Mo)	125.48	170.04	243.26	243.3
8	Tetravalent (Ce)	676.80	934.36	1256.40	1225.9
9	Trivalent (La)	306.60	420.53	606.26	621.2
10	Uranium (U)	70800.93	70128.34	69137.32	66771.30
11	More Volatile Main Group (Cd)	4.23	5.62	8.74	7.263
12	Less Volatile Main Group (Sn)	4.75	6.55	10.08	9.19

RN Class #	Class (representative)	BOC (kg)	MOC (kg)	EOC (kg)	SOARCA (kg)
16	Cesium Iodide (CsI)	17.53	24.31	35.15	34.82
17	Cesium Molybdate (Cs <sub>2</sub> MoO <sub>4</sub> )	154.76	212.15	298.46	302.47
	Total cesium class mass	128.67	176.53	248.83	251.76
	Total iodine class mass	8.56	11.87	17.17	17.01
	Total molybdenum class mass	166.53	226.30	322.41	323.52

### Rationale for Distribution

Varying the decay heat and inventory entails a large amount of data reduction and input generation for MELCOR and MACCS, which SNL has automated in support of similar efforts for Fukushima-related research [93]. Using plant-specific data, ORIGEN-S/ARP calculates decay heat and inventory, and a post-processing tool directly generates consistent MELCOR inputs of decay heat and lumped RN-class inventories (including class specific decay heats), along with consistent detailed nuclide input for MACCS.

The timing of the accident initiator relative to the last operating cycle (assumed to be cycle 20) is treated as inherently random; thus the first step of the decay heat uncertainty analysis involves uniform sampling of the time of reactor shutdown for three pre-chosen times: BOC, MOC, and EOC. This provides three unique sets of inventories and base decay heat curves. The second step involves unbiased simple random sampling of pre-created decay heat tables representing uncertainty on the three base decay heat curves themselves using uncertainties informed by the ANS-5.1-2005 decay heat standard [56]. The final integrated uncertain parameter is in the form of hundreds of nearly continuous variations of the three base decay power curves, with the total number corresponding with the number of MELCOR realizations. The uncertainty variations use unique fractional fission powers for each base power curve (for BOC, MOC, EOC) based on inventories of key fissile elements calculated by TRITON and ORIGEN-S. The modified decay powers are associated with the appropriate inventory from the base decay power curve for the three shutdown times to ensure a modified BOC decay power curve is never sampled on a realization using a MOC or EOC inventory. The decay powers and inventories are pre-generated before being sampled uniformly/discretely for MELCOR and MACCS inputs.

The times of shutdown in cycle 20 are chosen to be 7 days for BOC, 200 days for MOC, and 505 days for EOC. The decay power resulting from 0 to 2 days operation is so small compared to MOC and EOC that it may preclude gross core damage, even for an unmitigated STSBO; thus an operation time of 7 days is chosen for BOC. Additionally, the BOC operation time allows for quantifying the effects of significantly reduced decay power soon after scram (even before core uncovering). The MOC decay power, on the other hand, is relatively similar to the EOC decay power until about 18 hours after scram. This allows for investigating the influence of varied decay power during later stages of severe accident progression. The EOC operating time of 505 days reflects the decay power for the actual length of reactor operation and overall core burnup for cycle 20 at Surry. Figure 4-22 shows a comparison of the BOC to EOC ratio and the MOC to EOC ratio. Figure 4-22 further shows the variations between the three cycle times.

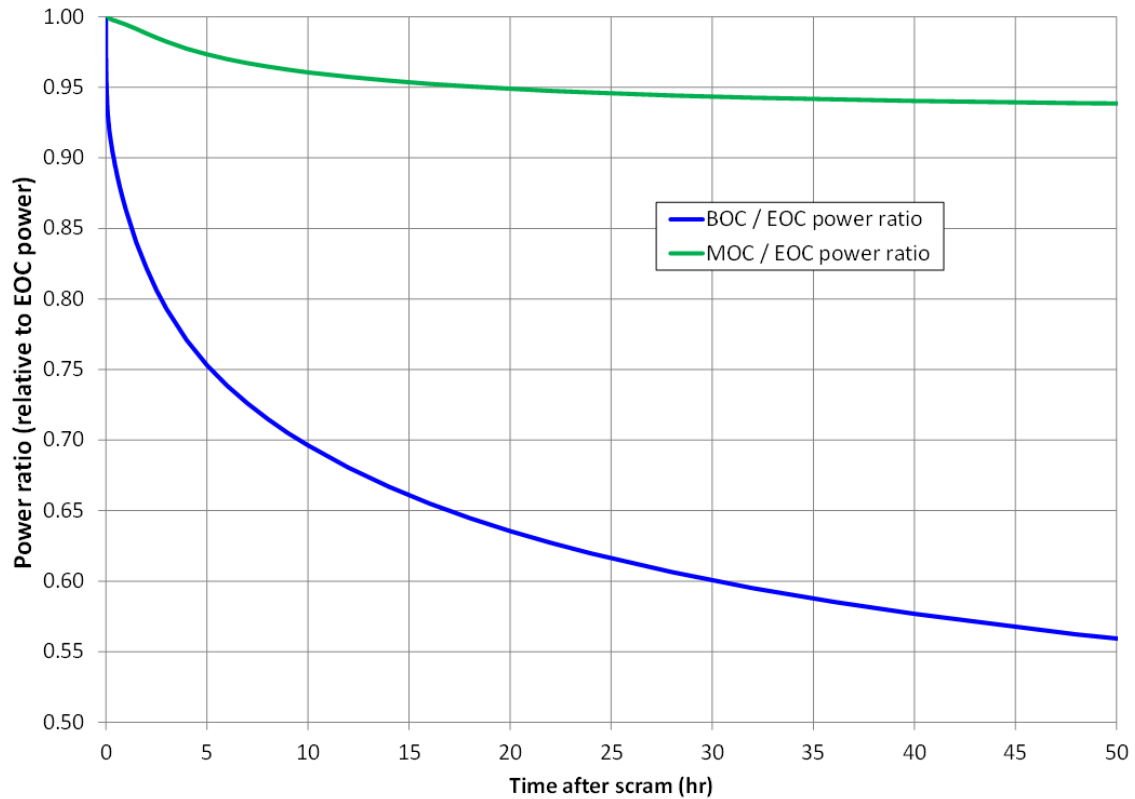


**Figure 4-22 BOC and MOC decay power relative to EOC decay power**

The multipliers derived from the ANS standard are applied to the three base decay heat curves using a simple rejection sampling technique to avoid any dubious and sudden increases in the resulting decay power curves. Therefore, the sampling guarantees monotonically decreasing decay powers (with respect to time) for each MELCOR realization. Figure 4-23 through Figure 4-26 show the resultant uncertainty decay heat curve horse tail plots for BOC, MOC, EOC, and all cycles combined, respectively.

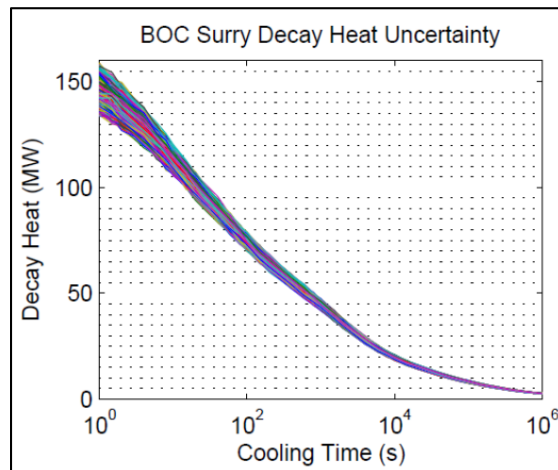


**Figure 4-23 BOC decay heat uncertainty**

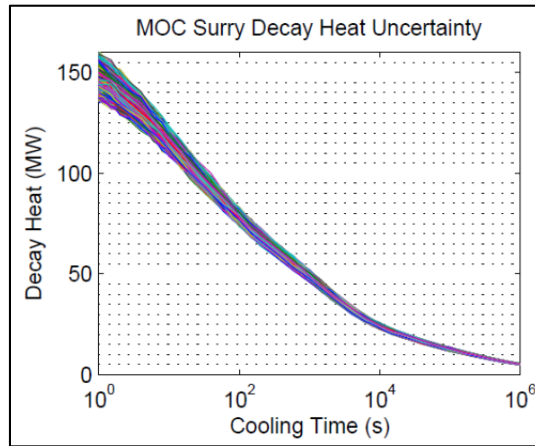


**Figure 4-24 MOC decay heat uncertainty**

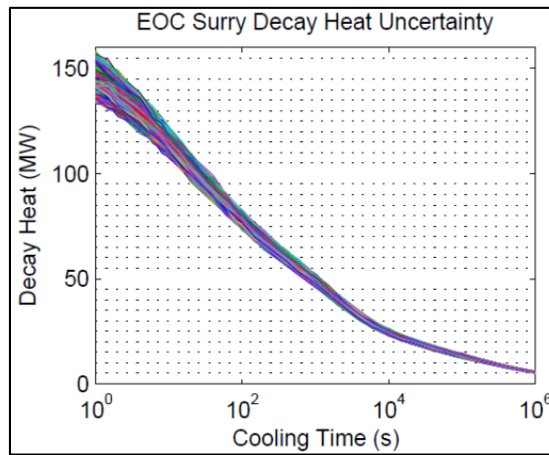


**Figure 4-25 EOC decay heat uncertainty**

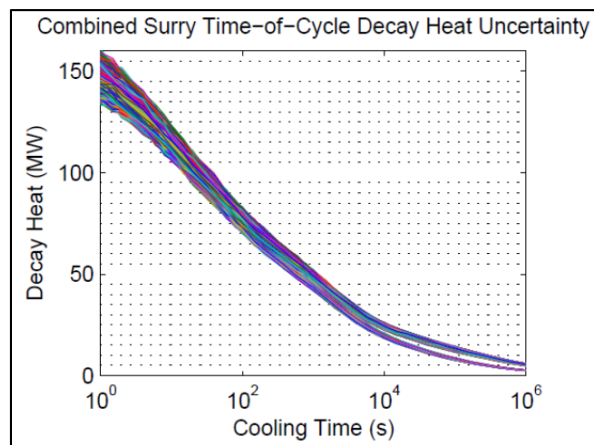


**Figure 4-26 Combined BOC, MOC, and EOC decay heat uncertainties**

#### 4.1.2.6 Effective Temperature at which the Eutectic Formed from Zircaloy Oxide and Uranium Oxide Melts (SC1132)

This parameter represents the temperature at which the eutectic formed from  $\text{UO}_2$  and  $\text{ZrO}_2$  melts. Within MELCOR this is input as a eutectic sensitivity coefficient (SC1132) and a melting temperature. By including the temperature of the eutectic reaction between  $\text{ZrO}_2$  and  $\text{UO}_2$  as a sampled parameter, general fuel failure of when the fuel collapses and when it becomes molten is affected. There are other failure mechanisms and possible eutectic reaction<sup>12</sup> between core materials, some of which are described in more detail in the related parameters section within Section 4.1.2.

The binary phase diagram for  $\text{ZrO}_2/\text{UO}_2$  suggests the melting point for equilibrium conditions is approximately 2800 K for a 50/50 molar mixture; hence this was the historical MELCOR default value. Any liquefaction below this temperature accounts for the effect of molten Zircaloy metal or alpha-Zr(O) 'wetting' the oxide surfaces. Observations of the Phebus and VERCORS experiments suggest that irradiated fuel and oxidized cladding exhibit eutectic liquefaction at significantly lower temperatures; thus the MELCOR default was subsequently modified to 2500 K. Following significant local cladding oxidation, the effective liquefaction of  $\text{ZrO}_2$  and  $\text{UO}_2$  mixtures results in local rod collapse as molten material, rather than as rubble or debris. The parameter treatment for this work attempts to approximate the combined uncertainties associated with burnup, eutectic composition, material properties, and non-equilibrium effects on  $\text{ZrO}_2/\text{UO}_2$  eutectic reactions.

The fuel melt associated with this parameter is a localized effect. This means that MELCOR evaluates the temperature independently for each core cell and allows the fuel in that specific cell to melt when it reaches a failure temperature, such as the temperature at which the eutectic formed from  $\text{UO}_2$  and  $\text{ZrO}_2$  melts. Thus, the entire core will not fail at once when the hottest region reaches the sampled temperature. It is possible that melting of a core cell can cause the subsequent failure of fuel above in the same radial ring that was previously supported by the failed cell. However, this is a physical effect and still only affects a section of a single ring, and keeping it a localized effect.

In MELCOR, eutectic reactions are approximated by user-modification of melting and failure temperatures in model input. Thus, to effectively represent the temperature at which the eutectic formed from  $\text{UO}_2$  and  $\text{ZrO}_2$  melts, the user must modify:

1. The sensitivity coefficient SC1132(1), which defines the cladding temperature resulting in rod collapse without Zr-metal cladding remaining (discussed further in Section 4.1.2.1), and
2. The melting temperatures of both  $\text{UO}_2$  and  $\text{ZrO}_2$  in the input deck (MP\_PRC records).

---

<sup>12</sup> It is noted that the pure  $\text{UO}_2/\text{ZrO}_2$  system has only a melting point, not a eutectic point. High burnup pins have complex intermetallic effects which are referred to as eutectic reactions in the VERCORS [52] experiments and the MELCOR users guide. This nomenclature is maintained for this analysis.

## Rationale for Distribution

Six experimental data points for eutectic induced core collapse are readily available from the VERCORS experiments to help inform the uncertainty distribution [52]. Table 4-6 shows the VERCORS test results along with the mean and standard deviation.

**Table 4-6 VERCORS test results for collapse temperature.**

Test	Collapse Temperature (K)
T1	2525
HT1	2550
HT2	2400
HT3	2525
V_6	2525
RT6	2350
<i>Mean</i>	2479
<i>Standard Deviation</i>	83

In selecting this experimental data, observed core slump is projected to a eutectic reaction. This was strongly indicated by the test results but cannot be definitively confirmed due to a lack of instrumentation.

The selection of a specific distribution is complicated by the lack of detailed experimental data over ranges of severe accident conditions and reactor operation (e.g. high burnup). While the VERCOR testing matrix does not provide randomly distributed evidence of eutectic formation temperatures, these tests do provide a range of temperatures over which eutectics were significant enough to cause core collapse. A normal distribution fitted to the data in Table 4-6 was used to assess uncertainty in the average core collapse temperature for higher burnup fuel. The simple parameter treatment is not intended to rigorously quantify eutectic effects on severe accidents and core degradation; such treatment is impossible when the MELCOR eutectic model is not activated. Rather, the proposed treatment roughly evaluates the influences that the physical state of the core debris has on core degradation kinetics and subsequent severe accident progression. A lower temperature for this parameter results in an increased generation of molten pools in the RPV during core disassembly. Alternatively, a higher temperature for this parameter results in a decreased generation of molten pool formation for  $ZrO_2$  and  $UO_2$  debris. The relocation and cooling of molten pools after formation are treated by several other models and parametric inputs in MELCOR; hence the eutectic parameter only affects the initial creation of molten pools for  $ZrO_2$  and  $UO_2$  immediately upon rod collapse.

Even though the testing data was derived from independent, identical tests, a normal distribution was fitted to the VERCORS data in order to describe the general range of potential collapse temperatures from VERCORS given varying environmental conditions, and is seen in Figure 4-27. This normal distribution has a mean of 2479 K and a standard deviation of 83. The red star in Figure 4-27 represents the 2800 K value used in SOARCA. Even left unbounded, the probability of sampling beyond these bounds is effectively *de minimis*, thus the bounds should not affect the results of this work.

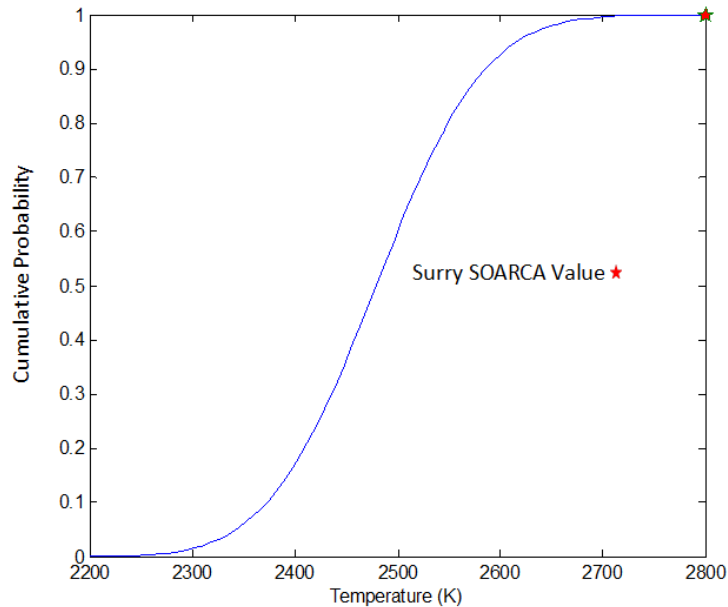


**Figure 4-27 CDF of eutectic melting temperature**

### **4.1.3 Ex-vessel Accident Progression**

#### **4.1.3.1 Hydrogen Ignition Criteria**

The hydrogen ignition criteria determines the ignition location for a hydrogen deflagration and the corresponding flammability limit (volume percent of hydrogen) to represent uncertainty in the direction of propagation from the ignition source for upward, horizontal, and downward propagation. This is accomplished by sampling on the location of the ignition source in each MELCOR control volume representing containment compartments. A discrete distribution was chosen with an equal probability for each of three bins that represent ignition location and corresponding flammability limit.

Hydrogen combustion has uncertainties in the ignition location, ignition timing, flammability limits, and combustion intensity. Ignition timing uncertainty includes both known sources like hot leg creep or presence of random ignition sources. Implementation of the hydrogen ignition criteria supports examination of two of these uncertainties (ignition location and flammability limits). It is assumed an ignition source is available. Although previous SOARCA calculations [3] included combustion at the default limit for spontaneous ignition (10% hydrogen concentration within the atmosphere), the presence of steam and other diluents precluded combustion in the containment during the unmitigated STSBO scenario, except upon the initial release of hydrogen-rich gas following hot leg creep rupture failure. The hydrogen ignition criteria are selected to explore the uncertainty in the lower limits of flammability. A key uncertainty in the lower limit for combustion is the location of the ignition source relative to the reactants. The flammability, or propagation, limits are greatly influenced by the initial direction of propagation from the ignition source. For example, the limits for hydrogen-air mixtures for upward, horizontal, and downward initial propagation of the flame are 4, 6, and 9 percent hydrogen, respectively, demonstrating the effect of buoyancy [55].

Sampling is performed on upward, horizontal, and downward propagation direction from the ignition source. Sampling is also performed on the location of the ignition source within a compartment. Each compartment, or control volume in MELCOR, is evaluated independently, but using the same sampled ignition location and flammability limit, so that ignition can occur in any compartment or multiple compartments simultaneously. At the flammability limits, the burn will begin at the ignition source, propagate from there, and develop into a deflagration throughout the compartment. The upward propagation, or ignition source near the bottom of the compartment, implies an upwardly progressing burn. The horizontal location implies an initially horizontal and upward propagation that moves across and upwards. Similarly, the upper location implies an initial propagation in all directions throughout the compartment. It is assumed that the ignition sources in these three categorizations of ignition location/propagation direction characterize the low flammability possibilities for a large-scale burn throughout a compartment.

### Rationale for Distribution

Sources of ignition could be present throughout the compartmentalized containment such that the location(s) where hydrogen would ignite and the direction(s) the flame(s) would need to propagate would be uncertain and random. The experimental information [55] relied upon in defining the sampling distribution for hydrogen lower flammability limits is limited to flame propagation in the primary directions of upward, horizontal, or downward. This suggests a discrete distribution is applicable. No information is available to suggest that any one direction is more likely than another and so a uniform weighting of the three discrete initial propagation directions (and corresponding lower flammability limits for hydrogen of 4, 6, and 9%) is appropriate. Figure 4-28 shows the discrete distribution for each ignition source location and initial propagation direction; each is equally likely.

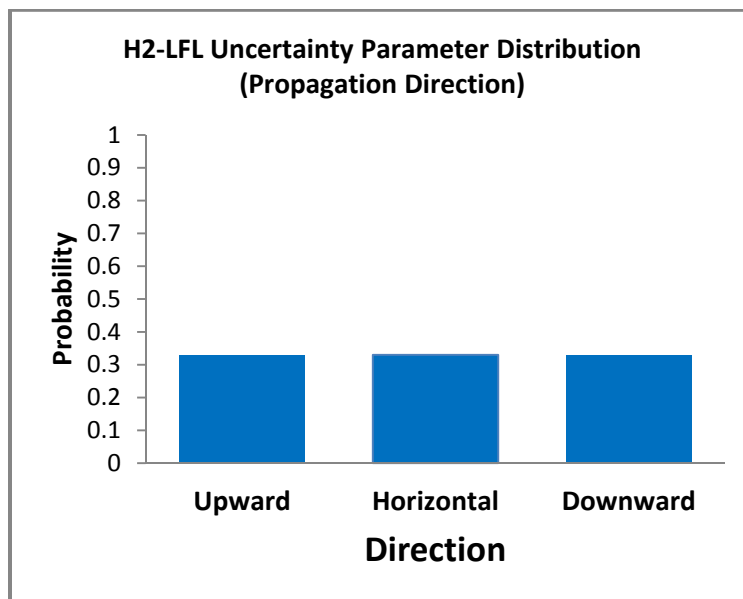


Figure 4-28 Uncertainty distribution for ignition propagation direction

#### 4.1.3.2 Secondary Side Decontamination Factor (ARTIST)

The ARTIST parameter determines the number of steam generator stages traversed by radionuclides following a SGTR, which is used to calculate decontamination factors for the MELCOR calculations. There are a total of seven stages, and a discrete distribution is used with an assigned probability to each of seven bins representing number of stages. This parameter is identified as SGTRLOC in the regression tables in Section 6.1.

Following an SGTR in a severe accident scenario, there is some portion of the radionuclide inventory that would be transported from the primary system to the secondary side and subsequently to the environment. However, there is a tortuous path through the steam generator that would result in a deposition of radionuclides; significantly reducing the total environmental release. The ARTIST facility hosted a series of tests to try to determine the amount of decontamination that occurs within a steam generator following an SGTR under various conditions. Results were extracted and interpreted from the ARTIST final report. They showed that deposition is essentially due to inertial impaction that results because large particles are unable to navigate the bends and obstacles while smaller particles can follow the flow stream. This is indicated by how abruptly the total DF drops to one (i.e., no decontamination) at lower particle sizes instead of slowly, asymptotically approaching one.

The ARTIST results are broken out into a DF per steam generator stage (separated by tube support plates) and are shown in Figure 4-29, as well as a separate DF for just the steam dryer and separator as shown in Figure 4-30. The applicable ARTIST results for the Surry scenario modeled in this work included three aerosol particle sizes and three measurement techniques (although not all types of measurement were conducted with every ARTIST test). Functions were fit to these results which were implemented into the MELCOR model as a model improvement detailed below further. The shape of the correlation between data for the various measurement methods and particle sizes for the steam separators and dryers in Figure 4-30 is consistent with decontamination by inertial impaction, but reflects the 'bounce' of large particles that prevent surface retention. This produces a specific DF that is applied to the release for each aerosol size bin instead of using the normal MELCOR aerosol capture and settling models on the secondary side.

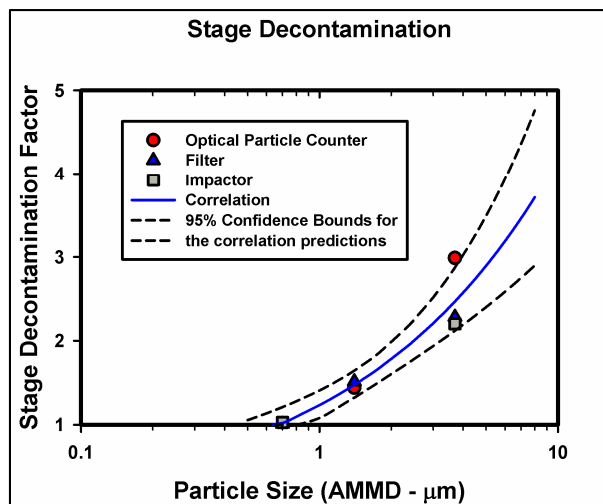
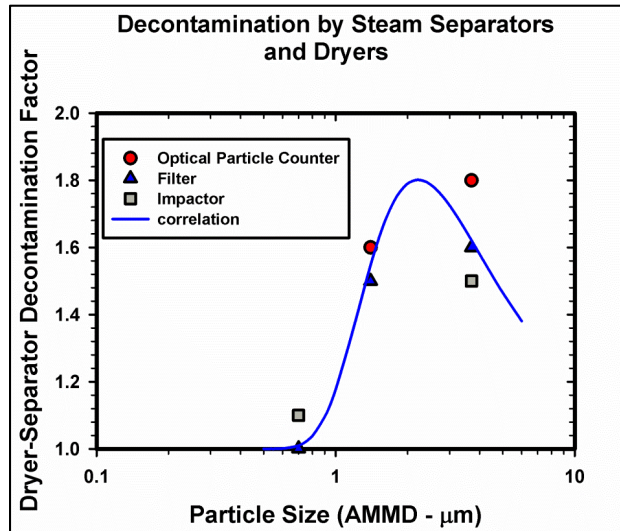


Figure 4-29 Decontamination factor per steam generator stage versus particle size and associated confidence bounds



**Figure 4-30 Decontamination factor from the separator and dryer versus particle size**

The total DF for mono-dispersed particles is dependent on the DF per stage to the power of the number of stages traveled past; thus the uncertainty in tube rupture location dominates uncertainty from the ARTIST experiment (shown by the dotted lines in Figure 4-29). As Surry has seven steam generator stages, a discrete distribution will be sampled for  $N$ ; where  $N$  is the number of stages traversed. The DF as a function of particle size shown in Figure 4-29 is applied aerosol size bin by aerosol size bin for each stage.

As previously stated, this parameter involves a model improvement in MELCOR that will change the DF from a single value of seven to a function that adjusts the DF based on aerosol particle size. In the new MELCOR improvement for each aerosol size bin, the median particle size will be used to determine two DFs based on the functions for a single steam generator stage and for the steam dryer and separator. The DF for a single stage will be raised to the  $N^{\text{th}}$  power, where  $N$  is the number of steam generator stages between the SGTR and the steam dryer and separator.  $N$  was sampled in this work to determine the axial temperature on the steam generator tube for input into the MELCOR control logic for an SGTR. This calculated total DF for the tube section will be multiplied by the DF from the steam dryer and separator function to yield a total DF which is what will be applied for that size bin.

Finally, the ARTIST tests were done with flow conditions and particles chosen to be representative of conditions in reactor accidents [7]. However, to scale the total DF exactly to MELCOR calculated flow conditions, the effective particle size used in the two DF functions is modified. Assuming that the dominant retention mechanism is inertial impaction, the test results can be scaled by preserving the Stokes number. The effective particle diameter,  $d_{eff}$ , was related to the actual particle diameter,  $d_p$ , by:

$$d_{eff} = d_p \left[ \frac{U_{acc} \rho_{acc} \mu_{test} 1}{U_{test} \rho_{test} \mu_{acc} \chi_{acc}} \right]^{1/2} = 1.4 \times 10^{-4} d_p \sqrt{\frac{U_{acc} \rho_{acc}}{\mu_{acc} \chi_{acc}}}$$

Eq. 4-32

where,  $U_{acc}$  and  $U_{test}$  are the superficial gas velocities (m/s) through the steam generators in the accident and in the test, respectively,  $\rho$  is density,  $\mu$  is gas viscosity, and  $\chi$  is the aerosol dynamic shape factor.

### Rationale for Distribution

Because the number of stages through which a particle travels is an integer value, a discrete distribution is used. Surry has seven steam generator stages, giving seven discrete bins. As indicated in Figure 19 of NUREG/CR-6365 [47], steam generator tube wall degradation has been observed in all steam generator stages. Thus, the likelihood of a spontaneous rupture is assumed to be equally probable for all steam generator stages. However, if there are no spontaneous ruptures at steady state conditions, it is highly unlikely a spontaneous rupture will occur during the select accident scenario, as the pressure differential across the steam generator tubes drops during the transient. Thus SGTRs observed in the modeled results of this work would be induced by thermal creep rupture, which propagates the growth of existing cracks. Thermal creep rupture is highly temperature dependent, so tube temperature is used to weight the discrete distribution of the spontaneous rupture phenomenon.

Normalized temperatures were taken from the 1/7<sup>th</sup> scale steam generator experiments, detailed in NUREG-1781 [44]. These normalized temperatures were near the midpoint of computational fluid dynamics predictions for a full-scale steam generator given in NUREG-1788 [45], making them applicable to this study. As the data was normalized axially, seven points are selected from a curve fit to the data, based on the actual locations of tube supports within the Surry steam generators. The distribution of temperatures is directly taken as the probability of failure in each location. This creates the discrete PDF distribution in Figure 4-31. Since temperatures are higher closer to the primary side inlet of the steam generator, there is a much greater probability at those locations (i.e.,  $N=7$  in Figure 4-31), but there will still be a significant number of samples throughout all seven tube locations.

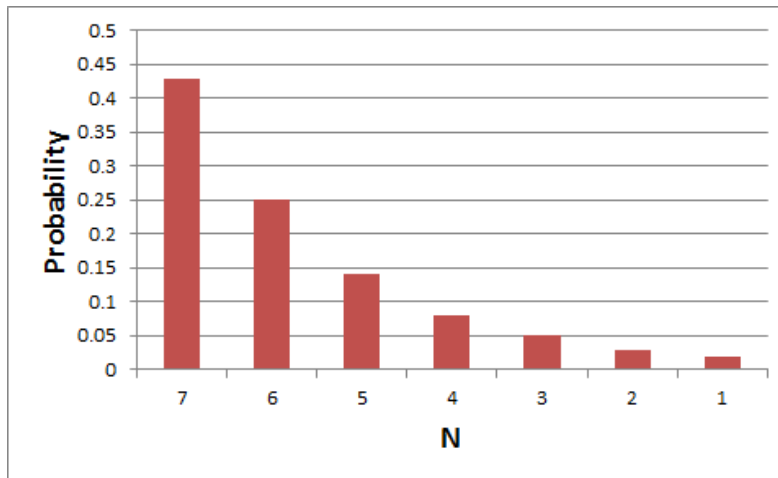


Figure 4-31 PDF for number of stages traversed after SGTR

#### 4.1.4 Containment Behavior

##### 4.1.4.1 Containment Design Leakage Rate (DLEAK)

Containment design leakage rate (DLEAK) is the leakage rate in %volume/day when containment pressure is at design pressure (45 psig). The leakage varies as containment pressure changes throughout the transient. DLEAK was sampled assuming uncertainty in the parameter can be reasonably represented by a uniform distribution having lower and upper bounds of 0.1 percent and 1.0 percent volume per day, respectively. The containment design leakage was implemented in the MELCOR Surry model by defining a flow path sized such that flowrate is limited by frictional resistance. For implementation in MELCOR, the leakage flow path is given a characteristic length to yield the sampled leakage, and these characteristic lengths are used in the regression analyses.

Prior to containment overpressure failure, radionuclide releases through nominal leakage tends to be relatively small (0.1% air volume per day at an overpressure ratio  $[P/P_{\text{Design}}]$  of 1). As an example, release fractions are less than  $10^{-4}$  of the core inventory (excluding noble gases) in the unmitigated SOARCA STSBO scenario (see Figure 5-36 in NUREG/CR-7110 Volume 2 [3]) before containment overpressure failure near 26 hours. Releases due to design leakage remained low and steady for about 20 hours before containment rebar failure in the SOARCA STBO, after which release fractions increased by several orders of magnitude due to containment functional failure (CFC parameter). This parameter can have an effect on population dose during the first day of the accident, and possibly during early evacuation. While the SOARCA STSBO exhibited relatively small early releases, uncertainty in the design leakage rate could increase radionuclide releases prior to containment functional failure.

#### Rationale for Distribution

The design basis leak rate for Surry is 0.1 percent per day; however, under certain conditions leakage may exceed this rate. NUREG-1493 identifies the design basis leak rate for Surry as 0.1 percent per day, but explains that technical specifications allow limited time operation with up to 1 percent per day containment leak rate [57]. NUREG-1493 [57] also states that the allowable leak rate can be increased by one to two orders of magnitude without significantly impacting the estimates of population dose in the event of an accident. Based on the NUREG-1493 discussion, the sampling of containment design leakage was bounded between the referenced technical specification of 1.0 percent and the stated design leakage of 0.1 percent volume per day at  $P/P_{\text{Design}}=1$ .

The base value for containment design leakage was implemented in the MELCOR Surry model by defining a flow path sized such that flowrate is limited by frictional resistance rather than by a choked flow condition. The flow path accommodates a 0.1 percent volume per day flow of steam at  $P/P_{\text{Design}}=1$ . It has a diameter of 0.0953", a length of 6'-3.2", and is absent from losses. Realizing flowrate in this flow path for fixed containment conditions to be proportional to the inverse of the square root of the length of the path, the desired variation in design leakage rate is accomplished by varying path length accordingly. A uniform discrete distribution of 10 lengths varying from 6'-3.20" to 0'-0.75" was sampled, where each length was associated with an even multiple of the base value of design leakage. The effective CDF of containment design leakage accomplished by this sampling of flow path length is presented in Figure 4-32. Figure 4-33 shows the range of design leak rate between the lower and upper bounds of 0.1 percent and 1.0 percent volume per day at  $P/P_{\text{Design}}=1$  for the MELCOR containment leakage model.

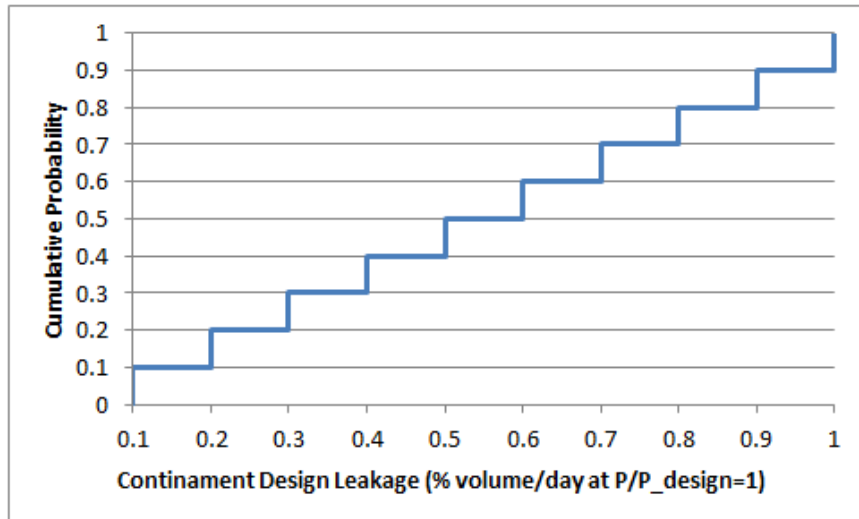


Figure 4-32 CDF of Containment Design Leakage

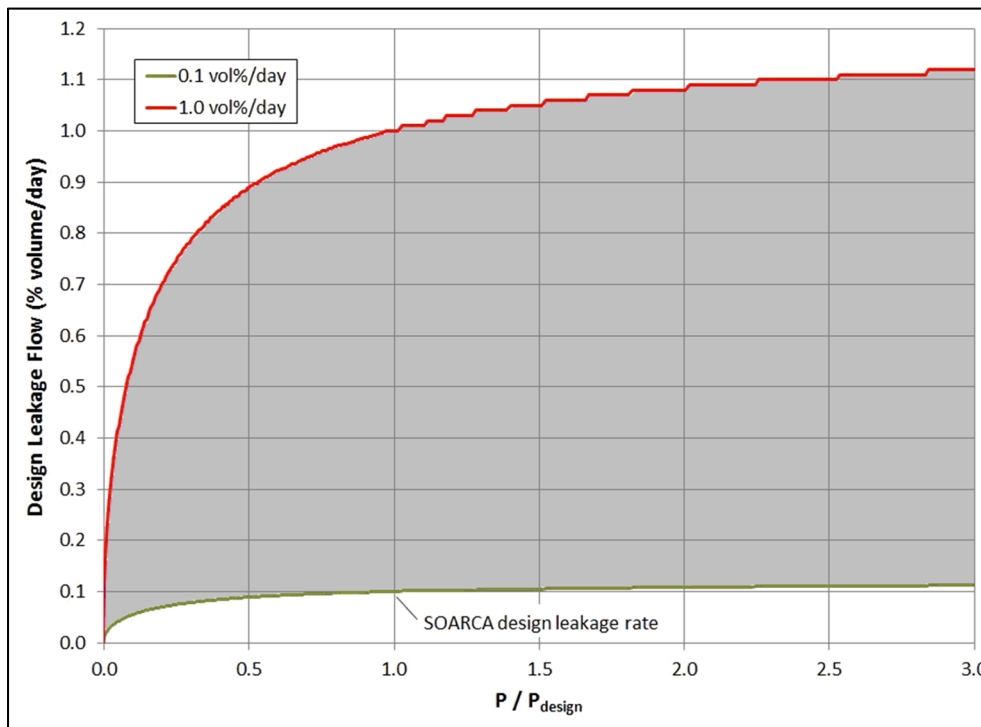


Figure 4-33 Range of containment design leakage

#### 4.1.4.2 Containment Fragility Curve (CFC)

The Containment Fragility Curve (CFC) refers to a set of containment pressure ratios at which failure modes occur and leakage increases. The ratio at which the lowest point in the curve, liner plate yield, occurs is sampled and the remainder of the data points can potentially shift,

depending on the sampling. Uncertainty in liner plate yield was represented with beta distribution ( $\alpha: 5.6; \beta: 6.3$ ) with a lower bound of 1.09 and an upper bound of 2.03 for  $P/P_{\text{Design}}$  (45 psig).

For accident scenarios without containment bypass, enhanced containment leakage due to overpressure is the dominant release path for radionuclides in the Surry MELCOR model used in SOARCA. The SOARCA model for containment overpressure failure is based on over 25 years of research. This research included both experimental and advanced computational efforts, such as the scaled PWR containment experiments at SNL (particularly the 1:4 for prestressed concrete and 1:6 for reinforced concrete) and nonlinear finite element simulations. These tests show that upon pressurization, PWR concrete containments exhibit significantly increased leakage before failing catastrophically due to the physically redundant arrangement of the steel-liner enclosed in a concrete shell. Large leakage effectively precludes catastrophic containment rupture for reasonable pressurization rates. Leakage following overpressure is most likely to occur near equipment hatches and other penetrations through the containment; these are regions of material and geometric discontinuities that cause high local stresses.

The SOARCA model for containment overpressure uses experimental data from the SNL 1:6 scaled experiments, since the Surry containment is reinforced concrete, in conjunction with a very simple NRC method to reconcile scale and the idealized nature of the experimental models. Specifically, the test data for normalized mass flow rate is used in the SOARCA MELCOR model while a set of very simple stress calculations provides the internal pressures at key stages of containment pressurization. This process yields tabular data of containment pressure vs. enhanced mass leak rate. Informed by the experimental observations, the hand-calculations estimate the internal containment pressures associated with the following events:

- Liner plate yield: 82.1 psig. Liner yield is defined to be the onset of enhanced containment leakage, and is associated with a leak rate that exceeds design leakage by an order of magnitude.
- Rebar yield: 119.36 psig
- 2 percent global containment strain: 126.71 psig.

In SOARCA, each of the calculated internal pressures was conservatively reduced 15 percent to roughly embody the large uncertainties associated with the rudimentary nature of the hand calculations, as well as uncertainties in material properties. With the spread of uncertainty being sampled for this parameter, this original conservatism can be removed.

The SOARCA model for containment overpressure is uncertain for several reasons. The scaled tests for containment overpressure were performed at ambient temperature with nitrogen, and did not consider the effects of high temperature steam, which could be saturated or superheated due to generation of non-condensable gases (from in-vessel oxidation and/or MCCI). The experimental models were non-prototypical with respect to aging, corrosion, and the arrangement of penetrations. Finally, the SOARCA hand-calculations for pressure at the various stages of containment overpressure are very simple and are reduced 15 percent rather arbitrarily. Therefore, the Surry UA treats the containment pressure at which to initiate the fragility (failure) curve as an uncertain parameter, and the treatment is informed by SOARCA, the 1:6 scale experiments, and finite element simulations for degraded containments [101].

## Rationale for Distribution

The data points shown in Figure 4-34 reflect leak rate data collected from the 1:6 scale experiments [58] and associated with NRC supplemental calculations of pressure for each stage of containment overpressure. These data points were generated in SOARCA to help inform the Surry containment leakage model. The three calculated pressures were all reduced 15 percent in SOARCA for conservatism; a fourth data point (liner plate yield shown at 1% volume / day in Figure 4-34) is adopted directly (both pressure and leak rate) from experimental data, but again with the pressure reduced 15 percent. The original SOARCA model [3] implemented a 3<sup>rd</sup> order polynomial through these data points and neglected the liner yield point; thus overpressure leakage before rebar yield was assumed to be subsumed by design leakage, and early enhanced leakage was assumed insignificant for calculation of integral releases. The Surry UA modeling approach was slightly different to facilitate uncertain parameter treatment of containment failure by overpressure and to maintain consistency with experimental observations. The Surry UA model considers functional failure to begin at liner plate yield, which is associated with a 1.0 percent mass/day leak rate (i.e., 10 times the original design leak rate, which is now an acceptable design basis leak rate under 10CFR50 Appendix J). This approach provides a model reflecting containment yield-before-rupture which was confirmed by the structural experts involved in the 1/6<sup>th</sup> scale reactor containment tests [102] as more realistic. Also, simple linear interpolation is used between the four data points of the fragility curve instead of a polynomial fit. The liner yield point is taken to be the sampled quantity from the CDF of overpressure ratio for the start of effective containment failure created in this work, and this is appropriate since past research has determined it to be the onset of significantly increased containment leakage.

After review of the containment research which documents finite element simulations for significant corrosion at mid-height of the containment [101][102], methodologies considered for severe accidents in NUREG/CR-6433 [103] and recent severe accident analyses in NUREG/CR-7149 [104], a CDF was created for the liner plate yield point of the CFC and is shown as the blue line in Figure 4-35. This CDF was also informed by discussions with containment experts and engineering judgment. It places the SOARCA pressure for liner plate yield ( $P/P_{\text{Design}} \approx 1.55$ ) significantly below the 50<sup>th</sup> percentile of the CDF, which reflects the conservatism introduced by the 15 percent reduction in the calculated pressure for liner plate yield. The majority of sampled values are between the SOARCA [3] value and the original experimental data point without conservatism of about 1.75. This reflects the best current state of knowledge about the most probable value to start overpressure leakage. The bounds of the distribution are set based on physical limits. The lower limit of  $P/P_{\text{Design}}$  of 1 is because while it would be possible to have containment degradation to the point of damage at atmospheric pressure, leakage below design pressure would be detected during outage testing. The upper limit is simply set to about the experimental point of rebar yield, which is an advanced damage state.

The CDF for the Surry UA differs from other CDFs (e.g., Surry IPE and NUREG/CR-6920), but is used to create sampled values for the liner yield pressure, which initiates overpressure leakage at a relatively low pressure and leak rate. Additionally, the CDF allows investigation into the interplay due to the effect of severe containment degradation with MACCS evacuation parameters (i.e., potential large early release frequency consequence analyses).

The data points beyond liner plate yield (rebar yield and beyond) with higher leak rates are lowered appropriately for  $P/P_{\text{Design}}$  according to the sampled  $P/P_{\text{Design}}$  for the liner plate yield data point along the CDF in Figure 4-35. However, these over pressure data points (rebar yield and

beyond) are not raised for a subsequently higher liner plate yield data point along the CDF. The rebar yield (~2.25  $P/P_{Design}$ ) and beyond data points in Figure 4-34 are considered the maximum value since they are based on experimental data and are considered fixed within structural mechanics (rebar yield and 2% global strain). While it could be envisioned that these data points could be reduced (e.g., corroded rebar), there is no justification to raise these data points within the current understanding of severe accident containment response.

As an example, consider the 20<sup>th</sup> and 80<sup>th</sup> percentile data from Figure 4-35. These percentiles translate to a  $P/P_{Design}$  of 1.45 and 1.75, respectively, for the liner plate yield data point in Figure 4-34. For the 20<sup>th</sup> percentile, the subsequent data points (rebar yield and beyond) are reduced for  $P/P_{Design}$  by ~0.1 (e.g., 2.155 for the rebar yield data point) and these new data points are linearly interpolated between the data points for the containment functional failure model in MELCOR. For the 80<sup>th</sup> percentile, the subsequent data points (rebar yield and beyond) remain at the same  $P/P_{Design}$  (e.g., 2.255 for the rebar yield data point) and the new liner plate yield data point is linearly interpolated with the original subsequent data points to produce the containment functional failure model in MELCOR.

Uncertainty in the leak rates are neglected, since estimations of experimental error are not readily available for the Surry UA. It is assumed that most of the uncertainty lies in the pressure associated with each of the four data points representing increasing leak rates, which were estimated by simple hand calculations informed by the experiments.

For compatibility with the MELCOR uncertainty engine, a beta distribution was fit to the CDF described above and shown in Figure 4-35. This distribution has the parameters: LB = 48.9 psi ( $P/P_{Design}$ =1.09), UB=103.6psi ( $P/P_{Design}$ =2.03),  $\alpha$  = 5.6,  $\beta$  = 6.3.

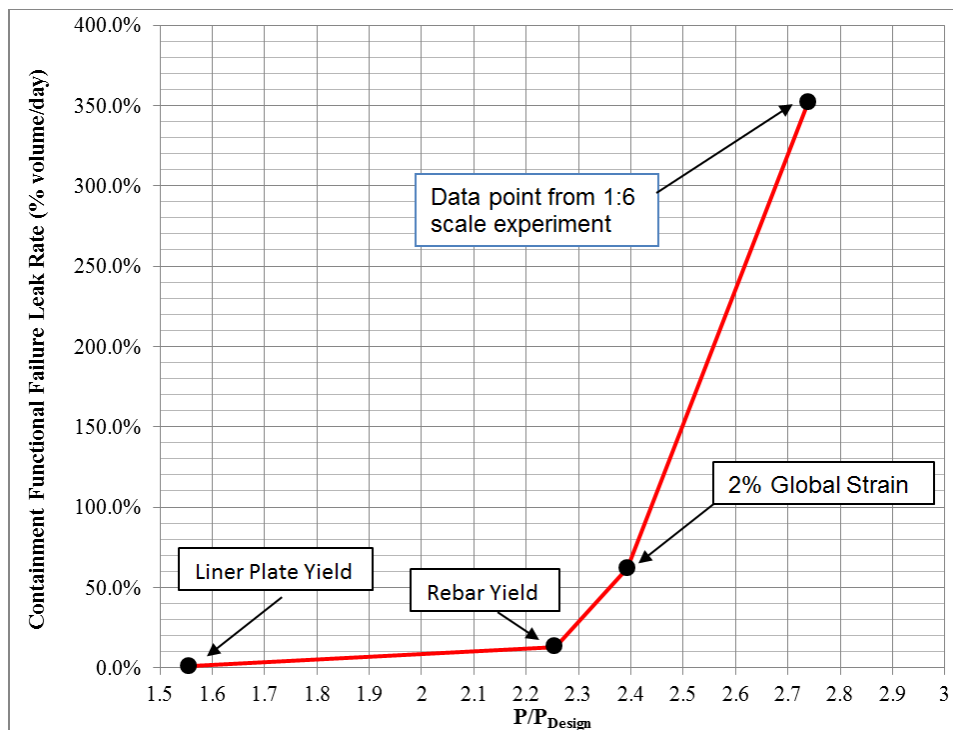
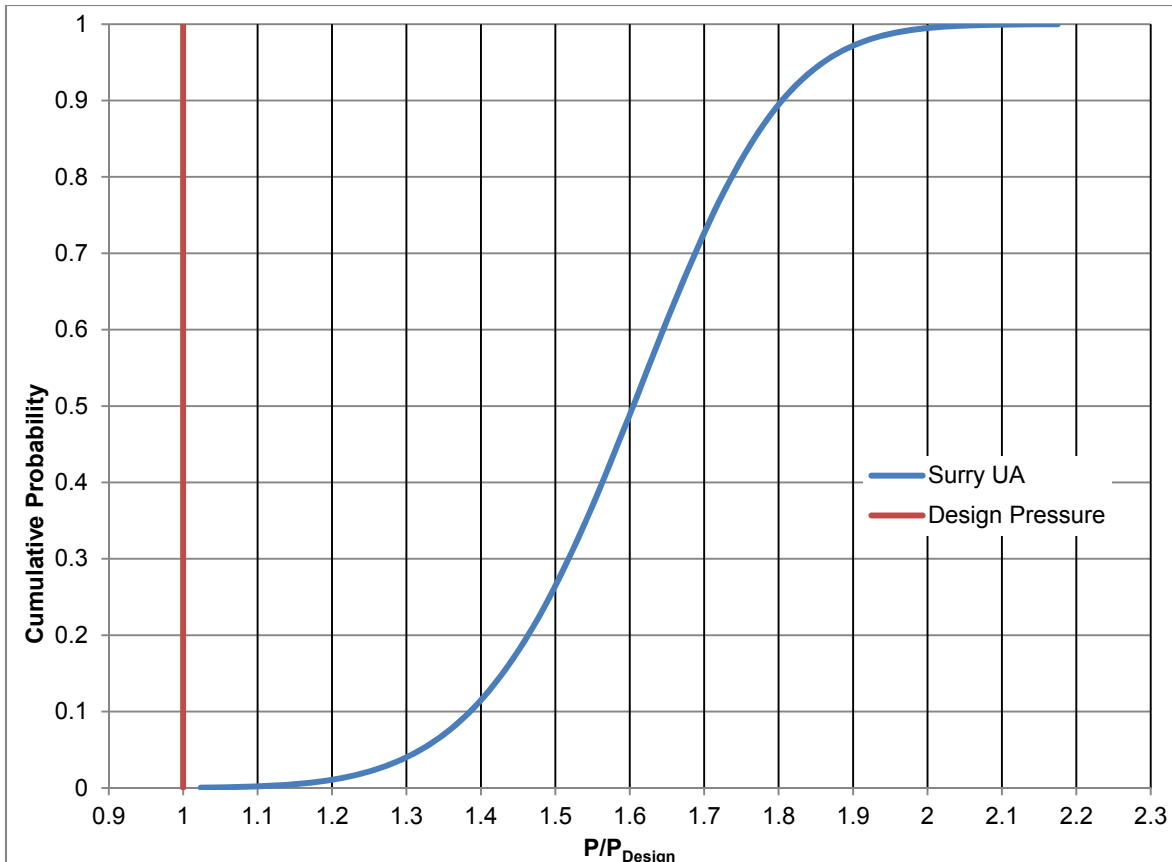


Figure 4-34 Containment functional failure leakage



**Figure 4-35 CDF for containment overpressure ratio for liner plate yield**

#### 4.1.4.3 Containment Convection Heat Transfer Multiplier

To address uncertainty in containment convection heat transfer, a multiplier (defined as XHTFCL in MELCOR) is modified for containment wall heat structures. The uncertainty in the unitless multiplier was represented by a triangular distribution with a mode of 1.4, a lower bound of 1.0 and an upper bound of 2.0. This parameter is identified as CONDENS in the regression tables in Section 6.1.

The heat deposited in concrete and steel in containment is significant in a MELCOR severe accident simulation and the rate at which the heat is deposited has associated uncertainty. Greater heat deposition rates relate to slower containment pressurization. Important to heat deposition rate (or heat transfer rate) is heat transfer coefficient (HTC). The calculation of HTC in MELCOR involves determining Nusselt number (Nu) as it does in the CONTAIN computer code [105]. Increasing the leading coefficient in the relation for Nu from 0.10 (default in MELCOR) to 0.14 (CONTAIN default) has historically been found to give more realistic results in comparisons with applicable experimental data [108]. Nu is a multiplier in the relation for HTC, and increasing the leading coefficient in the relation for Nu from 0.1 to 0.14 increases HTC by 40 percent. The value of 0.14 is only applicable to laminar natural circulation so its use in other accident sequences or models may require a new distribution.

## Rationale for Distribution

HTC can be increased in MELCOR by increasing the leading coefficient in the relation for Nu, just as in CONTAIN. Doing so, however, globally affects all heat structures in the model. A different means of increasing HTC is to increase the HTC multiplier XHTFCL individually associated with each heat structure. This was done in the UA calculations to each heat structure representing a wall of containment. Uncertainty in HTC was represented by employing a triangular probability distribution for the multiplier with mode 1.4, lower bound of 1.0 and upper bound of 2.0. The same specific multiplier was applied to all the containment walls in a given realization. The mode of 1.4 reflects the 40 percent increase reported as beneficial in the CONTAIN work. The value of 1.0 assigned to the lower bound is the default value of the multiplier. The value of 2.0 assigned to the upper bound reflects a doubling of the HTC MELCOR would assign on its own.

MELCOR documentation suggests that XHTFCL and mass transfer (i.e., condensation/evaporation) coefficient multiplier XMTFCL not be modified independently lest computational difficulties arise [7] (section 2.6). Consequently, multipliers XHTFCL and XMTFCL have been defined together as the same value in each realization. The associated PDF and CDF for the heat transfer coefficient and mass transfer multipliers given 500 samples are shown in Figure 4-36 and Figure 4-37, respectively.

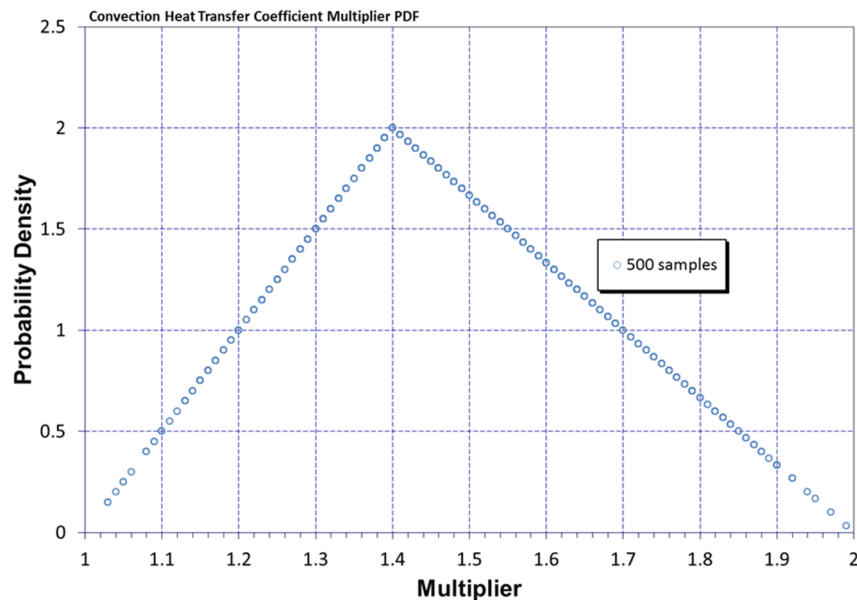
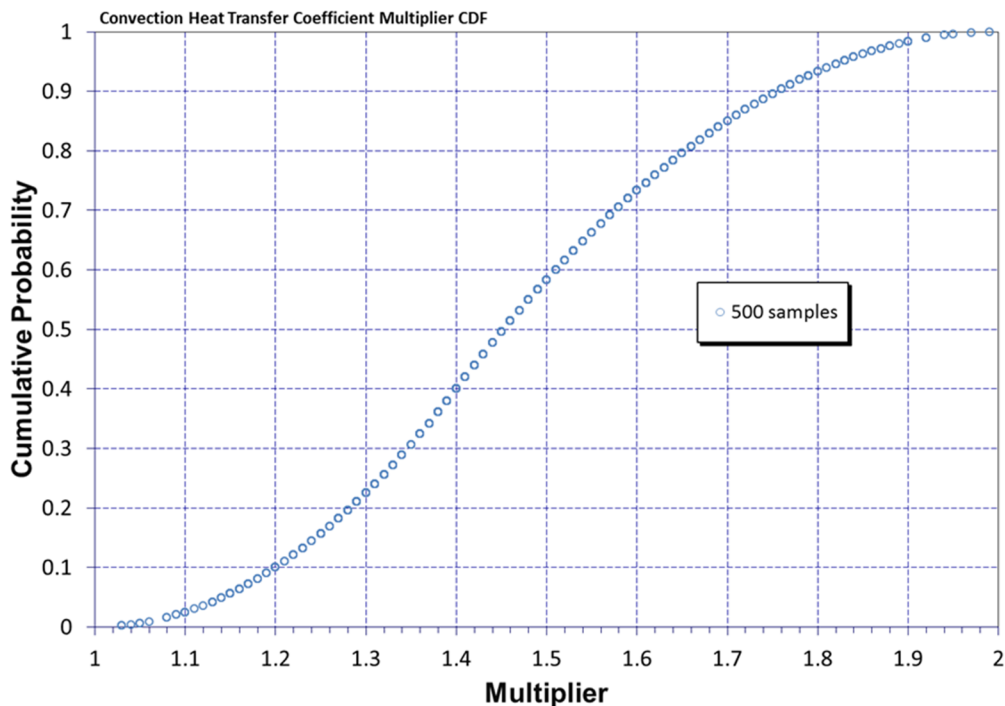


Figure 4-36 PDF of heat transfer coefficients and mass transfer multipliers



**Figure 4-37 CDF of heat transfer coefficients and mass transfer multipliers**

#### 4.1.5 Chemical Form (CHEMFORM I2)

##### 4.1.5.1 Chemical Form of Iodine

CHEMFORM I2 determines the fraction of total iodine in the fuel that is initially defined as gaseous, not aerosol. The uncertainty in the percent of gaseous iodine is represented with a truncated lognormal distribution ( $\mu$ : -9.94  $\sigma$ : 0.28) with a lower bound of 0 percent because there cannot be a negative amount of gaseous iodine. The range of gaseous iodine fraction is dependent on which time at cycle is selected.

Uncertainty in the gaseous iodine fraction in the total iodine released was identified as a key parameter and selected for evaluation of the sensitivity of SOARCA results. The presence of gaseous iodine remains an uncertain source term issue, especially with respect to long-term radioactive release mitigation issues. This is especially true after the comparatively much larger airborne aerosol radioactivity has settled from the atmosphere. Mechanistic modeling of gaseous iodine behavior is a technology still under development with important international research programs determining the dynamic behavior of iodine chemistry with respect to paints, wetted surfaces, buffered and unbuffered water pools undergoing radiolysis, and gas phase chemistry.

The Surry SOARCA analysis [3] assumed all released iodine combines with cesium to form cesium iodide (CsI) [3]. However, past radionuclide release studies, such as NUREG-1465 [115], have assumed that as much as 5 percent of the total iodine inventory is released as gaseous iodine. The current revision of NUREG-1465, ongoing at Sandia, has maintained this 5 percent gaseous iodine fraction as of the publication of this study. Additionally, recent

experiments at the Phebus facility show that gaseous iodine is found within containment [50]. With the different core make-ups of the various Phebus tests, the percentage of iodine in the containment that is gaseous has varied from as low as 0.2 percent to as high as 7 percent. Understanding the uncertainty regarding the chemical form of iodine is important because the iodine chemical behavior affects the amount and timing of iodine release from containment to the environment.

### Rationale for Distribution

Because there is a lack of understanding on gaseous iodine behavior from the Phebus tests, the recommended approach is that fission gas release to the fuel/cladding gap be used as a surrogate for the gaseous iodine fraction. This is an applicable surrogate because past research performed for reports such as WASH-1400 [78] (pg. IX-5) and NUREG/CR-7003 [79] (pg. 2-4) has shown that (i) the percentage of iodine released to the gap relative to the total inventory is similar to the corresponding percentage for noble gases like xenon and (ii) iodine and xenon have about the same diffusion coefficient. Second, analysis of used fuel rods has shown that iodine in the gap is gaseous. Finally, the consensus based on multiple severe accident experiments is that the iodine retained in the fuel rod and not transported to the gap will later be released in the form of CsI. Therefore, it is assumed that all gaseous iodine is located within the fuel/clad gap at essentially the same percentage as all fission gas.

Figure 4-38 summarizes data provided by the Atomic Energy and Alternative Energies Commission (CEA) from French reactors for low enriched uranium (LEU) and mixed oxide fuel. This data was obtained from Sandia interactions with CEA and is not available in referenceable material. The fuel was removed from operating reactors, and the cladding was punched to determine the gases present in the gap.

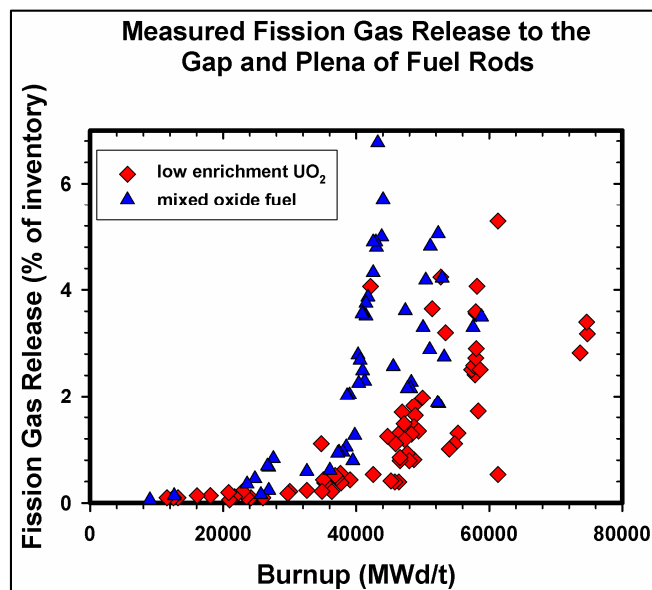


**Figure 4-38 French measured fission gas release to the fuel/cladding gap**

Surry uses exclusively LEU in its fuel, so the red data points were extracted from Figure 4-38. A 'best fit' curve is fit to the data, which is an exponential function. As stated in Section 4.1.2.5, specific plant information was provided for three different times in an operating cycle (i.e., BOC,

MOC, and EOC). This included specific burn-up data, in MWd/t, which was used to calculate an average burn-up for each time at cycle. These three average burn-ups are input to the curve fit to the French data, yielding gaseous iodine percentages of 0.1 percent, 0.18 percent, and 0.42 percent for each time at cycle, respectively. These values agree with the majority of Phebus tests, which showed the concentration of gaseous iodine in containment was generally <1 percent.

To create an uncertainty distribution, the absolute difference between each data point in Figure 4-38 and the exponential best-fit curve is calculated and normalized against burn-up. The spread of the transformed data fits well with a lognormal distribution with parameters  $\mu=-9.94$  and  $\sigma=0.28$ . The distribution is valid for any burn-up, although the lower limit of gaseous iodine must be truncated at 0.0 percent since it cannot be less than zero. The inverse of the lognormal distribution was randomly sampled externally, and using the specific burn-up value at each sampled time at cycle, a CDF for each time at cycle was created. As an example, the CDF for EOC is shown in Figure 4-39. Note, the best fit value for EOC of 0.42 percent is near the 50<sup>th</sup> percentile of the CDF and about 80 percent of the samples are below gaseous iodine of 1 percent, which is supported by the low to mid burn-up French data and the majority of the Phebus tests. Similar CDFs were created for BOC and MOC. The data points which form these CDFs are then used as the inputs to the MELCOR model.

The highest possible gaseous iodine percentage for EOC is about 3 percent which is lower than the previously held standard of 5 percent. Additionally, the French data also contains multiple points above a 3 percent threshold. However, based on the best fit to the data and the plant-specified burn-up values, sampling iodine this high is not justified. It is expected that gaseous iodine will release just like noble gases, and the results from 1 percent to 3 percent should be able to be extrapolated to 5 percent or above.

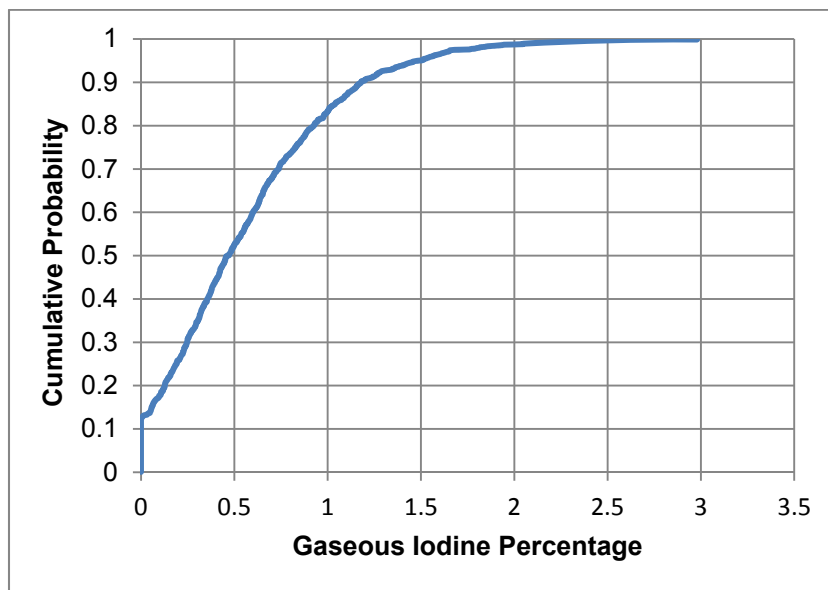


**Figure 4-39 CDF for the gaseous iodine percentage at EOC**

#### 4.1.5.2 Chemical Form of Cesium (CHEMFORM Cs)

CHEMFORM Cs determines the fraction of total available cesium in the fuel that becomes  $\text{Cs}_2\text{MoO}_4$ , with the remainder as  $\text{CsOH}$ . The uncertainty is represented with beta distribution ( $\alpha: 9; \beta: 3$ ) with a lower bound of 0 and an upper bound of 1.0.

As mentioned in Section 4.1.5.1, the first step in the speciation of cesium is the combination with most available iodine to form  $\text{CsI}$ . However, since there is generally much more cesium available than iodine, a significant amount of cesium remains to form other chemical classes by further speciation. The predominant next speciation of cesium described in the Surry SOARCA analysis [3] was based on detailed chemical analysis of the deposition and transport of the volatile fission products in the Phebus facility tests. The chemical analysis revealed molybdenum combined with cesium and formed cesium molybdate ( $\text{Cs}_2\text{MoO}_4$ ). This is based on cesium and molybdenum having been found deposited in the same locations that were at temperatures too high for cesium hydroxide to remain deposited. However, there was also evidence from the Phebus tests that cesium is revaporized at temperatures consistent with the cesium hydroxide chemical form. It is presumed that reactions between cesium molybdate and steam cause cesium hydroxide to form after release from the fuel. Prior to the Surry SOARCA analysis [3], the MELCOR default chemical form of remaining cesium (beyond the creation of  $\text{CsI}$ ) was 100 percent cesium hydroxide. Understanding the uncertainty regarding chemical form of cesium is important because cesium chemical behavior affects the amount and timing of the cesium release from containment into the environment (e.g., late phase revalorization of cesium).

#### Rationale for Distribution

The parameter being sampled is the fraction of cesium that becomes  $\text{Cs}_2\text{MoO}_4$  and so there are clear limits at 0.0 and 1.0. These limits also represent the spread in what was considered 'best practice' for cesium in past work where in SOARCA it was considered 100 percent cesium molybdate and prior to SOARCA the best practice had been 100 percent cesium hydroxide. So for this parameter, 0.0 and 1.0 will be used as the lower and upper limits, respectively. But physically, 0.0 and 1.0 can never be reached because the chemical potential for the other species would approach infinity. This supports the use of a beta distribution because the bounds are approached but never reached.

The best estimate for cesium partitioning based on examination of Phebus results indicates that outside of the primary system (and in containment) cesium will have a speciation of 80 percent  $\text{Cs}_2\text{MoO}_4$  and 20 percent  $\text{CsOH}$ . This may not represent the cesium distribution at the time of release from fuel, but within MELCOR there is no model for the cesium molybdate and steam reaction to form cesium hydroxide, so the environmental release forms need to be initialized within the fuel.

A beta distribution was created, using 0.8 as the mode and 0.0 and 1.0 as the bounds for  $\text{Cs}_2\text{MoO}_4$ . Because there is no information beyond the mode and the bounds, it is desirable for the mean and median to be about the same as the mode. The shape parameters of  $\alpha=9$  and  $\beta=3$  satisfy these criteria. Figure 4-40 shows the PDF of the distribution. This distribution represents the current thinking on cesium speciation based on the Phebus tests, using physical limits as bounds, which also agree with past best practices.

Partitioning the initial core inventory of cesium among certain allowable chemical forms for release and transport is managed within MELCOR input files that define the initial spatial mass

distribution of each chemical species and its associated decay heat. Changes to the mass fractions assumed for a particular chemical group directly affect the mass fractions of other chemical groups, and hundreds of individual input records within the MELCOR model for Surry. A script was written that takes input from the sampled continuous distribution and pre-creates the necessary MELCOR files. Fixed partition fractions are used to preserve mass balances.

Again, it should be noted that this distribution of cesium is applied to the amount of cesium remaining after it reacts with iodine to form CsI and after 4.65 percent of remaining cesium beyond form CsI is introduced to the fuel gap as CsOH, since there is no significant molybdenum within the fuel gap.

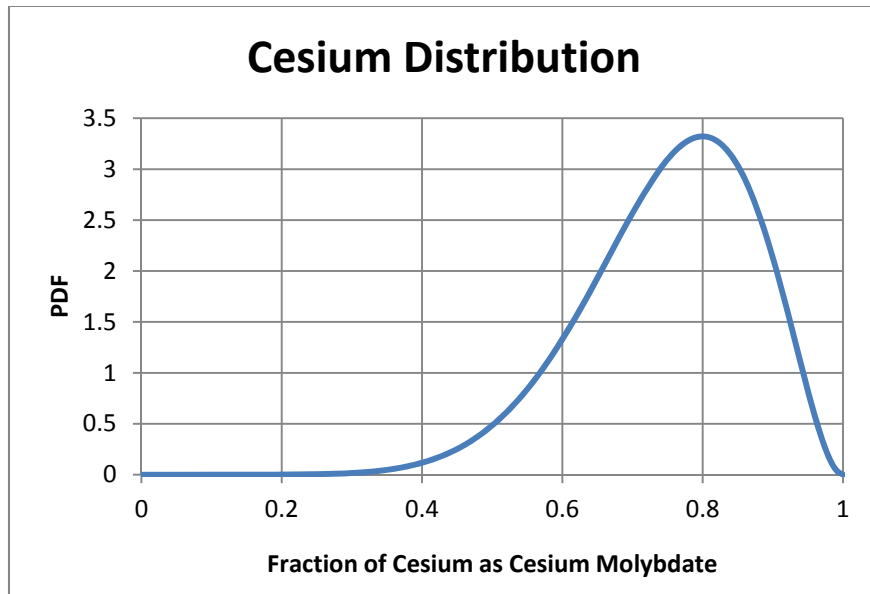


**Figure 4-40 PDF for the fraction of cesium as cesium molybdate**

#### **4.1.6 Aerosol Deposition**

The process of two or more aerosol particles colliding and combining to form a larger particle is known as agglomeration. The processes treating agglomeration in MELCOR are Brownian diffusion, differential gravitational settling, and turbulent agglomeration by shear and inertial forces. Aerosol particles are not usually assumed to be spherical, except when they include significant amounts of liquid. The effective aerosol densities may be significantly less than the bulk density of the materials of which the aerosols are composed.

##### **4.1.6.1 Dynamic Shape Factor**

The dynamic shape factor is defined as “the ratio of the actual resistance force of the nonspherical particle to the resistance force of a sphere having the same volume and velocity” [111]. This unitless dynamic shape factor is used to account for the stringing out of aerosol agglomerates in a linear or complex manner as opposed to growing as a perfect sphere. The dynamic shape factor is sampled directly, and the uncertainty of it is represented with a scaled beta distribution with the parameters of  $\alpha=1$  and  $\beta=5$  and bounds of 1.0 and 5.0.

A value of 1.0 is a perfect sphere and it is the lower limit for the dynamic shape factor. This value is also the default value in MELCOR and was used in the Surry SOARCA analysis [3].

### Rationale for Distribution

The MAEROS model in MELCOR is used to determine the mass concentration evolution of aerosols in a spatially homogenous volume, as well as deposition on surfaces and injection/removal from volumes. One of the critical assumptions of this model is that non-spherical particle effects are adequately parameterized with the dynamic shape factor, the collision shape factor, and the effective material density. The importance of these parameters is demonstrated in several uncertainty analyses of the MAEROS aerosol model performed in support of the development of the MELCOR program [106][107]. To determine the uncertainty of this model, the uncertainty of the dynamic shape factor is addressed.

Kasper et al [110] (Tables 9 and 10), experimentally measured values for the dynamic shape factor for linear chains with their long axis either parallel or perpendicular to the settling direction, as shown in Figure 4-41. As seen in Figure 4-41, the shape factor is reasonably linear with respect to the number of spheres. This data supports an upper bound of 2.8, with a weighting toward values less than 2.0. Compiled data from Hinds [111] (pg. 48) also supports a range of 1.0 to 2.04. However, Brockmann, J. E., et al [112], compiled data and models that yield a range of 1 to 10 for the dynamic shape factor. The same report includes a correlation for loosely-packed spheres which calculates dynamic shape factors will be in the range of 1 to 5 for void volumes ranging from 26 to 99 percent. Based on these sources, a range of 1 to 5 is reasonable and is the range used for this project.

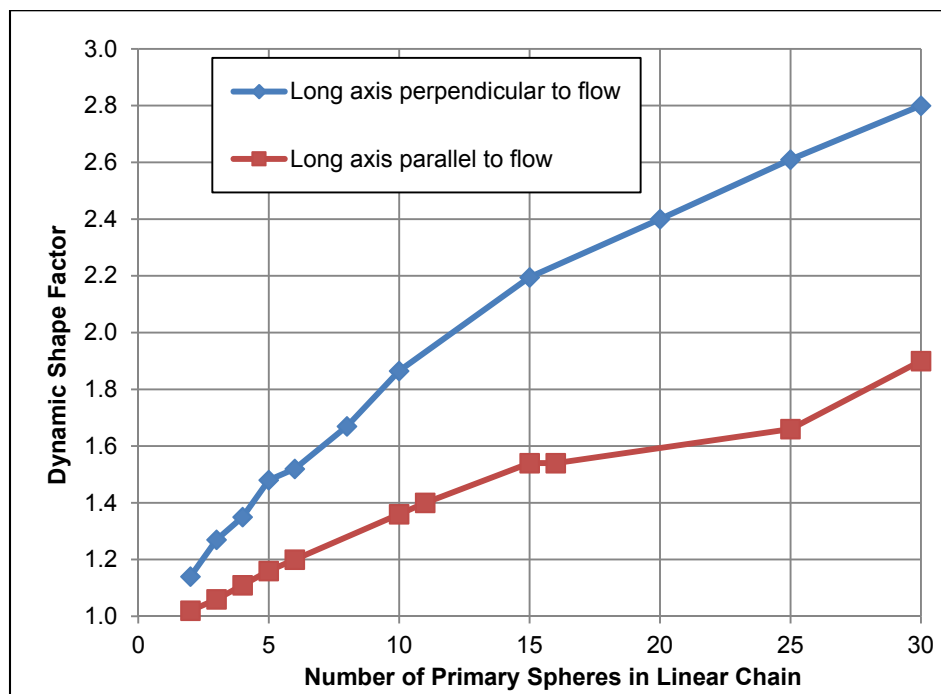


**Figure 4-41 Dynamic shape factor compared to number of spheres within a chain**

Although the bounds of the distribution were informed by the experiments described, these works cannot inform the shape of the distribution since they do not contain information on the

normal shape of aerosols during a severe accident. Kissane [113] compiled information on aerosols from a number of nuclear accident experiments, including the Phebus fission product tests (FPT). The report concluded, “Concerning particle shape, relatively compact particles without branching chain-like structures appear to be typical in the RCS;” although a visual inspection of post-test deposition images did show slight evidence of aerosol chains. Since a compact, spherical particle has a shape factor of 1.0, the distribution is weighted more heavily toward the lower end of the range (1.0). Additionally, most references support weighting more heavily in the 1.0 to 2.0 range. Because of this weighting, a beta distribution is used, with the parameters of  $\alpha=1$  and  $\beta=5$ , and the CDF of the distribution is shown in Figure 4-42. The  $\alpha$  parameter yields a function that has a peak as close as possible to the lower bound of 1.0, while the  $\beta$  parameter gives the desired shape to the PDF and yields about 75 percent of samples between 1.0 and 2.0 while still allowing some samples at physically possible values up to 5.0.

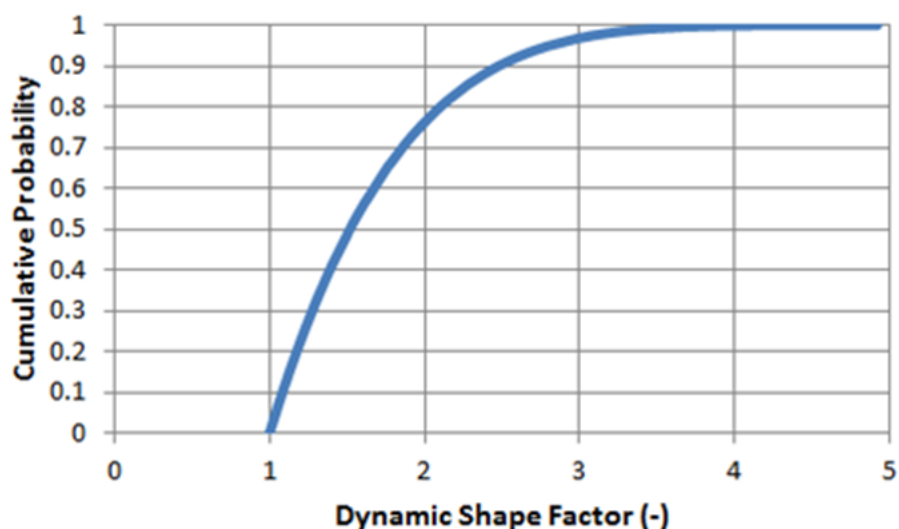


**Figure 4-42 CDF of the dynamic shape factor**

Additionally, there is a fundamental MELCOR limitation for aerosols in that the dynamic and collision shape factors and density are set globally at the beginning of the run and cannot be updated as the accident progresses. This means that the dynamic shape factor chosen from the uncertainty distribution cannot be changed during the accident progression.

## **4.2 Consequence Model Uncertainty (MACCS Inputs)**

The MACCS consequence model (Version 3.10.0.0 SVN-2560) was used in this analysis to calculate offsite doses and their effect on members of the public. Since the publication of NUREG/CR-7110 Volume 2 [3], MACCS and MELCOR have continued to be updated and improved, making a direct comparison with the Surry SOARCA analysis [3] not practical. To allow some comparison, the Surry SOARCA analysis [3] site file, which includes demographics, was maintained. This allows direct comparison of risk results, which is necessary to achieve the objective of quantifying the robustness of the original Surry STSBO by direct comparison of early and latent fatality risks. The early fatalities are those expected to occur within a relatively short period from the time of exposure (early health effects), and the latent cancer fatalities are those expected to occur over the lifetime of the exposed individuals [114]. The MACCS figures of merit were LCF risk and early fatality risk at specified distances.

Many of the uncertain MACCS parameters have both epistemic and aleatory contributions, and the combined effect adds complexity when developing the distributions. The focus of this UA is on epistemic uncertainty; however, some of the distributions developed for the uncertain inputs include aleatory uncertainty as well. For example, some of the evacuation parameters include the effects of weather, which is considered aleatory uncertainty. While the effects of adverse weather on evacuation speed are partially accounted for in the model, they are not fully accounted for and this leads to some uncertainty in the input parameters resulting from weather uncertainty. No effort was taken to deconvolve aleatory and epistemic uncertainties when they both contribute to individual parameters; instead, a simple approach is taken where weather is considered to be aleatory in nature, and all other uncertainties are considered to be epistemic in nature. A total of 622 parameters were sampled for the MACCS portion of the analysis. These parameters are described as parameter groups in Table 4-7.

Weather conditions that would apply in the case of a potential accident at some time in the future cannot be known in advance. MACCS accounts for weather variability by analyzing a statistically significant set of weather trials, and the modeled results are ensemble averages of weather that represent the full spectrum of meteorological conditions. This sampling strategy was chosen to represent the statistical variations of the weather and is consistent with MACCS best practices [6]. Emergency response to a potential accident cannot be predicted in advance either, because it is dependent on source term magnitude, time of day, weather, and site specific characteristics. Modeling of emergency response includes the timing of response actions related to protecting the public health and safety. MACCS represents protective action response activities through movement of cohorts. A cohort is defined as a segment of the population with unique response characteristics. The cohorts established in the best estimate analysis [3] were maintained for this UA and are listed below.

Cohort 1 represents the majority of the public residing within the 10 mile EPZ.

Cohort 2 represents the shadow evacuation population of 20 percent.

Cohort 3 represents the schools within the EPZ.

Cohort 4 represents the special facilities residents within the EPZ.

Cohort 5 represents the evacuation tail for the 0 to 10 mile public.

Cohort 6 represents the small fraction of the public that does not evacuate.

As described in Section 2, MACCS parameters expected to be important to the figures of merit were selected as uncertain inputs. Table 4-7 lists the distributions and bounds related to each parameter. For many of these parameters, the sampling approach is quite complex and is described in detail later in this section.

Several of the parameter distributions selected for this analysis are based on expert elicitation data captured in NUREG/CR-7161, "Synthesis of Distributions Representing Important Non-Site-Specific Parameters in Off Site Consequence Analysis" [69]. The United States and the Commission of European Communities conducted a series of expert elicitations to obtain distributions for uncertain variables used in health consequence analyses related to accidental release of nuclear material. The distributions reflect degrees of belief for non-site specific parameters that are uncertain and are likely to have significant or moderate influence on the results. The methodology in reference [69] used a resampling of the expert values and was based on the assumption of equal weights of the expert opinions.

**Table 4-7 Uncertain MACCS parameters applied in the analysis.**

Uncertain Parameter		Distribution type	Mode, $\alpha, \beta$	Lower Bound	Upper Bound	
Wet Deposition (CWASH1) (Section 4.2.1)		Log uniform		$10^{-6}$	$10^{-4}$	
Dry Deposition Velocities (VDEPOS, m/s) (Section 4.2.2)		Triangular	1	0.000405	0.000128	0.00128
			2	0.000373	0.000118	0.00118
			3	0.000488	0.000154	0.00154
			4	0.000823	0.00026	0.0026
			5	0.00161	0.000509	0.00509
			6	0.00329	0.00104	0.0104
			7	0.00636	0.00201	0.0201
			8	0.0104	0.0033	0.033
			9	0.013	0.0041	0.041
Groundshine Shielding Factors (GSHFAC)* (Section 4.2.3.1)		Continuous Linear				
Inhalation Protection Factors (PROTIN)* (Section 4.2.3.2)		Uniform				
Early Health Effects LD <sub>50</sub> Parameter (EFFACA)* (Section 4.2.4.1)	Hematopoietic	Continuous Linear				
	Pulmonary					
	Gastrointestinal					
Early Health Effects* Exponential Parameter (EFFACB) (Section 4.2.4.2)	Hematopoietic	Continuous Linear				
	Pulmonary					
	Gastrointestinal					
Early Health Effects Threshold Dose (EFFTHR)* (Section 4.2.4.3)	Hematopoietic	Continuous Linear				
	Pulmonary					
	Gastrointestinal					
Dose and Dose Rate Effectiveness Factor (DDREFA)* (Section 4.2.5.1)		Continuous Linear				
Lifetime Cancer Fatality Risk Factors (CFRISK) (Section 4.2.5.2)		Truncated Log normal	Varies by organ	Varies by organ	Varies by organ	
Long Term Inhalation Dose Coefficients (Section 4.2.5.3)		Log normal	Varies	Varies	Varies	
Crosswind Dispersion Linear Coefficient (CYSIGA, m) (Section 4.2.6.1)	A/B	Continuous Log triangular	0.7507	0.3002	1.8768	
	C		0.4063	0.1625	1.0158	
	D		0.2779	0.1112	0.6948	
	E/F		0.2158	0.0863	0.5395	
Vertical Dispersion Linear Coefficient (CZSIGA, m) (Section 4.2.6.2)	A/B	Continuous Log triangular	0.0361	0.0144	0.0903	
	C		0.2036	0.0814	0.509	
	D		0.2636	0.1054	0.659	
	E/F		0.2463	0.0985	0.6158	
Evacuation Delay (DLTEVA, hr) (Section 4.2.7.1)	Cohort 1	Triangular	2	1	4	
	Cohort 2		3	1	4	

Uncertain Parameter		Distribution type	Mode, $\alpha, \beta$	Lower Bound	Upper Bound
	Cohort 3		2.75	0.5	4
	Cohort 4		5	3	10
	Cohort 5		4	1	10
Evacuation Speed (ESPEED, mph) (Section 4.2.7.2)	Cohort 1	Triangular	1	0.5	12
	Cohort 2		5	0.5	15
	Cohort 3		1	0.5	15
	Cohort 4		5	0.5	20
	Cohort 5		10	0.5	20
Hotspot Relocation Time (TIMHOT, hr) (Section 4.2.7.3)		Uniform		12	30
Normal Relocation Time (TIMNRM, hr) (Section 4.2.7.4)		Uniform		16	48
Hotspot Relocation Dose (DOSHOT, rem) (Section 4.2.7.5)		Triangular	5	1	7.5
Normal Relocation Dose (DOSNRM, rem) (Section 4.2.7.6)		Triangular	1	0.5	2
Weather Trials - Aleatory Uncertainty (Section 4.2.8)					

\*Multiple values, refer to specific parameter section for discussion

#### 4.2.1 Wet Deposition Model (CWASH1)

CWASH1 is a linear factor in the expression for the wet deposition rate for aerosols. A log uniform distribution was used to represent uncertainty with a lower bound of  $10^{-6}$  and an upper bound of  $10^{-4}$ . Under rain conditions, wet deposition is very effective and rapidly depletes the plume. This process can produce concentrated deposits on the ground and create what is often referred to as a hotspot (i.e., an area of higher radioactivity than the surrounding areas) [80]. The epistemic uncertainty associated with CWASH1 is potentially important in reactor accident consequence calculations because increasing values for CWASH1 result in increased local concentrations of radionuclides deposited by rainfall events. In turn, such increased local radionuclide concentrations can have two opposing effects on radiation exposure and resulting health effects. First, high local radionuclide concentrations can increase early individual exposure and resulting early health effects. Second, high local radionuclide concentrations can increase the total fraction of a radionuclide release that is interdicted, and thus decrease long term population exposure and resulting latent health effects. This happens because the localized, high-concentration area created by the rain is likely to be interdicted, reducing the exposures to the residents in the long-term. Populations at longer distances receive less exposure because most of the plume has been washed out by the rain.

#### Rationale for Distribution

The model used in MACCS for wet deposition of aerosols over a unit area for a time interval  $[t_i, t_{i+1}]$  is formally given by

$$dC(t)/dt = -\lambda C(t) = -c_1 R^{c_2} C(t),$$

Eq. 4-33

where  $t$  = time (units: s),  $C(t)$  = vertically integrated aerosol concentration in the plume at time  $t$  (units: Bq/m<sup>2</sup>),  $\lambda = c_1 R^{c_2}$  = fractional removal rate for aerosols (units: 1/s),  $R$  = rainfall rate (units: mm/hr), and  $c_1$  (units: 1/s(mm/hr)<sup>c<sub>2</sub></sup>) and  $c_2$  (units: dimensionless) are constants used in the definition of  $\lambda$ . In turn,

$$\begin{aligned} D(t_i, t_{i+1}) &= C(t_i) - C(t_{i+1}) \\ &= C(t_i) - C(t_i) \exp[-\lambda(t_{i+1} - t_i)] \\ &\cong \lambda(t_{i+1} - t_i) C(t_i) \end{aligned}$$

Eq. 4-34

is the estimated aerosol deposition (units: kg/m<sup>2</sup>) that takes place over the time interval  $[t_i, t_{i+1}]$ .

In the computational implementation of aerosol deposition in MACCS, the rainfall rate  $R$  changes hourly for each rainfall event; however, the same values for  $c_1$  and  $c_2$  are used for all rainfall events. Although rainfall rate is taken into account in the definition of  $\lambda$ , it is well known that many additional properties of a rainfall event affect aerosol deposition, including (i) distribution of aerosol size, (ii) chemical and physical properties of aerosols, (iii) distribution of rain drop size, (iv) different aerosol removal rates within clouds (i.e., rainout) and below clouds (i.e., washout), and (v) short-term temporal variations in rainfall rate that are lost in reported hourly rainfall rates [56][60][61][62][63].

Given that MACCS uses fixed values for  $c_1$  and  $c_2$  for all rainfall events over the course of one year, the indicated range of properties that can affect aerosol deposition presents a major challenge in defining uncertainty distributions for  $c_1$  and  $c_2$ . Specifically, the values used for  $c_1$  and  $c_2$  in MACCS are compromise values that are used for a large number of different rainfall situations, while being the most appropriate values to use for only a few of these situations. As a result, the epistemic uncertainty distributions for  $c_1$  and  $c_2$  should characterize the uncertainty in the locations of the most appropriate values to use for  $c_1$  and  $c_2$  given that a single value for  $c_1$  and a single value for  $c_2$  are used for all rainfall events. Given the manner in which  $c_1$  and  $c_2$  are used in MACCS, care must be taken to avoid using distributions for  $c_1$  and  $c_2$  that are intended to characterize the variability in  $c_1$  and  $c_2$  over the range of individual rainfall events, as the use of such distributions may produce unrealistic uncertainty analysis results. For example, the results of the expert elicitations for the wet deposition of aerosols in Appendix A of [64] appear to be for aleatory uncertainty over individual rainfall events.

The strategy adopted here to quantify the epistemic uncertainty associated with values for  $c_1$  and  $c_2$  chosen for universal use (i.e., for all rainfall conditions in a year of weather data) was first to look at the results of a number of studies that obtained values for  $c_1$  and  $c_2$  from data for real rainfall events or from computational models that incorporate effects that are difficult to quantify for observational data (e.g., [56], Tables 10 and 11; [61], Tables 7-11; [62], Table 3; [63], Equations (16) and (21); [65], Table 1; [66], Equations (1) and (2); [67], Figures 2 and 3; [68], Table 9). Next, choose a range of possible values for  $c_1$  and  $c_2$  that is representative of

these values, while avoiding extreme values. The outcome of this effort was a range of  $[10^{-6}, 10^{-4}]$  for  $c_1$  and a fixed value of 0.7 for  $c_2$ . A fixed value for  $c_2$  was selected because, given a potential range of perhaps  $[0.6, 0.8]$  for  $c_2$ , the effects of the much larger range for  $c_1$  should dominate the effects of the uncertainty associated with  $c_2$ . Given the absence of a reason to assign a particular distribution to the possible values for  $c_1$ , a log-uniform distribution is specified for the indicated range of  $[10^{-6}, 10^{-4}]$  so that each order of magnitude is assigned the same probability (i.e., 0.5). The CDF is presented in Figure 4-43.

The CWASH2 parameter was also considered, but there are insufficient data to support development of a defensible distribution. Although this would be a reasonable parameter to evaluate, it was not included because there are insufficient data to support development of a defensible distribution. Furthermore, CWASH1 captures the effect of wet deposition sufficiently such that it was not necessary to evaluate CWASH2 as an exploratory parameter.

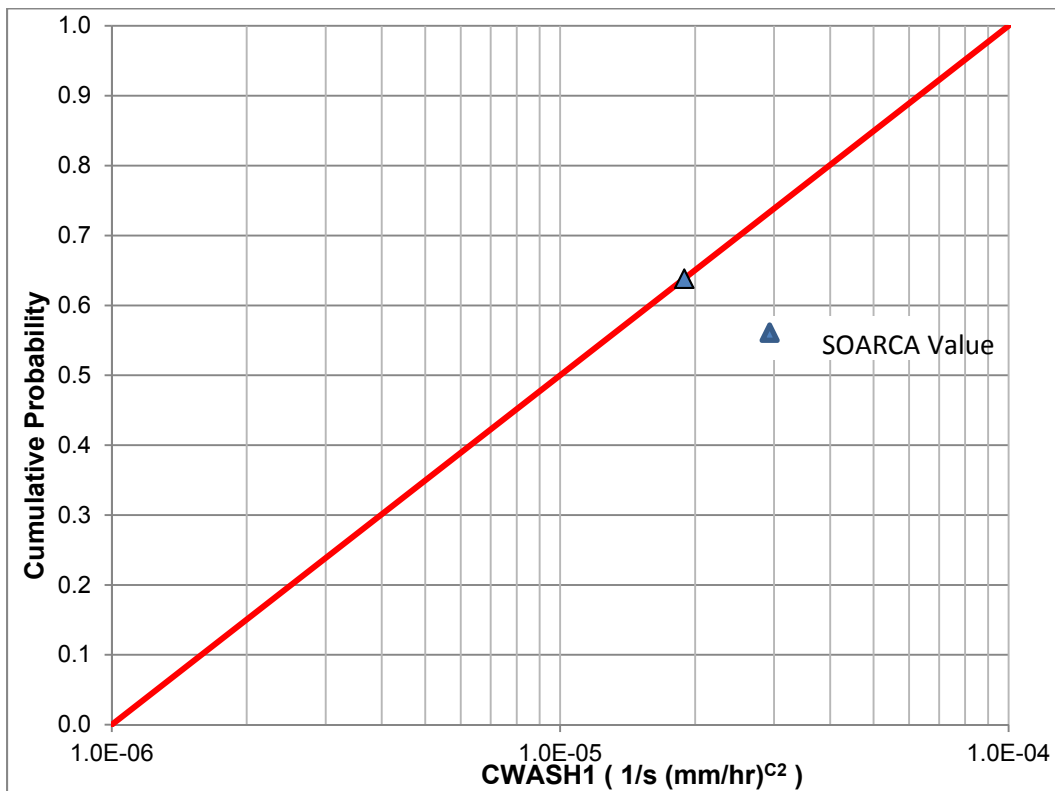


Figure 4-43 CDF of the linear coefficient CWASH1

#### 4.2.2 Dry Deposition Velocities (VDEPOS)

Dry deposition velocities are established by aerosol bins to represent the dependence of deposition velocity on particle size. A triangular distribution is used to represent uncertainty in each of nine aerosol particle sizes. Dry deposition is the only mechanism for deposition onto the ground for more than 90 percent of the hours of the year at Surry (i.e., the hours during which precipitation does not occur). Since long-term exposures usually contribute more than 50 percent of the overall exposure, deposition is important because deposited material is the only

source of exposure during the long term. Furthermore, the PB UA indicated that dry deposition velocity is the most important parameter of all those considered for individual latent cancer risk.

Dry deposition involves a variety of mechanisms that cause aerosols to deposit, including gravitational settling, impaction onto surface irregularities, including buildings and other manmade structures, and Brownian diffusion. Dry deposition is a much slower process than wet deposition, but occurs continuously, whereas, wet deposition occurs intermittently. Larger values of dry deposition velocity result in larger long-term doses at shorter distances and smaller doses at longer distances. The converse is also true that smaller values of dry deposition velocity result in smaller long-term doses at shorter distances and larger doses at longer distances.

### **Rationale for Distribution**

As a starting point, the distributions for dry deposition velocity use the expert elicitation data in NUREG/CR-6244 [64]. These expert data are evaluated in Revision 1 of *Synthesis of Distributions Representing Important Non-Site-Specific Parameters in Off-Site Consequence Analysis* [69], Section 3. The expert data show uncertainty ranges of nearly five orders of magnitude for small particles (0.1  $\mu\text{m}$ ) and about three orders of magnitude for large particles (10  $\mu\text{m}$ ). These ranges seem larger than should be expected for representative values that are to be applied to an entire year of weather trials. In reviewing the expert elicitation documents, it is likely that the experts interpreted the uncertainty to represent instance by instance uncertainties rather than representative values for a large set of weather trials to represent one year of weather data.

In NUREG/CR-4551, Vol. 2, Rev.1, Part 7, pp. 2-18 to 2-20 [70] the authors describe the uncertainty in deposition velocity for NUREG-1150 [10]. In that study, a single deposition velocity was used to characterize the entire range of aerosol sizes that would be released into the atmosphere during a reactor accident. The best estimate, based on empirical equations and physical models, was that deposition velocity is 0.3 cm/s and that the reasonable range of uncertainty is 0.03 to 3 cm/s, a range of a factor of 100. This range accounts for uncertainties in aerosol size, wind speed, surface roughness, and aerosol density. Of these uncertainties, aerosol size is explicitly accounted for in the current study, but uncertainty in the other three parameters should have an effect on the overall uncertainty in deposition velocity. This reasoning should lead to an uncertainty range for a specific aerosol size that is less than two orders of magnitude, which is clearly narrower than the range provided in the expert elicitation study. Another parameter not discussed in the NUREG-1150 documentation is aerosol shape factor, but this should have a relatively minor contribution to uncertainty in deposition velocity.

Estimation of the importance of wind speed, surface roughness, and aerosol density can be made from Eq. 4-35, which is equation 3.1 in [69]. The coefficients  $a$  through  $f$  were chosen to be 50<sup>th</sup> percentile values from Table 3-1 in the same reference. For establishing a range of deposition velocities considering uncertainties in surface roughness and wind speed, the important parameters in the equation are  $e$  and  $f$ , which are respectively 1.061 and 0.169 in the table. By examining the meteorological data file for Surry, a representative range for wind speed is 1 to 10 m/s, with 2.2 m/s being the annual mean wind speed at Surry. From Equation 4-35, this range in wind speed leads to about a factor of 5 in deposition velocity. A representative range for surface roughness at Surry is 0.1 to 0.6 m [3]. Based on Equation 4-35, this range in surface roughness leads to about a factor of 2 in deposition velocity. Aerosol density has a significant effect for larger particles and a negligible effect for small particles, as can be seen from Figure 2-13 in [70]. For larger particles, a range of 4 in particle density corresponds to a

range of about 2 in deposition velocity. For small aerosols, particle density has almost no effect on deposition velocity and for that reason it is not included here. From this discussion, assuming that the influences of wind speed and surface roughness are independent, which is reasonable, then the uncertainty range in deposition velocity to account for these effects should be about a factor of 10.

$$\ln(v_d) = a + b(\ln d_p) + c(\ln d_p)^2 + d(\ln d_p)^3 + e \cdot z_0 + f \cdot V$$

Eq. 4-35

Where

$d_p$  = hydrodynamic particle diameter, ( $\mu\text{m}$ )

$z_0$  = surface roughness, m

$v_d$  = deposition velocity, cm/s

$V$  = wind speed, m/s

$a, b, c, d, e, f$  = correlation coefficients

The above discussion corresponds to the following equation, which is simply the difference in Eq. 4-35 evaluated at an upper bound and a lower bound set of values:

$$\begin{aligned} \ln(v_d)_{UB} - \ln(v_d)_{LB} &= \ln\left(\frac{(v_d)_{UB}}{(v_d)_{LB}}\right) = e \cdot [(z_0)_{UB} - (z_0)_{LB}] + f \cdot [(V)_{UB} - (V)_{LB}] \\ &= 1.061 \cdot (0.6 - 0.1) + 0.169 \cdot (10 - 1) \end{aligned} \quad \text{Eq. 4-36}$$

Where

$UB$  indicates an upper bound value

$LB$  indicates a lower bound value

Solving Eq. 4-36 for the ratio of the upper bound to the lower bound value of deposition velocity produces a factor of about 8. This value is rounded up to a factor of 10 to account for variations in particle size and density within a bin.

To construct distributions to be used in this study for each aerosol size, the 50<sup>th</sup> percentile values from the expert elicitation are used as the modes of a set of triangular distributions. These values were chosen because, although the distributions from the expert elicitation process are considered too wide, the median values from these distributions should represent best estimates from the group of experts. The lower and upper bounds of triangular distributions are chosen to be the mode divided and multiplied by the square root of 10, respectively. The 50<sup>th</sup> percentile values from the expert elicitation (modes of the triangular distributions) are evaluated from Eq. 4-35 with choices for surface roughness to be 0.1 m and wind speed to be the mean Surry wind speed, 2.2 m/s. The distribution parameters are tabulated in Table 4-8 and shown in Figure 4-44.

**Table 4-8 Dry deposition velocities.**

Triangular Distributions	Deposition Velocity (m/s)		
Representative Aerosol Diameter ( $\mu\text{m}$ )	Lower Bound	Mode	Upper Bound
0.15	1.28E-04	4.05E-04	1.28E-03
0.29	1.18E-04	3.73E-04	1.18E-03
0.53	1.54E-04	4.88E-04	1.54E-03
0.99	2.60E-04	8.23E-04	2.60E-03
1.8	5.09E-04	1.61E-03	5.09E-03
3.4	1.04E-03	3.29E-03	1.04E-02
6.4	2.01E-03	6.36E-03	2.01E-02
12	3.30E-03	1.04E-02	3.30E-02
20	4.10E-03	1.30E-02	4.10E-02

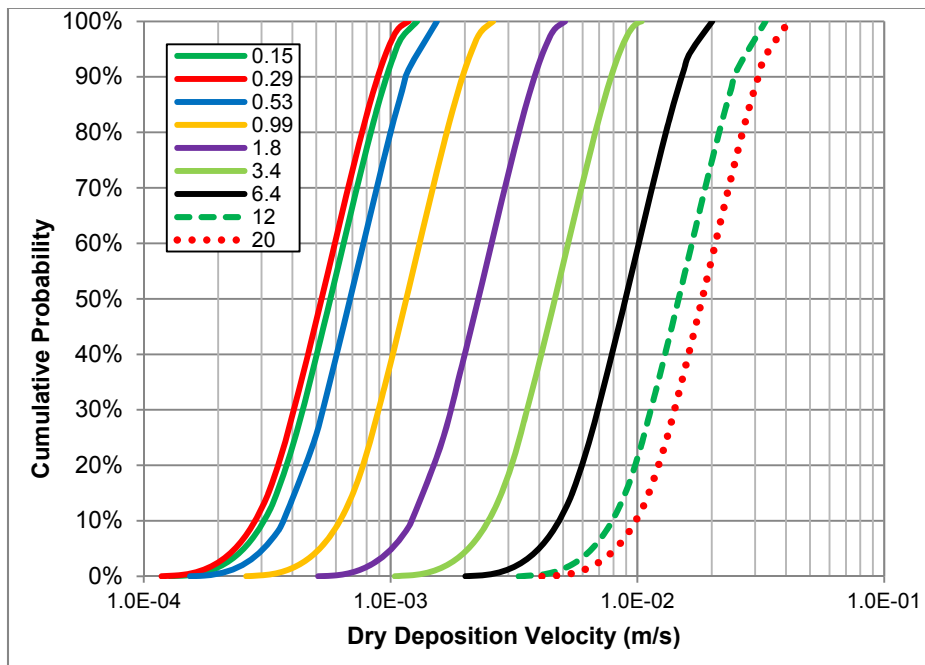


**Figure 4-44 CDF of dry deposition velocities for mass median diameters representing MACCS aerosol bins**

VDEPOS is assumed to be perfectly rank-order correlated across aerosol sizes. This prevents small aerosols from depositing faster than large aerosols, which would contradict our understanding of aerosol physics. Rank-order correlation is the most commonly used method of computing a correlation coefficient using the rank order of the sampled values between two variables, rather than the absolute value sampled from the distribution.

### **4.2.3 Shielding Factors (GSHFAC and PROTIN)**

As described in the MACCS code manual [76], in general the dose equation for an early exposure pathway in a given spatial element is the product of the radionuclide concentration, dose conversion factor, duration of exposure, and a shielding or protection factor. For the cloud inhalation exposure pathway, the quantities are the ground-level air concentration within a spatial element, inhalation dose conversion factor, duration of exposure, and inhalation protection factor. For the groundshine pathway, the quantities are the ground concentration, groundshine dose conversion factor, duration of exposure, and groundshine shielding factor. MACCS calculates groundshine dose as though an individual were located on an infinite flat plane onto which deposition occurs, consistent with Federal Guidance Report (FGR) 12 [76]. The shielding factor accounts for effects of surface roughness and shielding offered by a building or set of buildings that block a portion of the gamma radiation.

The shielding or protection factor is a unitless quantity used to reduce the radiation dose to account for protection provided by a given protective action or mitigating environmental condition. Shielding or protection factors are specified by the user for the cloudshine, inhalation, groundshine, and skin dose exposure pathways, and for three activity types (evacuation, normal activity, and sheltering) [76]. A shielding factor of unity represents the limiting case of a person receiving the full dose (i.e., standing outdoors and completely unprotected from exposure), and a shielding factor of zero represents the limiting case of complete shielding from the exposure. As part of the SOARCA project, Dr. Keith Eckerman provided an updated technical basis and methodology for radiation dose and health risk estimation [72]. This reference provided much of the basis for the shielding factors, as described below, and other risk factors discussed within this study.

During the investigation of the cloudshine shielding factor, CSFACT, issues were identified regarding the source data, which was an unpublished internal Sandia document "Recommendations for MACCS2 Parameter Uncertainty Distributions," prepared by Heames, et al. in 2003. The internal Sandia report was an attempt to use data from expert elicitation to create distributions for MACCS parameters, and was based on an earlier Sandia letter report [71]. However, while the distributions in Gregory [71] for inhalation and groundshine are identical to Heames, there is no distribution in Gregory [71] for cloudshine and no supporting discussion. Physically, cloudshine shielding and inhalation protection are completely different. Protection from cloudshine represents the fraction of radiation from a plume external to a structure is able to reach the interior of the structure; inhalation protection is the fraction of the external concentration that leaks into a structure and is able to be inhaled. Because physically the two distributions should not be identical and because there is no discussion in either source regarding the basis for a distribution for cloudshine shielding factor, a point value was used in the UA. Since the cloudshine pathway is typically a small contributor to overall dose in MACCS analyses, using a point value for the shielding factor should have a minor effect on the estimated uncertainties.

#### **4.2.3.1 Groundshine Shielding Factors (GSHFAC)**

The values of GSHFAC are important because the doses received from groundshine are directly proportional to these factors and groundshine is usually the most important of the long-term dose pathways. Uncertainty exists in factors that affect GSHFAC, such as indoor residence time, household shielding value, and departures from the infinite flat plane assumptions. There are additional contributions to uncertainty in the energy deposited within a human organ for a specified incident radiation, which is represented by the groundshine

deposited energy (GSDE) scaling factor. GSDE is a dimensionless scaling factor used to account for the amount of ionizing radiation energy deposited within various human organs from external radiation emanating from the ground. These uncertainties of the deposition in individual organs stem from age, height, and weight variations of the exposed population and are incorporated into GSDE uncertainty; but GSDE is not a specific MACCS input. So the uncertainty in GSDE is incorporated into GSHFAC uncertainty distribution, as explained below. The two mechanisms, shielding from structures and energy deposition into organs, are independent and so are treated as being uncorrelated.

### **Rationale for Distribution**

Piecewise uniform distributions (normal activity, sheltering, and evacuation) for the combined GSHFAC and GSDE uncertainty were implemented in MACCS as an overall uncertainty for GSHFAC. Construction of this distribution function is described in the following paragraphs.

The piecewise uniform values used in GSHFAC represent a combination of uncertainty derived from NUREG/CR-6526 [73] and uncertainty in GSDE. Gregory et al. [71] evaluated the expert data to derive distributions for groundshine from NUREG/CR-6526. In Gregory et al. [71], three types of activity, normal, sheltering, and evacuation, are evaluated for the groundshine dose pathway, resulting in three sets of shielding factors, shown on Figure 4-45.

Regarding GSDE, to simplify the implementation of uncertainty in the energy deposited within a human organ for a specified incident radiation, Eckerman [72] recommends that a single triangular distribution be applied as a multiplicative factor for all radionuclides and for all organs. Eckerman [72] recommends a triangular distribution with a minimum of 0.5, a peak (mode) of 0.8, and a maximum of 1.5 which incorporates variations in ionizing radiation energy and human body variations from age, sex, height, and weight. The triangular distribution used to represent uncertainty in the dose coefficients for GSDE is shown in Figure 4-46.

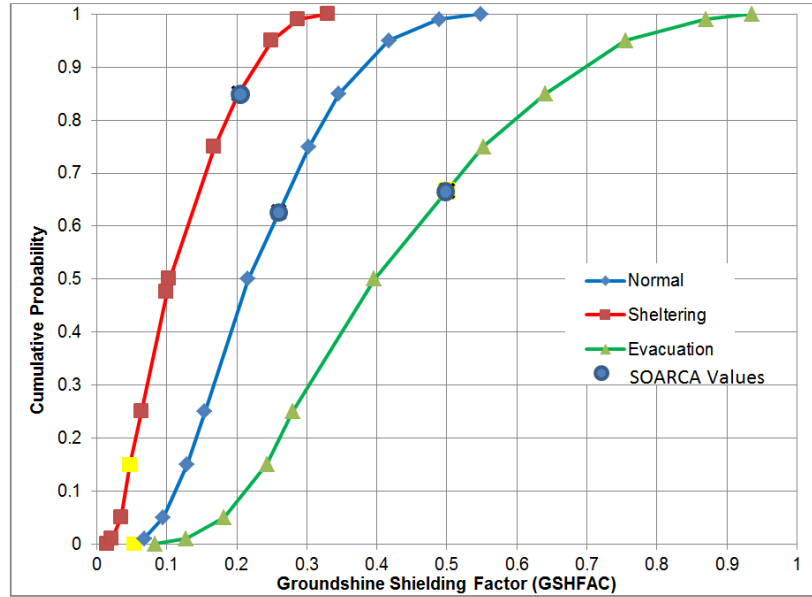
Furthermore, Eckerman [72] suggests that the uncertainties in organ-specific groundshine dose conversion factors are highly correlated. As a result, this UA combines the uncertainty in GSHFAC and the uncertainty in the dose coefficients (i.e., through the GSDE uncertainty distribution) into a single uncertainty factor, which can be implemented as an overall uncertainty in the GSHFAC input for MACCS. The uncertainties in the GSHFAC and the groundshine dose coefficients are treated as uncorrelated, since they have no relation (i.e., the shielding from a building (GSHFAC) does not bear upon variations in organ geometry or variations in ionizing radiation energy).

Figure 4-47 shows the combination of uncertainty in GSHFAC and GSDE for all cohorts considered. For long-term groundshine exposure, the distribution is assumed to be the same as for normal activity. GSHFAC is specified to be the same for each of the six cohorts in this UA, with one exception. Cohort 4, which is the population in special facilities, uses the same shielding factors for normal activity as for sheltering because this cohort is normally indoors and resides in fairly stout concrete structures that provide better shielding than typical housing.

The distributions for normal activity and evacuation are uncorrelated, i.e., a rank correlation coefficient of 0.0. The distributions for normal activity and sheltering are correlated with a rank correlation coefficient of 0.8 because both represent fractions of time spent indoors. The distributions for sheltering and evacuation are taken to be uncorrelated. The distributions for normal activity and long-term groundshine shielding factors are considered perfectly rank

correlated (RRC is 1.0). No correlation is assumed between GSHFAC and inhalation protection factors (PROTIN).

Figure 4-47 shows the final piecewise uniform distributions used for GSHFAC. The Surry SOARCA [3] values are also provided for the normal, sheltering, and evacuation activities and long-term activity. The long-term shielding factor is taken to be identical to the value for normal activity during the emergency phase.



**Figure 4-45 Cumulative distribution functions of GSHFAC for normal activity, sheltering, and evacuation based on expert elicitation data**

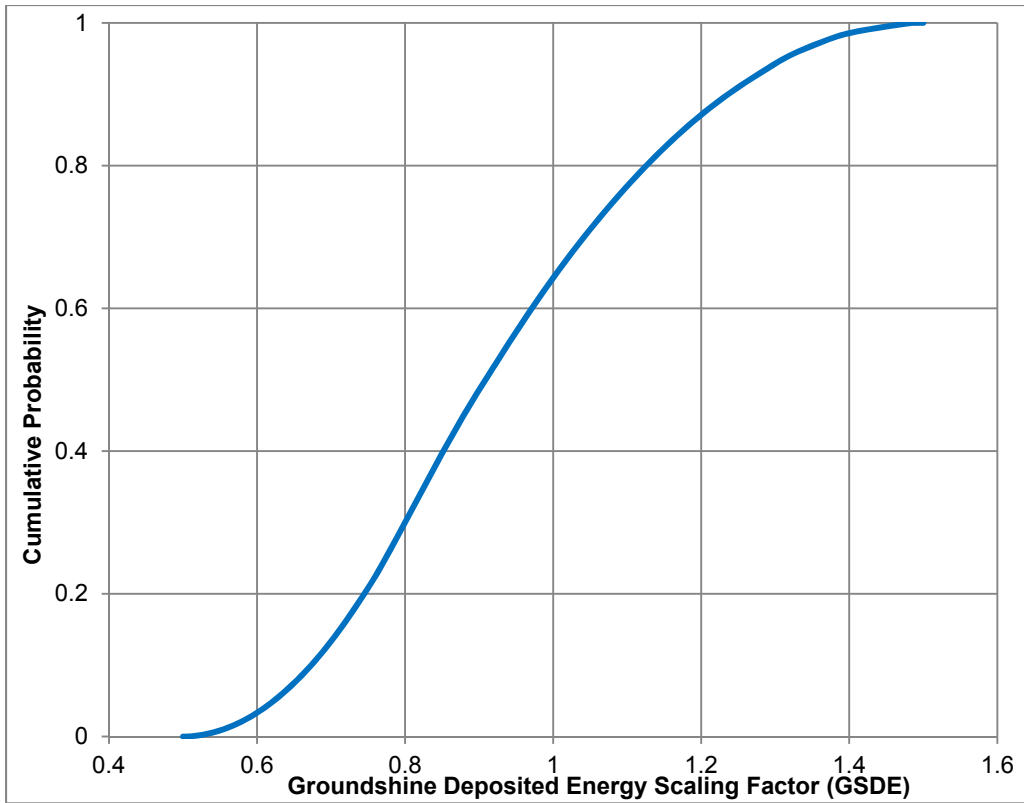


Figure 4-46 Cumulative distribution function of GSDE

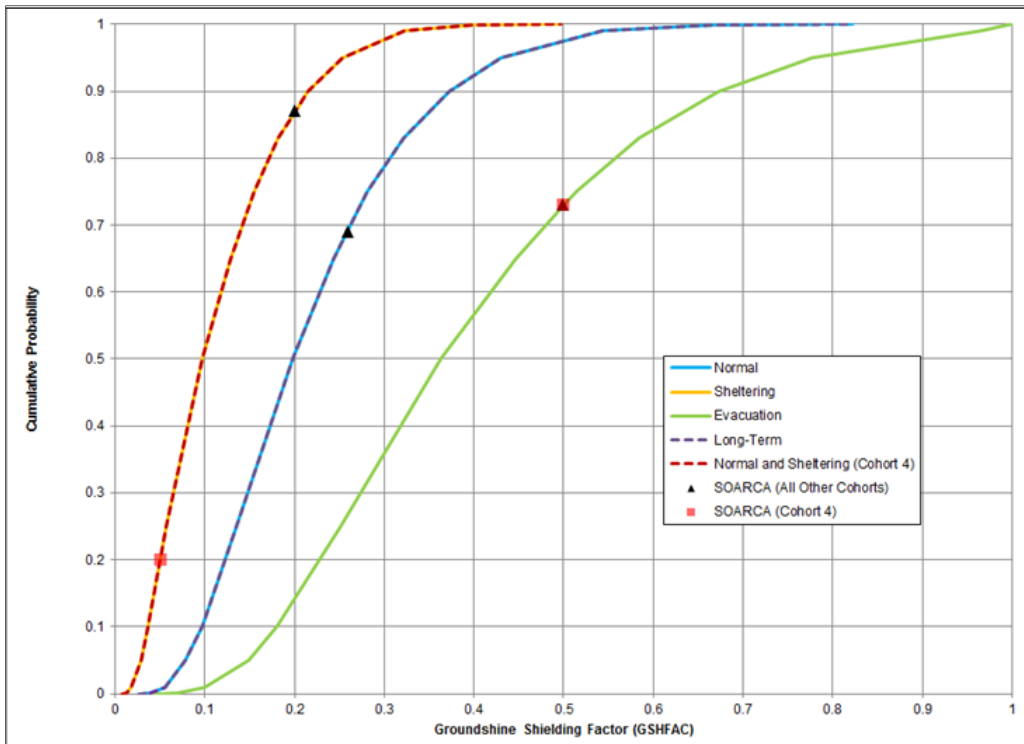


Figure 4-47 CDF of GSHFAC accounting for uncertainty in GSDE

**Table 4-9 Groundshine shielding factor distribution parameters. A value of unity represents full groundshine for a person standing on an infinite flat plane with uniform concentration; a value of zero represents complete shielding.**

Continuous Linear Distributions	Groundshine Shielding Factor (-)		
	Evacuation for All Cohorts	Normal Activity for All but Cohort 4 and Long-Term Activity for Entire Population	Sheltering for All Cohorts and Normal Activity for Cohort 4
0	0.0415	0.0265	0.0075
0.001	0.0692	0.0394	0.0120
0.01	0.1001	0.0552	0.0179
0.05	0.1491	0.0784	0.0286
0.1	0.1804	0.0967	0.0361
0.25	0.2504	0.1354	0.0563
0.5	0.3635	0.1979	0.0969
0.65	0.4464	0.2433	0.1288
0.75	0.5146	0.2816	0.1549
0.83	0.5843	0.3211	0.1818
0.9	0.6717	0.3719	0.2148
0.95	0.7768	0.4297	0.2533
0.99	0.9665	0.5441	0.3226
0.999	N/A	0.6660	0.3975
1	1.0000	0.8220	0.4965

#### 4.2.3.2 Inhalation Protection Factors (PROTIN)

The inhalation dose protection factor is represented by PROTIN. Population dose is reduced through the PROTIN inhalation protection factor based on the activity the population is engaged in, such as sheltering, evacuating, or performing normal activities. The inhalation shielding factors used in the MACCS calculation are important because the doses received from inhalation are directly proportional to these factors and dose is a key metric in this analysis. The distributions used in this UA are derived from NUREG/CR-6526 [73] which collected data from an expert elicitation panel on deposited material and external doses. The expert data indicates that there is a large range of uncertainty in current expert best estimates on the inhalation protection factor.

#### Rationale for Distribution

Gregory et al. [71] evaluated the expert data in [73] to derive distributions for the inhalation protection factor. Three distributions were derived, one each for normal activity, sheltering, and evacuation. Only data from the U.S. expert were used to determine the time spent in various structures (outdoors, vehicles, and low-, medium-, and high-shielded buildings). These data provided the needed information for the normal activity type. The times were shifted towards outdoors in vehicles for evacuation and shifted towards high shielded buildings for sheltering. To determine the final distributions from all the experts, the air concentration ratios

(indoors/outdoors) were considered for both normally ventilated buildings and buildings with all windows closed.

In reviewing these distributions, it appears that the ranges of the distributions are too large, especially for sheltering and evacuation, with the protection factor for sheltering skewed toward too little protection and evacuation skewed toward too much protection. The experts seemed to be answering the question of what are the maximum and minimum possible protection factors for any individual person in the zone, whereas for this work, a representative value for all people in the zone is needed.

To verify that these judgments are correct, the Gregory distributions were compared to distributions for inhalation protection factor given in NUREG/CR-4551 [70], which were prepared for NUREG-1150. This source recommended a uniform distribution from 0.15 to 1.0 for normal activity, a uniform distribution from 0.1 to 0.4 for sheltering, and a constant value of 1.0 (no protection) for evacuation.

The recommended distribution for normal activity is similar to the distribution in [71]; whereas, the distribution for sheltering has a significantly smaller range because it only allows for relatively high amounts of protection, indicating sheltering is in stouter building structures. In practice sheltering may be enforced wherever people currently are (shelter in place), so the higher values in [71] are plausible for some individuals but not for an entire cohort.

Thus, the decision was made to use the distributions for sheltering and normal activities from [71], except with a truncation at the 0.2 and 0.8 quantiles of each CDF to be representative of cohorts instead of a single member of a cohort. New CDFs were drawn, using the .02 and 0.8 quantile values as the upper and lower bound while maintaining the 0.5 quantile value and shape of the distributions. The distributions are defined to be piecewise-uniform to reflect information from the expert elicitation. Figure 4-48 also shows the SOARCA values as black triangles, which were obtained from the NUREG-1150 defaults [10].

The single inhalation protection factor of 1 for evacuation [70] is significantly different than the values from the distribution in [71], which includes low values for PROTIN that are difficult to defend. Additionally, the SOARCA default for evacuation of 0.98, which came from NUREG/CR-6953, Volume 1 [74], is still considered the best estimate. Therefore, the best judgment was to create a uniform distribution from 0.9 to 1.0, which allows for a limited uncertainty investigation in PROTIN for evacuation but doesn't include high amounts of protection indicated in Gregory that do not seem physically possible for an entire cohort.

The distribution for the long-term inhalation protection factor is assumed to be the same as the distribution for normal activity during the emergency phase. PROTIN must be specified for each cohort (population group) in a MACCS analysis. In the Surry SOARCA analysis [3], shielding values for Cohorts 1, 2, 3, 5, and 6 are identical. Cohort 4 represents special facilities, which had different shielding values in the Surry SOARCA analysis [3]. Because normal activity for Cohort 4 would be approximately the same as sheltering due to the robust nature of the special facility buildings, the distribution for normal activity was chosen to be the same as for sheltering for Cohort 4. These distributions are shown in Figure 4-48 as dashed lines overlaying the base distributions.

The distributions for normal activity and sheltering are correlated with a rank correlation coefficient of 0.75, based on the assumption that the majority of normal activity is indoors. Therefore, if sheltering is sampled with a lower value, normal activity should also be a lower

value. The distributions for normal activity and long-term inhalation are also perfectly rank correlated. No correlations are assumed between PROTIN and the groundshine shielding factor (GSHFAC) for any of the three activity types, evacuation, normal activity, and sheltering.

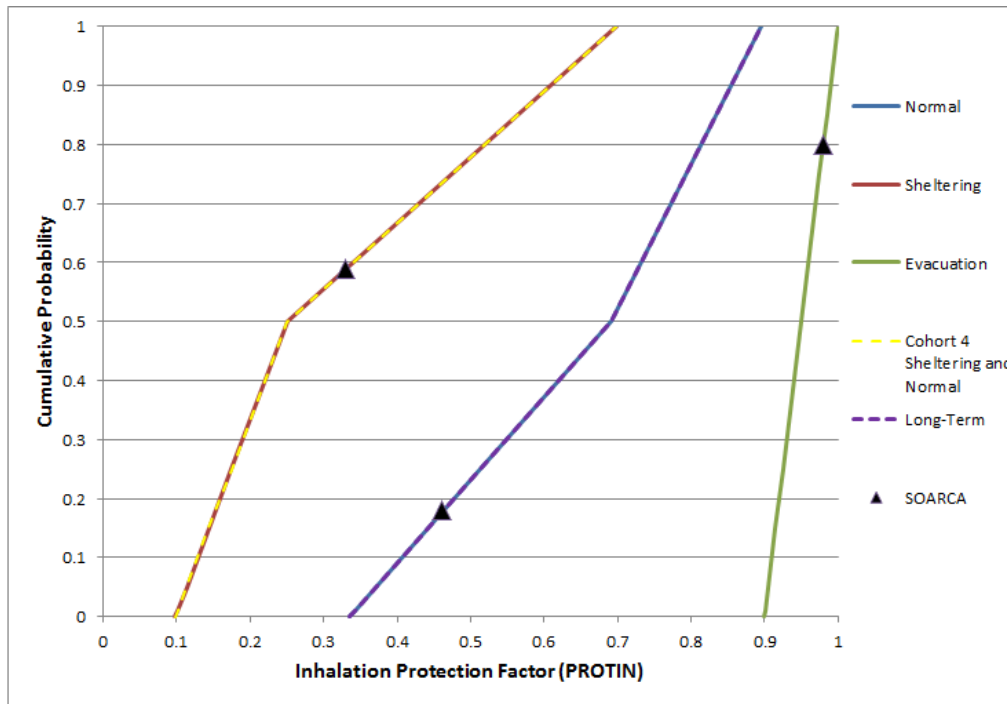


Figure 4-48 CDFs of PROTIN for normal activity, sheltering, and evacuation

Table 4-10 Inhalation protection factor distribution parameters. A value of unity represents direct inhalation from a passing plume; a value of zero represents complete protection.

Quantile Value	Inhalation Protection Factor (-)		
	Implemented as a Uniform Distribution	Continuous Linear Distributions	
	Evacuation for All Cohorts	Normal Activity for All but Cohort 4 and Long-Term Activity for Entire Population	Sheltering for All Cohorts and Normal Activity for Cohort 4
0	0.9	0.3355	0.09825
0.01	N/A	0.34263	0.101305
0.05	N/A	0.37115	0.113525
0.15	N/A	0.44245	0.144075
0.25	N/A	0.51375	0.174625
0.5	N/A	0.692	0.251
1	1.0	0.896	0.6985

#### 4.2.4 Early Health Effects (EFFACA, EFFACB, EFFTHR)

When radioactive material is inhaled and retained in the respiratory system, an individual may continue to receive a radiation dose for long periods of time after the material was inhaled. Depending on particle size and chemical form, clearance mechanisms may remove the material from the body or transport it from the respiratory system to other organs of the body. The MACCS early health effects model accounts for dose protraction from radioactive material inhaled and retained within the body and calculates an effective acute dose, i.e., a one-day dose that would induce the same effects as the protracted dose [76]. External radiation is only received during the exposure period, so dose protraction is not usually an issue.

The individual risk of an early fatality is modeled in MACCS using a three-parameter hazard function, expressed in Eq. 4-37 for specified target organs (i.e., red bone marrow, lungs, and stomach) with an acute dose threshold. The early health effects parameters represented in the equation include:

- Early Health Effects LD50 Parameter (EFFACA),
- Early Health Effects Exponential Parameter (EFFACB), and
- Early Health Effects Threshold Dose (EFFTHR).

The Weibull function contains the EFFACA parameter for the lethal dose to 50 percent of the population ( $LD_{50}$ ), EFFACB as an exponential parameter that defines the steepness of the dose-response function, and a threshold dose defined by EFFTHR.

$$H = 0.693 \left( \frac{DOSE}{EFFACA} \right)^{EFFACB}$$

Eq. 4-37

Where:

$H =$	hazard function for individual risk of an early fatality (unitless)
$DOSE =$	effective acute dose (Gy) to a target organ. DOSE is set to zero when it is below the threshold, EFFTHR
$EFFACA =$	$LD_{50}$ (Gy) for a specific health effect
$EFFACB =$	the exponential parameter in the hazard function (unitless)

All three of the variables used to determine the individual risk of early fatality in Eq. 4-37 are treated as uncertain. Furthermore, there are three values for each of the parameters for the three organs listed above. A dose to each of the organs is associated with a specific type of early fatality, as follows: (1) an acute dose to the red bone marrow is used to assess occurrences of the hematopoietic syndrome, (2) an acute dose to the lungs is used to assess occurrences of the pulmonary syndrome, and (3) an acute dose to the stomach is used to assess occurrences of the gastro-intestinal syndrome.

When estimating early health effects, it is appropriate to use gray (Gy) as the unit of measure for doses. Doses measured in gray and Sieverts (Sv) are the same for low linear energy transfer (LET) radiation (gamma and beta), but different for high LET radiation (alpha). Doses in Sieverts are based on a standard radiation weighting factor for high LET radiation of 20; doses from high LET radiation in units of gray are based on either a value of unity or a nonstandard value for radiation weighting factor. In the case of latent health effects, a Sievert captures the biological effects of radiation in terms of the risk of cancer induction. In the case of early health effects, a nonstandard radiation weighting factor of 10 is used for acute doses. This difference is because

high LET radiation has a different biological impact for early health effects than it does for latent health effects.

#### **4.2.4.1 Early Health Effects LD<sub>50</sub> Parameter (EFFACA)**

The EFFACA parameter represents LD<sub>50</sub>, the lethal dose to 50 percent of the population, in the hazard function for a target organ [76]. The effective acute dose commitment period is up to one year for inhaled radionuclides. The EFFACA distribution is based on data provided for the estimation of four types of early health effects, hematopoietic syndrome, gastrointestinal syndrome, pulmonary syndrome, and pneumonitis [69]. The first three of these early health effects are potentially fatal and are included in the documented results. Pneumonitis is generally nonfatal, and was not reported.

#### **Rationale for Distribution**

The EFFACA distribution for the three target organs considered are piecewise uniform and are based on linear interpolation between data points taken from Table 6-1 of Bixler et al. [69]. The basis for the EFFACA distribution are uncertain characteristics associated with estimation of four types of early health effects, and are taken directly from Bixler et al. [69] and are derived expert elicitation values provided in NUREG/CR-6545. The parameter distributions and SOARCA values associated with the three fatal, early health effects are shown on Figure 4-49. The upper and lower bounds of each of the distributions incorporate the entire range of the expert elicitation data [69].

Bixler et al. [69] recommended that EFFACA be correlated with the early health effects threshold parameter (EFFTHR) for the same health effect using a 1.00 rank correlation coefficient [69].

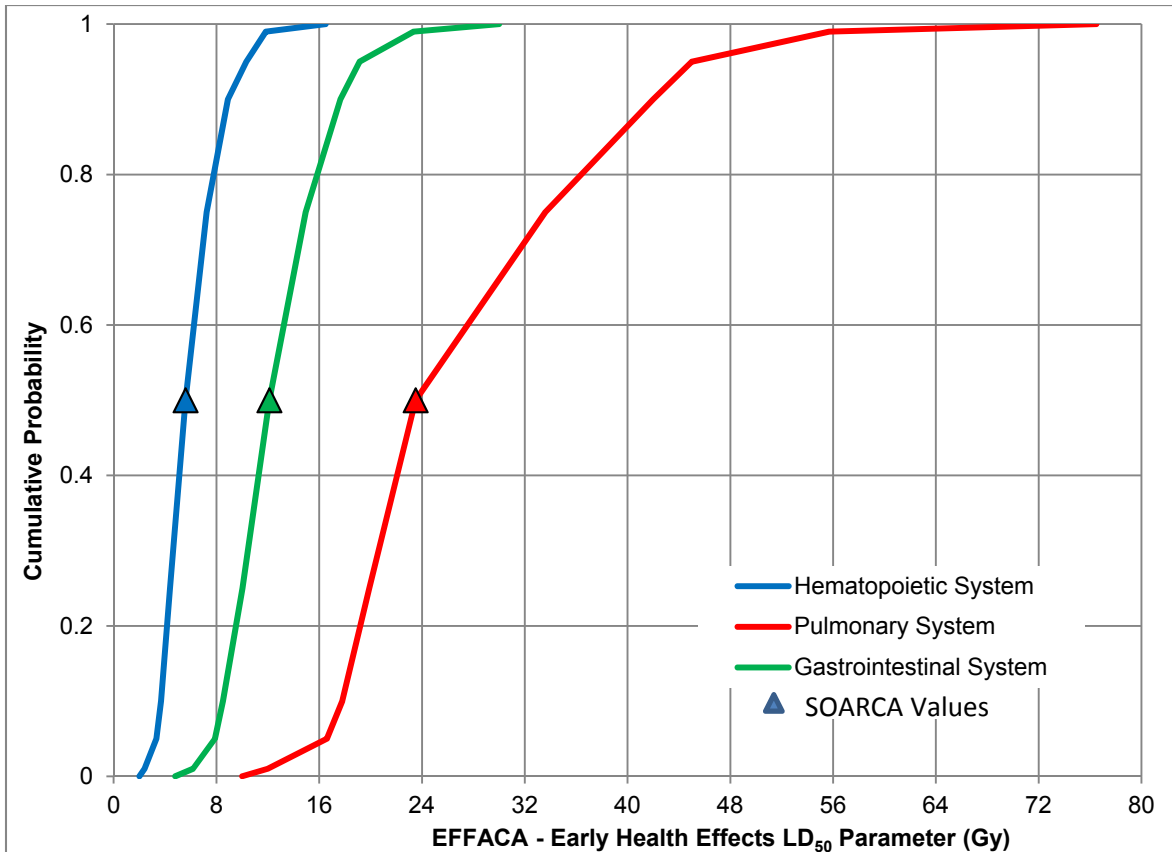


**Figure 4-49 CDFs of EFFACA for specified health effects**

#### 4.2.4.2 Early Health Effects Exponential Parameter (EFFACB)

The EFFACB parameter represents the exponential or shape factor in the hazard function for the target organ [76]. The same target organs identified with EFFACA are considered here. Again, pneumonitis is nonfatal, was not included as an uncertain parameter, and does not contribute to any reported results.

#### Rationale for Distribution

The EFFACB distribution for all three target organs considered are piecewise uniform, and are based on linear interpolation between data points taken from Table 6-1 of Bixler et al. [69]. The basis for the EFFACB distributions is derived from NUREG/CR-6545 and evaluated by Bixler et al. [69]. The parameter distributions and SOARCA values associated with these three potentially fatal early health effects for EFFACB are shown on Figure 4-50. The Surry SOARCA values [3] are the median values from these distributions, as shown in the figure. The upper and lower bounds of each of the three distributions incorporate the entire range of the expert elicitation data [69].

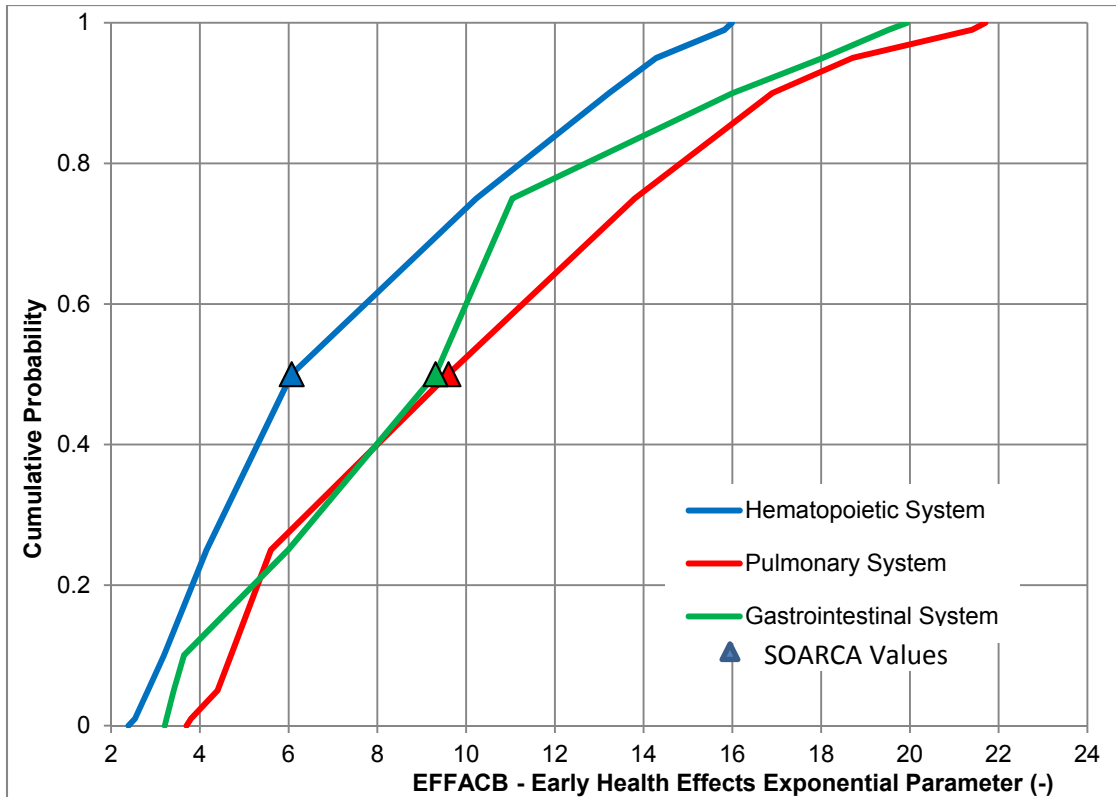


**Figure 4-50 CDFs of EFFACB for specified health effects**

#### 4.2.4.3 Early Health Effects Threshold Dose (EFFTHR)

The EFFTHR parameter represents the threshold dose associated with the target organ [76]. The same target organs identified with EFFACA and EFFACB are considered here. Pneumonitis is not included for the reasons discussed above.

#### Rationale for Distribution

The EFFTHR distribution for all three target organs considered are piecewise uniform, and are based on linear interpolation between data points taken from Table 6-1 of Bixler et al. [69]. The EFFTHR distributions are derived from NUREG/CR-6545 and evaluated by Bixler et al. [69]. The parameter distributions and SOARCA values associated with these three potentially fatal early health effects for EFFTHR are shown on Figure 4-51. The Surry SOARCA values [3] were chosen to be the medians of these distributions. The upper and lower bounds of each of the three distributions incorporate the entire range of the expert elicitation data [69].

For each health effect, EFFTHR is correlated with the early health effects LD<sub>50</sub> parameter (EFFACA) for the same health effect using a rank correlation coefficient of 1.00 [69].

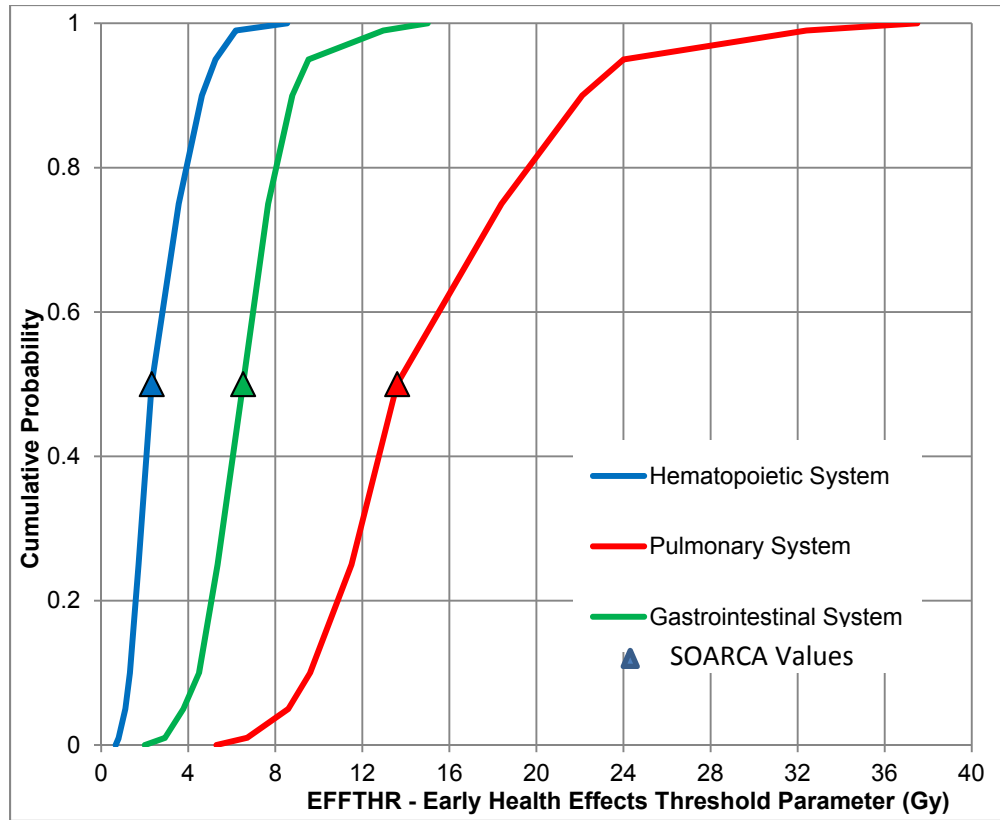


**Figure 4-51 CDFs of EFFTHR for specified health effects**

#### 4.2.5 Latent Health Effects (DDREFA, CFRISK, Long-Term Inhalation Dose Coefficients)

##### 4.2.5.1 Dose and Dose Rate Effectiveness Factor (DDREFA)

The dose and dose rate effectiveness factor (DDREFA) is a dimensionless dose- and organ-dependent reduction factor. Epidemiological studies used in the development of radiation exposure risk models involved subjects who experienced high radiation doses delivered in a relatively short time period [72]. There is evidence that indicates that the biological response per unit dose at low doses may be an overestimation if one extrapolates from observations made with high, acutely delivered doses [72]. The degree of overestimation is commonly expressed in terms of a dose and dose rate effectiveness factor. DDREFA is used in MACCS to modify the organ-specific lifetime cancer fatality risk factors (CFRISKS) in order to distinguish between low and high dose exposures incurred during the early phase. There is significant uncertainty in DDREFA because there is a large amount of scatter in dose-response data at lower dose levels.

For this analysis, low dose is defined as 0.2 Gy (20 rad) or less and low dose rate is defined as 0.1 mGy/min (600 mrad/hr) or less [72]. MACCS only considers dose and not dose rate in the implementation of DDREFA. In MACCS, doses received during the emergency phase are divided by DDREFA when the committed dose is less than 0.2 Gy. Doses received during the long-term phase are assumed to be controlled by the habitability criterion to be well below 0.2 Gy, so these doses are always divided by DDREFA in the calculation of latent health effects.

## Rationale for Distribution

Age- and gender-averaged cancer mortality risk uncertainties were developed for SOARCA [3][72]. Additionally, Eckerman [72] recommends a PDF specific for breast cancer and all other types of cancer for low LET radiation. However, the PDFs provided did not integrate to unity; therefore, the PDF equations were normalized as shown in Figure 4-52. An upper limit of DDREFA is 3.0 for breast and 8.0 for other cancers [72].

Eckerman recommended that high LET radiation be assigned a DDREFA of unity (1.0) with no uncertainty [72]; however, the distinction between low and high LET radiation to an organ cannot be distinguished within the MACCS framework; therefore, the PDFs suggested for low LET radiation are applied to all types of radiation. To implement the uncertainty in DDREFA, the CDF was segmented into equally spaced quantiles to construct a piecewise uniform distribution as shown in Figure 4-53. The SOARCA values are represented in Figure 4-53 by the blue triangles.

The value of DDREFA for each organ is independent of the other organs and so they are not correlated [72]. The DDREFA for each organ has a corresponding CFRISK parameter, and these parameters are also uncorrelated.

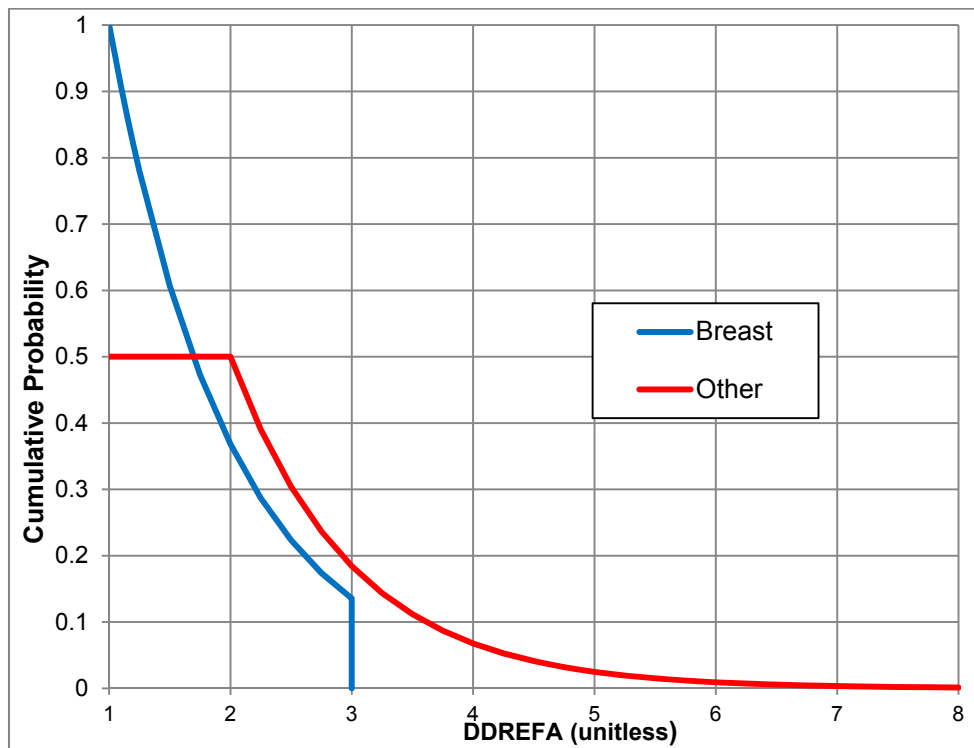


Figure 4-52 Normalized PDFs for DDREFA for breast and other cancers

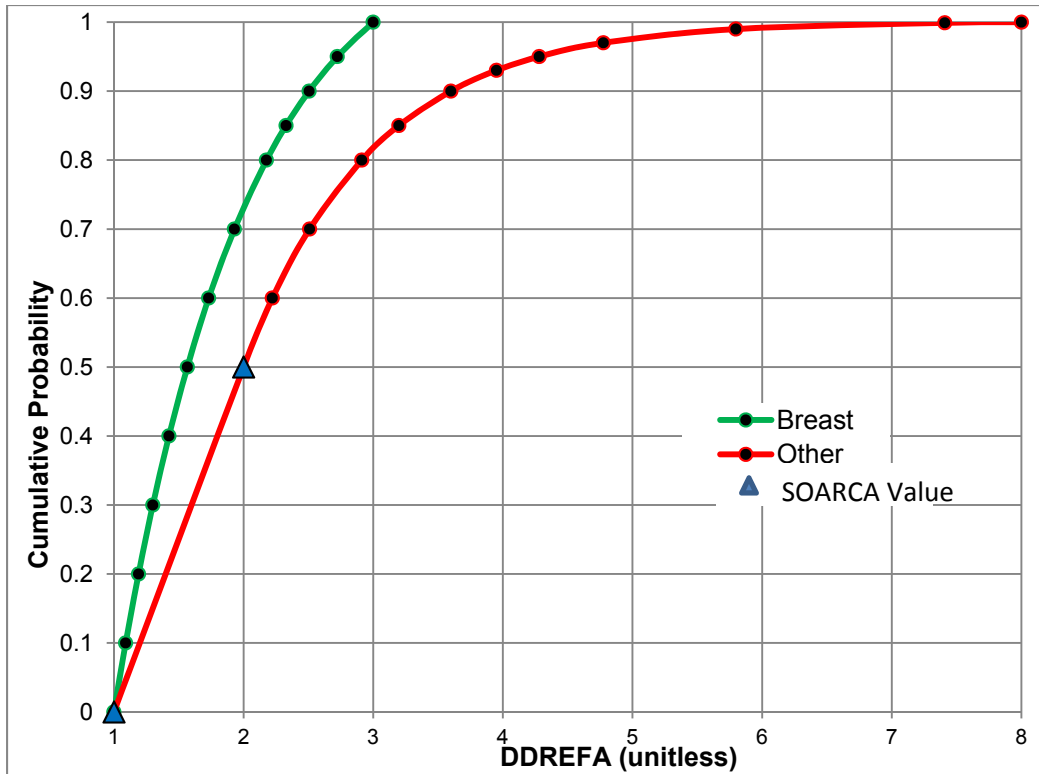


Figure 4-53 CDFs of DDREFA for breast and other cancer types

#### 4.2.5.2 Lifetime Cancer Fatality Risk Factors (CFRISK)

The lifetime cancer fatality risk factors (CFRISK) are based on a 50-year lifetime dose commitment to specified target organs (risk/Sv). The probability of a lifetime cancer fatality is calculated separately for each cancer syndrome related to each target organ and is based on the technical approach described in the National Academy of Sciences / National Research Council Biological Effects of Ionizing Radiation (BEIR) V report. The BEIR V risk models are used in FGR-13.

Radiation dose to organs and tissues of the body are involved in the decision to allow the evacuated population to return and in the estimation of the potential health effects in the population. Return of the population falls within the scope of radiation protection and uses the standard dosimetric quantities of radiation protection, i.e., effective doses. Estimation of health effects involves calculating doses to specific organs and applying cancer risk factors to estimate the number of excess cancer fatalities in a population. Both the dose coefficients (Section 4.2.5.3) and risk factors are uncertain. Uncertainties in the cancer fatality risk factors are evaluated in this section.

#### Rationale for Distribution

Truncated log-normal distributions were selected for the cancer fatality risk factors based on guidance from Keith Eckerman [72]. Estimates of the gender and age averaged uncertainty in CFRISK for each of the organs used for latent health effects were obtained from Eckerman [72]; whereas, the estimates used in the earlier Surry SOARCA analysis were from BEIR V [3] (the blue triangles in Figure 4-54).

The uncertainty distributions provided by Eckerman [72] indicate that cancer risk for leukemia seems to be relatively well quantified; lung, breast, colon, and residual (cancer sites not explicitly identified – esophagus, stomach, skin, ovaries, bladder, kidney, etc.) are moderately well quantified; and thyroid, liver, and bone are relatively poorly quantified. Eckerman [72] concluded this based on the premise that inconsistency in expert judgment is a valid measure of uncertainty in CFRISK.

Each log normal distribution is truncated at  $\pm 3$  sigma for each distribution. This represents a truncation at quantile 0.001 and 0.999. CFRISK for each organ is considered independent of the other organs and therefore the risk factors are not correlated [72].

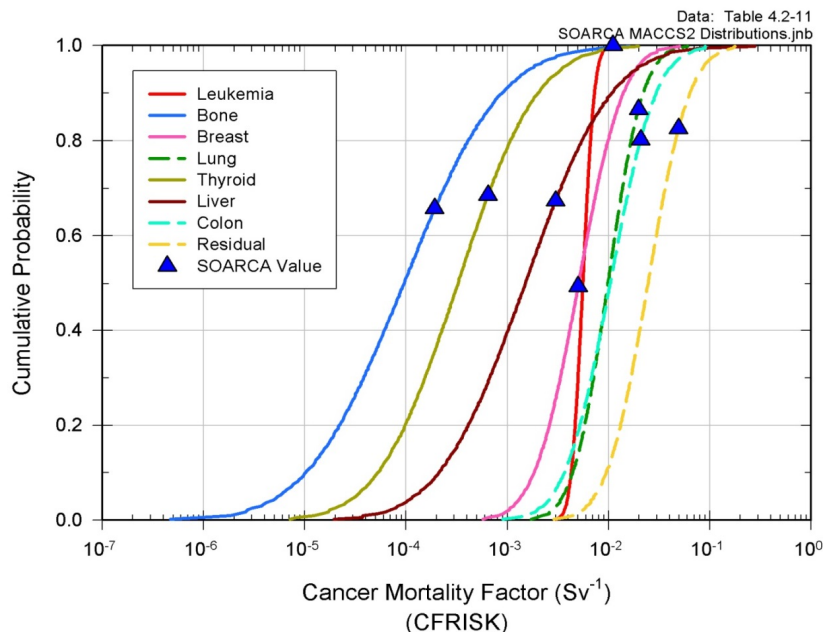


**Figure 4-54 CDF for CFRISK for each of the organs included in the analysis**

#### 4.2.5.3 Long-Term Inhalation Dose Coefficients

The long-term inhalation dose coefficients are used to calculate the committed organ-specific equivalent dose or the committed effective dose (Sv) from the inhalation of 1 Bq of a radionuclide over a 50-year commitment period. Uncertainties in inhalation dose coefficients were examined by Pawel et al. [75] to evaluate the uncertainties in the cancer risk coefficients of FGR-13. Based on the Eckerman report for SOARCA [1], the assignment of uncertainty distributions to long-term inhalation dose coefficients for individual radionuclides is difficult because these values are the end products of complex calculations. These calculations involve a collection of uncertain biokinetics and dosimetric coefficients and assumptions, which Pawel et al. [75] determined to be the largest uncertainty for most risk coefficients.

The LCF risk factors in MACCS are based on the technical approach described in BEIR V in which long-term inhalation dose coefficients are part of that approach. The assessment of the uncertainty in dose is evaluated on the basis of sensitivity analyses in which various combinations of plausible biokinetics and dosimetric models are used to generate alternative dose coefficients, such as those discussed in Pawel et al [75], and Eckerman report [72].

## Rationale for Distribution

For the long-term dose coefficients related to the inhalation pathway, Eckerman [72] recommends that the uncertainty distributions for the coefficients be treated as truncated log normal distributions with the geometric means and standard deviations for the 58 radionuclides listed in Table 4-9. The upper and lower values used to create the distributions are assumed to represent the 90 percent confidence interval for each dose coefficient.

For an individual radionuclide, the long-term inhalation dose coefficients are treated as correlated with a rank correlation coefficient of 1.0 for all of the organs except the lung. The lung is correlated with a rank correlation coefficient of -1.0 with the dose coefficients of all of the other organs (red bone marrow, bone, breast, thyroid, liver, colon, and 'residual'). This, in effect, means that only one input is sampled independently (e.g., long-term inhalation dose coefficient for the red bone marrow) to represent all organ-specific long-term inhalation dose coefficients uncertainty. The logic behind this is that the inhaled radionuclides may spend more or less time (residence time) in the lungs, depending on the chemical form of the radionuclide and its solubility, and subsequently after departing from the lung, the radionuclide is carried through the blood stream to other systemic tissues. Thus, the longer the time spent in the lungs, the greater the dose in the lungs and the less the dose to the other systemic tissues. The shorter the time spent in the lungs, the smaller the dose in the lungs and the greater the dose to the other systemic tissues. MACCS uses the bone as the corresponding organ to correlate the other organ-specific long-term inhalation dose coefficients.

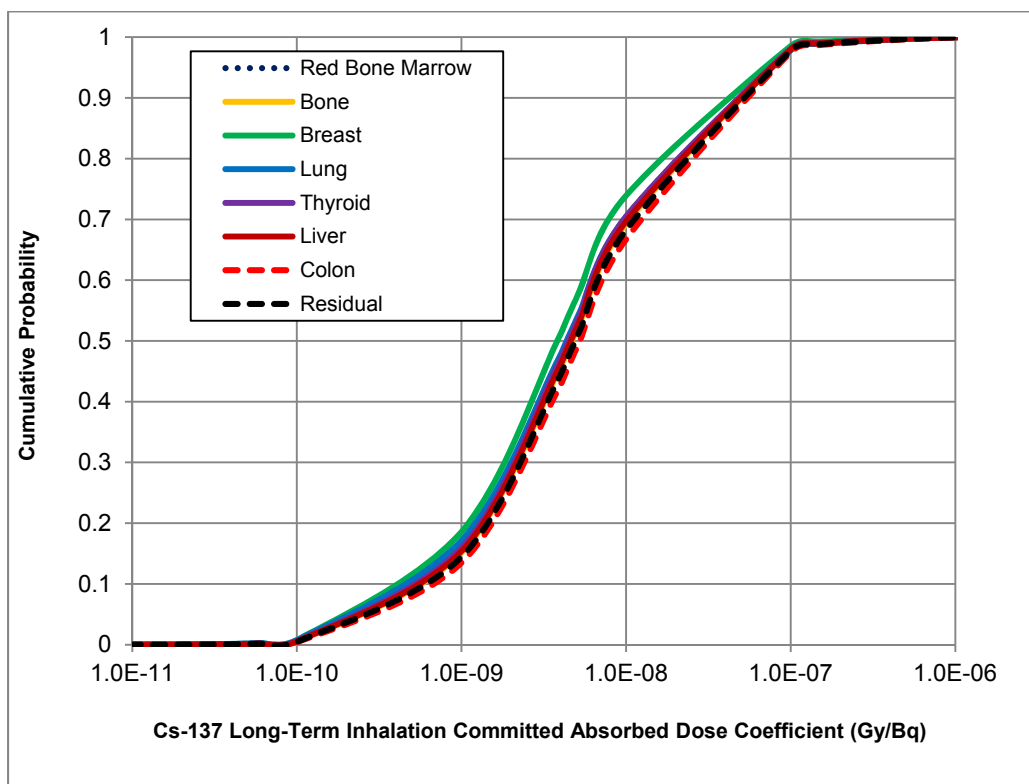
There are 69 radionuclides considered in the Surry SOARCA analysis [3]. Of those, only 58 radionuclides have nonzero dose coefficients for inhalation. In this UA, these 58 radionuclides, listed in Table 4-11, are assigned uncertain long-term inhalation dose coefficients for each of the eight organs used in this analysis, which are lung, red bone marrow, bone, breast, thyroid, liver, colon, and residual. The residual dose coefficient represents the collection of organs that are not specifically represented and that are important for cancer induction.

Figure 4-55 and Figure 4-56 provide examples of the truncated log normal distributions for two radionuclides, Cs-137 and Pu-241, for the eight different organs included in this analysis. Uncertainties in the acute inhalation dose coefficients (used to estimate the early health effects discussed in Section 4.2.4) were considered to be less important and were not included in this UA.

SOARCA did not include the ingestion dose pathway and neither does this UA. Uncertainty in groundshine dose coefficients is treated through uncertainty in the groundshine shielding factors, as explained above. Cloudshine uncertainty is not treated because it is a relatively unimportant dose pathway, compared with groundshine and inhalation.

**Table 4-11 Radionuclides treated as having uncertain inhalation dose coefficients.**

Radionuclides							
Co-58	Y-90	Nb-97	Te-127	I-132	Ba-140	Pr-144	Cm-242
Co-60	Y-91	Mo-99	Te-127m	I-133	La-140	Nd-147	Cm-244
Rb-86	Y-91m	Tc-99m	Te-129	I-134	La-141	Np-239	
Rb-88	Y-92	Ru-103	Te-129m	I-135	La-142	Pu-238	
Sr-89	Y-93	Ru-105	Te-131	Cs-134	Ce-141	Pu-239	
Sr-90	Zr-95	Ru-106	Te-131m	Cs-136	Ce-143	Pu-240	
Sr-91	Zr-97	Rh-103m	Te-132	Cs-137	Ce-144	Pu-241	
Sr-92	Nb-95	Rh-105	I-131	Ba-139	Pr-143	Am-241	



**Figure 4-55 Cs-137 lifetime inhalation dose coefficient distributions for organs included in the consequence analysis**

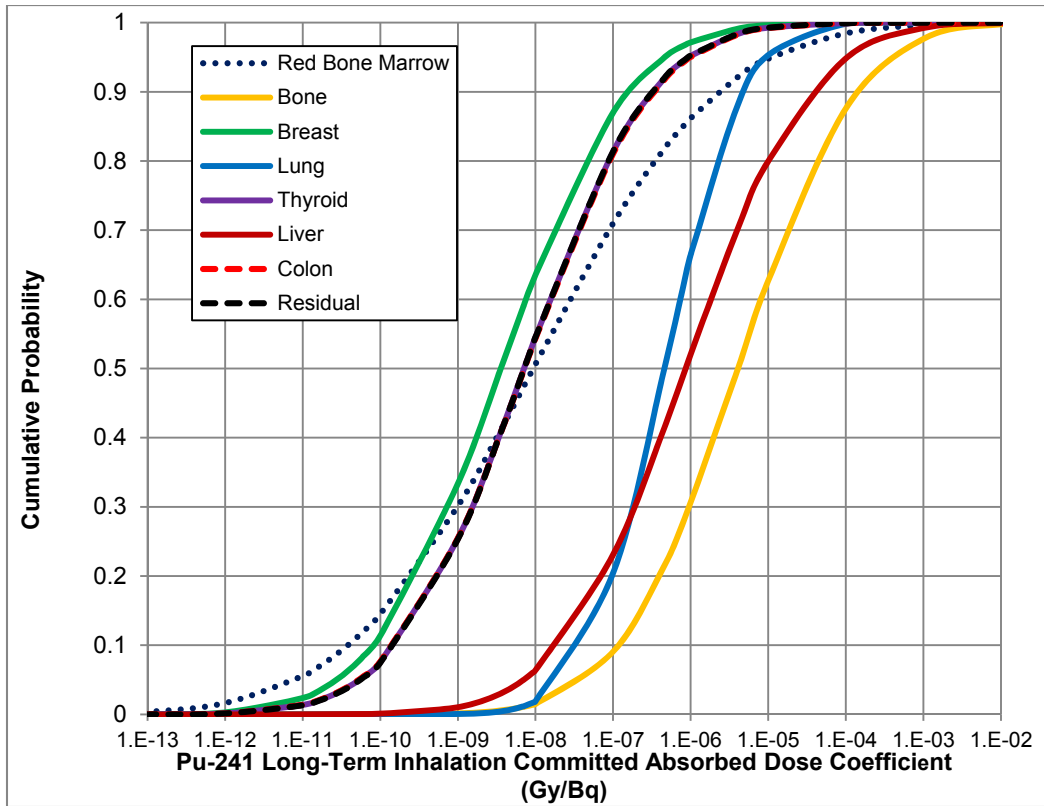


**Figure 4-56 Pu-241 long-term inhalation dose coefficient distributions for organs included in the consequence analysis**

#### **4.2.6 Dispersion (CYSIGA, CZSIGA)**

Dispersion of a radioactive plume following a severe accident directly affects doses to members of the population and resulting health effects. Thus, the dispersion parameters used to estimate atmospheric dispersion are important to the outcome of the calculation. The coefficients used to calculate dispersion were chosen to be the median values from an expert elicitation for SOARCA, but there is significant uncertainty in these values.

In terms of predicted health effects, these parameters tend to have a non-linear effect when using the linear, no-threshold (LNT) hypothesis for estimating latent health effects because dispersion influences the amount of land that is interdicted. Dispersion has an even greater influence on estimated health effects when truncation is used in the dose-response model because a smaller dose to an individual can reduce a nonzero risk to zero and, conversely, a larger dose can raise a zero risk to be nonzero.

Within MACCS, plume dispersion is calculated using the Gaussian plume model, shown in Eq. 4-38 for the simple case of an unbounded plume.

$$\chi(x, y, z) = \frac{Q}{2\pi \bar{u} \sigma_y \sigma_z} \exp \left[ -\frac{1}{2} \left( \frac{y}{\sigma_y} \right)^2 \right] \exp \left[ -\frac{1}{2} \left( \frac{z - h}{\sigma_z} \right)^2 \right]$$

Eq. 4-38

where  $\chi(x,y,z)$  is the air concentration at a downwind location  $(x,y,z)$ ,  $Q$  is the source strength,  $\bar{u}$  is the mean wind speed,  $h$  is the release height, and  $\sigma_y$  and  $\sigma_z$  are the standard deviations of the normal crosswind and vertical concentration distributions, respectively.  $Q$  and  $h$  are determined by the accident sequence, while  $\bar{u}$ ,  $\sigma_y$ , and  $\sigma_z$  are functions of weather. Uncertainty in  $\sigma_y$  is used to capture the uncertainty in crosswind dispersion. The function used to define  $\sigma_y$  is given in Eq. 4-39.

$$\sigma_y = CYSIGA \cdot x^{CYSIGB}$$

Eq. 4-39

where  $x$  is the downwind distance and  $CYSIGA$  and  $CYSIGB$  are empirical constants chosen to fit observed results. A value for both of the constants must be entered for each of the six Pasquill-Gifford stability classes (A-F).

In this work, it was beneficial to only sample one of the two constants to simplify the specification of uncertainty. Bixler et al. [69] characterized the uncertainty as an uncertainty in  $CYSIGA$  and this characterization is used here.

#### 4.2.6.1 Crosswind Dispersion Linear Coefficient (CYSIGA)

The crosswind dispersion linear coefficient is represented by  $CYSIGA$ . The SOARCA best estimate values for  $CYSIGA$  were chosen to be the median of the results of an expert elicitation [69]. Distributions were fit to the expert data and these were roughly lognormal. The median of the distributions is considered to be a reasonable best estimate value for this parameter; however, the distributions created from the elicitation are not used in this analysis. The expert data indicate about one order-of-magnitude uncertainty within the 90 percent confidence interval and about two orders of magnitude at the 100 percent confidence interval.

In retrospect, it appears that the experts considered the question: what is the uncertainty in the dispersion at a specific point in time, i.e., for a specific weather instance. The appropriate question for this UA is: what is the uncertainty in dispersion that is representative of a year of weather data? The second question leads to a narrower distribution because a single set of dispersion parameters is selected to represent a whole year of weather variability.

There are a number of other sources for  $CYSIGA$ , three of which are given as examples in the MACCS User's Guide [76]. These values were compared to the best estimate values from expert elicitation. It was found that 2/3rds of the values were within a factor of 3 of the best estimate value and were about evenly distributed between larger and smaller. These historic values (from 1977, 1979, and 1989) were used by multiple experts in constructing their distributions, showing they continue to be regarded as reasonable bases to estimate dispersion.

Additionally, NUREG/CR-6853 [77], compared results from MACCS (a Gaussian plume code) with 3 other codes for transport and dispersion and found that the results from the 4 codes were within a factor of 2 for compass averaged concentrations and 3 for sector specific concentrations. This factor can be considered to be an approximation of the uncertainty in transport and dispersion. As a first-order approximation at short distances, the uncertainty in plume concentration is inversely proportional to the uncertainty in  $\sigma_y$  multiplied by the uncertainty in  $\sigma_z$ . Accounting for an uncertainty in concentration of a factor of three above and below the median corresponds to a range of uncertainty in CYSIGA from 1/1.73 to 1.73 times the median assuming that both cross-wind and vertical dispersion have the same ranges of uncertainty. If this range is considered to be the uncertainty at the 90 percent confidence level, the entire range of uncertainty is reasonably chosen to be bounded by factors of 1/2.5 and 2.5 on the median value for CYSIGA.

### Rationale for Distribution

The 50<sup>th</sup> percentile of the distribution from the expert elicitation [35] is a reasonable and defensible choice for the best estimate value to use for CYSIGA. Expert elicitation results are based on a combined category for stability classes A and B and a combined category for stability classes E and F, yielding 4 distributions for A/B, C, D, and E/F. Based on the previous discussion, the bounds of the distribution are set to be a factor of 2.5 higher and lower than the best estimate value for each weather class. All calculated values are found in Table 4-12.

In the previous Peach Bottom UA, a piecewise log-uniform distribution was used for CYSIGA because the expert elicitation data were approximately lognormal [2]. Since the range of uncertainty was chosen to be different for this analysis, a simpler log-triangular distribution was chosen. This choice is consistent with a most likely value at the center of the distribution and a likelihood that decreases as the bounds are approached. A log-triangular distribution was used instead of a triangular one because it gives equal sampling weight on either side of the mode when using a multiplicative factor for the lower and upper bounds.

**Table 4-12 Log-triangular values for dispersion parameter CYSIGA for each stability class.**

Class	Lower Bound	Mode	Upper Bound
A/B	.3002	.7507	1.8768
C	.1625	.4063	1.0158
D	.1112	.2779	0.6948
E/F	.0863	.2158	0.5395

CYSIGA and CZSIGA are perfectly rank correlated across the four stability classes. These values are also perfectly rank correlated with the values of CZSIGA, the vertical dispersion parameters discussed below. This indicates that uncertainty in CYSIGA is partially caused by changing weather conditions that would result in an increase or decrease in both the crosswind and vertical dispersion together. It also ensures that the order between the stability classes is preserved. The CDF is presented in Figure 4-57.

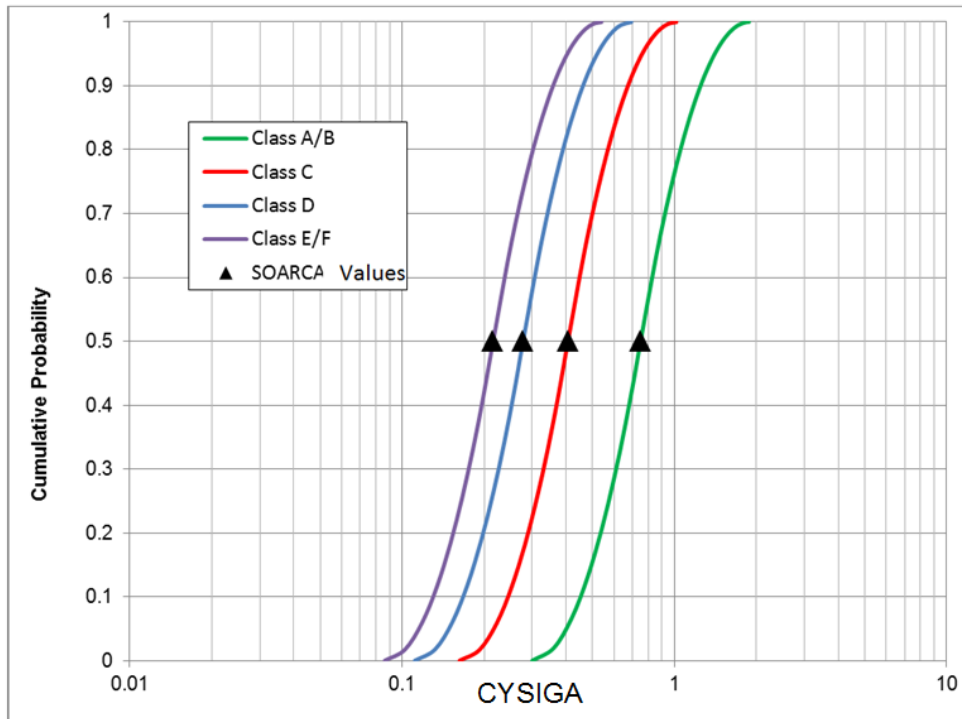


**Figure 4-57 CDFs of CYSIGA for individual stability classes**

**4.2.6.2 Vertical Dispersion Linear Coefficient (CZSIGA)**

The SOARCA best estimate values for CZSIGA were also based on the results of an expert elicitation [69]. Distributions were fit to the expert data, which were again roughly lognormal. The best estimate values used in SOARCA were chosen to be the 50<sup>th</sup> percentile of the distributions, and that value is appropriate as a median value in the UA for Surry. However, the distribution for CZSIGA has the same issues as the one for CYSIGA described above, so a narrower distribution is developed and used in this work. The same approach described in the previous subsection leads to distribution bounds on CZSIGA that are also factors of 2.5 above and below the median value for each stability class.

**Rationale for Distribution**

The 50<sup>th</sup> percentile of the distribution from the expert elicitation [69] is a reasonable and defensible choice for the best estimate value for CZSIGA. Based on the previous discussion, the bounds are set at a factor of 2.5 higher and lower than the best estimate value for each stability class. The distribution parameters are provided in Table 4-13.

CZSIGA distributions are perfectly rank correlated with each other and across the weather stability classes. They are also rank correlated with the crosswind coefficients (CYSIGA). This indicates that uncertainty in CZSIGA is partially caused by changing weather conditions that would result in an increase or decrease in both the crosswind and vertical dispersion together. It also ensures that the order between the stability classes is preserved. Figure 4-58 shows the CDFs of a log-triangular distribution for each of the four SOARCA stability class groupings.

**Table 4-13 Log-triangular values for dispersion parameter CZSIGA for each stability class.**

Class	Lower Bound	Mode	Upper Bound
A/B	.0144	.0361	.0903
C	.0814	.2036	.509
D	.1054	.2636	.659
E/F	.0985	.2463	.6158

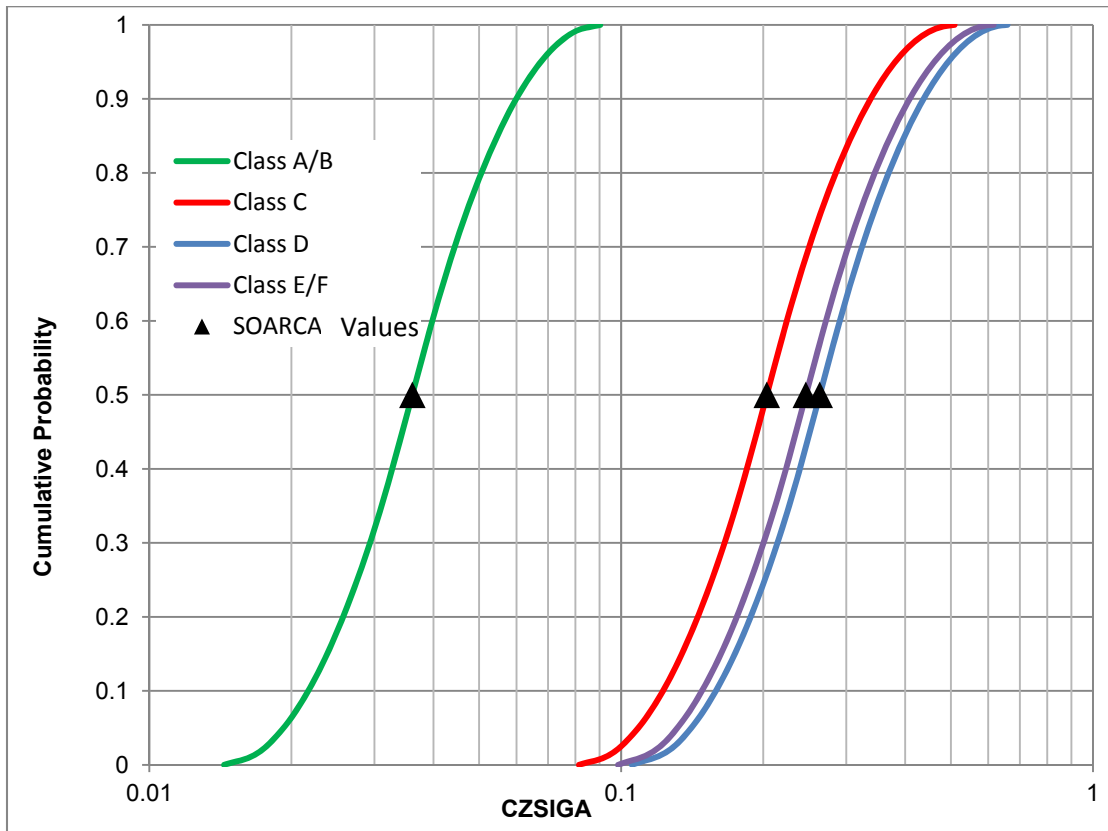


**Figure 4-58 CDFs of CZSIGA for individual stability classes**

#### **4.2.7 Emergency Response (Evacuation and Relocation)**

MACCS input parameters related to emergency response and evacuation were developed primarily from the 2012 Surry Evacuation Time Estimate (ETE) study [82]. The ETE provided the mobilization times, travel times for cohorts, and evacuation route information. Licensees are required under Appendix E, “Emergency Planning and Preparedness for Production and Utilization Facilities,” to 10 CFR Part 50 and 10 CFR 50.47, “Emergency Plans,” to estimate the time to evacuate the EPZ. Appendix E.IV.3 to 10 CFR 50 provides that nuclear power reactor licensees shall use ETEs in the formulation of protective action strategies. Therefore, it may be expected that the information in the ETE report will be used in the response decisions.

In the Surry SOARCA analysis [3], information from the 2001 Surry ETE was used to develop these response times [3]. NRC has since published updated guidance for developing ETEs in 2005 and 2011 [86][87]. The 2012 Surry ETE [82] follows the current guidance and includes detailed demographic information and measures of effectiveness that were useful in developing the delay and speed parameter values for each cohort. The cohorts established in the Surry SOARCA analysis [3] were maintained for this UA and are described below.

Cohort 1 represents the public residing within the 10-mile EPZ. One cohort was used to represent the entire public within the EPZ. Current analyses [91] separate the public into smaller population segments, creating additional cohorts to represent the response of the public. Expanding the number of cohorts was a new advancement in MACCS when SOARCA was initiated, and due to concerns over computer run time, which never materialized, it was determined at the time that a maximum of 6 cohorts should be used.

Cohort 2 represents the shadow evacuation which was defined as 20 percent of the population within the area 10 miles beyond the EPZ. A shadow evacuation typically occurs after widespread news of a nearby emergency is broadcast, and residents outside the official evacuation zone begin to evacuate. The area of 10 to 20 miles was specific to SOARCA. More current research [15] and ETE guidance [86] suggests that 20 percent of the population of the area extending 5 miles beyond the evacuation area is appropriate. However, to maintain a consistent demographic population distribution for risk comparisons, the Surry SOARCA [3] approach of 20 percent of the public from the area 10 to 20 miles beyond the EPZ was maintained.

Cohort 3 represents the schools within the EPZ. The 2012 Surry ETE report identifies sufficient resources for a single wave evacuation with enough buses to serve all of the schools [82].

Cohort 4 represents special facilities residents within the EPZ and includes ambulatory, wheelchair bound, and bedridden patients. Special facilities can take longer to evacuate than the general public because special transportation resources must be mobilized and loading patients must be done with care. The facilities evacuate individually following facility-specific evacuation plans [88].

Cohort 5 represents the evacuation tail for the 0 to 10 mile public. The evacuation tail is the last 10 percent of the general public and as such follows the general public evacuation [84]. The initial speed of the tail is the same as the final speed of the general public, but because the tail enters the roadway network late in the event, the roadways begin to clear, and the tail eventually has a faster evacuation speed [84].

Cohort 6 represents a small fraction of the public assumed to refuse to evacuate. A value of 0.5 percent was used in NUREG-1150 and has been applied in subsequent studies, including SOARCA [3]. This value is supported through recent research which included a survey of evacuees by Mitchell, et al that identified 98.4 percent of the public evacuated in response to the Graniteville chemical spill [12][13]. Thus, 1.6 percent of the public did not evacuate in this event. The EPZ has a siren system and backup capabilities to alert the public, and the EPZ population receives emergency response information at least annually; therefore, response from the EPZ public may be expected to be more efficient than the ad hoc evacuation for Graniteville. Additionally, as identified in a national telephone survey of EPZ residents, the public has a good

understanding of the emergency response expectations [15]. The speed and delay parameters are not applicable to this cohort, but the relocation parameters apply.

Figure 4-59 shows a typical response timeline as implemented in MACCS.

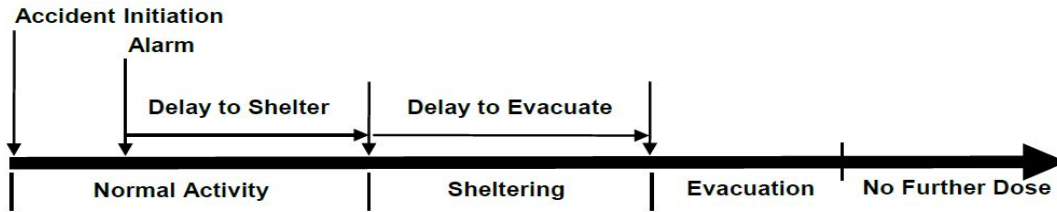


**Figure 4-59 General response timeline representing MACCS activities**

For each cohort, MACCS uses the following duration and travel speed parameters:

- Delay to shelter (DLTSHL) represents the duration of time from the accident initiation until the population becomes aware of the emergency and begins sheltering. During this period, shielding parameters are applied assuming normal activity.
- Delay to evacuate (DLTEVA) represents the duration of time from the start of sheltering to the start of evacuation. During this period, shielding parameters are applied assuming sheltering.
- Duration of beginning phase (DURBEG) of evacuation is the first of three emergency response time periods in MACCS and is typically used to represent the time from start of travel until evacuees are in the evacuation queue. This phase begins when the sheltering period ends. During this phase, a travel speed (ESPEED1) is applied for each cohort. For each of the three evacuation phases, shielding parameters are applied for evacuation.
- Duration of middle phase (DURMID) of evacuation is typically used to represent the time of travel after DURBEG until the cohort travels beyond the EPZ. This period begins when DURBEG ends. During this phase a second travel speed (ESPEED2) is applied for each cohort.

The third and final phase of evacuation is defined as the period of time from the end of DURMID to the end of the early phase, which is 7 days from the time of the first radiation release in this analysis and in SOARCA [1]. During this phase, a third travel speed (ESPEED3) is used to represent the travel speed beyond the EPZ. The population travels at ESPEED3 until they have reached a distance of 30 miles from the plant, at which point they are modeled to receive no further early phase radiation exposure. As distances increase radially beyond the EPZ, the roadway network becomes more expansive providing increased capacity which facilitates greater speeds.

It is not necessary to make each of the above parameters uncertain. In determining which parameters to select, it was decided that one delay parameter and one speed parameter would adequately represent the uncertainty of the set. Because DURBEG and ESPEED1 represent the early part of the evacuation (only 15 minutes for most cohorts), assessing the uncertainty for this duration would be of less interest than assessing the middle phase which comprises most of

the travel time inside the EPZ. The third phase occurs primarily beyond the EPZ and at faster speeds and would also be of less interest. Therefore, ESPEED2 was selected to be uncertain because this occurs during the middle phase when congestion within the network is at its greatest, and vehicles are slowly moving out of the EPZ.

When a General Emergency is declared, licensees have 15 minutes to make a declaration and provide a protective action recommendation (PAR) to the offsite response organizations (OROs). After receipt of the accident declaration, OROs make a protective action decision, activate sirens, and issue an Emergency Alert System (EAS) message. The data used in Surry for this time period was developed from exercise information. A sensitivity analysis was conducted on delaying notification in the Surry SOARCA analysis by one hour [3]. The results showed there was little effect from this delay [3].

The effect of weather is partially addressed in emergency response. An evacuation speed multiplier was used to reduce travel speed when precipitation is occurring, as indicated from the meteorological data file. This multiplier is used to address adverse weather, consisting of rain, ice, or snow, any of which can affect the response. The evacuation speed multiplier was set at 0.7, which reduces the ESPEED values to 70 percent of the fair weather travel speed.

In addition to speed and delay, relocation parameters are sampled to reflect uncertainty in post-evacuation activities. Relocation was first introduced in the CRAC model [78] to instantaneously remove the public from areas that exceed specified dose limits at a specified time after plume arrival. This evolved into the MACCS hotspot and normal relocation parameters. Following a release of radioactive material, levels of deposition can vary resulting in areas with elevated dose rates called hotspots [80] which may warrant the relocation of residents from affected areas. These areas of elevated contamination would typically be identified after the initial evacuation, but still during the early phase, based on dose projections from state, utility, and federal agency computer modeling and field measurements.

The U.S. Environmental Protection Agency (EPA) protective action guides (PAGs) for evacuation are typically used in MACCS as the dose thresholds at which the public would be relocated. When these thresholds are exceeded, OROs would be expected to relocate individuals from the affected areas. This application is typically considered for residents beyond the EPZ, but also applies to residents within the EPZ who may have refused to follow the initial evacuation orders. It is assumed these individuals will relocate when they understand a release has occurred, and they are informed they are located in elevated dose areas. MACCS implements relocation with the hotspot and normal relocation parameters, which are specific to the MACCS model.

Hotspot and normal relocation are determined in MACCS based on the total effective dose commitment projected to be received by an individual who remained in place for the entire emergency phase period while engaging in normal activity. The pathways used for calculating the total effective dose commitment are cloudshine, groundshine, direct inhalation, and resuspension inhalation. The reference time for the relocation dose criteria is plume arrival. Relocated individuals are removed from the problem for the duration of the emergency phase and receive no additional dose during this phase [6].

#### **4.2.7.1 Evacuation Delay (DLTEVA)**

The evacuation delay (DLTEVA) defines the duration of the sheltering period that occurs immediately before evacuation. Lengthy delays could increase the potential for receiving dose.

However, there are reasons for expecting such delays to be limited; for example, there is high confidence in the alert and notification system used to warn the public. Sirens are tested at least monthly and the performance characteristics for siren systems are maintained under the Reactor Oversight Process (ROP). The ROP data for Surry showed a 99.9 percent performance indicator at the time of the Surry SOARCA analysis [3]. Furthermore, research has found that EPZ residents understand actions that may be expected during an emergency and are well prepared, with 20 percent of EPZ residents having go-bags and are ready to leave promptly [15]. Wolshon et al. [84] found that delay is not uniform with most of the evacuees experiencing a smaller delay (e.g., 90 percent of the public evacuates in about 60 percent of the response time). The variation in public response makes this a good candidate for the UA. Information used to develop the DLTEVA distribution was obtained from the ETE report [82].

### **Rationale for Distribution**

A triangular distribution is used to represent DLTEVA uncertainty because there is some confidence in the mode which was based on a site specific telephone survey conducted to support the ETE [82]. Delays can occur for many reasons, and this is represented by the bounds. Delays can increase due to a slow response to the evacuation order, a need to wait for the return of commuters, a need to wait for public transportation, a need to shut down operations prior to leaving work, etc. Likewise, those members of the public with go-bags may respond rapidly, with little or no delay. Because delays vary individually, they would not apply to the entire cohort. However, MACCS moves cohorts as a whole based on population fraction; therefore, compromise values, based on the ETE data, are used to represent the entire cohort response.

The DLTEVA parameter is applied at the cohort level. Response timing is sampled for each cohort. Cohort 1 represents the first 90 percent of the 0-10 mile public (the EPZ). The SOARCA baseline DLTEVA value was 1 hour [3]. A mode of 2 hours represents the expected time, which is taken as an approximate average of the mobilization time for residents with and without commuters as presented in the ETE report [82]. A lower bound of 0 hours would indicate there is no delay after the public has been notified. Such conditions could occur as demonstrated in spontaneous evacuations where some people leave when they observe an emergency, such as a fire, but prior to receiving evacuation orders [88]. However, it would not be realistic that the entire cohort would leave immediately. With a mode of 2 hours and understanding that there are situations where the public may become aware of a need to evacuate prior to receiving formal notification, 1 hour was judged to be reasonable for the lower bound of the entire cohort. With regard to the upper bound, the ETE report shows the longest the general public cohort (the first 90 percent of the public) is expected to take 4 hours [82] in the case of residents waiting for commuters to return home during snow, and this was used for the upper bound.

Cohort 2 represents the shadow evacuation in the 10 to 20 mile area. The size of the shadow evacuation can be influenced by communication during the emergency. The timing and content of messaging can cause the shadow to increase or decrease and can cause residents to leave earlier or later in the event depending on the perceived risk of the residents [88]. The shadow evacuation typically begins shortly after the general evacuation begins. The lower bound for Cohort 2 is established as 1 hour, which allows time for the general evacuation to get underway. The 1 hour value was based on analyst judgment and review of emergency evacuation information [81]. A value of 5 hours was judged to be reasonable for the upper bound. A mode of 3 hours was judged reasonable to reflect this cohort usually follows the evacuees from the hazard area (e.g., the general public cohort).

Cohort 3 represents the schools within the EPZ. When the SOARCA project [1] was initiated, it was decided at the time to select a winter weekday scenario that includes school evacuation. Although this scenario only occurs on weekdays over a range of a few hours, it challenges the response agencies with additional logistics and responsibilities. For this scenario, the Virginia Department of Emergency Management would notify schools when a Site Area Emergency (SAE) is declared [3]. This notification triggers activities to mobilize buses and evacuate the schools. The baseline SOARCA DLTEVA was 1 hour based on the 2001 ETE, which assumed that transportation resources were immediately available. The ETE report [82] identifies sufficient resources for a single wave evacuation, indicating there are enough buses to serve every school at the same time. A lower bound of 0.5 hours was judged reasonable for this cohort. This includes time for OROs to notify the schools and assumes the evacuation occurs in the morning at the beginning of school or in the afternoon at the end of school when buses are already mobilized. The 2012 ETE report provides school bus mobilization times that range from 145 minutes to 180 minutes [82]. An upper bound of 4 hours was established to account for the mobilization time and potential delay in notification, communication with drivers, delay in travel due to weather or other impediments, etc. A mode of 2.75 hours was selected to represent an average of the mobilization times presented in the ETE [82].

Cohort 4 represents the special facilities within the EPZ and was modeled in SOARCA [3] with a DLTEVA of 11 hours based on the 2001 ETE. There are 12 special facilities identified in the 2012 Surry ETE [82], and these facilities would evacuate as resources are available. It is not necessary, to model each facility individually; therefore, special facilities are modeled as a group. The departure was set later in the evacuation with a time that represents an average of when the facilities may depart. The 2012 ETE report identifies 3 hours as the average time for buses to arrive at the facilities. Additional time was estimated for loading the residents prior to beginning the evacuation [82]. It is unlikely resources for all facilities could be obtained and mobilized much faster than 3 hours, because the ETE report identifies there are insufficient ambulances to complete the evacuation in a single wave, making a second wave necessary. Therefore, 3 hours was judged reasonable for the lower bound. A mode of 5 hours was judged reasonable to reflect the vehicle mobilization time, lack of transportation resources to mobilize in a single wave, and the time to load residents. A factor of 2 was applied to the mode providing a value of 10 hours. The factor of 2 was based on analyst judgment which considered there are cooperative agreements with neighboring counties to acquire additional resources. This gives confidence that resources would eventually become available. However, additional time would be needed to acquire these resources, and for such an event, there could be competing priorities with the cooperative agreement counties. The upper bound may also represent a potential delay in availability of transportation resources, communication with drivers, delay in travel due to weather, or other impediments.

Cohort 5 represents the evacuation tail for the 0 to 10 mile public. The SOARCA [3] DLTEVA value was 11 hours, based on the 2001 ETE. In the 2012 ETE [82], Scenario 6 represents the midweek winter day good weather evacuation, which is similar to the SOARCA scenario. The 2012 ETE report shows that 90 percent of the general public completes their evacuation in about 4 hours, which is the time the tail would begin. The evacuation ends at about 6 hours. A lower bound of 3 hours was judged reasonable to reflect efficient evacuation of the general public. An upper bound of 10 hours was judged reasonable to reflect a range of potential delays that contribute to the tail, such as waiting for commuters, shutting down equipment, and other delays. A mode of 4 hours was selected based on the ETE [82] which represents the expected time for this scenario.

Table 4-14 provides a listing of the cohorts and the values used in the triangular distribution. The cohort sampling approach is shown in Figure 4-60. Evacuation delays are sampled independently for each cohort. Although it was intended the evacuation tail be correlated with the public, because the tail leaves after the public, the modeling was not implemented in this manner. This modeling error would likely have a negligible effect on the results. For each cohort the timing of evacuation is specified independently at each radial distance in the grid (a ring). These values are rank correlated so that the entire cohort begins to evacuate at approximately the same time.

**Table 4-14 MACCS uncertain parameters – evacuation delay.**

Parameter	SOARCA Value	Mode	Bounds
Cohort 1 (0-10 Public)	1.0	2.0	LB = 1.0 hr. UB = 4.0 hr.
Cohort 2 (10-20 Shadow)	1.0	3.0	LB = 1.0 hr. UB = 4.0 hr.
Cohort 3 (Schools)	1.0	2.75	LB = 0.5 hr. UB = 4.0 hr.
Cohort 4 (Special Facilities)	11	5.0	LB = 3.0 hr. UB = 10.0 hr.
Cohort 5 (Evacuation Tail)	11	4.0	LB = 1.0 hr. UB = 10.0 hr.

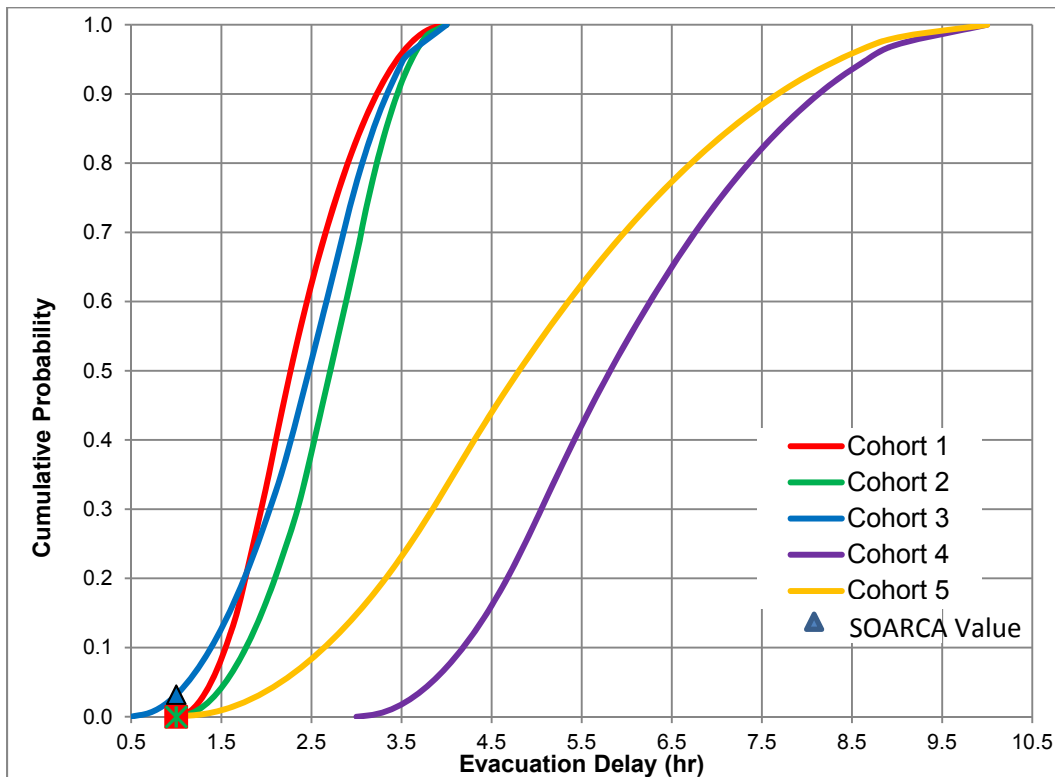


**Figure 4-60 CDF of DLTEVA for each cohort**  
(Note: Cohort 4 and 5 SOARCA values fall outside of their respective CDFs)

#### **4.2.7.2 Evacuation Speed (ESPEED)**

The ESPEED2 parameter represents the speed for each of the evacuating cohorts for the duration of the middle phase. As mentioned earlier, the Surry SOARCA analysis [3] values were based on the Surry ETE report dated 2001. The current Surry ETE report [82] includes additional detail, measures of effectiveness, and updated time estimates.

##### **Rationale for Distribution**

A triangular distribution was used to represent uncertainty because there is confidence that the mode derived from the ETE report is the most likely value. The ETE report was developed following NRC guidance and reviewed by NRC staff. Average speeds for the entire roadway network and for select evacuation routes are provided in the ETE [82]. These speeds can vary by cohort depending on the evacuation routes selected by each cohort, the location of the cohort within the EPZ (e.g., schools may be near the edge of the EPZ), and the time the cohort enters the roadway.

For Cohort 1 (the 0-10 mile public) the Surry SOARCA [3] speed was 1 mph based on the 2001 ETE report and accounted for MACCS loading the entire public cohort at one time. In reality, evacuating residents would load the roadway network over a longer period of time and travel at different speeds based on congestion at the time they enter the roadway network. The current ETE identifies an average network speed of about 12 mph for the duration of the evacuation [82]. This average speed includes the beginning, middle and late phases in MACCS, and includes areas west of the James River, which experience a faster free flow speed (i.e., unimpeded traffic flow) and areas east of the river, which experience congested flow as illustrated in Chapter 7 of the ETE report [82]. Because the speed is being sampled for the middle phase duration, a lower bound of 0.5 mph is judged reasonable and reflects a potential for congestion and impediments to the evacuation. Such impediments can range from drivers stopping to ask emergency personnel questions to power outages that affect stoplights or infrastructure damage that requires alternate routes. An upper bound of 12 mph was judged reasonable to represent the average speed identified in the ETE report, which represents evacuation under normal conditions. A mode of 1 mph was judged reasonable, again accounting for MACCS loading the entire public cohort at one time and accounting for the fact that the parameter is ESPEED2 which occurs during the congested period. The current ETE shows speeds of less than 2 mph on several evacuation routes under normal conditions [82].

Cohort 2 represents the 10 to 20 mile shadow evacuation which is travelling on different roadways than the EPZ population, thus the speeds are not directly related to the EPZ evacuees. The speed was set at 1 mph in the Surry SOARCA analysis [3] because most of the shadow population is located in the densely populated areas east of the James River. The lower bound is established at 0.5 mph. Although shadow evacuations occur in response to emergencies, the effect of the shadow evacuation on the evacuees from the EPZ is seldom significant. This is quantified in Appendix M of the ETE study [82] which shows that an increase in the shadow population to 25 percent of the public has no effect on the ETE, and an increase to 60 percent, only has a 25 minute increase on the ETE. The upper bound of 15 mph was judged reasonable to account for limited traffic congestion and increased roadway capacity beyond the EPZ. A mode of 5 mph was judged reasonable to reflect these evacuees are beyond the congested EPZ when they begin their travel.

For Cohort 3 (schools), a speed of 10 mph was used in the Surry SOARCA analysis [3] because schools are notified directly, allowing them to begin evacuation prior to the general public. For

this accident scenario, schools are assumed to receive orders to evacuate after declaration of the SAE, which is about 2.5 hours prior to the general public [3]. The 2012 ETE shows the schools require approximately 3 hours to mobilize buses. This puts the school cohort on the evacuation route during periods when traffic congestion is building. The current ETE report shows average speeds for the school evacuation ranging from 1.1 mph to 33 mph. The school speeds largely depend on the proximity to the EPZ boundary and the level of congestion on the evacuation routes travelled. The school with a 33 mph speed is located about 0.5 miles from the southeast edge of the EPZ; thus, this school evacuates ahead of the rest of the population on uncongested roadways and is not typical of other schools. Most of the average speeds for schools were estimated at less than 10 mph [82]. A lower bound of 0.5 mph was judged reasonable to account for congestion and potential impediments to the evacuation. An upper bound of 15 mph was judged reasonable based on the potential for less congestion due to evacuation early in the event, which could occur in the mornings or afternoons while buses are already mobilized. A mode of 1 mph was chosen based on the speeds used for the general public and the current ETE which shows the schools evacuating with the general public [3].

Cohort 4 represents the special facilities within the EPZ which were modeled in the Surry SOARCA analysis [3] as starting evacuation later in the event, near the end of the peak traffic congestion. The lower bound of 0.5 mph was judged reasonable to represent these evacuees entering the roadway network during heavy congestion. These facilities evacuate individually, and the potential exists to enter the roadway network when traffic congestion is heavy. The upper bound of 20 mph was judged reasonable to represent evacuating late in the event when roadways are less congested. This would be consistent with sheltering for an extended period until specialized vehicles arrive to support the evacuation. A mode of 5 mph was judged reasonable reflecting facilities that evacuate independently, on average, are likely to enter the roadway network while some congestion exists.

Cohort 5 represents the evacuation tail for the EPZ public, which begins evacuation at the end of the general public evacuation. The initial speed of the tail is the same as the general public because they enter the roadway immediately behind the general public. As evacuees exit the EPZ, the roadways begin to clear and the evacuation speed of the tail increases [84]. The lower bound was set at 0.5 mph because the tail enters the roadway network at the end of the peak congestion, which is represented by the lower bound for Cohort 1. The upper bound of 20 mph represents roadways that are relatively free of congestion once the majority of vehicles have left the area. A mode of 10 mph was judged reasonable to reflect that in most instances, the tail has left late enough that there is less congestion.

Table 4-15 provides a listing of the cohorts and the values used in the triangular distribution. Cohorts are sampled as shown on Figure 4-61. Evacuation speeds are perfectly rank correlated between cohorts.

**Table 4-15 MACCS uncertain parameters – evacuation speeds.**

Cohort	SOARCA Value	Mode (mph)	Bounds (mph)
Cohort 1 (0-10 Public)	1 mph	1.0	LB = 0.5 UB = 12.0
Cohort 2 (10-20 Shadow)	1 mph	5.0	LB = 0.5 UB = 15.0
Cohort 3 (Schools)	10 mph	1.0	LB = 0.5 UB = 15.0
Cohort 4 (Special Facilities)	10 mph	5.0	LB = 0.5 UB = 20.0
Cohort 5 (Evacuation Tail)	10 mph	10.0	LB = 0.5 UB = 20.0

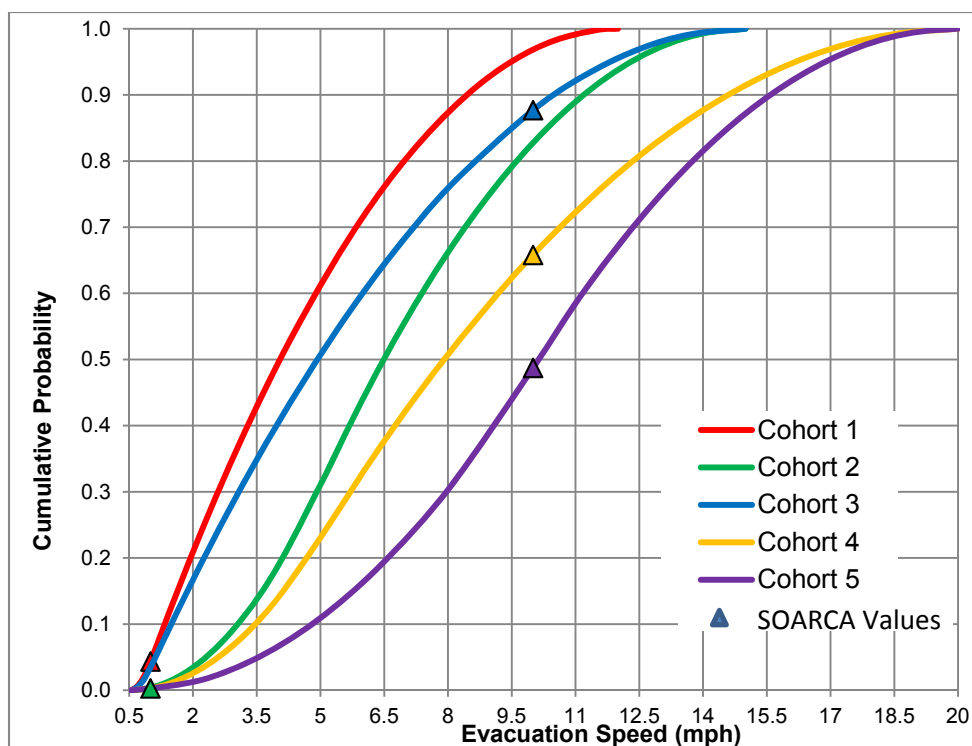


**Figure 4-61 CDFs of ESPEED for each cohort**

### 4.2.7.3 Hotspot Relocation Time (TIMHOT)

The hotspot relocation time (TIMHOT) is the estimated time needed to relocate residents from areas that exceed the hotspot dose threshold (DOSHOT). This user specified time is implemented in MACCS after plume arrival. The relocation time should include all temporal elements that contribute to the relocation activities. This includes time for OROs to define the affected areas, develop messaging and initiate the EAS to notify the public. This also includes time for the public to prepare to leave and travel out of the affected area. Each of these elements can be influenced by factors such as size of the affected area, number of affected

residents, location of residents when the warning is received, available resources to coordinate the relocation, clarity of data, weather, etc. Notification may be augmented by route alerting (which is identified in the state emergency plan), Reverse 911<sup>®</sup>, or other communication methods [81].

MACCS implements this parameter by removing the entire affected population from the dose equation a point in time, the time specified by TIMHOT after plume arrival. Because relocation occurs over a period of time, this was developed as an average for the affected population. Establishing a distribution to account for a range of source terms, population densities, and other characteristics that influence relocation is challenging.

### **Rationale for Distribution**

A uniform distribution was used to represent uncertainty, because the potential influences in activity duration during the emergency make any value within the range described below possible. Few of the time contributing activities can be estimated with confidence prior to an event, such as the affected area, affected population, available transportation infrastructure, need for traffic control, and plume travel speed. There are no empirical data available related to prompt relocation of residents. NUREG/CR-7110 Volume 2 [3] used a relocation time of 24 hours.

Relocation is expected to occur after evacuation is complete. This approach allows emergency responders who were supporting the evacuation to transition to relocating residents, and helps limit extra traffic in areas where the evacuees are travelling. The lower bound was developed based on an optimal relocation implemented promptly after plume arrival. Capabilities exist to project hotspot areas, and OROs could request the public make preparations to leave, prior to the release. Relocation could then begin promptly once it is determined the plume has passed. Assuming the public is prepared to leave, the final time element is travel out of the affected area. A review of the SOARCA results from NUREG/CR-7110 Volume 2 [3] shows that the release fraction of cesium for the STSBO scenario may only exceed the hotspot dose threshold in a few areas up to 5 miles beyond the EPZ. Therefore, the affected area may be small and associated population for hotspot may represent only a small fraction of the population. From SecPop [83], the 2010 population within the radial area 5 miles beyond the EPZ (i.e., 10 to 15 miles from the plant) is about 150,000. The Surry emergency response scenario includes an assumption that 20 percent of the population in this area evacuates as a shadow evacuation, which reduces the number of people potentially affected by hotspots [3]. It is assumed 20 percent of the remaining residents may need to be relocated due to exceeding the hotspot criteria. Considering the number of people potentially affected and the need for authorities to notify these people and support the relocation, a lower bound value of 12 hours after plume arrival was judged reasonable.

The upper bound represents conditions in which there is a delay in relocation, which could occur for many reasons. For example, OROs may decide to wait until the morning, rather than trying to mobilize families at night. Loss of communication, infrastructure damage, or OROs focused on activities within the EPZ or having other conflicting priorities could contribute to such a delay. Because relocation is based on projected dose over the emergency phase, it may not have the same priority as other urgent requirements. It is also possible that response officials may choose to shelter in place for a period of time. A value of 30 hours after plume arrival was judged reasonable for the affected area. The CDF is presented in Figure 4-62.

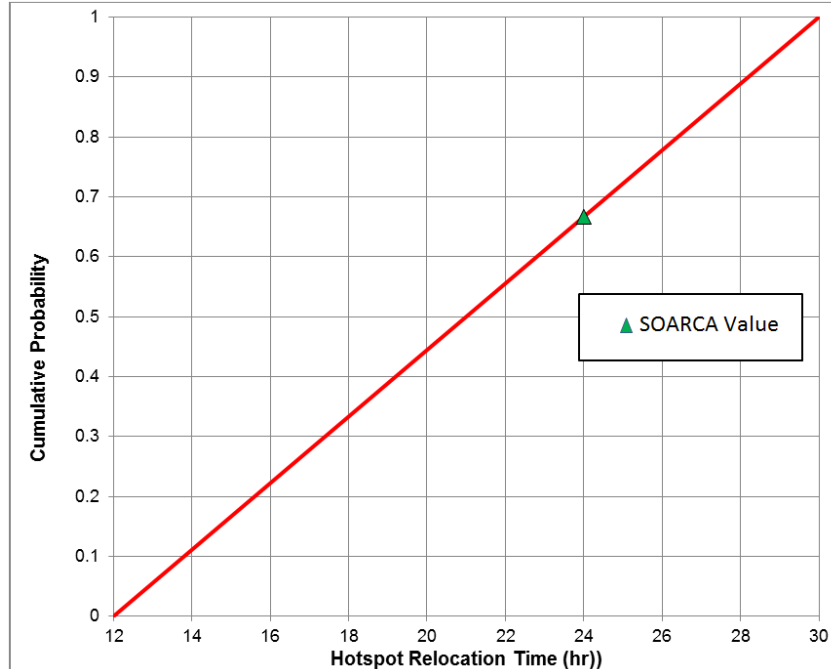


**Figure 4-62 CDF of TIMHOT**

#### 4.2.7.4 Normal Relocation Time (TIMNRM)

The normal relocation time (TIMNRM) is the time to relocate residents from areas that exceed the normal dose threshold (DOSNRM). This user specified time is relative to plume arrival. The time includes the elements described for the hotspot relocation time (TIMHOT). In addition, time may be needed to allow clearance of residents relocated due to the hotspot criteria. Again, establishing a distribution to account for a range of source terms, population densities, and other characteristics that influence relocation is challenging. Furthermore, because DOSNRM is a relatively low dose threshold, the size of the area could be large and could have a correspondingly large population. MACCS implements this parameter by removing the entire affected population from the dose equation at a point in time, the specified TIMNRM after plume arrival. As with TIMHOT, a compromise time is developed by considering the influencing factors.

#### Rationale for Distribution

A uniform distribution is used to represent uncertainty in TIMNRM because the potential influences in activity duration during the emergency make any value within the range described below possible for the same reasons described with TIMHOT. However, normal relocation has a lower dose threshold and may not be implemented with the same urgency as hotspot relocation. No empirical data related to prompt relocation of residents after an evacuation was identified. This lack of data also supports use of a uniform distribution. NUREG/CR-7110 Volume 2 [3], used a normal relocation time of 36 hours.

Similar to TIMHOT, the lower bound is developed based on an optimal response where OROs relocate residents promptly after plume arrival. A review of the SOARCA baseline results [3] shows that the release fraction of cesium could exceed the normal dose threshold over most of the area 5 miles beyond the EPZ. From SecPop [83], the 2010 population within the radial area

5 miles beyond the EPZ is about 150,000. The Surry scenario includes an assumption that 20 percent of this population evacuates as a shadow evacuation [3], and it is assumed another 20 percent of the public are relocated under the hotspot criteria. Thus for this analysis, about 95,000 residents remain in the area and could potentially be relocated (this assumes the entire remaining population in this area is relocated). Early notifications can be accomplished via EAS messaging, but route alerting would still be necessary and would take a few hours. For this size of population, traffic control would likely be established to support a relocation effort. Because the compromise time reflects the entire affected population, which is dispersed throughout the 5 mile radial area beyond the EPZ (approximately 400 square miles), a lower bound of 16 hours after plume arrival was judged reasonable.

The upper bound represents conditions where OROs are focused on activities within the EPZ or have other conflicting priorities which delay relocation activities. Furthermore, they may delay relocation until daylight hours. Because this relocation is due to a 1 rem dose projected over the emergency phase, it may not have the same priority as other urgent requirements. An upper bound of 48 hours after plume arrival was judged reasonable. The CDF is presented in Figure 4-63.

TIMNRM is perfectly rank correlated with the hotspot relocation time (TIMHOT) because MACCS requires TIMNRM be less than TIMHOT.

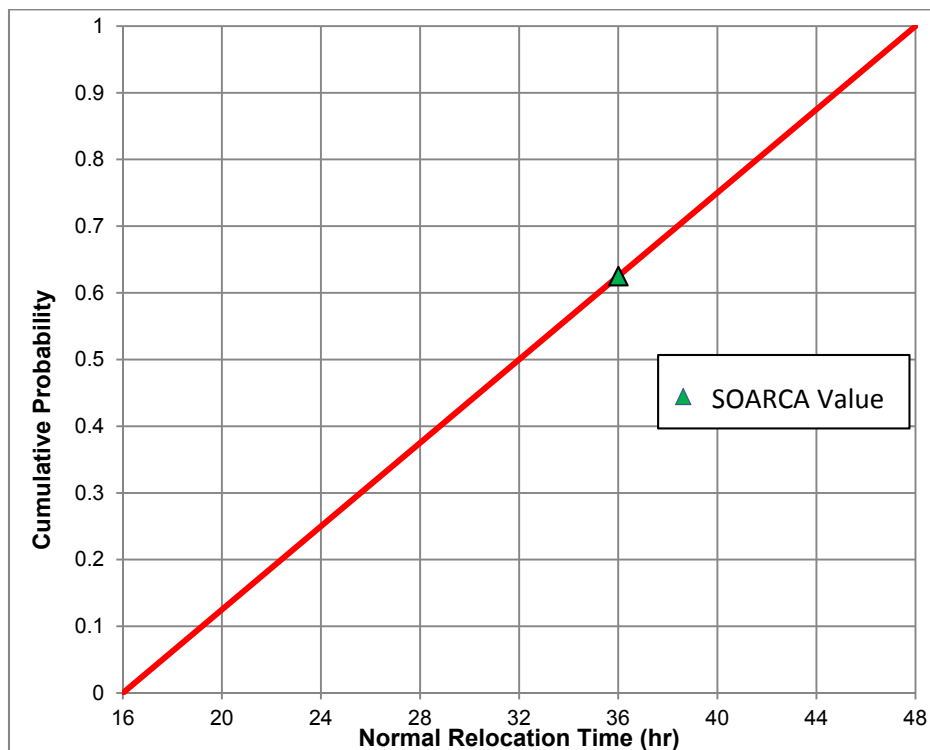


Figure 4-63 CDF of TIMNRM

#### 4.2.7.5 Hotspot Relocation Dose (DOSHOT)

The hotspot relocation dose (DOSHOT) is a projected dose used to initiate hotspot relocation. If the total dose to individuals exceeds DOSHOT, those people are relocated (i.e., removed from the analysis) at a user specified hotspot relocation time (TIMHOT) [76] in the early phase.

DOSHOT is often [3][6] represented as the upper bound of the projected dose range provided in the EPA PAG Manual (Table 1-1. Planning Guidance and Protective Action Guides for Radiological Incidents) [85]. This should not be confused with the EPA PAG Manual criteria for relocation, which is specified for the intermediate phase [85].

### Rationale for Distribution

A triangular distribution is used to represent the uncertainty in DOSHOT because the mode is considered to be the most likely value (5 rem) based on the EPA PAGs [85]. For the Surry SOARCA analysis [3], 5 rem projected over the emergency phase was used based on the upper evacuation bound in the EPA PAG Manual [85]. The range was developed recognizing that ORO decisions are influenced by many factors that could result in a higher or lower value.

The EPA PAG Manual provides a range of 1 to 5 rem for implementing protective actions and explains that under normal conditions, evacuation should be implemented if residents are expected to receive 1 rem over a 4 day emergency phase [85]. The upper bound for this distribution was increased 50 percent above the EPA PAG to 7.5 rem, based on analyst judgment. The lower bound was set at 1 rem, which is the mode of the normal relocation criteria (DOSNRM) as described in Section 4.2.7.6. The CDF is presented in Figure 4-64.

DOSHOT is perfectly rank correlated (i.e., coefficient of 1.0) with the normal relocation dose (DOSNRM) because MACCS requires DOSNRM to be less than DOSHOT.

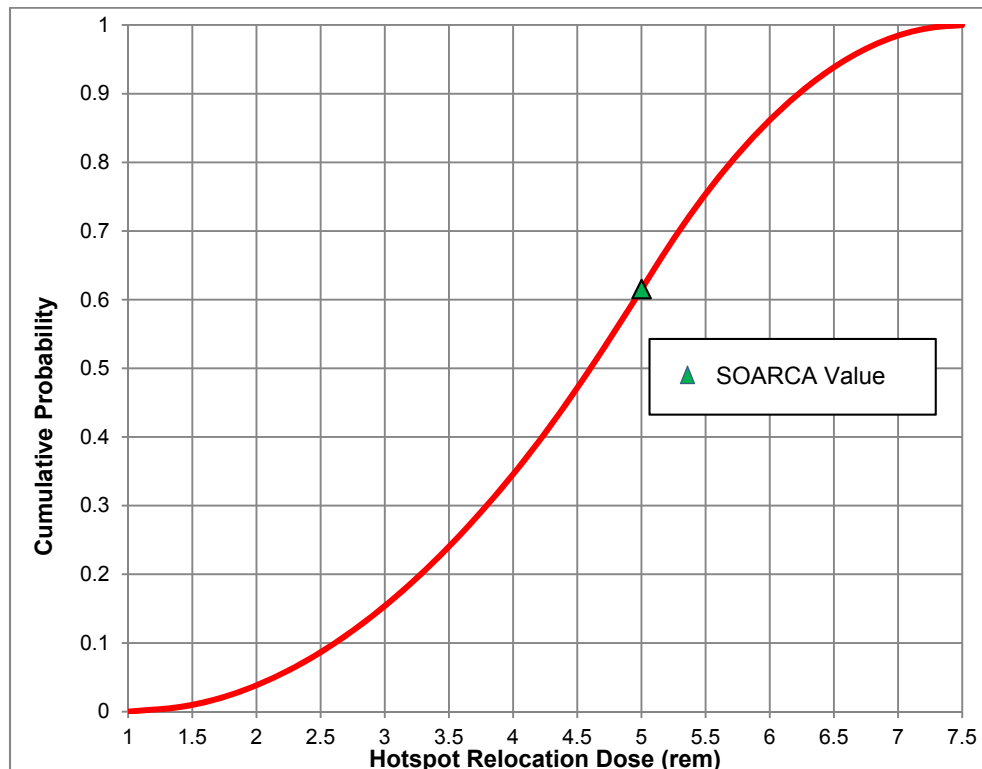


Figure 4-64 CDF of DOSHOT

#### 4.2.7.6 Normal Relocation Dose (DOSNRM)

The normal relocation dose (DOSNRM) is a projected dose used to initiate normal relocation. If the total dose to individuals exceeds DOSNRM, those people are relocated (i.e., removed from the analysis) at a user specified normal relocation time (TIMNRM) [76] in the early phase. DOSNRM is typically [3][6] represented as the lower bound of the projected dose range provided in Table 1.1 of the EPA PAG Manual [85].

##### Rationale for Distribution

A triangular distribution is used because the mode (1 rem) is considered to be the most likely value based on EPA PAGs. For the Surry SOARCA analysis [3], a projected dose of 1 rem was used based on the lower evacuation bounds in Table 1.1 of the EPA PAG Manual [85]. A range was developed because OROs may implement a higher or lower value.

It is assumed that OROs would attempt to meet the EPA PAG barring unforeseen circumstances. Therefore, using judgment, the upper bound for this distribution was increased by a factor of two over the mode to 2 rem. The lower bound of 0.5 rem was judged reasonable. A low threshold value causes the size of the affected area to increase, which would increase the number of people requiring relocation. The number of people affected would likely influence ORO decisions on the lower threshold value. The CDF is presented in Figure 4-65.

DOSNRM is perfectly rank correlated with the hotspot relocation dose (DOSHOT) because MACCS requires DOSNRM to be less than DOSHOT.

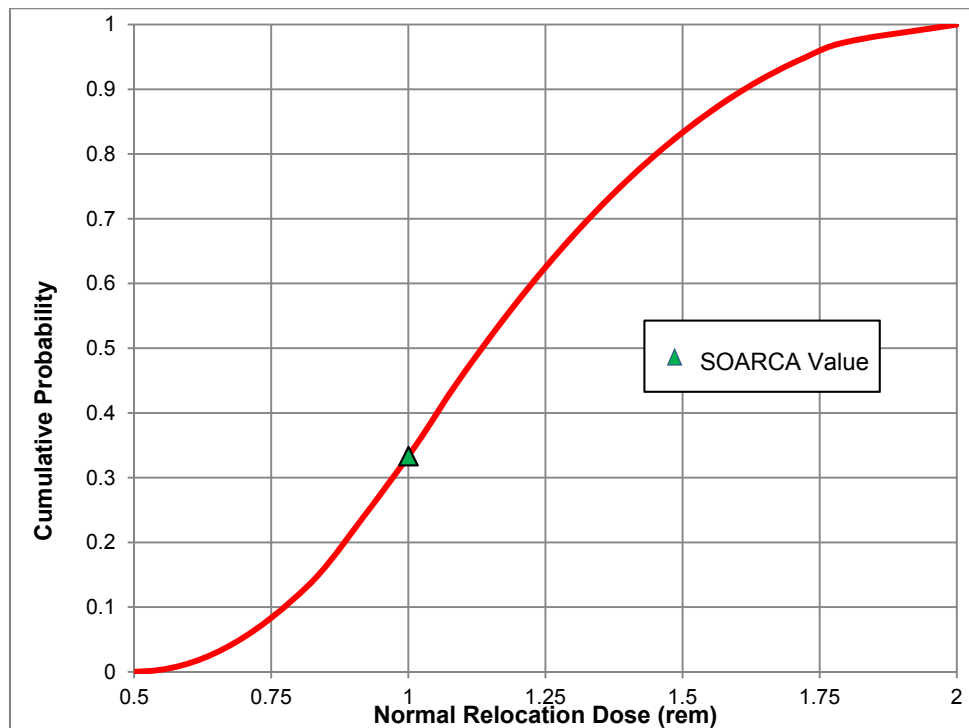


Figure 4-65 CDF of DOSNRM

#### 4.2.8 Weather

Weather binning approach is used to categorize similar sets of weather data based on wind speed, stability class, and the occurrence of precipitation. For the non-uniform weather-bin sampling approach used for SOARCA, the number of trials selected from each bin was the maximum of 12 trials and 10 percent of the number of trials in the bin. Some bins contain fewer than 12 trials. In those cases, all of the trials within the bin are used for sampling. This strategy results in roughly 1,000 weather trials for the Surry weather data used in this analysis.

The best estimate offsite consequence values are the expected (mean) value of the probability distribution obtained from a large number of weather trials. The UA uses the same weather-sampling strategy adopted for SOARCA, as reported in the MACCS Best Practices document, and also applied in the Peach Bottom UA [2][6].

One or more years of archived weather data from a reactor site is the starting point for evaluating the variability in consequences that can result from uncertain weather at the time of a future, hypothetical, atmospheric release of radioactive material. The inherent assumption in using historical data to quantify the consequences of a future event is that future weather data will be statistically similar to historical data. This has been a good assumption from past experience, as established by the body of work created when plants perform consequence analyses to support license extensions. That work looks specifically at two consequence measures: population dose and economic losses. For those results, the general observation has been that mean consequence values have been the same when evaluated for five, usually consecutive, weather years to within about  $\pm 10$  percent. The expectation is that this observation will be equally valid for future weather, although the variation could be larger for specific consequence measures.

Consequence analysis using MACCS is based on one year of archived data from a single weather tower. Most commonly, the weather tower is on the actual site of the nuclear power plant and is fairly close (less than a kilometer) to the location from which a source term would be emitted, were an accident to occur. This is the case for the Surry consequence analysis. Two years of archived weather data were obtained from the site and one of those years, 2004, was selected for this consequence analysis. Measurable precipitation (at least 0.01 in.) occurred during 6.9% of the hours of 2004. More details about the weather data used for Surry are provided in NUREG/CR-7110 Vol. 2 [3].

Meteorological data are measured at two elevations on a single weather tower and those measurements are used to construct four, hourly values to characterize the influence of weather. The hourly values represent integral or averaged values over hour-long intervals for each hour of a 365-day year (a total of 8760 data points). The hourly values in the meteorological data file are (1) wind direction, (2) wind speed, (3) stability class, and (4) precipitation rate. Wind direction and wind speed are measured at a fine time resolution (e.g., every 5 s) and averaged over the one-hour intervals. Stability class is constructed from temperatures measured at two elevations and evaluated according to criteria in Reg. Guide 1.23 [92]. One parameter in the meteorological data file, mixing layer height, is recorded as a seasonal average rather than an hourly value. The mixing layer heights serve as upper boundaries for vertical dispersion of a plume. There are eight values for mixing layer height, and these are for morning and afternoon, averaged over each of the four seasons. A morning value generally corresponds to the minimum of the mixing layer height over a 24-hour period; the afternoon value generally corresponds to the maximum of the mixing layer height over a 24-

hour period. All of these eight values are used to analyze a set of weather trials that represent the entire year and every hour of the day.

MACCS has several options for treatment of meteorological data, which include the ability to directly input weather data, or the ability to sample weather data from an external input file. Sampling options include a strategy that uses meteorological bins defined by the user (weather binning), or one or more random samples from each day of the weather file. Weather binning is a type of importance sampling used to categorize similar sets of weather data based on wind speed, stability class, and the occurrence of precipitation. With regard to wind direction, the assumption is that sampling within each weather bin is sufficient to adequately represent the wind rose, i.e., the likelihood of the wind blowing in each compass direction, for that bin. Accounting for the fact that each plume segment travels in its own direction, as explained below, this assumption should be satisfied.

The weather sampling strategy adopted for SOARCA and this Surry UA uses the weather-binning approach in MACCS. The weather binning structure is the same as the one in NUREG-1150 [10], which consists of 16 predefined bins for combinations of stability class and wind speed and 20 user-defined bins for rain occurring before the plume travels 32 km (20 miles). The rain bins differentiate rain intensity and the distance the plume travels before rain begins. Each hour of weather in the meteorological data file is placed into one of the weather bins, with the rain bins taking priority over the wind-speed/stability-class bins. The definition of these weather bins is provided in the Table 4-16. The probability of weather in each weather bin is proportional to the number of hours of data that go into that bin, and thus the weather bins are not equally probable. The probability of a sample (weather trial) drawn from a weather bin is accounted for in the sampling method. A weather trial uses a selected hour from one of the bins as the initial hour of weather corresponding to a release into the atmosphere. Subsequent hours of a weather trial follow the sequence of data from the weather file, as explained below.

**Table 4-16 Rain bins and wind speed and stability class bins.**

		<i>Rain Bins</i>					
Rain Distance (miles)	Rain Intensity (mm/hr)						
	0 - 2	2 - 4	4 - 6	> 6			
< 2 miles	Bin 17	Bin 18	Bin 19	Bin 20			
2 - 3.5 miles	Bin 21	Bin 22	Bin 23	Bin 24			
3.5 - 7 miles	Bin 25	Bin 26	Bin 27	Bin 28			
7 - 13 miles	Bin 29	Bin 30	Bin 31	Bin 32			
13 - 20 miles	Bin 33	Bin 34	Bin 35	Bin 36			
> 20 miles	Not a rain bin – use wind speed and stability class binning						
		<i>Wind Speed and Stability Class Bins</i>					
Stability Class	Wind Speed u (m/s)						
	0 - 1	1 - 2	2 - 3	3 - 5	5 - 7	> 7	
A/B	Bin 1			Bin 2			
C/D	Bin 3	Bin 4	Bin 5	Bin 6	Bin 7	Bin 8	
E	Bin 9	Bin 10	Bin 11	Bin 12			
F/G	Bin 13	Bin 14	Bin 15	Bin 16			

The number of weather trials selected from each bin was the maximum of 12 trials and 10 percent of the number in the bin. Some bins contain fewer than 12 trials. In those cases, all of the trials within the bin are used in the set of weather trials. This strategy results in roughly 1,000 weather trials to represent the 8,760 hours of data in a 365-day year for the Surry UA. A sensitivity study conducted for the Peach Bottom UA [2] showed that this sampling strategy matched the mean results that would have been obtained by choosing every hour in the weather file (8760 samples) within 3% for health risks evaluated with the linear, no-threshold (LNT) dose-response assumption and within 12% for health risks evaluated with the two non-LNT dose-response assumptions. Since the same sampling strategy was chosen for Surry as Peach Bottom, the expectation is that the accuracy should be similar.

A weather trial in MACCS is significantly more complex than if it were modeled with just a point value of weather data. A weather trial is defined by the starting hour of weather data from the meteorological data file. However, the weather trial uses as much data from the meteorological data file as required to transport plume segments through and out of the computational grid. An overall atmospheric release (source term) for the Surry UA is described by 50 to 100 plume segments, depending on the occurrence of steam generator tube rupture. Each plume segment represents the quantity of radionuclides released over a one-hour period from a specific release path (e.g., leakage through a failed steam generator tube). Each plume segment can travel in a different direction, and it is affected by the hourly data, i.e., wind speed, stability class, and precipitation rate, taken from the weather file starting with the hour of its release from the source location until it exits the computational grid.

An illustration of the way plume segments move through the grid is shown in the following two snapshots from a plume animation. Figure 4-66 shows four consecutive plume segments, where the tail of one segment happens to align in distance traveled, but not in direction, with the head of the next. The plume segments are colored purple, green, yellow, and red in order of increasing radius in the first snapshot. The wind is shifting from northwest to northeast, as indicated by the directions of the segments. Figure 4-67 also shows four plume segments, where each has moved outward along its centerline toward the edge of the grid. One plume segment has disappeared off the grid and a new one has been created in an even more easterly direction than the previous segments. Each segment has its own width, depending on the amount of dispersion that has occurred as it experiences varying weather conditions along its path. Each segment also has a unique length, depending on the speed of the wind during its release.

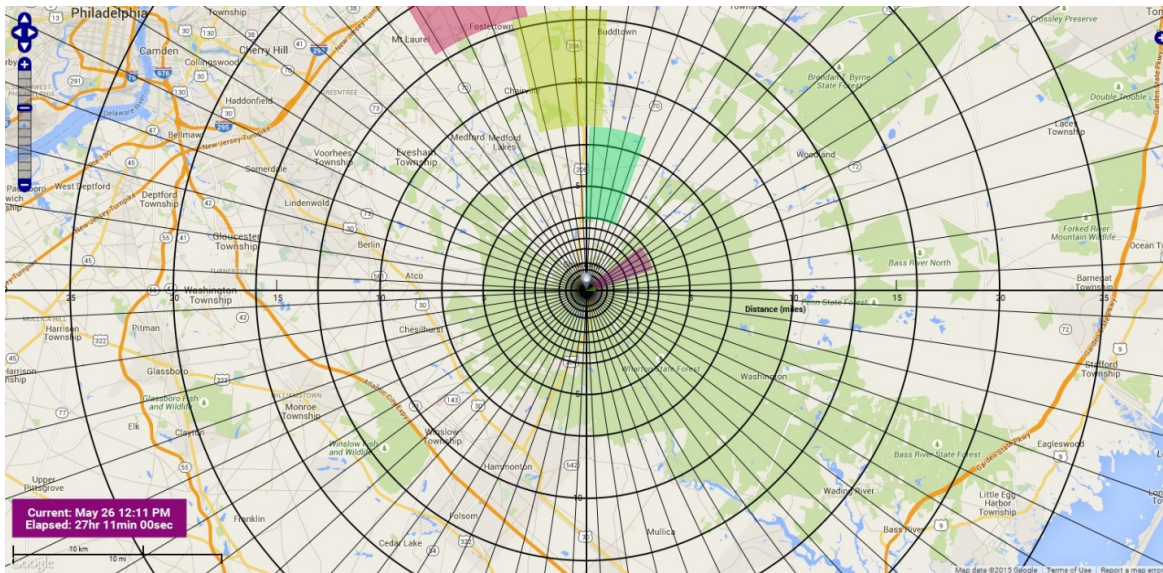


**Figure 4-66** Illustration of four consecutive plume segments, where the tail of one segment aligns in distance traveled, but not in direction, with the head of the next segment

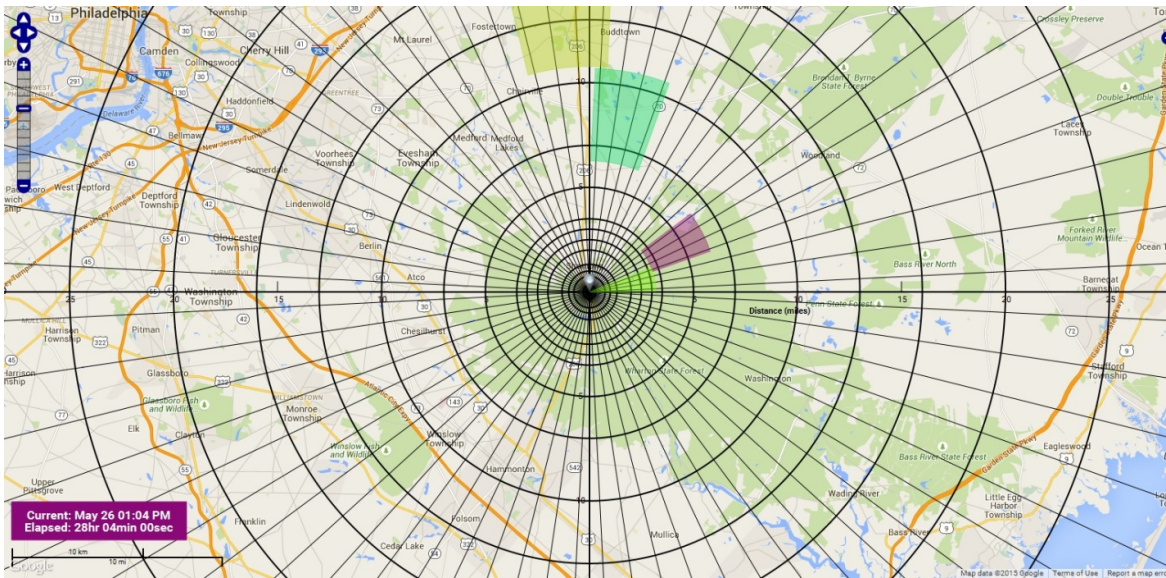


**Figure 4-67** Illustration of four consecutive plume segments with tails that do not align

#### 4.2.9 MACCS Correlated Parameters

Many of the parameters in the analysis have correlations. Some of these are perfectly rank ordered and others have rank correlation coefficients between -1.0 and +1.0. Unless specified in Table 4-17 below, parameters are not correlated.

**Table 4-17 MACCS correlated parameters.**

<b>Input Parameter</b>	<b>Perfectly Rank-Order Correlated with</b>	<b>Comments</b>
PROTIN(2)	LPROTIN	Long-term is tied to normal activity
GSHFAC(2)	LGSHFAC	Long-term is tied to normal activity
TIMHOT	TIMNRM	HOT is always less than NRM
DOSHOT	DOSNRM	HOT is always greater than NRM
EFFTHR(1)	EFFACA(1)	Red bone marrow
EFFTHR (2)	EFFACA (2)	Lungs
EFFTHR (3)	EFFACA (3)	Stomach
CYSIGA(1)	CYSIGA(2-6)	All weather conditions
CYSIGA(1)	CZSIGA(1-6)	All weather conditions
ESPEED(2)-1	ESPEED(2)-(2-5)	Middle Phase of Espeed for all Cohorts evacuating
VDEPOS(1)	VDEPOS(2-10)	All particle size bins
Co-58_ICH(1)	Co-58_ICH(2,4-9)	Lifetime inhalation dose coefficient
Co-60_ICH(1)	Co-58_ICH(2,4-9)	Lifetime inhalation dose coefficient
Rb-86_ICH(1)	Co-58_ICH(2,4-9)	Lifetime inhalation dose coefficient
Rb-88_ICH(1)	Co-58_ICH(2,4-9)	Lifetime inhalation dose coefficient
Sr-89_ICH(1)	Co-58_ICH(2,4-9)	Lifetime inhalation dose coefficient
Sr-90_ICH(1)	Co-58_ICH(2,4-9)	Lifetime inhalation dose coefficient
Sr-91_ICH(1)	Co-58_ICH(2,4-9)	Lifetime inhalation dose coefficient
Sr-92_ICH(1)	Co-58_ICH(2,4-9)	Lifetime inhalation dose coefficient
Y-90_ICH(1)	Co-58_ICH(2,4-9)	Lifetime inhalation dose coefficient
Y-91_ICH(1)	Co-58_ICH(2,4-9)	Lifetime inhalation dose coefficient
Y-91m_ICH(1)	Co-58_ICH(2,4-9)	Lifetime inhalation dose coefficient
Y-92_ICH(1)	Co-58_ICH(2,4-9)	Lifetime inhalation dose coefficient
Y-93_ICH(1)	Co-58_ICH(2,4-9)	Lifetime inhalation dose coefficient
Zr-95_ICH(1)	Co-58_ICH(2,4-9)	Lifetime inhalation dose coefficient
Zr-97_ICH(1)	Co-58_ICH(2,4-9)	Lifetime inhalation dose coefficient
Nb-95_ICH(1)	Co-58_ICH(2,4-9)	Lifetime inhalation dose coefficient
Nb-97_ICH(1)	Co-58_ICH(2,4-9)	Lifetime inhalation dose coefficient
Mo-99_ICH(1)	Co-58_ICH(2,4-9)	Lifetime inhalation dose coefficient
Tc-99m_ICH(1)	Co-58_ICH(2,4-9)	Lifetime inhalation dose coefficient
Ru-103_ICH(1)	Co-58_ICH(2,4-9)	Lifetime inhalation dose coefficient
Ru-105_ICH(1)	Co-58_ICH(2,4-9)	Lifetime inhalation dose coefficient
Ru-106_ICH(1)	Co-58_ICH(2,4-9)	Lifetime inhalation dose coefficient
Rh-103m_ICH(1)	Co-58_ICH(2,4-9)	Lifetime inhalation dose coefficient
Rg-105_ICH(1)	Co-58_ICH(2,4-9)	Lifetime inhalation dose coefficient
Te-127_ICH(1)	Co-58_ICH(2,4-9)	Lifetime inhalation dose coefficient
Te-127m_ICH(1)	Co-58_ICH(2,4-9)	Lifetime inhalation dose coefficient
Te-129_ICH(1)	Co-58_ICH(2,4-9)	Lifetime inhalation dose coefficient
Te-129m_ICH(1)	Co-58_ICH(2,4-9)	Lifetime inhalation dose coefficient
Te-131_ICH(1)	Co-58_ICH(2,4-9)	Lifetime inhalation dose coefficient
Te-131m_ICH(1)	Co-58_ICH(2,4-9)	Lifetime inhalation dose coefficient
Te-132_ICH(1)	Co-58_ICH(2,4-9)	Lifetime inhalation dose coefficient
I-131_ICH(1)	Co-58_ICH(2,4-9)	Lifetime inhalation dose coefficient

Input Parameter	Perfectly Rank-Order Correlated with	Comments	
I-132_ICH(1)	Co-58_ICH(2,4-9)	Lifetime inhalation dose coefficient	
I-133_ICH(1)	Co-58_ICH(2,4-9)	Lifetime inhalation dose coefficient	
I-134_ICH(1)	Co-58_ICH(2,4-9)	Lifetime inhalation dose coefficient	
I-135_ICH(1)	Co-58_ICH(2,4-9)	Lifetime inhalation dose coefficient	
Cs-134_ICH(1)	Co-58_ICH(2,4-9)	Lifetime inhalation dose coefficient	
Cs-136_ICH(1)	Co-58_ICH(2,4-9)	Lifetime inhalation dose coefficient	
Cs-137_ICH(1)	Co-58_ICH(2,4-9)	Lifetime inhalation dose coefficient	
Ba-139_ICH(1)	Co-58_ICH(2,4-9)	Lifetime inhalation dose coefficient	
Ba-140_ICH(1)	Co-58_ICH(2,4-9)	Lifetime inhalation dose coefficient	
La-140_ICH(1)	Co-58_ICH(2,4-9)	Lifetime inhalation dose coefficient	
La-141_ICH(1)	Co-58_ICH(2,4-9)	Lifetime inhalation dose coefficient	
La-142_ICH(1)	Co-58_ICH(2,4-9)	Lifetime inhalation dose coefficient	
Ce-143_ICH(1)	Co-58_ICH(2,4-9)	Lifetime inhalation dose coefficient	
Ce-144_ICH(1)	Co-58_ICH(2,4-9)	Lifetime inhalation dose coefficient	
Pr-143_ICH(1)	Co-58_ICH(2,4-9)	Lifetime inhalation dose coefficient	
Pr-144_ICH(1)	Co-58_ICH(2,4-9)	Lifetime inhalation dose coefficient	
Nb-147_ICH(1)	Co-58_ICH(2,4-9)	Lifetime inhalation dose coefficient	
Np-239_ICH(1)	Co-58_ICH(2,4-9)	Lifetime inhalation dose coefficient	
Pu-238_ICH(1)	Co-58_ICH(2,4-9)	Lifetime inhalation dose coefficient	
Pu-239_ICH(1)	Co-58_ICH(2,4-9)	Lifetime inhalation dose coefficient	
Pu-240_ICH(1)	Co-58_ICH(2,4-9)	Lifetime inhalation dose coefficient	
Pu-241_ICH(1)	Co-58_ICH(2,4-9)	Lifetime inhalation dose coefficient	
Am-241_ICH(1)	Co-58_ICH(2,4-9)	Lifetime inhalation dose coefficient	
Cm-242_ICH(1)	Co-58_ICH(2,4-9)	Lifetime inhalation dose coefficient	
Cm-244_ICH(1)	Co-58_ICH(2,4-9)	Lifetime inhalation dose coefficient	
Linear correlation coefficients			
Input Parameter	Rank-Order Correlated With	Correlation Coefficient	Comments
PROTIN(2)	PROTIN(3)	0.75	Applies to all evacuation cohorts for normal activity and sheltering inhalation protection factors
GSHFAC(2)	GSHFAC(3)	0.8	Applies to all evacuation cohorts for normal activity and sheltering groundshine shielding factors

## 4.3 Quality Assurance Review of Input Parameters

### 4.3.1 MELCOR QA Review

Each uncertain MELCOR parameter was input into the Surry SOARCA model using a combination of existing MELCOR input records, new control and tabular, the .mapped and .vars files, and external data files. To confirm that the implementation of the parameters was done correctly, a QA review for each parameter was performed using the first set of fifty uncertainty runs along with select one-off sensitivities.

The QA involved multiple activities. First, the created input files and associated MELCOR output variables were checked to ensure that the proper values were used. Second, plots of key results

were checked to see that they matched with expectations based on certain values of the parameters. If there was not a run in the uncertainty set that used a needed value for a parameter, a sensitivity analysis was run where that value was manually selected.

This review was completed for each parameter, and it is not necessary to document the approach results of the entire effort. The process for QA of the SV thermal failure temperature and associated open fraction is described, which was typical. First, several realizations were spot checked between the uncertainty engine output file and the MELCOR input files to ensure that values matched. Second, the values in the uncertainty engine output file were plotted to ensure they matched the expected curves based on the distribution types selected. Finally, to check the output to see that the model responded as expected, a realization was sought where there was thermal failure of the SV. In the 50 realizations of the set used, there were no thermal SV failures, because stochastic cycling failure, liquid failure, or a hot leg creep rupture had occurred first in this smaller set of realizations. Therefore, a one-off sensitivity was run where the thermal failure parameter was set to a very low value of 670 K, while the number of cycles to both normal and liquid failure was set high. The temperature of the SV with the lowest setpoint is shown in Figure 4-68, along with the corresponding valve open fraction.

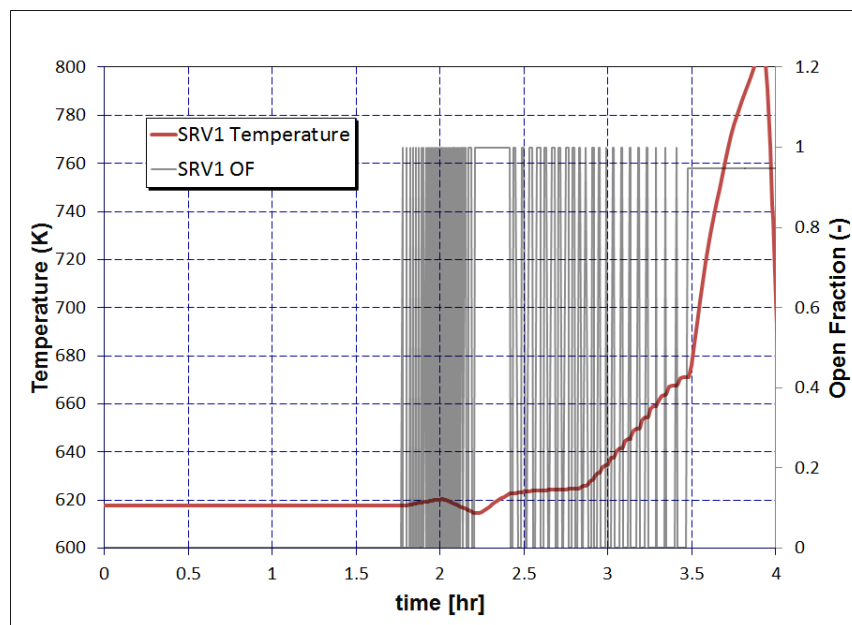


**Figure 4-68 SV1 temperature and open fraction for thermal failure sensitivity**

The temperature of the SV is modeled to only change when the valve is open and passing liquid or hot gases. As shown in Figure 4-68, the temperature stays steady until the first opening at which point it has a slight increase and then decrease during the early cycles. This can be explained by most of the early cycles being liquid cycles, which can actually have a slight cooling effect. Cycles after 2.5 hours are mainly hot steam, and at this point the SV temperature starts to increase steadily. The rate of SV heat-up increases corresponding with the temperature of the primary system, as observed at about 3 hours. Just before 3.5 hours, the SV temperature reaches the failure point of 670K and correctly, the valve fails open with an open fraction of 0.9487, which was the other sampled parameter value. The system pressure (not shown) also decreases rapidly at this time, as expected. This QA verified that the SV failure

temperature and corresponding open fraction are sampled correctly and were also implemented into the model correctly.

This general QA approach was implemented for each of the uncertain MELCOR parameters. Other single sensitivities were conducted, such as varied containment liner yield pressure, a secondary SV sticking open, and primary SV1 failing closed. A number of errors were found, both in the sampling of values and in the model enhancements done for their implementation. All of the identified errors were corrected before the final uncertainty realizations were run.

#### **4.3.2 MACCS QA Review**

The QA review of the MACCS input deck included comparing the Surry model inputs with the specified values identified in Section 4.2.

Dose coefficients were an important element of the QA review. A comprehensive table of mean dose coefficients and variances for eight organs was created using data from a report developed by Keith Eckerman to support SOARCA [72]. The dose coefficients were calculated by taking the natural log of the inhalation dose coefficients from Appendix B of Eckerman's report. Appendix B tabulates dose coefficients for the eight cancer sites and represents their uncertainties in terms of a log-normal distribution. The variance was calculated by also taking the natural log of the standard deviation values found in Table B-2 of Eckerman's report. The natural log of both the dose coefficient and variance were reviewed individually from the MACCS run. Of the 928 values reviewed, 7 values were found incorrect and were corrected for Surry.



## 5. UPDATED MELCOR BASE CASE

### 5.1 Source Term Model (MELCOR)

The calculations performed for the UA, results of which are presented in Section 6.0, were generated with an updated version of the MELCOR Surry SOARCA STSBO model that included the changes identified in earlier sections and in Appendix A. The updated model addresses issues identified in the course of this project and enhancements to improve model fidelity and support parameter distributions.

#### 5.1.1 Updated Best Estimate Run

As a central reference for comparison, a MELCOR calculation was performed for the Surry unmitigated STSBO scenario, where the value of each of the uncertain parameters in the UA was specified as the value determined to be most likely or most physically representative. Table 5-1 identifies the values used in this base calculation for the uncertain parameters sampled in the UA and differences, if any, from the Surry SOARCA [3] values are identified.

**Table 5-1 Values used for or associated with UA uncertain parameters in the base calculation.**

#	Variable	Best estimate	Original SOARCA Value [3]	Rationale ('SOARCA' refers to original single run)
1	Primary SV stochastic failure to close (SVLAMFTC)	45	256	Mean of samples; differs from SOARCA, but representative of newer SV failure data
2	Primary SV stochastic failure to open (SVLAMFTO)	N/A	N/A	This failure mode is sampled in the UA but because the expected number of cycles is greater than FTC it does not occur in the best estimate. SOARCA did not consider this failure
3	Primary SV failure to close due to passing water (SVWTR)	25	N/A	About 0.5 on the CDF for the mean and 50 <sup>th</sup> curves; SOARCA did not consider this failure
4	Primary SV thermal seizure criterion (SVFAILT)	1000 K	1000 K	0.5 on the CDF and SOARCA value maintained
5	Primary SV open area fraction upon either stochastic or thermal failure (SVOAFRAC)	0.5	1.0	0.5 on the CDF; SOARCA assumed fully open on failing but distribution is more supported
6	Secondary SV stochastic failure to reclose (SVLAMFTC-S/G)	45	256	About 0.5 on the CDF for the mean and 50 <sup>th</sup> curves; differs from SOARCA, but representative of newer SV failure data
7	Reactor Coolant Pump Seal Leakage (RCPSL)	21 gpm per pump for entirety of transient	21 with possibility to increase	Highest probability discrete bin; SOARCA allowed for increased leakage based on saturation conditions but new uncertainty logic does not support timing variability
8	Steam Generator Tube Thickness (modeled as tube outer diameter)	.0106335	N/A	Mode of symmetric triangular distribution and 0.5 on CDF; SOARCA did not consider
9	Hot SG Tube Temperature Multiplier	.44	N/A	0.5 on the CDF; SOARCA did not consider

#	Variable	Best estimate	Original SOARCA Value [3]	Rationale ('SOARCA' refers to original single run)
10	Zircaloy melt breakout temperature (SC1131(2))	2350 K	2400 K	0.5 on the CDF; logically supported considering new data is slightly lower than SOARCA value
11	Material Properties: temperature at which the eutectic formed from ZrO <sub>2</sub> and UO <sub>2</sub> melts (ZrO <sub>2</sub> /UO <sub>2</sub> )	2479 K	2800 K	Mode of normal distribution; SOARCA value is melting point for a 50/50 molar mixture and wasn't modified because of the presence of time-at-temperature model; new MELCOR default is 2500 K – close to mode
12	Molten clad drainage rate (SC1141(2))	0.2	0.2	SOARCA value maintained; not at 0.5 of the CDF but justified by the CORA experiments
13	Radial molten debris relocation time constant	60 s	60 s	SOARCA value maintained, uncertainty range set to observe importance. No technical justification to modify best estimate.
14	Solid radial debris relocation time constant	360 s	360 s	SOARCA value maintained, uncertainty range set to observe importance. No technical justification to modify best estimate.
15	Decay Heat Cycle	MOC, base decay heat	EOC, base decay heat	Assuming an accident can happen on any day of the cycle, MOC is closest to the majority of days. SOARCA used a Sequoyah EOC ORIGEN run, UA ORIGEN runs are now Surry specific. Decay heat does not have to be adjusted because the base ORIGEN decay heat is the mode of a normal distribution.
16	Containment Leakage Rate (% Volume per day at P/Pd = 1) Leak	0.55	0.1	0.5 on the CDF; SOARCA was design basis value, determined leakage would never be lower than this but could be up to 1.0 so strong justification to change best estimate
17	Containment Fragility Curve (CFC) Rupture	1.6 for liner yield, other points stay same	1.55	0.5 on the CDF; also approximately represents SOARCA value with 15% conservatism removed
18	Hydrogen ignition criteria (H <sub>2</sub> LFL)	6%	10%	Median value of discrete distribution; all bins are lower than SOARCA value but are technically justified
19	Secondary side decontamination factor (ARTIST) – N represents number of stages after SGTR	N=7	N/A	Highest probability discrete bin; SOARCA used a DF of 7 for any SGTR, new modeling supersedes this
20	Gaseous Iodine fraction (CHEMFORM-I)	0.00182	0.0	0.5 on MOC CDF; MOC needed since selected as inventory best estimate; SOARCA had no gaseous iodine but a small amount is technically justified
21	Cesium fraction (CHEMFORM-Cs)	0.8 Cs <sub>2</sub> MoO <sub>4</sub>	1.0 Cs <sub>2</sub> MoO <sub>4</sub>	Best estimate based on Phebus tests and mode of created PDF; SOARCA value was based on an earlier interpretation of Phebus results
22	Containment Condensation Rate – (XMTFCL)	1.4	1.0	Mode of PDF and best estimate based on comparisons to CONTAIN and experiments; parameter not considered by SOARCA so default was used
23	Radionuclide (RN) Package Reference Manual: Dynamic Shape Factor	1.5	1.0	0.5 on CDF, data suggests range of 1-2 is most likely, SOARCA value of 1 is for perfect spheres which is physical lower bound

Noteworthy aspects in the results of the base UA calculation include that:

1. An over-cycling FTC of the lowest set-point SV on each of the 3 SGs occurred and the failures happened within 3 min of each other.
2. An over-cycling FTC of the lowest set-point SV on the pressurizer occurred.
3. Hot leg nozzle rupture occurred on Loop A rather than on Loop C (to which the pressurizer surge line connects).
4. Energetic hydrogen deflagrations occurred in containment.
5. No SGTR occurred nor came close to occurring.
6. Containment design pressure and the pressure associated with liner yield were both exceeded.
7. Containment pressure associated with rebar yield was not reached by 48 hr but pressure was trending towards this point being exceeded shortly thereafter.
8. The largest contributor to containment pressurization was the continuous heating of original RCS coolant recast as steam in the containment (rather than addition of non-condensable gasses to the atmosphere from core-concrete interaction as was anticipated).
9. Releases to the environment of iodine and cesium were small, 0.073 percent and 0.029 percent of the inventory at scram, respectively.
10. Concrete ablation from core-concrete interaction slowed a little by the end of the MELCOR calculation at 48 hours, but was continuing.

Key event times in the base UA calculation are listed in Table 5-2.

**Table 5-2 Key event timing in the base UA calculation.**

Event	Time (hh:mm)
STSBO – loss of all AC and DC electrical power, AFW unavailable	00:00
Reactor trips Main steam isolation valves (MISVs) close RCP seal leakage initiates at 21 gpm/pump	00:00
RCP seal failure (enhanced leakage)	-*
SG SV fails to close	01:11
SG dryout	01:22
PRT rupture disk breaks	02:09
RPV water level reduces to TAF	02:40
Pressurizer SV fails to close	03:00
First fission product gap release	03:22

Event	Time (hh:mm)
SGTR	-*
Loop A hot leg nozzle rupture	04:28
1 <sup>st</sup> hydrogen burn	04:28
Accumulators begin discharging	04:28
Accumulators empty	04:29
RPV dry	05:33
RPV lower head breach	07:41
Reactor cavity dry	07:46
Containment pressure reaches design (45 psig)	25:01
Containment liner yields	41:05
Release of elemental iodine to the environment exceeds 1.0%	43:37
Containment rebar yields	-*
End of calculation	48:00

\*Indicates event did not occur

Figure 5-1 through Figure 5-19 present histories of various conditions in the base Surry UA STSBO calculation. Attributes of the figures are discussed below.

The primary pressure for the base case is shown in Figure 5-1. The cooling influence that exists as long as water resides in the SGs is evident early (during the first hour or so) in this figure. Full-loop natural circulation facilitates the cooling, efficiently transporting fission product decay heat from the core to the SGs. The stronger cooling that develops in response to SG SVs failing to close, due to a decrease in saturation temperature with depressurization, can be seen as can the depressurizations associated with a pressurizer SV failing to close and a hot leg nozzle rupturing. Interestingly, Hot Leg Nozzle A ruptured instead of Hot Leg Nozzle C. Nozzle C rupture was thought to be more likely due to venting through the pressurizer SVs which instills hot gas flows preferentially through the Hot Leg C nozzle.

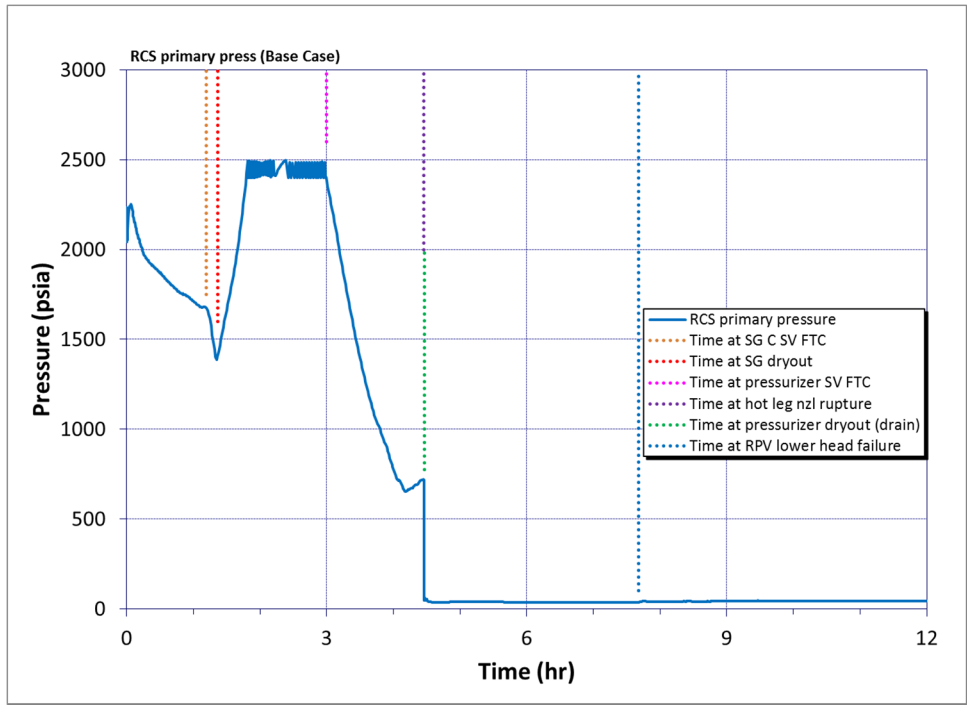


**Figure 5-1 RCS primary press (Base Case)**

Figure 5-2 shows SG pressure history. Pressure relief primarily through secondary SV operation but additionally through leakage past the MSIVs dictates pressure until SV failures to close vent the SGs to atmospheric pressure.

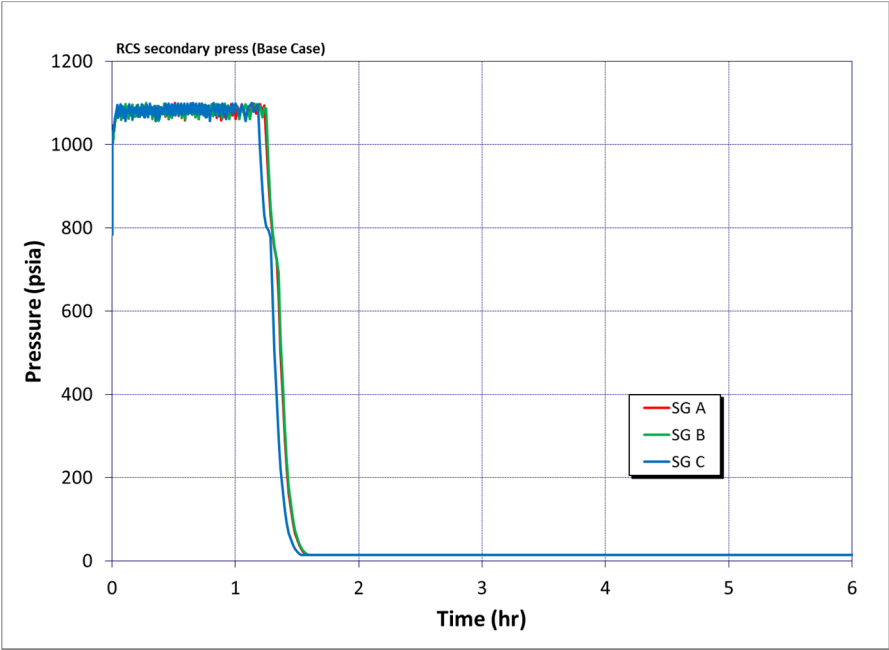


**Figure 5-2 RCS secondary press (Base Case)**

RCS level response is shown in Figure 5-3. This figure shows there is water holdup in the pressurizer prior to the pressurizer SV failure to close, even though the hot leg is dry. Accumulator injection is evident.

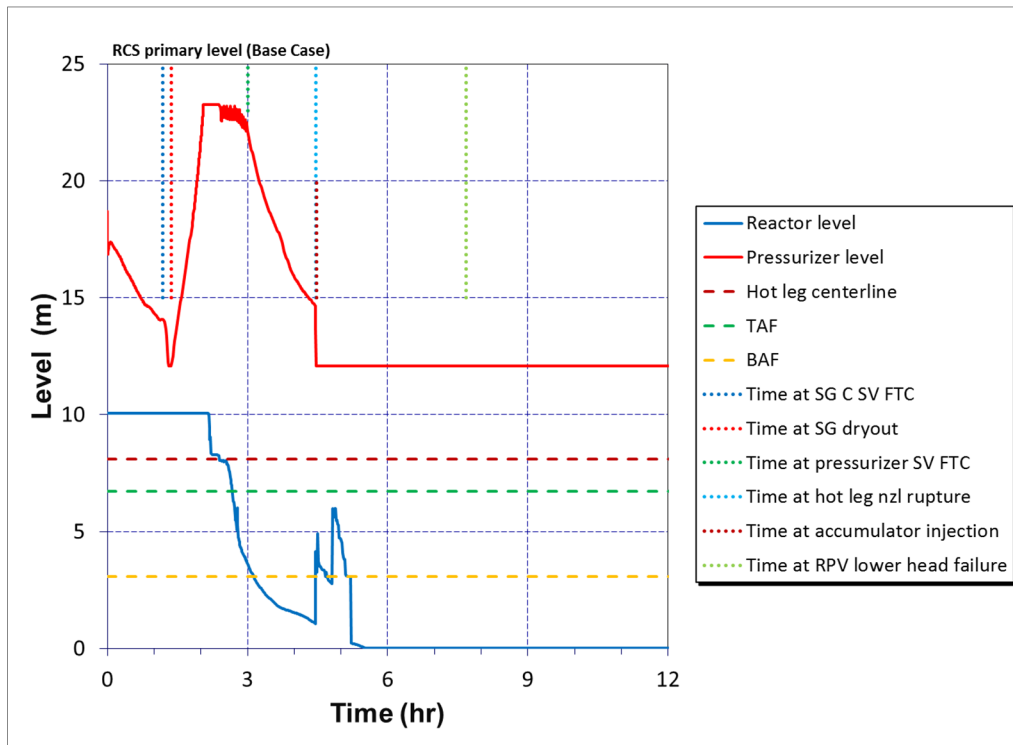


Figure 5-3 RCS primary level (Base Case)

Figure 5-4 shows the history of combined leakage from the RCS through the RCP seals. Note that there is no damage assumed to result to the seals in the course of the base calculation. The seals simply continue to leak at the baseline amount of 21 gpm/pump (at design pressure), provided there is still water in the RCS.

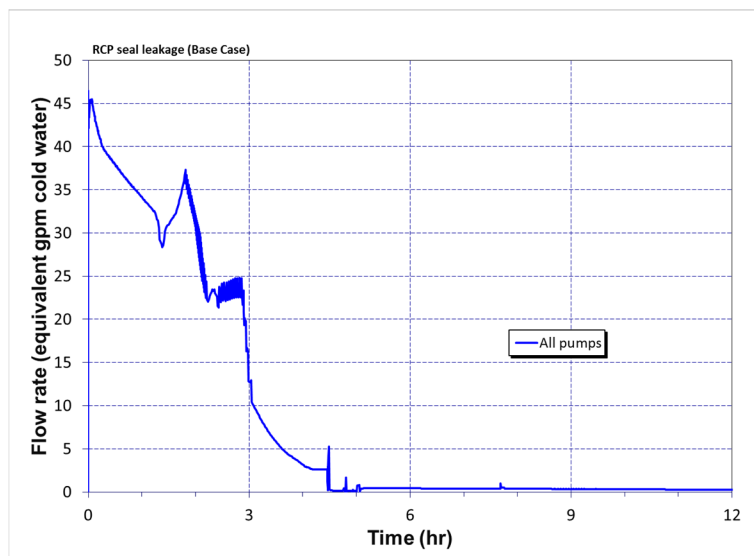
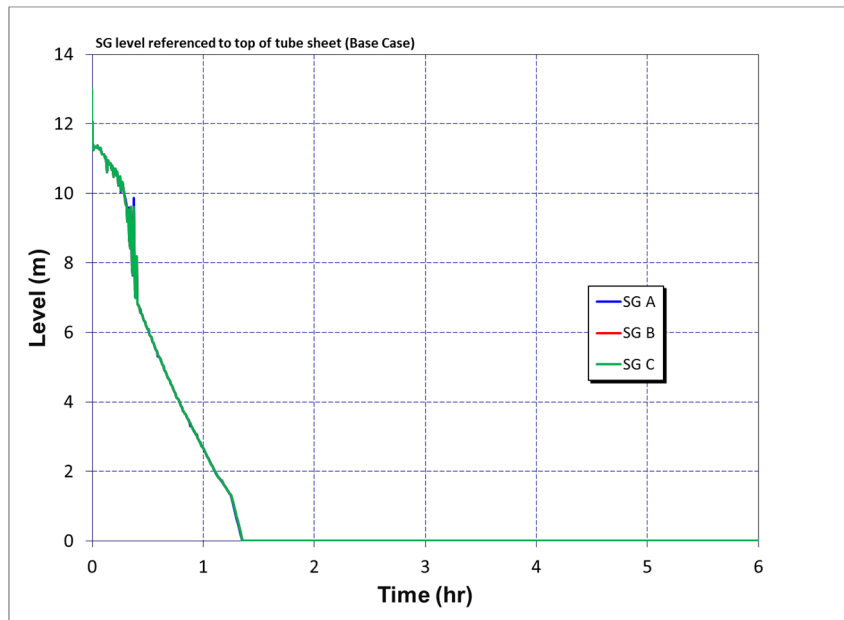


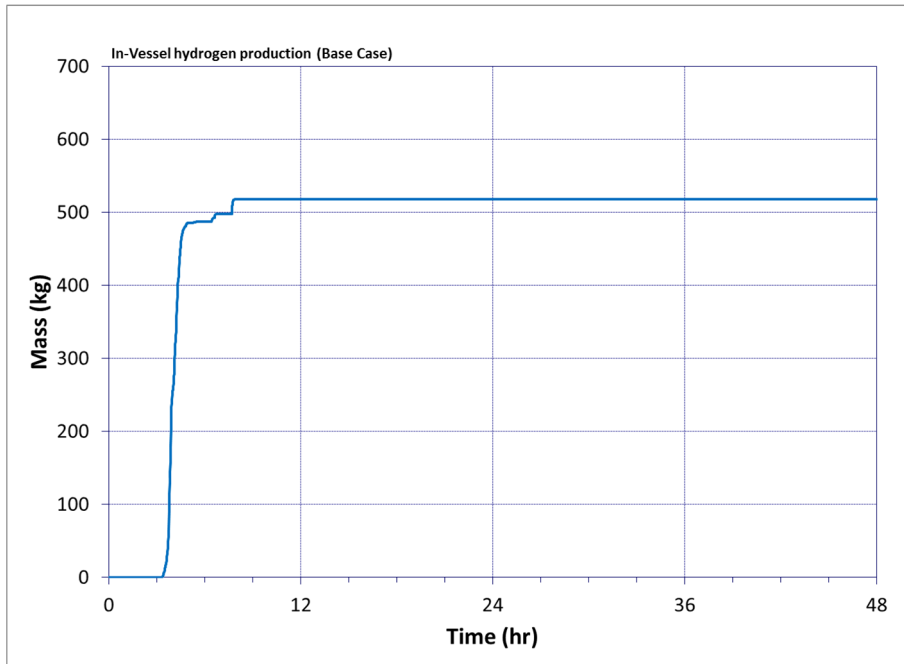
Figure 5-4 RCP seal leakage (Base Case)

SG level response is shown in Figure 5-5. All three SGs have essentially the same water level trend. Level decreases continuously in the absence of any feedwater delivery. The late steepening in level decline towards dryout reflects SVs on the SGs failing to close.

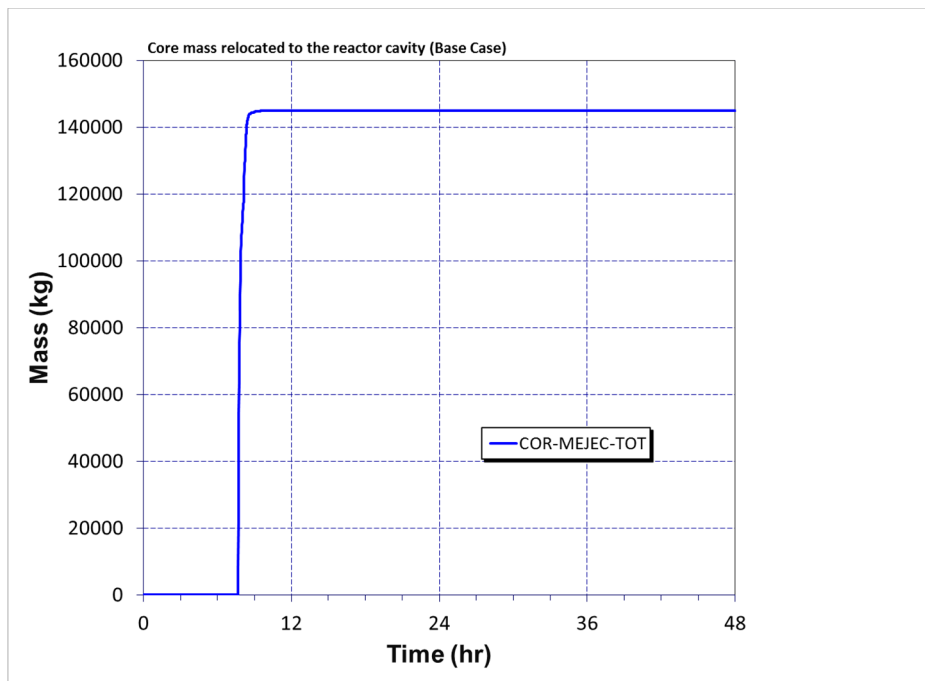


**Figure 5-5 SG level referenced to top of tube sheet (Base Case)**

Figure 5-6 and Figure 5-7 show the hydrogen produced inside the RPV through oxidation of fuel cladding and steel and the mass of core debris relocated to the reactor cavity, respectively. Each shows a large, singular event, although there is some minimal later production of hydrogen. Of greater interest are the initiation timing, duration, and magnitude of hydrogen production and relocated mass.



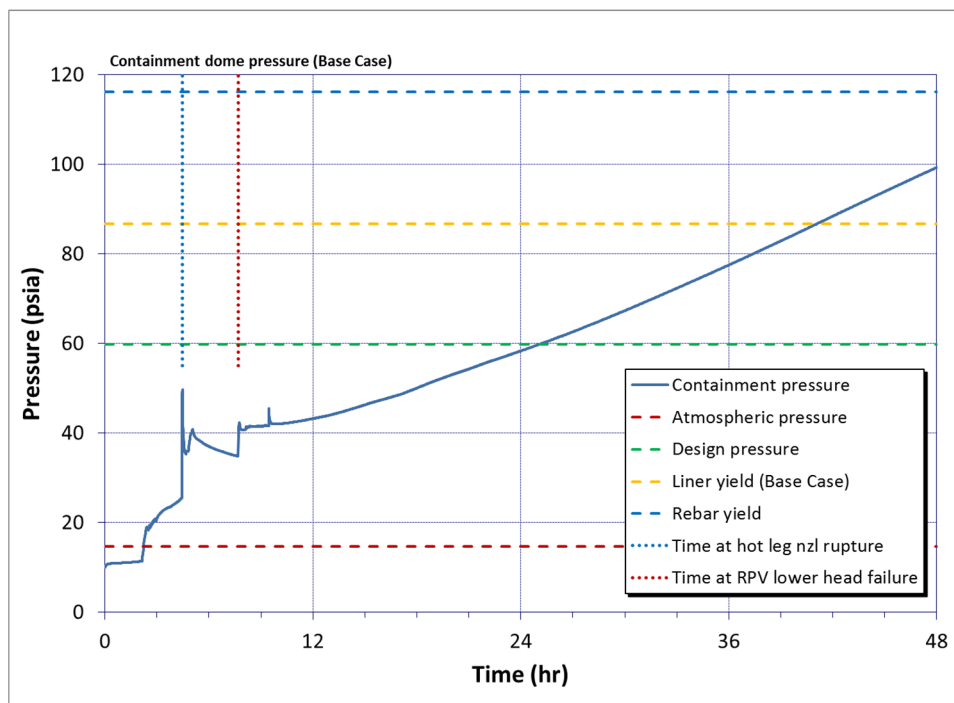
**Figure 5-6 In-Vessel hydrogen production (Base Case)**



**Figure 5-7 Core mass relocated to the reactor cavity (Base Case)**

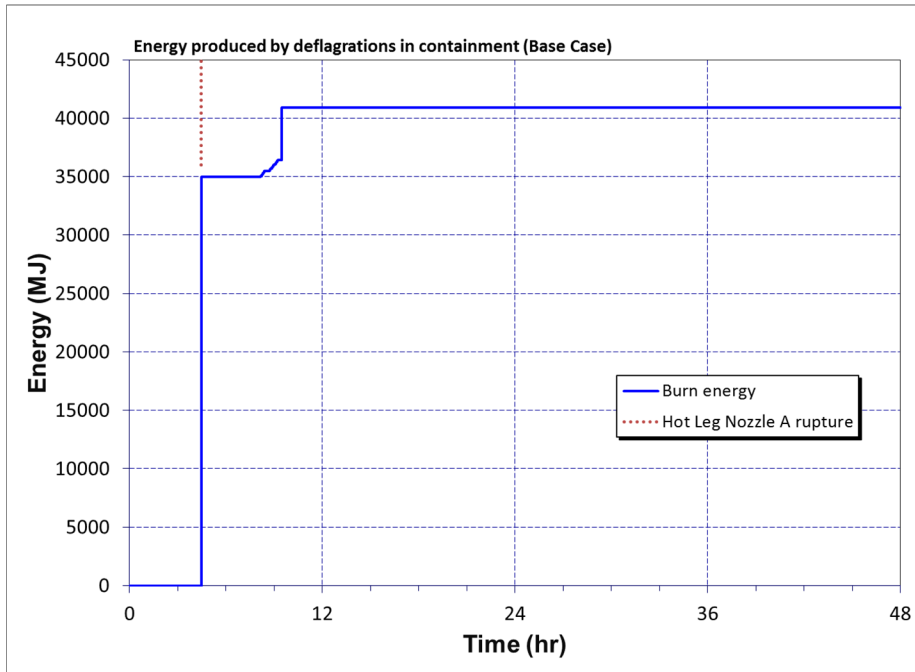
Figure 5-8 presents containment pressure in the base UA unmitigated STSBO calculation. Pressure starts off sub-atmospheric consistent with Surry containment design. Once the SGs dry out, RCS inventory swells and RCS pressure increases causing the lowest set-point SV on the pressurizer to vent the system to the PRT. Once the energy absorbing capacity of the PRT

is reached, the rupture disk on the tank breaks at 2 hours 9 minutes. Containment pressure jumps in response and then rises steadily as the pressurizer SV, without the PRT intervening, relieves directly to containment. Pressure jumps again when the hot leg nozzle on Loop A ruptures, immediately and fully venting the RCS primary system to containment and initiating a hydrogen deflagration within lower containment. Energy and mass additions to containment then abate and containment pressure trends down as core damage proceeds. Pressure jumps one more time when the lower head of the reactor pressure vessel fails dropping core debris into the water pool standing on the reactor cavity floor. The pool vaporizes quickly. From this point on, containment pressure trends continually higher as heat from fission product decay in the core debris on the containment floor raises the temperature of the whole of containment. Non-condensable gas generation from core-concrete interaction contributes slightly to the pressurization. The design pressure of containment is exceeded as is the pressure associated with yielding of the containment steel liner. The pressure associated with the yielding of rebar in the bounding containment concrete is not reached within the 48 hour extent of the MELCOR calculation. Interesting with respect to the pressurization of containment is that the largest contribution is from continuous heating of original RCS coolant recast as steam in the containment atmosphere (rather than to the addition of non-condensable gasses to the atmosphere from core-concrete interaction as was anticipated). This contribution is described in greater detail in the discussion of the concrete sensitivities in Section 6.1.7.



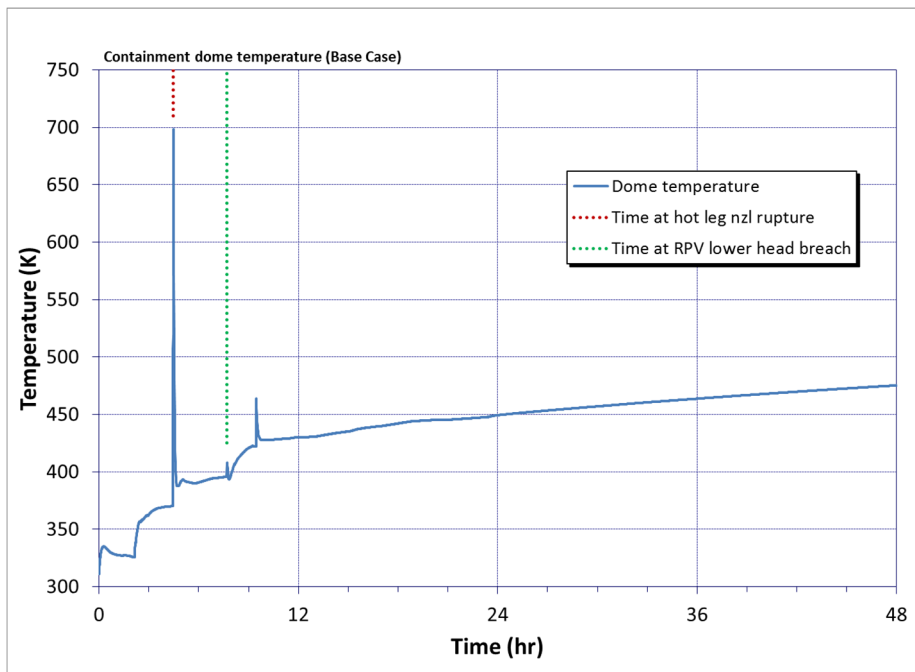
**Figure 5-8 Containment pressure (Base Case)**

The energy produced by deflagrations in containment is illustrated in Figure 5-9, which shows there are two main deflagrations, one at hot leg nozzle creep, and a second about an hour after lower head failure. There are also very minor deflagrations right at lower head failure.



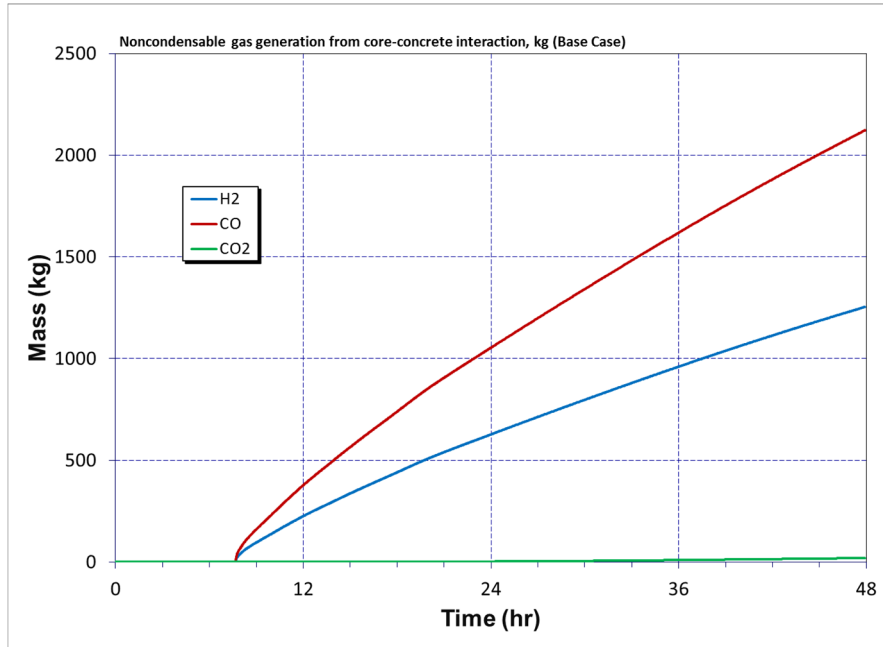
**Figure 5-9 Energy produced by deflagrations in containment (Base Case)**

The influence of deflagrations can be seen as spikes in the plot of containment atmospheric temperature in Figure 5-10.

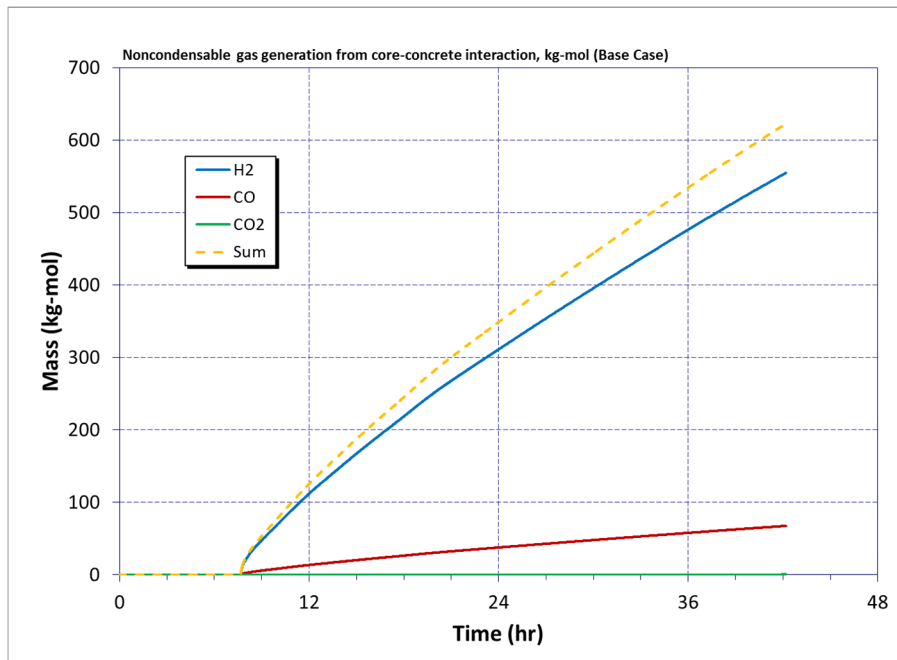


**Figure 5-10 Containment dome temperature (Base Case)**

Non-condensable gas generation from core-concrete interaction in units of kg and kg-mol are shown in Figure 5-11 and Figure 5-12, respectively. These effects are described in greater detail in the discussion of the concrete sensitivities in Section 6.1.7.

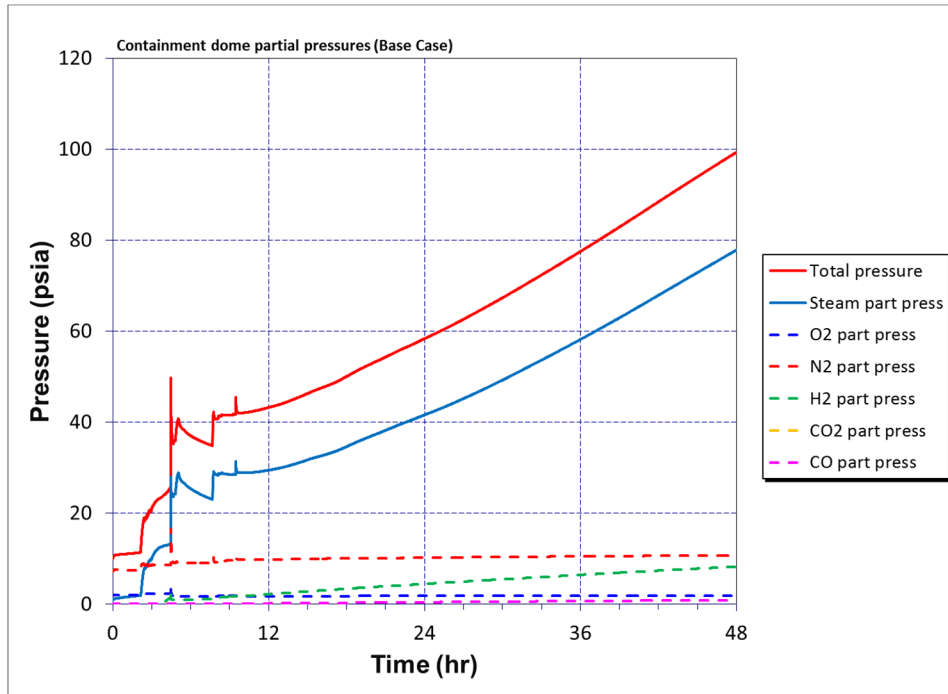


**Figure 5-11 Noncondensable gas generation from core-concrete interaction, kg (Base Case)**



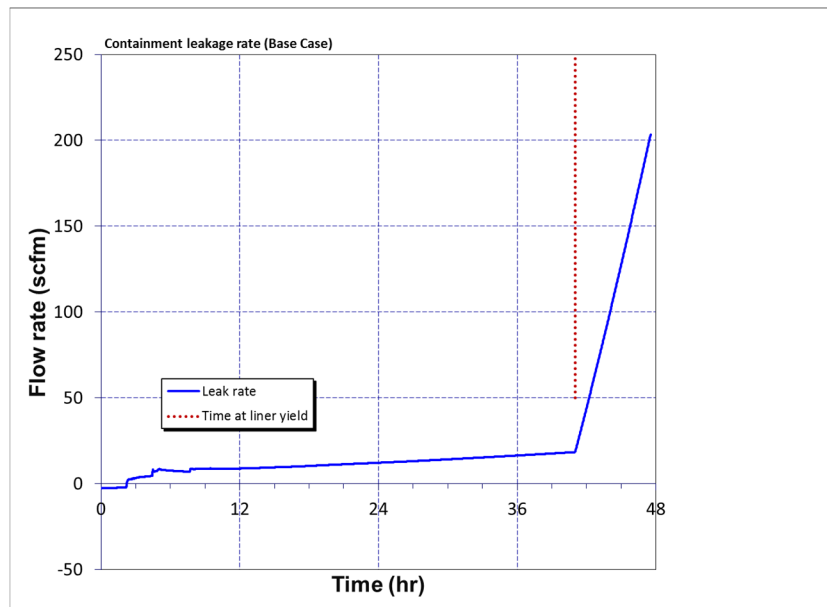
**Figure 5-12 Noncondensable gas generation from core-concrete interaction, kg-mol (Base Case)**

Figure 5-13 shows the partial pressures of containment atmosphere constituents, and clearly illustrates that pressurization of steam by decay heat is the primary driver for overall containment pressurization.



**Figure 5-13 Containment dome partial pressures (Base Case)**

The rate of gas leakage from containment to the environment is presented in Figure 5-14 where the increased leakage developed at liner yield is evident.



**Figure 5-14 Containment leakage rate (Base Case)**

Figure 5-15 shows indications of the largest creep damage accumulation in the tubes of SGs A, B and C. Accumulation approaching the value associated with rupture (unity) is not seen, which indicates there is no SGTR nor any approach to an SGTR occurring in the base UA STSBO calculation. This is partially due to the best estimate value for tube thickness and partially due to the early depressurization of the primary side, reducing the pressure differential across the tubes.

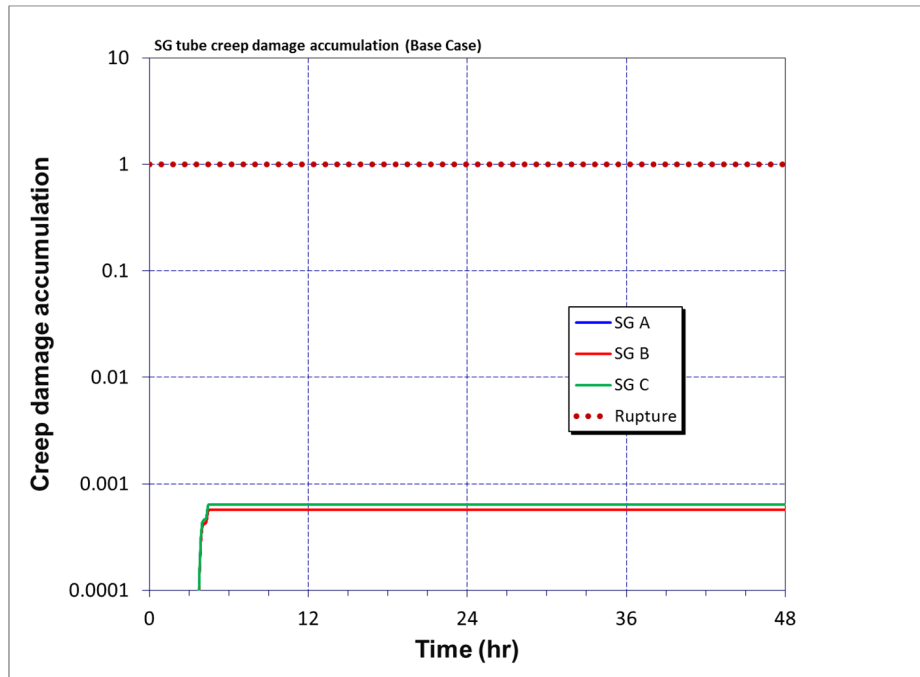


**Figure 5-15 SG tube creep damage accumulation (Base Case)**

Figure 5-16 and Figure 5-17 show the fractional distribution throughout the RCS, of iodine as elemental gaseous iodine and as cesium-iodide aerosol combined. The early decrease of iodine on the primary side is a combination of hot leg creep, releasing airborne iodine to containment, and RPV dry-out, which releases iodine captured by the primary coolant. The sharp increase in iodine resident in containment coincident with a sharp decrease resident in the RCS is attributable to the PRT drying out and releasing much of its inventory of radionuclides to the containment atmosphere. The PRT is considered part of the RCS in the MELCOR model. There is also some late revaporization of iodine deposited in the RCS, evidenced by the gradual increase of 'containment total' following PRT dryout. However, very little iodine release to the environment, 0.073 percent of the inventory at scram, is indicated as of 48 hours.

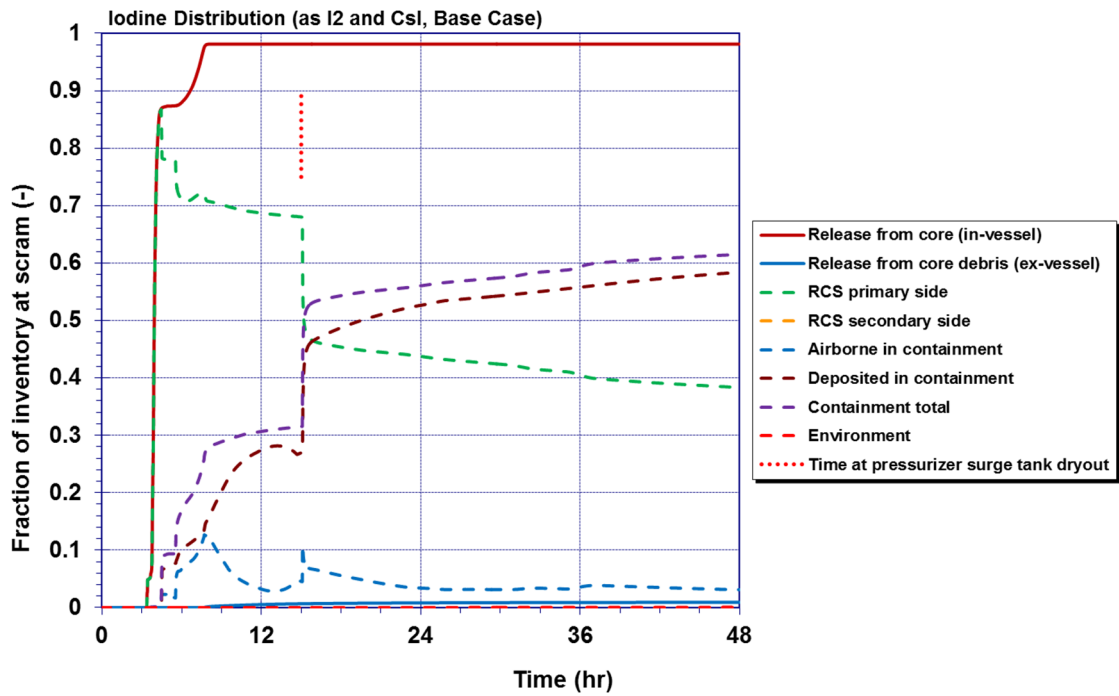


Figure 5-16 Iodine distribution (as I2 and CsI, Base Case)

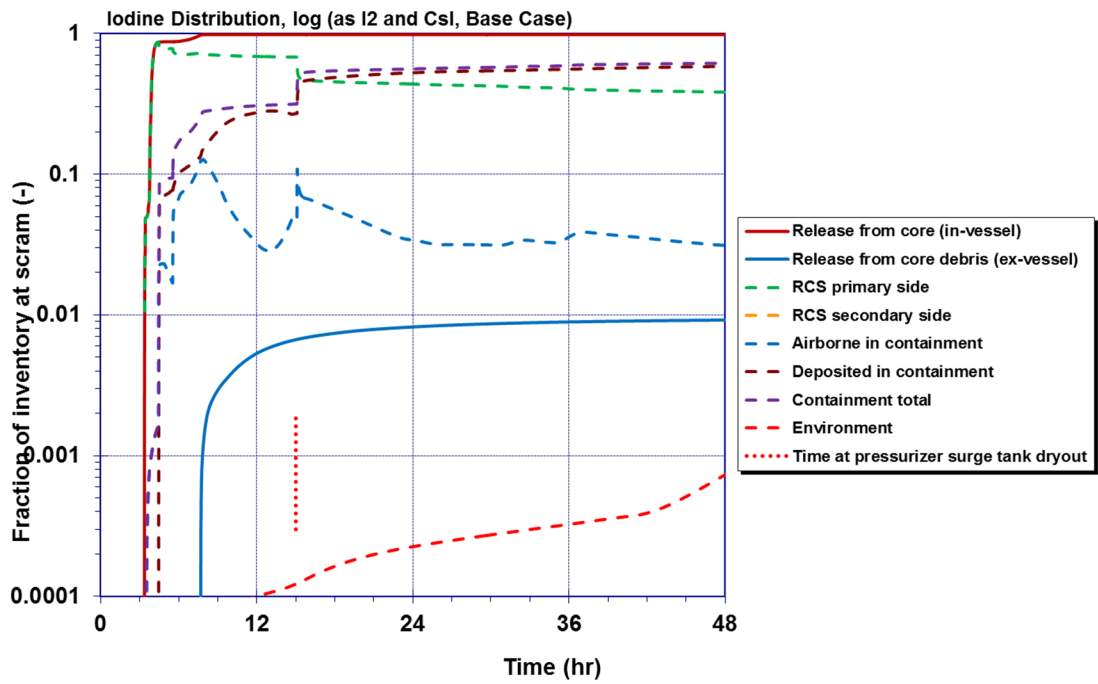


Figure 5-17 Iodine distribution (log, as I2 and CsI, Base Case)

Figure 5-18 and Figure 5-19 show the same information as Figure 5-16 and Figure 5-17 but for cesium rather than iodine. The cesium is as combined aerosols of cesium hydroxide, cesium iodide and cesium molybdate. The same general trends as observed in the iodine figures are also seen for cesium. As in the case of iodine, very little Cs release to the environment, 0.029 percent of the inventory at scram, is indicated as of 48 hours. Chemisorption of Cs from CsOH binds 7.69 percent of the Cs inventory at scram permanently to stainless steel structures within the RPV, not evidenced in the figures.

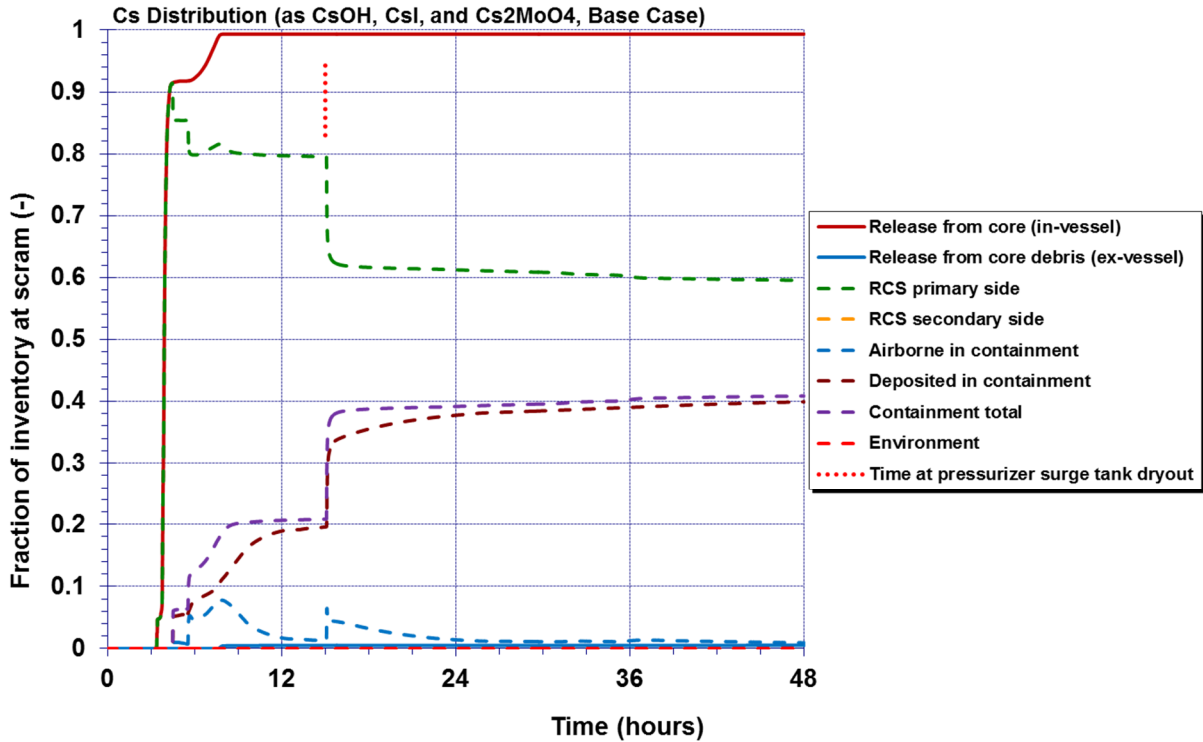
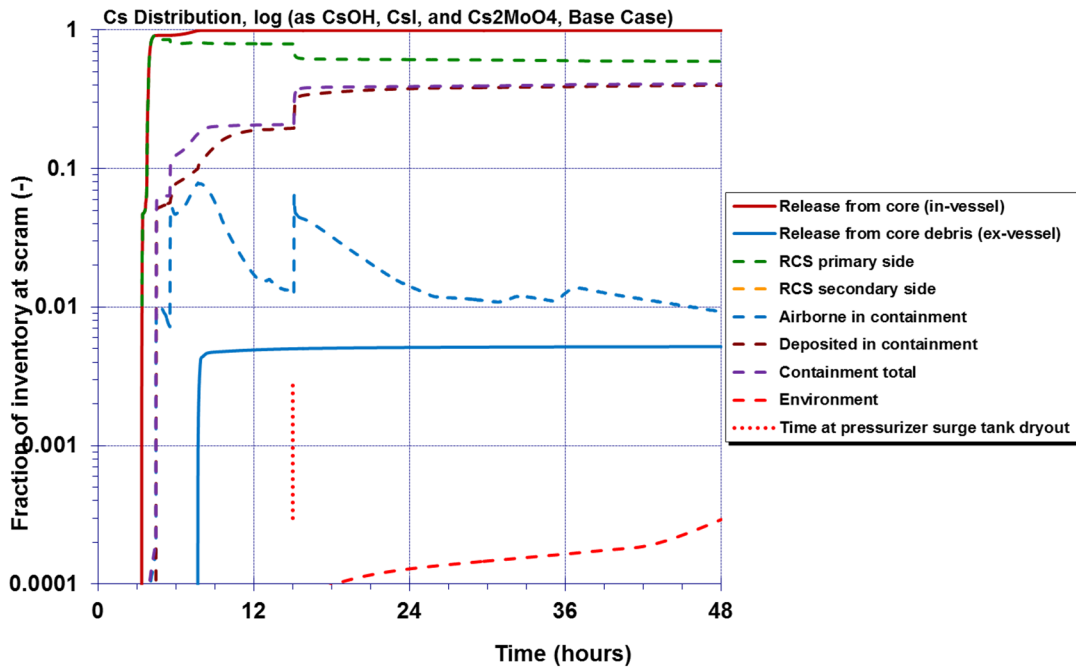
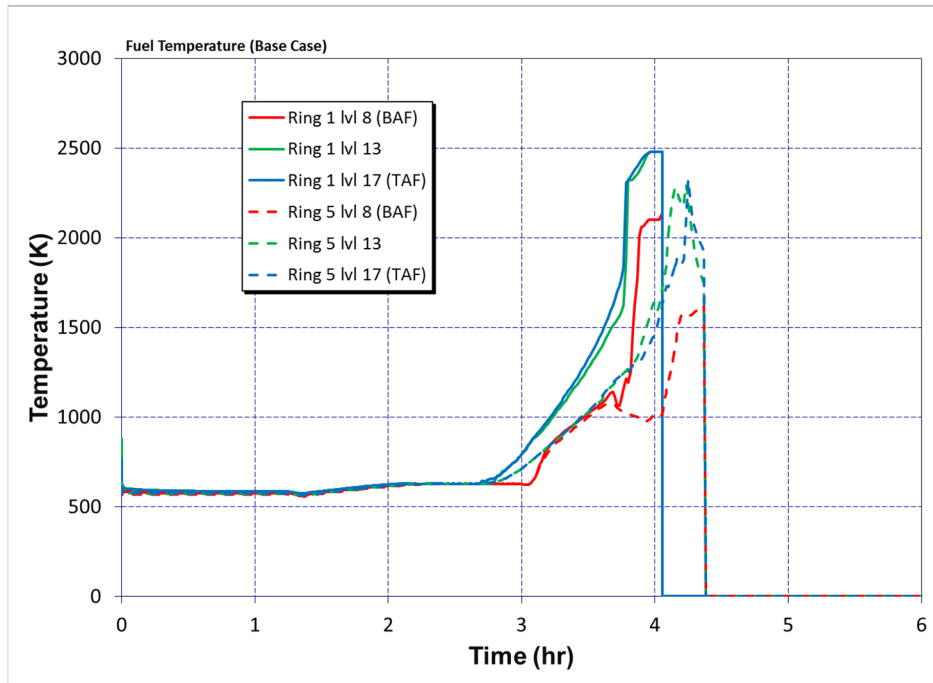


Figure 5-18 Cs distribution (as CsOH, CsI, and Cs<sub>2</sub>MoO<sub>4</sub>, Base Case)



**Figure 5-19 Cs distribution (log, as CsOH, CsI, and Cs<sub>2</sub>MoO<sub>4</sub>, Base Case)**

Central and peripheral fuel temperatures high and low in the core are presented in Figure 5-20. These temperature trends show fuel relocation events and also show how within MELCOR radial and axial differences lead to different heating rates and relocation times.



**Figure 5-20 Fuel temperature (Base Case)**

Water depth on the floor of the reactor cavity and ablation of cavity concrete are shown in Figure 5-21. Water in the cavity is very rapidly boiled off following lower head failure. Ablation continues throughout the 48 hours of the modeled transient.

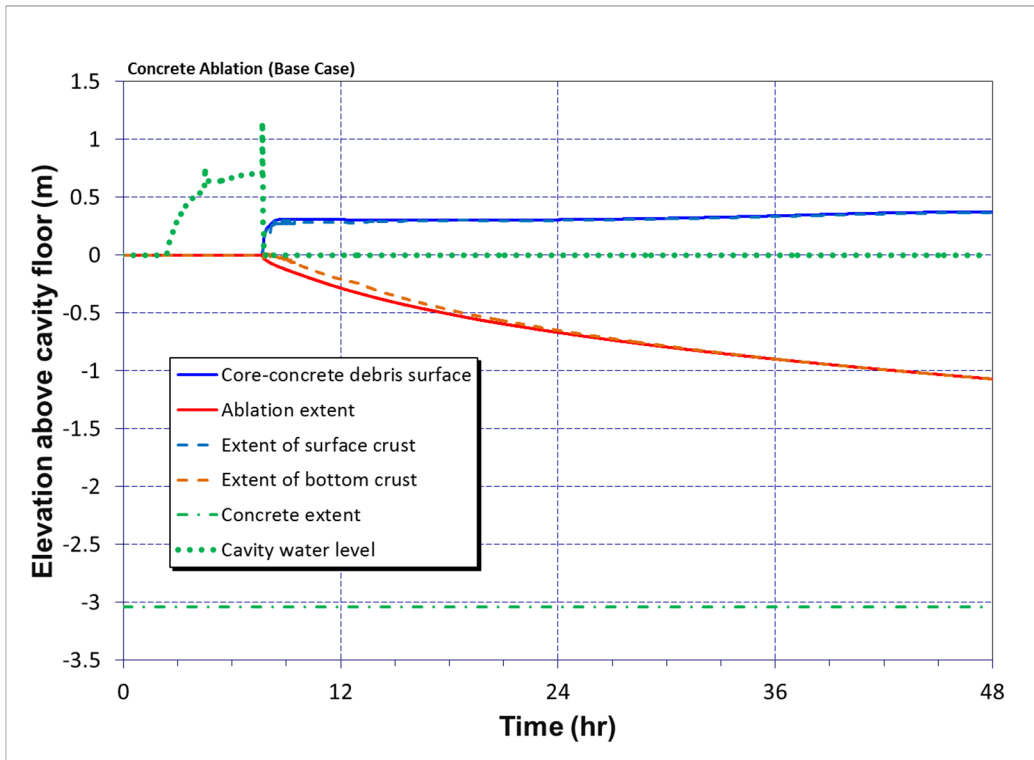


Figure 5-21 Concrete ablation and cavity water depth (Base Case)



## **6. SOARCA MODEL PARAMETER UNCERTAINTY AND SENSITIVITY ANALYSES**

### **6.1 Source Term Parameter Uncertainty Analysis**

There were 24 MELCOR parameters that were selected for sampling in the UA. Sandia used a high performance computing cluster to execute a Monte Carlo simulation with 1200 MELCOR runs, of which 1003 were successful. Each run is identified with a unique realization number. In the 1003 successful realizations, the following results were observed within the 48 hour run time:

- An SGTR occurred in 104 realizations; this number may reflect a slight conservatism considering the assumption that the most damaged tube is in the hottest region;
- A hot leg nozzle rupture occurred in 930 realizations;
- In every realization that an SGTR occurred, a hot leg nozzle rupture also occurred;
- A failure of one or more RCS secondary side safety valves (SG safety valves) to close occurred in 954 realizations ;
- An SV on the RCS primary side (on the pressurizer) failed to close in 686 realizations ;
- Individual safety valves on the RCS primary side failed to open in 10 realizations but as a system all 3 sequential valves never failed to open simultaneously;
- The steel containment liner yielded and tore in 742 realizations;
- Containment concrete rebar yielded (and the concrete fractured) in 72 realizations; and
- In 162 realizations, the noble gas release to the environment had not accrued to 1 percent of the total inventory by 48 hours.

Regression analyses were then performed on the full set of realizations, a set with only SGTRs, and a set without SGTRs (e.g., the non-SGTR set) as identified in Table 6-1. For the full set and the non-SGTR set, regression analyses were performed for BOC, MOC, and EOC. These separate analyses were performed to understand the extent to which the SGTRs dominate the results and the effects of time at cycle. The results were then reviewed against the figures of merit established for the analysis, including iodine and cesium release to the environment, hydrogen production, and release timing.

**Table 6-1 MELCOR regression analyses completed.**

Output Parameter Data set used based on occurrence of SGTR												
Cycle	Cs_frac			I_frac			H2_Prod			Release Timing		
	SGTR	Non-SGTR	Both	SGTR	Non-SGTR	Both	SGTR	Non-SGTR	Both	SGTR	Non-SGTR	Both
All	✓	✓	✓	✓	✓	✓	✓	✓	✓		✓	✓
BOC		✓	✓		✓	✓		✓	✓			
MOC		✓	✓		✓	✓		✓	✓			
EOC		✓	✓		✓	✓		✓	✓			

Regression tables provide summaries of the analysis. The first four major columns in the tables are labeled with the regression technique used to create the results. The last two columns contain average values of the main (individual, independent) contribution of the parameter on the result metric and the conjoint influence<sup>13</sup> of the parameter on the result metric. These are calculated as arithmetic averages of the overall contributions from the four regression techniques as described in Section 3. Values of main contribution greater than 0.02 and conjoint contributions greater than 0.1 are considered significant and are highlighted. The parameters in the first column of the tables are ordered by the values in the column labeled Main Contribution, thus the most important parameters appear in rank order at the top of the table.

For some of the parameters, it was more desirable to include a post-calculated parameter in the regression calculations that more meaningfully capture the translation of the sampled input to reactor system behavior. Several parameters were post-calculated (see Table 6-2) for use in regressions, based on both the sampled input and actual behavior, and also to attempt complete coverage of the uncertainty space. Also included are those parameters for which the input is slightly different than the description in Chapter 4.

**Table 6-2 Post-calculated regression parameters.**

#	Parameter Name	Description	Notes
1	SVOAFRAC	Overall open fraction of the 3 primary SV system at 48 hours	Value is 0 if there are no SV failure, 1 if there is liquid failure, the sampled open fraction if only the first SV fails partially open, and the sum of the sampled open fractions if multiple SVs fail partially open
2	SV_STATUS	Failure mode of the 3 primary SV system	Similar to open fraction but only looking at failure mode, a value of 0 is no SV failure, 1 is cycling failure partially open

<sup>13</sup> Conjoint influence is the influence of two or more input parameters acting together, which may have synergistic effects that would not be uncovered by studying the influence of each parameter separately and individually.

#	Parameter Name	Description	Notes
3	SV_NBCYC	Number of cycles experienced by the 3 primary SV system	If the lowest setpoint SV fails, the value is the sampled number of cycles to failure, if multiple SVs fail, the value is the sum of the cycles experienced by each value, if no SV failure occurs, the value is the sampled value for cycles to failure, which is a simplification
4	CYCLE	Integral baseline decay energy at 48 hours, representing time at cycle	The calculation of baseline energy separates out the decay heat aspect of time at cycle from the change in radionuclide inventory portion
5	DEV_DEC_HEAT	Percent change in actual integrated 48 hr decay energy for each realization from the baseline energy for the appropriate time at cycle	Without using a percent change, the integrated 48 hr energy for each realization just mirror the CYCLE parameter. This calculation captures the importance for small deviations in decay heat from the baseline curves
6	TUBTHICK	SG tube outer diameter (m) representing tube thickness	The parameter description in Chapter 4 is written as tube thickness, but the actual necessary MELCOR input is outer diameter, so a conversion is performed
7	DLEAK	Flow path length (m) yielding desired design leakage	Chapter 4 described the parameter as sampling on %vol/day leakage but in practicality 10 discrete flow path lengths were defined that yield the desired leakage. These lengths are inputs to regression calculations

### 6.1.1 Iodine Release Fraction to Environment

Iodine is created by fission of uranium within the reactor fuel. It is a volatile fission product, and can be released as an elemental gas, or bound together with cesium as Csl, an aerosol. Because of its volatility, a portion of iodine transports to the fuel-cladding gap, leading to early releases when gap failure occurs. Iodine has a relatively short half-life (i.e. high specific activity) compared to other fission products, particularly I-131 with a half-life of 8 days, and can dominate early health effects, if releases occur before or during evacuation.

Typical of severe accident analyses, iodine release from fuel is near 100 percent of its total inventory. The reason environmental releases are much lower is due to hold-up and deposition in both the primary system and in containment. However, in MELCOR, iodine assigned to the gaseous phase is not deposited and remains airborne, available for release to the environment. Additionally, there can be events in which containment is bypassed and in those cases environmental releases are typically much higher.

Iodine release is an indicator for both timing and magnitude of fuel damage. Timing of fuel relocation events, such as failure of support structures and lower head failure, can also be indicated by iodine releases. Additionally, environmental release fraction magnitudes provide evidence on the condition of containment and strongly influence early health effects.

### 6.1.1.1 Comparison to SOARCA and Horsetail Plot

The environmental release fraction of all iodine (percentage of initial iodine inventory) at 48 hours is a primary figure of merit for the analysis. Figure 6-1 shows the time dependent release fractions for the first 300 successful realizations, as well as the calculated mean, median, and 5<sup>th</sup> and 95<sup>th</sup> percentiles of all realizations. There is a clear bifurcation in the results, with the higher release fractions representing SGTR realizations, and the remainder of the realizations having much lower releases. The non-SGTR realizations are all below 0.01 with the majority even below 0.001. At 48 hours, the results are well distributed, with no clear splits except the SGTRs. However, some of the realizations are increasing at 48 hours, while some remain relatively constant.

There is a wide spread between the calculated mean, median, and 95<sup>th</sup> percentile curves. The 95<sup>th</sup> percentile falls in the SGTR realizations, the median in the non-SGTR realizations, while the mean is in between where no actual realizations exist. There is also a significant time difference between the mean and median, with the median releasing about two hours later. This is due to how the mean and median are calculated. Because the SGTR releases are about up to two orders of magnitude higher than the other runs, they disproportionately influence the mean, which is not representative of any specific realization. Meanwhile, the median takes the middle realization at each time, so it is representative of a non-SGTR at all times although not necessarily the same realization at all times. Thus, the timing difference between the median and mean is indicative of the timing difference in releases from SGTRs and non-SGTRs. The calculated 5<sup>th</sup> percentile curve has an associated initial release time that is much later than the calculated median curve, and the 5<sup>th</sup> percentile remains under 0.01 percent at 48 hours.

All four calculated curves are relatively steady by 20 hours, but the median and 5<sup>th</sup> percentile start increasing again shortly after. As described in detail in a subsequent section, late increases in release fractions are primarily due to containment failure, which is driven by heating of steam from decay heat remaining in ex-vessel melt. The 95<sup>th</sup> percentile has no observable late increase as it represents an SGTR, which is a containment bypass event. Therefore, containment liner failure does not have a large impact as all significant releases have already occurred. As the mean is primarily influenced by the SGTR realizations, it also does not exhibit a late increase.

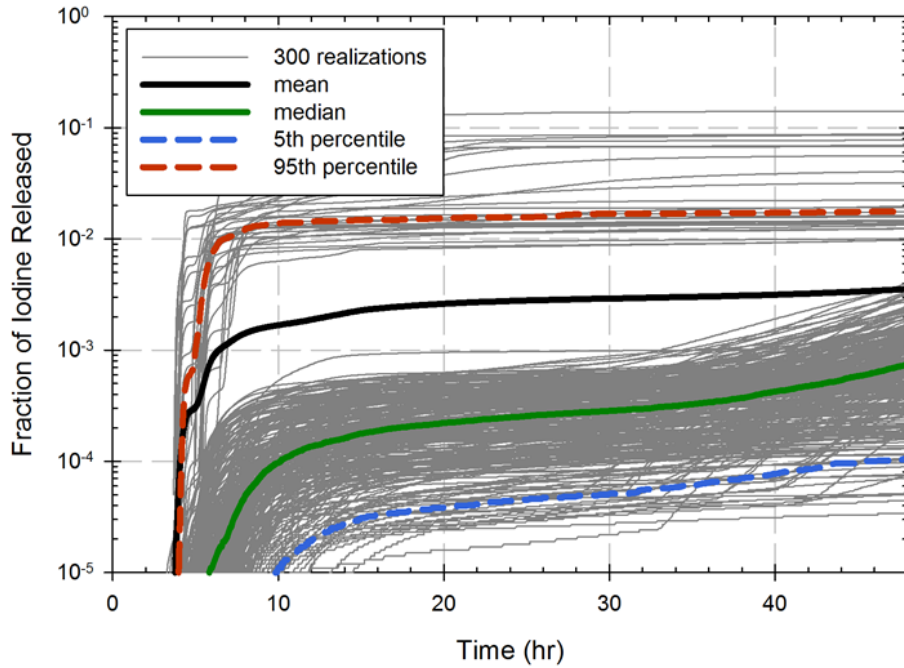


**Figure 6-1 Iodine release fractions over 48 hours with mean, median, 5<sup>th</sup> and 95<sup>th</sup> percentiles**

Figure 6-2 illustrates the cumulative probabilities for the fraction of iodine release for selected time intervals.

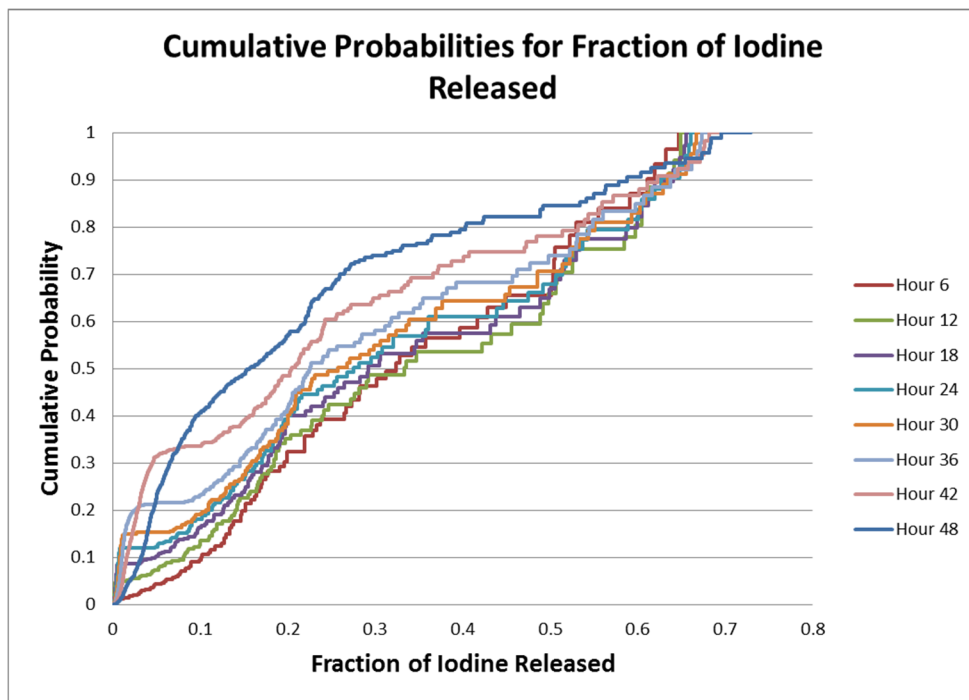


**Figure 6-2 Cumulative probabilities for the fraction of iodine release for selected time intervals**

As shown in Figure 6-3, the environmental release fraction of iodine in the original SOARCA STSBO run is about 0.0065 at 48 hours. This is much higher than the UA median 48 hour release and similar to the mean. The timing of the release is very close to the calculated median. The SOARCA releases are much lower than either the mean or median (and near the 5<sup>th</sup> percentile) until about 26 hours, at which point they rapidly increase above both calculated curves before leveling off after 40 hours.

The two major differences between the original Surry SOARCA [3] model and the new realizations are related to sampling of nominal containment leakage and the containment failure model. The lower limit of leakage sampling was set at the SOARCA value, meaning essentially all new realizations have larger nominal leakage. This increases earlier releases by having slightly larger mass flows to the environment, and it has the secondary effect of partially subduing containment pressure. Because this is a sampled parameter, the effects of leakage are captured in regression results.

The containment failure curve was also modified in this work. Figure 6-4 displays the curve for the original Surry SOARCA [3] run on the left, with the modified UA curve on the right. Both curves use three of the same data points, based on scaled containment testing at Sandia. However, the original SOARCA model removed the liner plate yield point and fit a parabolic function to the remaining three data points, which results in the enhanced failure leakage not initiating until much higher containment pressures. With the liner plate yield point included, and a linear fit between the four points, the Surry UA model starts enhanced leakage much earlier. The effect, combined with other sampled parameters such as time at cycle and nominal leakage, is that in the UA realizations containment pressure remains lower for a longer time period. Although the original SOARCA runs have a higher failure set-point, the failure is more dramatic with greater amounts of revaporization due to simultaneous pressure decrease and temperature increase and larger mass flows resulting in a greater iodine environmental release fraction. The effect of the revised containment failure curve cannot be seen in the regression results, as the change to the basic shape of the containment failure curve that predicts more of a yield-before-break behavior was made to the base input deck.

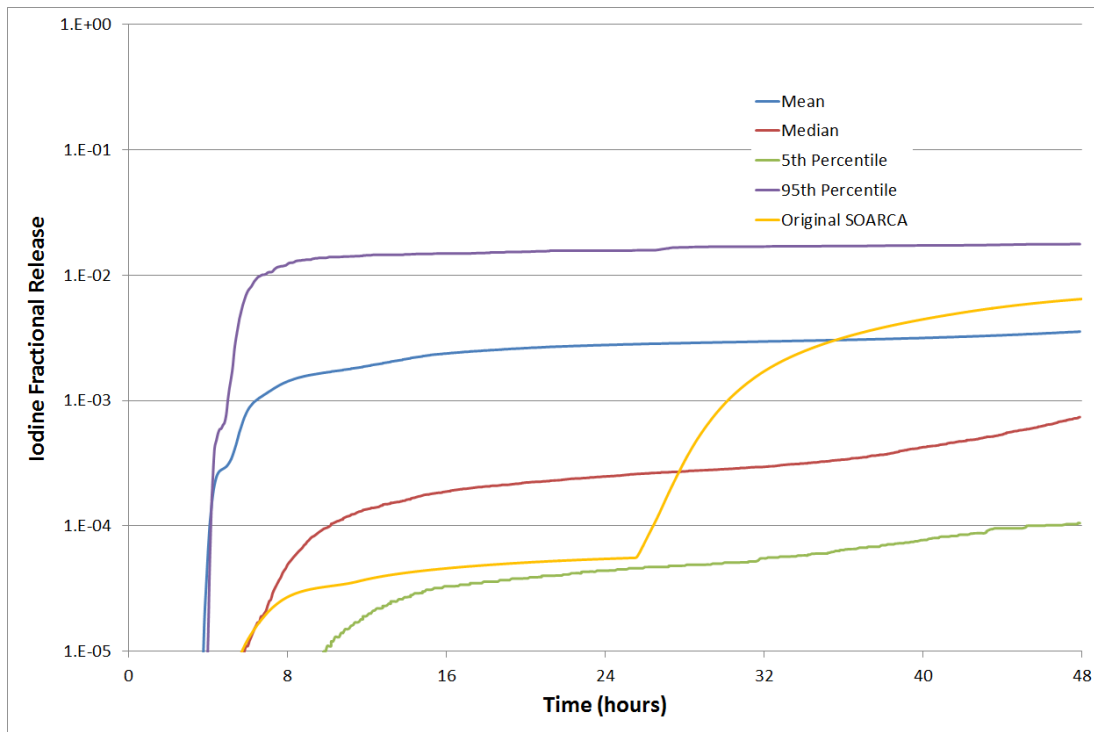


**Figure 6-3 Comparison of iodine release fraction in the original SOARCA STSBO to the calculated values of all successful realizations**

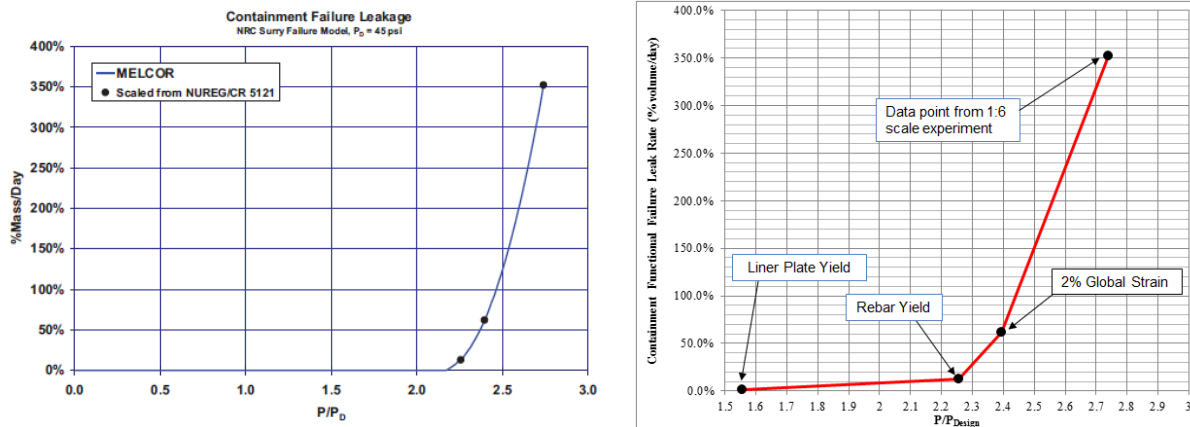


**Figure 6-4 Comparison of containment failure models used for the original SOARCA STSBO and the UA realizations**

**6.1.1.2 Regression Tables and Scatterplots**

Regression analyses were performed with all successful realizations. Three sets were done, one for all realizations, one for just SGTR realizations, and one for non-SGTR realizations. Additional regressions were done for the three times at cycle independently (BOC, MOC, and

EOC). SGTR parameters dominated the regression results for all realizations, and since SGTR results have a unique section elsewhere in this report, Table 6-3 shows the results for just the non-SGTR realizations. In the following section, Key Parameters, each of the top six parameters, as well as other parameters of interest, have a technical rationale as to why they may contribute to uncertainty in iodine release fractions.

The main result is that time at cycle is identified by each technique as explaining half or more of the overall variance for iodine release fractions. It is also identified as having a high conjoint contribution, indicated by the yellow highlighting. After this, the next five parameters stay in essentially the same order with one major exception (containment leakage from rank regression) and explain essentially all the remaining model uncertainty. Each of the methods successfully explains the majority of overall iodine release variability.

Scatterplots were produced for the parameters ranked most important by the arithmetic average of the regression techniques. Such plots are useful for verifying relationships between the parameter input values and iodine release fractions indicated by the regressions. It can also be visually identified when a regression may be fitting to noise. The scatterplots of most interest are displayed in the respective parameter sections.

**Table 6-3 Regression analysis of iodine release fraction for non-SGTR realizations.**

Final R <sup>2</sup>	Rank Regression		Quadratic		Recursive Partitioning		MARS		Main Contr.*	Conjoint Contr. *
	0.77		0.92		0.88		0.82			
Input	R <sup>2</sup> contr.	SRRC	S <sub>i</sub>	T <sub>i</sub>	S <sub>i</sub>	T <sub>i</sub>	S <sub>i</sub>	T <sub>i</sub>		
CYCLE	0.51	0.69	0.39	0.50	0.37	0.60	0.40	0.40	0.380	0.102
CFC	0.04	-0.21	0.09	0.15	0.08	0.25	0.12	0.16	0.074	0.080
DLEAK	0.11	0.32	0.08	0.11	0.04	0.10	0.09	0.09	0.073	0.029
CHEMFORMI2	0.03	0.18	0.06	0.10	0.09	0.29	0.11	0.17	0.063	0.089
DEV_DEC_HEAT	0.03	-0.18	0.06	0.11	0.03	0.16	0.08	0.11	0.043	0.063
PARTSHAPE	0.02	0.15	0.04	0.06	0.02	0.11	0.07	0.11	0.034	0.041
SC1132	0.00	0.07	0.01	0.02	0.00	0.01	0.01	0.03	0.005	0.011
SV_STATUS	0.00	0.09	0.02	0.09	---	---	---	---	0.004	0.023
CONDENS	0.01	-0.07	0.01	0.01	---	---	0.00	0.01	0.004	0.003
SV_NBCYC	---	---	---	---	0.00	0.00	0.01	0.01	0.002	0.000
SRVFAILT	---	---	0.00	0.01	0.00	0.01	0.00	0.00	0.002	0.005
SGTRLOC	0.00	0.05	0.00	0.02	0.00	0.02	---	---	0.002	0.009
RDSTC	0.00	0.04	---	---	0.00	0.01	---	---	0.001	0.001
CHEMFORMCS	---	---	0.00	0.01	---	---	0.00	0.01	0.001	0.005
SG_B_SV_cycl	---	---	---	---	---	---	0.00	0.01	0.001	0.001
TUBETEMP	---	---	0.00	0.01	0.00	0.01	---	---	0.001	0.005
RCPSL	0.00	0.06	---	---	---	---	---	---	0.001	0.000
RDMTC	---	---	---	---	---	---	0.00	0.00	0.000	0.000
TUBTHICK	0.00	0.03	---	---	0.00	0.00	---	---	0.000	0.000
SVOAFRAC	0.00	-0.08	0.00	0.01	0.00	0.02	---	---	0.000	0.009
SC1131	0.00	-0.03	0.00	0.02	---	---	0.00	0.01	0.000	0.009
SV_WTR_CYC	---	---	---	---	0.00	0.01	0.00	0.00	0.000	0.003

\* highlighted if main contribution larger than 0.02 or conjoint contribution larger than 0.1

### 6.1.1.3 Key Parameters for non-SGTR Realizations

#### Time at Cycle (CYCLE)

This parameter determines the burn-up of the core, which in turn affects baseline decay heat and radionuclide inventories. For iodine specifically, this determines timing of fuel heat-up, which in turn causes initial radionuclide releases, and later in the accident progression, the rate of containment pressurization. Additionally, the amount of gaseous iodine is sampled differently based on the time at cycle, with the least at BOC (cycle = 1) and the most at EOC (cycle = 3). Each of the regression techniques lists time at cycle as by far the most important in iodine release fractions. The scatterplot (Figure 6-5) clearly shows the trend of increasing iodine release fraction as time at cycle increases.

The differentiation between BOC and the other two is primarily caused by the difference in base decay heat, which is much lower at BOC. Because the decay heat is so low, containment pressurization occurs slowly and the rebar yield set-point is not reached. When gross containment rebar failure occurs, mass flow rates to the environment are increased, and some deposited aerosols are revaporized, allowing them to be transported out of containment. The effect of containment pressure is described in more detail in a later section.

Between MOC and EOC, the primary difference is the sampling of gaseous iodine, since the base decay heat curves are very close between the two. Gaseous iodine has much higher release fractions since MELCOR does not model adsorption of gaseous iodine on structures. The gaseous iodine remains in the atmosphere, available for containment leakage. This is represented in the scatterplots in that MOC and EOC have a close lower bound, which is when there is little to no gaseous iodine, but EOC has a much higher range since gaseous iodine can be sampled that much higher at EOC.

Time at cycle was also identified as having a high conjoint contribution to uncertainty, meaning there is interplay between time at cycle and at least one other parameter. This is expected since time at cycle drives containment failure (the second parameter) and influences Chemform I2 sampling (fourth). Each of these also has medium conjoint contributions.

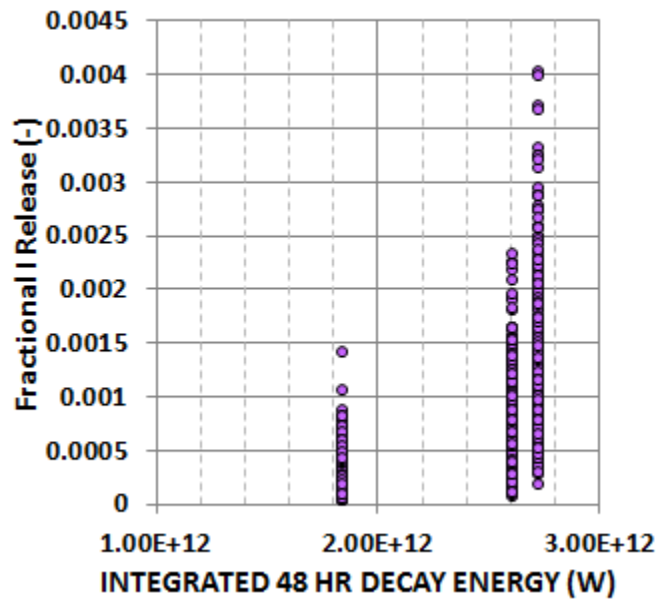


**Figure 6-5 Scatterplot of iodine release fraction versus integrated decay energy representing time at cycle input values**

### Containment Failure (CFC)

This parameter represents the ratio of actual containment pressure to design pressure at which liner plate yield occurs. This is the starting point for the containment failure model, detailed in Section 4.1.4.2. Sampling of this ratio at a lower value results in containment liner failure at lower pressures. This was identified as the second most important parameter by all regression techniques, except rank regression which listed it third. It has some conjoint influence, most likely with time at cycle, since this drives the containment pressurization. SRRC<sup>14</sup> indicated that there is a negative trend, with iodine releases increasing as this parameter decreases. The

<sup>14</sup> Standardized rank regression coefficients (SRRC) display the rank regression coefficients after they have been standardized to take out the unit influence. The rank regression coefficient is an indication of the strength of the influence.

scatterplot, Figure 6-6, does give confirmation; with the highest outliers all being at low sampled input values, and a clear trend, especially around 1.5.

There are two physical rationales for why increased flow out of the containment (which occurs after rupture) increases the iodine release fraction. First and most obvious, any aerosols that remain suspended in the atmosphere, as well as any gaseous iodine, are transported more effectively into the environment with greater flow rates. But also important is that the pressure drop upon rebar failure leakage leads to revaporization of some of the previously deposited iodine aerosols, both in the primary system and on containment structures, making them available for transport to the environment.

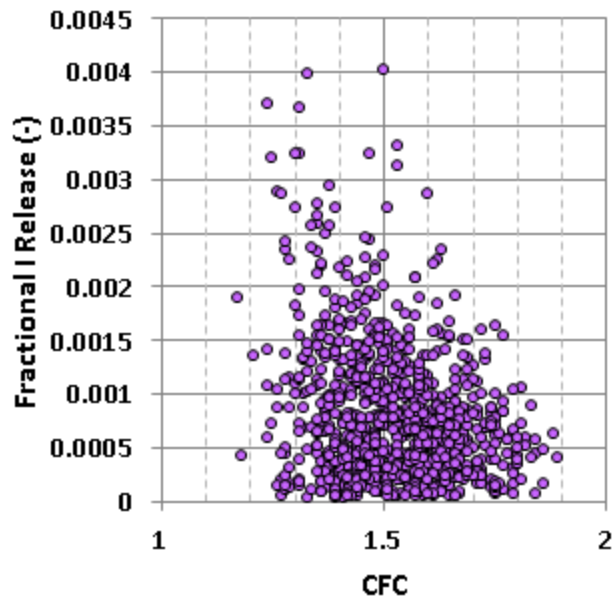


**Figure 6-6 Scatterplot of iodine release fraction versus containment failure input values**

### **Containment Leakage (DLEAK)**

The amount of nominal leakage from containment is sampled. Prior to enhanced leakage due to containment liner yield, this is the only release path for radionuclides to the environment, excluding bypass events like an SGTR. Within MELCOR, it is input as the calculated flow path length which yields the flow resistance needed to give the desired leakage at design pressure. This flow path is effectively a hole in containment and does not represent a tortuous pathway, however simply resizing the hole has negative choked flow impacts. Because the flow path lengths were pre-calculated, the leakage parameter was divided into 10 discrete bins that mirror the intended uniform continuous distribution.

Containment leakage was identified by all of the regression techniques as having a top six contribution to uncertainty, although the rank ranged from second to fourth. The scatterplot, Figure 6-7, shows an interesting result, in that although the range of iodine release fractions is approximately the same at all leakages, there is a firm lower bound that raises with increasing leakage rates. This may be an indicator that regardless of the amount of gaseous iodine, there

is some amount of aerosol that is quickly released before there is time for deposition in containment and this aerosol release is highly dependent on the leakage rate. Thus, it is suspected that the grouping at the lower limit reflect runs with little to no gaseous iodine and possibly no containment rebar yield, while the upward spread shows the sampling on the amount of gaseous iodine.

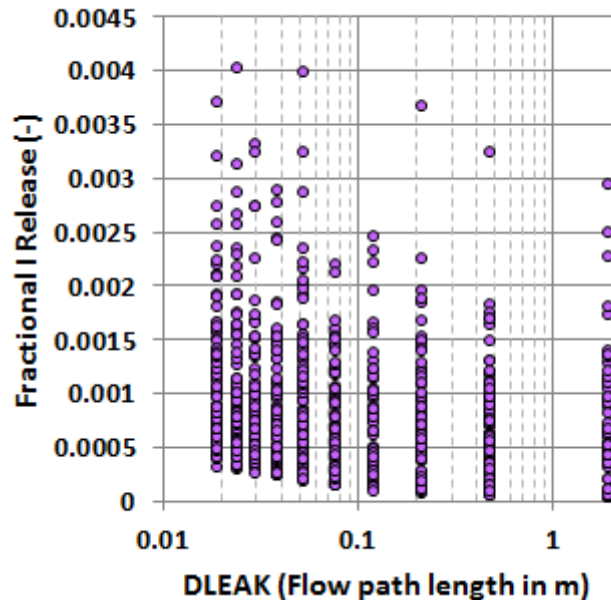


**Figure 6-7 Scatterplot of iodine release fraction versus containment leakage input values**

### **Chemform I2 (CHEMFORMI2)**

This parameter determines the fraction of total iodine that will be gaseous and elemental. The remainder binds with cesium to form CsI, an aerosol. The range of potential values depends on the time at cycle, with BOC having the lowest range for gaseous fraction and EOC the highest. Chemform I2 was identified as anywhere from the second to fourth most important parameter in explaining uncertainty by every regression technique. It also has a relatively large conjoint contribution, which is an expected result, based on the described range dependence on time at cycle sampling, suggesting observed trends may be partially just an additional indicator for time at cycle.

In Figure 6-8, the scatterplot shows a clear linearly increasing trend between the fraction of gaseous iodine and total iodine release fraction. Gaseous iodine releases at greater percentages than CsI since MELCOR does not model gaseous iodine adsorption on walls or surfaces and there is minimal retention in either the primary system or containment. It does, however, become well mixed throughout the entire containment volume, which is why it does not instantaneously release at 100 percent when containment fails, since flow rates are still dependent on volumetric fractions. Regardless, since total iodine release fraction combines the release of gaseous I2 and aerosol CsI, the more gaseous iodine present, the higher the total release will be.

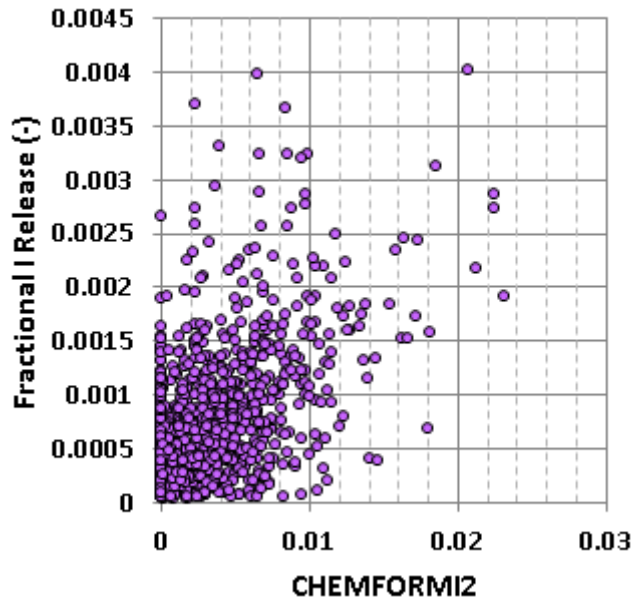


**Figure 6-8 Scatterplot of iodine release fraction versus Chemform I2 input values**  
*(higher gaseous iodine leads to greater release to environment)*

#### Decay Heat (DEV\_DEC\_HEAT)

This parameter applies uncertainty to the base decay curves provided by the time at cycle parameter. For the purposes of the regression analyses, the total decay energy at 48 hours is integrated from each decay heat curve. A percentage difference is then calculated between the individual realization and the base decay energy for the corresponding time at cycle. This percentage difference is the x-axis in the scatterplot in Figure 6-9. Using this difference removes the overlap between MOC and EOC and only looks at the variation introduced by this parameter, divorcing it from time at cycle.

Decay heat uncertainty was listed as the fifth highest contributor to overall iodine uncertainty. SRRC from Rank Regression indicates a negative trend, in that iodine release fractions are higher with a lower decay heat, which is a counterintuitive result, especially considering the time at cycle results. However, looking at the scatterplot it appears to be mostly a fit to noise, and the fact that high outliers are at lower decay heat is probably coincidence.

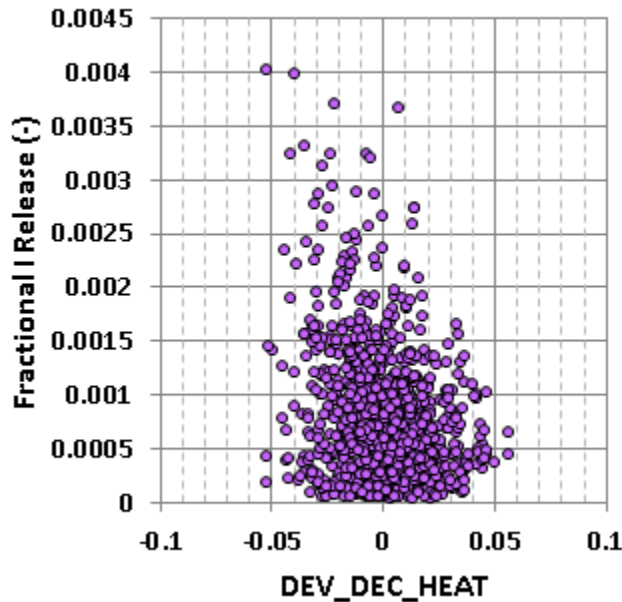


**Figure 6-9 Scatterplot of iodine release fraction versus decay heat deviations**

**Dynamic Shape Factor (PARTSHAPE)**

This parameter accounts for increased drag force for nonspherical aerosol particles. A perfect sphere has a shape factor of 1.0. Although this is identified as a top six parameter by each regression technique, it does not explain a large portion of the uncertainty. This lower importance is visible in the scatterplot (Figure 6-10), which may show a minor trend toward higher release with higher shape factors, but mostly resembles noise.

Within MELCOR, the dynamic shape factor influences the amount of agglomeration (effective particle size), as well as three deposition processes: gravitational settling, Brownian diffusion, and thermophoresis. Sampling a higher value of the dynamic shape factor yields more agglomeration and increased aerodynamic drag and allows aerosols to remain in the atmosphere longer available for release, while also reducing deposition, especially gravitational settling. The majority of iodine is aerosol, so it is an expected result that increasing shape factor increases environmental releases. It was unexpected that this effect would have significantly lower importance than time at cycle, which is the top parameter. This again emphasizes the importance of gaseous iodine.

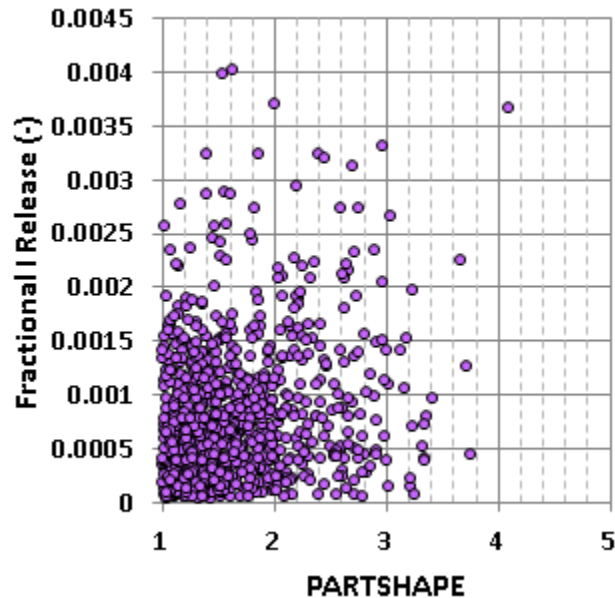


**Figure 6-10 Scatterplot of iodine release fraction versus dynamic shape factor input values**

#### **Other Parameters**

When looking at the regression results for all successful realizations, two parameters completely dominated the results: tube thickness and SV open fraction. Both of these relate to the frequency and severity of SGTRs and have an anticipated conjoint influence. The tube thickness essentially acts as a stress multiplier on the creep rupture equation and since the secondary is always depressurized, it is the primary determinant on whether an SGTR occurs. Primary SV open fraction also impacts the probability of SGTR occurrence, since it partially determines the pressure differential across the tubes. Once there is an SGTR, the open fraction of the secondary SV determines the flow area to environment, with a full open SV leading to the highest environmental releases. SGTR results are described in much more detail in a subsequent section (section 6.1.5), but are mentioned here as well considering their dominance over regression results for all realizations and the fact that those releases are 1 to 2 orders of magnitude larger.

There are no other parameters that were outside the top six parameters that still had a significant contribution to uncertainty in iodine release fractions, nor is there a parameter that was expected to be important for iodine that does not appear.

#### **6.1.1.4 Time at Cycle Independent Results**

Because time at cycle is such a predominant factor differentiating between runs, regressions were run independently for each time at cycle, removing it as a parameter. Results are very different for the BOC regression as opposed to MOC and EOC. First, as described in more detail in the following section, containment pressure never increases enough by 48 hours to have over-pressure failure for BOC realizations. Thus containment failure is not one of the most important parameters and design leakage dominates. Second, the sampling for the amount of

gaseous iodine is very low at BOC which is why the Chemform I2 parameter has relatively lower importance. Finally, since there is no rebar yield and infrequent liner yield, decay heat variation which also influences containment pressurization has lower importance and the dynamic shape factor which influences release whether it is design leakage or containment failure, has higher relative importance. Since a number of parameters have been removed or reduced in importance, SV open fraction raises in importance. This varies the flow rate of iodine in the primary system leaking into containment before hot leg or lower head failure, but supporting information indicates it may also be a fit to noise. No other parameter has an independent contribution to uncertainty for BOC realizations, and those with large conjoint contribution are due to an error in the Quadratic regression technique, in which occasionally the technique identifies no parameters with independent influence but many with large conjoint influence. These results are ignored. However, even considering all these differences, uncertainty is still dominated by nominal containment leakage and the dynamic shape factor.

At MOC and EOC, there is little variation besides the removal of the time at cycle parameter. The top 6 parameters for all realizations, minus time at cycle, remain as the top contributors to iodine uncertainty in approximately the same order, with a few exceptions. Chemform I2 has higher importance at EOC than MOC, since the sampling range is much larger at EOC. Dynamic shape factor is also slightly more important for MOC, since not all MOC realizations reach containment rebar yield, but deposition is important regardless. Design leakage is less of a contributor for EOC since almost all these realizations reach containment liner yield, with some reaching rebar yield, which greatly increases releases. Similar to BOC, there are a couple parameters in the EOC result with large conjoint influence, but again they are due to an error with the Quadratic regression technique. There were no unexpected results in the regression analyses at MOC and EOC, but they do emphasize the difference at BOC.

#### **6.1.1.5 Timing and Other Effects**

As observed in Figure 6-1, there are no obvious timing bifurcations for the onset of iodine release which are spread about evenly from 4 to 10 hours. Almost all of the releases are steady between about 15 and 30 hours. After this point, the majority of releases increase again, although a number, particularly SGTR realizations, remain steady. This is the only clear split observed from the horsetail results, aside from the SGTR realizations which have releases that are 1 to 2 orders of magnitude higher.

In addition to the key figures of merit, horsetail plots were also produced for primary pressure and containment pressure. Figure 6-11 shows the horsetail for containment pressure, with an inset with a comparison to the original SOARCA pressure. The results show a clear bifurcation, starting at about 5 hours. Analysis of select realizations showed that the upper split represents all MOC and EOC realizations, while the lower split is made up of BOC realizations. The key difference is decay heat. The initial pressure increases in containment are caused by release of steam from the primary system, which start boiling earlier at MOC and EOC. Late containment pressurization is driven by direct heating of the steam already in containment by the decay heat remaining in the fuel after it has been discharged through the lower head of the RPV into containment.

The combination of these two effects means that at 48 hours, the highest BOC containment pressure is only 70 psia in any realizations. In the original SOARCA run, containment rebar failure leading to enhanced leakage started at about 120 psia. Although the liner yield failure point is sampled, it never reaches 70 psia. Thus, while most of the MOC and EOC realizations experience liner yield and some experience rebar failure accompanied by some revaporization

of deposited aerosols at BOC these are never reached at 48 hours and all releases to environment are through nominal leakage. If the runs were extended to 72 or 96 hours, it is expected that all realizations would have increased release fractions and the majority of BOC realizations would reach containment liner yield. This finding emphasizes the importance of controlling containment pressure in a real accident and suggests that late addition of water may have an adverse effect by creating an additional steam source and pressurizing containment.

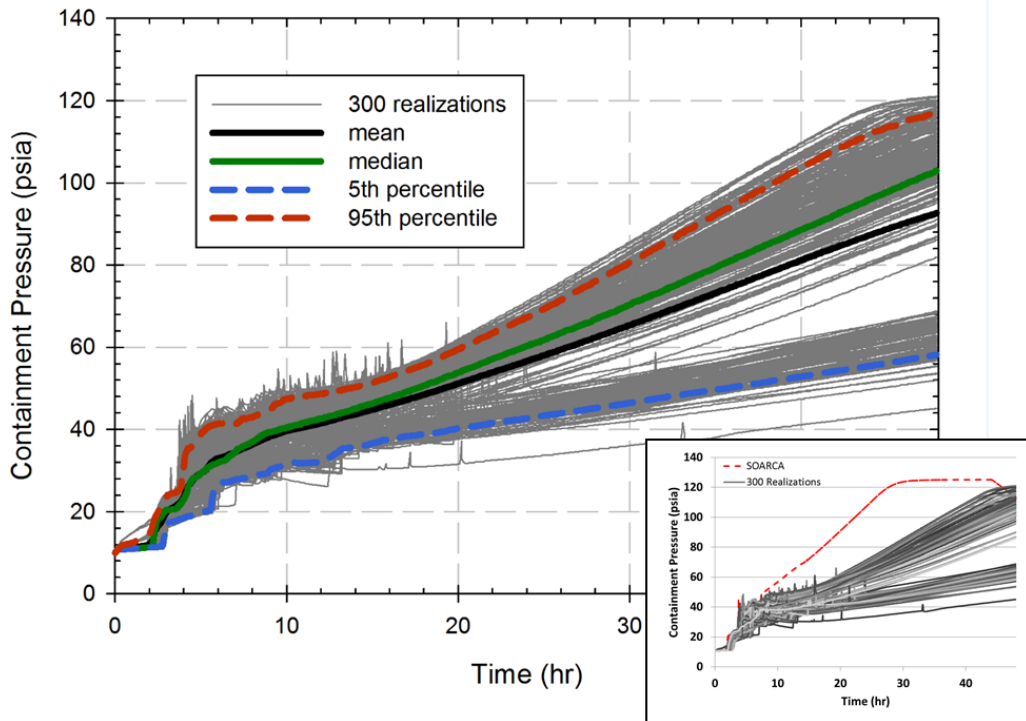


**Figure 6-11 Containment pressure over 48 hours with mean, median, 5<sup>th</sup> and 95<sup>th</sup> percentiles, and the original SOARCA result**

#### 6.1.1.6 Iodine Release Fraction to Environment – Conclusions

Iodine environmental release fractions are significantly lower than the original SOARCA run, primarily caused by slower containment pressurization, driven by multiple parameters including time at cycle and nominal containment leakage, and a modification to the containment failure model. There is a large split between SGTR and non-SGTR cases, in that SGTRs have one to two orders of magnitude higher release fractions. For non-SGTRs (90% of realizations), the spread of release fractions, excluding low outliers, is about one order of magnitude. The most important parameter for the non-SGTR realizations is time at cycle, which both influences the containment pressurization and the amount of gaseous iodine. Chemform I2 also influences the amount of gaseous iodine, which releases in higher amounts than aerosolized iodine. As expected, aerosol shape factor is important, as are parameters that determine flow rates to environment: leakage and especially containment failure. Releases increase with containment liner yield and more so at rebar failure where some revaporization can occur, but many realizations do not reach failure in 48 hours (including all BOC realizations), so those releases level out and nominal leakage is the top parameter. If the runs went out to 72 or 96 hours, it is expected that all or almost all would have increased iodine release fractions. Tube thickness

and SV open fraction determine whether a SGTR occurs. For SGTR realizations, the primary factor of importance on release magnitude is the secondary SV open fraction, which determines the flow area to the environment. The timing of pressurizer relief tank dry-out was found in single realization analysis to be important to release fraction magnitudes because all aerosols retained in the pool are instantly revaporized upon dry-out, but since none of the parameters are a good surrogate for dry-out time, it does not appear in the regression results presented in this section.

### **6.1.2 Cesium Release Fraction to Environment**

Radioisotopes of cesium are created by fission of uranium. Cesium is volatile but readily binds with other elements to form aerosols. Specifically, it is known to bind with iodine as CsI, molybdenum as  $Cs_2MoO_4$ , and water as CsOH. Because of its volatility, a portion of cesium transports to the fuel-cladding gap, leading to early releases to the RCP upon the occurrence of gap failure. Cesium has a relatively long half-life (approximately 30 years for Cs-137, 2 years for Cs-134) compared to other high yield fission products and dominates late health effects. Typical of severe accident analyses, cesium release from fuel is near 100 percent of its total inventory. The reason most environmental releases are low in this UA is due to hold-up and deposition in the primary system and in containment. For bypass scenarios such as the SGTR realizations, environmental releases are typically much higher.

Cesium release is an indicator for both timing and magnitude of fuel damage. Timing of fuel relocation events, such as failure of support plates and lower head failure, can be indicated by studying cesium releases along with other reactor conditions. Additionally, environmental release fraction magnitudes provide evidence on the condition of containment and strongly influence late health effects.

There is an expected correlation between cesium and iodine environmental releases, since a portion of cesium bonds with iodine. Figure 6-12 shows the release fractions for each, sorted by realization. There is a very strong linear correlation shown. This is partially due to the bonding as CsI, but since only a portion of cesium goes into CsI, it also generally indicates that parameters with high importance to iodine releases would also be expected to have importance to cesium releases.

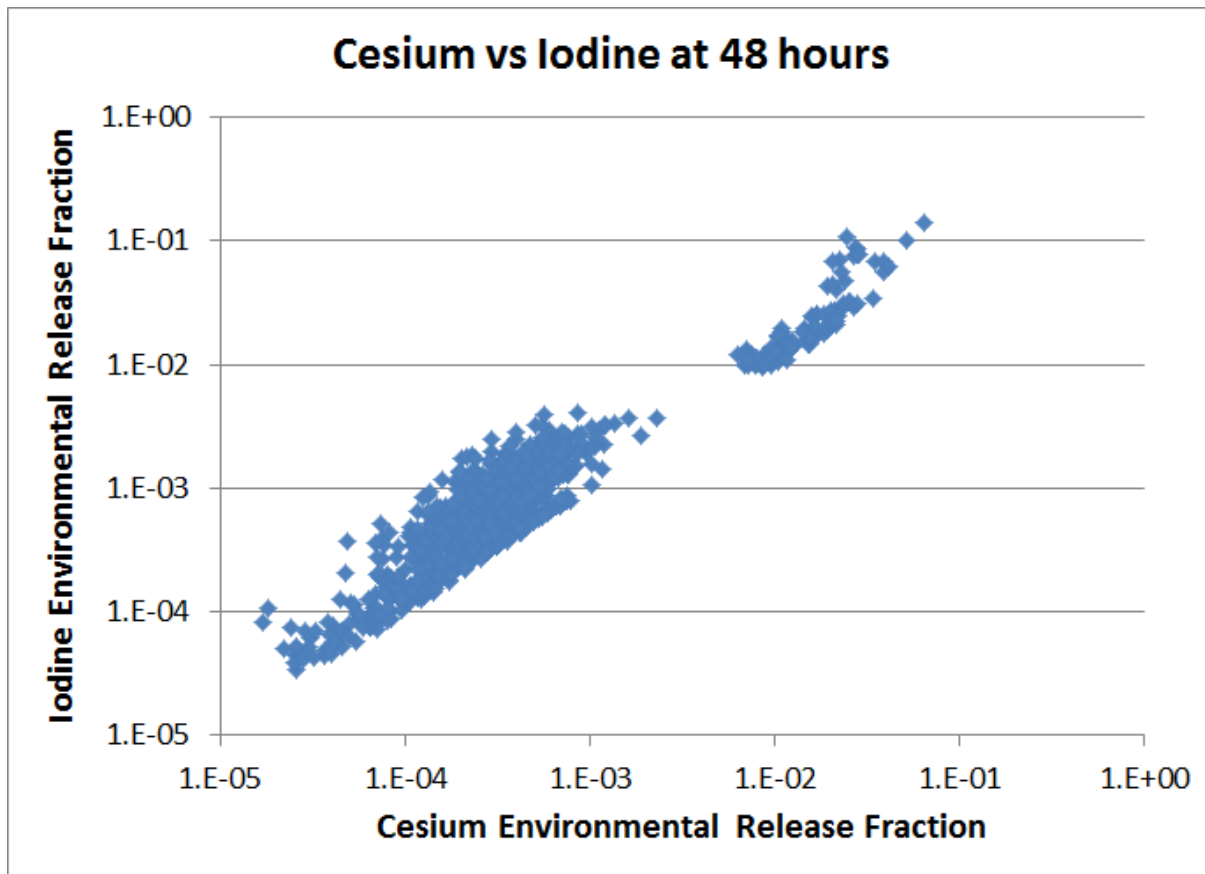


**Figure 6-12 Comparison of cesium and iodine environmental release fractions at 48 hours**

### 6.1.2.1 Comparison to SOARCA and Horsetail Plot

The environmental release fraction of all cesium (percentage of initial cesium inventory) at 48 hours is a primary figure of merit for the analysis. Figure 6-13 shows the time dependent release fractions for the first 300 successful realizations, as well as the calculated mean, median, and 5<sup>th</sup> and 95<sup>th</sup> percentiles of all realizations. There is a clear bifurcation in the results, with the higher release fractions representing SGTR realizations, and the remainder of the realizations having much lower releases. The release fractions for non-SGTR realizations are almost all below 0.001 at 48 hours, while the SGTR realizations are in the 0.01 range. Throughout the analysis, the results are well distributed, with no clear splits except the SGTRs. However, some of the realizations are increasing at 48 hours, while some remain relatively constant.

There is a wide spread between the calculated mean, median, and 95<sup>th</sup> percentile curves. The 95<sup>th</sup> percentile falls in the SGTR realizations, the median in the non-SGTR realizations, while the mean is in between where no actual realizations exist. There is also a significant time difference between the mean and median, with the median releasing much later in time. This is due to how the mean and median are calculated. As the SGTR releases are about two orders of magnitude higher than the other runs, they disproportionately influence the mean, which is not representative of any specific realization. Meanwhile, the median takes the middle realization at each time, so it is representative of a non-SGTR at all times although not necessarily the same realization at all times. The calculated 5<sup>th</sup> percentile curve has an associated initial release time

that is much later than the calculated median curve, and the 5th percentile remains under a release fraction of 1.0E-4 at 48 hours.

All four calculated curves are relatively steady by 20 hours, but the median and 5<sup>th</sup> percentile start increasing again around 40 hours. As described in detail in a subsequent section, late increases in release fractions are primarily due to containment liner yield, which is driven by heating of steam in containment from decay heat remaining in ex-vessel melt. The 95<sup>th</sup> percentile has no observable late increase as it represents an SGTR, which is a containment bypass event. Therefore, the containment failure model does not have a large impact as all significant releases have already occurred. As the mean is primarily influenced by the SGTR realizations, it also does not exhibit a late increase.

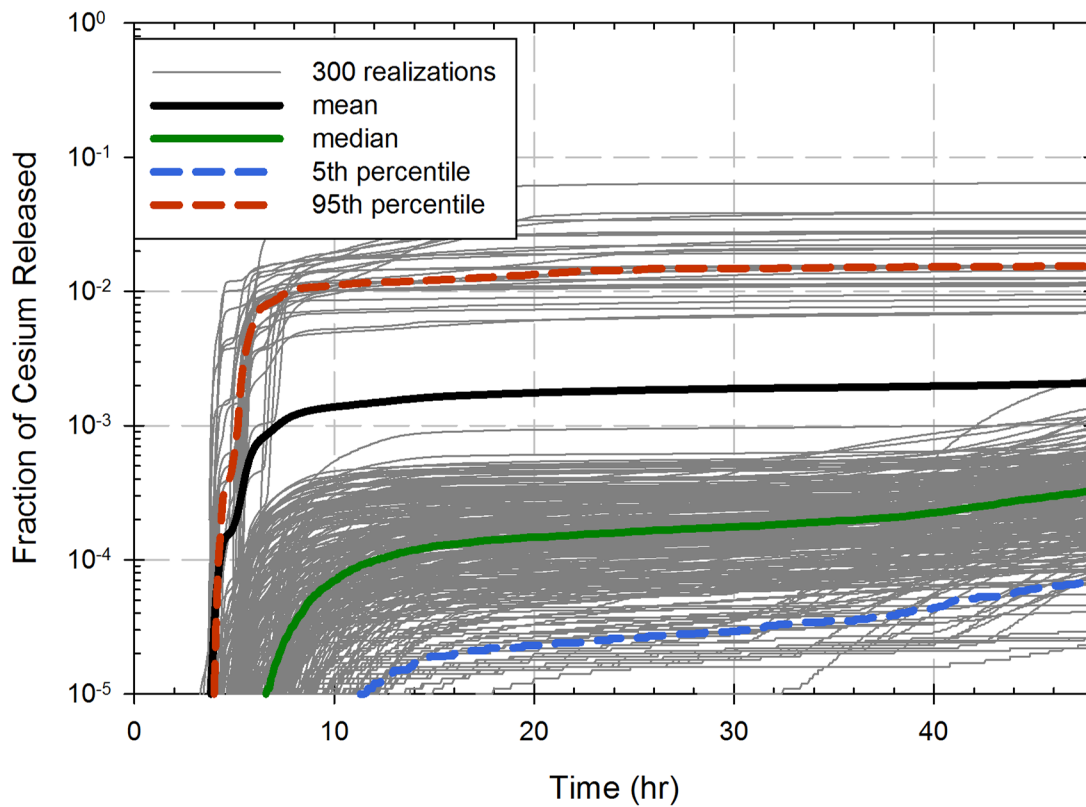


**Figure 6-13 Cesium release fractions over 48 hours with mean, median, 5<sup>th</sup> and 95<sup>th</sup> percentiles**

Figure 6-14 illustrates the cumulative probabilities for the fraction of cesium release for selected time intervals.

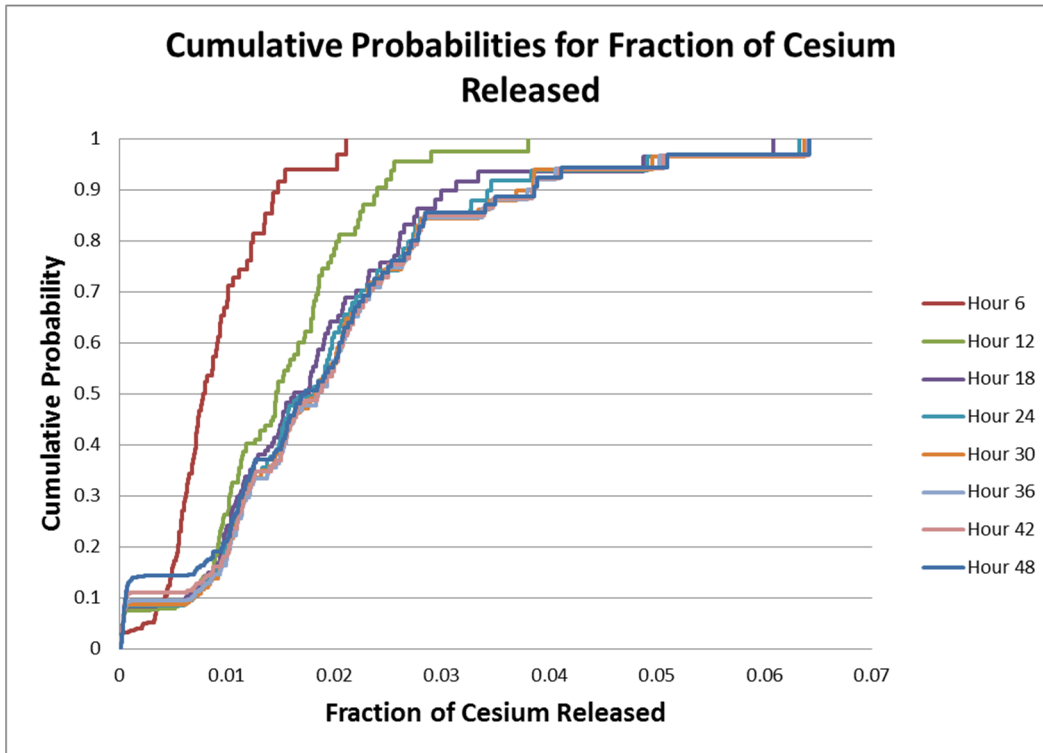


**Figure 6-14 Cumulative probabilities for the fraction of cesium release for selected time intervals**

As shown in Figure 6-15, the environmental release fraction of cesium at 48 hours in the SOARCA STSBO run is about 0.0006, which falls at about the midpoint of the mean and median realizations, putting it at the upper end of the non-SGTR realizations. However, the initial release timing is much closer to the median than the mean, although slightly earlier than the median. This is to be expected as the original SOARCA run did not include an SGTR but had high burn-up fuel (corresponding closest to EOC). The early SOARCA releases are much lower than either the mean or median and in fact are very close to the 5<sup>th</sup> percentile at 24 hours. At this point the SOARCA release fraction increases rapidly, above the median.

The two major differences between the Surry SOARCA model [3] and the new realizations are related to sampling of nominal containment leakage and the containment failure model. The lower limit of leakage sampling was set at the Surry SOARCA value [3], which caused essentially all of the UA realizations to have larger nominal leakage. This increases earlier releases by having slightly larger mass flows to the environment, and it has a secondary effect of partially subduing containment pressure. Because this is a sampled parameter, the effects of leakage are captured in regression results.

The containment failure curve was also modified in this work. Figure 6-16 displays the curve for the Surry SOARCA run on the left, with the modified UA curve on the right. Both curves use three of the same data points, based on scaled containment testing at Sandia. However, the Surry SOARCA model [3] removed the liner plate yield point and fit a parabolic function to the remaining three data points, which results in the enhanced failure leakage not initiating until much higher containment pressures. With the liner plate yield point included, and a linear fit between the four points, the Surry UA model starts enhanced leakage much earlier. The effect,

combined with higher sampling of nominal leakage, is that in the UA realizations containment pressure remains lower for a longer time period. Although the original SOARCA runs have a higher failure set-point, the failure is more dramatic with greater amounts of revaporization due to simultaneous pressure decrease and temperature increase and larger mass flows resulting in a greater cesium environmental release fraction. Comparison between the Surry SOARCA results for cesium and iodine (in Figure 6-15 and Figure 6-3, respectively) indicate that iodine experiences much more revaporization (by an order of magnitude) subsequent to containment rebar failure, at which point the pressure trend levels out and begins to decrease again while the temperature continues to increase. This large revaporization is rarely seen in the UA results since rebar failure pressure is almost never reached and instead the containment pressure and temperature trends gradually increase together through 48 hours. The effect of the revised containment failure curve in Figure 6-16 cannot be seen directly in the regression results. While the liner plate yield pressure is a sampled parameter, the change to the basic shape of the containment failure curve (CFC) that predicts more of a yield-before-break behavior was made to the base input deck.

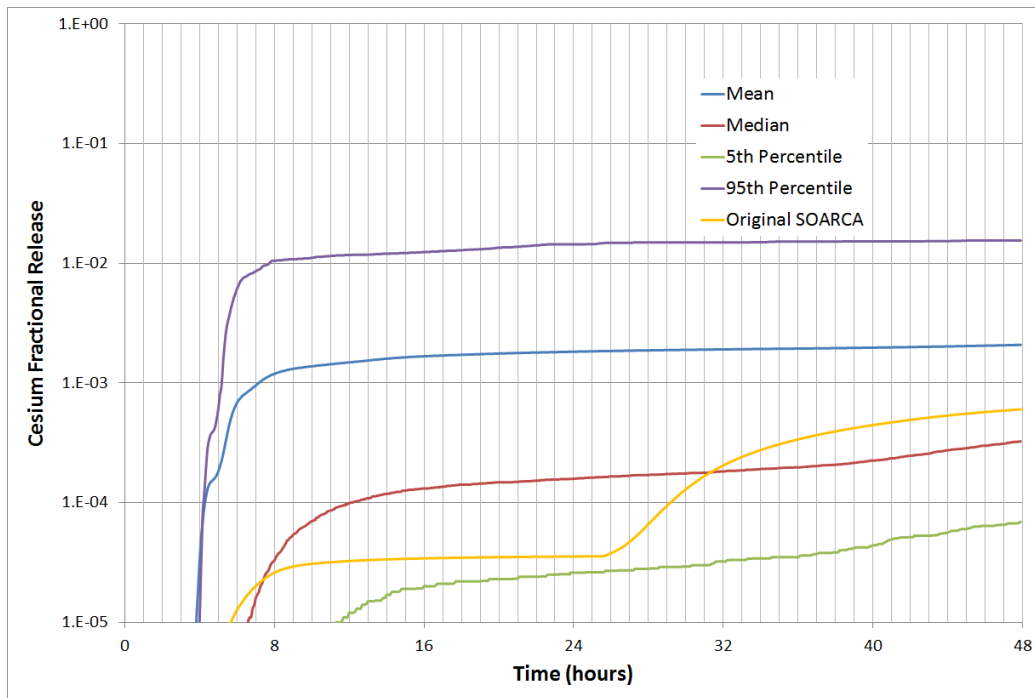


**Figure 6-15 Comparison of cesium release fraction in the original SOARCA STSBO to the calculated values of all successful realizations**

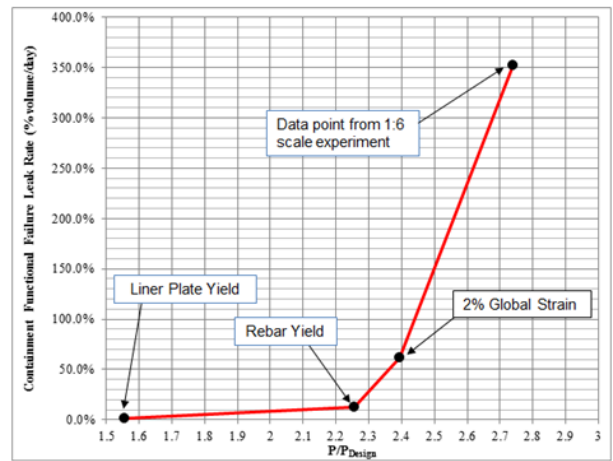
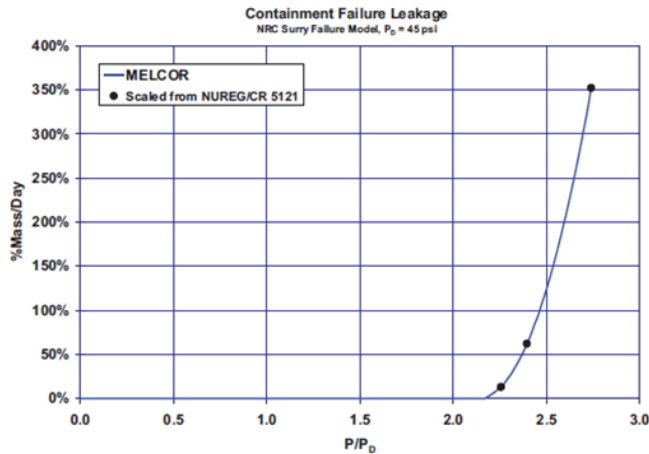


**Figure 6-16 Comparison of containment failure models used for the Surry SOARCA STSBO and the Surry uncertainty analysis**

### 6.1.2.2 Regression Tables and Scatterplots

Regression analyses were performed with all successful realizations. Three sets were done, one for all realizations, one for just SGTR realizations, and one for non-SGTR realizations. Additional regressions were done for the three times at cycle independently (BOC, MOC, and EOC). SGTR parameters dominated the regression results for all realizations, and since SGTR results have a unique section elsewhere in this report (section 6.1.5), Table 6-4 shows the results for just the non-SGTR realizations. In the following section, Key Parameters, technical rationale is provided regarding why the parameters may contribute to uncertainty in cesium release fractions.

Design leakage is the most important parameter, identified by each regression technique as responsible for almost half of the variation in results. The next two parameters in Table 6-4, time at cycle and shape factor, identified in order by each technique, explain the majority of the remaining uncertainty. The fourth, fifth and sixth parameters are identified in order with two minor exceptions, and are the only other significant main contributors to uncertainty. Each of the methods explains over half of overall cesium release variability.

**Table 6-4 Regression analysis of cesium release fraction in non-SGTR realizations.**

Final R <sup>2</sup>	Rank Regression		Quadratic		Recursive Partitioning		MARS		Main Contr.*	Conjoint Contr. *
	0.67		0.79		0.83		0.68			
Input	R <sup>2</sup> contr.	SRRC	S <sub>i</sub>	T <sub>i</sub>	S <sub>i</sub>	T <sub>i</sub>	S <sub>i</sub>	T <sub>i</sub>		
<i>DLEAK</i>	0.35	0.58	0.29	0.34	0.25	0.48	0.35	0.35	0.258	0.077
<i>CYCLE</i>	0.15	0.42	0.19	0.29	0.12	0.30	0.20	0.20	0.135	0.073
<i>PARTSHAPE</i>	0.05	0.23	0.12	0.16	0.09	0.33	0.18	0.21	0.085	0.081
<i>CFC</i>	0.04	-0.20	0.07	0.12	0.03	0.20	0.11	0.12	0.050	0.060
<i>DEV_DEC_HEAT</i>	0.02	-0.15	0.04	0.07	0.05	0.23	0.05	0.06	0.031	0.061
<i>CHEMFORMCS</i>	0.03	-0.16	0.03	0.06	0.00	0.05	0.04	0.04	0.020	0.022
<i>SVOAFRAC</i>	0.01	-0.12	0.00	0.05	0.01	0.10	0.01	0.04	0.006	0.044
<i>SC1132</i>	0.01	0.07	0.00	0.02	0.00	0.02	0.01	0.03	0.004	0.015
<i>TUBTHICK</i>	0.00	0.03	0.01	0.00	0.00	0.02	---	---	0.003	0.006
<i>CONDENS</i>	0.00	-0.06	0.00	0.02	0.00	0.02	0.01	0.01	0.003	0.011
<i>SGTRLOC</i>	0.01	0.07	0.00	0.01	---	---	0.00	0.01	0.002	0.003
<i>RDSTC</i>	0.00	0.06	---	---	0.00	0.02	0.00	0.01	0.001	0.005
<i>SC1131</i>	0.00	-0.04	0.00	0.00	0.00	0.02	---	---	0.001	0.004
<i>RCPSL</i>	0.00	0.08	---	---	0.00	0.01	0.00	0.01	0.001	0.003
<i>SRVFAILT</i>	---	---	---	---	---	---	0.00	0.01	0.000	0.001
<i>SV_STATUS</i>	---	---	0.00	0.06	---	---	0.00	0.00	0.000	0.016
<i>SG_B_SV_cycl</i>	---	---	0.00	0.01	0.00	0.01	---	---	0.000	0.008
<i>TUBETEMP</i>	---	---	0.00	0.01	0.00	0.01	---	---	0.000	0.006
<i>CHEMFORMI2</i>	---	---	---	---	---	---	0.00	0.00	0.000	0.000

\* highlighted if main contribution larger than 0.02 or conjoint contribution larger than 0.1

### 6.1.2.3 Key Parameters for non-SGTR Realizations

#### Containment Leakage (DLEAK)

The amount of nominal leakage from containment is sampled. Prior to increased leakage due to containment liner yield, this is the only release path for radionuclides to the environment, excluding bypass events like an SGTR. Within MELCOR, it is input as the calculated flow path length which yields the flow resistance needed to give the desired leakage at design pressure. This flow path is effectively just a hole in containment and doesn't represent a tortuous pathway, however simply resizing the hole has negative choked flow impacts. Because the flow path lengths were pre-calculated, the leakage parameter was divided into 10 discrete uniform bins that mirror the intended uniform continuous distribution.

Design leakage was identified by each regression technique as the largest contributor to uncertainty. Its influence was primarily independent, with little conjoint contribution. This is a logical result, as the majority of these cases have late or no containment liner yield, leaving this leakage as the only release pathway for cesium. The scatterplot (Figure 6-17) shows a clear trend of increase release fraction with decreasing flow path length (higher leakage). There is also an interesting result in that there is a clearly increasing lower bound with higher leakage. This may indicate that due to the design leakage, there is some amount of aerosolized cesium that is quickly released to the environment before there is time for deposition in containment.

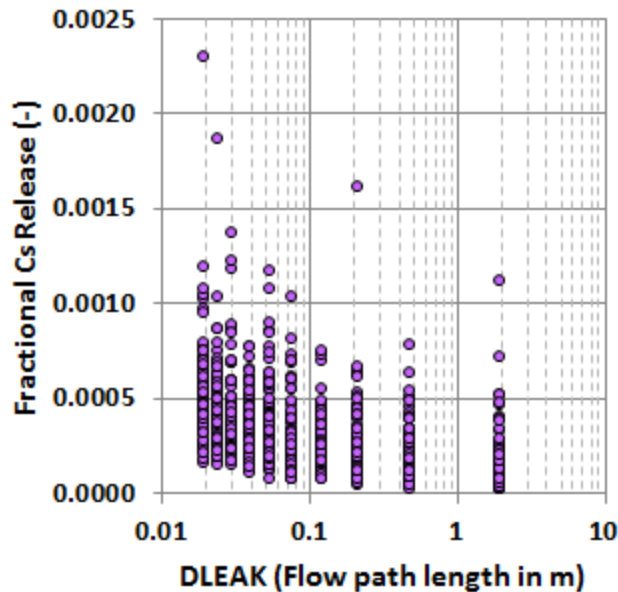


**Figure 6-17 Scatterplot of cesium release fraction versus containment leakage input values**

**Time at Cycle (CYCLE)**

This parameter specifies the burn-up of the core, as indicated by the total baseline decay energy at 48 hours. For cesium specifically, this determines timing of fuel heat-up, which in turn causes initial radionuclide releases, and later in the accident progression, the rate of containment pressurization. Each regression technique identified time at cycle as the second largest contributor to uncertainty. Its influence was primarily independent, with little conjoint contribution.

The scatterplot (Figure 6-18) shows that the largest difference in cesium release fraction is between EOC and the other two. BOC and MOC have approximately the same range and distribution of release fractions. It is an unexpected result that MOC and EOC should have a visibly different range and distribution, considering how close the total decay energy is. It is suspected that this little increase in decay energy is necessary to pressurize containment to the rebar yield set-point. The closeness of MOC and EOC total decay energy also hides the time dependence of the decay heat. MOC and EOC are very close early in the accident sequence, but the difference grows greater late in the sequence, when rebar yield might potentially be reached. When gross containment failure occurs, mass flow rates to the environment are increased, and small amounts of deposited aerosols are revaporized, allowing them to be transported out of containment. The effect of containment pressure is described in more detail in a later section (section 6.1.2.5).

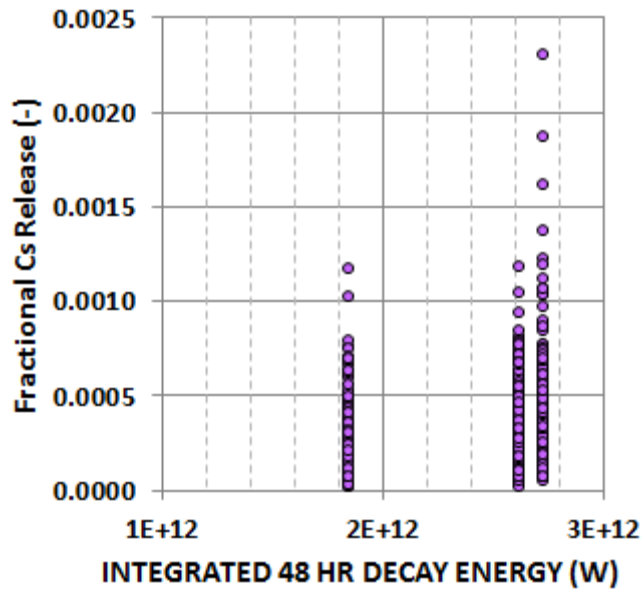


**Figure 6-18 Scatterplot of cesium release fraction versus integrated decay energy representing time at cycle input values**

#### **Dynamic Shape Factor (PARTSHAPE)**

This parameter accounts for increased drag force for nonspherical aerosol particles. A perfect sphere has a dynamic shape factor of 1.0. Shape factor is identified by all regression techniques as the third most important parameter in explaining uncertainty in cesium production, with minimal conjoint influence. However, although the scatterplot (Figure 6-19) does show a minor trend of increasing release fraction with larger shape factors, the majority resembled noise.

Within MELCOR, the dynamic shape factor influences the amount of agglomeration (effective particle size), as well as three deposition processes: gravitational settling, Brownian diffusion, and thermophoresis. A higher sampling of the dynamic shape factor yields more agglomeration and increased aerodynamic drag and allows aerosols to remain in the atmosphere longer available for release, while also reducing deposition, especially gravitational settling. All of cesium is aerosol, thus it is an expected result that increasing shape factor increases environmental releases.

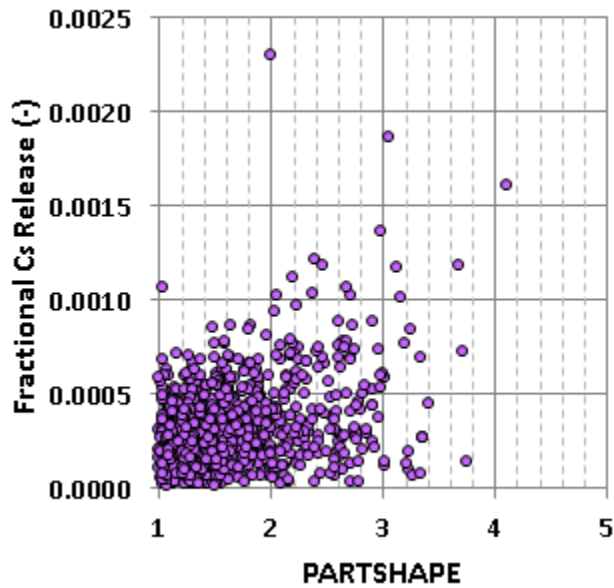


**Figure 6-19 Scatterplot of cesium release fraction versus dynamic shape factor input values**

### Containment Failure (CFC)

This parameter represents the ratio of actual containment pressure to design pressure at which liner plate yield occurs. This is the starting point for the containment failure model, detailed in Section 4.1.4.2. Sampling of this parameter at a lower value results in containment liner yield at lower pressures. This was identified as a top six parameter by all regression techniques, although not always as the fourth highest. SRRC, from the rank regression technique, indicated that there is a negative trend, with cesium releases increasing as this parameter decreases. The scatterplot (Figure 6-20) does give slight confirmation, with the highest outliers all being at low sampled input values, but the majority of the plot resembles noise. This supports the lower importance of this parameter, as compared to the top three.

There are two physical rationales for why increased flow out of the containment (which occur after rupture) increases the cesium release fraction. First and by far the most important, any aerosols that remain suspended in the atmosphere, or those entrapped aerosols instantaneously released to the atmosphere when any pool in a control volume dries out, are transported more effectively into the environment with greater flow rates. Of secondary importance is the large pressure drop that occurs upon rebar yield (and concrete failure) while containment temperature continues to increase can lead to the revaporization of some of the previously deposited cesium aerosols, making them available for transport to the environment. The relative lower position of this parameter is due to the fact that many realizations do not reach liner yield and almost none reach rebar yield, and may also indicate that the primary chemical forms of cesium do not revaporize at large rates, since this parameter had higher importance for iodine.

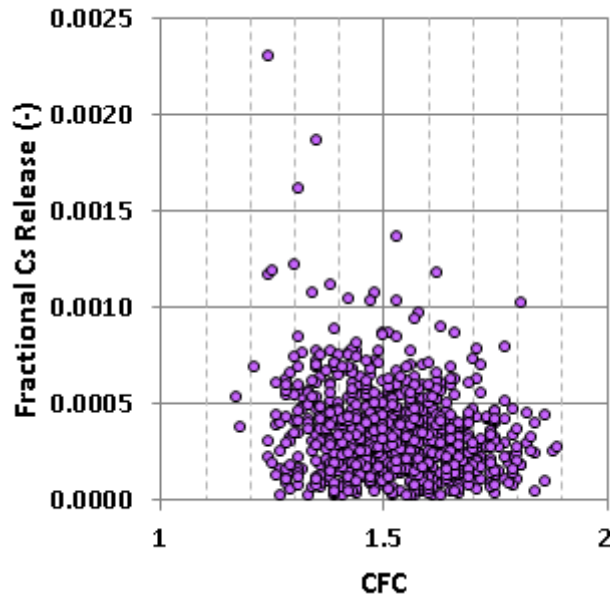


**Figure 6-20 Scatterplot of cesium release fraction versus containment failure input values**

**Decay Heat (DEV\_DEC\_HEAT)**

This parameter applies uncertainty to the base decay curves provided by the time at cycle parameter. For the purposes of the regression analyses, the total decay energy at 48 hours is integrated from the decay heat curves, and then a percentage difference from the baseline total decay energy for each corresponding time at cycle is calculated. This reduces the parameter to only looking at differences as compared to base decay heat and removes a decay heat overlap between MOC and EOC.

Decay heat uncertainty was identified by each regression technique as having importance in the top six, but with a low contribution to the total uncertainty. This is confirmed by the scatterplot in Figure 6-21, which mostly resembles noise. There is a minor trend toward higher release fractions with lower decay energy, which is a counterintuitive result as higher decay heat drives earlier releases from fuel and late containment pressurization. Given the low overall importance of this parameter, this is likely a coincidental result.

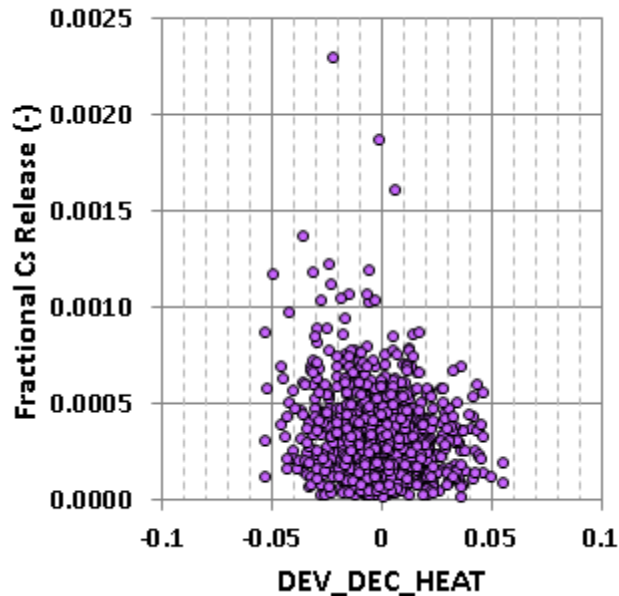


**Figure 6-21 Scatterplot of cesium release fraction versus decay heat deviation**

#### **Chemform Cs (CHEMFORMCS)**

This parameter determines the chemical speciation of cesium remaining after bonding with iodine to form CsI into  $Cs_2MoO_4$  and CsOH, which may release from fuel as a vapor but quickly cools to aerosolize. Chemform Cs was identified by all but one regression technique as a top six (but very low) contributor to overall uncertainty, while recursive partitioning did not identify it at all. The scatterplot (Figure 6-22) shows a fit to noise, with no clear trend visible, confirming relative low importance.

The  $Cs_2MoO_4$  and CsOH classes can have different release rates from fuel and revaporization potentials. Each of these could significantly impact environmental releases. The fact that Chemform Cs has such low relative importance indicates that either the definitions of these chemical classes are very similar or that any differences in these physical processes are swamped by other effects such as containment leakage.

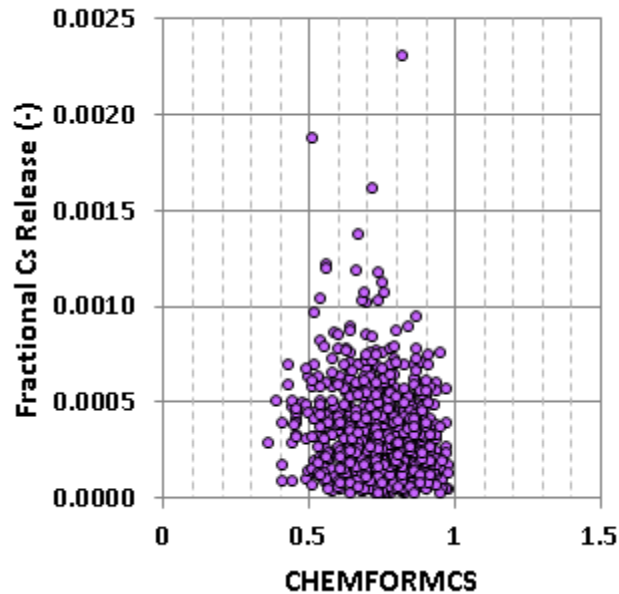


**Figure 6-22 Scatterplot of cesium release fraction versus Chemform Cs input values**

### Other Parameters

When looking at the regression results for all successful realizations, two parameters completely dominated the results: tube thickness and SV open fraction. Both of these relate to the frequency and severity of SGTRs and have an anticipated conjoint influence. The tube thickness essentially acts as a stress multiplier on the creep rupture equation and since the secondary is always depressurized, it is the primary determinant on whether an SGTR occurs. Primary SV open fraction also impacts the probability of SGTR occurrence, since it partially determines the pressure differential across the tubes. Once there is an SGTR, the open fraction of the secondary SV determines the flow area to environment, with a full open SV leading to the highest environmental releases. SGTR results are described in much more detail in a subsequent section, but are mentioned here as well considering their dominance over regression results for all realizations and the fact that those releases are 1 to 2 orders of magnitude larger.

Chemform I2 has an impact on the total amount of aerosol mass, because additional gaseous iodine means the formation of less CsI. This difference was theorized to potentially impact the amount of agglomeration, deposition, and subsequent releases. It has very minor or no importance from both regression results for non-SGTR realizations and all realizations. Due to this, it is concluded that the hypothesized impact of total aerosol mass is not present. There are no other parameters that were expected to be important in cesium environmental release fractions.

#### 6.1.2.4 Time at Cycle Independent Results

Because there are few realizations that reach rebar yield and cesium molybdate revaporizes less readily than cesium iodide following containment failure, design leakage and particle shape factor already dominate results for all realizations. This leads to fewer differences between BOC, MOC, and EOC. There were two key differences identified. First, since BOC realizations

never reach containment liner yield, the containment failure curve and those parameters affecting containment depressurization have no importance, while SV open fraction which affects the flow rate of cesium to containment prior to hot leg or lower head failure, has increased importance. Second, dynamic shape factor is the top contributor to uncertainty for EOC realizations, followed by design leakage and containment failure, since increased deposition impacts the release regardless of the containment pathway. Otherwise, there were no unexpected results in time at cycle independent regression results for cesium environmental release fractions.

#### **6.1.2.5 Timing and Other Effects**

As observed in Figure 6-14, there are no obvious timing bifurcations for the onset of cesium release which are spread about evenly from 4 to 10 hours. Almost all of the releases are steady between about 15 and 30 hours. After this point, the majority of releases increase again, although there are some, particularly SGTR realizations that remain steady. It is difficult to distinguish these from the scatterplot. The only clear split observed on the horsetail is the SGTR realizations, with releases that are 1-2 orders of magnitude higher.

In addition to the key figures of merit, horsetail plots were also produced for primary pressure and containment pressure. Figure 6-23 shows the horsetail for containment pressure, with an inset comparison to the original SOARCA pressure. The results show a clear bifurcation, starting at about 5 hours. Analysis of select realizations showed that the upper split represents all MOC and EOC realizations, while the lower split is made up of BOC realizations. The key difference is decay heat. The initial pressure increases in containment are caused by release of steam from the primary system, which start boiling earlier at MOC and EOC. Late containment pressurization is driven by direct heating of the steam already in containment by the decay heat remaining in the fuel after it has been discharged through the lower head of the RPV into containment.

The combination of these two effects means that at 48 hours, the highest BOC containment pressure is only 70 psia. In the original SOARCA calculation [3], containment rebar rupture leading to enhanced leakage started at about 120 psia. Although the liner yield failure point is sampled, it never reaches 70 psia in any realization. Thus, while most of the MOC and EOC realizations experience liner yield and some experience rebar rupture accompanied by some revaporization of deposited aerosols, at BOC these are never reached at 48 hours and all releases to environment are through nominal leakage. If the runs were extended to 72 or 96 hours, it is expected that all realizations would have increased release fractions, and the majority of BOC realizations would reach containment liner yield. This finding emphasizes the importance of controlling containment pressure in a real accident and suggests that late addition of water may have an adverse effect by creating an additional steam source and pressurizing containment.

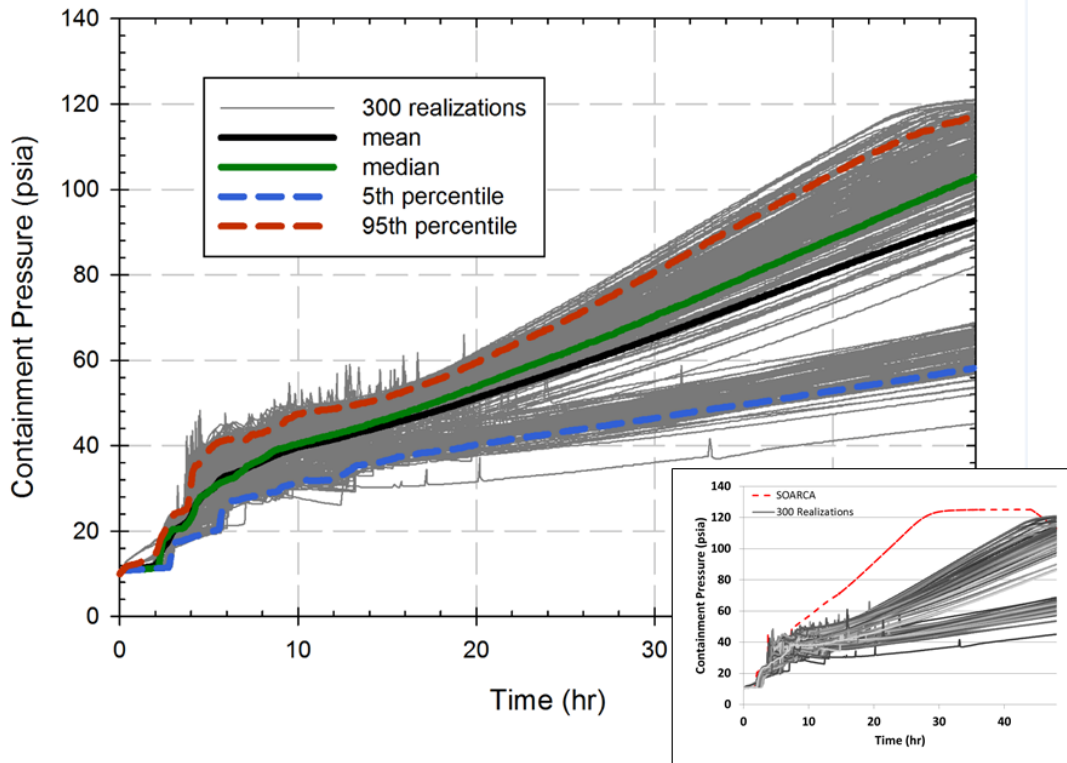


**Figure 6-23** Containment pressure over 48 hours with mean, median, 5<sup>th</sup> and 95<sup>th</sup> percentiles, and the original SOARCA result

### 6.1.2.6 Cesium Release Fraction to Environment – Conclusions

Cesium environmental release fractions are, equal to or lower than the Surry SOARCA calculation [3], except when an SGTR occurs. The lower release is primarily caused by slower containment pressurization, driven by multiple parameters including time at cycle and nominal containment leakage, and a modification to the containment failure model. There is a large split between SGTR and non-SGTR realizations, with SGTRs having one to two orders of magnitude higher release fractions. For non-SGTRs (90% of realizations), the spread of release fractions, excluding low outliers, is one order of magnitude. As expected, there is a very strong correlation between the parameters with highest importance for iodine releases and those for cesium releases. The most important parameter for the non-SGTR realizations is nominal containment leakage, which provides a pathway to the environment and slightly influences the timing of containment liner yield. Time at cycle and dynamic shape factor explain the majority of remaining uncertainty, with time at cycle determining containment pressurization rates and shape factor the amount of deposition of cesium aerosols. Releases increase with containment liner yield, and especially rebar yield and concrete rupture, but BOC realizations never reach either failure in 48 hours. At MOC and EOC, containment liner yield becomes more important and rebar yield is occasionally reached. However, these effects do not significantly change time at cycle independent regression results. The relative lower importance of containment failure indicates that cesium molybdate reevaporizes in lower amounts than cesium iodine, although this is not a predominant release mechanism for either. If the runs were conducted to 72 or 96 hours, it is expected that all or almost all would have increased cesium release fractions, and

regression rankings would likely change if most realizations achieve containment failure. The chemical form of cesium, while always in the top six parameters, never explained a large amount of the uncertainty. Tube thickness and SV open fraction determine whether an SGTR occurs. For SGTR realizations, the primary factor of importance on release magnitude is the secondary SV open fraction, which determines the flow area to the environment. The timing of pressurizer relief tank dry-out was found in single realization analysis to be important to release fraction magnitudes, because all aerosols retained in the pool are instantly revaporized upon dry-out. But since none of the parameters are a good surrogate for dry-out time, it does not appear in the regression results presented in this section.

### **6.1.3 Hydrogen Production**

Hydrogen production in the Surry model is primarily due to oxidation reactions of the Zircaloy fuel cladding, although there is also a small amount produced by oxidation of stainless steel structures. Cladding oxidation will continue until Zircaloy interior to the zirc oxide shell melts, breaks through the oxide layer, and relocates. Oxidation can continue, depending on the drainage rate, until the fuel itself reaches melting temperature and relocates to cooler regions of the core.

The onset of hydrogen release and total production are thus indicators of fuel temperature, leading to the onset of cladding oxidation and fuel melt, and also indicates the total amount of fuel damage. Release of hydrogen is also an indicator for radionuclide releases as these occur during the fuel damage progression. The amount of hydrogen produced in-vessel, along with the ex-vessel production of hydrogen and other NCGs during MCCI, are also the primary influences on whether deflagration and detonation conditions are reached in containment, which cause pressure increases leading to increased containment leakage and greater fission product releases to environment.

#### **6.1.3.1 Comparison to SOARCA and Horsetail Plot**

The total amount of hydrogen produced at 48 hours is the primary figure of merit for the analysis. Figure 6-24 shows the time dependent production for the first 300 successful realizations, as well as the calculated mean, median, and 5<sup>th</sup> and 95<sup>th</sup> percentiles of all realizations. As shown by the 5<sup>th</sup> and 95<sup>th</sup> percentiles, which exclude rare outliers, total production is between about 250 and 600 kg of hydrogen. Figure 6-25 illustrates the cumulative probabilities for the quantity of hydrogen produced for selected time intervals, which shows that after 6 hours, there are even distributions with no obvious splits. The high and low outliers are still very important and are analyzed in the single realization section. The mean and median of the realizations essentially overlap at all times, with about 400 kg of total hydrogen produced by 48 hours. The timing of the onset of hydrogen production is essentially the same for the mean, median, and 95<sup>th</sup> percentile curves, while for the 5<sup>th</sup> percentile, it is about 2 hours later. This timing difference is indicative of a larger split at the onset of hydrogen production, which is discussed in the timing section. However, almost every realization has stopped hydrogen production by 20 hours.

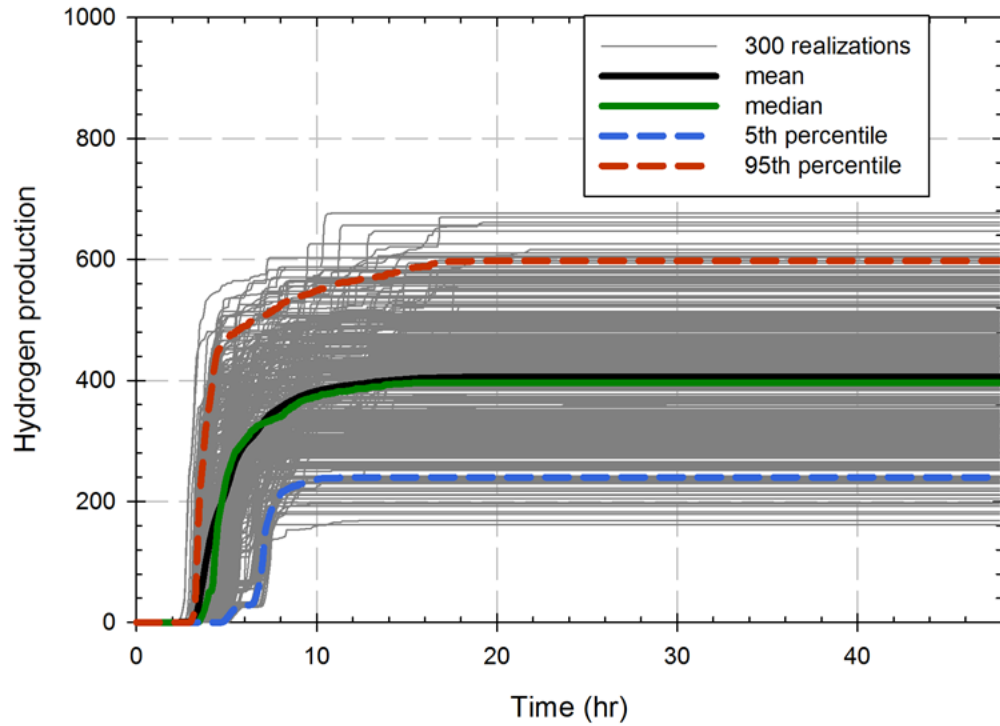


**Figure 6-24 Total Hydrogen production over 48 hours with mean, median, 5th and 95th percentiles**

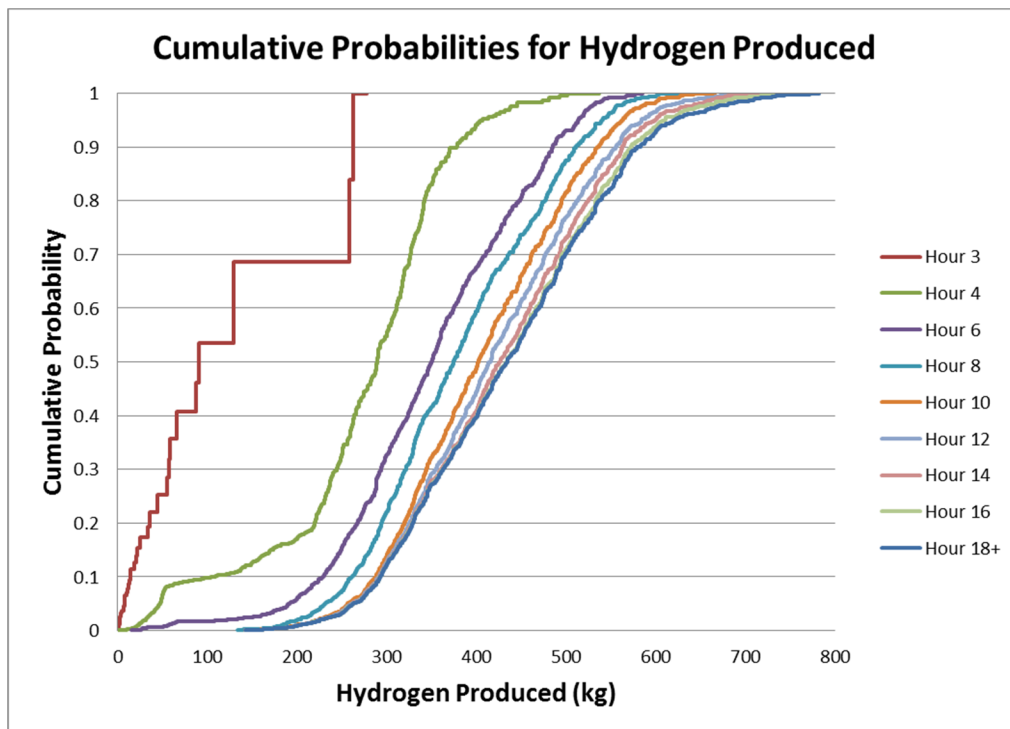


**Figure 6-25 Cumulative probabilities for the quantity of hydrogen produced for selected time intervals**

As shown in Figure 6-26, the total amount of hydrogen produced in the original SOARCA STSBO run was 349 kg, slightly lower than the mean and median but well within the bounds of the results. The timing of the onset of production is about the same as all but the 5<sup>th</sup> percentile curves. For the first hour of release, the original SOARCA results most closely matched the 95<sup>th</sup> percentile curve. This is likely because the original SOARCA deck used a high burn-up core with near end of cycle decay heat. The new results have time at cycle sampled, with the original SOARCA results being closest to the EOC sampling. For the next 3 hours, the original SOARCA results mirror the mean and median until about 8 hours, at which SOARCA H2 production stops, while the mean and median continue to increase. Each individual realization has a hard stop point to hydrogen production, similar to original SOARCA, but the increases in mean and median from 5 to 16 hours are because these curves are calculated from all realizations and do not represent any single realization for the full 48 hours. As will be described in more detail in a later section, BOC realization have later start times to hydrogen production but a generally higher total, which is what influences the mean and median after 8 hours. Any single realization has a distinct stopping point for hydrogen production when fuel relocation occurs, which would match the shape of the original SOARCA curve.

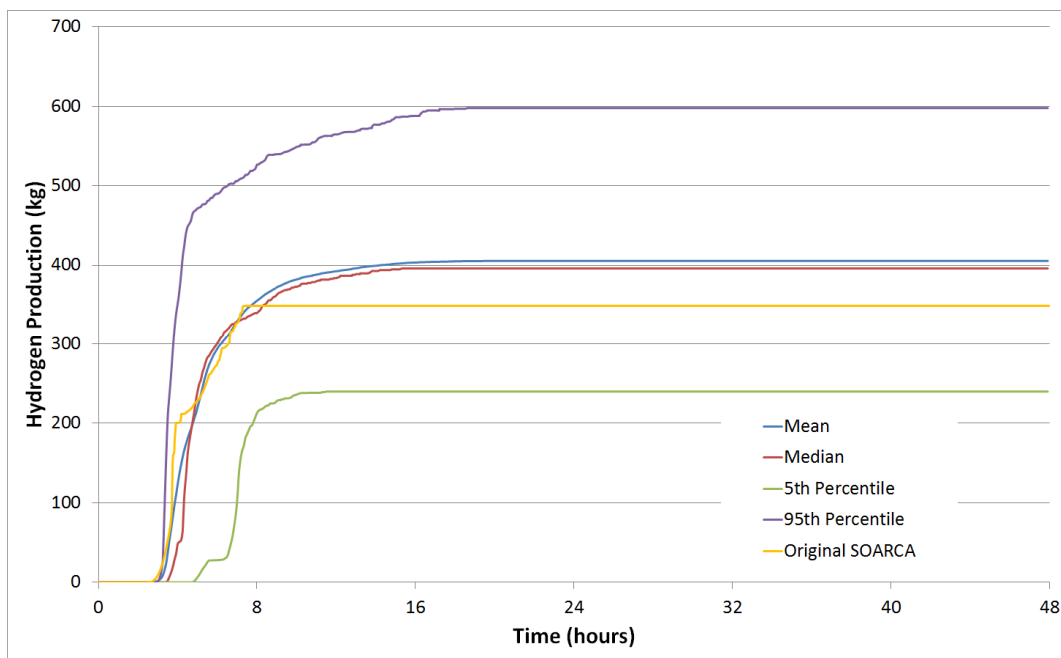


**Figure 6-26 Comparison of hydrogen production in the original SOARCA STSBO to the calculated values of all successful realizations**

### 6.1.3.2 Regression Tables and Scatterplots

Regression analyses were performed with all successful realizations. Three sets were done, one for all realizations, one for just SGTR realizations, and one for non-SGTR realizations. Additional regressions were done for the three times at cycle independently (BOC, MOC, and EOC). SGTR parameters dominated the regression results for all realizations, and since SGTR results have a unique section (section 6.1.5), Table 6-5 shows the results for just non-SGTR realizations. In the following section, Key Parameters, for each of the top six parameters, as well as other parameters of interest, a technical rationale is provided regarding why these parameters may contribute to uncertainty in hydrogen production.

The main result from the regression analysis is that a parameter related to SV failures (either SV open fraction or SV failure mode) was identified by each regression technique as clearly having the top contribution to uncertainty in hydrogen production. Each technique then ranked effective melting temperature and time at cycle as the second and third most important, in order. After these four parameters, there are no others that have a significant contribution to hydrogen uncertainty, and no parameters have a large conjoint contribution. Each regression technique successfully explains at least half of the total uncertainty in hydrogen production.

**Table 6-5 Regression analysis of hydrogen production in non-SGTR realizations.**

Final R <sup>2</sup>	Rank Regression		Quadratic		Recursive Partitioning		MARS		Main Contr.*	Conjoint Contr.*
	0.54		0.73		0.88		0.71			
Input	R <sup>2</sup> contr.	SRRC	S <sub>i</sub>	T <sub>i</sub>	S <sub>i</sub>	T <sub>i</sub>	S <sub>i</sub>	T <sub>i</sub>		
<i>SVOAFRAC</i>	0.03	0.23	0.52	0.54	0.31	0.45	0.54	0.54	0.266	0.046
<i>SC1132</i>	0.16	0.41	0.19	0.22	0.19	0.42	0.20	0.24	0.151	0.087
<i>CYCLE</i>	0.08	0.32	0.14	0.16	0.17	0.31	0.14	0.13	0.106	0.047
<i>SV_STATUS</i>	0.25	0.30	0.04	0.04	---	---	0.03	0.03	0.076	0.000
<i>SC1131</i>	---	---	0.01	0.04	0.02	0.18	0.01	0.06	0.010	0.066
<i>SV_NBCYC</i>	0.01	-0.13	0.01	0.00	0.00	0.05	0.02	0.02	0.007	0.015
<i>RCPSL</i>	0.00	0.06	0.02	0.05	---	---	0.02	0.01	0.007	0.007
<i>DLEAK</i>	---	---	0.01	0.01	---	---	---	---	0.001	0.000
<i>RDSTC</i>	---	---	0.00	0.01	0.00	0.01	0.00	0.00	0.001	0.004
<i>SGTRLOC</i>	0.00	0.07	---	---	---	---	0.00	0.00	0.001	0.000
<i>SC1141</i>	---	---	0.00	0.01	0.00	0.01	0.00	0.00	0.001	0.006
<i>CHEMFORMI2</i>	---	---	---	---	0.00	0.03	0.00	0.01	0.001	0.010
<i>DEV_DEC_HEAT</i>	---	---	---	---	0.00	0.01	---	---	0.001	0.004
<i>SG_B_SV_cycl</i>	---	---	---	---	0.00	0.01	0.00	0.00	0.001	0.003
<i>TUBETEMP</i>	---	---	---	---	0.00	0.02	0.00	0.00	0.000	0.006
<i>TUBTHICK</i>	---	---	---	---	0.00	0.01	0.00	0.00	0.000	0.003
<i>CFC</i>	---	---	---	---	---	---	0.00	0.01	0.000	0.001
<i>PARTSHAPE</i>	---	---	0.00	0.01	---	---	---	---	0.000	0.001
<i>CONDENS</i>	---	---	0.00	0.00	---	---	---	---	0.000	0.000
<i>RDMTC</i>	---	---	---	---	0.00	0.01	---	---	0.000	0.004
<i>H2LFL</i>	---	---	---	---	0.00	0.01	---	---	0.000	0.003
<i>SV_WTR_CYC</i>	---	---	---	---	0.00	0.01	---	---	0.000	0.003

\* highlighted if main contribution larger than 0.02 or conjoint contribution larger than 0.1

### 6.1.3.3 Key Parameters

#### Pressurizer SV Open Fraction (SVOAFRAC)

This parameter indicates the open fraction of the primary SV system at 48 hours. It is post-calculated based on actual failure conditions, using the sampled inputs. If one SV experienced liquid failure, the open fraction is 1.0 since it always fails fully open. If there are no SV failures at 48 hours, the open fraction is 0.0, which is a simplification, because it did experience some cycling, but it was judged to be the most appropriate single value representation. Finally, if one SV experienced cycling failure, the sampled open fraction is used and if multiple SV experience cycling failure, their open fractions are summed.

Open fraction was identified by the three more advanced regression techniques as having the largest contribution to uncertainty in hydrogen production. The scatterplot (Figure 6-27) does show a possible parabolic trend, with hydrogen production increasing with open fractions from 0 to 0.5, but then decreasing above 0.5. This would explain why rank regression did not identify this parameter with high importance, as it only looks for a linear trend.

This trend can potentially be explained by steam flow rates. When the primary SV is more fully open, steam leaves the RPV quickly and can halt oxidation by steam limiting and cooling of the fuel. However at low open fractions, there is little steam flow and localized oxidation could be effectively steam limited. There may be an ideal middle ground where a moderate steam flow over the hot fuel rods leads to the most oxidation. Alternately, it is possible that the parabolic trend observed is a coincidence and that the scatterplot is showing mostly noise, with a small linear trend of increased hydrogen production with higher open fractions (quicker depressurization). The presence of SV status, number of SV cycles, and RCP seal leakage in the list of parameters with some contribution does indicate there is a real relation between hydrogen production and pressurization state.

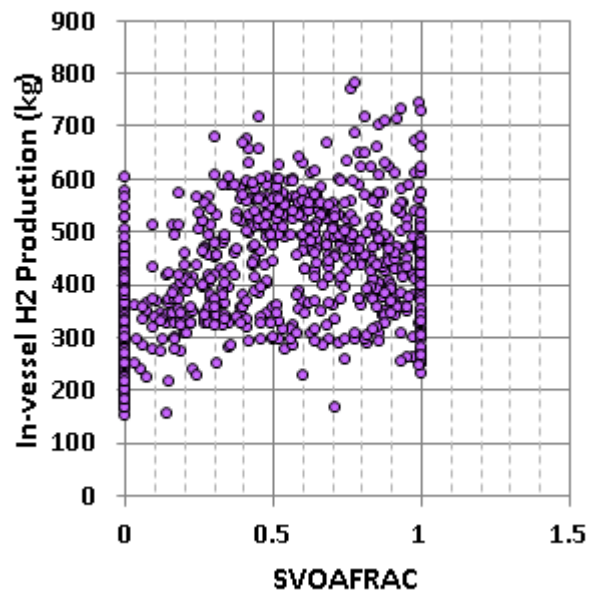


**Figure 6-27 Scatterplot of in-vessel hydrogen production versus SV 48 hour post-calculated open fraction**

#### **Temperature at which the Eutectic Formed from UO<sub>2</sub> and ZrO<sub>2</sub> Melts (SC1132)**

This parameter is a surrogate for a number of material interactions that lead to fuel melt and relocation. Effectively, it determines that temperature at which the eutectic formed from UO<sub>2</sub> and ZrO<sub>2</sub> melts which is when standing fuel rods turn to molten debris. This parameter was identified as the second most important by all four regression methods. Additionally, the scatterplot (Figure 6-28) shows a clear linearly increasing trend for the temperature at which the eutectic formed and hydrogen production. This was the scatterplot that showed the most obvious, distinct trend, again emphasizing the importance of this parameter.

The physical rationale for the trend exhibited by the scatterplot is that oxidation rates increase with rising temperature. If the fuel is allowed to reach a higher temperature before melting the rate of oxidation will accordingly be larger, producing more hydrogen. Additionally, regardless of increasing oxidation rate, the longer the fuel stands in a hotter location and continues oxidizing before being relocated to cooler regions increases the total amount of hydrogen produced.

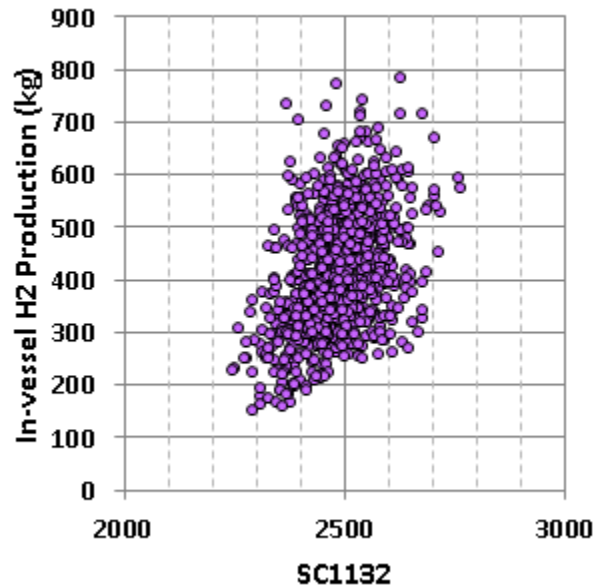


**Figure 6-28 Scatterplot of in-vessel hydrogen production versus eutectic melt temperature input values**

### **Time at Cycle (CYCLE)**

The time at cycle determines the burnup of the core, which has two main effects: decay heat and radionuclide inventories. The integrated decay energy at 48 hours is represented by this parameter, separating out just the decay heat aspect of time at cycle, and representing that MOC and EOC are much closer than MOC is to BOC. The amount of decay heat is the primary factor in initial core heat up and the time to onset of oxidation. Thus BOC runs ( $\sim 1.8E12$  J) start oxidation and hydrogen production later than MOC ( $2.6E12$  J) and EOC ( $2.7E12$  J) runs. All four regression techniques indicated time at cycle was the third most important parameter in explaining uncertainty.

Although oxidation starts earlier with increased burn-up, the scatterplot (Figure 6-29) shows that there is a slight trend of lower total hydrogen production with higher burn-up. The reason for the trend is that higher decay heat at MOC and EOC and the earlier onset of oxidation leads to more rapid fuel heat up, melt, and relocation to cooler regions of the vessel, suppressing oxidation. An unexpected and interesting result was identified where, exclusively in terms of total hydrogen production, it may be more beneficial to have an accident with a higher burn-up core.

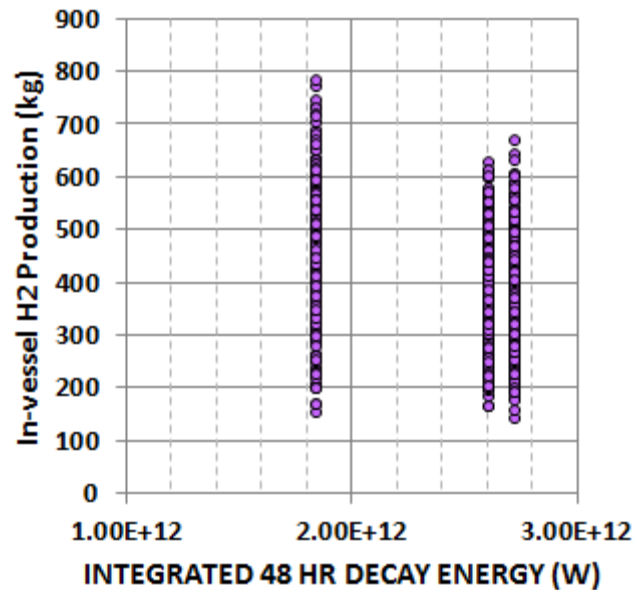


**Figure 6-29 Scatterplot of in-vessel hydrogen production versus integrated decay energy representing time at cycle input values**

**Pressurizer SV Status (Failure Mode) (SV\_STATUS)**

This parameter gives a discrete value to signify the final state of the primary SV system at 48 hours, with a value of 0 signifying there were no SV failures, 1 signifying that one or more SV's experienced cycling failure partially open, and 2 signifying that one or more SV's experienced liquid failure fully open. This is not a sampled parameter and rather is post-processed based on actual failures. Essentially this parameter contains most of the same information as the open fraction, but removes the spread from 0.0 to 1.0 in an attempt to see if just the failure mode is important.

Only rank regression identified this parameter as having a large contribution to hydrogen uncertainty, but it was the top parameter for rank regression. Looking at the scatterplot in Figure 6-30, although the spread of results is certainly different for each mode, it is hard to visually identify a linear trend. However, the largest amount of hydrogen production occurs when there is cycling failure and the system is at least partially depressurized. This generally matches the result from the open fraction parameter. It is likely that this parameter is capturing the same trends as the open fraction and not identifying a unique contribution.

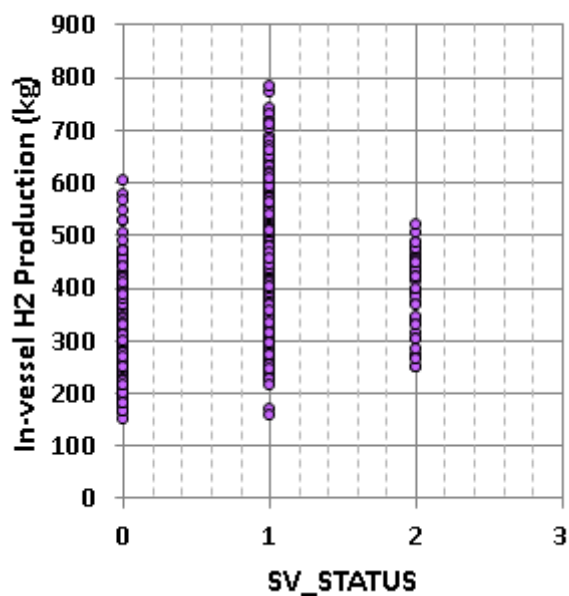


**Figure 6-30 Scatterplot of in-vessel hydrogen production versus SV status values**

**Zircaloy Breakout Temperature (SC1131)**

This parameter determines the temperature at which molten Zircaloy breaks through the oxide layer, effectively suppressing oxidation. Rank regression did not identify this parameter as important, while the other three calculated only a very low contribution to uncertainty. This is confirmed by the scatterplot in Figure 6-31 which resembles noise. There is potentially a small trend toward more hydrogen production with high temperatures. This would be an expected result, since higher temperatures allow more time for oxidation. It was expected that this would have higher importance, since it stops the oxidation process. If the regression was performed at a time during core damage instead of 48 hours, it is possible that this parameter would increase in importance.

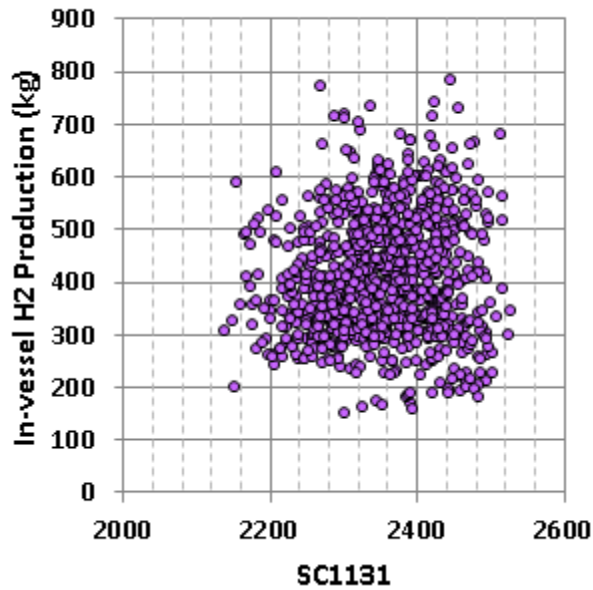


**Figure 6-31 Scatterplot of in-vessel hydrogen production versus Zircaloy breakout temperature input values**

### **SV Cycles to Failure (SV\_NBCYC)**

This parameter gives the number of normal cycles until a primary SV fails partially open. It is based mostly on the sampled input, since in the majority of realizations only the first SV fails, but in cases where the first SV fails mostly closed and the second SV cycles and fails, the parameter sums the cycles for each. There are cases where the number of cycles is great enough that no SV failures occur. In these cases, this parameter is assigned the sampled number of cycles to first SV failure, which means that hydrogen production for large values of this parameter have minimal meaning.

Three of the regression techniques calculated that this parameter has a contribution to hydrogen uncertainty, although in all three cases, the contribution is very minimal. The scatterplot (Figure 6-32) shows what resembles an exponentially decreasing curve with increasing number of cycles, although this may be a coincidence considering the untrustworthiness of high number of cycles. Regardless, a simple linear trend does still show lower hydrogen production with greater number of cycles (higher probability of staying pressurized), a trend that matches the other SV parameters.

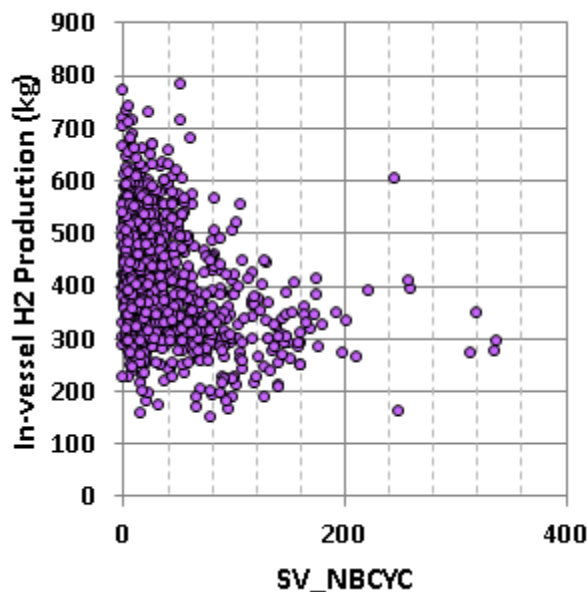


**Figure 6-32 Scatterplot of in-vessel hydrogen production versus SV cycles to failure values**

### Other Parameters

RCP seal leakage has a minor contribution to hydrogen uncertainty, although it was outside the top six most important parameters. Since this parameter contributes to whether the system is pressurized during fuel damage, similar to SV failure and open fraction, it is not surprising that it has some contribution to the uncertainty in hydrogen production. It has a positive SRRC value, indicated that there is more hydrogen produced with greater depressurization rates, which matches the trends observed in SV parameters.

Neither molten clad drainage rate nor decay heat deviation was listed in the top six most important parameters, although each has a very minor conjoint contribution. This drainage rate determines the time it takes to relocate molten materials to cooler regions of the vessel. As it has a significant impact on core damage progression, it was expected to contribute to the amount of oxidation. Decay heat is the driver for core temperature increases, and even small variations would be expected to have some impact on the amount of hydrogen produced. Their absence from the top parameters may indicate the importance is less than expected, or that over 48 hours, their effects are dampened by other parameters. It is suspected that if the regression was performed at a time during fuel damage, these could both raise in importance.

No other parameters had an independent contribution to hydrogen production uncertainty, nor are there any other parameters that were expected to have a significant contribution that didn't.

#### 6.1.3.4 Time at Cycle Independent Results

Because time at cycle is such a predominant factor differentiating between runs, regressions were run independently for each time at cycle, removing it as a parameter. The key result, is that the top two parameters, SV open fraction and effective eutectic melting temperature,

remain the two parameters dominating uncertainty for all time at cycles. SV status is a top 3 parameter for MOC and EOC, but again it seems to be only a surrogate for open fraction. Other top six parameters, Zircaloy breakout temperature and the two relating to primary system pressure, RCP seal leakage and number of SV cycles, retain some minor importance, but never overtake the top two. SGTR location and design leakage make the top six parameters for BOC, but in both cases this appears to be a fit to noise and there are no observable trends in the scatterplot and no physical reason why they would contribute to hydrogen production.

#### **6.1.3.5 Timing and Other Effects**

There is an observed timing difference in the onset of hydrogen production, shown in the horsetail in Figure 6-24. There is a clear split between the majority of releases, which are about evenly distributed between 3 and 6 hours, and the late releases at about 7 hours. Each of the important parameters was analyzed to determine the primary cause. It was demonstrated (see Figure 6-33) that primary system depressurization was the most important parameter in the timing, with time at cycle secondary. In the figure “Early” refers to a SV failing open after 10 or less cycles and depressurizing the system very early and “Late” refers to realizations without any SV failures before late hot leg creep rupture.

Specifically, time at cycle determines the first initiation of hydrogen production, with all MOC and EOC productions starting about the same time, but BOC realizations delayed by about an hour. However, whether the system is pressurized determines whether hydrogen production, caused by oxidation, increases rapidly or is delayed by about two hours until significant production. Therefore the MOC and EOC realizations with early depressurization make up the earliest high releases, signified by the 95<sup>th</sup> percentile curve on the horsetail. The majority of hydrogen production curves in Figure 6-24, including the calculated median and mean curves, are a combination of MOC and EOC realizations with later or no depressurization and BOC realizations with early depressurization. And the clearly observed late split, signified by the 5<sup>th</sup> percentile, is BOC realizations with late or no depressurization. However, regardless of the timing of the onset of hydrogen production, BOC realizations generally have higher total production at 48 hours, confirming the conclusions from the time at cycle parameter section.

This analysis provides partial confirmation of the regression techniques, which identified depressurization parameters (SV open fraction, SV status, and SV number of cycles) as the largest contributors to hydrogen production, and time at cycle as the third most important parameter. It also shows that although some of the effects of the parameters may be washed out by only regressing at 48 hours and not during core damage, the techniques do still seem to identify the important parameters in some order. It is likely that the effective melting temperature is the driver for total production for each realization, which is why the regression techniques identify it as the second most important parameter.

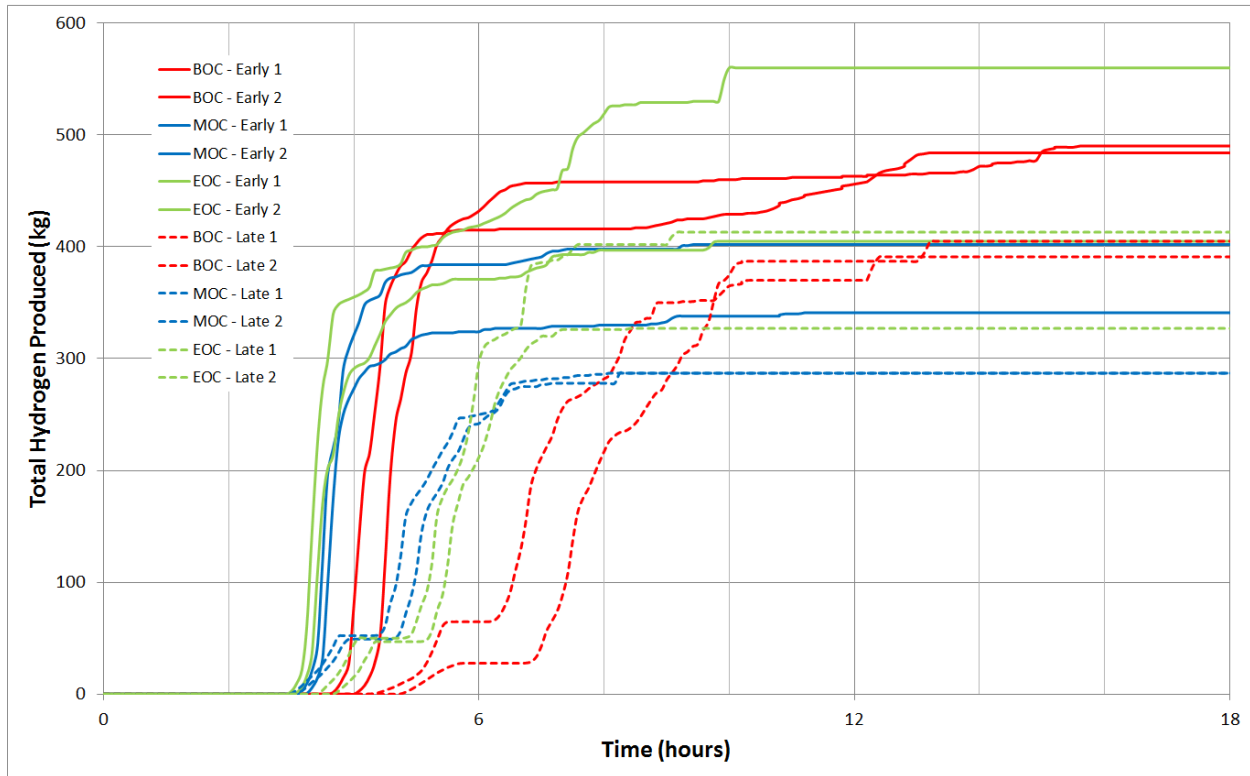


**Figure 6-33 Select realizations demonstrating the timing differences for the onset of Hydrogen productions**

### 6.1.3.6 Hydrogen Production Conclusions

In-vessel hydrogen production at 48 hours is a similar magnitude to the original SOARCA STSBO run. The range of total production, indicated by the 5<sup>th</sup> and 95<sup>th</sup> percentile curves, is from about 250-600 kg, or a spread of about 350 kg. This can also be represented as a departure from the mean and median of a factor of about 1.5. Regression results for hydrogen uncertainty are essentially the same, regardless as to whether there is an SGTR or not. The two most important parameters early in hydrogen production, indicated by the timing analysis are primary system depressurization, followed by time at cycle both of which are also important in the regression analysis. The impact of depressurization is most likely due to the rate of steaming and the flow rates of steam leaving the vessel. Flow rates of steam that are too high or too low can both halt oxidation. The magnitude of the total hydrogen generation by 48 hours, indicated by the regression analyses, is driven by effective melt temperature and secondarily by the time at cycle, both of which determine the amount of time the fuel remains in place before relocation. Depressurization and effective melt temperature remain as the most important parameters for all time at cycle independent regression analyses. There is not always agreement between the four regression techniques, emphasizing the benefit of using multiple techniques.

### 6.1.4 Time of Release

To determine parameters important in the start time of the release, a regression analysis was performed using the time of release as a metric. In the Peach Bottom UA [2], a 1 percent release of iodine was used as the metric for the time of release analysis; however in the Surry

uncertainty realizations, only SGTRs, which represent about 10 percent of the realizations, had releases of iodine greater than 1 percent. Thus for Surry, the time at which 1 percent of noble gases were released to the environment was used as the metric. With the noble gas metric, there were 162 of the 1003 realizations that did not reach the criteria by 48 hours. For these 162 realizations, 48 hours was used as the input to the regression.

The earliest releases in the uncertainty realizations were SGTRs, which exceeded the release timing threshold from about 4 to 8 hours. This is the same time core damage is occurring, as indicated by the onset of hydrogen production. However, non-SGTR realizations do not exceed the release timing threshold until 24 hours at the earliest, well after core damage. This is primarily due to the release paths from containment.

#### **6.1.4.1 Comparison to SOARCA**

The initial timing of the three primary figures of merit, hydrogen production, iodine release, and cesium release, are compared to the Surry SOARCA [3] timing in their respective report sections. The timing of 1 percent environmental release of noble gases was not a key metric for the original Surry SOARCA calculation [3], but the time extracted from the report was at about 1.125 days, or approximately  $9.7E4$  seconds. This was just after the start of increased containment leakage upon failure. The timing for the Surry SOARCA calculation [3] was earlier than almost all non-SGTR realizations. The reason is because with new modeling enhancements, containment liner yield is reached much later (or not at all) in all the uncertainty realizations, as described in detail in previous sections. Thus, the earlier timing of the Surry SOARCA [3] 1 percent release is an expected result.

#### **6.1.4.2 Regression Tables and Scatterplots**

Regression analyses were performed with all successful realizations. For the release timing figure of merit, one regression analysis was performed for all realizations and one for non-SGTR realizations. Table 6-6 and Table 6-7 show the regression results for non-SGTR realizations and all realizations, respectively. In the following section, Key Parameters, a technical rationale is provided for the top parameters contributing to timing of release variability, as well as a rationale for why parameters that were expected to be important may not be for the specified metrics.

The main result from the regression analysis is that the design leakage is the top parameter in both regression results, especially for non-SGTR realizations where it dominates uncertainty. SV open fraction and tube thickness are important for all realizations, as they are the primary contributors to whether an SGTR occurs and have a conjoint influence. Finally, time at cycle contributes significantly to uncertainty in both regression analyses. No other parameters were found to have high importance.

In the timing of release section, scatterplots for parameters that explain a large portion of uncertainty and visually show a clear trend or interesting result are displayed, and are identified as being either for all realizations or for non-SGTR realizations.

Table 6-6 Regression analysis of release timing for non-SGTRs.

Final R <sup>2</sup>	Rank Regression		Quadratic		Recursive Partitioning		MARS		Main Contr.*	Conjoint Contr. *
	0.76		0.95		0.93		0.87			
Input	R <sup>2</sup> contr.	SRRC	S <sub>i</sub>	T <sub>i</sub>	S <sub>i</sub>	T <sub>i</sub>	S <sub>i</sub>	T <sub>i</sub>		
DLEAK	0.48	0.69	0.52	0.58	0.55	0.63	0.59	0.58	0.499	0.044
CYCLE	0.23	0.51	0.28	0.33	0.30	0.38	0.33	0.33	0.263	0.041
CFC	0.03	0.18	0.04	0.06	0.03	0.08	0.05	0.05	0.035	0.025
SVOAFRAC	0.01	0.10	0.04	0.05	0.01	0.04	0.02	0.02	0.017	0.014
DEV_DEC_HEAT	0.01	0.09	0.01	0.01	0.00	0.01	0.01	0.01	0.006	0.005
SV_STATUS	---	---	0.01	0.01	---	---	---	---	0.003	0.001
CONDENS	0.00	0.04	0.00	0.00	0.00	0.00	0.00	0.00	0.003	0.000
SC1141	---	---	0.00	0.01	0.01	0.00	0.00	0.00	0.002	0.002
RCPSL	0.00	0.10	0.00	0.00	---	---	0.00	0.00	0.002	0.001
SGTRLOC	0.00	0.02	0.00	0.01	0.00	0.01	---	---	0.001	0.006
SC1132	0.00	-0.04	---	---	---	---	0.00	0.00	0.001	0.000
CHEMFORMCS	---	---	---	---	0.00	0.01	0.00	0.00	0.001	0.001
TUBTHICK	---	---	---	---	0.00	0.00	0.00	0.00	0.001	0.000
PARTSHAPE	0.00	-0.05	---	---	---	---	---	---	0.001	0.000
SV_NBCYC	---	---	---	---	0.00	0.01	---	---	0.000	0.002
SC1131	0.00	0.02	0.00	0.01	0.00	0.00	---	---	0.000	0.002
H2LFL	0.00	-0.02	0.00	0.00	---	---	---	---	0.000	0.001
TUBETEMP	---	---	0.00	0.01	---	---	0.00	0.00	0.000	0.003

\* highlighted if main contribution larger than 0.02 or conjoint contribution larger than 0.1

Table 6-7 Regression analysis of release timing for all realizations.

Final R <sup>2</sup>	Rank Regression		Quadratic		Recursive Partitioning		MARS		Main Contr.*	Conjoint Contr. *
	0.62		0.75		0.91		0.79			
Input	R <sup>2</sup> contr.	SRRC	S <sub>i</sub>	T <sub>i</sub>	S <sub>i</sub>	T <sub>i</sub>	S <sub>i</sub>	T <sub>i</sub>		
DLEAK	0.35	0.57	0.14	0.18	0.15	0.21	0.14	0.15	0.176	0.029
TUBTHICK	0.04	0.22	0.24	0.33	0.20	0.60	0.25	0.53	0.151	0.220
SVOAFRAC	0.05	0.21	0.29	0.36	0.13	0.49	0.19	0.47	0.132	0.200
CYCLE	0.15	0.42	0.10	0.11	0.07	0.11	0.10	0.10	0.091	0.014
CFC	0.02	0.14	0.01	0.04	0.01	0.03	0.02	0.01	0.012	0.011
DEV_DEC_HEAT	0.01	0.09	0.01	0.02	---	---	0.01	0.01	0.006	0.003
TUBETEMP	0.00	-0.06	0.01	0.03	0.00	0.06	0.01	0.03	0.005	0.025
RCPSL	0.00	-0.09	0.01	0.01	---	---	0.01	0.01	0.005	0.001
SV_STATUS	0.00	0.08	0.01	0.04	---	---	---	---	0.002	0.007
RDSTC	---	---	0.00	0.01	0.00	0.01	0.00	0.01	0.001	0.005
SGTRLOC	---	---	0.00	0.01	---	---	0.00	0.00	0.001	0.002
CONDENS	0.00	0.05	---	---	0.00	0.01	0.00	0.00	0.001	0.005
SG_B_SV_cycl	---	---	0.00	0.01	0.00	0.00	---	---	0.001	0.001
SC1132	0.00	-0.04	---	---	---	---	---	---	0.001	0.000
SV_NBCYC	---	---	0.00	0.02	0.00	0.00	0.00	0.01	0.001	0.007
SC1141	---	---	0.00	0.01	0.00	0.00	---	---	0.000	0.003
RDMTTC	---	---	---	---	0.00	0.00	0.00	0.01	0.000	0.005
SRVFAILT	---	---	0.00	0.01	0.00	0.01	---	---	0.000	0.004

\* highlighted if main contribution larger than 0.02 or conjoint contribution larger than 0.1

### 6.1.4.3 Key Parameters

#### Containment Design Leakage (DLEAK)

The rate of nominal containment leakage (% volume/day) occurring before containment liner yield is sampled. It is input as a discrete flow path length (m), with smaller lengths corresponding to larger leakage. Prior to containment liner yield, this is the only pathway for radionuclide release to the environment. This parameter was listed as having the largest main contribution to release timing uncertainty by the regression analyses for all realizations and for non-SGTR realizations.

The scatterplot for non-SGTR realizations Figure 6-34 shows that this parameter only has a significant difference for the 4 highest leakage bins (0.7 to 1.0%) For the remainder, the approximate ranges and distributions for time are about the same, between 1.0E5 and 1.8E5 seconds. Below this point, timing decreases significantly as leakage increases. This is an expected result, as increased design leakage provides a greater flow rate to the environment, allowing 1 percent release to be reached earlier. The high importance of this parameter is due in part to the fact that containment liner yield is not reached in many of the uncertain realizations. Of the many scatterplots produced as part of the regression analyses, this was the only one that showed a clear relationship between input and release timing.

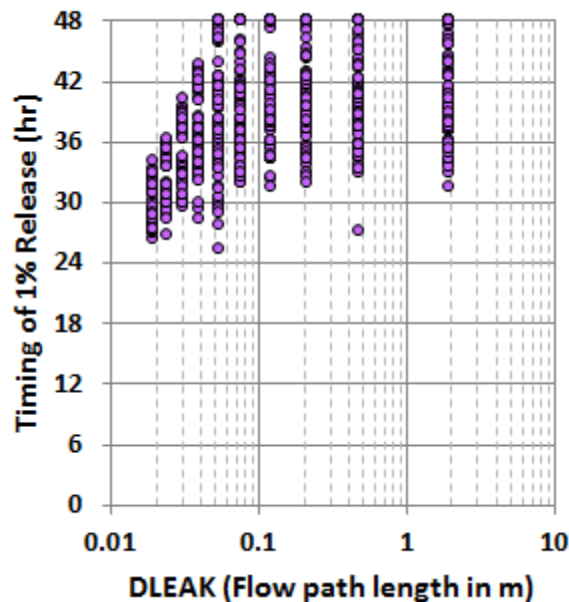
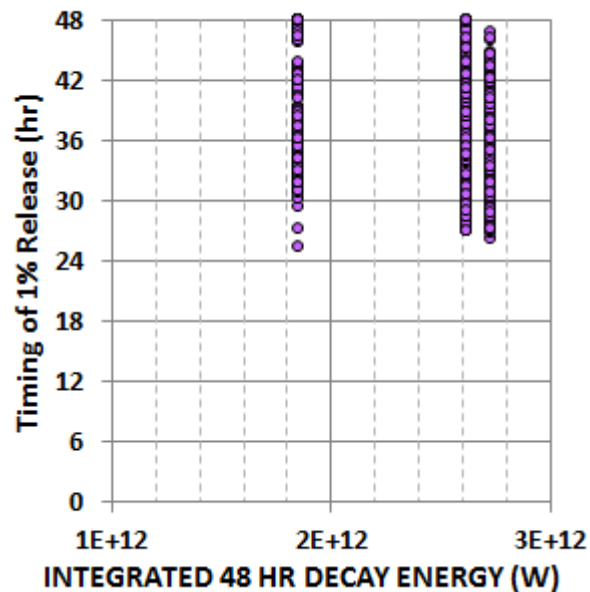


Figure 6-34 Scatterplot of timing of release versus design leakage flow path length input values

#### Time at Cycle (CYCLE)

The time at cycle parameter specifies the burn-up of the core, as indicated by the total baseline decay energy at 48 hours. The parameter was the second highest contributor to timing uncertainty for non-SGTR realizations, and fourth highest contributor for all realizations.

The scatterplot for non-SGTR realizations Figure 6-35 shows that the range of results for BOC and MOC are approximately the same, but that at EOC, the upper and lower bounds are shifted very slightly towards earlier timing. The trend toward earlier releases with increased decay heat is expected, since decay heat is the primary driver of late containment pressurization, determining whether failure pressures are reached. However, it was unexpected that there is not a more marked difference and that the only minor difference seen was between MOC and EOC, especially considering the small differences in base energy between MOC and EOC compared to BOC. However, this mirrors the results observed in the cesium release section, so the small increase must determine whether failure is reached in some realizations.



**Figure 6-35 Scatterplot of timing of release versus integrated decay energy representing time at cycle input values**

### Tube Thickness (TUBTHICK)

This parameter is converted directly from sampled input (which is thickness) to outer diameter in meters, both of which represent the effective thickness of damaged steam generator tubes. Since tube thickness goes into the calculation for hoop stress, the sampling of this thickness is effectively also sampling a stress multiplier on the creep equation. This parameter was the second highest contributor to timing uncertainty for all realizations, but had no importance for non-SGTR realizations. This was an expected result, if no SGTR occurs, the thickness of the tube has no impact on the accident progression, and any importance would have been a non-physical fit to noise.

The scatterplot for all realizations in Figure 6-36 shows that the big difference is between the timing of the SGTR realizations compared to non-SGTR realizations. Releases of 1 percent for SGTRs occur at about  $2.0E4$  seconds (5.5 hours), 20 hours earlier than the earliest non-SGTR realizations. Within the non-SGTR grouping (the higher grouping in the scatterplot), there is no trend observed where timing changes with the tube thickness, which is again expected as there should be no impact on non-SGTR for all tube thicknesses. The hard upper bound is the end of

the calculated transient, 48 hours, meaning 1% noble gas release wasn't reached by this time. In the SGTR grouping (the lower grouping in the scatterplot), there may be a minor trend toward earlier release with lower thickness, which would be physical since a more damaged tube would fail slightly earlier. However, this trend does not seem to be significant and the high contribution of this parameter is almost entirely due to the determination of whether an SGTR occurs, for which the parameter needs to be sampled at about 0.0105 m or lower.

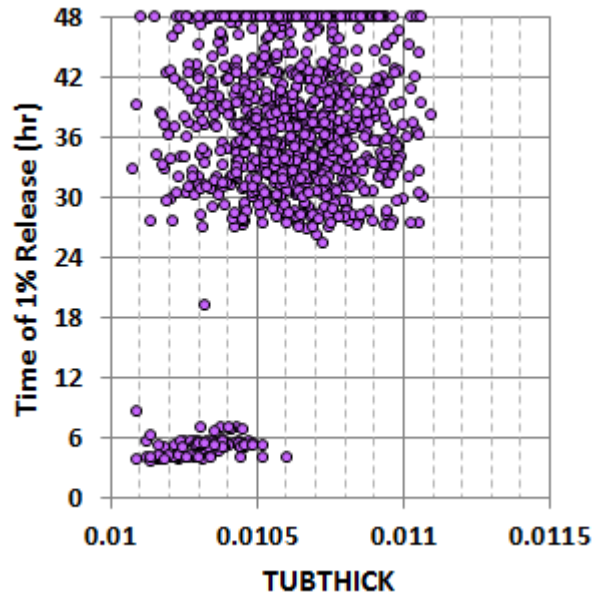


**Figure 6-36 Scatterplot of timing of release versus tube thickness input values**

### SV Open Fraction (SVOAFRAC)

The SV open fraction parameter has a partial indicator for the open fraction of the primary and secondary SV systems at 48 hours. It is post-calculated based on actual failure conditions of the primary SV, using the sampled inputs (see Hydrogen section). However this representation of open fraction is not always applicable for secondary SVs. Since they are not modeled to experience liquid failure and there is only one of 5 SVs modeled per loop, it always fails partially open, and would be more accurately represented by the direct input value.

The parameter was identified as the third largest main contributor to timing uncertainty for all realizations, with a conjoint contribution with tube thickness, and the fourth largest for non-SGTR realizations, although with a relatively low contribution. Similar to tube thickness, the scatterplot Figure 6-37 shows that the only real difference is between SGTR and non-SGTR realizations, and there are no obvious trends in either timing grouping. The vertical groupings at 0 and 1 are realizations where the primary SV experienced either no failure or liquid failure, respectively, and the hard upper bound is the end of the calculated transient, 48 hours, meaning 1% noble gas release wasn't reached by this time. As described in more detail in the tube rupture section, the open fraction of the primary SV has an impact on whether an SGTR can occur, which is why it has higher importance for all realizations and a conjoint contribution with tube thickness.

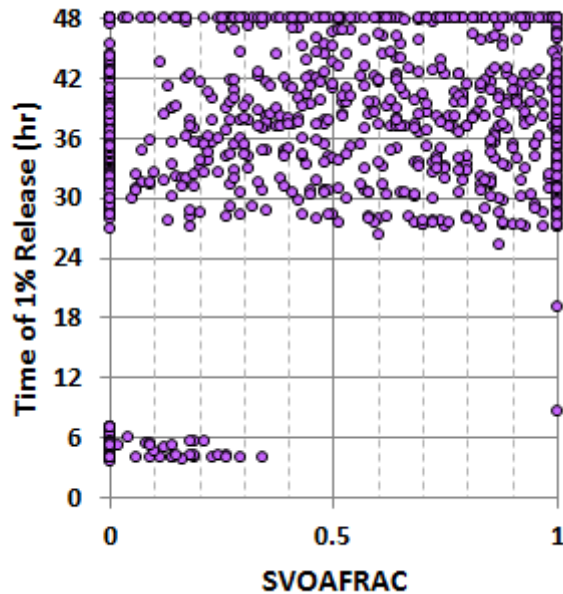


**Figure 6-37 Scatterplot of timing of release versus SV open fraction input values**

**Other Parameters – Containment failure curve, decay heat, and fuel failure parameters**

The containment failure curve (CFC) and decay heat (DEV\_DEC\_HEAT) have very minor contributions to timing uncertainty in both regression analyses. As they contribute to containment pressurization and leakage area to the environment, both were expected to have some importance. The lower contribution for the containment failure curve is due to the fact that even with the liner yield point being sampled, many realizations never reach this point and only have design leakage, and even fewer reach rebar yield. As for the decay heat parameter, the lower importance is because the variation on the base decay heat curves (determined by the time at cycle parameter) is much lower than the differences between the base curves themselves.

No parameters that influence the fuel melt progression, such as effective eutectic melting temperature or Zircaloy breakout temperature, had any contribution to timing uncertainty in either regression analyses. Since no environmental releases can begin until at least cladding rupture occurs, it was expected that these parameters may have some importance. The absence of these parameters from the results indicates that even though the release horsetails in Figure 6-1 and Figure 6-13 show a variation of about 6 hours in the onset of environmental releases, the containment parameters, particularly design leakage completely subsume this variation. No other parameters had a large independent contribution to release timing uncertainty, nor are there any other parameters that were expected to have a significant contribution.

**6.1.4.4 Time at Cycle Independent Results**

No time at cycle independent regressions were run for the release timing figure of merit because as time at cycle was not a dominant parameter for these results, there was no reason to believe that its effect was obscuring the effect of other parameters.

#### **6.1.4.5 Timing and Other Effects**

Since this metric is a single value of time, compared to a 48 hour trend for other key metrics such as hydrogen production, there are no trends or bifurcations to observe from horsetail plots. The only key split is between SGTR and non-SGTR realizations, and this split has been analyzed.

#### **6.1.4.6 Time of Release Conclusions**

There is a large timing difference between SGTR and non-SGTR realizations, with non-SGTR realizations meeting the 1 percent environmental release criteria about 20 to 40 hours later, if they meet the criteria at all. In fact, 18 percent of non-SGTR realizations do not release 1 percent of noble gases by 48 hours. In the original SOARCA analysis, the timing difference was about 25 hours, at the lower end of this range. Since almost all noble gases enter containment quickly after core damage, this indicates that the flow rates to the environment for SGTRs is significantly larger than the flow rates associated with design leakage, even when sampled at the highest bin. This was tested through one-off calculations and results show that flow rates to environment through the secondary side (combination of MSIV leakage and a stuck open secondary SV) are approximately three orders of magnitude greater than nominal leakage, regardless of any uncertainty sampling. However since only 10 percent of runs have SGTRs, and because the majority of realizations do not reach containment liner yield, design leakage is the highest contributor to release timing uncertainty in regression results for all realizations and for non-SGTR realizations. The two parameters that determine whether an SGTR occurs, tube thickness and SV open fraction, have high importance for all realizations. Finally, time at cycle, the determinant for base decay heat which drives containment pressurization leading to greater leakage and in some cases containment liner yield, has a large contribution to uncertainty in both regression analyses. All these were expected results based on insights from the other figures of merit. Two new insights are the observation that some realizations that do not release 1 percent of noble gases by 48 hours and that parameters which influence the timing of core damage, such as effective eutectic melting temperature, have limited importance when compared to containment related parameters. Note that this conclusion is specific to this regression analysis. The single realization investigation in Section 6.1.6 shows instances where these parameters have large importance.

#### **6.1.5 Steam Generator Tube Rupture**

A number of model enhancements were made to the Surry MELCOR deck, since the original SOARCA [3] calculation, which greatly improved steam generator tube representation. First, a single tube model was added that represents the hottest tube. The single tube is in addition to the heat structure representing the average temperature of the remainder of the tubes. Second, baseline leakage from the MSIVs was implemented on the secondary system leading to secondary depressurization within a few hours of the accident initiation. Third, cycling failure of the secondary SVs was included and the open fraction of the failed SV was sampled, further enhancing the modeling of time to depressurization. Finally, a new parameter, SG tube thickness, was added and sampled that induced an effective stress multiplier on the single tube representative of previously damaged tubes. With these changes, it was expected that some number of SGTRs would be calculated in the 1200 uncertain realizations.

A total of 104 SGTRs were observed out of 1003 successful realizations; this fraction may reflect a slight conservatism considering the assumption that the most damaged tube is in the

hottest region. These SGTR realizations have environmental releases of cesium and iodine that are 1 to 2 orders of magnitude greater than the median releases and generally occur earlier, making them primary contributors to total offsite consequences. As a result of this importance, separate regression analyses were performed for the SGTR realizations, the results of which are in this section.

#### **6.1.5.1 Comparison to SOARCA**

In the original SOARCA calculation for Surry [3], there was an STSBO scenario that included induced (forced) SGTRs. A sensitivity analysis was done to vary the flow area, representative of one or two failed tubes. In these runs, a secondary SV was stuck open at 3 hours and then an SGTR was modeled to occur when the creep damage index exceeded 5 percent, which was at 3 hr 33 min [3]. The SOARCA calculations [3] had only 14 minutes between the induced SGTR and hot leg creep rupture. Figure 6-38 shows the environmental release fractions for cesium and iodine for 1 and 2 tube SGTRs. In comparison to the SGTR realizations in the cesium and iodine horsetails (Figure 6-1 and Figure 6-13), the SOARCA results fall within the spread, although on the lower side in both cases.

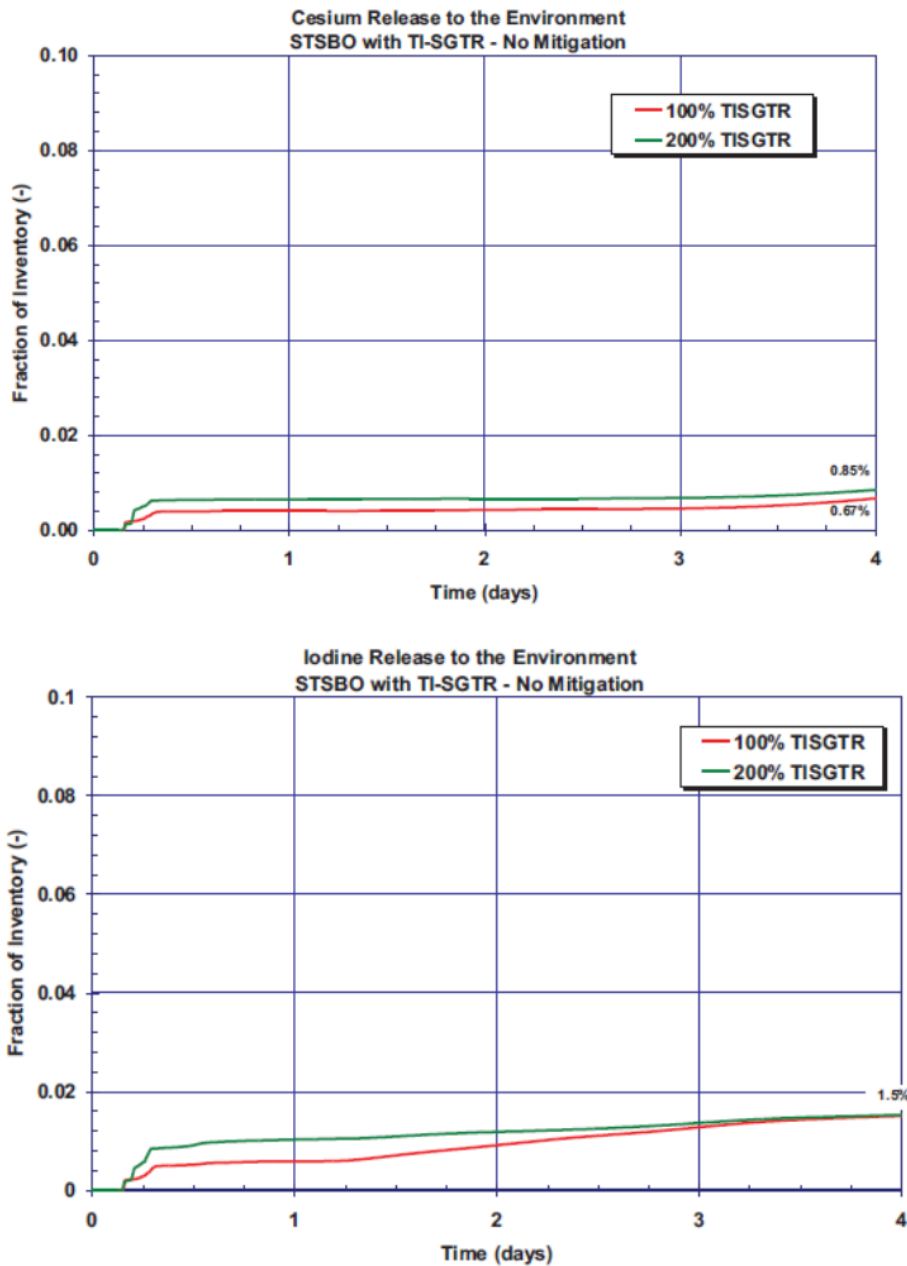


**Figure 6-38 Cesium and iodine environmental release fractions from original SOARCA SGTR sensitivities**

In addition to the model enhancements, there are three primary differences between the Surry SOARCA [3] SGTRs and those in the uncertainty realizations. First, the flow area to the environment is different in the UA. Surry SOARCA [3] assumed a stuck open secondary SV. Although these SGTR realizations also generally have stuck open secondary SVs, the open fraction is varied, and there is also leakage modeled through the MSIV. Second, the Surry SOARCA [3] calculation had a prescribed secondary DF of 7 applied to all aerosol size bins. With the UA realizations, the secondary decontamination amount is calculated by the code for each class, based on sampled break location and velocities. In one spot-checked SGTR, total

DFs for smaller particles in bins 1 to 4 were less than 2 for the entirety of the 48 hour transient, while those for the larger particle bins ranged from 4 to 1E6. Differences in the break location can have an even larger impact based on the power factor. It is difficult to compare releases between calculations with such disparities in total DFs. Third, due to the sampling of numerous parameters that influence core temperatures and primary system depressurization, the timing of hot leg creep varies somewhat between realizations, as does the timing of the SGTR based on time at cycle, tube temperature, and other parameters. This yields a wide range of times between SGTR and hot leg creep. As will be described in more detail in the timing section, this difference has a large impact on total releases.

### **6.1.5.2 Regression Tables and Scatterplots**

Regression analyses were performed for just SGTR realizations and non-SGTR realizations. This section gives the regression results for just SGTR realizations for the cesium release and iodine release metrics. The SGTR parameters dominated the regression results for all realizations. To describe the influence from only the SGTR realizations, results from all realizations are not reported in this section. Table 6-8 and Table 6-9 show the regression results for the SGTR realizations, for iodine and cesium, respectively. In the following section, Key Parameters, there is a technical rationale given for the top parameters contributing to cesium and iodine release variability, as well as an explanation for parameters that were expected to be important, but did not show importance for the specified metrics.

The main result from the regression analysis is that the SV open fraction and SG tube thickness contribute to the vast majority of uncertainty. It appears that there may have been over-predicting of conjoint influence, especially by the quadratic and MARS techniques for iodine, indicated by the huge difference between independent (main) and conjoint contribution. Additionally, the very large total  $R^2$  for the quadratic technique additionally suggests over-fitting. However, this does not diminish the importance of the top two parameters. SGTR location was a notable absence from the top parameters. Outside the top two, parameters that were important for iodine and cesium releases for non-SGTR realizations retain a very marginal importance.

**Table 6-8 Regression analysis of iodine release fraction for SGTRs.**

	Rank Regression		Quadratic		Recursive Partitioning		MARS		Main Contr.*	Conjoint Contr. *
Final R <sup>2</sup>	0.59		0.98		0.88		0.78			
Input	R <sup>2</sup> contr.	SRRC	S <sub>i</sub>	T <sub>i</sub>	S <sub>i</sub>	T <sub>i</sub>	S <sub>i</sub>	T <sub>i</sub>		
SVOAFRAC	0.16	0.51	0.15	0.80	0.60	0.86	0.03	0.97	0.213	0.532
TUBTHICK	0.29	-0.32	---	---	0.03	0.07	0.02	0.97	0.082	0.260
DLEAK	0.04	0.17	0.02	0.77	0.01	0.05	0.01	0.02	0.015	0.261
PARTSHAPE	0.05	0.22	---	---	0.01	0.01	---	---	0.015	0.002
CYCLE	0.03	0.21	0.01	0.00	0.00	0.00	0.00	0.00	0.012	0.001
SC1131	---	---	---	---	0.04	0.23	---	---	0.010	0.056
CHEMFORMCS	---	---	0.00	0.06	0.02	0.06	0.00	0.05	0.006	0.045
SGTRLOC	---	---	0.02	0.03	---	---	---	---	0.005	0.005
RCPSL	0.02	0.18	---	---	---	---	---	---	0.005	0.000
SV_STATUS	---	---	0.01	0.16	---	---	0.00	0.01	0.002	0.053
SRVFAILT	---	---	---	---	0.00	0.04	0.00	0.00	0.001	0.010
RDSTC	---	---	---	---	---	---	0.00	0.02	0.001	0.004
H2LFL	---	---	0.00	0.02	---	---	0.00	0.02	0.001	0.011
RDMTC	---	---	---	---	0.00	0.04	---	---	0.001	0.010
TUBETEMP	---	---	---	---	0.00	0.01	0.00	0.02	0.000	0.008
SV_WTR_CYC	---	---	---	---	---	---	0.00	0.06	0.000	0.015
CFC	---	---	---	---	---	---	0.00	0.03	0.000	0.007
DEV_DEC_HEAT	---	---	---	---	---	---	0.00	0.02	0.000	0.006
SC1132	---	---	---	---	---	---	0.00	0.01	0.000	0.003
SC1141	---	---	---	---	---	---	0.00	0.01	0.000	0.002

\* highlighted in yellow if main contribution larger than 0.02 or conjoint contribution larger than 0.1

**Table 6-9 Regression analysis of cesium release fraction for SGTRs.**

	Rank Regression		Quadratic		Recursive Partitioning		MARS		Main Contr.*	Conjoint Contr. *
Final R <sup>2</sup>	0.54		1.00		0.81		0.54			
Input	R <sup>2</sup> contr.	SRRC	S <sub>i</sub>	T <sub>i</sub>	S <sub>i</sub>	T <sub>i</sub>	S <sub>i</sub>	T <sub>i</sub>		
SVOAFRAC	0.13	0.58	0.30	0.75	0.39	0.71	---	---	0.188	0.234
TUBTHICK	0.21	-0.27	0.00	0.02	0.07	0.14	0.36	0.36	0.115	0.023
SV_STATUS	---	---	0.04	0.12	---	---	0.33	0.33	0.072	0.026
CYCLE	0.08	0.34	0.00	0.02	0.06	0.12	0.22	0.22	0.062	0.024
PARTSHAPE	0.12	0.36	0.00	0.00	0.05	0.09	0.09	0.09	0.052	0.011
CHEMFORMCS	---	---	---	---	0.06	0.27	---	---	0.015	0.058
DLEAK	---	---	0.04	0.59	---	---	---	---	0.014	0.184
SC1141	---	---	0.00	0.00	0.01	0.06	---	---	0.004	0.013
SV_WTR_CYC	---	---	0.01	0.09	---	---	0.00	0.00	0.003	0.028
SGTRLOC	---	---	0.01	0.03	---	---	---	---	0.003	0.009
H2LFL	---	---	0.00	0.00	0.00	0.00	0.00	0.00	0.002	0.001
SC1131	---	---	0.00	0.00	0.01	0.01	0.00	0.00	0.002	0.002
RDSTC	---	---	0.00	0.00	---	---	---	---	0.001	0.000
SRVFAILT	---	---	0.00	0.01	---	---	0.00	0.00	0.000	0.004
CONDENS	---	---	0.00	0.00	---	---	0.00	0.00	0.000	0.002
RDMTC	---	---	---	---	0.00	0.02	0.00	0.00	0.000	0.006
RCPSL	---	---	---	---	0.00	0.00	0.00	0.01	0.000	0.001
SC1132	---	---	---	---	---	---	0.00	0.01	0.000	0.001
SV_NBCYC	---	---	---	---	---	---	0.00	0.00	0.000	0.001
DEV_DEC_HEAT	---	---	---	---	---	---	0.00	0.00	0.000	0.000
TUBETEMP	---	---	---	---	---	---	0.00	0.00	0.000	0.000

\* highlighted in yellow if main contribution larger than 0.02 or conjoint contribution larger than 0.1

### 6.1.5.3 Key Parameters

#### SV Open Fraction (SVOAFRAC)

The SV open fraction parameter represents a partial indicator for the open fraction of both the primary and secondary SV system at 48 hours. The open fraction is post-calculated based on actual failure conditions of the primary SV, using the sampled inputs (see Hydrogen section). However this representation of open fraction is not always applicable for secondary SVs. Since SVs are not modeled to experience liquid failure and there is only one of 5 SVs modeled per loop, the first SV always fails partially open. Thus a value of 0, which is a large percentage of results as shown in the scatterplot (Figure 6-39), is only accurate for primary SVs, while secondary SVs would be more correctly represented by the directly sampled input value. The solution for future runs is to sample open fraction for primary and secondary SVs separately.

Open fraction was identified by most of the advanced regression techniques as having the largest contribution to uncertainty in release fractions for SGTRs.

The lack of SGTRs with open fractions between 0.4 and 1.0 in the scatterplot appears to be due to a complicated interplay with the primary SVs. A primary SV failing with an open fraction greater than 0.5 will tend to depressurize quickly. Since the secondary side is always depressurized due to MSIV leakage, this means there will be no pressure difference to induce a break. Figure 6-40 and Figure 6-41 show the primary and secondary pressures for realization

1151, which had tube thickness in the lowest 10 percent of the CDF and a failed primary SV with an open fraction of 0.49, and realization 119, which had tube thickness at about the 50<sup>th</sup> percentile of the CDF, but a failed primary SV with an open fraction of 0.23. Each realization had approximately the same primary pressure up to 2 hours, and while there was a difference in secondary depressurization timing due to one instance of a stuck open secondary SV, in both realizations all three steam generators were at atmospheric pressure by 3 hours. However, primary depressurization rate varied significantly after 3 hours. In realization 1151 where there is an SGTR, there is a pressure difference of about 1750 psi at the point of the rupture, while in realization 119 the pressure difference is less than 1000 psi. This indicates that regardless of tube thickness, the pressure difference must be greater than 1000 psi during the period of core damage for an SGTR to occur. This supports the regression results placing open fraction higher than tube thickness in importance.

Further evidence that lack of primary depressurization is the reason for the SGTR is that 75 of the 104 SGTRs had no primary SV failure, keeping the primary side pressurized, and none had liquid failure, which would always occur early since later SV cycles have no liquid. Additionally, SGTR realizations with no primary SV failure were checked to see what the sampled SV open fraction was, i.e. what the open fraction would have been had there been a SV failure. The sampled values captured the whole range from 0 to 1, meaning there is no connection between open fraction and SGTR occurrence except the impact on primary depressurization.

While it seems clear that primary SV open fractions can have an impact on the probability of SGTR occurrence, there are two reasons why secondary SV open fractions have an impact, especially on the trend toward larger releases with a larger open fraction. First, the secondary SV open fraction has an impact on the depressurization timing for the secondary side; although, since the number of secondary SV cycles is not a top parameter, and there is always depressurization by MSIV leakage, this probably is not the primary reason. Second, and more importantly, the open fraction of the secondary SV determines the flow area to the environment after an SGTR, with a larger open fraction resulting in generally higher releases, a trend seen in the scatterplots, even in the limited data from 0 to 0.4 as shown in Figure 6-39.

During the testing for this parameter, an error was identified in the application which may have actually reduced SV open fraction contribution to uncertainty. The error was in the sampled open fraction which was only correctly input for loop B, while SVs on loop A and C always failed closed. This error did not impact the likelihood of SGTR occurrence, since the MSIV leakage always depressurizes the secondary side. Although SGTRs still occurred in loops A and C and there were environmental releases due to MSIV leakage, the additional leakage path through a stuck-open SV was not included. Since many of the SGTRs were in loop B, the range of possible results is believed to be captured, but it is possible more of the SGTRs would have been at the higher, not lower, end of the release range.

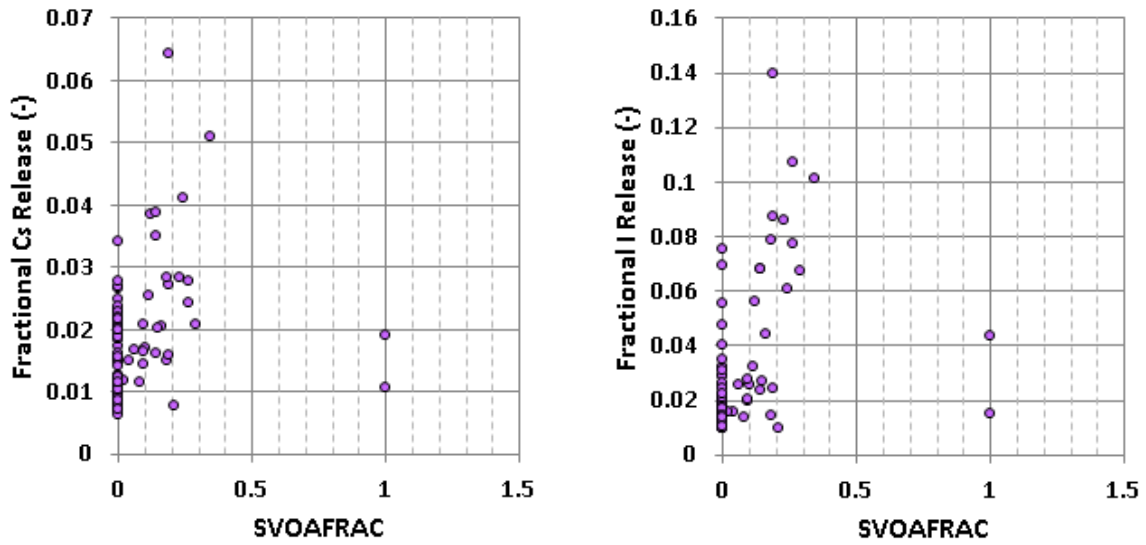


Figure 6-39 Scatterplot of cesium and iodine release fractions versus SV open fractions

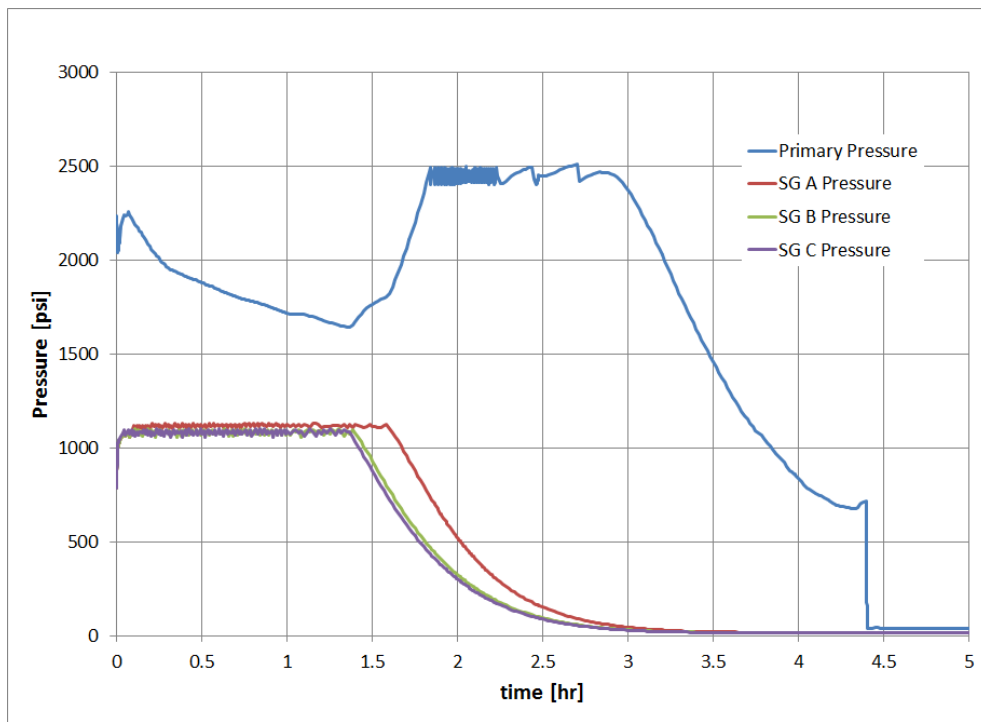
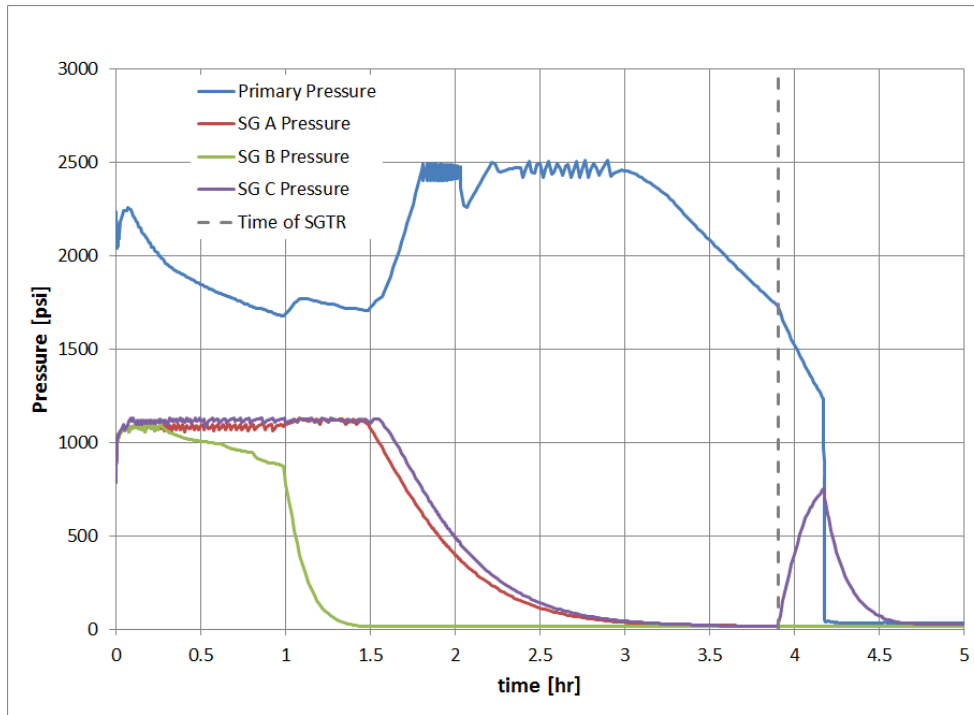


Figure 6-40 Primary and secondary pressure for realization 1151



**Figure 6-41 Primary and secondary pressure for realization 119**

### **SG Tube Thickness (TUBTHICK)**

The SG tube thickness was directly sampled from input and represents the effective thickness of damaged steam generator tubes. Since tube thickness goes into the calculation for hoop stress, the sampling of this thickness is effectively also sampling a stress multiplier on the creep equation. Half of the regression techniques for iodine and cesium identified this as the first or second most important parameter, and overall it was second in both tables by arithmetic average. The scatterplots in Figure 6-42 show a trend toward higher release fractions at lower tube thickness. This would be an expected result since a more damaged tube would reach creep failure earlier, allowing more time between the SGTR and hot leg creep rupture.

However, the most important aspect of this parameter is not captured in the regression of the magnitude of the releases, but is in the probability of an SGTR to occur. The sampled range of tube outer diameter was 0.0101 m to 0.0111 m, and with the exception of three minor outliers, there are no SGTRs with a sampled value greater than 0.0105 m (stress multiplier of 2.8) and 44 of 94 are lower than 0.0103 m (stress multiplier of 3.4). This is in good agreement with previous research on SGTRs [32].

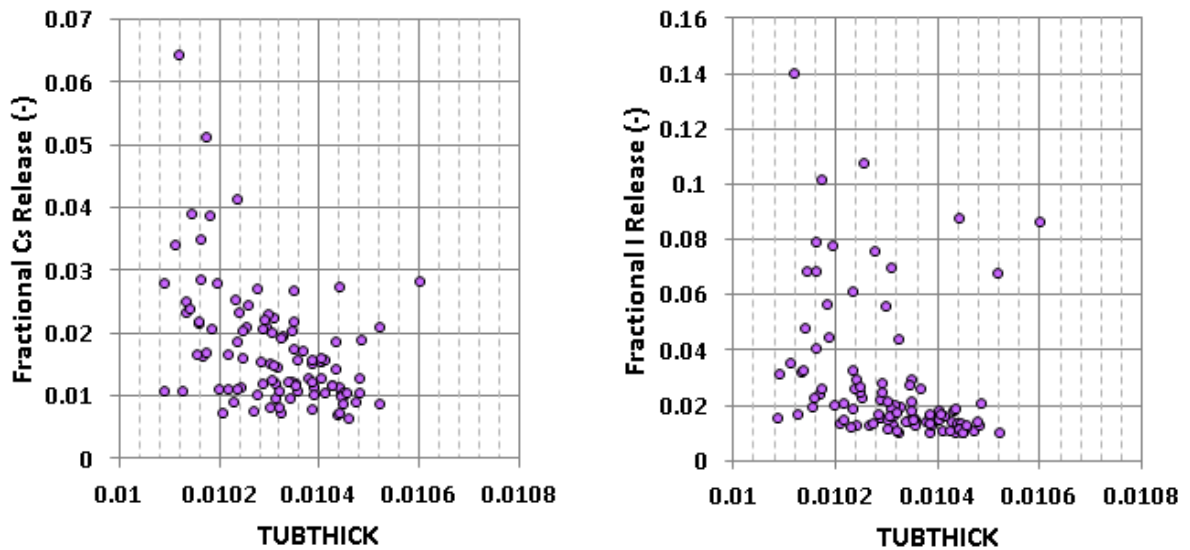


**Figure 6-42 Scatterplot of cesium and iodine release fractions versus steam generator tube thickness input values**

### SGTR Location (SGTRLOC)

The SGTR location for the secondary site rupture determines the location of the tube that ruptures in an SGTR. This was developed with the ARTIST parameter in Section 4. SGTR location is a direct input. Since the location of the SGTR determines the DF applied to the release, it was expected to be perhaps the most important parameter in cesium and iodine release fractions for SGTRs. However, it was only identified by the quadratic regression for cesium and iodine and was 10<sup>th</sup> and 8<sup>th</sup>, respectively, in the weighted list of contributors.

The SGTR location was plotted versus cesium environmental release fraction for all SGTR realizations (Figure 6-43). This plot shows that although there is a much larger range in location 7, the remaining locations have about the same range of releases. However, when looking at only SGTRs that have a secondary SV open fraction of 0.0 (Figure 6-44) to remove the effect of open fraction, there is a clear linearly higher trend of releases with changing location, except for the outliers in location 2. These scatterplots show that although SGTR location and consequential DF have an impact when all other factors are kept constant, other effects such as SV open fraction and timing of hot leg creep are more important influences on release fractions for all SGTR realizations. This explains why SGTR location had a limited importance in the regression results, compared to the expected importance.

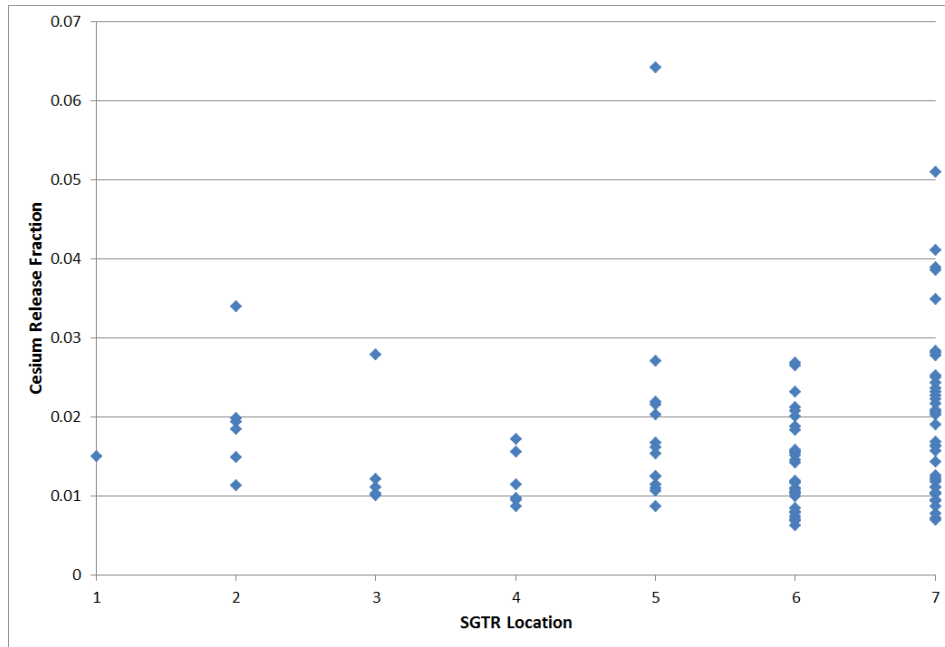


**Figure 6-43 Scatterplot of cesium release fraction versus SGTR location input values for all SGTRs**

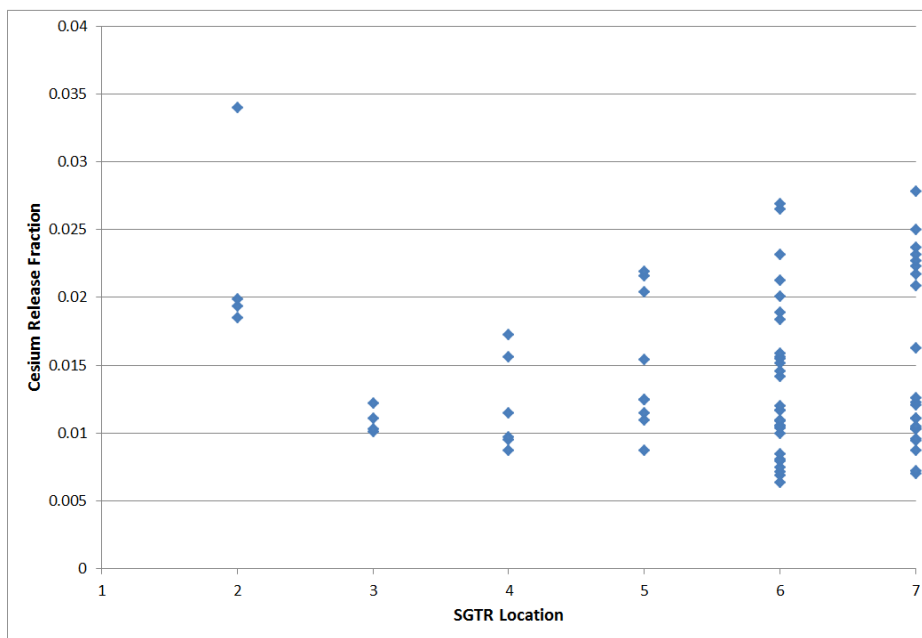


**Figure 6-44 Scatterplot of cesium release fraction versus SGTR location input values for SGTRs with a SV open fraction of 0.0**

### Hottest Tube Normalized Temperature (TUBETEMP)

The hottest tube normalized temperature parameter gives the normalized temperature for the hottest tube based on CFD results. The parameter is used, along with the actual inlet and outlet temperature calculated by MELCOR, to determine the temperature of the hottest tube at all

points in time. Since temperature is one of the primary inputs into the creep rupture formulation, this parameter was expected to contribute to whether or not an SGTR occurs. This parameter did not rank as important in the regression results for either cesium or iodine release, because during core damage, temperature rises so quickly that regardless of sampling, the necessary temperature will be reached in about the same time. The reason the temperature increases quickly is that while decay heat increases fuel temperature gradually, the exothermic oxidation reaction results in a much more rapid increase of fuel temperature up to the temperatures at which SGTRs occur. Figure 6-45 shows the maximum fuel and hottest tube temperature plotted on one axis, with creep damage fraction on the other. Creep occurs at a fraction of 1.0. Both realizations in the figure are EOC cases that experienced tube ruptures. In realization 356, the hottest tube was sampled at the lowest end of the parameter distribution, and in realization 441, was sampled at the highest end. There are minor differences in fuel temperature, possibly due to decay heat, but the differences in hottest tube temperature caused by the sampling are much more significant. For example, at 3.5 hours the fuel temperatures are 42 K different, but the hottest tube is 79 K hotter. Although it takes realization 356 20 minutes to catch up to realization 441 hottest tube temperatures, the difference in the timing of SGTR is only 5 minutes. This shows the exponential nature of creep damage accruing and explains why normalized hottest tube temperature is not a key parameter in release fractions.

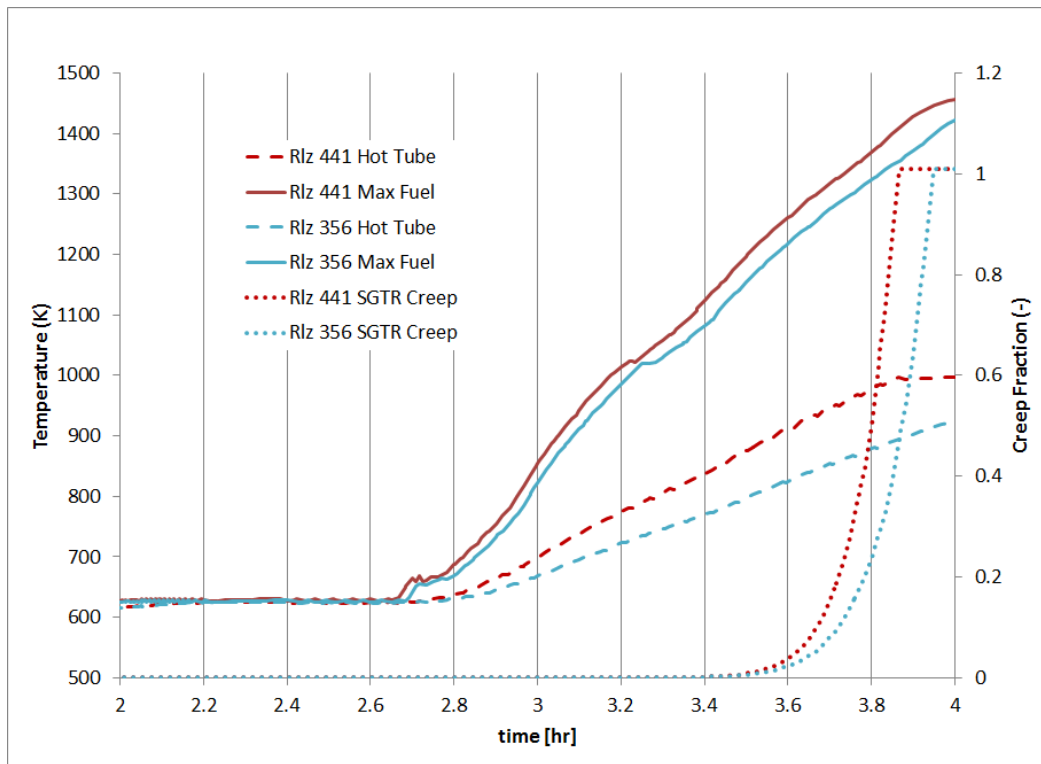


**Figure 6-45 Maximum fuel and hottest tube temperature, and creep damage fraction for realizations 356 (blue) and 441 (red)**

#### Other Parameters – Design Leakage, Dynamic Shape Factor, Time at Cycle

Design leakage is listed in Table 6-6 as the third most important parameter for iodine and in Table 6-7 as the seventh most important for cesium. However in both cases, there is essentially no individual contribution, but there is a large conjoint contribution identified by the quadratic

regression technique. The only other parameter with a large conjoint contribution for both regressions was SV open fraction. There is no technical justification for why the sampled values for design leakage and open fraction, primary or secondary, should have interplay. Because it was only identified by one regression technique, it appears to be an overfit to a limited number of realizations.

Dynamic shape factor and time at cycle were both important in non-SGTR realizations due to aerosol deposition and containment pressurization, respectively. They were both identified as a top six parameter by both regression analyses, although neither with a large contribution. Their presence implies that either there are minimal releases from containment after hot leg creep, or that there is deposition within the RCS before the rupture location and that time at cycle helps determine SGTR timing. Due to the relatively low contribution, no further investigation was performed.

SV status (indicating failure mode) had a medium contribution for cesium, but was only identified by the MARS regression technique, which did not identify open fraction as an important parameter. A review of supporting data, and the difference between MARS and the three other techniques, shows that SV status was very likely taken as a surrogate for SV open fraction. No other parameters had a large independent contribution to SGTR cesium and iodine environmental release fraction uncertainty, nor are there any other parameters that were expected to have a significant contribution.

#### **6.1.5.4 Hydrogen Regression Results**

One key result from the hydrogen regression analysis run for the SGTR realizations was that SV open fraction, which was the top contributor for non-SGTR realizations, was barely identified as a contributor. This is likely related to the fact that almost all open fractions are less than 0.4, not allowing a hydrogen trend to develop. The other two most important parameters from the non-SGTR realizations, effective melting temperature and time at cycle, are still the top two parameters. It was expected that there would be no changes since the rupture of a single tube does not cause primary depressurization and should have no impact on the core damage progression. The one major deviation appears explainable due to limited range of the open fraction parameter, and its contribution may have been overfit by advanced regression techniques.

#### **6.1.5.5 Time at Cycle Independent Results**

No time at cycle independent regressions were run for the SGTR realizations because there were not enough realizations in each to have meaningful results. Additionally, since time at cycle was not a dominant parameter for these results, it would not be masking any other important parameters.

#### **6.1.5.6 Timing and Other Effects**

The primary timing factor for SGTR, in terms of environmental releases, is the time between the SGTR and the hot leg creep rupture. During this period all releases from fuel are preferentially transporting to the environment through the tube rupture, and not into containment. Although some releases will still go through the SGs after hot leg creep, it is a lower percentage, and release magnitude is determined by the secondary SV open fraction, as described earlier.

Two SGTR realizations were chosen, from extensive review of the results. Each realization was an MOC run with the tube rupture occurring in the lower plenum (location N=7), and having RCP seal leakage of 21 gpm. Plots were made for primary and secondary pressure, maximum cladding temperature, and the creep fraction (creep occurs at 1) for both the hottest tube and the hot leg. The primary difference between the two is that in realization 243 (Figure 6-46) the primary RCS remains fully pressurized at the time of SGTR as no pressurizer SV sticks open, while in realization 751 (Figure 6-47) a pressurizer SV sticks open and the primary RCS is partially depressurized at the point of the SGTR. Iodine release fractions at 48 hours were 1 percent for realization 243, and 6.1 percent for realization 751.

For both realizations, the secondary is fully depressurized before the onset of SG tube creep by MSIV leakage in realization 243 and a stuck open secondary SV in realization 751. Additionally, since these are both MOC realizations, clad temperature is very similar for both. SG tube creep starts earlier for realization 751, partially due to differences in parameters like tube thickness and temperature, but also likely because the stuck open pressurizer SV drives hot steam from the core preferentially towards one loop, driving temperature increase in that SG earlier. The other key differences is that although core temperature is actually slightly higher at 4 hours in realization 751 than realization 243, hot leg creep fraction is a lower in realization 751 and increases a little slower. This is due to the fact that the primary is slightly depressurized in realization 751, and both pressure and temperature drive creep damage. Thus, the timing difference between SGTR and hot leg creep in these two realizations is partially due to differences in sampled parameters that directly impact SGTRs, such as tube thickness, but also different reactor conditions like pressure and temperature, which are also influenced by other sampled parameters.

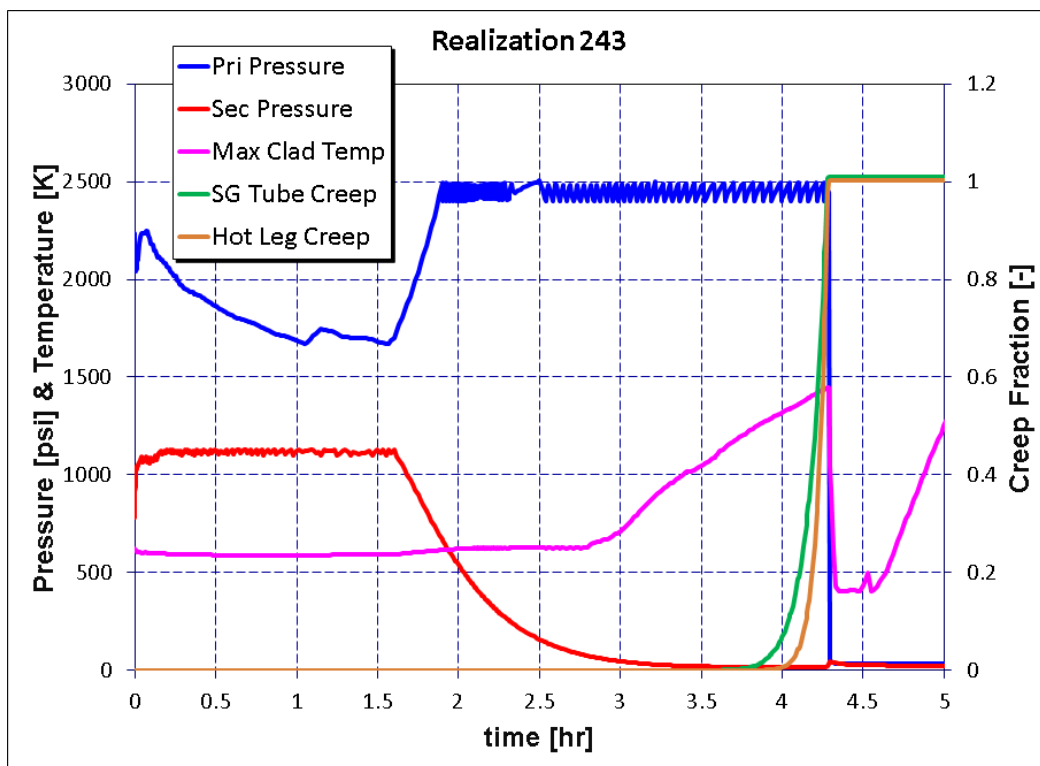
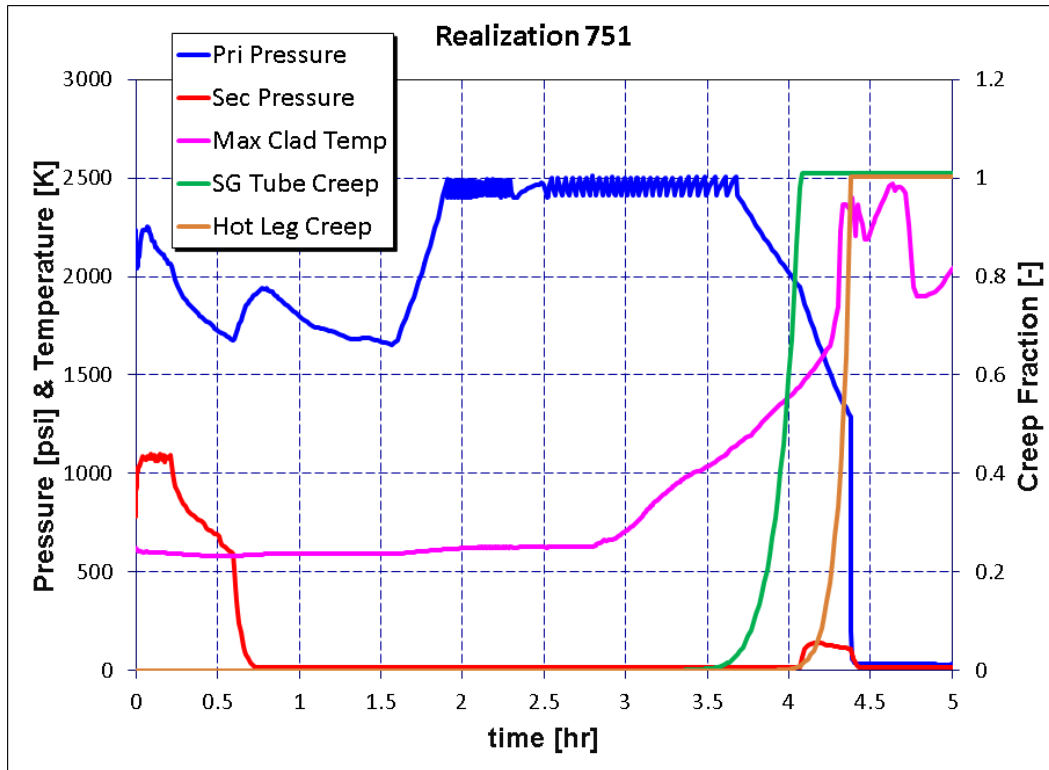


Figure 6-46 Pressure, temperature and creep fractions for Rlz 243



**Figure 6-47 Pressure, temperature and creep fractions for Rlz 751 with stuck open pressurizer SV**

The time of tube rupture and hot leg creep was extracted for each SGTR realization. The time difference has a minimum of 0.12 min, maximum of 143.8 min, mean of 28.1 min and standard deviation of 31.1 min.

### 6.1.5.7 Steam Generator Tube Rupture Conclusions

Environmental release fractions from SGTR realizations are 1 to 2 orders of magnitude larger than the remainder of the uncertainty realizations. A key result is the determination that SGTRs are both temperature and pressure induced. An SGTR will only occur when there is a significant pressure differential between the primary and secondary sides during fuel heat-up, leading to elevated hottest tube temperature. A direct comparison to the Surry SOARCA [3] STSBO with induced SGTR is not possible because of timing differences and differences in decontamination factors and flow areas on the secondary side, in addition to the significant model changes. The two most important parameters contributing to release fraction uncertainty are SV open fraction and tube thickness. The open fraction determines not only the pressure differential between primary and secondary, but also increases the flow area to the environment following an SGTR. Tube thickness acts as a stress multiplier on the creep equations and an SGTR required a stress multiplier of about 3 or higher. Two parameters that were expected to have a large impact, hottest tube temperature and SGTR location, did not contribute. This was due to the exponential nature of creep damage with any elevated temperature for hottest tube temperature, and the respectively greater contribution of open fraction for SGTR location. The timing of hot leg creep, in comparison to the SGTR timing, had a large impact on total releases, and has an average of 28 minutes. This timing is influenced by a number of different parameters, both affecting the conditions of the hottest tube and the general reactor system,

and did not show up directly in regression results. There were no significant differences for hydrogen production for SGTR realizations, other than the lack of open fraction.

### **6.1.6 Analysis of Select MELCOR Individual Realizations**

Additional insights related to accident progression can be obtained through investigation of single realizations. A set of single realizations was chosen for investigation in greater detail to identify phenomena driving the Cs and I releases to the environment and in-vessel hydrogen production. The set was selected from those realizations where early or late release was observed or low or high release magnitudes were observed. The realizations investigated, and the values of their sampled parameters, are identified in Table 6-10. Table 6-11 and Table 6-12 present the timing of key events, important occurrences and attributes, the magnitudes of Cs and I releases, and the amounts of hydrogen produced in-vessel in the realizations. The results discussed in this section represent only those few single realizations evaluated.

Several phenomena described below were found to influence the course of an individual calculation.

- Occurrence of an SGTR,
- Failure to close of a safety valve serving a steam generator that suffers an SGTR,
- Energetic hydrogen/carbon monoxide burns in containment,
- Steel containment liner yielding (tearing),
- Containment building rebar yielding and resulting concrete fracture,
- Timing of the PRT dryout,
- The number of successful cycles experienced by the system of 3 parallel safety valves serving the primary-side of the RCS,
- Chemisorption of Cs from CsOH into the stainless steel of the RPV internals,
- Fission product aerosol impaction in the tube bundle on the boiler side of a faulted steam generator,
- Ready dispersion of elemental gaseous iodine ( $I_2$ ), and
- Slowed core damage progression.

Several of the uncertain parameters considered in the UA, as their sampled values varied from calculation to calculation, were found to affect particular phenomenon in the list above, either promoting, discouraging, or influencing the strength of a phenomenon. The influential parameters were identified as:

- The amount of time spent by the reactor at power since refueling, i.e., a BOC, MOC or EOC state of the reactor core at the onset of the SBO,

- The melting temperature of the  $\text{UO}_2\text{-ZrO}_2$  eutectic,
- Containment leakage dependence on pressure,
- The fractional open position of an RCS secondary-side safety valve following a failure to close,
- The fractional open position of an RCS primary side SV following a failure to close,
- The pressure at which the containment steel liner will yield,
- The elevation within a steam generator tube bundle where an SGTR occurs,
- The fraction of total I inventory initialized in the fuel-cladding gap as gaseous, and
- The fraction of total Cs inventory initialized in the form of CsOH.

**Table 6-10 Select individual realization uncertain parameter values.**

Parameter	Value by realization											
	Base	9	48	50	66	236	495	562	667	856	965	1126
Secondary safety valve open area fraction given FTC	0.50	0.60	0.87	0.81	0.37	0.04	0.02	0.34	0.06	0.89	0.51	0.78
RCP seal leakage at seal failure (gpm)	21	21	21	21	21	21	21	21	21	182	21	21
SG tube thickness (mm)	0.791	0.867	0.884	0.617	0.979	0.545	0.472	0.334	0.334	0.996	0.807	0.781
Hottest normalized SG tube temperature	0.440	0.416	0.419	0.497	0.439	0.463	0.389	0.466	0.432	0.445	0.386	0.476
Zircaloy melt breakout temperature (K)	2350	2425	2383	2377	2392	2404	2374	2257	2367	2367	2379	2447
Melting temperature of UO <sub>2</sub> -ZrO <sub>2</sub> eutectic (K)	2479	2517	2472	2383	2433	2246	2620	2511	2314	2412	2288	2628
Molten clad drainage rate (kg/m-s)	0.2	0.35	1.11	0.44	0.23	0.18	0.67	1.38	0.86	0.36	0.35	0.33
Solid core debris radial relocation time constant (s)	360	762.9	546.9	609.3	653.7	870.8	340.3	133.8	183.1	217.8	390.3	573.1
Molten core debris radial relocation time constant (s)	60	75.8	21.8	47.2	50.0	34.3	77.9	30.0	90.4	32.0	57.6	50.1
Containment leakage at P/P <sub>d</sub> =1.0 (% vol/day)	0.54	1.00	0.60	0.89	0.10	0.30	0.80	0.80	0.89	0.40	0.20	0.70
Ratio of P/P <sub>d</sub> at containment steel liner yield	1.6	1.24	1.24	1.5	1.33	1.51	1.6	1.45	1.49	1.45	1.63	1.79
Direction of H <sub>2</sub> /CO burn propagation	horiz	down	down	down	up	up	horiz	down	up	down	up	up
Number of tube bundle grid spacers above an SGTR	7	5	7	5	5	1	7	7	5	7	3	7
Multiplier on containment steam condensation rate	1.4	1.18	1.04	1.3	1.46	1.9	1.47	1.39	1.72	1.84	1.38	1.23
Shape factor associated with aerosol setting	1.5	2	3.12	1.63	1.03	1.09	1.25	1.04	2.45	2.86	1.07	1.36
BOC, MOC or EOC state of reactor core	MOC	EOC	BOC	EOC	BOC	BOC	EOC	EOC	EOC	BOC	BOC	BOC
Percentage of I as I <sub>2</sub>	0.18	0.23	0.14	2.07	0.00	0.00	0.02	0.60	0.70	0.26	0.38	0.38
Fraction of Cs as Cs <sub>2</sub> MoO <sub>4</sub>	0.80	0.82	0.74	0.8	0.83	0.62	0.76	0.53	0.67	0.69	0.95	0.74

**Table 6-11 Select individual realization timing of key events, key occurrences/attributes, Cs and I releases and in-vessel H<sub>2</sub> production.**

Event	Timing by realization (hours:minutes)											
	Base	9	48	50	66	236	495	562	667	856	965	1126
STSBO – loss of all AC and DC electrical power, AFW unavailable	0:00	0:00	0:00	0:00	0:00	0:00	0:00	0:00	0:00	0:00	0:00	0:00
Reactor trips MSIVs close RCP seal leakage initiates at 21 gpm/pump	0:00	0:00	0:00	0:00	0:00	0:00	0:00	0:00	0:00	0:00	0:00	0:00
RCP seal failure	None	None	None	None	None	None	None	None	None	00:13	None	None
1 <sup>st</sup> SG safety valve failure to close	1:11	1:24	0:21	0:07	0:25	0:06	0:50	0:08	0:46	0:06	0:21	0:13
SG dry out	1:22	1:24	1:35	1:26	1:53	1:50	1:30	1:35	1:26	1:54	1:38	1:44
PRT rupture disk breaks	2:09	2:06	2:33	2:02	2:49	2:48	2:13	1:59	2:13	2:55	2:47	2:41
RPV water level reduces to TAF	2:40	2:36	3:08	2:29	3:28	3:25	2:44	2:42	2:44	2:38	3:25	3:17
RCS primary depressurization initiates consequential to a pressurizer SV failing to fully close at this time or earlier	3:00	3:35	4:22	2:16	4:46	5:13	None	2:57	3:41	None	3:59	4:09
First fission product gap release	3:22	3:26	4:30	2:58	4:59	4:48	3:36	3:26	3:32	4:32	4:29	4:31
SGTR	None	None	None	None	None	5:15	4:03	3:55	3:42	None	None	None
Hot leg nozzle rupture	4:28	4:09	5:48	4:27	5:57	5:25	4:09	4:10	4:11	5:27	None	5:52
1 <sup>st</sup> hydrogen burn	4:28	4:09	5:48	4:27	5:57	6:31	5:08	4:10	4:11	6:29	5:50	5:12
Accumulators discharge	4:28	4:09	4:55	3:13	5:57	5:26	4:09	4:10	4:11	5:27	5:06	4:49
RPV dry	5:33	7:17	11:24	7:45	10:13	10:04	7:37	7:29	6:29	11:00	3:59	4:09
RPV lower head breach	7:41	7:15	14:32	7:41	10:11	10:05	9:17	4:10	8:03	11:57	14:23	14:58
PRT dry	15:00	39:42	10:15	7:46	5:57	5:13	4:00	4:10	4:11	None	11:43	11:56
Containment pressure reaches design (45 psig)	25:01	20:18	36:26	19:08	47:59	None	21:58	26:42	23:43	42:54	None	38:54
Containment steel liner yields (and tears)	None	25:10	None	30:40	None	None	36:00	38:24	34:26	None	None	None
Containment rebar yields/concrete fractures	None	39:04	None	45:40	None							
End of calculation	48:00	48:00	48:00	48:00	48:00	48:00	48:00	48:00	48:00	48:00	48:00	48:00

**Table 6-12 Select individual realization timing of key events, key occurrences/attributes, Cs and I releases and in-vessel H<sub>2</sub> production.**

Key occurrences/ attributes	Value by realization											
	Base	9	48	50	66	236	495	562	667	856	965	1126
Combined actual number of successful cycles experienced by the 3-valve RCS primary side safety valve system	46	61	59	31	57	48	58	8	37	7	47	52
SGTR occurrence (Yes/No)	No	No	No	No	No	Yes	Yes	Yes	Yes	No	No	No
Containment steel liner yields and tears (Yes/No)	Yes	Yes	Yes	Yes	No	No	Yes	Yes	Yes	No	No	No
Containment rebar yields/concrete fractures (Yes/No)	No	Yes	No	Yes	No	No	No	No	No	No	No	No
In-vessel H <sub>2</sub> production (kg)	518	369	481	396	464	196	354	370	142	366	361	782
Fractional chemisorption of Cs	0.07	0.04	0.05	0.04	0.05	0.02	0.02	0.11	0.02	0.02	0.03	0.05
Time at PRT dry out (Early/Late)	Early	Late	Early	Early	Early	Early	Early	Early	Early	None	Early	Early
Time when noble gas release to the environment exceeds 1% (hr)	> 48:00	26:19	25:22	29:24	> 48:00	5:58	5:15	3:59	3:56	> 48:00	> 48:00	40:13
Fractional Cs release to the environment by 48 hr	0.0003	0.0023	0.0012	0.0009	0.0000	0.0151	0.0118	0.0510	0.0168	0.0003	0.0000	0.0002
Fractional I release to the environment by 48 hr	0.0007	0.0037	0.0014	0.0041	0.0000	0.0158	0.0156	0.1015	0.0255	0.0003	0.0001	0.0003
Cs mass released to the environment by 48 hr (kg)	0.0517	0.5766	0.1506	0.2174	0.0033	1.9417	2.9430	12.6820	4.1864	0.0403	0.0022	0.0201
I mass released to the environment by 48 hr (kg)	0.0087	0.0641	0.0121	0.0699	0.0003	0.1351	0.2676	12.6820	0.4373	0.0029	0.0007	0.0022

The comparisons described below between contrasting select individual calculations illustrate the influence of phenomena identified as important to the progression of the uncertainty calculations. Understood dependencies of the phenomena on the uncertain parameters are described for each of the realizations investigated.

RLZ 9 exhibits the largest fractional release of Cs to the environment of all the realizations that did not experience an SGTR. Interesting in this case is the late introduction at 39.7 hours of Cs compounds from the dried-out PRT as aerosols to the containment atmosphere. Coincidentally, this introduction occurred soon after the time when containment pressure reached the value associated with concrete rebar failure. Containment leakage increased markedly at this point and CsOH, CsI and Cs<sub>2</sub>MoO<sub>4</sub> aerosols introduced when the PRT dried out released to the environment. Figure 6-48, Figure 6-49 and Figure 6-50 show the distribution of Cs throughout the model, containment pressure and containment leakage rate for RLZ 9, respectively. For

comparison, the PRT dried out at 15 hours in the base UA calculation before containment liner yield and rebar failure. The aerosols introduced to the containment atmosphere at PRT dry out largely deposited in containment before increased leakage to the environment developed.

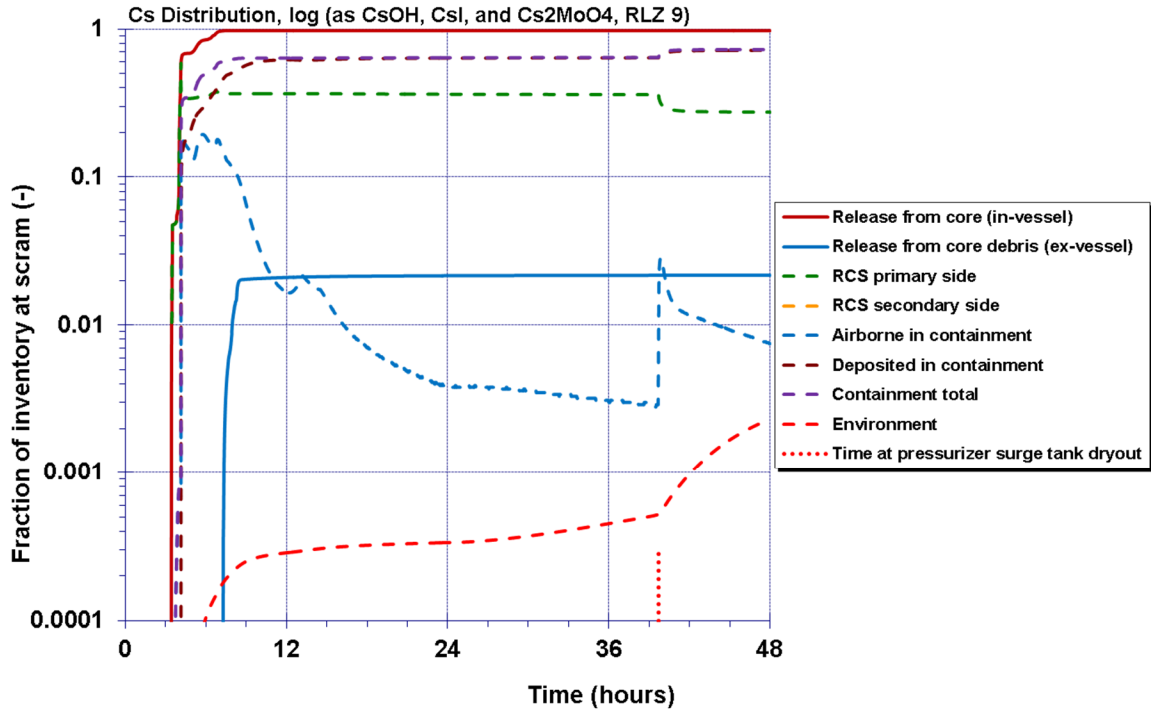


Figure 6-48 RLZ 9 Cs distribution

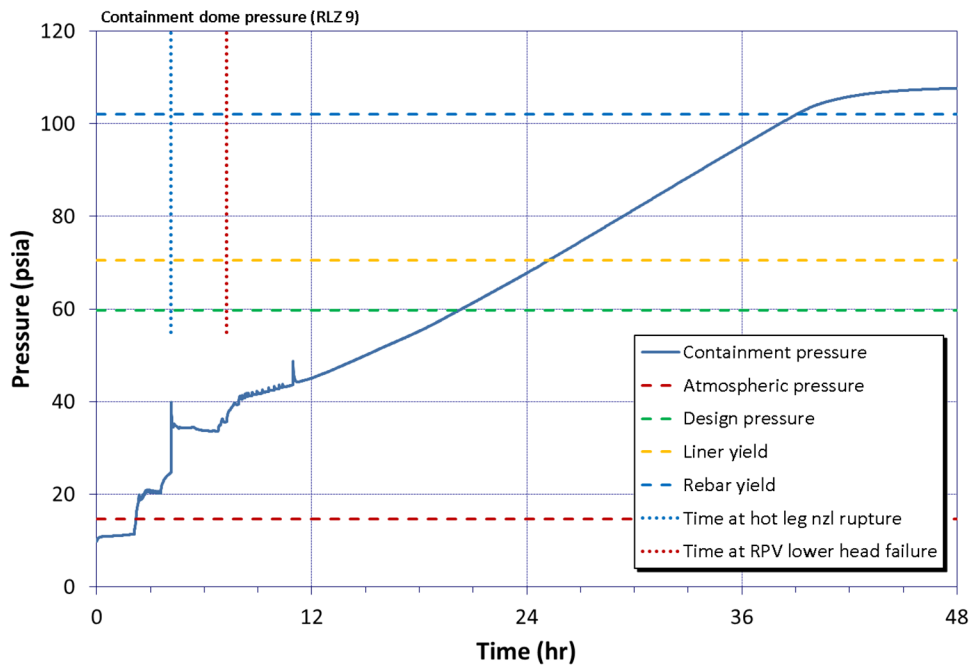


Figure 6-49 RLZ 9 containment pressure

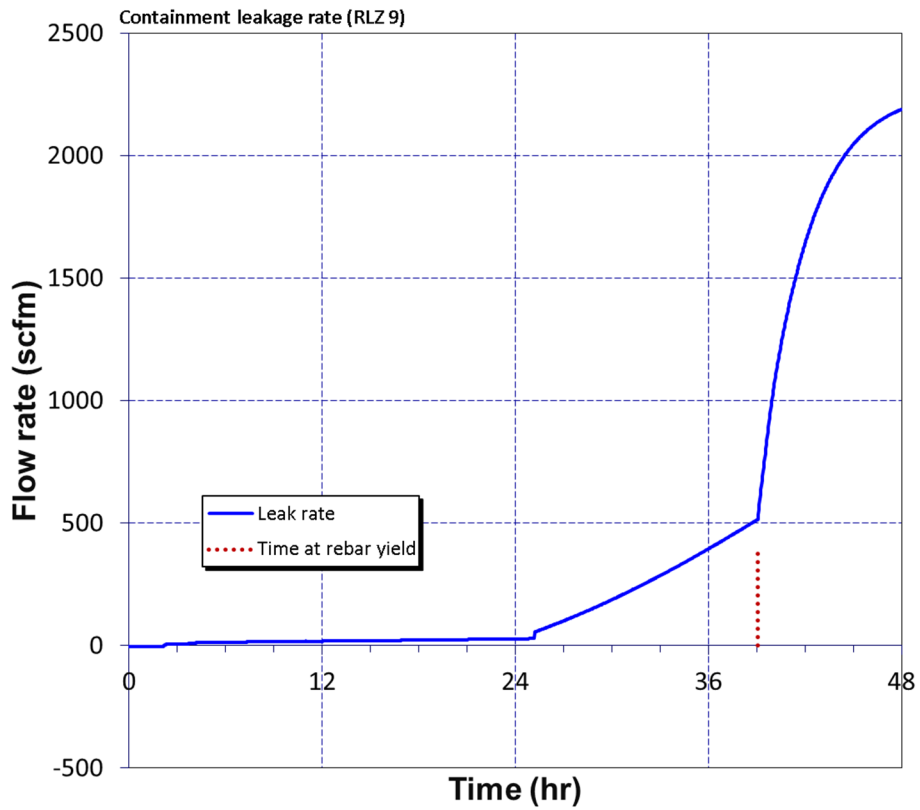
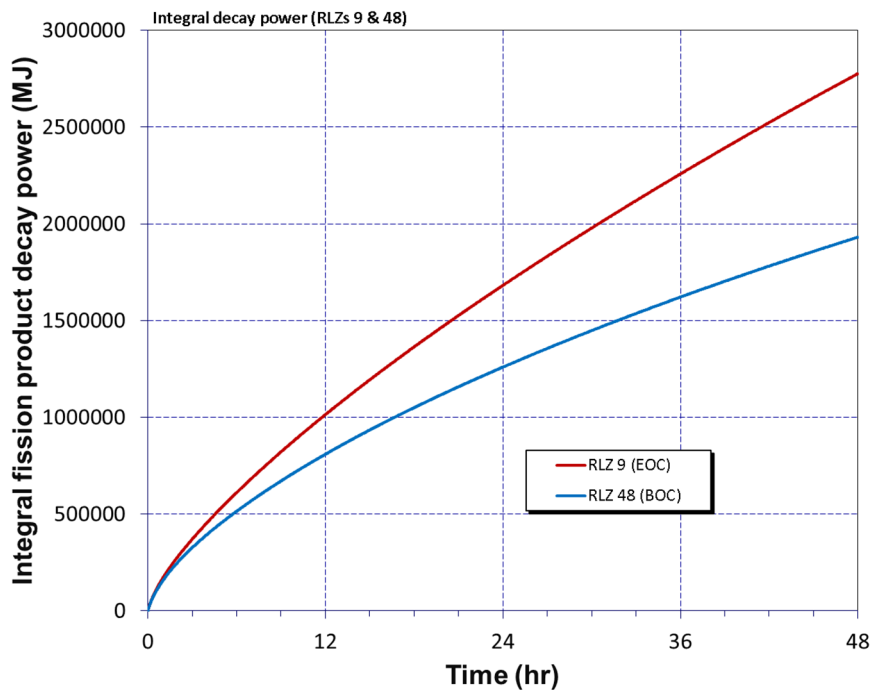


Figure 6-50 RLZ 9 containment leakage rate

RLZ 48 experienced the largest fractional release of Cs to the environment of all the realizations that did not experience an SGTR and where BOC fission product inventories were represented. Comparisons can be made between this case and RLZ 9 to identify dependencies attributable to when in the fuel cycle the accident initiates. RLZ 9 had EOC fission product inventories represented and the highest Cs release to the environment of all realizations that did not experience an SGTR. Figure 6-51 presents integral fission product decay power for the two calculations. Figure 6-52, Figure 6-53 and Figure 6-54 present containment pressure, temperature and leakage rate between the two calculations, respectively. The higher decay heat of EOC Case 9 relates to greater containment temperature and hence greater containment pressure. The greater pressure in turn relates to greater containment leakage eventually even failing the rebar in the reinforced concrete.



**Figure 6-51 RLZs 9 and 48 integral fission product decay power**

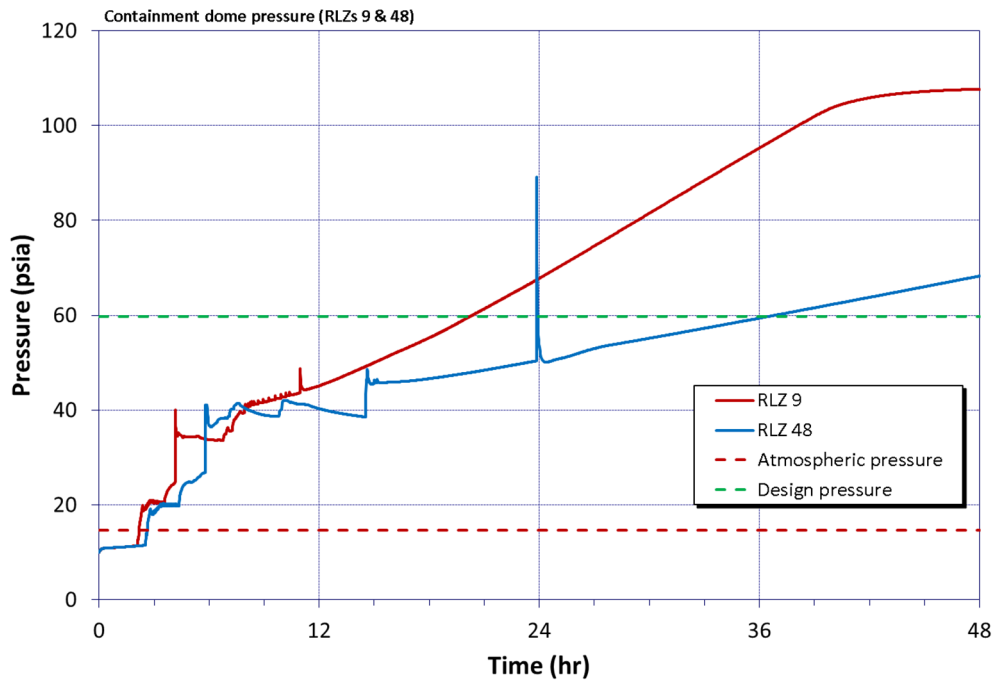


Figure 6-52 RLZs 9 and 48 containment pressure

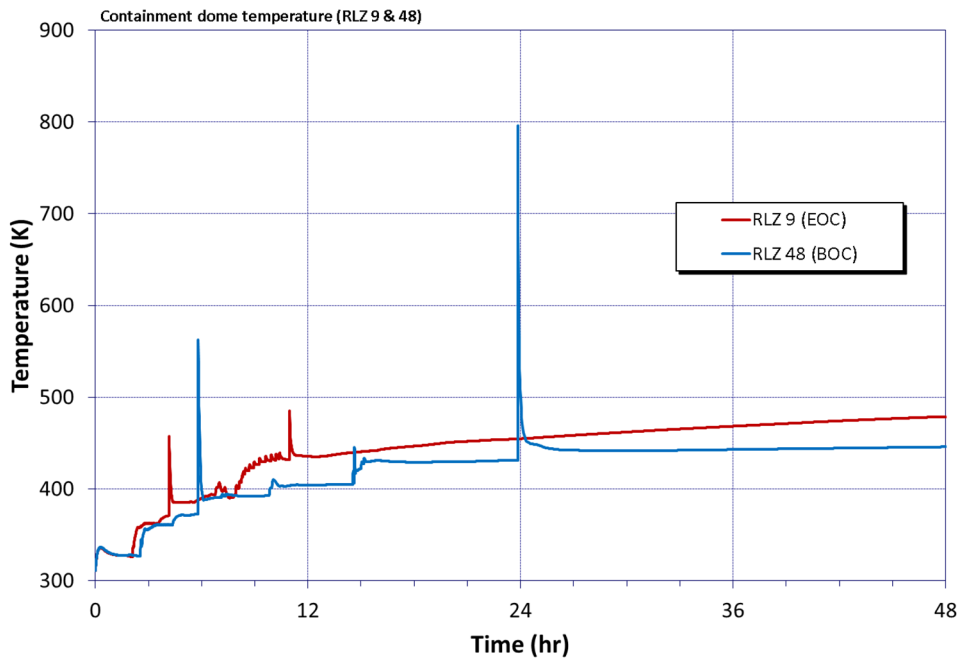
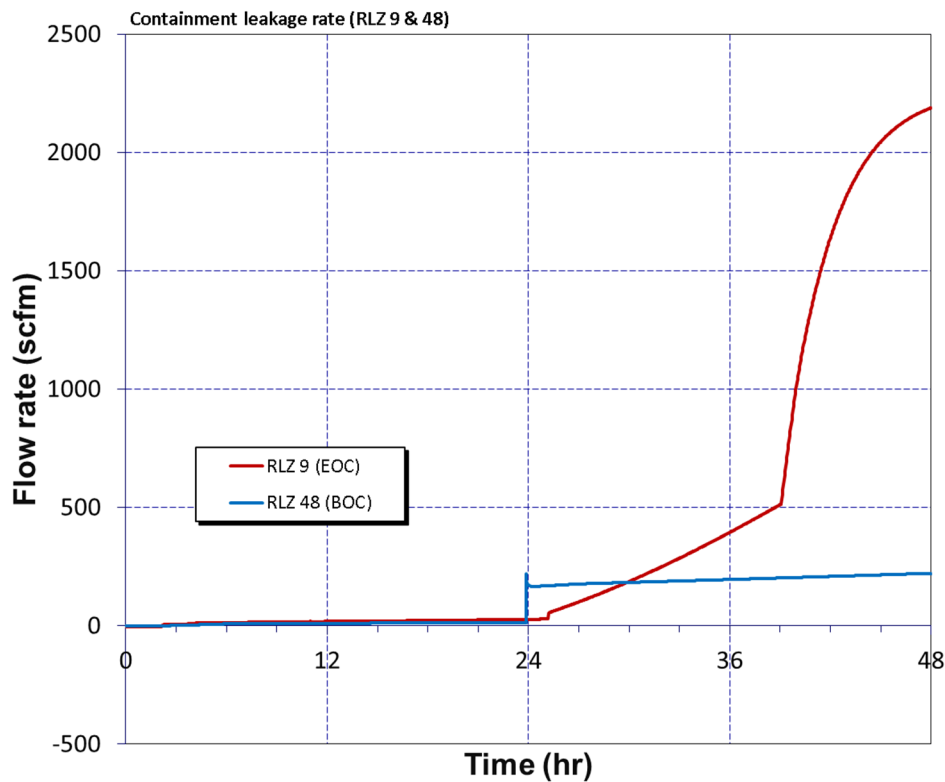


Figure 6-53 RLZs 9 and 48 containment temperature



**Figure 6-54 RLZs 9 and 48 containment leakage rate**

RLZ 965 contrasts with RLZ 9 in that it exhibits the smallest fractional release of Cs to the environment of all the realizations that did not experience an SGTR. The sampled values of several uncertain parameters contribute to this result, including:

- fission product decay power consistent with a BOC state of the reactor core,
- a small containment leakage rate of 0.20 percent vol/day at  $P/P_{\text{design}} = 1.0$ , and
- a large pressure requirement for tearing the steel containment liner plating of  $1.63 \times P_{\text{design}}$ .

Core damage was largely slowed in RLZ 965 due to the RCS pressure boundary remaining intact, with only a leaking unseated safety valve and leaking RCP seals, until the RPV lower head failed. There was no hot leg nozzle rupture in this calculation. Accumulator injection took place over hours rather than minutes. The RCS still largely depressurized before lower head failure.

Beyond the slowed core damage and associated late RPV lower head failure, the BOC state of the reactor core appeared to be a large contributor to the small release of fission products to the environment in RLZ 965. The reduced heating of the containment environment by BOC decay heat in this calculation compared to the heating by MOC or EOC decay heat in other calculations related to lower containment pressure over the 48 hour duration considered. Containment pressure in RLZ 965 did not reach containment design pressure much less the

pressure required to tear the steel containment liner or fail rebar in the concrete containment. All of these pressure thresholds were exceeded in RLZ 9. The lower pressure of RLZ 965 meant less leakage from the containment to the environment and hence less Cs release. Early PRT dry out in the calculation allowed time for the associated aerosols introduced to containment to settle before greater containment leakage at higher containment pressure ensued.

RLZ 50 exhibits the largest fractional release of I to the environment of all the realizations that did not experience an SGTR. The major contributors to the relatively large release are a high (2.07 %) percentage of elemental (gaseous) iodine specified as initially in the fuel-cladding gap and EOC decay heat defined for the reactor core. The gaseous iodine releases from the fuel early in core damage progression as fuel cladding bursts. No deposition mechanisms in the MELCOR calculation affect the gas as it vents from the RCS and resides in the containment atmosphere. Consequently, the full initial inventory of gaseous iodine becomes uniformly distributed throughout containment and releases to the environment as the containment leaks. Containment leakage is pronounced in the calculation due to the strong heating of the containment environment and the associated strong containment pressurization resulting from the high decay power of the EOC reactor core state. Masses of I released to the environment as gas and aerosol are of the same order of magnitude as can be seen in Figure 6-55.

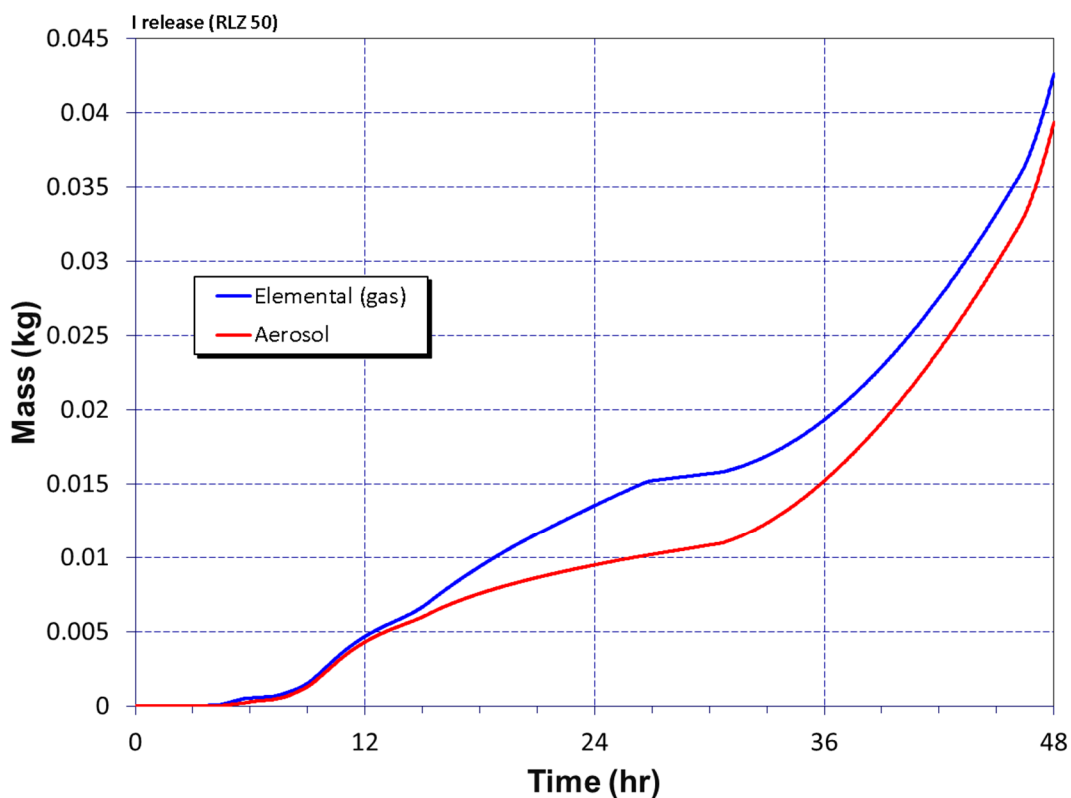


**Figure 6-55 RLZ 50 I release to the environment**

RLZ 66 contrasts with RLZ 50 in that it exhibits the smallest fractional release of I to the environment of all the realizations that did not experience an SGTR. The small release is attributable to no gaseous I being initialized in the core, BOC decay heat, and small

containment leakage being specified. RLZ 50 had a relatively large amount of gaseous I initialized, EOC decay heat, and medial containment leakage specified. Containment leakage to 48 hours differed dramatically between the calculations as can be seen in Figure 6-56.

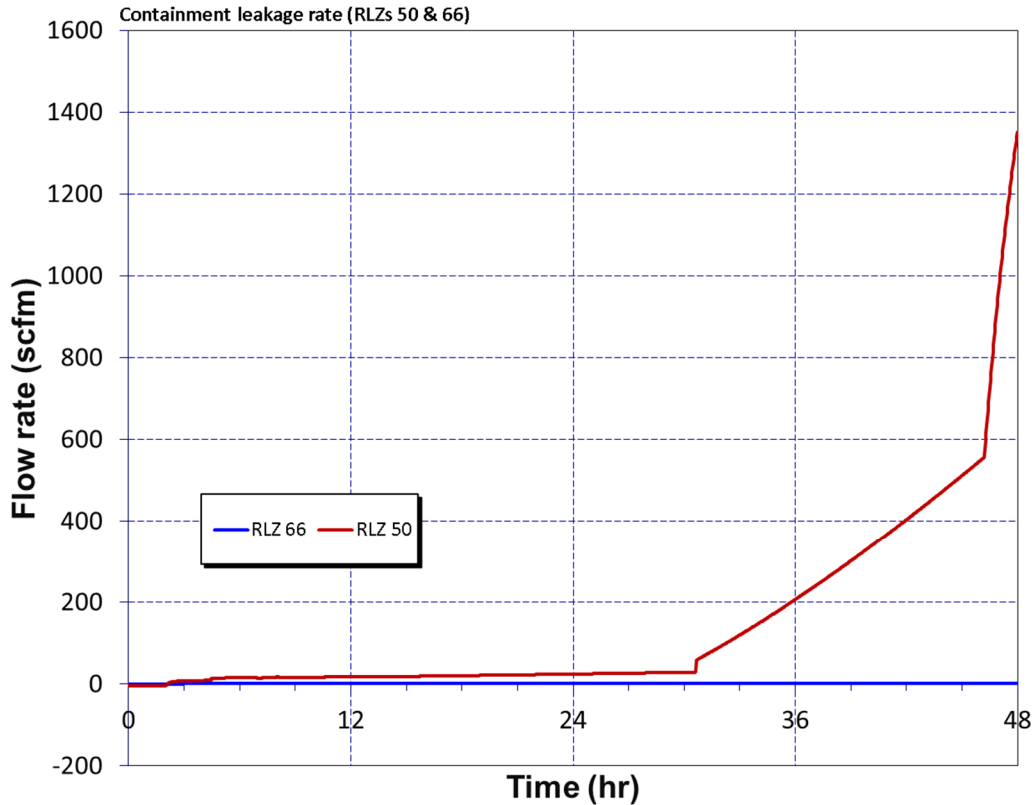


**Figure 6-56 RLZs 50 and 66 containment leakage rate**

RLZ 495 experienced an SGTR low in the SG-B tube bundle and an SG-B safety valve FTC but with a small open fraction (0.02). The realization resulted in a medial Cs release among the realizations that experienced an SGTR and was singled out as the reference SGTR case for which to compare other SGTR cases.

RLZ 236 experienced an SGTR high in the SG-B tube bundle and an SG-B safety valve FTC but with a small open fraction (0.04). Results of this realization were compared to those of RLZ 495 to illustrate the influence on fission product release to the environment of differing degrees of aerosol deposition in the affected SG. Table 6-13 presents a comparison between the two calculations where differences are evident in the DFs associated with aerosol deposition in the tube bundles (on the boiler sides) and steam separators and driers. DFs are included separately for the CsOH, CsI and Cs<sub>2</sub>MoO<sub>4</sub> radionuclide classes. DF is consistently higher in RLZ 495 where the SGTR was low in the tube bundle which forced aerosols to negotiate the full vertical extent of the bundle in their bypass of containment.

**Table 6-13 Comparison of boiler-side aerosol deposition in a steam generator in the event of an SGTR high or low in the tube bundle.**

RLZ 495 - SGTR low in tube bundle								
Deposited in faulted SG (kg)			Released thru the SGTR to the environment (kg)			Associated DF		
CsOH	CsI	Cs <sub>2</sub> MoO <sub>4</sub>	CsOH	CsI	Cs <sub>2</sub> MoO <sub>4</sub>	CsOH	CsI	Cs <sub>2</sub> MoO <sub>4</sub>
1.3178	0.7467	7.7048	1.3890	0.5275	2.1760	1.95	2.42	4.54
RLZ 236 - SGTR high in tube bundle								
Deposited in faulted SG (kg)			Released thru the SGTR to the environment (kg)			Associated DF		
CsOH	CsI	Cs <sub>2</sub> MoO <sub>4</sub>	CsOH	CsI	Cs <sub>2</sub> MoO <sub>4</sub>	CsOH	CsI	Cs <sub>2</sub> MoO <sub>4</sub>
0.3813	0.1353	1.0664	0.7951	0.2736	1.7310	1.48	1.49	1.62

RLZ 562 experienced an SGTR low in the SG-B tube bundle and an SG-B safety valve FTC but with a significant open fraction (0.34). Results of this realization were compared to those of RLZ 495 to illustrate the influence on fission product release to the environment of differing degrees to which a safety valve on the faulted SG remains open after failing to close. Table 6-14 presents a comparison between the two calculations where differences in fractional release of CsOH, CsI and Cs<sub>2</sub>MoO<sub>4</sub> to the environment are evident. While releases associated with containment leakage are comparable between the calculations, total leakage to the environment is substantially greater in RLZ 562, at least in the case of CsOH and CsI. Fractional releases of CsOH, CsI and Cs<sub>2</sub>MoO<sub>4</sub> are 4.45, 6.59 and 1.08 times greater in RLZ 562, respectively. These greater releases identify an intuitive influence on the degree to which a safety valve in the faulted SG remains open after failing to close, whereby a more open condition relates to larger releases.

**Table 6-14 Cs release via containment leakage and containment bypass in RLZs 495 and 562.**

SGTR case	Containment leakage (fraction)			Containment bypass leakage (fraction)			Total leakage (fraction)		
	CsOH	CsI	Cs <sub>2</sub> MoO <sub>4</sub>	CsOH	CsI	Cs <sub>2</sub> MoO <sub>4</sub>	CsOH	CsI	Cs <sub>2</sub> MoO <sub>4</sub>
RLZ 495 – insignificant (0.04) faulted SG safety valve FTC open fraction	4.14E-04	4.98E-04	2.75E-04	1.88E-02	1.47E-02	7.96E-03	1.92E-02	1.52E-02	8.24E-03
RLZ 562 – significant (0.34) faulted SG safety valve FTC open fraction	2.85E-04	4.67E-04	1.13E-04	8.50E-02	9.95E-02	8.81E-03	8.53E-02	1.00E-01	8.92E-03

RLZ 48 exhibited the earliest release of a cumulative 1 percent of the initial noble gas inventory in the core to the environment of all realizations that did not experience an SGTR. Interesting with respect to this timing is that the values of uncertain parameters specified in RLZ 48 do not suggest that an early release would occur, and it likely would not have but for a particularly energetic hydrogen/carbon monoxide burn that increased containment pressure sufficiently to tear the steel containment liner. Figure 6-57 shows the coincidence of a marked increase in containment leakage rate and an energetic hydrogen/carbon monoxide burn approximately 24 hours into the calculation. It is this tear in the containment liner that facilitated the early release of noble gas to the environment.<sup>15</sup>

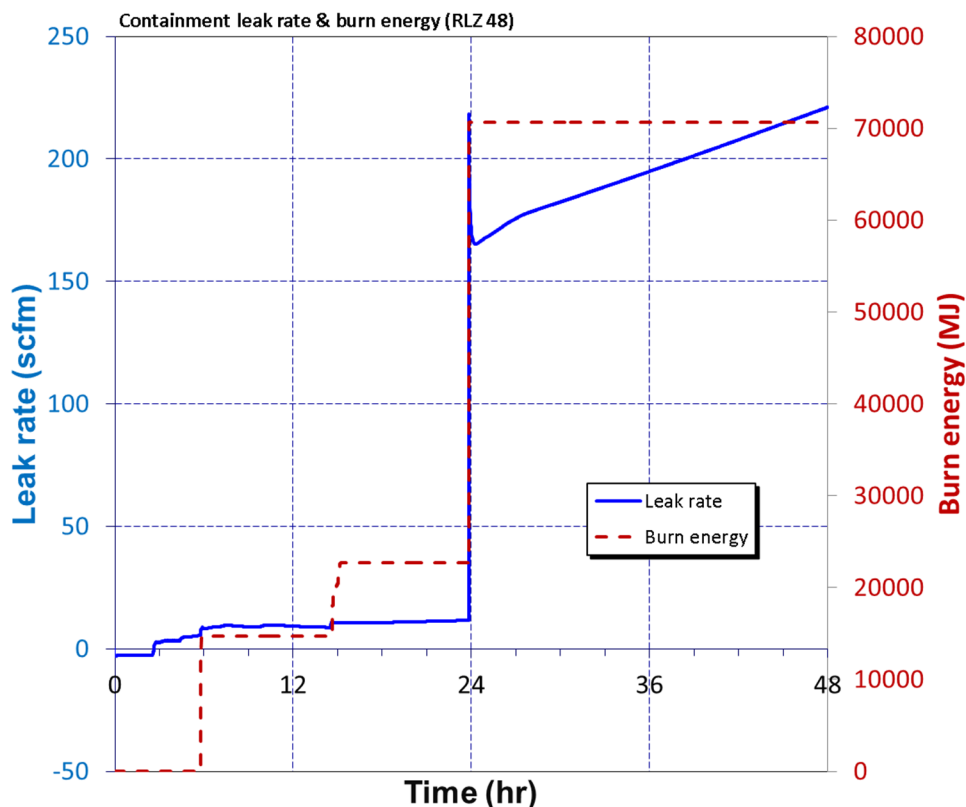


**Figure 6-57 Containment leak rate and burn energy in RLZ 48**

RLZ 856 did not release a cumulative 1 percent of the initial noble gas inventory to the environment within the 48 hour duration. This was the case for 162 realizations. RLZ 856 did not include an SGTR. No single uncertain parameter seems to be responsible for the late

<sup>15</sup> During the review of the individual realizations, an error was identified in the UA lean limit hydrogen combustion modeling (see Appendix A.2.4.7 for a description). The UA lean ignition logic did not properly enforce the steam inerting threshold. Considering the stoichiometric requirements of adequate oxygen and hydrogen, the model could allow ignition at 4 percent to 7 percent higher steam concentrations than intended. The bulk control volume steam concentration in Realization 48 was in the steam inerted range during the burn at 24 hours. A review of the UA realization release signatures suggested that only two realizations were affected. Due to uncertainties in non-uniform gas distributions, ignition is possible but considered very unlikely (i.e., requires gas non-uniformity and a strong ignition source for lean and wet conditions).

release in this calculation. Two parameters appear to be important, including a BOC fission product inventory (and associated decay heat) and restrictive containment leakage. Phenomena that appear important are no steel containment liner tear, and no rebar failure/containment concrete fracture.

The low decay heat associated with the BOC fission product inventory is responsible for the intact integrity of containment to 48 hours in that the containment environment heats and pressurizes slower.

Interesting in RLZ 856 is that a large 182 gpm leakage per pump at 13 min was specified for the uncertain pump leakage parameter but the time for water level to drop to the top of active fuel (TAF) differed little from that in the base calculation which had leakage of 21 gpm per pump. This is true even though the 3-safety valve system serving the RCS primary side failed open after only 7 cycles as opposed to the base calculation which failed open after 46 cycles. It is possible that the increased leakage in RLZ 856 caused enough depressurization that the 7 cycles took much longer than the first 7 cycles in the base case, but regardless it was expected that there would be a noticeable difference in time to TAF.

RLZ 1126 experienced the most in-vessel hydrogen production of all the realizations. In contrast, RLZ 667 experienced the least in-core hydrogen production of all the realizations. Most of the uncertain parameters can be ruled out as influential here based on established dependencies leaving the following as possible contributors to the variance seen in the amount of hydrogen produced in-vessel through the oxidation of zircaloy and steel:

- zircaloy melt breakout temperature,
- melting temperature of  $\text{UO}_2\text{-ZrO}_2$  eutectic,
- molten clad drainage rate,
- solid core debris radial relocation time constant,
- molten core debris radial relocation time constant, and
- BOC, MOC or EOC state of the reactor core at the onset of the SBO.

The value of each of these parameters varies significantly between RLZs 667 and 1126, making it difficult to ascertain the individual importance by comparing these two calculations alone. The regression analysis identified the melting temperature of the  $\text{UO}_2\text{-ZrO}_2$  eutectic and the BOC, MOC or EOC state of the reactor core as important to hydrogen production. Not included in the above list are the uncertain parameters associated with RCS primary-side safety valve operation, i.e., the:

- number of cycles (flowing vapor) to valve failure to open or failure to close,
- number of cycles (flowing liquid) to valve failure to open or failure to close,
- elevated temperature at which a safety valve will fail to close, and the
- fractionally open position a valve would have given that it failed to close.

A dependency materialized in the UA calculations, whereby hydrogen production varied dependent on the function of the 3 parallel safety valves on the pressurizer serving to vent the primary side of the RCS. An aggregate parameter that effectively embodies all of the uncertain parameters associated with operation of the pressurizer safety valves is the number of successful cycles experienced by the 3-valve system. Figure 6-58 illustrates this dependence wherein an association can be seen between the number of successful cycles experienced by

the 3-valve system and the amount of hydrogen produced – more cycles leading to less hydrogen production.

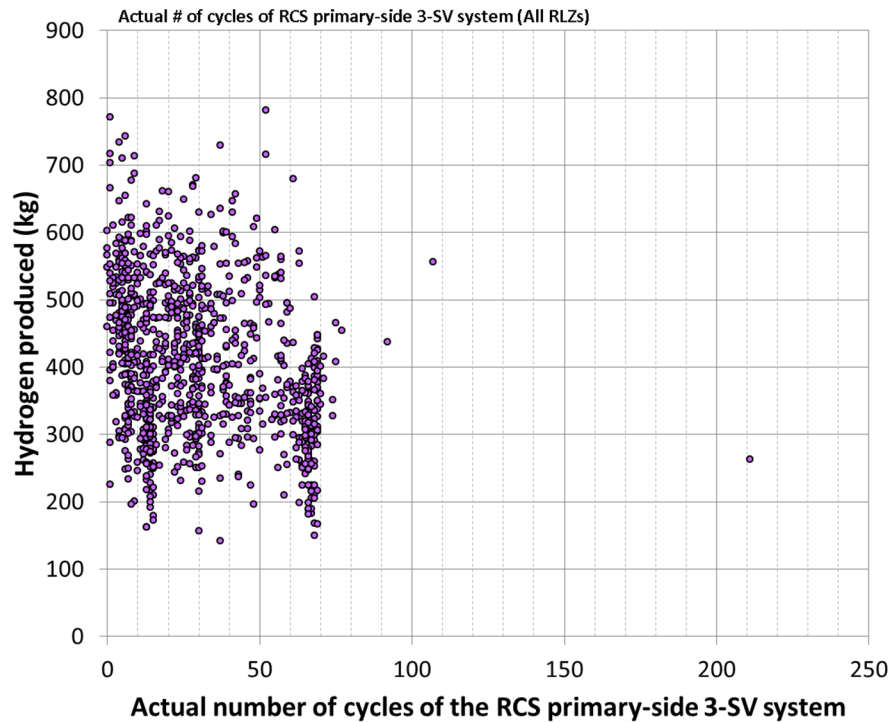


**Figure 6-58 In-vessel H<sub>2</sub> production versus actual number of cycles of the RCS primary-side 3-safety valve system**

Important to realize in considering the actual number of cycles experienced by the pressurizer 3-safety valve system is this aggregate parameter is not the same number-of-cycles parameter investigated in the regression analyses. That parameter is an estimate of cycles to failure based on input considerations (i.e., stochastic failure rate) and it often differs largely from the actual number of cycles to failure experienced, due to the stochastic modeling and physical evolution of the reactor system (i.e., primary system pressure). Negligible importance is identified in the regression analysis on the estimated cycles to failure with respect to the metric of in-vessel hydrogen production. Importance is instead identified on failed open or failed closed status and fractional open area. These conditions are all embodied in the actual number of safety valve system cycles. For example, if the first valve of the 3-valve system fails to close but remains only slightly open, pressure relief moves up to the second valve and a successful cycle is counted for the system. If on the other hand the first valve fails fully open, the system depressurizes, valve cycling ends and no further cycling counts are registered.

The parameters judged to be important with respect to in-vessel hydrogen production are:

- The melting temperature of the UO<sub>2</sub>-ZrO<sub>2</sub> eutectic – higher temperatures relating to greater production per regression analysis and single-realization comparisons.

- The BOC, MOC or EOC state of the reactor core at the onset of the SBO – longer burnup state relating to less production as seen in scatter plots and suggested by single-realization comparisons.
- The number of cycles experienced by the RCS primary-side safety valves (on the pressurizer) as a system of 3 valves – more cycles relating to less production.
- Speciation of Cs as predominantly CsOH or Cs<sub>2</sub>MoO<sub>4</sub> looked to be important generally in the UA calculations in that significant chemisorption of Cs from CsOH occurred. The chemisorption took place in the reactor vessel where Cs was stripped from CsOH vapor and seized by stainless steel. Once chemisorbed, the Cs was immobile and unavailable for release to the environment. Chemisorbed Cs amounts in the select individual realizations are reported in Table 6-10.

### 6.1.7 MELCOR Analysis Extended to 72 Hours

In the base uncertainty analysis, all MELCOR realizations were run to 48 hours. An analysis of selected realizations was also performed to evaluate physical effects that impact environmental release fractions, particularly containment failure, that might occur beyond 48 hours. The additional analysis included extending the MELCOR calculations for 9 individual MELCOR realizations to 72 hours. The realization numbers and the basis for selecting each are provided in Table 6-15. For each individual case, containment pressure, containment leakage rate, ablation depth, and iodine and cesium distributions are plotted.

**Table 6-15 72 hour individual cases.**

#	Realization #	Motivating factor
1	Base Case	The base case is the updated best estimate run described in Section 5.1.1.
2	965	Minimal environmental releases at 48 hours (this case had the lowest cesium release fraction and near lowest iodine). Calculation will identify if these increase by 72 hours.
3	243	SGTR occurring very close to hot leg creep. The 72 hour calculation will show how release fractions change with both pathways open at about the same time.
4	14	SGTR occurring long before hot leg creep. The 72 hour calculation will show how release fractions change with a large timing gap between these events to be compared against #3.
5	S32*	SGTR with no hot leg creep. The 72 hour calculation will show how much release fractions increase when only a bypass flow path is available to compare against #3 and #4.
6	19	Containment pressure near rebar yield point. The 72 hour calculation will show if there is a jump in release fractions when this increased failure point is reached.
7	53	Containment pressure that has plateaued (this case has very low sampling of CFC). The 72 hour calculation will show whether release fractions continue to increase long after the rebar yield point is reached and pressure stabilizes and then starts to decrease.
8	1017	BOC with highest 48 hour pressure (this case had high sampling of decay heat but only reached design pressure at 48 hours). The 72 hour calculation will show whether containment pressure will reach liner plate yield for a BOC realization at 72 hours.
9	9	Very late PRT dry-out (39 hours). The 72 hour calculation will show whether release fractions continue to increase if PRT dry-out, which re-introduces entrained fission products back into the atmosphere, occurs after containment failure.

\* There was no realization in the base uncertainty analysis that included an SGTR with no hot leg creep. This realization was selected from the number of tubes sensitivity and included the failure of 5 tubes.

## Base Case

The base case realization included the updated parameter values for each of the uncertain parameters with MOC average decay heat. By 48 hours containment pressure reached the liner yield point, but not rebar yield as shown in Figure 6-59. There is a large increase in containment leakage rate once the liner yield point is reached, as shown in Figure 6-60. The pressure and leakage continue to increase uniformly until about 58 hours, at which point pressure reaches the rebar yield point, and there is another significant increase in leakage rate. The containment pressure trend quickly turns over and reaches a plateau, although there is no pressure decrease by 72 hours.

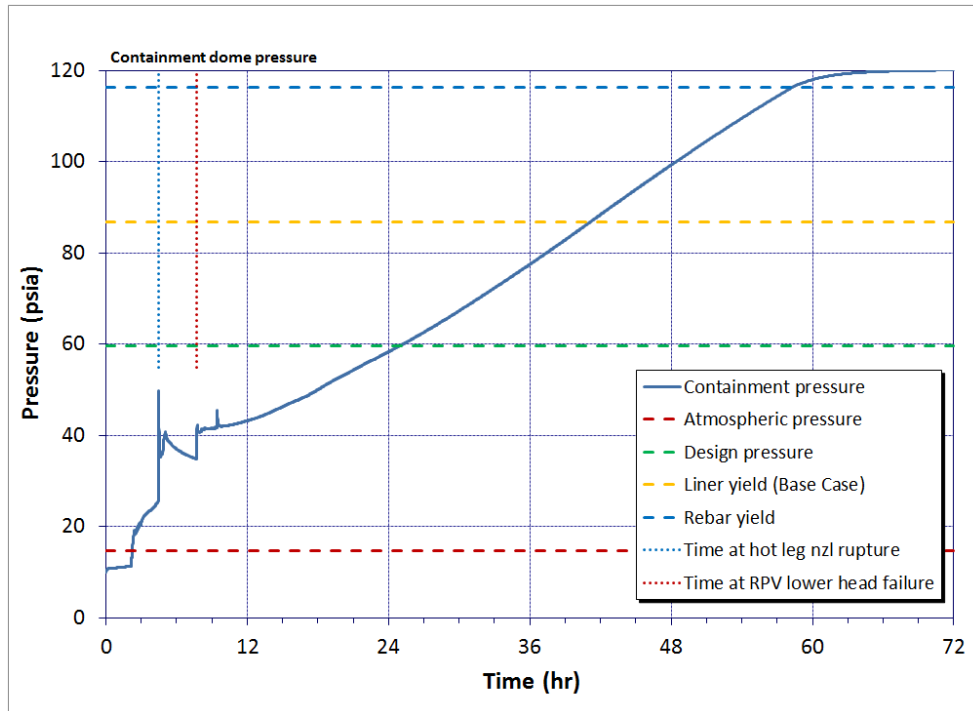
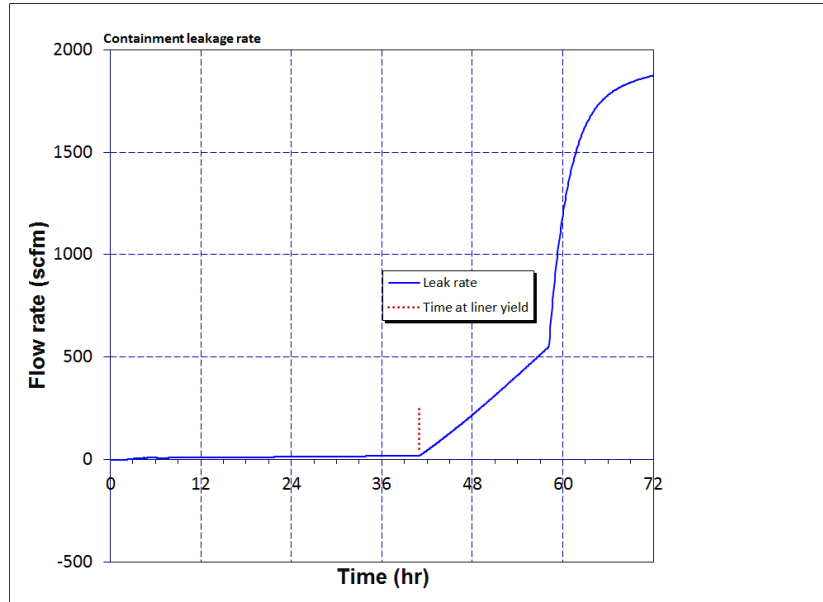
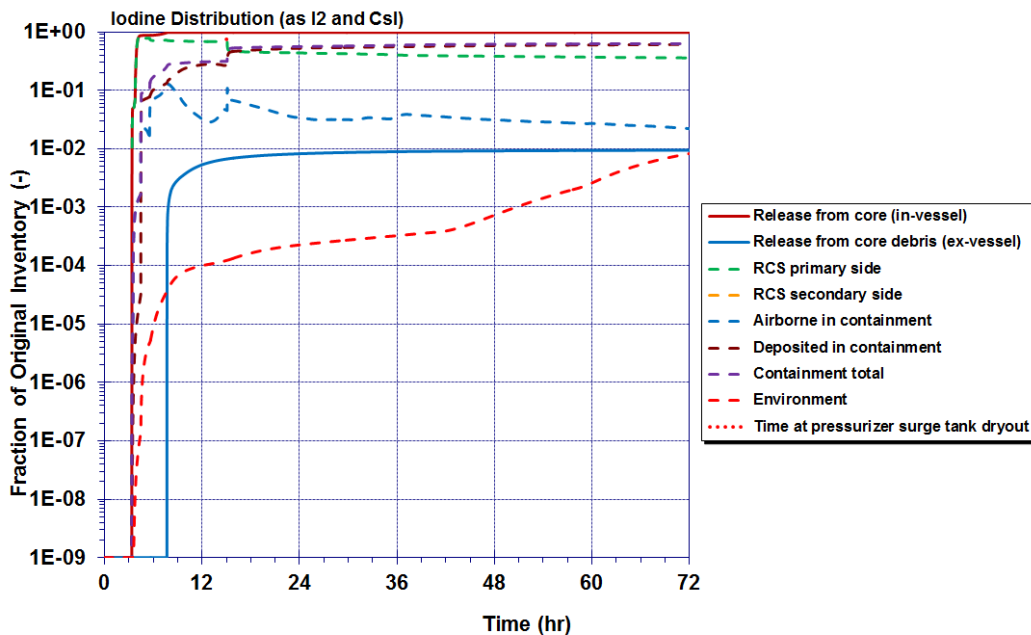


Figure 6-59 Base case containment pressure



**Figure 6-60 Base case leakage rate**

The iodine distribution does not change significantly from 48 to 72 hours as shown in Figure 6-61. There was a slope change when the liner yield point was reached at approximately 42 hours but no corresponding increase when rebar yield is reached. Even without a slope increase there is an order of magnitude total increase in iodine release fraction from 48 to 72 hours, with the total at 72 hours at 1 percent without a noticeable asymptote. Cesium showed the same general behavior, with a 72 hour release fraction of about 0.4 percent.



**Figure 6-61 Base case iodine release fractions**

## Realization 965

Even at 72 hours, containment pressure never reached liner yield in this realization, as shown in Figure 6-62. Environmental releases of iodine and cesium leveled out by 48 hours and there are only minor increases to 72 hours.

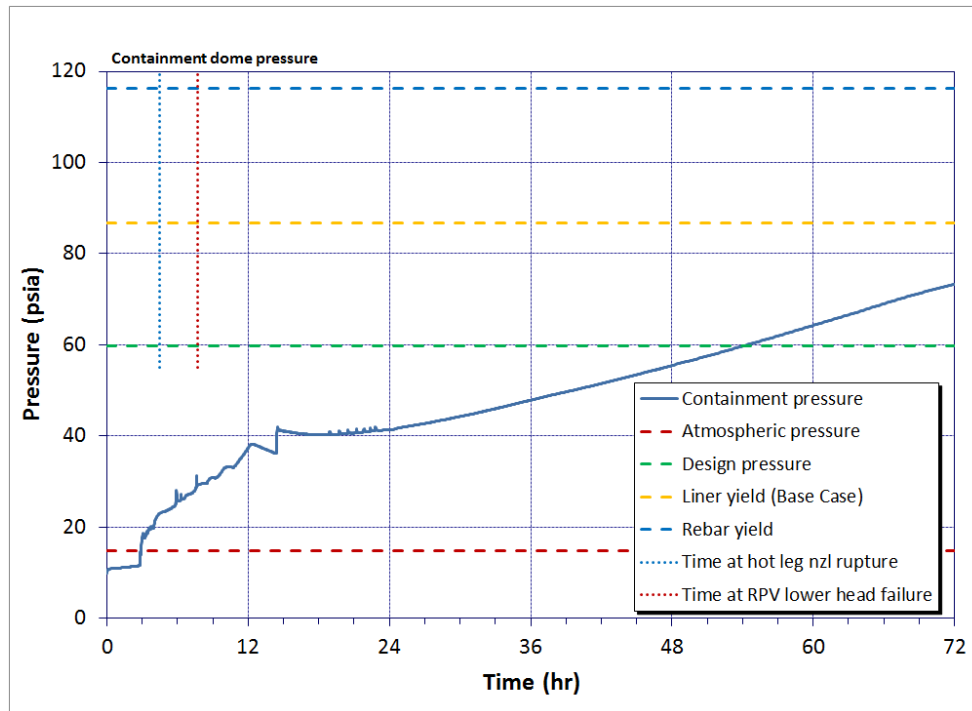


**Figure 6-62 Realization 965 containment pressure**

## Realization 243

In this realization, the SGTR occurred very close to the time of hot leg creep, and environmental releases of cesium and iodine had leveled out well before 48 hours, as shown in Figure 6-63. After 48 hours, containment pressure continues to increase and reaches the rebar yield point; however there is no corresponding increase in environmental release fractions. The only noticeable change in the cesium distribution in Figure 6-64 is that the amount in the containment atmosphere decreases throughout the transient, but the location of the corresponding increase is visually unclear. The conclusion is that the hot leg creep stops large environmental releases through the SGTR flow path, but the releases that did occur during that small time period still dwarf any additional releases from late containment failure.

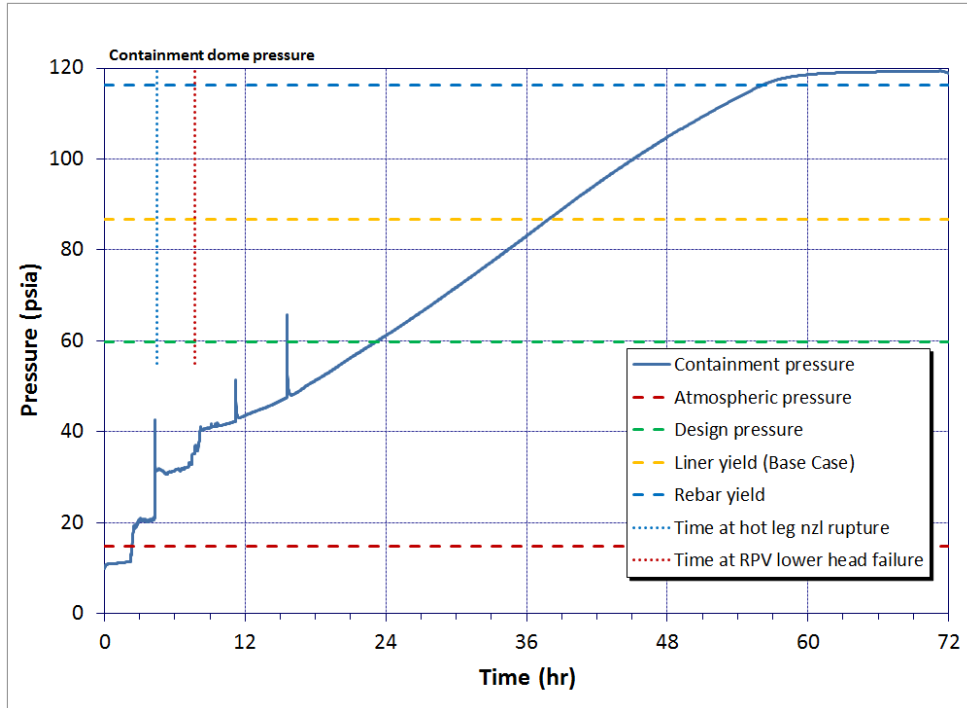


Figure 6-63 Realization 243 containment pressure

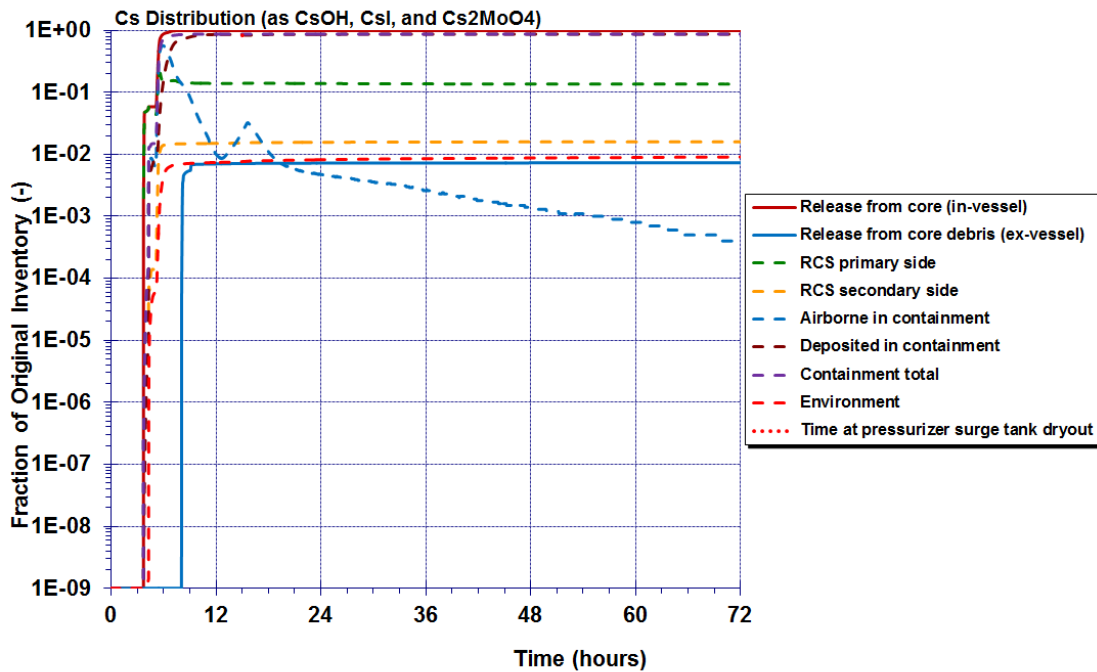


Figure 6-64 Realization 243 cesium release fractions

## Realization 14

The key difference between this realization and Realization 243 is the SGTR occurs well before hot leg creep, as shown in Figure 6-65. This leads to a much higher environmental release fraction for cesium and iodine, although almost all of the release is still in the first 6 hours, as shown in Figure 6-66. Containment pressure is also suppressed as the SGTR flow path allows steam to bypass containment until the point of hot leg creep. Design pressure is not reached at 72 hours. There are no new or unexpected impacts from 48 to 72 hours, with only a slow increase in containment pressurization and a slow reduction of airborne radionuclides in containment.

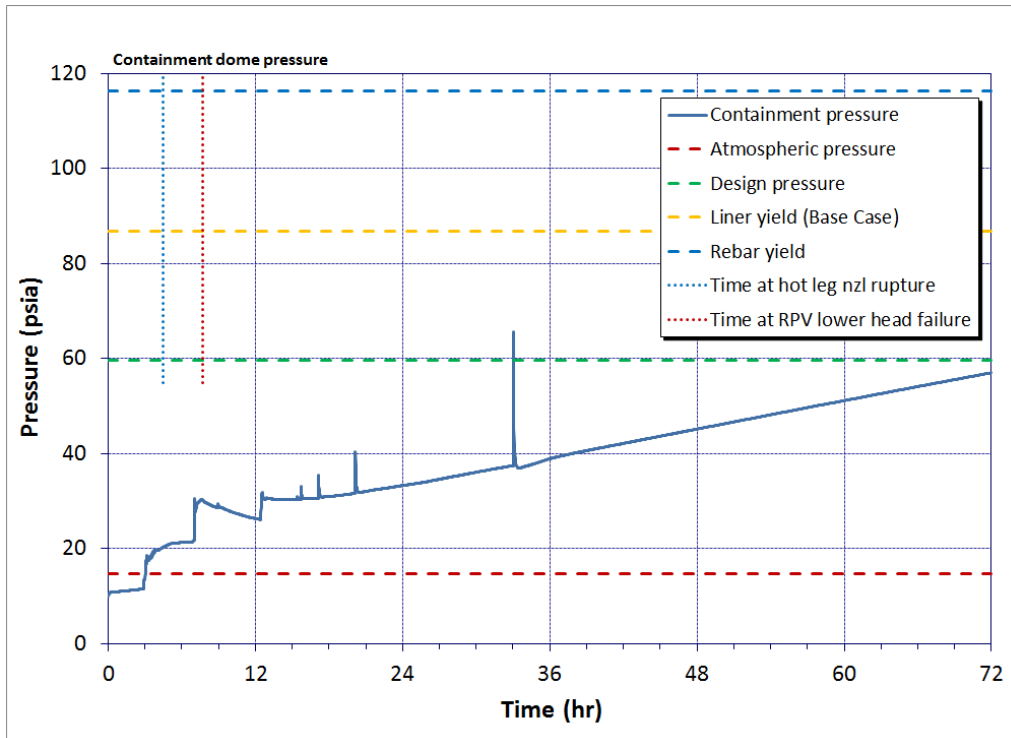
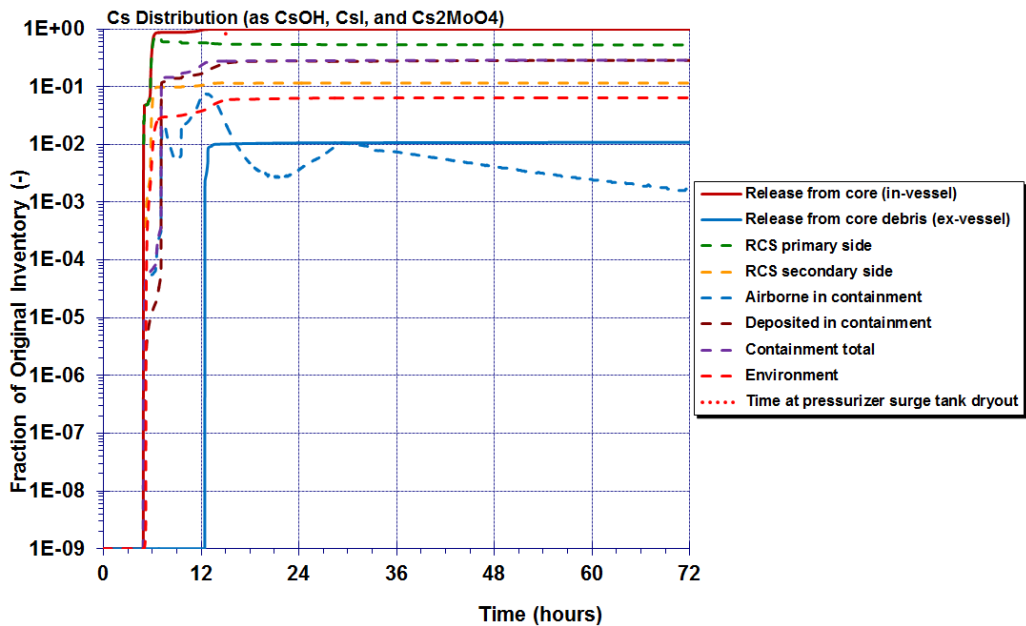


Figure 6-65 Realization 14 containment pressure



**Figure 6-66 Realization 14 cesium release fractions**

**Realization S32**

With no hot leg creep in this realization, environmental release fractions are high, with almost no radionuclides in containment, as shown in Figure 6-67. Containment pressure is suppressed. These are early effects in the sequence, and there are no important changes from 48 to 72 hours. Interestingly, at 72 hours the cesium is almost exactly evenly distributed between the primary side, secondary side, and environment. This seems to be a coincidental result, as the iodine distribution is more divided.

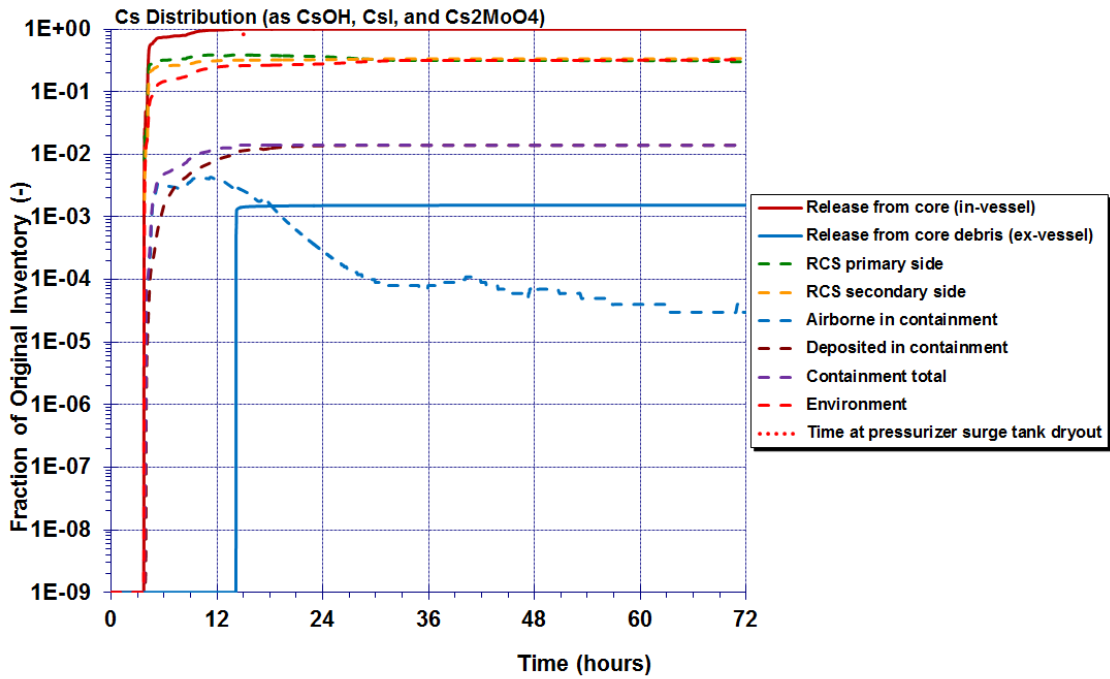


Figure 6-67 Realization S32 cesium release fractions

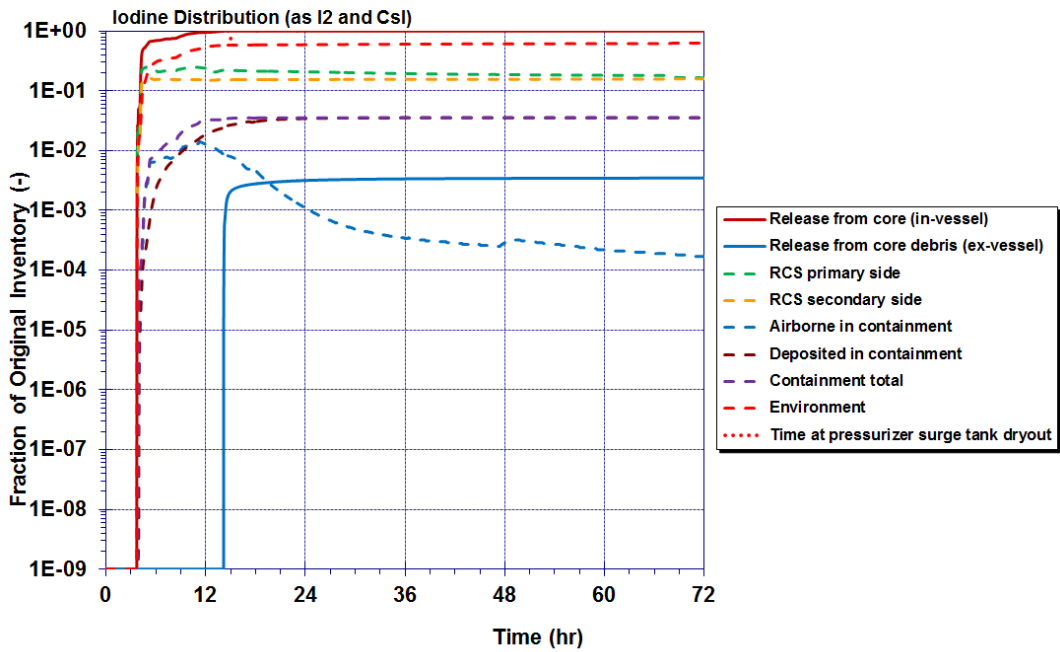


Figure 6-68 Realization S32 iodine release fractions

## Realization 19

This realization shows almost the exact same behavior in Figure 6-69 as the base case, except slightly earlier. Rebar yield is reached at about 51 hours, and there is a plateau of containment pressure. Containment leakage continues to increase, as shown in Figure 6-70, but at a much slower rate. However, even at 72 hours, neither containment pressure or containment leakage have begun to decrease. Iodine and cesium environmental release fractions (Figure 6-71) continue to increase to 72 hours, but starting at 60 hours (pressure plateau) the rate of increase is diminished. However, there is still almost an order of magnitude increase from 48 to 72 hours.

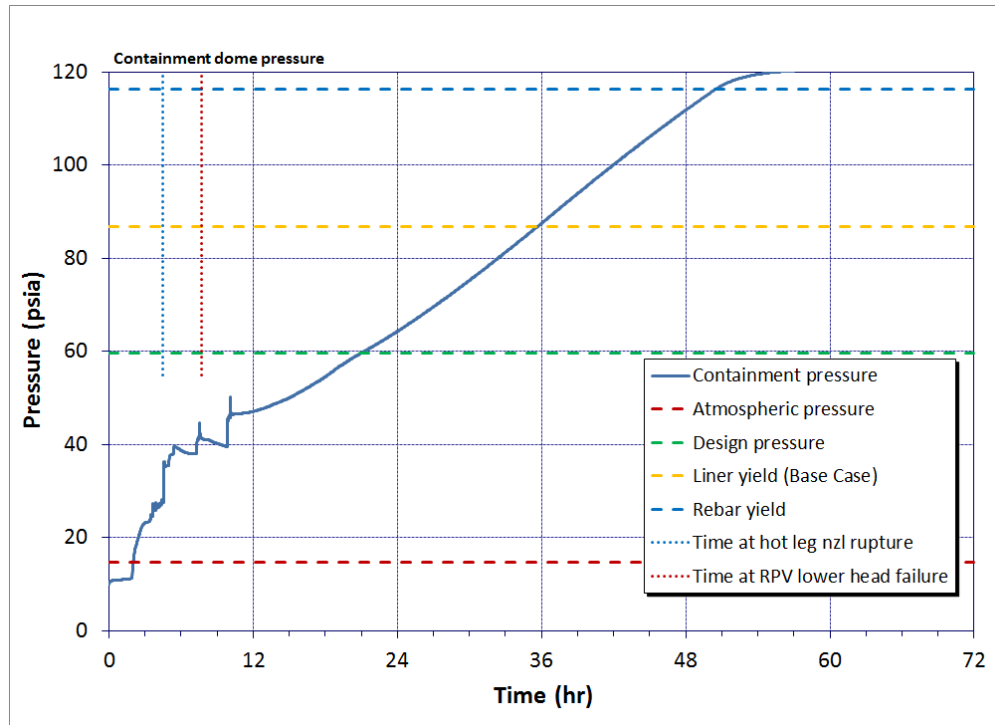
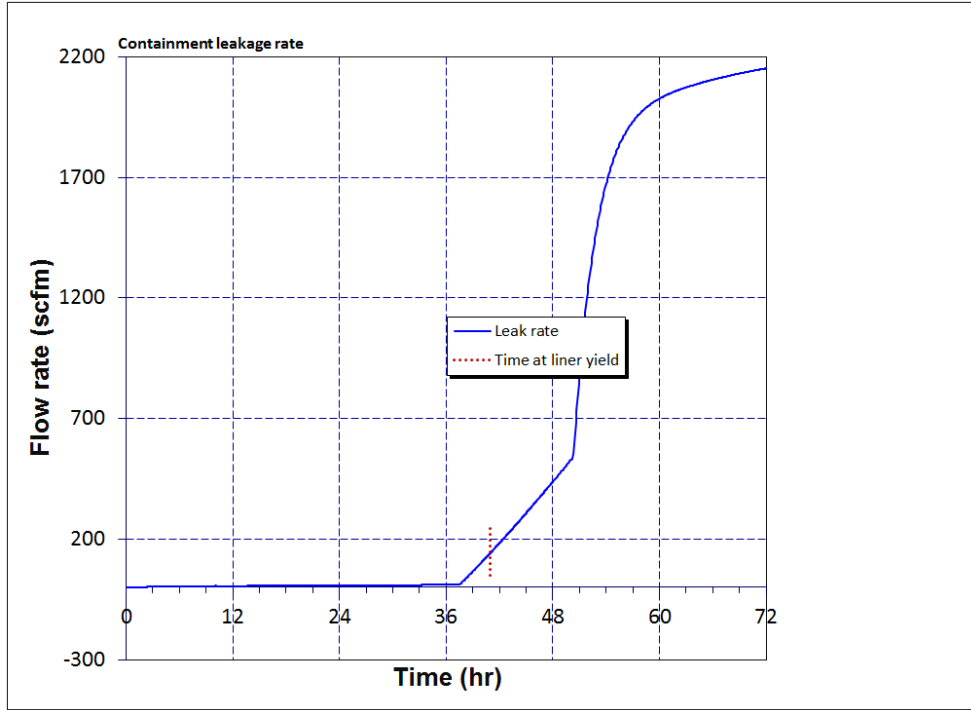
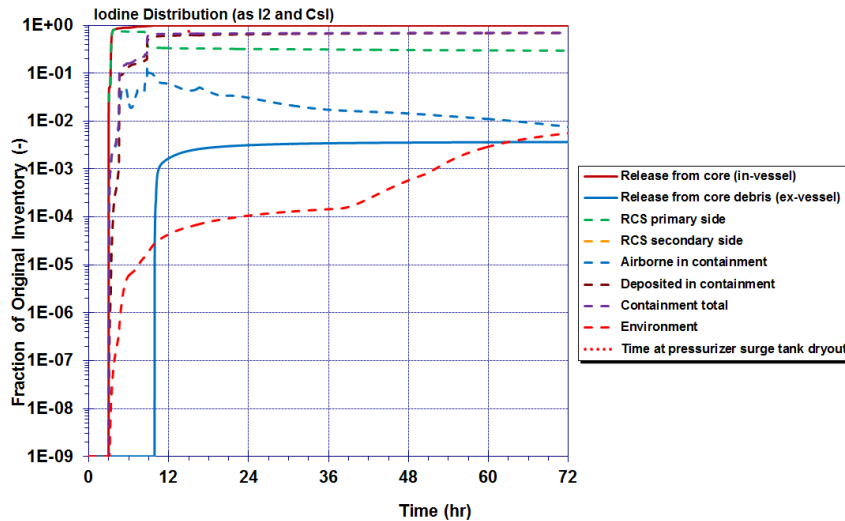


Figure 6-69 Realization 19 containment pressure



**Figure 6-70 Realization 19 leakage rate**



**Figure 6-71 Realization 19 iodine release fractions**

**Realization 53**

In this realization, the containment pressure plateau had been reached by 48 hours, as shown in Figure 6-72. At about 62 hours, containment leakage coupled with the drying out of the containment sump which removed a steam source, leads to containment pressure decrease and leak rate decrease. It was anticipated that a large late release in iodine and cesium could

occur, since decreases in pressure while the containment atmosphere temperature continued to rise may cause increased amounts of revaporization of deposited aerosols. However, a large late release in iodine and cesium was not observed, by 72 hours environmental release fractions for both cesium and iodine have basically leveled out as shown in Figure 6-73. This case also had the greatest amount of concrete ablation, likely because decay heat was high, and still more than 1.5 meters in thickness of concrete remained, as shown in Figure 6-74.

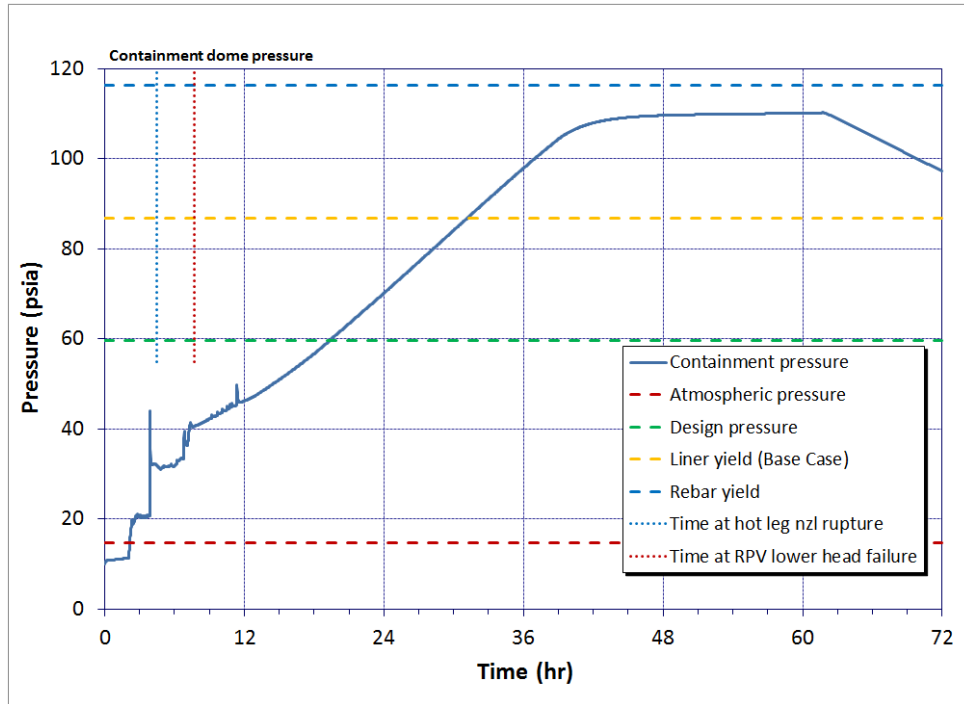


Figure 6-72 Realization 53 containment pressure

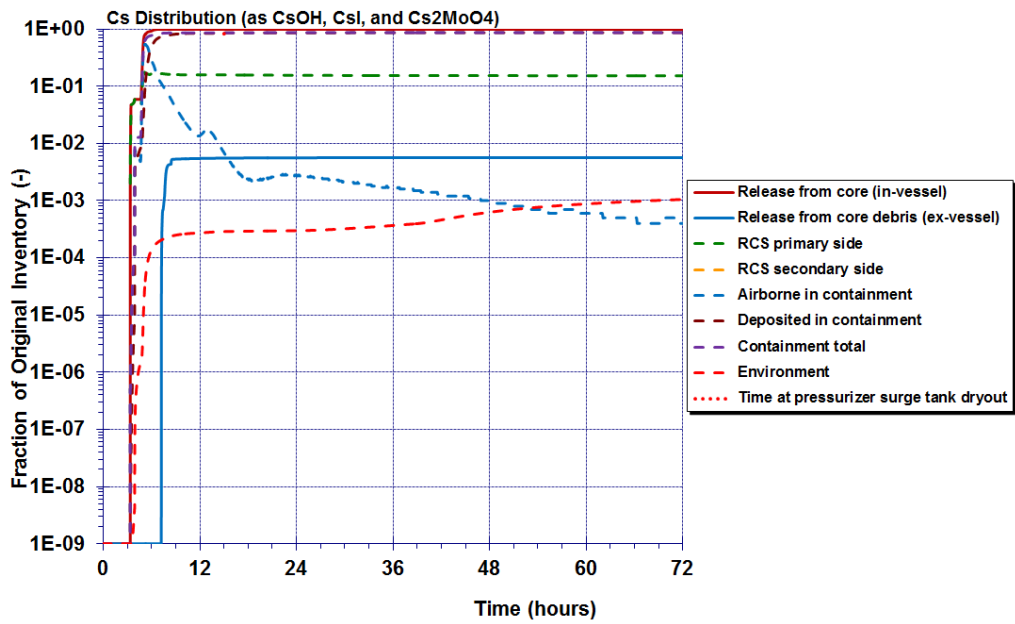


Figure 6-73 Realization 53 cesium release fractions

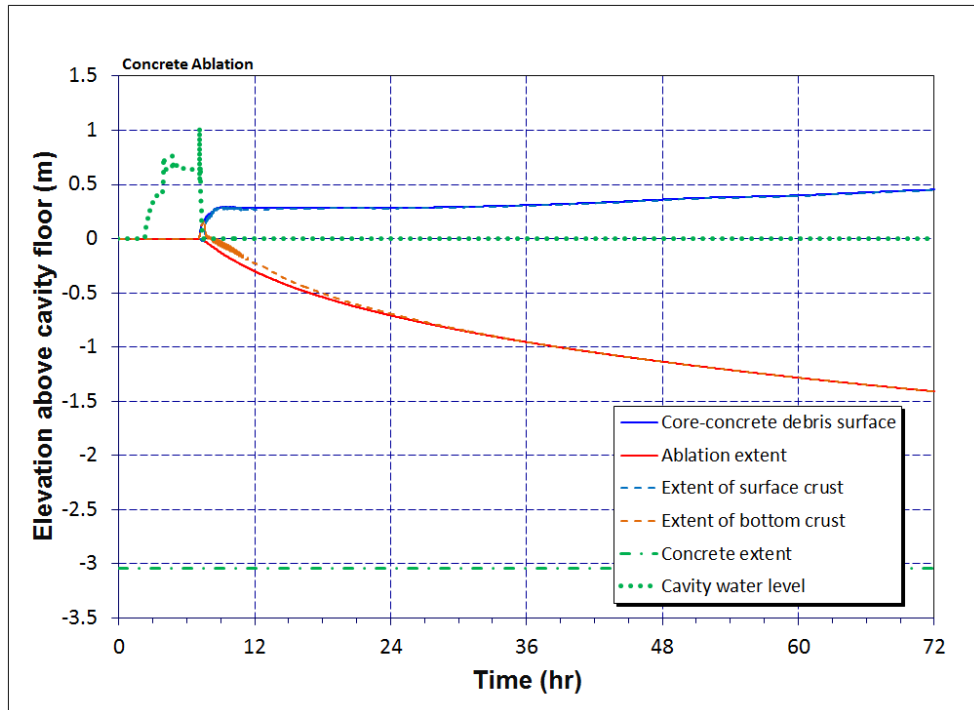
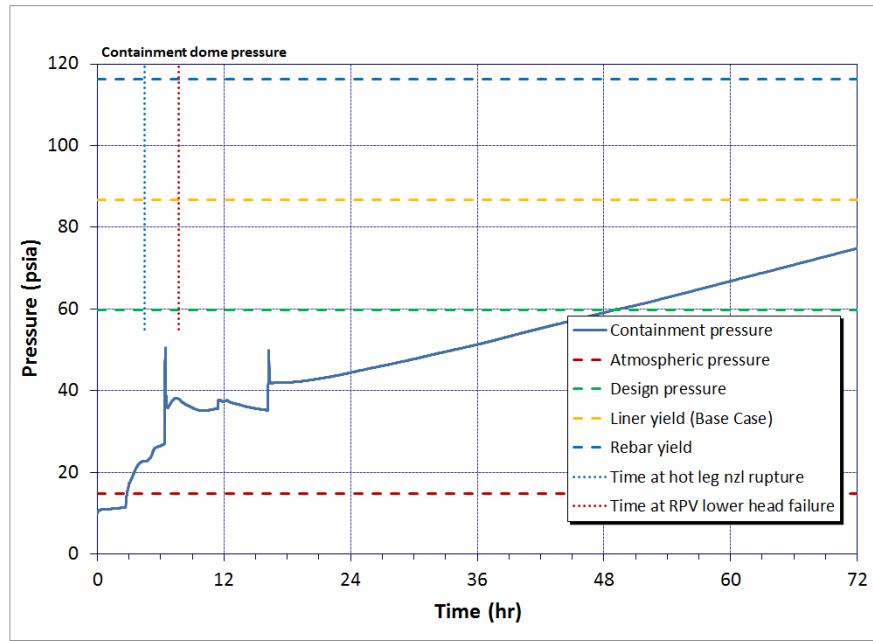


Figure 6-74 Realization 53 concrete ablation

## Realization 1017

Even though this realization had the highest decay heat of any BOC realization, by 72 hours containment pressure did not reach the liner yield point, as shown in Figure 6-75. Leakage remains low and there are essentially no changes in environmental release fractions from 48 to 72 hours for cesium or iodine.



**Figure 6-75 Realization 1017 containment pressure**

## Realization 9

The PRT dries out at about 40 hours in this realization. In the cesium distribution (Figure 6-76), a large increase in the amount of airborne radionuclides in containment can be seen at this time, accompanied by a reduction in the amount on the primary side. The environmental release fraction for cesium also starts to increase at this time. It continues to increase from 48 to 72 hours, but only from about 0.2 percent to 0.5 percent. At 72 hours, the release fraction has essentially leveled out again. This realization also had a late decrease in containment pressure as shown in Figure 6-77 (after the plateau), but this was not accompanied by any large increases in release fractions.

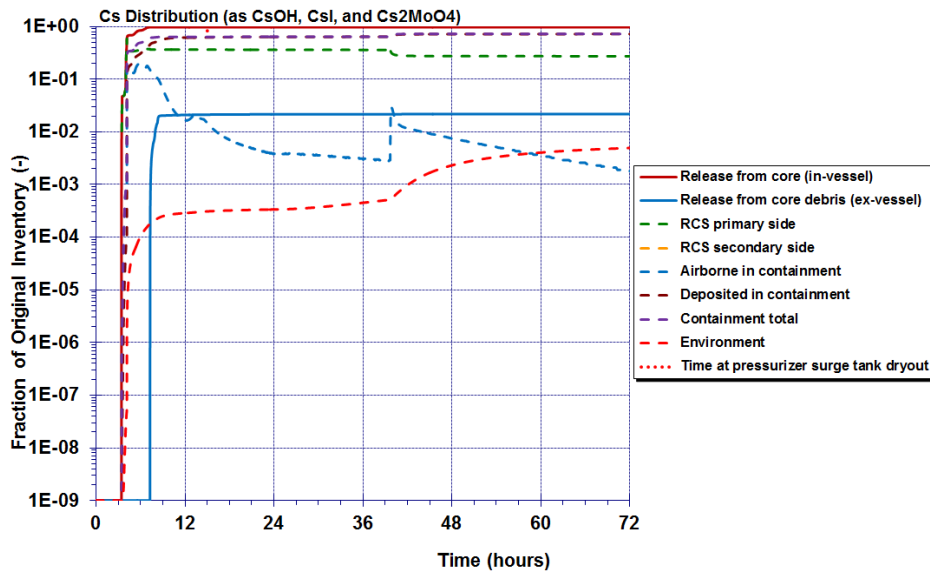


Figure 6-76 Realization 9 cesium release fractions

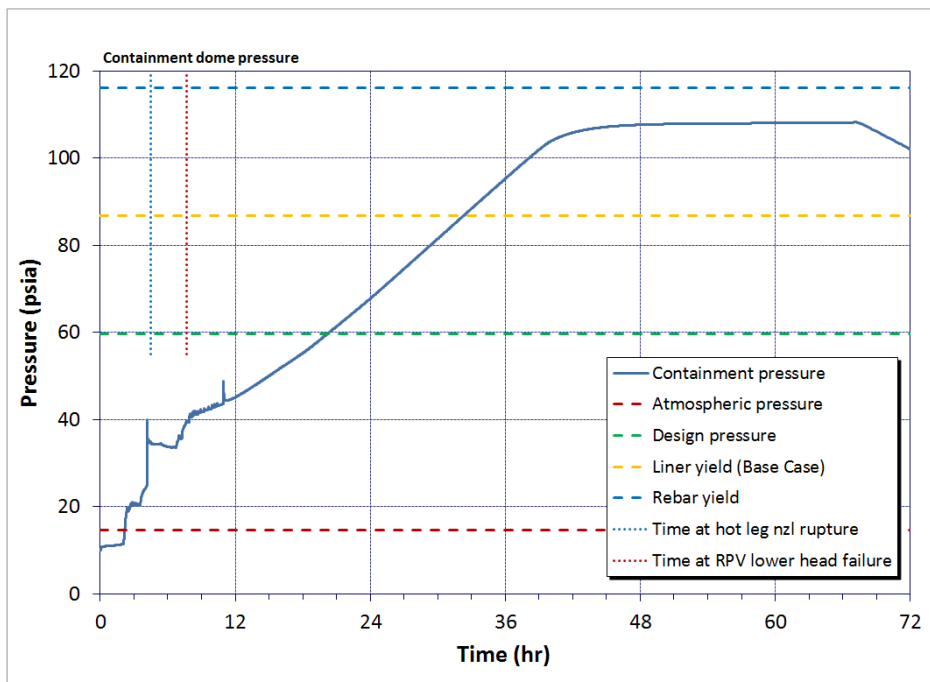


Figure 6-77 Realization 9 containment pressure

Because containment pressure was generally observed to increase from 48 to 72 hours, unless the rebar yield point was reached, further investigation was performed beyond 48 hours. The above subset of single realizations was extended to 72 hours. In summary, the cases where rebar yield was reached, the pressure levels off (to a plateau) and then gradually begins to decrease as the leakage more than compensates for steam generation and heating of the atmosphere. There are marked increases in cesium and iodine environmental release at the

point of liner yield, with some increases of an order of magnitude from 48 to 72 hours. Such increases did not occur with rebar yield only. There appear to be no realizations that could ablate through all available concrete by 72 hours, nor are there any BOC realizations that will reach liner yield by 72 hours.

## **6.1.8 MELCOR Sensitivity Analyses**

Selected sensitivity analyses were conducted on MELCOR parameters to understand the contributions of individual uncertain inputs to the uncertainty in analysis results. Supplemental sensitivity analyses, which were conducted early in the project, were used to inform decisions related to parameters selected and developed for the project.

### **6.1.8.1 SGTR Number of Tubes Joint Sensitivity**

A joint sensitivity analysis was performed to understand the effects of the number of tubes ruptured. The joint sensitivity sampled on a reduced set of parameters judged to be most important to variations in SGTR behavior. For all uncertainty realizations, it was assumed that if an SGTR occurred, it would have the flow area equal to a double-ended guillotine break (DEGB) of a single tube. This tube was assumed to be the most damaged tube in the hottest region of the steam generator. However, there is a possibility that multiple flawed tubes could fail nearly simultaneously in the hottest region, or that a number of small cracks in multiple tubes could form that would have the equivalent flow area of a DEGB of more than one tube. To account for these possibilities, a probability distribution was created for the number of tubes failing upon an SGTR, and a joint sensitivity analysis was performed to look at how environmental releases and the accident sequence would change with the failure of multiple tubes.

A total of 130 realizations were executed, of which 97 were successful runs. This was reasonably consistent with the MELCOR success rate for the rest of the analyses. In this analysis, the number of tubes, SGTR location, secondary SV open fraction, and primary SV open fraction were sampled. Unlike in the base uncertainty run, primary and secondary SV open fractions were sampled independently. SGTR location and secondary SV open fraction were included to see if the effects of multiple tubes on release fractions were larger than the effects from these parameters, and primary SV open fraction was included to provide some variation in SGTR timing in relation to hot leg creep rupture.

#### **6.1.8.1.1 Distribution**

To inform the distribution, six preliminary MELCOR sensitivity calculations were conducted using the base case model, except that tube thickness was input as the lower bound of its uncertainty distribution, to ensure an SGTR. Instead of using the default of SGTR failure area of 1 tube, the number of tubes was varied (1, 2, 3, 5, 10, and 20). The upper bound was selected based on CFD results in NUREG-1922 [46], which indicated that 18 to 20 tubes would be in the hottest tube bin for a full-sized steam generator. Additionally, an NRC consequential SGTR report, currently in draft format (subsequently referred to as C-SGTR Report) estimates that if there is thermally induced SGTRs in non-flawed tubes, about 20 would fail simultaneously. As these sensitivities were created using the base case model, each run had an early SV sticking partially open on both the primary and secondary sides. Thus, at the time of SGTR (about 3.5 hours) the secondary side was completely depressurized and the primary had partially depressurized to about 1000 psi.

A key result from the sensitivities was that only the 20 tube run had instantaneous equilibration of the primary to secondary pressure differential and a preclusion of hot leg creep rupture. With 5 tubes, pressures began to equilibrate, and with 10 tubes, pressure did equilibrate, but in a matter of minutes rather than instantaneously. In both cases there was still hot leg creep rupture. This does not agree with NUREG-1570 [31], and the C-SGTR report, both of which indicate that only 3 or more tubes must fail to prevent creep rupture due to a minimal pressure differential. The second key result of the sensitivities is that environmental release fractions of iodine and cesium at 10 hours (after core damage is completed) have a limited difference above 5 tubes (they increase almost linearly from 1 to 3). It was concluded that with more than 5 tubes failing, the limiting flow is to the environment through MSIV leakage and a partially stuck-open secondary SV not the SG tubes, thus even though the accident progression can be different, environmental releases are more similar.

Since the number of tubes is a discrete number, a discrete distribution is used for how many will fail in each realization. The lower bound is 1 tube, as sampling 0 tubes would defeat the purpose of the sensitivity. Although NUREG-1922 and the C-SGTR report might suggest 20 tubes as the upper bound, there are a number of technical justifications that indicate failure of 20 tubes is too many. First, the C-SGTR assumes that with thermal failure of flawed tubes, 20 tubes would fail. In the uncertainty results for this project, it was observed that an SGTR never occurred unless the stress multiplier was greater than 2, indicating a significantly flawed tube, so the C-SGTR assumption of 20 is not valid for this scenario.

The C-SGTR report included a section calculating the flaw distribution for steam generator tubes, including the build-up of thermally induced damage and leakage. This calculation for the number of flawed tubes yields, for a representative Westinghouse SG, 2.8 percent of tubes having some wear but only 0.235 percent having large flaws generated in the last cycle. This is about 24 total tubes with large flaws, required for MELCOR to predict an SGTR, for the 3 Surry SGs. Most tube damage mechanisms are random, making it unlikely the most flawed tubes would all be in the hottest region. The C-SGTR report also used this flaw distribution to calculate the probability of 1 tube having a DEGB, 2 tubes, and more than 2, using a DEGB to represent the flow area of some number of smaller leaks, common modeling practice. This calculation gave a probability of 1.3E-2 for 1 tube, 8.2E-5 for 2 tubes, and a negligible probability for more than 2 tubes. NUREG-1570 also confirmed that the failure of each additional tube would be more than an order of magnitude less likely. This result is very reasonable, considering the low number of most flawed tubes and the high likelihood they will not be co-located.

The above discussion suggests a distribution to sample 1 and 2 tubes, with 2 tubes being more than an order of magnitude lower probability. However, there is some justification to go up to 5 tubes, primarily that 1 tube failing can impact neighboring tubes, and that there are some damage mechanisms that would damage co-located tubes. NUREG-1570 concluded that the bursting of a steam generator tube under severe accident conditions would cause severe erosion of neighboring tubes. It also concluded that a jet of water or steam from a small tube crack can fail an adjacent tube in a few minutes to an hour. Even though there has never been a spontaneous SGTR in the U.S. that failed an adjacent tube, the possibility is non-zero. Additionally, wear damage caused by a foreign object would be co-located, however, it would not necessarily be in the hottest region and this damage type has been significantly diminished by modern practices.

Therefore, the distribution for the number of tubes failing is defined as a discrete distribution from 1 tube to 5 tubes. To most accurately represent current probabilities, each additional tube failing would have a probability an order of magnitude or more lower of occurrence. However,

with the limited number of realizations, this would not yield enough samples from 3 to 5 tubes to provide any statistically significant results. Instead, each additional tube has a probability that is a factor of 2 lower, except 4 and 5 tubes which are equal so that the PDF (Figure 6-78) sums to 1. This is not a physical representation, but instead ensures that there will be enough sampling of each bin. It is also conservative, since higher number of tubes failing leads to larger environmental releases. The inclusion of the failure of 3 to 5 tubes incorporates the potential for co-located damage and failure of neighboring tubes following the bursting of a single tube. Additionally, in the 5 tube sensitivity run, the primary and secondary pressures were trending toward pressure equilibration until hot leg creep occurred. Thus some 5 tube cases may preclude hot leg creep from happening, especially with the sampling of primary SV open fraction providing a range of pressure differentials. Finally, since flow from the secondary side is the limiting factor with failure of more than a few tubes, 10 and 20 tubes failing, while having some tiny physical likelihood, do not need to be sampled as the range of releases with 4 and 5 tubes should be inclusive.

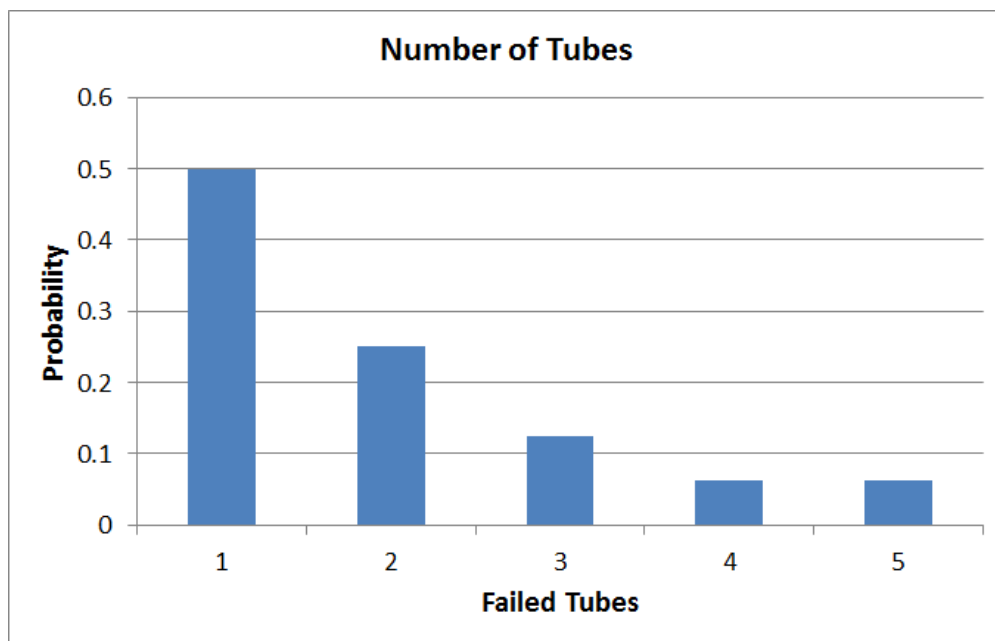


**Figure 6-78 PDF of number of tubes simultaneously failing upon an SGTR**

#### 6.1.8.1.2 Horsetail Plots

For the 97 sensitivity realizations that successfully reached 48 hour completion, horsetail plots were produced for fractional releases to the environment of iodine (Figure 6-79) and cesium (Figure 6-80). Both horsetails were color-coded to identify which curves are associated with which number of tubes input. There are two key results from the two horsetails. The first key result is that releases for 1 tube are higher than the majority of the 104 SGTR cases in the 1003 uncertainty realizations (see Figure 6-1 and Figure 6-11). There is one important factor in explaining this difference. In those realizations, the open fractions of the primary and secondary SVs were the same sampled value. Since there needed to be a pressure differential to cause an SGTR, there were no SGTRs where the primary SV open fraction was greater than 0.4, meaning that the secondary SV open fraction was also always less than 0.4. In this joint sensitivity, the open fractions are sampled independently so secondary SV open fraction can range from 0.01 to 1.0, allowing for greater flow rates to the environment and thus, higher

release fractions. Additionally, as described in Section 6.1.5.3, there was an error identified in the sampled secondary SV open fraction in loops A and C causing them to always fail closed, driving releases down. Thus for this joint sensitivity, SGTRs were forced to occur in only loop B, further increasing releases.

The second key result is the increasing release fractions with additional tubes. With a couple overlapping exceptions, releases for 2 tubes are higher than 1 tube, and releases for 3 tubes are higher than 2 tubes. However, the releases for 3 to 5 tubes show no clear differences and seem to randomly overlap. This gives additional evidence to support the conclusion that flows from the secondary side limit releases with more than a few tubes failing and also confirms the upper limit on the number of tubes sampled is reasonable. These two key results hold true for both iodine and cesium.

One other visual difference from the horsetails is that for 1 tube after the initial puff release there is a gradual increase over the next 10 hours or so. This trend is seen to a lesser extent with 2 tubes. For 3 or more tubes the initial release is almost all of the total release, and the releases usually level out within 6 hours. At the time of the SGTR, most gap releases have occurred, and some releases from the fuel, but fuel has not yet melted and relocated. Radionuclides that have been released up to that point are primarily deposited in the primary system. The higher the number tubes failing simultaneously, the larger the instantaneous depressurization of the primary will be, and it is postulated that there will be more revaporization of the deposited radionuclides. This would lead to a larger puff release to the environment. For the 1 tube realizations this effect would be minimal and most deposited aerosols would remain until dry-out events put them back in the atmosphere, at which time hot leg creep would have occurred. However, since this is an additional flow path, not all radionuclides will be transported to the secondary side, resulting in a more gradual environmental release. This postulated conclusion was not investigated in more detail. Early increased releases for multiple tubes, after the initial puff, are a result of additional fuel melting. Late increased releases may be due to containment liner yield.

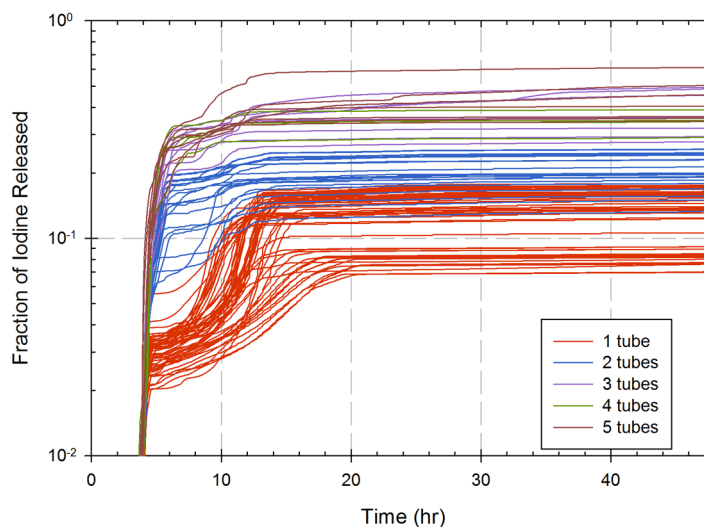


**Figure 6-79 Iodine environmental release fraction with number of tubes color-coded**

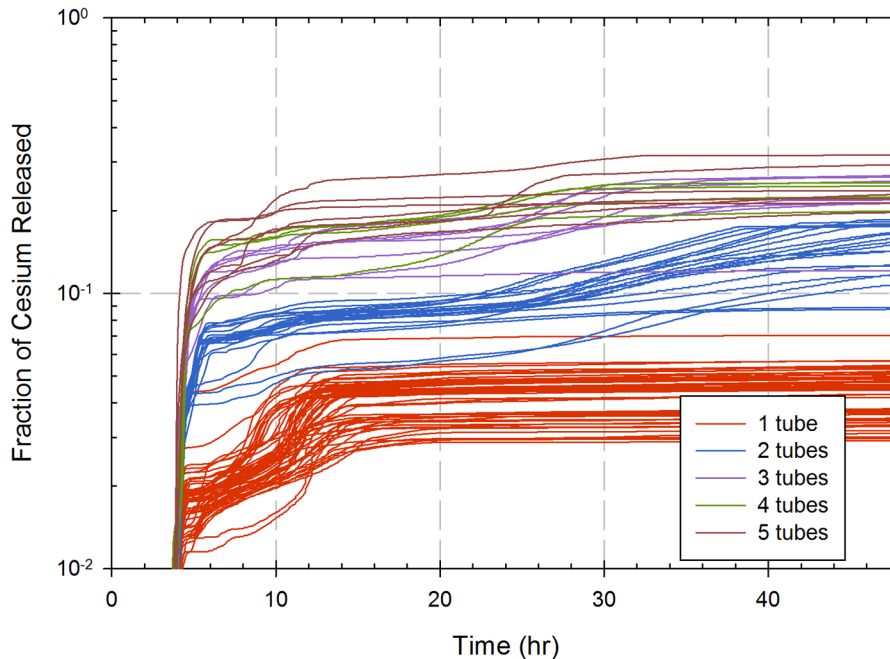


**Figure 6-80 Cesium environmental release fraction with number of tubes color-coded**

A limited regression analysis was conducted for this joint sensitivity. Data was extracted at 48 hours for cesium and iodine release fractions for all successful realizations. These data were used to create scatterplots for each parameter, which are displayed in the respective subsections below. For the basic regression, linear trend lines were fit to the scatterplots and the  $R^2$  value displayed.

#### 6.1.8.1.3 Parameters

##### Number of Tubes

Understanding the effects of the number of failed tubes was the motivating factor for this joint sensitivity. Based on the six early sensitivities (described in Section 6.1.7.1.1), it was expected to have the largest impact on environmental release fractions. This was confirmed by the step changes seen in the horsetails, where the spread from 1 tube, is small compared to the total range when varying the number of tubes up to 5. To compare directly to the other sampled parameters, two scatterplots (Figure 6-81) were created for iodine and cesium release fractions at 48 hours. Consistent with the horsetails, the step changes from 1 to 2 tubes and from 2 to 3 tubes are observed. The ranges of releases for 3 to 5 tube bins are very similar. However, mostly because of outliers in 3-5 tubes the linear trend line still shows a very good fit to the data, especially considering the step changes from 1 to 2 tubes, and from 2 to 3 tubes. The trend of larger releases with increasing number of tubes failing is a very expected result since it increases the flow area for radionuclides to bypass containment and delays hot leg creep rupture.

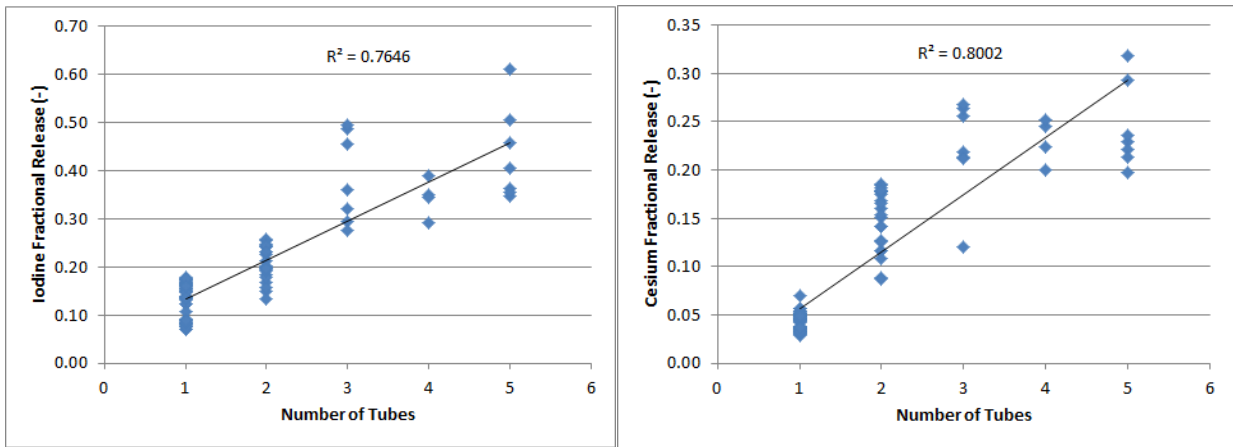


**Figure 6-81 Scatterplots of iodine and cesium release fractions versus number of failed tubes input values**

### Secondary SV Open Fraction

Sampling was conducted on the open fraction of the secondary SV upon failure at 45 cycles, which is the best estimate value. In this joint sensitivity secondary SV open fraction was sampled separately from the primary SV open fraction. The input values are used directly to create the scatterplots in Figure 6-82. Neither scatterplot shows an obvious trend, confirmed by the linear trend lines which have essentially no fit. The expected physical trend would be a larger open fraction leading to higher release fractions, as the flow area to the environment would be larger. There is some evidence of this trend with larger releases, above 0.2 for iodine and 0.1 for cesium. This indicates that when 1 tube fails, this failure area is limiting in terms of environmental releases but when multiple tubes fail, the limiting area is MSIV leakage and the stuck open SV, making the open fraction more important with the failure of multiple tubes. These results also indicate that for 1 tube, time between SGTR and hot leg creep rupture is more important for release fractions than secondary SV open fraction.

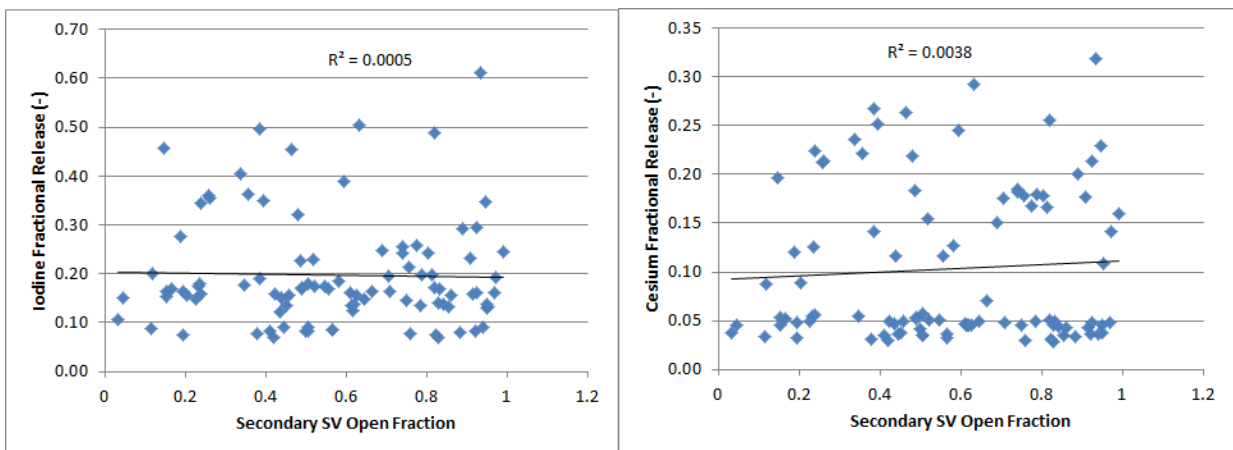


**Figure 6-82 Scatterplots of iodine and cesium release fractions versus secondary SV open fraction input values**

## SGTR Location

Sampling was conducted on the number of steam generator stages after the break location, using the same uncertainty distribution as the ARTIST parameter in the main uncertainty analysis. The SGTR location is a direct input. The location of the SGTR determines the DF applied to the release. In the regression analysis of the SGTRs in the base uncertainty realizations, this parameter showed a low importance, despite its determination of the DF. It was included in this joint sensitivity as a test to confirm this result.

As shown in the scatterplots for iodine and cesium release fractions (Figure 6-83), the result was partially confirmed. The linear trend lines show essentially no fit to the data. However, this may have been partially due to the high outliers at 1 and 4. The ranges of releases at locations 5 to 7 are approximately similar but have a much higher upper bound than the remainder of the locations, excluding high outliers. This may be partially due to limited sampling at locations 1 to 3, but even considering that limitation, there seems to be a clear step change between locations 4 and 5. The conclusion is that when many other parameters are fixed, the calculated DFs, based on SGTR location, impact release fractions, but the importance of location is low compared to some other parameters. A similar conclusion was reached in the SGTR section (section 6.1.5).

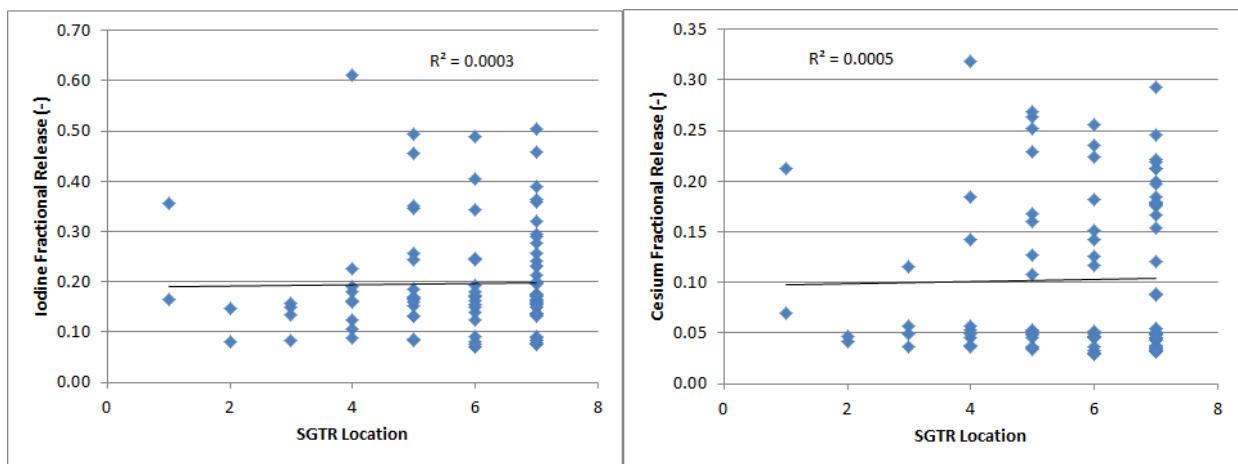


**Figure 6-83 Scatterplots of iodine and cesium release fractions versus SGTR location input values**

## Primary SV Open Fraction

Sampling was conducted on the open fraction of the primary SV upon failure at 45 cycles, which is the best estimate value. Primary SV open fraction was included in this joint sensitivity to provide some variation in the timing of the SGTR relative to hot leg creep and was sampled separately from the secondary SV open fraction. Unlike in the base uncertainty realizations, this is the only failure mode for the primary SVs, so there is no post-processing required and the input values are used directly to create the scatterplots of iodine and cesium release fractions in Figure 6-84.

To ensure that SGTRs occurred in these realizations, primary SV open fraction was only sampled from 0.1 to 0.5 (using a uniform distribution), since in the SGTR section it was shown that if the open fraction was any larger it would depressurize the primary too quickly and there

would be no pressure differential from the primary to the secondary side to cause an SGTR. Therefore, it wasn't expected to have the large importance that it did in that section, since all these realizations had an SGTR. However, there is still a physical trend that a larger open fraction (and quick primary depressurization) increases release fractions. This is because the pressure differential between the primary system and the containment determines, along with temperature, the timing of hot leg creep. With a lower pressure differential, hot leg creep occurs later, and almost all flows of radionuclides go from the primary through the SGTR into the environment, and not into containment. This trend is seen in the scatterplots, and confirmed by the linear trend line, but with a relatively low importance as compared to the number of tubes.

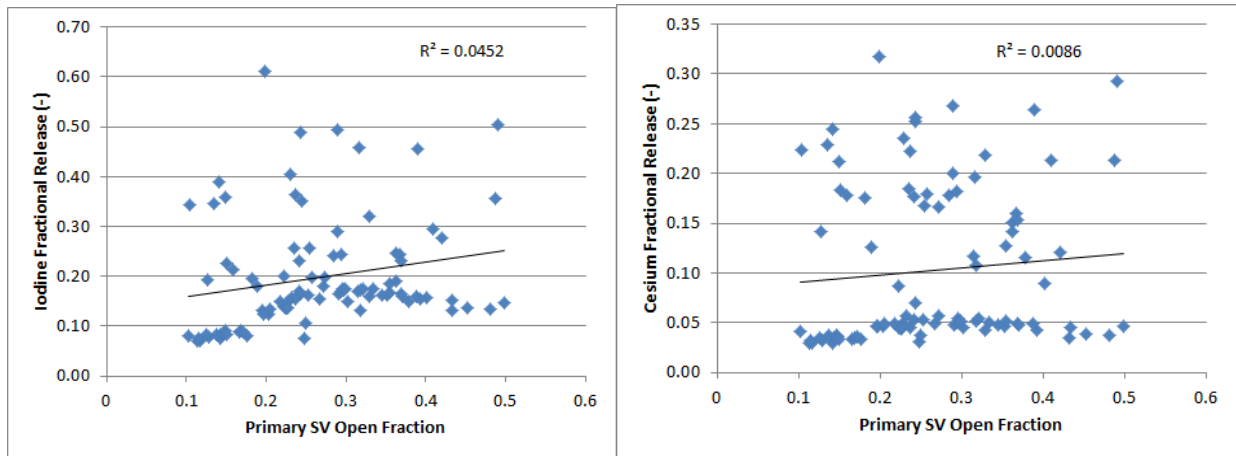


**Figure 6-84 Scatterplots of iodine and cesium release fractions versus primary SV open fraction input values**

#### 6.1.8.1.4 Timing and Other Effects

Time at cycle, decay heat, tube thickness, and tube temperature are all kept constant for this joint sensitivity, therefore all SGTRs occur at approximately the same time. The primary timing difference in these realizations is when hot leg creep rupture occurs. Two realizations were selected and plotted to illustrate how much small differences in reactor conditions can affect the timing, primary and secondary pressure, maximum cladding temperature, and creep fraction (indicates the amount of creep that has occurred, failure happens at a value of 1.0) for both the SG tube and the hot leg. Both realizations have a primary SV open fraction at 0.23. Realization 29 (Figure 6-85) had a failure of 5 tubes, and realization 62 (Figure 6-86) had a failure of 1 tube. The environmental release fraction for iodine was 40 percent for realization 29, one of the highest releases, and 16 percent for realization 62.

At the time of SGTR (about 3.5 hours), both primary pressure and maximum cladding temperatures are essentially equal between the two realizations. Additionally, the secondary side is depressurized to atmosphere in both. The major difference is primary depressurization following the SGTR. At 4 hours, which is about when hot leg creep damage begins for realization 62, there is a 600 psi difference between the two realizations. Additionally, as realization 29 depressurizes, a small dip in the temperature is observed at about 3.5 hours, leading to a very slight delay in reaching peak clad temperature. The combination of decreased primary pressure and slight delay in temperature increase results in hot leg creep occurring about 3.5 hours later in realization 29. This is important, because before hot leg creep, the vast

majority of radionuclides released from fuel will be transported to the secondary side and subsequently, the environment.

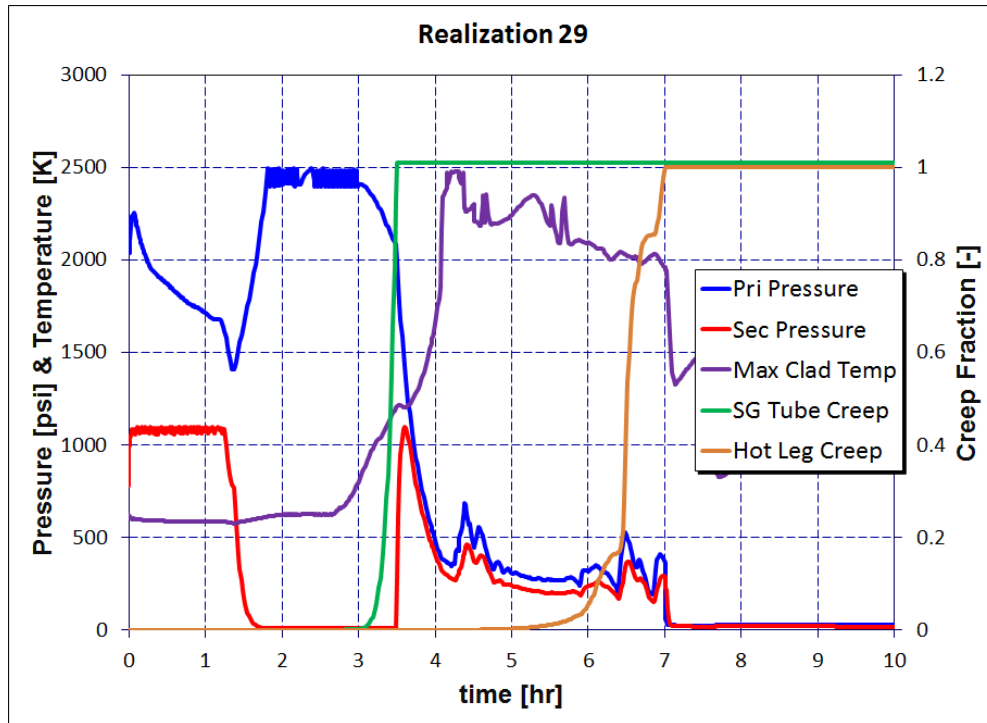
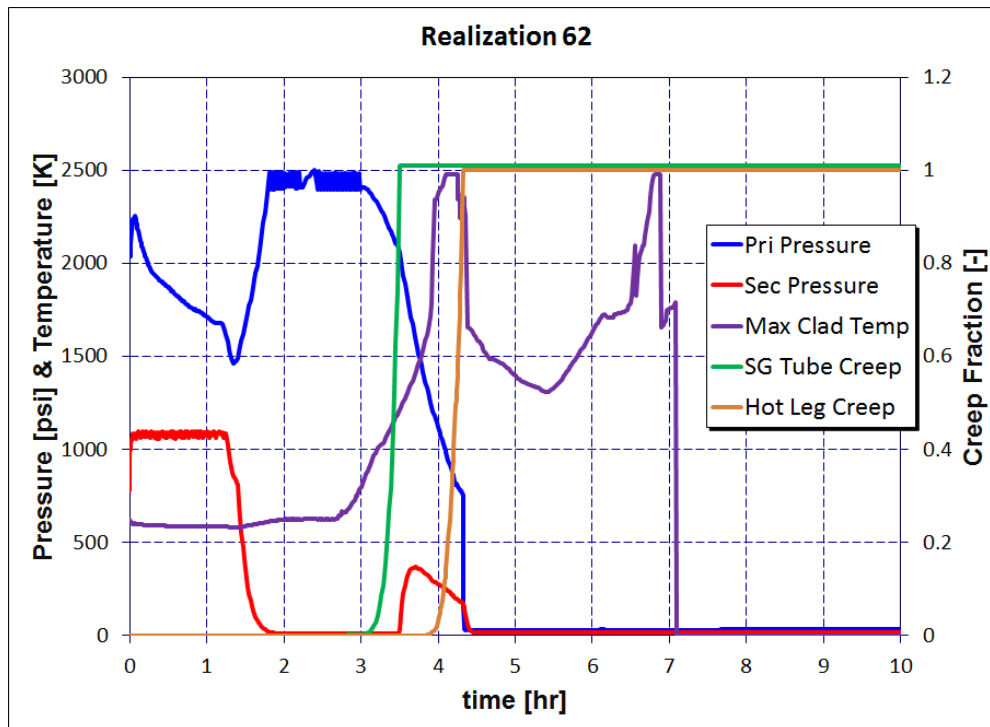


Figure 6-85 Pressure, temperature and creep fractions for Rlz 29



## **Figure 6-86 Pressure, temperature and creep fractions for Rlz 62**

There is one realization, 32, that did not have creep rupture. This was also a case where there was failure of 5 tubes. The key difference between realization 32 and 29 is that the secondary SV open fraction for 32 is 0.93 as opposed to 0.34 for 29. Because the open fraction is so large it allows the primary and secondary to quickly drop to atmospheric pressure, instead of equilibrating at about 500 psi like realization 29, thus there is no pressure differential to drive hot leg creep, regardless of temperature.

### **6.1.8.1.5 SGTR Number of Tubes Failed Joint Sensitivity Conclusions**

To determine the effect of having more than one SG tube failing on environmental release fractions for cesium and iodine, a distribution was created to sample failure of 1 to 5 tubes. Sampling was performed on the number of tubes, primary and secondary SV open fraction, and SGTR location. Releases for 1 tube were slightly higher than the majority of base uncertainty SGTR realizations as secondary SV open fraction was sampled on the full range, hot leg creep timing was varied and an error in the loops A and C was bypassed. There are step increases in release fractions for the failure of 2 and 3 tubes, but no significant difference from 3 to 5 tubes. This indicates that when 3 or more tubes fail, flow to environment is limited by MSIV leakage and the stuck open secondary SV, and not by the flow through the SG tubes. Another key result is that releases from 1 tube increase more gradually while 3 to 5 tubes has more of a quick puff release, potentially due to revaporization. The number of tubes parameter dominated results, with none of the other 3 sampled parameters having a significant additional impact. A large factor in the total release fractions is the time of hot leg creep relative to the SGTR. This timing is primarily due to depressurization rate, based on the number of tubes failing and exacerbated by the primary SV open fraction. One realization, with 5 tubes failing, had no hot leg creep leading to the highest release fractions.

### **6.1.8.2 Sensitivity on Concrete Aggregate**

The Surry SOARCA MELCOR analyses [3] included a limestone based aggregate for the containment concrete, which is the aggregate identified in the reference MAAP file. However, during the UA activities, it was discovered that the Surry Power Station actually used a basaltic aggregate. This was confirmed by review of a 1989 Virginia Tech Report associated with license renewal which contained some petrographic examination results of concrete core samples taken from the Unit 2 containment structure. Since the type of concrete can have a major effect on the MCCI, and containment pressure and temperature responses, which can ultimately determine functional failure of containment, a sensitivity analysis was conducted to determine the potential differences between the use of limestone and basaltic concrete. This sensitivity helps quantify the effect of the appropriate concrete type with regard to the Surry SOARCA calculation [3]. Two nearly identical MELCOR calculations were performed with only the concrete type varied between the two calculations. The first used a basaltic aggregate concrete, and the second used a limestone based concrete aggregate. Both of these concrete types were selected from the MELCOR default list [8]. The MELCOR files used for the concrete and rebar sensitivity analyses are listed in Table 6-16.

**Table 6-16 Sensitivity on concrete type and rebar file names.**

File Name	Description
Surry_UA_base_3_28_15	The Surry UA base case used for comparison for all MELCOR sensitivities within this report. The concrete is basaltic with 17% by mass rebar.
Surry_Old_Concrete	The Surry_UA_base_3_28_15 file except the concrete is limestone.
Surry_No_Rebar	The Surry_UA_base_3_28_15 file except the concrete has no rebar.
Surry_30%_Rebar	The Surry_UA_base_3_28_15 file except the concrete has 30% by mass rebar.

Figure 6-87 shows the differences of the MCCI debris surface and ablation depth between the two analyses. Figure 6-88 shows the contributions and sum total of the MCCI non-condensable gases (NCGs) for both analyses. As seen in Figure 6-87, the basaltic concrete shows a more vigorous MCCI than with limestone concrete. However from Figure 6-88, the limestone concrete has approximately 30 percent greater release of NCGs. These results are in line with previous EPRI analyses [116], and as with the EPRI analyses are the result of the inverse relationship between the downward heat transfer coefficient to the effective decomposition enthalpy, which results in a higher ablation rate for basaltic concrete but lower NCG generation due to the increased cooling effect of the higher ablation rate on the corium.

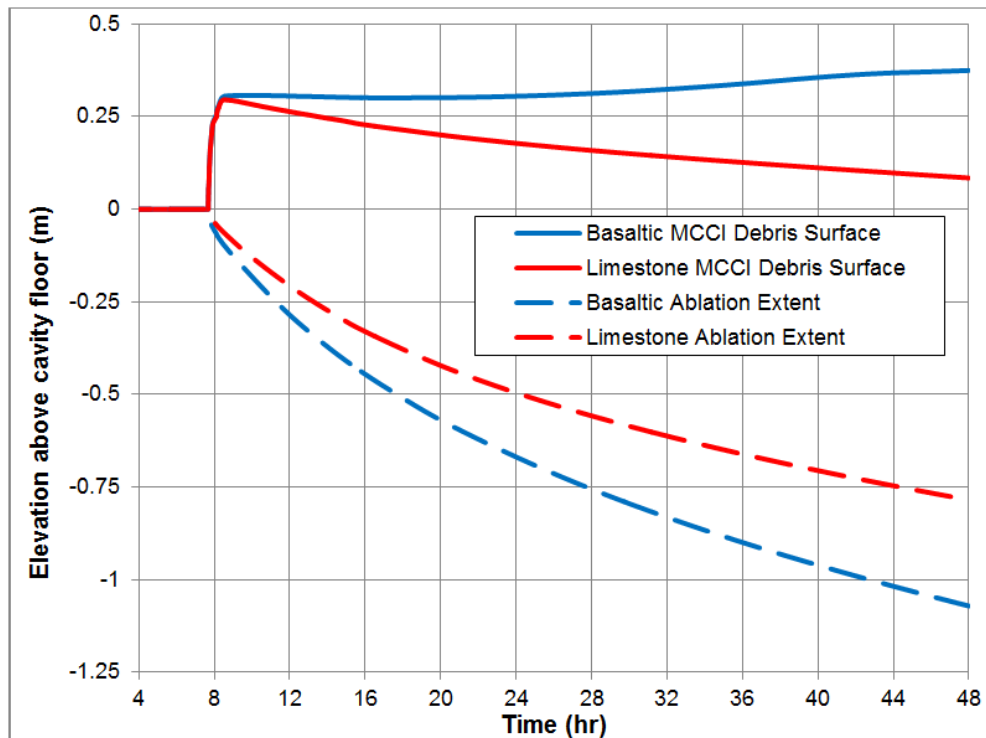


**Figure 6-87 MCCI debris surface and ablation depth**

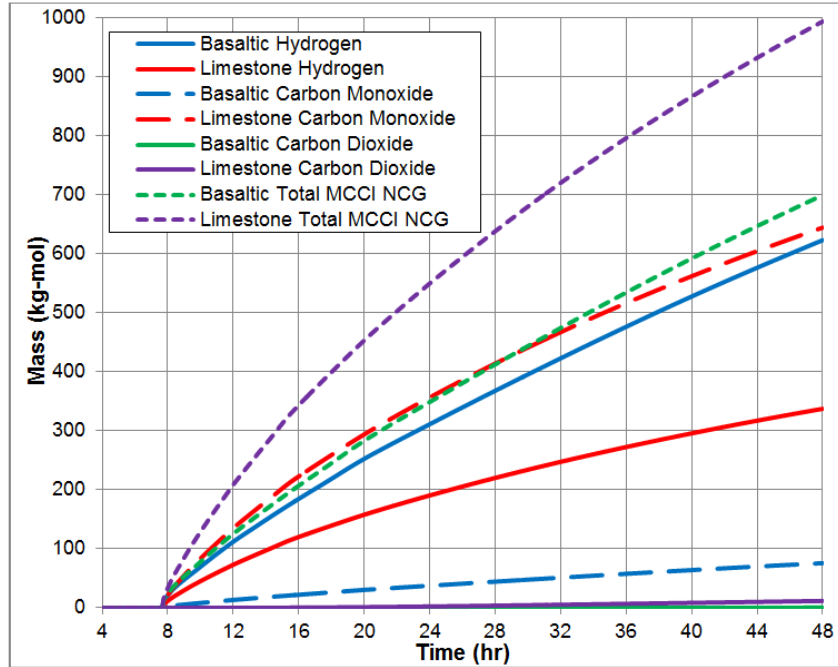


**Figure 6-88 MCCI non-condensable gas contribution and sum total**

Figure 6-89 and Figure 6-90 show the containment pressure response and containment temperature response, respectively, for the two analyses. From these figures it is interesting to note that containment pressure (~9.5%) and temperature (~2%) vary little between the calculations even though the mass of gas generated by core concrete interaction varies by approximately 30 percent. These results are again in line with previous EPRI analyses [116].

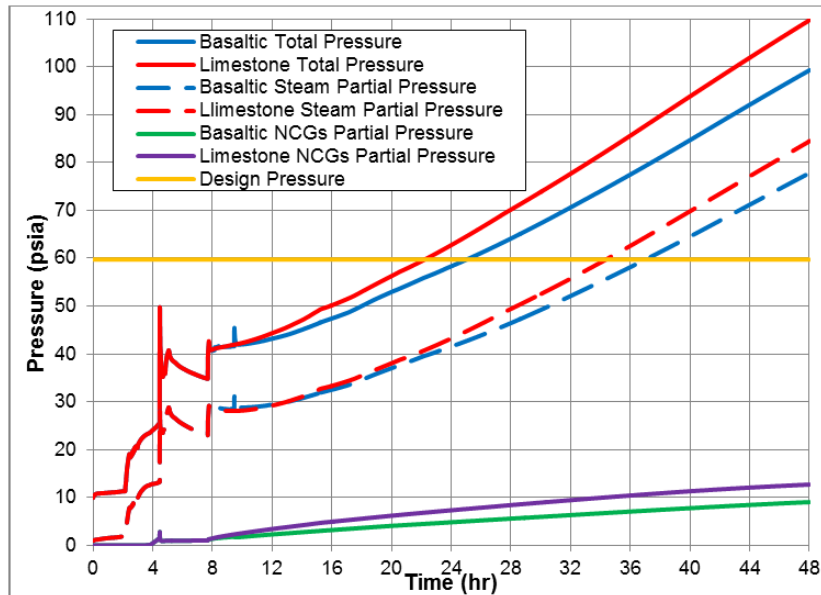


**Figure 6-89 Containment pressure response**

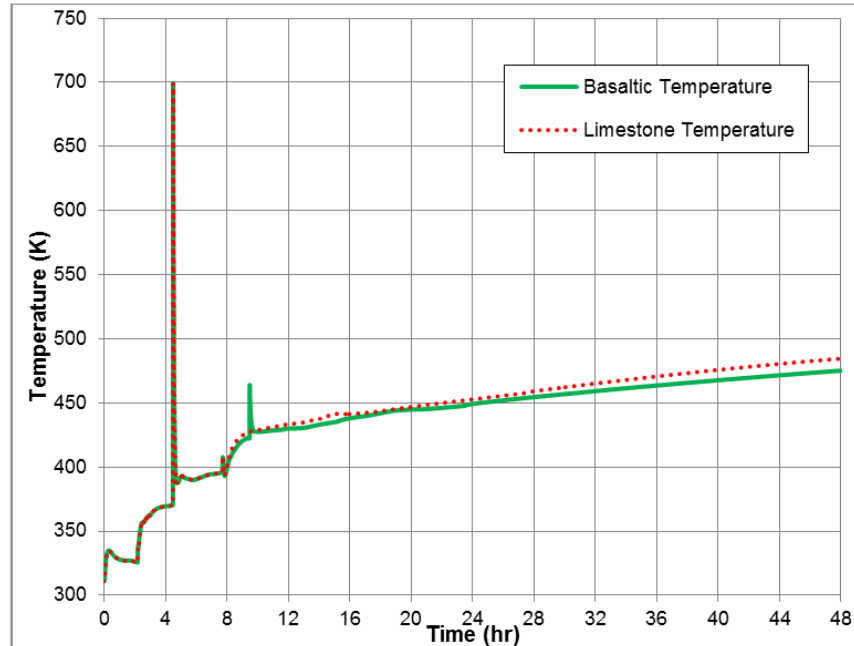


**Figure 6-90 Containment temperature response**

As seen in Figure 6-89, the key observation to make in considering these results is that most of the pressure in containment is attributable to the partial pressure of steam. The partial pressures of NCGs generated by MCCI do not contribute much to the overall pressure, so differences in the amounts of gas generated do not either. Instead, containment pressure increase over the long term is due to continued heating of the containment and the containment atmosphere by decay heat generated in the core debris resident on the containment floor as seen in Figure 6-91. The energy (~9.2%) between basaltic and limestone concrete shown in Figure 6-91 accounts for approximately 97 percent of the total containment pressure difference between basaltic and limestone concrete shown in Figure 6-89 at the end of the simulations (48 hours).

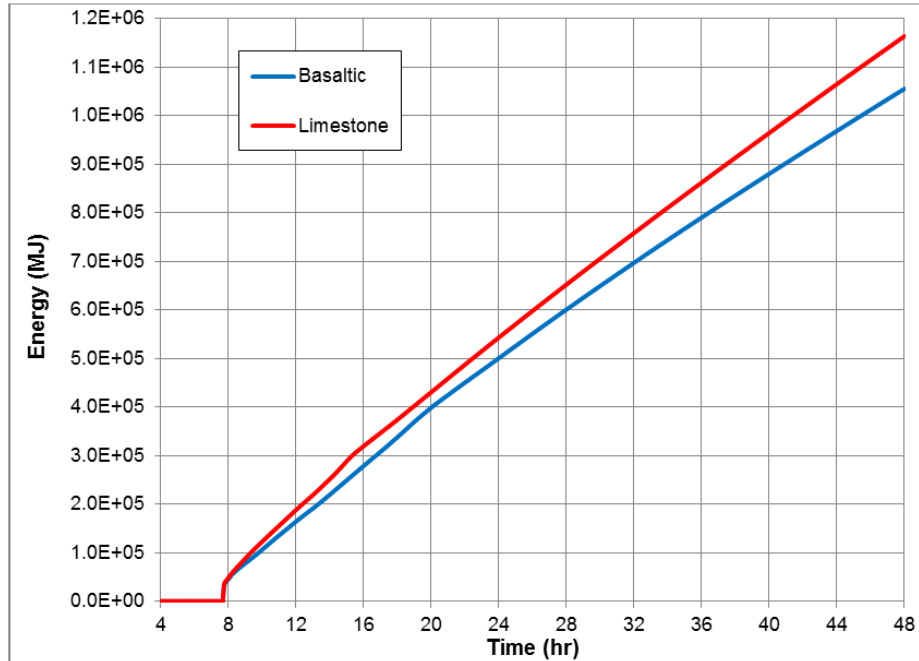


**Figure 6-91 Energy transfer from the cavity to containment atmosphere**

In Figure 6-92, the environmental release fraction from limestone concrete for cesium and iodine is greater than the basaltic concrete at the end of the 48 hour simulation. This is attributed to the increased containment pressurization in the limestone concrete analysis which reaches liner yield (i.e., functional failure of containment) at approximately 36.5 hours as compared to basaltic concrete analysis which reaches liner yield at approximately 41 hours. Since the releases from both analyses are so low (i.e., <0.2%) for both cesium and iodine, these releases can be essentially considered the same.

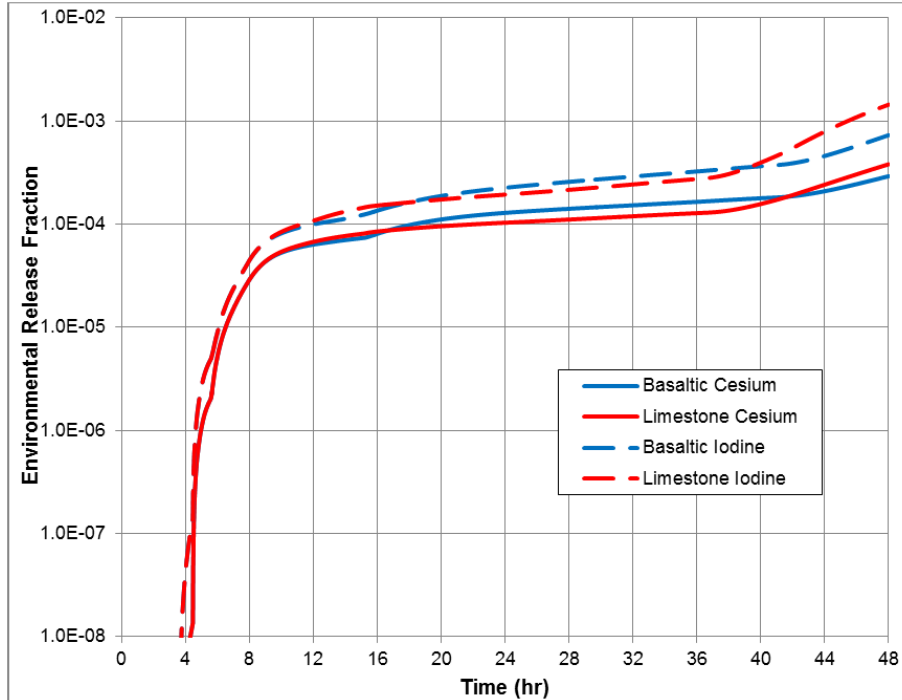


**Figure 6-92 Environmental release fraction of cesium and iodine**

From these analyses, the only contributing factor that is important in the long term is the containment pressurization. This pressurization is due to continued heating of the containment and the containment atmosphere by decay heat generated in the core debris resident on the containment floor as seen in Figure 6-91.

### 6.1.8.3 Rebar Mass within the Concrete

The Surry SOARCA analyses [3] considered the Surry Power Station concrete to contain 17 percent by mass of rebar. This sensitivity analysis was developed after discussions with the Level 3 PRA team revealed their analysis used a lower percent of rebar. This sensitivity considers two extreme instances for MCCI and containment response with regards to zero percent and approximately double (30%) rebar by mass within the concrete. Although zero percent would never be expected, analyzing zero percent supports quantification of the effect of the rebar. Figure 6-93 shows the MCCI debris surface and ablation extent for all three cases considered. The debris surface is the same for all three cases. However, the ablation extent for the no rebar and 30 percent rebar cases is about 5 percent less and about 6 percent greater, respectively, when compared to the base case. This ablation depth results in NCG contribution for the no rebar and 30 percent rebar cases of 1 percent greater and 4 percent less, respectively, when compared to the base case. This NCG differentiation, as well as the MCCI hydrogen contribution, can be seen in Figure 6-94.

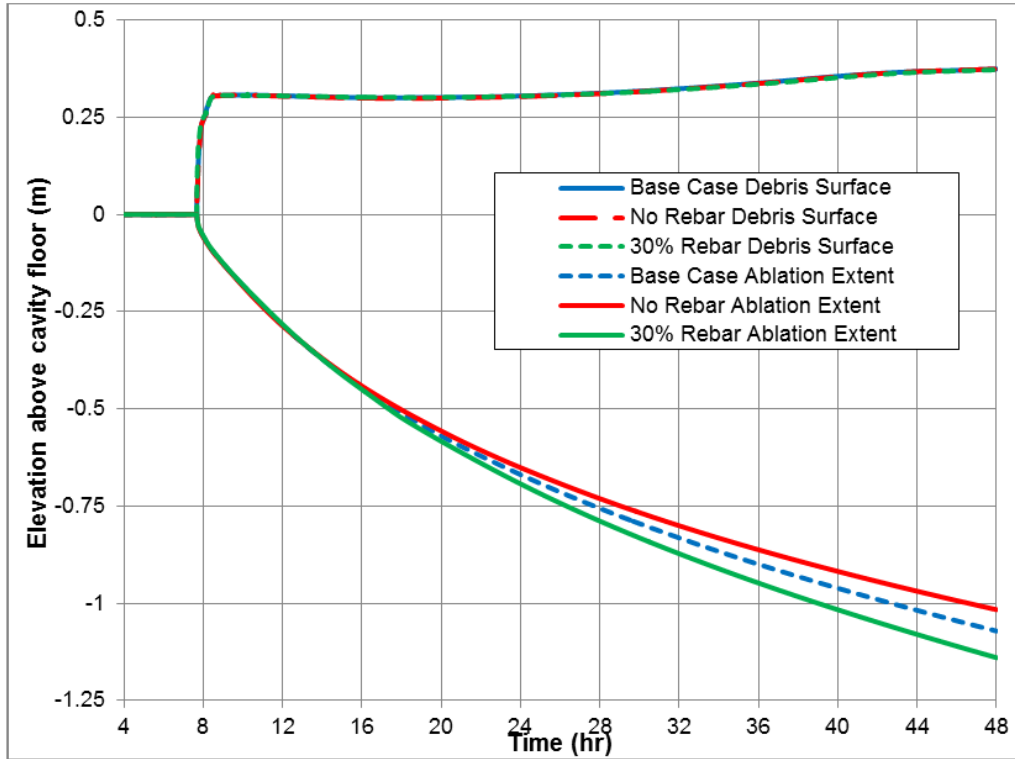


Figure 6-93 MCCI debris surface and ablation depth for varied rebar

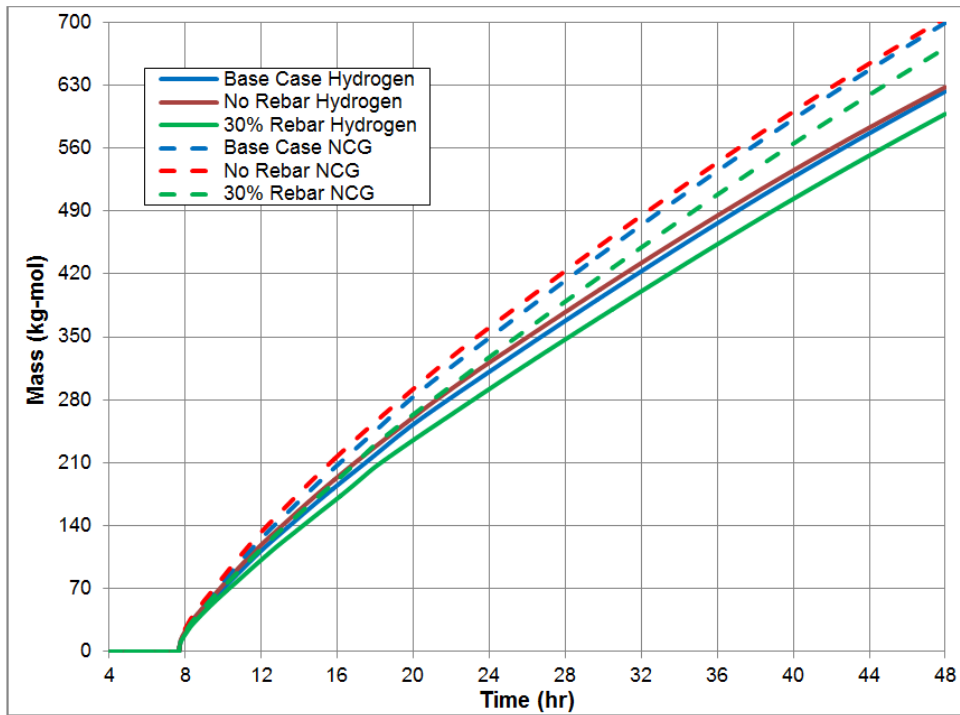
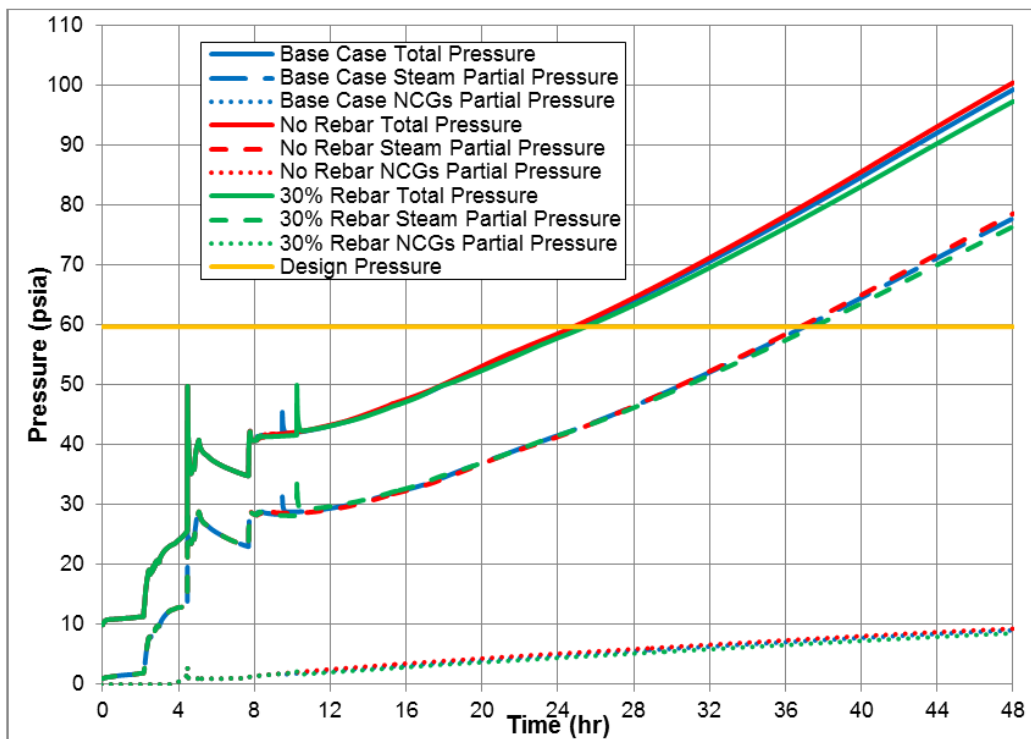


Figure 6-94 MCCI NCG contribution for varied rebar

For the same reasons discussed in Section 6.1.7.1, the overall NCG contribution is small as seen in Figure 6-95. The total containment pressure for the no rebar and 30 percent rebar cases is 1 percent greater and 2 percent less, respectively, when compared to the base case. Additionally, the containment temperature response between the three cases is small and can be seen in Figure 6-96. The containment temperature response for the no rebar and 30 percent rebar cases is less than a 1 percent difference when compared to the base case.

Figure 6-95 and Figure 6-96 indicate that the amount of rebar used does not appear to have a significant, if any difference in the containment response. However, the amount of rebar does have a secondary effect for hydrogen deflagration pressure response after hot leg failure. As seen in Figure 6-95 and Figure 6-96, for post hot leg failure the pressure and temperature rise from deflagration is the result of additional hydrogen and carbon monoxide production from MCCI due to high amounts of rebar (i.e., iron within the rebar reacts with water and carbon dioxide to generate iron oxide and hydrogen and carbon monoxide, respectively). While there are small hydrogen deflagrations for the no rebar case, the deflagrations within the MELCOR CAV package do not carry into a full containment deflagration. The base and 30 percent rebar cases have an instance in which the MELCOR CAV package deflagrations which does carry over into full containment deflagrations and are observed in Figure 6-95 and Figure 6-96 at 9.5-hours and 10.25-hours, respectively.



**Figure 6-95 Containment pressure response for varied rebar**

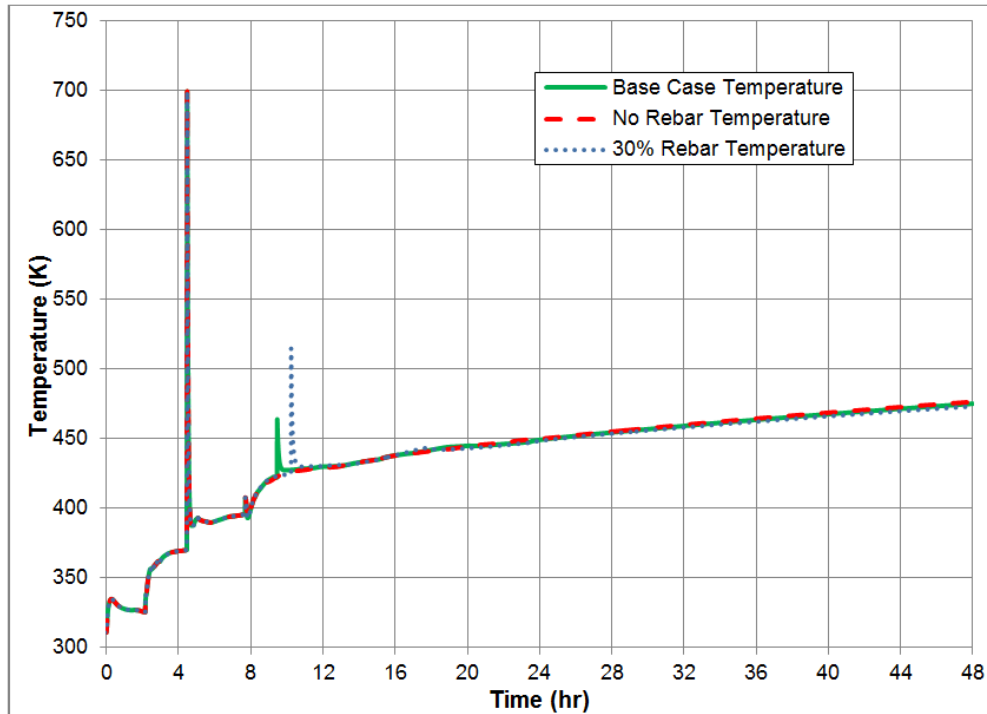


**Figure 6-96 Containment temperature response for varied rebar**

Similar to the discussion in Section 6.1.7.1, the containment pressure increase over the long term is due to continued heating of the containment and the containment atmosphere by decay heat generated in the core debris resident on the containment floor as seen in Figure 6-97. The total energy transfer from the cavity to containment atmosphere for the no rebar and 30 percent rebar cases is 3 percent greater and 3 percent less, respectively, when compared to the base case.

In Figure 6-98, the environmental release fraction from the no rebar and 30 percent rebar cases for cesium are 16 percent and 11 percent less, respectively when compared to the base case at the end of the 48 hour simulation. Additionally in Figure 6-98, the environmental release fraction from the no rebar and 30 percent rebar cases for iodine are 6 percent and 15 percent less, respectively, when compared to the base case at the end of the 48-hour simulation. The base case having slightly higher environmental release fractions is attributed to revaporization of airborne material within containment near the end (40 to 44 hours) of the simulation. However, since the releases from these analyses are so low (i.e., <0.1%) for both cesium and iodine, these releases can be essentially considered the same.

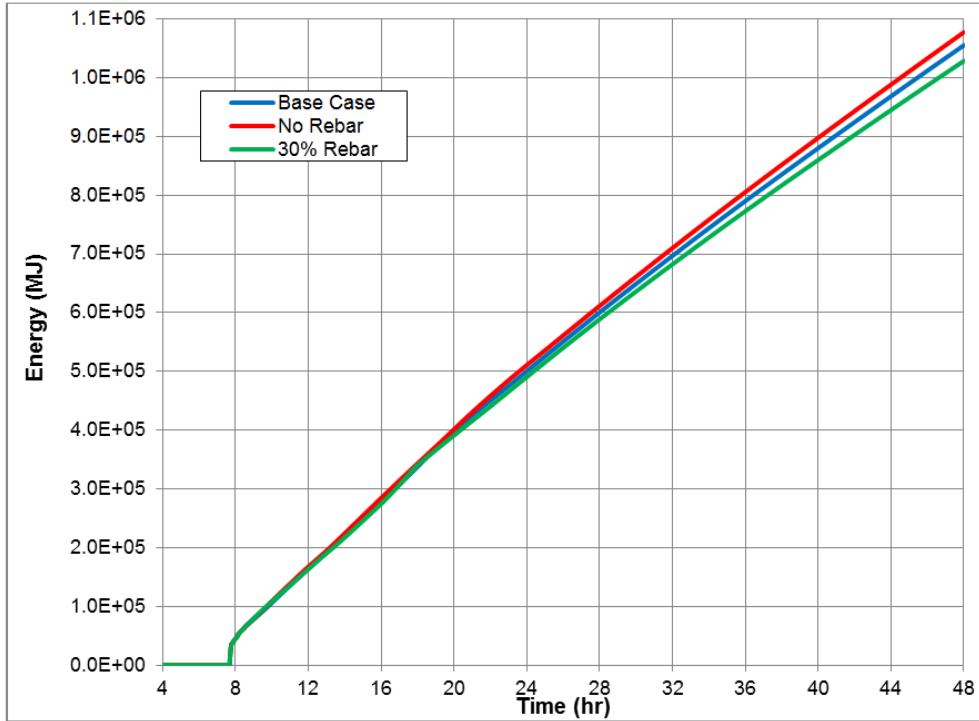


**Figure 6-97 Energy transfer from the cavity to containment atmosphere for varied rebar**

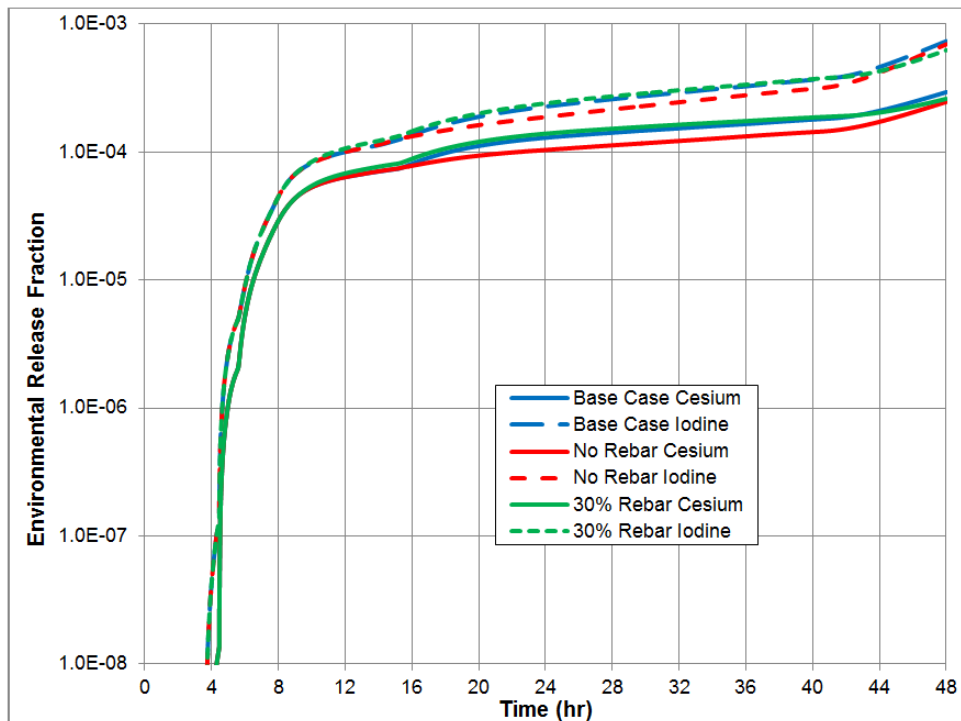


**Figure 6-98 Environmental release fraction of cesium and iodine for varied rebar**

From these sensitivity analyses, the contributing factors that are of note are the following:

- Overall, there is very little difference in the effects from the amount of rebar considered within the concrete.
- Hydrogen deflagrations which carry over into a full containment hydrogen burn have a strong correlation between the amount of rebar within the concrete due to the additional amount of combustible gases (hydrogen and carbon monoxide) generated from MCCI with the rebar.

#### 6.1.8.4 Supplemental Sensitivity Analysis on Leakage from the MSIV

An early sensitive set was run for MSIV leakage. In this set, 4 realizations were performed. The first two were run using the design technical specification for MSIV leakage at a BWR – 11.5 scfh (standard cubic feet per hour). To apply this leakage to the MELCOR model, Eq. 6-1 was used along with a simple two control volume MELCOR model, with the specified pressure differences. A flow path was sized between the two volumes to yield the desired leakage rate. This open fraction, and associated hydraulic diameter were input in the Surry model and run to see the leakage at operating pressure. The other difference between these first two runs was the pressure of control volume (CV) 281 (TURBINE) which is a time-independent CV that essentially represents the remainder of the steam system and environment past the MSIVs. In the original SOARCA model, this CV has a pressure just below the main steam line. This was maintained for the first realization. The second realization set the pressure to atmosphere to be more representative of the environment and less so of the remainder of the reactor system. It was found that regardless of the pressure of CV 281, MSIV leakage at 11.5 scfh did not result in any depressurization of the secondary side during the transient. The third and fourth realizations were run at 10x and 100x BWR MSIV design leakage, respectively, done by scaling up the size of the new flow path. These realizations were also done with CV 281 at atmospheric pressure, as this promotes more significant flows through the MSIV as compared to a pressurized system. It was found that with leakage at ten times the design value, there was still no depressurization of the secondary system. One hundred times design leakage did slightly depressurize the secondary side, but it was not significant at the time of hot leg creep.

$$u = \frac{SCFH}{A} * \frac{1 m^3}{35.315 ft^3} * \frac{1 hr}{3600 sec} * \frac{P_{std}}{P_{cv}} * \frac{T_{cv}}{T_{std}}$$

Eq. 6-1

Where:

u	=	flow path velocity (m/s)
SCFH	=	specified leak rate (scfh)
A	=	flow path area (m <sup>2</sup> )
P <sub>std</sub>	=	standard pressure (1 atm, 14.7 psia)
P <sub>cv</sub>	=	pressure of fluid entering flow path (testing value 39.7 psia)
T <sub>cv</sub>	=	temperature of fluid entering flow path (Surry S.S. Value)
T <sub>std</sub>	=	standard temperature (68°F = 528°R)

Since the sensitivity showed minimal depressurization up to 100x BWR design leakage and there was no PWR-specific value, the results of this sensitivity support the removal of MSIV leakage as a parameter. However, subsequent to the running of these sensitivities, SMEs concluded that BWR design leakage would have no bearing on PWR MSIV performance, primarily because there is no PWR technical specification and thus, no testing of PWR MSIVs.

As a result of the lack of testing and subsequent lack of machining to meet the specification, the SME best estimate is strongly held that the secondary would be depressurized in the modeled accident. Thus, an MSIV leakage area of 0.5 in<sup>2</sup> was used for each steam line. This is larger than 100x BWR design leakage, but is consistent with recent NRC work, including the consequential SGTR project.

#### **6.1.8.5 Supplemental Sensitivity on all Primary SVs Failing Closed**

Failure modeling was significantly enhanced for primary SVs as part of the UA model enhancements. New failure modes were added, including the potential for a SV to fail in the closed position due to stochastic over-cycling. This modeling was included for all three primary SVs. In this STSBO scenario, there is no availability of PORVs, leaving SVs and RCP seal leakage as the only means of primary system pressure relief, which is needed once boiling is initiated in the core region. With the potential for all three primary SVs to fail in the closed position, it was unknown whether RCP seal leakage would be sufficient to depressurize the system, and if not, what the response of the MELCOR code would be to a significant over-pressurization of the primary system.

To test the response, a sensitivity set was run, based on the best estimate deck at the time, which had no SV failures, in which all three primary SVs fail closed after only 2 cycles apiece. In the first sensitivity, RCP seal leakage was left at 21 gpm/pump. Following this, two more sensitivities were run with enhanced leakage at 182 gpm/pump and 480 gpm/pump. Primary pressures for all three sensitivities are compared to the best estimate run in Figure 6-99.

For all cases, the pressure is essentially equivalent until 13 minutes, at which point the RCP seal leakage increases in the 2<sup>nd</sup> and 3<sup>rd</sup> sensitivities. After this point, the 21 gpm/pump sensitivity continues to mirror the best estimate pressure until just before two hours, when pressure reaches the setpoint of the lowest SV. There are the 6 cycles needed to fail the three SVs closed, and then the pressure rapidly increases past the SV set points up to a pressure of about 20 MPa, at which time rapid depressurization occurred. Further analysis of the output files showed that depressurization was a result of a gross failure of the RPV lower head at high pressure. This was an unexpected result. Intuitively, the thick steel lower head would not be the weakest point of the primary system, but this result illuminated the fact that MELCOR did not have any other locations in the primary where over-pressure failure modeling was implemented.

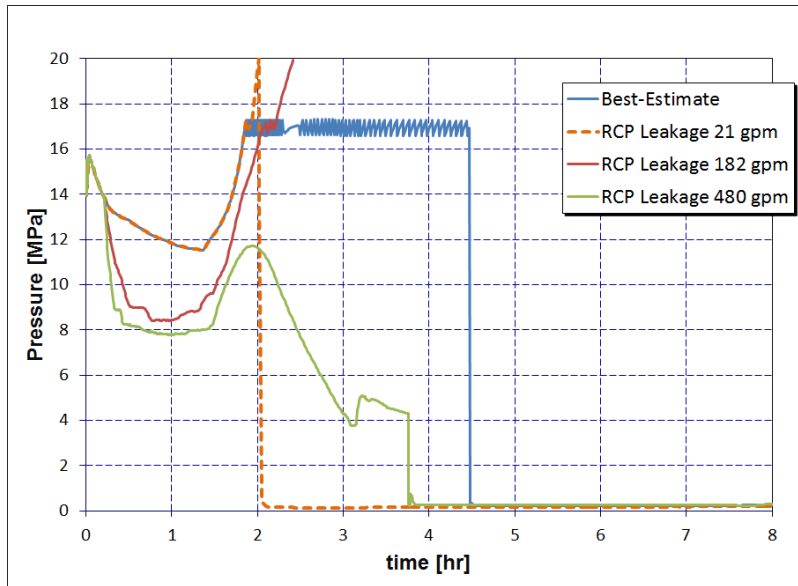


**Figure 6-99 Comparison of primary pressures for select values of pump seal leakage**

The two sensitivities with higher RCP seal leakage (182 gpm/pump and 480 gpm/pump) were then run to observe what would happen with the MELCOR cases where all three SVs failed closed but RCP seal leakage was greater than the best estimate. In both cases, at 13 minutes the primary system starts to depressurize rapidly. The pressure stabilizes at about 1 hour and stays relatively steady until the steam generators dry out, which is observed in Figure 6-99 where beginning at about 1 hour, all plots start to increase as boiling in the RPV drives pressure up. With leakage of 182 gpm/pump there is still not enough leakage area to compensate for this large amount of boiling, and pressure increases to the same point where lower head over-pressurization occurred, at which time the run failed. However, with the largest leakage of 480 gpm/pump the leakage area was large enough to compensate for the RPV boiling and the run eventually depressurizes to containment ambient pressure.

The RCP seals leak at least a small amount regardless of the scenario. Therefore, it was judged to be a weak point of the primary system, although not the only weak point. It was assumed that if primary pressure rises above the highest setpoint SV (17.3 MPa or 2514 psig) to a pressure of 18.96 MPa or 2750 psig, RCP seal leakage will increase to the largest amount, 480 gpm/pump, representing the greatest amount of seal damage. This enhanced leakage based on primary pressure was instituted into the MELCOR model and was used in all uncertainty realizations, precluding gross failure of the lower head. Although none of the uncertainty realizations had all 3 primary SVs fail closed, this sensitivity nevertheless identified a limitation in the MELCOR Surry input model that was made more physical.

## 6.2 Offsite Consequences

The results of the consequence analyses are presented in terms of risk to the public for each of the probabilistic source terms analyzed. The reported risk metrics are individual LCF and early-fatality risks to residents within circular and annular regions centered on the reactor site. They are averaged over the entire residential population within each region. The risk values represent the predicted number of fatalities divided by the population for the selected dose-response model. These risk metrics account for the distribution of the population within the

circular or annular region and for the interplay between the population distribution and the wind rose probabilities.

All results are presented as conditional risks, which are the risks predicated on the accident occurring. The absolute risk is the product of the core damage frequency for the accident scenario and the conditional risk for that scenario, and is discussed where applicable. The absolute risk is the likelihood of receiving a latent fatal cancer or early fatality for an average individual living within specified radii of the plant per year of plant operation (i.e., LCF risk per reactor year (pry) or early-fatality risk pry).

### 6.2.1 Latent Cancer Fatality Risk

This subsection describes the primary results for the uncertainty analysis of LCF risk. This subsection is divided further by dose-response model. Linear, no-threshold results are presented first, followed by the results for which health effects are linear with thresholds, truncated for annual doses below the US background, including medical radiation, of 620 mrem/yr and below 5 rem/yr provided that the lifetime dose is less than 10 rem. This latter dose response model is based on a position statement from the Health Physics Society and is labeled HPS. Regression analyses were completed for the spatial intervals and dose thresholds as identified in Table 6-17.

**Table 6-17 MACCS regression analyses completed by spatial intervals and dose threshold.**

Output Parameter									
Data set used based on occurrence of SGTR									
Spatial Interval (miles)	LNT			Truncated Background			HPS		
	SGTR	Non-SGTR	Both	SGTR	Non-SGTR	Both	SGTR	*Non-SGTR	Both
0 to 10	✓	✓	✓	✓	✓	✓	✓	✓	✓
0 to 20	✓	✓	✓	✓	✓	✓	✓	✓	✓
0 to 30	✓	✓	✓	✓	✓	✓	✓	✓	✓
0 to 40	✓	✓	✓	✓	✓	✓	✓	✓	✓
0 to 50	✓	✓	✓	✓	✓	✓	✓	✓	✓
10 to 20	✓	✓	✓	✓	✓	✓	✓	✓	✓
20 to 30	✓	✓	✓	✓	✓	✓	✓		✓
30 to 40	✓	✓	✓	✓	✓	✓	✓		✓
40 to 50	✓	✓	✓	✓	✓	✓	✓		✓

\*For this set only one value was not equal to zero from 20-30 and all values were zero for 30-40 and 40-50

#### 6.2.1.1 Results for LNT Dose Response

Table 6-18 and Table 6-19 show statistical results for mean, individual, LCF risk conditional on an STSBO accident occurring from the MACCS uncertainty analysis at nine spatial intervals representing concentric circles and annular areas all centered on the Surry site. In these tables, mean indicates that results are averaged over weather variability, within the spatial interval, and

over the set of 1003 realizations. Each of the statistics in the table represents the overall epistemic (state of knowledge) uncertainty for the groups of MELCOR (Level 2) and MACCS (Level 3) inputs that were treated as uncertain (cf., Section 4.2). The results show that mean conditional risks are on the order of  $10^{-5}$  and diminish with distance from the plant.

Figure 6-100 and Figure 6-101 show the CCDFs for the same circular and annular areas summarized in Table 6-18 and Table 6-19. The points on the curves represent the mean LCF risk over variable weather for each of the 1003 realizations representing epistemic uncertainty in this UA and are conditional on an STSBO occurring. The curves show that the conditional risks span the range of  $10^{-8}$  to nearly  $10^{-3}$  per event. The curves display a distinct shoulder at a probability of approximately 0.1. This represents the transition from events with no SGTR above the shoulder to events with SGTR below the shoulder.

**Table 6-18 Mean, individual LCF risk using LNT dose response, conditional on an STSBO occurring for five circular areas centered on Surry site.**

	0-10 miles	0-20 miles	0-30 miles	0-40 miles	0-50 miles
<b>Mean</b>	2.84E-05	1.60E-05	1.09E-05	6.97E-06	5.33E-06
<b>Median</b>	6.29E-06	3.06E-06	1.95E-06	1.18E-06	8.86E-07
<b>5<sup>th</sup> Percentile</b>	6.87E-07	3.47E-07	2.27E-07	1.38E-07	1.04E-07
<b>95<sup>th</sup> Percentile</b>	1.74E-04	1.01E-04	7.04E-05	4.51E-05	3.51E-05

**Table 6-19 Mean, individual LCF risk using LNT dose response, conditional on an STSBO occurring for four annular areas centered on Surry site.**

	10-20 miles	20-30 miles	30-40 miles	40-50 miles
<b>Mean</b>	1.13E-05	4.72E-06	2.79E-06	1.85E-06
<b>Median</b>	1.76E-06	6.45E-07	3.69E-07	2.37E-07
<b>5<sup>th</sup> Percentile</b>	2.15E-07	7.89E-08	4.39E-08	2.90E-08
<b>95<sup>th</sup> Percentile</b>	7.20E-05	2.95E-05	1.76E-05	1.25E-05

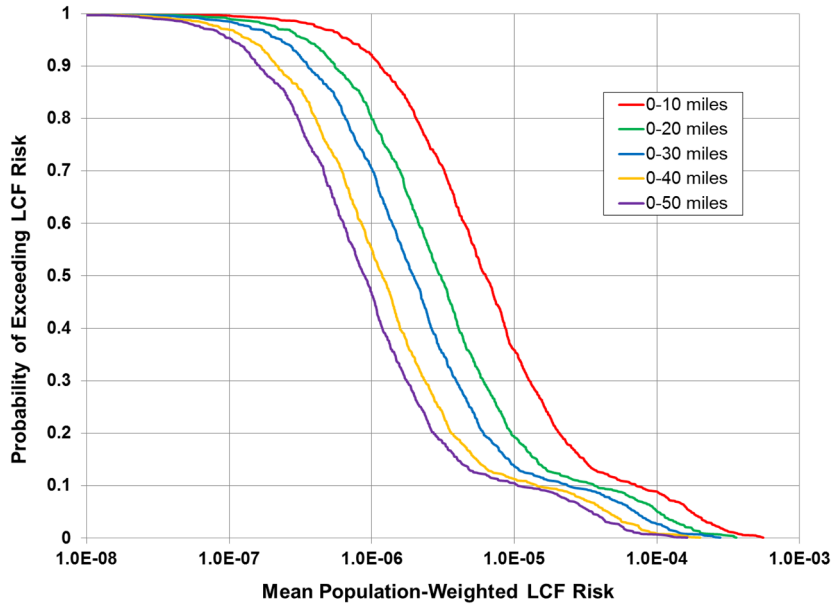


**Figure 6-100 Complementary cumulative distribution functions of mean, population-weighted LCF risk (based on LNT dose response) conditional on an STSBO occurring for five circular areas centered on the Surry site**

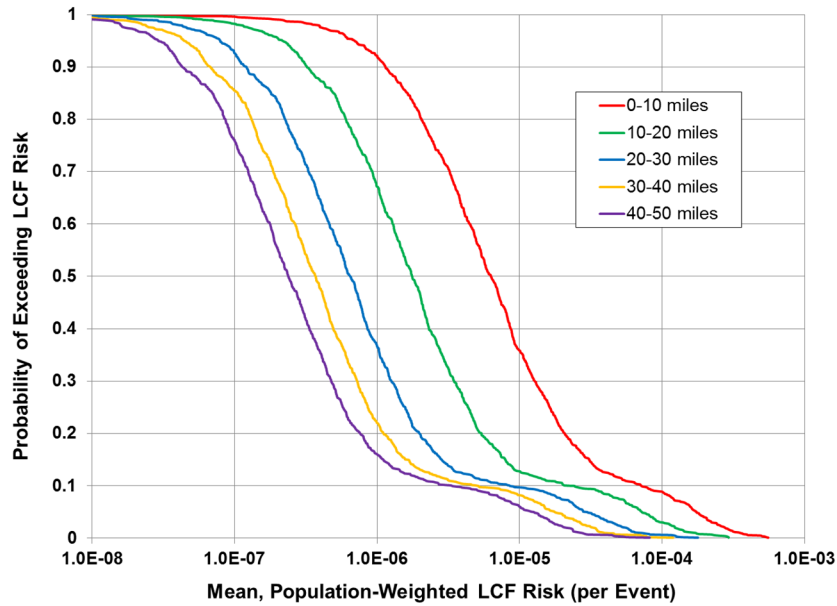


**Figure 6-101 Complementary cumulative distribution function of mean, population-weighted LCF risk (based on LNT dose response) conditional on an STSBO occurring for five annular areas centered on the Surry site**

The emergency phase used in this analysis is the first seven days following the beginning of release into the environment. The long-term phase immediately follows the emergency phase and lasts for 50 years. Figure 6-102 shows the fraction of the total risk from the emergency phase for the set of LCF risk results shown in Figure 6-101. Two key features are apparent from

this figure. First, the large majority of the LCF risk based on the linear no-threshold dose response is from the long-term phase at all five distance intervals, even for the realizations with SGTR. The mean values from the five distributions are 0.01, 0.15, 0.17, 0.16, and 0.16 for distance intervals 0 to 10, 10 to 20, 20 to 30, 30 to 40, and 40 to 50 miles, respectively. Only a handful of realizations have emergency-phase contributions to risk that exceed those from the long-term phase. Second, the curve for the distance range from 0 to 10 miles has a very different character than those for the other distance ranges because evacuation is very effective in reducing risk during the emergency phase for the population living within the EPZ. Most of the overall risk within 10 miles is to the 0.5 percent of the public that is assumed to not evacuate; however, some of the risk is to the slowly evacuating cohorts for the realizations with relatively early releases, mainly the realizations with SGTR.

The core damage frequency for an STSBO at Surry provided in NUREG/CR-7110 Volume 2 is  $2 \times 10^{-6}$  pry. Thus, the absolute risk of an STSBO based on a LNT dose-response model, including the possibility of an induced SGTR, is estimated to be about  $6 \times 10^{-11}$  pry ( $2 \times 10^{-6}$  pry  $\cdot$   $3 \times 10^{-5}$  conditional risk from Table 6-18) to a member of the population living within 10 miles of the reactor site; for comparison, the absolute risk for an STSBO with and without SGTR in the original SOARCA study was about  $3 \times 10^{-10}$  pry.

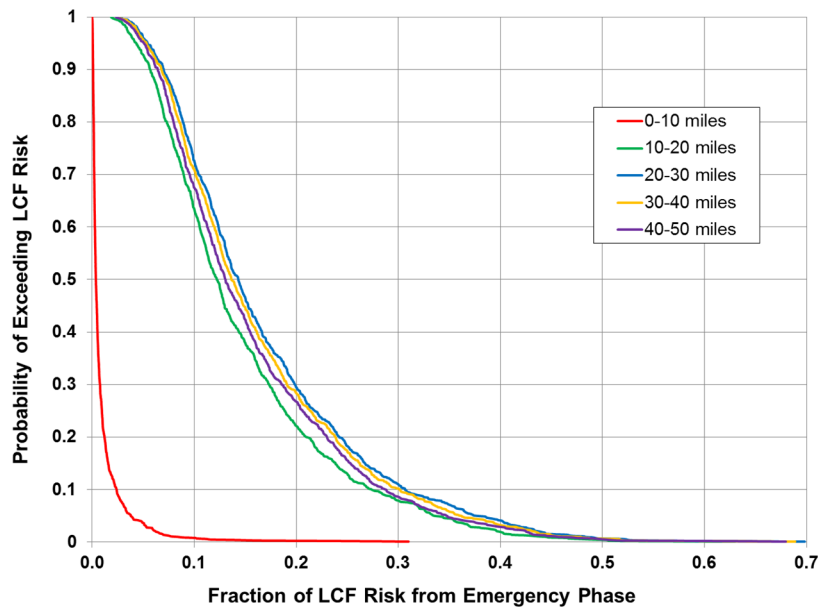


**Figure 6-102 Complementary cumulative distribution functions of fraction of the population-weighted LCF risk (based on LNT dose response) from the emergency phase for residents within five annular areas centered on the Surry site**

### 6.2.1.2 Results for Linear Dose Response Truncated below US Annual Background

Table 6-20 and Table 6-21 show statistical results for mean, individual, LCF risk conditional on an STSBO accident occurring from the MACCS uncertainty analysis at nine spatial intervals representing concentric circles and annular areas all centered on the Surry site. In these tables, mean indicates that results are averaged over weather variability, within the spatial interval, and over the set of 1003 realizations. Each of the statistics in the table represents the overall

epistemic (state of knowledge) uncertainty for the groups of MELCOR (Level 2) and MACCS (Level 3) inputs that were treated as uncertain (cf., Section 4.2). The results show that mean conditional risks are less than  $10^{-5}$  within 10 miles and diminish with distance from the plant. The mean values in these tables are about an order-of-magnitude lower than those in Table 6-18 and Table 6-19 based on the LNT dose-response model. The 5<sup>th</sup> percentile results are all zero and the median results are nearly zero within 10 miles and identically zero for the population living beyond 10 miles. Only the risks above the median contribute significantly to the mean.

Figure 6-103 and Figure 6-104 show the complementary cumulative distribution functions for the same circular and annular areas summarized in Table 6-18 and Table 6-19. The points on the curves represent the mean LCF risk over variable weather for each of the 1003 realizations representing epistemic uncertainty in this UA and are conditional on an STSBO occurring. The curves show that the conditional risks span the range of  $10^{-14}$  to about  $10^{-4}$  per event. The curves display a distinct shoulder at a probability of approximately 0.1. This represents the transition from events with no SGTR above the shoulder to events with SGTR below the shoulder.

Figure 6-104 shows that the probability of a nonzero risk is less than unity within 10 miles (approximately 0.94 of the results are nonzero) when annual doses less than 620 mrem do not contribute to health effects. The probability diminishes sharply at longer distances. For example, the probability is only about 0.17 that the LCF risk is greater than zero at distances greater than 10 miles. The probabilities drop to 0.11, 0.10, and 0.10 at distances of 20, 30, and 40 miles, respectively. A probability of 0.10 corresponds to the shoulder in the risk curve shown in the figure.

The distinction between emergency-phase and long-term-phase risks is blurred for this dose-response model because dose truncation is performed for each year. The first year includes the emergency phase and a portion of the long-term phase, so no breakdown can be provided for risks during the two individual phases.

**Table 6-20 Mean, individual LCF risk using US annual background dose-response model, conditional on an STSBO accident for five circular areas centered on the Surry site.**

	0-10 miles	0-20 miles	0-30 miles	0-40 miles	0-50 miles
<b>Mean</b>	3.11E-06	2.14E-06	1.42E-06	8.39E-07	6.01E-07
<b>Median</b>	1.14E-09	3.14E-10	1.73E-10	8.89E-11	6.05E-11
<b>5<sup>th</sup> Percentile</b>	0.00E+00	0.00E+00	0.00E+00	0.00E+00	0.00E+00
<b>95<sup>th</sup> Percentile</b>	2.54E-05	1.66E-05	1.08E-05	6.18E-06	4.24E-06

**Table 6-21 Mean, individual LCF risk using US annual background dose-response model, conditional on an STSBO accident for four annular areas centered on the Surry site.**

	10-20 miles	20-30 miles	30-40 miles	40-50 miles
<b>Mean</b>	1.78E-06	5.45E-07	2.20E-07	9.43E-08
<b>Median</b>	0.00E+00	0.00E+00	0.00E+00	0.00E+00
<b>5<sup>th</sup> Percentile</b>	0.00E+00	0.00E+00	0.00E+00	0.00E+00
<b>95<sup>th</sup> Percentile</b>	1.32E-05	3.24E-06	1.12E-06	4.24E-07

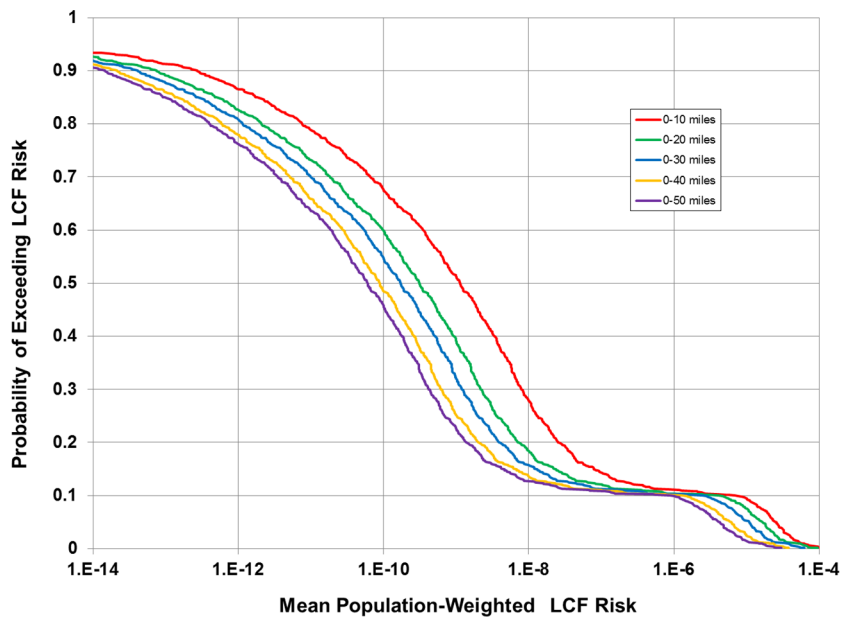


**Figure 6-103 Complementary cumulative distribution function of mean, population-weighted LCF risk (based on US background dose truncation) conditional on an STSBO accident for five circular areas centered on the Surry site**

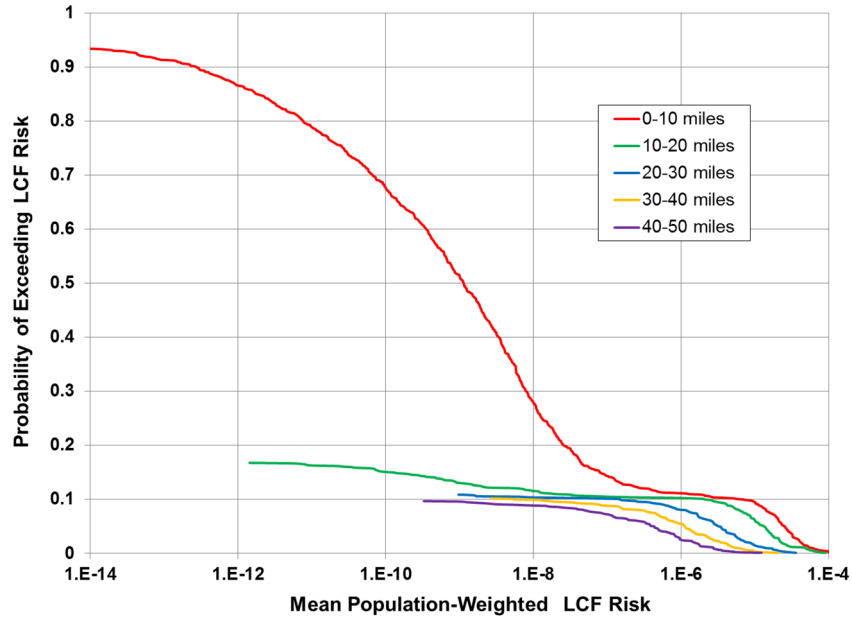


**Figure 6-104 Complementary cumulative distribution function of mean, population-weighted LCF risk (based on US background dose-response model) conditional on an STSBO accident for five annular areas centered on the Surry site**

### 6.2.1.3 Results for Linear Dose Response Truncated Using the HPS Model

Table 6-22 and Table 6-23 show statistical results for mean, individual, LCF risk conditional on an STSBO accident occurring from the MACCS uncertainty analysis at nine spatial intervals representing concentric circles and annular areas all centered on the Surry site. In these tables, mean indicates that results are averaged over weather variability, within the spatial interval, and over the set of 1003 realizations. Each of the statistics in the table represents the overall epistemic (state of knowledge) uncertainty for the groups of MELCOR (Level 2) and MACCS (Level 3) inputs that were treated as uncertain (cf., Section 4.2). The results show that mean conditional risks are less than  $10^{-6}$  and diminish with distance from the plant. The 5<sup>th</sup> percentile results are all zero and the median results are nearly zero within 10 miles and identically zero beyond 10 miles. Only the risks above the median contribute significantly to the mean.

Figure 6-105 and Figure 6-106 show the complementary cumulative distribution functions for the same circular and annular areas summarized in Table 6-18 and Table 6-19. The points on the curves represent the mean LCF risk over variable weather for each of the 1003 realizations representing epistemic uncertainty in this UA and are conditional on the accident occurring. The curves show that the conditional risks span the range of  $10^{-14}$  to about  $10^{-4}$  per event. The curves display a distinct shoulder at a probability of approximately 0.1. This represents the transition from events with no SGTR above the shoulder to events with SGTR below the shoulder.

Figure 6-104 shows that the probability of a nonzero risk is less than unity within 10 miles (approximately 0.85 of the results are nonzero) when annual doses less than 5 rem do not contribute to health effects (provided lifetime doses do not exceed 10 rem. The probability diminishes sharply at longer distances. For example, the probability is only about 0.12 that the

LCF risk is greater than zero at distances greater than 10 miles. The probabilities drop to 0.10, 0.09, and 0.07 at distances of 20, 30, and 40 miles, respectively. A probability of 0.10 corresponds to the shoulder in the risk curve shown in the figure, below which SGTRs dominate. This shows that even some of the SGTR sequences do not produce annual doses greater than 5 rem at distances beyond 30 miles.

The distinction between emergency-phase and long-term-phase risks is blurred for this dose-response model because dose truncation is performed for each year. The first year includes the emergency phase and a portion of the long-term phase, so no breakdown can be provided for risks during the two individual phases.

**Table 6-22 Mean, individual LCF risk using HPS dose-response model, conditional on an STSBO accident occurring for five circular areas centered on the Surry site.**

	0-10 miles	0-20 miles	0-30 miles	0-40 miles	0-50 miles
<b>Mean</b>	5.29E-07	4.37E-07	2.78E-07	1.54E-07	1.07E-07
<b>Median</b>	3.15E-12	8.69E-13	4.77E-13	2.46E-13	1.67E-13
<b>5th percentile</b>	0.00E+00	0.00E+00	0.00E+00	0.00E+00	0.00E+00
<b>95th percentile</b>	1.67E-06	2.14E-06	1.20E-06	6.22E-07	4.25E-07

**Table 6-23 Mean, individual LCF risk using HPS dose-response model, conditional on an STSBO accident occurring for four annular areas centered on the Surry site.**

	10-20 miles	20-30 miles	30-40 miles	40-50 miles
<b>Mean</b>	4.03E-07	8.33E-08	2.26E-08	7.61E-09
<b>Median</b>	0.00E+00	0.00E+00	0.00E+00	0.00E+00
<b>5th percentile</b>	0.00E+00	0.00E+00	0.00E+00	0.00E+00
<b>95th percentile</b>	1.35E-06	8.63E-08	9.46E-09	9.98E-10

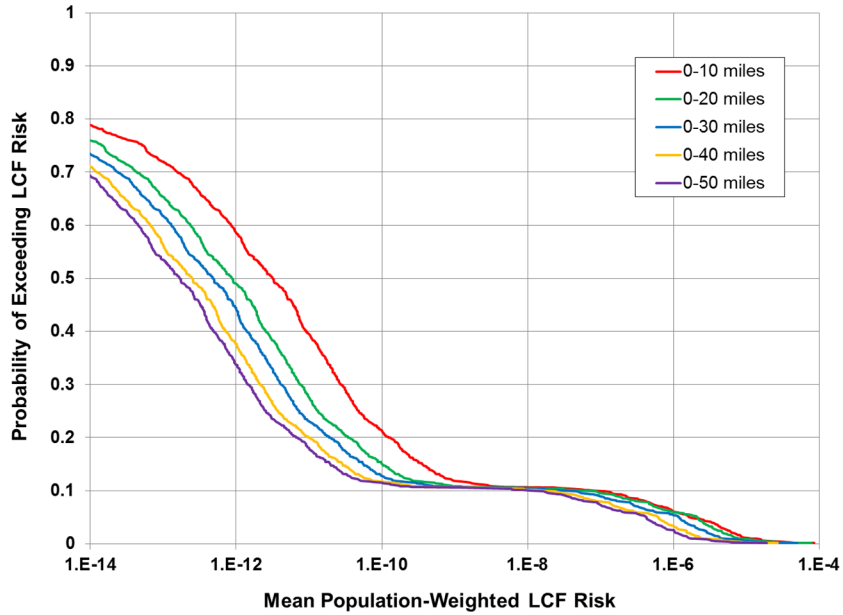


**Figure 6-105 Complementary cumulative distribution function of mean, population-weighted LCF risk (based on HPS dose-response model) conditional on an STSBO accident for five circular areas centered on the Surry site**

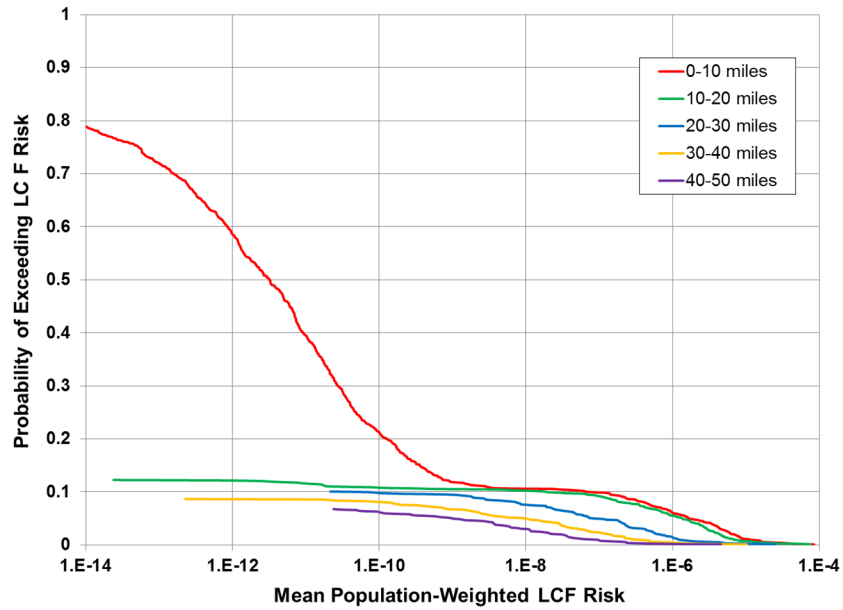


**Figure 6-106 Complementary cumulative distribution function of mean, population-weighted LCF risk (based on HPS dose-response model) conditional on an STSBO accident for five annular areas centered on the Surry site**

## 6.2.2 Early Fatalities

Only one realization had a nonzero risk for early fatalities. Within this realization, only a few of the weather trials had doses large enough to exceed the dose threshold for early fatalities to occur and the reported conditional risk was approximately  $7 \cdot 10^{-13}$  within a 2-mile radius of the site. This number is so small that it is essentially zero.

## 6.2.3 Regression Analysis

As part of the statistical analysis of the MACCS UA, a series of regression methods were applied to determine which input parameters most affect LCF risk and early-fatality risk. The four regression methods, Rank regression, Quadratic regression, Recursive partitioning, and MARS, are described in Section 3.

### 6.2.3.1 Regression Analysis of Latent Cancer Fatality Risk Using LNT

Each of the four regression techniques was applied to the 1003 realizations that were evaluated in this UA. Regression analyses for nine distance intervals were performed. Five circular areas with outer radii of 10, 20, 30, 40, and 50 miles were evaluated; annuli (rings) from 10 to 20 miles, 20 to 30 miles, 30 to 40 miles, and 40 to 50 miles were also evaluated. The combination of regression techniques and distance intervals resulted in a set of 36 results. A complete set of regression analyses were also performed on the subset of the realizations that did not involve induced SGTRs and those that did involve SGTRs. This resulted in 104 regression results. A subset of these results is discussed in this subsection. The results that are not discussed here have similar trends to those that are included and so do not provide different insights.

#### 6.2.3.1.1 All Cases

Table 6-24 through Table 6-26 show the regression results for mean LCF risks from the complete set of 1003 realizations. The results are based on the LNT dose-response model at three distance intervals from the site: 0 to 10 miles, 10 to 20 miles, and 0 to 50 miles. The word 'mean' is used to indicate a statistical mean over variable weather.

The first four major columns in the tables are labeled with the regression technique used to create the results. The last two columns contain average values of the main (individual, independent) contribution of the parameter on the result metric and the conjoint influence of the parameter on the result metric. These are calculated as arithmetic averages of the overall contributions from the four regression techniques ( $R^2$  from rank regression and  $S_i$  from the others) and an arithmetic average of the values of  $(\text{Final } R^2) * (T_i - S_i)$  for the three nonlinear regression techniques (i.e., all but rank regression). More detail is provided in Section 3.3.2.

Values of main contribution greater than 0.02 are considered significant, are highlighted, and are discussed in subsequent paragraphs. Conjoint contributions greater than 0.1 are also considered significant and are highlighted. The parameters in the first column of the tables are ordered by the value in the column labeled Main Contribution, so the most important parameters appear in rank order at the top of the table.

The first two parameters in all three regression tables are TUBTHICK, the initial tube thickness of the most damaged steam generator tube, and SVOAFRAC, which indicates the open area of the relief valves on the primary side of the reactor. This parameter is important to the extent that it influences the depressurization of the reactor primary. These parameters influence whether

the accident progression is driven toward a steam generator tube rupture or not. Both parameters have large values in the Main and Conjoint Contribution columns. The large conjoint contributions of these parameters and the lack of significant conjoint influence for the other parameters indicate that these parameters have a synergistic influence. The TUBTHICK parameter directly affects the initial damage state of one of the steam generator tubes; the SVOAFRAC parameter is related to the depressurization of the RCS after SV failure and thus influences the pressure differential across the damaged steam generator tube. Tube thickness and pressure differential across the tube controls the likelihood of a steam generator tube rupture. Thus, they have a critical influence on both the magnitude and timing of the release and directly influence LCF risk. Both parameters are negatively correlated with risk because risk increases when the weakest tube is thin and pressure differential across the tube is large.

**Table 6-24 Mean, individual, LCF risk regression results within a 10-mile circular area for all realizations based on LNT.**

Input	Rank Regression		Quadratic		Recursive Partitioning		MARS		Main Contr.*	Conjoint Contr.*
	R <sup>2</sup> contr.	SRRC	S <sub>I</sub>	T <sub>I</sub>	S <sub>I</sub>	T <sub>I</sub>	S <sub>I</sub>	T <sub>I</sub>		
Final R <sup>2</sup>	0.54		0.60		0.86		0.74			
TUBTHICK	0.04	-0.20	0.33	0.53	0.30	0.86	0.35	0.80	0.189	0.309
SVOAFRAC	0.03	-0.18	0.23	0.40	0.09	0.55	0.11	0.45	0.082	0.250
CYCLE	0.18	0.44	0.01	0.02	0.01	0.01	0.02	0.02	0.050	0.005
GSHFAC.2	0.13	0.35	0.02	0.05	0.00	0.00	0.01	0.03	0.038	0.011
DLEAK	0.08	0.26	0.01	0.04	0.01	0.01	0.00	0.01	0.022	0.010
CFRISK.8	0.02	0.15	0.02	0.05	0.00	0.06	0.02	0.08	0.011	0.037
SV_STATUS	---	---	0.04	0.04	---	---	---	---	0.006	0.000
DDREFA.8	0.01	-0.12	0.00	0.02	0.00	0.05	0.00	0.03	0.004	0.025
CYSIGA.1	0.02	-0.13	---	---	---	---	---	---	0.004	0.000
TUBETEMP	---	---	0.02	0.02	0.00	0.00	0.01	0.03	0.004	0.006
DEV_DEC_HEAT	0.01	-0.09	0.00	0.03	0.00	0.03	0.01	0.02	0.004	0.015
VDEPOS.1	0.01	0.09	0.01	0.01	0.00	0.04	---	---	0.003	0.011
CFRISK.7	0.01	0.09	---	---	---	---	---	---	0.002	0.000
CFC	0.01	-0.09	---	---	---	---	0.00	0.01	0.002	0.001
CFRISK.6	0.01	0.07	---	---	---	---	0.00	0.02	0.002	0.003
PROTIN.2	---	---	---	---	0.01	0.09	---	---	0.001	0.023
CHEMFORMCS	0.01	-0.06	---	---	---	---	---	---	0.001	0.000
SGTRLOC	0.00	0.06	0.00	0.01	---	---	---	---	0.001	0.002
CFRISK.2	---	---	0.00	0.03	---	---	---	---	0.001	0.005
LA.140_I.9	---	---	0.00	0.04	0.00	0.03	0.00	0.01	0.000	0.018
PARTSHAPE	---	---	0.00	0.01	0.00	0.01	---	---	0.000	0.004
CHEMFORMI2	---	---	---	---	0.00	0.02	0.00	0.01	0.000	0.009

\* highlighted if main contribution larger than 0.02 or conjoint contribution larger than 0.1

**Table 6-25 Mean, individual, LCF risk regression results within a 10- to 20-mile annular area for all realizations based on LNT.**

	Rank Regression		Quadratic		Recursive Partitioning		MARS		Main Contr.*	Conjoint Contr.*
Final R <sup>2</sup>	0.38		0.59		0.85		0.73			
Input	R <sup>2</sup> contr.	SRRC	S <sub>i</sub>	T <sub>i</sub>	S <sub>i</sub>	T <sub>i</sub>	S <sub>i</sub>	T <sub>i</sub>		
TUBTHICK	0.04	-0.21	0.29	0.45	0.35	0.89	0.30	0.82	0.181	0.311
SVOAFRAC	0.02	-0.15	0.19	0.34	0.08	0.56	0.11	0.48	0.071	0.255
GSHFAC.2	0.11	0.32	0.02	0.04	---	---	---	---	0.030	0.005
DLEAK	0.08	0.26	0.01	0.09	---	---	---	---	0.020	0.017
CYCLE	0.05	0.23	---	---	---	---	0.01	0.03	0.014	0.004
CFRISK.8	0.01	0.13	0.02	0.03	0.00	0.01	0.02	0.07	0.009	0.019
SV_STATUS	---	---	0.04	0.10	---	---	0.00	0.01	0.007	0.016
TUBETEMP	---	---	0.01	0.03	0.00	0.02	0.00	0.02	0.004	0.012
DDREFA.8	0.02	-0.12	0.00	0.03	0.00	0.00	---	---	0.004	0.005
PROTIN.2	---	---	0.01	0.02	0.00	0.03	0.01	0.04	0.004	0.018
VDEPOS.1	---	---	0.01	0.02	0.00	0.08	0.01	0.04	0.004	0.031
CYSIGA.1	0.01	-0.10	---	---	---	---	---	---	0.003	0.000
CFRISK.7	0.01	0.10	---	---	---	---	---	---	0.003	0.000
CFRISK.6	0.01	0.06	0.01	0.14	---	---	0.00	0.01	0.002	0.027
PARTSHAPE	0.00	0.05	0.00	0.03	0.01	0.03	---	---	0.002	0.013
CFRISK.2	---	---	0.01	0.05	---	---	---	---	0.002	0.008
DEV_DEC_HEAT	0.01	-0.10	---	---	0.00	0.00	---	---	0.002	0.000
DDREFA.1	---	---	0.00	0.03	0.00	0.01	0.00	0.06	0.002	0.022
CHEMFORMI2	---	---	0.00	0.02	0.01	0.01	---	---	0.002	0.004
CFC	0.01	-0.08	---	---	---	---	---	---	0.001	0.000
CWASH1.	0.01	0.07	---	---	0.00	0.01	0.00	0.01	0.001	0.004
CHEMFORMCS	0.01	-0.06	---	---	---	---	---	---	0.001	0.000

\* highlighted if main contribution larger than 0.02 or conjoint contribution larger than 0.1

**Table 6-26 Mean, individual, LCF risk regression results within a 50-mile circular area for all realizations based on LNT.**

	Rank Regression		Quadratic		Recursive Partitioning		MARS		Main Contr.*	Conjoint Contr.*
Final R <sup>2</sup>	0.37		0.60		0.86		0.59			
Input	R <sup>2</sup> contr.	SRRC	S <sub>i</sub>	T <sub>i</sub>	S <sub>i</sub>	T <sub>i</sub>	S <sub>i</sub>	T <sub>i</sub>		
TUBTHICK	0.04	-0.21	0.26	0.43	0.35	0.89	0.47	0.88	0.194	0.269
SVOAFRAC	0.02	-0.14	0.21	0.37	0.08	0.55	0.12	0.53	0.071	0.247
GSHFAC.2	0.12	0.34	0.02	0.06	0.00	0.05	---	---	0.033	0.022
DLEAK	0.07	0.24	0.01	0.08	---	---	---	---	0.018	0.014
CYCLE	0.05	0.23	0.00	0.01	0.00	0.02	0.01	0.01	0.014	0.006
SV_STATUS	---	---	0.04	0.11	---	---	---	---	0.008	0.013
CFRISK.8	0.01	0.13	0.01	0.04	0.00	0.04	---	---	0.005	0.016
DDREFA.8	0.02	-0.12	0.00	0.02	0.00	0.01	0.00	0.01	0.004	0.009
DEV_DEC_HEAT	0.01	-0.09	0.01	0.06	---	---	---	---	0.004	0.009
CFRISK.6	0.01	0.06	0.01	0.11	0.00	0.01	0.00	0.00	0.003	0.022
CFRISK.7	0.01	0.11	---	---	---	---	---	---	0.003	0.000
SV_NBCYC	---	---	0.01	0.04	---	---	0.00	0.01	0.002	0.007
PARTSHAPE	0.00	0.05	0.00	0.02	0.01	0.02	0.00	0.01	0.002	0.008
CYSIGA.1	0.01	-0.09	---	---	---	---	---	---	0.002	0.000
PROTIN.2	---	---	0.01	0.01	0.00	0.03	---	---	0.002	0.007
CWASH1.	0.01	0.08	---	---	---	---	---	---	0.002	0.000
CHEMFORMI2	---	---	---	---	0.01	0.01	0.00	0.02	0.002	0.003
CFC	0.01	-0.07	---	---	---	---	---	---	0.001	0.000
CHEMFORMCS	0.01	-0.06	---	---	---	---	---	---	0.001	0.000
VDEPOS.1	---	---	0.00	0.03	---	---	---	---	0.001	0.004
CFRISK.2	---	---	0.00	0.05	0.00	0.03	0.00	0.00	0.001	0.019
CE.143_ICH.9	---	---	---	---	0.00	0.00	0.00	0.00	0.001	0.000

\* highlighted if main contribution larger than 0.02 or conjoint contribution larger than 0.1

The third parameter in Table 6-24 is CYCLE, which corresponds to the point during the fuel cycle at which the accident occurs (i.e., BOC, MOC, and EOC). This sampled value directly affects the MELCOR source term calculation through decay heat and it directly affects the MACCS consequence analysis through fission product inventory. Of all the sampled parameters, this is the only parameter that has such a dual status. Because the activities of the fission products in the fuel increase with burnup, this parameter can have a significant influence on risk. The activities of shorter lived isotopes increase with burnup only until secular equilibrium is established; however, the activities of longer lived isotopes, like Cs-137, can nearly double from BOC to EOC. Because the longer lived isotopes have a significant effect on LCF risk, especially in the long-term phase, this parameter is significant to the predicted results. The correlation between CYCLE and predicted risk is positive, as expected.

The fourth parameter in Table 6-24 and the third parameter in the other two tables is GSHFAC.2, which is the groundshine shielding factor for normal activity during the emergency phase. This parameter is fully rank-correlated with the value of groundshine shielding factor used for the long-term phase. Normal activity is averaged for the population over a normal week of activity, including time spent indoors at home, at work, outdoors, and commuting. Groundshine is not a particularly important dose pathway during the emergency phase, but is generally the dominant dose pathway during the long-term phase. Since the groundshine dose received by any individual during the long-term phase is directly proportional to the long-term groundshine shielding factor, it is important for latent cancer risk. This is especially so when the long-term-phase dominates the emergency-phase contribution to risk. This parameter is positively correlated with LCF risk, which indicates that greater design leakage positively influences risk.

The fifth parameter in Table 6-24 and the fourth parameter in the other the two tables is the containment leak path length (DLEAK), which is the leak path length for design basis leakage from containment. The rate of leakage from containment responds inversely to the value of this parameter, so increasing values of this parameter cause risk to diminish. This parameter is negatively correlated with LCF risk.

The scatter plots provided in Figure 6-107 through Figure 6-111 show the trends between the five most important inputs for LCF risk within a 50-mile circular area, as discussed in the preceding paragraphs. The trends in these figures are very similar for the other circular and annular areas that were evaluated in this study. The plots qualitatively show the sign and strength of the correlation between the parameters and LCF risk, although the trend is sometimes hard to distinguish by eye because of the density of the dots. Additionally, these plots show the dual nature of the source terms: the points at the top of each plot generally correspond to realizations with an SGTR; the points below generally correspond to realizations with no SGTR. Scatter plots in which the group of points corresponding to SGTR is shifted right or left indicate a correlation between the variable and the occurrence of an SGTR.

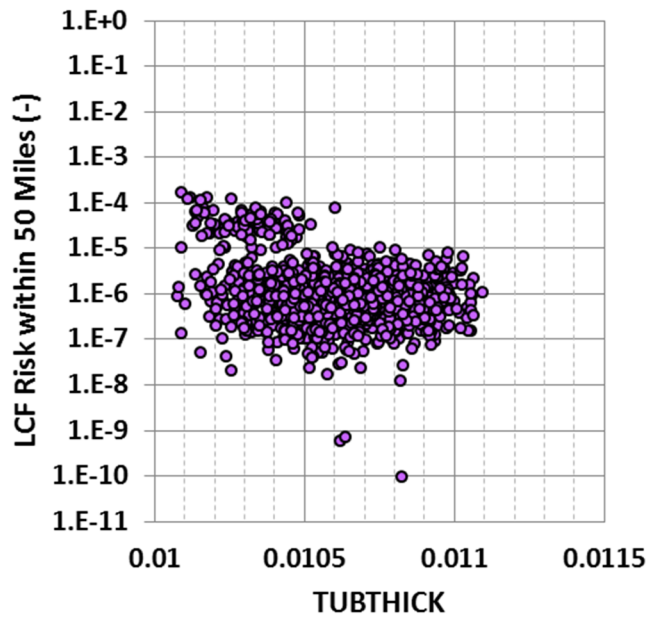


Figure 6-107 Scatter plot of mean, individual, LCF risk within a 50-mile circular area for all realizations, versus steam generator tube thickness, TUBTHICK, conditional on an STSBO accident

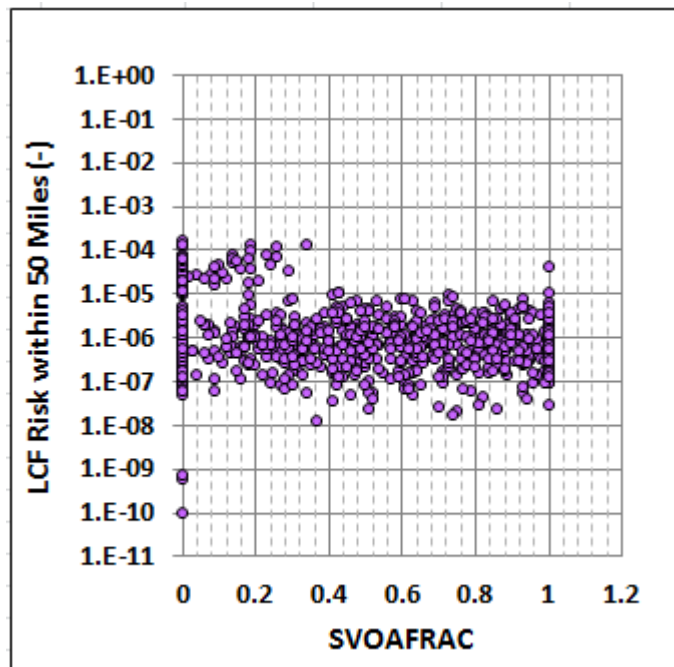


Figure 6-108 Scatter plot of mean, individual, LCF risk within a 50-mile circular area for all realizations, versus safety valve open area fraction, SVOAFRAC, conditional on an STSBO accident

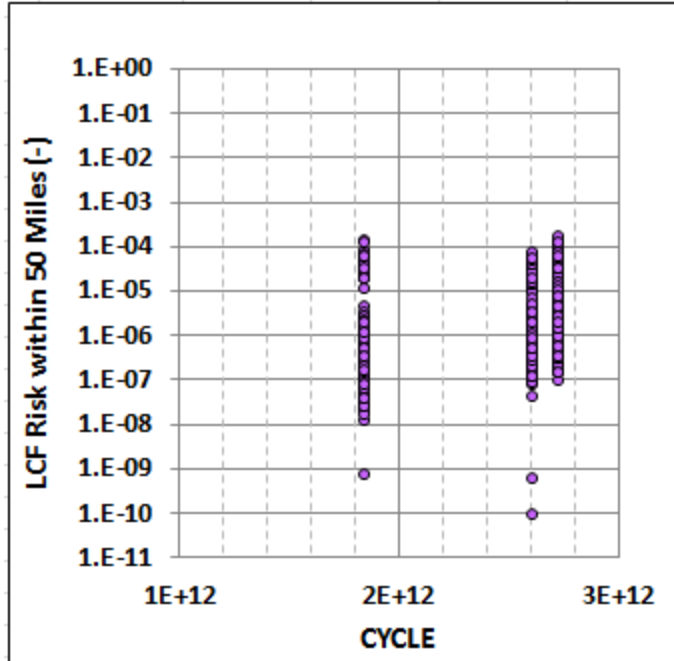


Figure 6-109 Scatter plot of mean, individual, LCF risk within a 50-mile circular area for all realizations, versus time in the fuel cycle, CYCLE, conditional on an STSBO accident

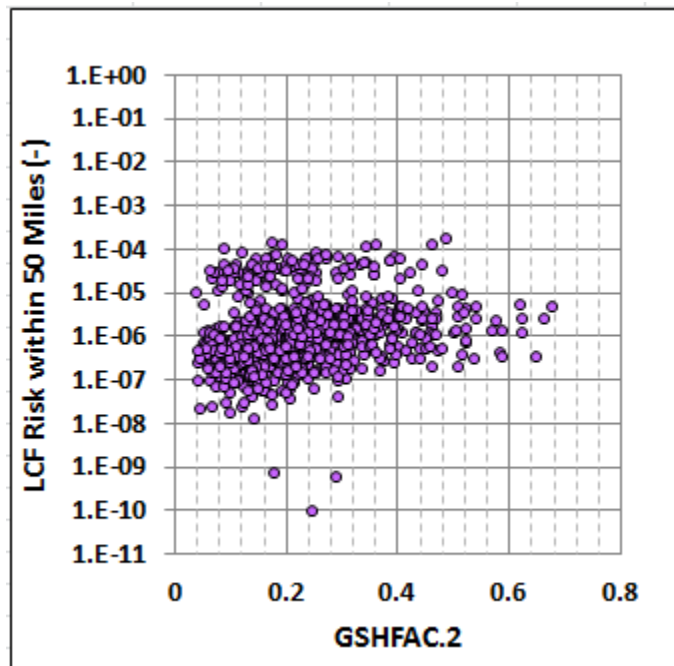
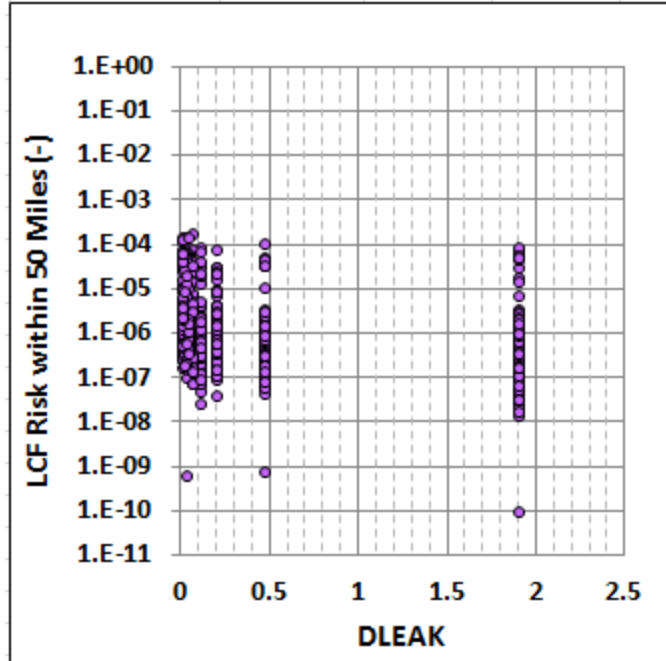


Figure 6-110 Scatter plot of mean, individual, LCF risk within a 50-mile circular area for all realizations, versus groundshine shielding factor, GSHFAC.2, conditional on an STSBO accident



**Figure 6-111 Scatter plot of mean, individual, LCF risk within a 50-mile circular area for all realizations, versus containment leakage path length, conditional on an STSBO accident**

Figure 6-107 and Figure 6-108 show negative correlations between TUBTHICK and SVOAFRAC with LCF risk, respectively, primarily because the cluster of points representing SGTR is shifted to the left. Figure 6-109 shows a positive correlation between time of the accident during the fuel cycle and LCF risk. This figure clearly shows the discrete nature of the distribution: the left group of points corresponds to BOC; the middle group corresponds to MOC; and the group on the right corresponds to EOC. Figure 6-110 shows a positive correlation between groundshine shielding factor (GSHFAC.2) and LCF risk. Groundshine doses increase with the shielding factor, so this relationship is expected. Realizations with and without an SGTR display the same trend. Figure 6-111 shows a slightly negative trend between containment leakage path length and LCF risk. Leakage rate and path length are inversely related, so this trend is expected.

#### 6.2.3.1.2 Cases Involving Steam Generator Tube Rupture

The subset of realizations in which SGTR occurs are described in this subsection. The MELCOR parameters that control SGTR do not dominate in this set of realizations because SGTR is a precondition for the set of realizations that are evaluated; however, one of these MELCOR parameters does appear on the list of important parameters and is discussed below.

Table 6-27 through Table 6-29 show the important input parameters identified by the regression analyses at the same three radial intervals shown in the preceding subsection. Three parameters are highlighted as being important at all three of the distance ranges: (1) steam generator tube thickness, TUBTHICK; (2) aerosol deposition velocity for the smallest aerosol bin, VDEPOS.1; and (3) groundshine shielding factor for normal activity and/or sheltering, GSHFAC.2 and/or GSHFAC.3, respectively. The two groundshine parameters, GSHFAC.2 and GSHFAC.3, are rank correlated with a coefficient of 0.8. They are considered together in this

discussion. The groundshine shielding factor for normal activity is correlated with the long-term groundshine shielding factor with a correlation coefficient of 1.0, and so these can be treated as a single parameter. All ten aerosol deposition velocities (for 10 size bins) are correlated with a coefficient of 1.0, so the deposition velocities behave almost as if they are a single uncertain parameter.

Steam generator tube thickness (TUBTHICK) affects the timing of failure in addition to the probability of failure of a steam generator tube. The timing of tube failure affects the source term and, through it, the LCF risk. Aerosol deposition velocities (represented by VDEPOS.1) a MACCS input parameter, was identified as one of the most important parameters in the Peach Bottom UA [2] because it controls the quantity of material deposited, which affects long-term consequences through the groundshine pathway. Groundshine shielding factor (GSHFAC.2 or GSHFAC.3) was identified in the preceding subsection as one of the most important parameters for the full set of realizations, and it appears here as one of the most important parameters for the SGTR cases as well.

Three additional parameters are identified as important for two of the three distance intervals: (1) cancer fatality risk factor for residual cancers, CFRISK.8; (2) the containment leak path length, DLEAK; and (3) the I-134 lifetime inhalation dose coefficient for the lungs, I.134\_I.9. The cancer fatality risk factor for residual cancers is the largest of the set of risk factors and was also identified as important in the Peach Bottom UA [2]. The leak path length controls the rate of containment leakage and it contributes to the overall release even when an SGTR occurs. Finally, the inhalation dose coefficient for I-134 is very important for accident scenarios with early releases. The half-life of I-134 is only 52.5 min. but its initial core activity is the largest of the iodine isotopes. The lung dose coefficient is negatively rank correlated with the dose coefficients for the other organs, and thereby represents the effects of all of the I-134 inhalation lifetime dose coefficients.

**Table 6-27 Mean, individual, LCF risk regression results within a 10-mile circular area for realizations with SGTR based on LNT.**

	Rank Regression		Quadratic		Recursive Partitioning		MARS		Main Contr.*	Conjoint Contr. *
Final R <sup>2</sup>	0.66		1.00		0.71		0.51			
Input	R <sup>2</sup> contr.	SRRC	S <sub>i</sub>	T <sub>i</sub>	S <sub>i</sub>	T <sub>i</sub>	S <sub>i</sub>	T <sub>i</sub>		
CFRISK.8	0.12	0.33	---	---	---	---	0.28	0.28	0.067	0.000
VDEPOS.1	0.12	0.25	---	---	0.01	0.07	0.26	0.26	0.065	0.013
TUBTHICK	---	---	0.02	0.22	0.15	0.43	0.12	0.12	0.065	0.130
GSHFAC.3	0.09	0.21	---	---	0.04	0.29	0.25	0.25	0.063	0.059
I.134_ICH.9	0.02	0.19	0.01	0.01	0.18	0.24	0.00	0.01	0.040	0.016
SV_STATUS	---	---	0.11	0.31	---	---	0.00	0.00	0.037	0.067
DLTEVA_5.7	0.06	0.14	---	---	0.08	0.22	---	---	0.029	0.033
DLEAK	0.01	0.09	0.08	0.59	---	---	0.00	0.00	0.023	0.171
CO.60_ICH.9	---	---	0.07	0.08	---	---	---	---	0.023	0.002
CFRISK.6	0.03	0.21	0.01	0.01	---	---	0.09	0.10	0.021	0.001
PROTIN.2	0.05	0.16	0.02	0.07	0.01	0.02	---	---	0.017	0.023
SVOAFRAC	---	---	---	---	0.07	0.12	0.00	0.00	0.016	0.013
CYCLE	0.03	0.14	0.02	0.03	---	---	---	---	0.012	0.006
SR.91_ICH.9	0.04	-0.17	---	---	---	---	---	---	0.011	0.000
GSHFAC.2	0.02	0.23	0.01	0.01	0.01	0.03	0.00	0.00	0.007	0.008
RH.105_ICH.9	0.03	0.22	---	---	---	---	0.00	0.01	0.007	0.001
DLTEVA_2.8	0.02	-0.08	---	---	---	---	---	---	0.004	0.000
TE.132_ICH.9	0.01	-0.15	---	---	---	---	0.00	0.00	0.004	0.000
DLTEVA_5.8	0.01	0.09	0.00	0.08	---	---	---	---	0.004	0.025
DLTEVA_3.5	---	---	0.01	0.16	---	---	---	---	0.003	0.049
DLTEVA.2	---	---	0.01	0.01	---	---	---	---	0.003	0.002
DLTEVA.7	---	---	---	---	0.01	0.07	0.00	0.00	0.001	0.014

\* highlighted if main contribution larger than 0.02 or conjoint contribution larger than 0.1

**Table 6-28 Mean, individual, LCF risk regression results within a 10- to 20-mile annular area for realizations with SGTR based on LNT.**

Final R <sup>2</sup>	Rank Regression		Quadratic		Recursive Partitioning		MARS		Main Contr.*	Conjoint Contr.*
	0.66		1.00		0.79		0.56			
Input	R <sup>2</sup> contr.	SRRC	S <sub>i</sub>	T <sub>i</sub>	S <sub>i</sub>	T <sub>i</sub>	S <sub>i</sub>	T <sub>i</sub>		
VDEPOS.1	0.12	0.29	0.02	0.04	0.17	0.20	0.30	0.30	0.110	0.014
DLTEVA_4.8	---	---	0.02	0.11	0.26	0.31	0.00	0.00	0.076	0.041
GSHFAC.3	---	---	0.07	0.15	---	---	0.25	0.25	0.070	0.025
GSHFAC.2	0.15	0.33	---	---	0.11	0.32	---	---	0.061	0.055
CYSIGA.1	0.04	-0.22	0.06	0.07	---	---	0.14	0.13	0.044	0.003
RCPSL	0.08	0.29	0.02	0.13	---	---	0.08	0.07	0.036	0.036
I.134_ICH.9	0.02	0.14	---	---	0.10	0.18	0.00	0.00	0.024	0.021
DLTEVA.2	---	---	0.01	0.06	0.02	0.07	0.08	0.08	0.023	0.029
TUBTHICK	0.03	-0.16	0.01	0.12	---	---	0.10	0.09	0.022	0.037
DLEAK	0.04	0.08	0.04	0.46	---	---	---	---	0.020	0.139
PROTIN.2	0.06	0.16	---	---	0.00	0.01	---	---	0.014	0.003
DLTEVA_5.6	0.01	-0.13	---	---	---	---	0.06	0.07	0.012	0.001
DLTEVA_5.8	0.04	0.11	---	---	---	---	0.00	0.00	0.010	0.001
DLTEVA_5.7	0.02	0.14	0.01	0.27	0.01	0.05	---	---	0.010	0.098
SVOAFRAC	---	---	---	---	0.04	0.14	---	---	0.010	0.028
CS.136_ICH.9	0.02	0.16	---	---	0.01	0.01	---	---	0.007	0.001
DLTEVA_2.4	0.02	0.15	---	---	---	---	---	---	0.004	0.000
TIMHOT.	0.01	-0.12	---	---	0.00	0.01	0.00	0.00	0.003	0.002
CFRISK.6	---	---	0.01	0.31	0.00	0.00	0.00	0.00	0.003	0.100
DLTEVA_2.8	0.01	-0.13	---	---	---	---	---	---	0.002	0.000
CFRISK.7	---	---	---	---	0.01	0.05	---	---	0.002	0.011
DLTEVA_2.11	---	---	---	---	0.01	0.04	0.00	0.00	0.002	0.009

\* highlighted if main contribution larger than 0.02 or conjoint contribution larger than 0.1

**Table 6-29 Mean, individual, LCF risk regression results within a 50-mile circular area for realizations with SGTR based on LNT.**

Final R <sup>2</sup>	Rank Regression		Quadratic		Recursive Partitioning		MARS		Main Contr.*	Conjoint Contr.*
	0.69		1.00		0.79		0.63			
Input	R <sup>2</sup> contr.	SRRC	S <sub>i</sub>	T <sub>i</sub>	S <sub>i</sub>	T <sub>i</sub>	S <sub>i</sub>	T <sub>i</sub>		
TUBTHICK	---	---	0.04	0.15	0.15	0.55	0.16	0.16	0.087	0.142
VDEPOS.1	0.11	0.31	---	---	0.02	0.06	0.25	0.25	0.071	0.010
GSHFAC.3	---	---	---	---	0.00	0.03	0.27	0.27	0.057	0.008
GSHFAC.2	0.16	0.29	0.02	0.10	0.06	0.20	0.00	0.01	0.056	0.064
CFRISK.8	0.05	0.29	0.02	0.05	0.01	0.01	0.14	0.15	0.041	0.011
SVOAFRAC	---	---	0.01	0.27	0.09	0.15	0.00	0.00	0.025	0.104
DLEAK	0.04	0.09	0.03	0.61	0.03	0.10	0.00	0.01	0.023	0.214
CYSIGA.1	---	---	0.00	0.01	0.01	0.00	0.09	0.08	0.019	0.004
DLTEVA_5.6	0.02	-0.16	---	---	---	---	0.09	0.09	0.019	0.000
RCPSL	0.07	0.23	---	---	---	---	---	---	0.018	0.000
DLTEVA_4.8	---	---	0.00	0.04	0.06	0.36	---	---	0.017	0.093
SR.91_ICH.9	0.01	-0.10	0.02	0.05	0.03	0.09	---	---	0.013	0.027
PROTIN.2	0.05	0.17	---	---	---	---	---	---	0.013	0.000
CFRISK.7	0.03	0.16	0.01	0.20	---	---	0.00	0.00	0.010	0.064
DLTEVA_5.8	0.04	0.09	---	---	---	---	---	---	0.009	0.000
TE.132_ICH.9	0.03	-0.10	---	---	---	---	---	---	0.008	0.000
DLTEVA_2.11	---	---	0.02	0.16	0.00	0.02	---	---	0.007	0.052
DLTEVA.2	---	---	0.02	0.02	---	---	---	---	0.007	0.000
TIMHOT.	0.02	-0.18	0.01	0.11	---	---	---	---	0.007	0.034
DLTEVA_2.4	0.02	0.17	---	---	---	---	0.00	0.00	0.006	0.001
DLTEVA_2.8	0.02	-0.14	---	---	---	---	0.00	0.00	0.005	0.001
I.134_ICH.9	0.02	0.14	---	---	0.01	0.07	0.00	0.00	0.005	0.017

\* highlighted if main contribution larger than 0.02 or conjoint contribution larger than 0.1

The scatter plots provided in Figure 6-112 through Figure 6-118 show the trends between the six most important inputs (seven including both of the groundshine shielding factors) and LCF risk, as discussed in the preceding paragraphs. The trends in these figures are for the 50-mile circular area, but they are very similar for the other circular and annular areas that were evaluated in this study. The plots indicate the sign of the correlation between the parameters and LCF risk, although the trend is sometimes hard to distinguish by eye.

The steam generator tube wall thickness (TUBTHICK) is negatively correlated with LCF risk (Figure 6-112), as observed above when all realizations were considered in the regression analysis. This means that thinner walls, which are more likely to fail early, lead to higher risks. This makes intuitive sense. The correlation between the MACCS aerosol deposition velocity (VDEPOS.1) and LCF risk is positive (Figure 6-113), indicating that more deposition within moderate distances from the plant enhances the LCF risk. The impact of deposition is mainly through the groundshine pathway during the long-term phase. The MACCS parameter for groundshine shielding factor also affects doses from the groundshine pathway, which dominates the long-term health effect risk. The groundshine shielding factors (GSHFAC.2 and GSHFAC.3) are positively correlated with risk because a higher value increases doses through this pathway (Figure 6-114 and Figure 6-115). That means that higher values of the shielding factor are associated with higher risks, as they should be. The MELCOR parameter for containment leakage path length (DLEAK) is negatively correlated with LCF risk for the SGTR cases (Figure 6-117), just as it is for the full set of realizations. The shorter the path length, the higher is the leakage rate, and so the greater the LCF risk. Finally, increases in the I-134 inhalation dose coefficient (I.134\_ICH.9) cause increases in LCF risk and this parameter is an important contributor when releases are early enough that most of the activity has not decayed prior to exposure (Figure 6-118).

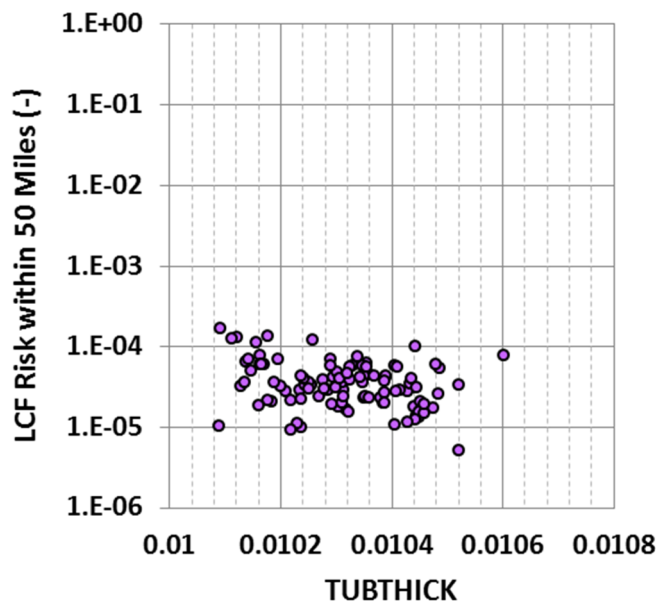


**Figure 6-112 Scatter plot of mean, individual, LCF risk within a 50-mile circular area for realizations involving SGTR, conditional on an STSBO accident, versus steam generator tube thickness, TUBTHICK**

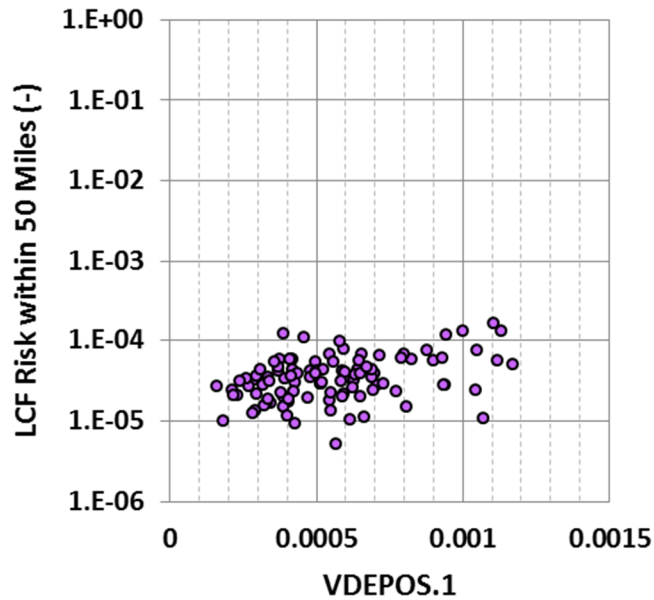


**Figure 6-113 Scatter plot of mean, individual, LCF risk within a 50-mile circular area for realizations involving SGTR, conditional on an STSBO accident, versus aerosol deposition velocity, VDEPOS.1**

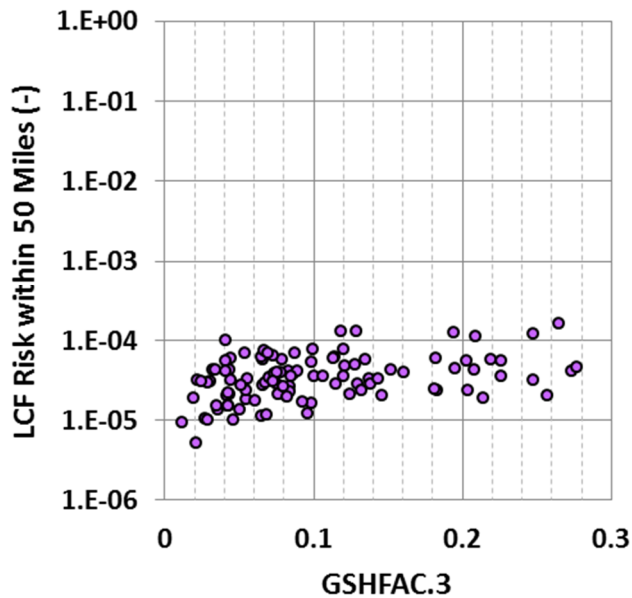


**Figure 6-114 Scatter plot of mean, individual, LCF risk within a 50-mile circular area for realizations with SGTR, conditional on an STSBO accident, versus groundshine shielding factor for emergency phase sheltering, GSHFAC.3**

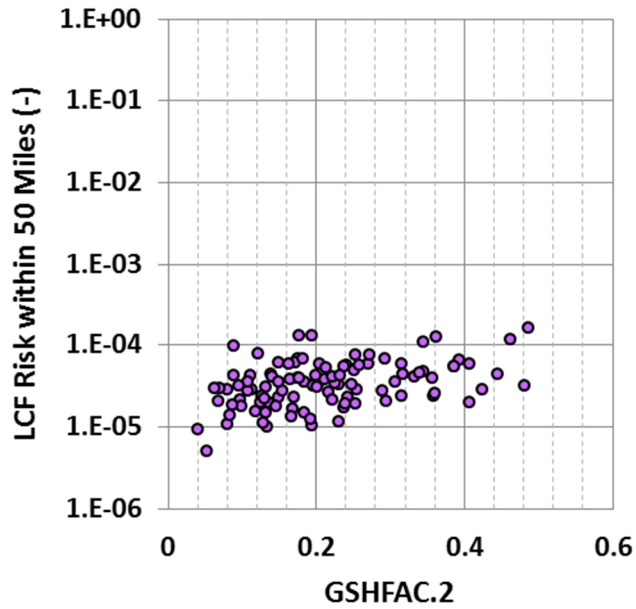


**Figure 6-115 Scatter plot of mean, individual, LCF risk within a 50-mile circular area for realizations with SGTR, conditional on an STSBO accident, versus groundshine shielding factor for normal activity during the emergency phase, GSHFAC.2**

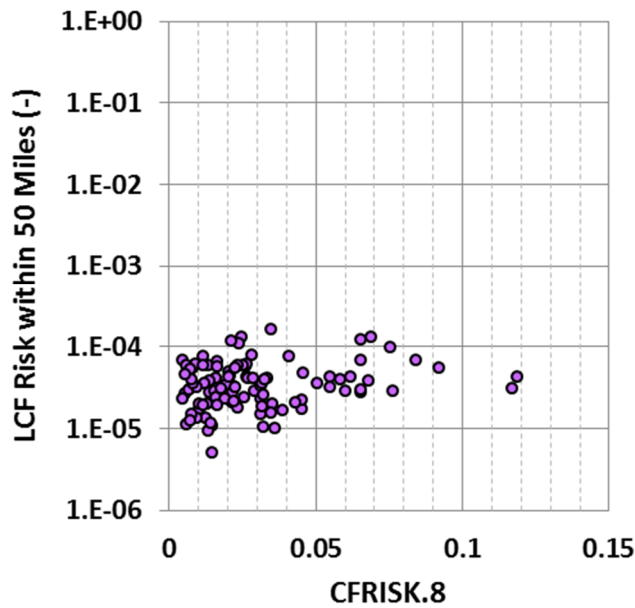


**Figure 6-116 Scatter plot of mean, individual, LCF risk within a 50-mile circular area for realizations involving SGTR, conditional on an STSBO accident, versus cancer fatality risk factor for the residual organ, CFRISK.8**

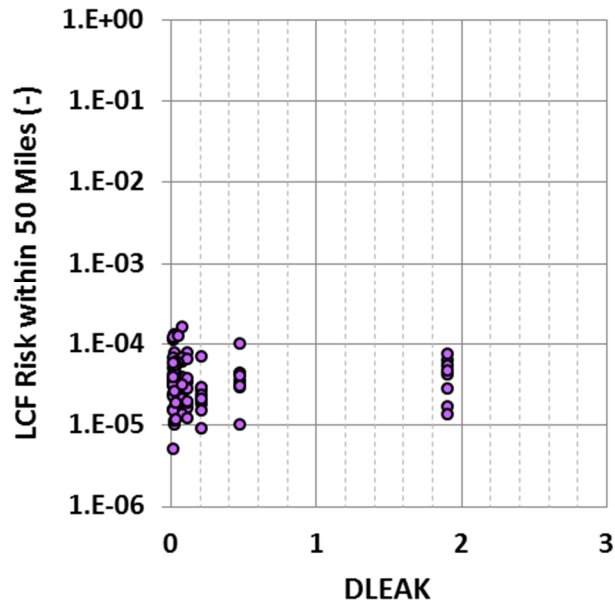


**Figure 6-117 Scatter plot of mean, individual, LCF risk within a 50-mile circular area for realizations involving SGTR, conditional on an STSBO accident, versus containment leak path length, DLEAK**

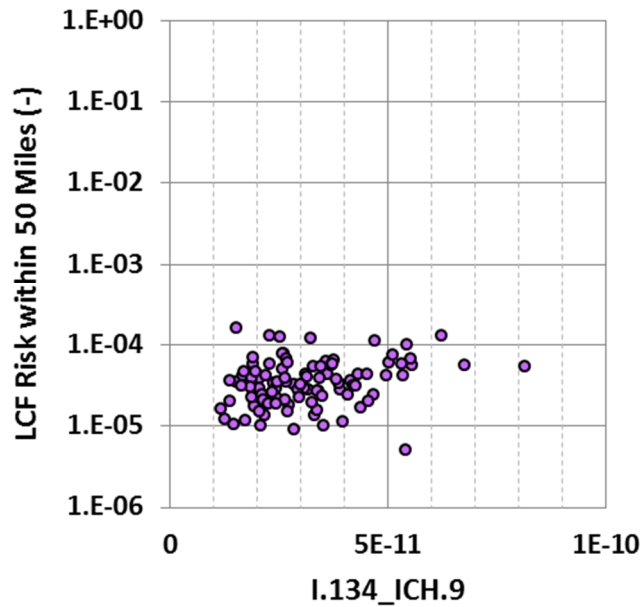


**Figure 6-118 Scatter plot of mean, individual, LCF risk within a 50-mile circular area for realizations involving SGTR, conditional on an STSBO accident, versus I-134 inhalation dose coefficient for the lungs, I.134\_ICH.9**

6.2.3.1.3 Cases not Involving Steam Generator Tube Rupture

The subset of realizations in which an SGTR does not occur is described in this subsection. The MELCOR parameters that control steam generator tube rupture do not dominate in this set of cases because SGTR is eliminated from the set of realizations that are evaluated.

Table 6-30 through Table 6-32 show the important input parameters identified by the regression analyses at the same three radial intervals shown in the two preceding subsections. The four most important parameters appear in the same order in all three intervals. The most important parameter is the time during the fuel cycle at which the accident occurs, CYCLE. Second is the groundshine shielding factor for normal activity during the emergency phase, GSHFAC.2, which is fully correlated with the groundshine shielding factor for the long-term phase. The third most important input parameter is the containment leakage path length, DLEAK, which is inversely proportional to containment leakage rate. This parameter has an elevated importance for the cases without an SGTR because containment leakage is the dominant release pathway. The fourth most significant parameter on the list is cancer fatality risk factor for residual cancers, CFRISK.8. Residual cancers are larger than any of the individual cancer types that are modeled and thus this parameter is more important than the other cancer risk factors.

**Table 6-30 Mean, individual, LCF risk (based on LNT) regression results within a 10-mile circular area for realizations that do not involve SGTR.**

Input	Rank Regression		Quadratic		Recursive Partitioning		MARS		Main Contr.*	Conjoint Contr.*
	R <sup>2</sup> contr.	SRRC	S <sub>i</sub>	T <sub>i</sub>	S <sub>i</sub>	T <sub>i</sub>	S <sub>i</sub>	T <sub>i</sub>		
Final R <sup>2</sup>	0.73		0.83		0.84		0.59			
CYCLE	0.27	0.52	0.14	0.23	0.18	0.55	0.30	0.30	0.179	0.128
GSHFAC.2	0.19	0.44	0.22	0.38	0.18	0.54	0.25	0.27	0.166	0.152
DLEAK	0.12	-0.33	0.06	0.20	0.03	0.16	0.09	0.09	0.062	0.077
CFRISK.8	0.03	0.16	0.04	0.07	0.02	0.14	0.07	0.07	0.030	0.040
CYSIGA.1	0.03	-0.18	0.02	0.02	0.01	0.04	0.04	0.05	0.019	0.012
VDEPOS.1	0.02	0.12	0.02	0.06	0.01	0.24	0.03	0.07	0.017	0.081
PARTSHAPE	0.01	0.09	0.01	0.03	0.00	0.04	0.05	0.06	0.012	0.018
CFRISK.7	0.01	0.12	0.02	0.03	0.00	0.02	0.03	0.03	0.012	0.007
CFC	0.02	-0.13	0.02	0.03	0.00	0.02	0.02	0.02	0.010	0.009
DEV_DEC_HEAT	0.01	-0.08	0.02	0.04	0.00	0.04	0.02	0.04	0.010	0.021
CFRISK.6	0.01	0.09	0.02	0.07	0.00	0.04	0.01	0.01	0.009	0.023
DDREFA.8	0.01	-0.11	0.01	0.03	0.01	0.03	---	---	0.006	0.014
CHEMFORMCS	0.01	-0.09	---	---	---	---	0.02	0.03	0.005	0.001
GSHFAC.3	---	---	0.02	0.07	---	---	---	---	0.005	0.014
CFRISK.4	0.01	0.09	---	---	---	---	---	---	0.002	0.000
CFRISK.3	---	---	---	---	---	---	0.01	0.02	0.001	0.003
SV_NBCYC	---	---	0.00	0.02	---	---	0.00	0.00	0.001	0.005
SGTRLOC	0.00	0.04	0.00	0.03	---	---	0.00	0.00	0.000	0.009
CFRISK.1	---	---	---	---	0.00	0.12	---	---	0.000	0.033
DLTEVA_5.12	---	---	---	---	0.00	0.04	---	---	0.000	0.011
ZR.95_ICH.9	---	---	---	---	0.00	0.03	---	---	0.000	0.008

\* highlighted if main contribution larger than 0.02 or conjoint contribution larger than 0.1

**Table 6-31 Mean, individual, LCF risk (based on LNT) regression results within a 10- to 20-mile annular area for realizations that do not involve SGTR.**

Final R <sup>2</sup>	Rank Regression		Quadratic		Recursive Partitioning		MARS		Main Contr.*	Conjoint Contr.*
	0.72		0.84		0.83		0.65			
Input	R <sup>2</sup> contr.	SRRC	S <sub>i</sub>	T <sub>i</sub>	S <sub>i</sub>	T <sub>i</sub>	S <sub>i</sub>	T <sub>i</sub>		
CYCLE	0.30	0.56	0.16	0.25	0.19	0.60	0.29	0.29	0.194	0.141
GSHFAC.2	0.15	0.40	0.19	0.31	0.15	0.52	0.21	0.25	0.143	0.144
DLEAK	0.12	-0.34	0.06	0.20	0.03	0.14	0.11	0.11	0.066	0.067
CFRISK.8	0.03	0.15	0.04	0.09	0.02	0.15	0.07	0.07	0.029	0.050
CYSIGA.1	0.03	-0.17	0.02	0.03	0.00	0.02	0.03	0.03	0.017	0.008
PARTSHAPE	0.01	0.10	0.02	0.03	0.00	0.02	0.05	0.08	0.014	0.017
CFRISK.7	0.01	0.12	0.01	0.02	0.01	0.07	0.03	0.02	0.012	0.018
CFC	0.02	-0.13	0.01	0.02	0.00	0.04	0.02	0.02	0.011	0.012
DEV_DEC_HEAT	0.01	-0.09	0.02	0.05	0.01	0.05	0.02	0.03	0.011	0.025
CFRISK.6	0.01	0.09	0.03	0.08	---	---	0.02	0.05	0.010	0.022
VDEPOS.1	0.01	0.09	0.02	0.03	0.01	0.23	0.01	0.04	0.009	0.072
CFRISK.4	0.01	0.10	0.02	0.05	---	---	0.01	0.02	0.007	0.011
CHEMFORMCS	0.01	-0.08	---	---	0.00	0.13	0.03	0.02	0.006	0.035
GSHFAC.3	---	---	0.02	0.05	---	---	---	---	0.004	0.010
RCPSL	---	---	0.01	0.08	---	---	0.00	0.01	0.004	0.019
DDREFA.8	0.01	-0.11	---	---	0.00	0.05	---	---	0.003	0.014
DDREFA.4	0.01	-0.07	---	---	---	---	---	---	0.002	0.000
PROTIN_3.3	---	---	---	---	0.01	0.02	---	---	0.001	0.004
CFRISK.3	---	---	---	---	---	---	0.01	0.04	0.001	0.007
ZR.95_ICH.9	---	---	---	---	0.00	0.02	---	---	0.001	0.005
CHEMFORMI2	---	---	0.00	0.02	---	---	---	---	0.001	0.004
PROTIN.2	---	---	---	---	0.00	0.02	---	---	0.000	0.006

\* highlighted if main contribution larger than 0.02 or conjoint contribution larger than 0.1

**Table 6-32 Mean, individual, LCF risk (based on LNT) regression results within a 50-mile circular area for realizations that do not involve SGTR.**

Final R <sup>2</sup>	Rank Regression		Quadratic		Recursive Partitioning		MARS		Main Contr.*	Conjoint Contr.*
	0.72		0.84		0.82		0.67			
Input	R <sup>2</sup> contr.	SRRC	S <sub>i</sub>	T <sub>i</sub>	S <sub>i</sub>	T <sub>i</sub>	S <sub>i</sub>	T <sub>i</sub>		
CYCLE	0.29	0.54	0.14	0.23	0.18	0.55	0.28	0.28	0.185	0.128
GSHFAC.2	0.16	0.41	0.19	0.30	0.18	0.56	0.22	0.26	0.155	0.144
DLEAK	0.12	-0.34	0.06	0.20	0.03	0.16	0.10	0.11	0.065	0.077
CFRISK.8	0.03	0.16	0.04	0.06	0.01	0.11	0.06	0.07	0.027	0.037
PARTSHAPE	0.01	0.09	0.02	0.02	0.00	0.03	0.05	0.07	0.015	0.013
CYSIGA.1	0.03	-0.15	0.01	0.02	0.01	0.03	0.03	0.03	0.014	0.009
CFC	0.02	-0.13	0.02	0.09	0.01	0.06	0.02	0.02	0.013	0.035
DEV_DEC_HEAT	0.01	-0.08	0.01	0.09	0.01	0.03	0.02	0.04	0.011	0.031
CFRISK.6	0.01	0.09	0.03	0.08	---	---	0.02	0.06	0.011	0.023
VDEPOS.1	0.01	0.09	0.02	0.03	0.01	0.22	0.01	0.05	0.010	0.070
CFRISK.7	0.01	0.12	---	---	0.00	0.06	0.02	0.03	0.008	0.017
CHEMFORMCS	0.01	-0.08	0.01	0.02	0.00	0.04	0.02	0.03	0.007	0.016
DDREFA.8	0.01	-0.11	---	---	0.01	0.08	0.01	0.02	0.006	0.021
GSHFAC.3	---	---	0.02	0.07	---	---	---	---	0.006	0.014
CFRISK.4	0.01	0.10	---	---	---	---	0.01	0.01	0.003	0.001
RCPSL	---	---	0.01	0.13	---	---	---	---	0.003	0.034
CFRISK.3	---	---	---	---	---	---	0.01	0.04	0.002	0.006
CWASH1.	0.01	0.07	---	---	---	---	---	---	0.001	0.000
SGTRLOC	---	---	0.00	0.02	---	---	---	---	0.001	0.004
CM.242_ICH.9	---	---	---	---	0.00	0.05	---	---	0.001	0.013
CFRISK.1	---	---	---	---	0.00	0.08	---	---	0.001	0.020
PROTIN.2	---	---	0.00	0.02	---	---	---	---	0.000	0.005

\* highlighted if main contribution larger than 0.02 or conjoint contribution larger than 0.1

The scatter plots provided in Figure 6-119 through Figure 6-122 show the trends between the four most important inputs and LCF risk, as discussed in the preceding paragraph. The trends in

these figures are for the 50-mile circular area, but they are very similar for the other circular and annular areas that were evaluated in this study. The plots indicate the sign and degree of the correlation between the parameters and LCF risk, although the trend is sometimes hard to distinguish by eye. The trends are also indicated by the sign of SRRC in the above tables.

Figure 6-119 clearly shows a trend between time during the fuel cycle (CYCLE) and LCF risk. The trend indicates a positive correlation, which indicates that LCF risk increases with fuel burnup. Cs-137 activity nearly doubles from BOC to EOC, and this isotope is a dominant contributor to long-term groundshine doses. The plot indicates that the difference between BOC and MOC is greater than the difference between MOC and EOC. Similarly, Figure 6-120 shows a clear trend between groundshine shielding factor for normal activity during the emergency phase (GSHFAC.2, which is correlated with a coefficient of 1.0 with groundshine shielding factor during the long-term phase) with LCF risk. The value during the long-term phase has a greater influence on risk than the value during the emergency phase because of the extended period over which groundshine contributes to dose. Increases in the shielding factor corresponds to an increase in groundshine dose and, thus, to an increase in LCF risk. The containment leakage path length, DLEAK, which is inversely related to leakage rate, is negatively correlated with the LCF risk. That means that higher leakage rates lead to higher LCF risk, as expected. Finally, the residual cancer fatality risk factor, CFRISK.8, is positively correlated with LCF risk. Thus, cancer risks increase with this factor, as expected. While all of the cancer risk factors should be positively correlated with LCF risk, residual cancers are the largest contributor and thus are more important than the other risk factors.

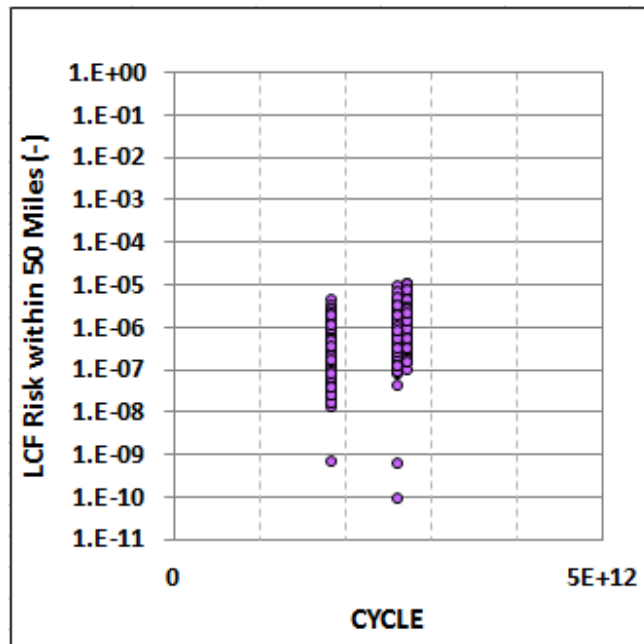


**Figure 6-119 Scatter plot of mean, individual, LCF risk (based on LNT) within a 50-mile circular area for realizations that do not involve SGTR, conditional on an STSBO accident, versus time during the fuel cycle, CYCLE**

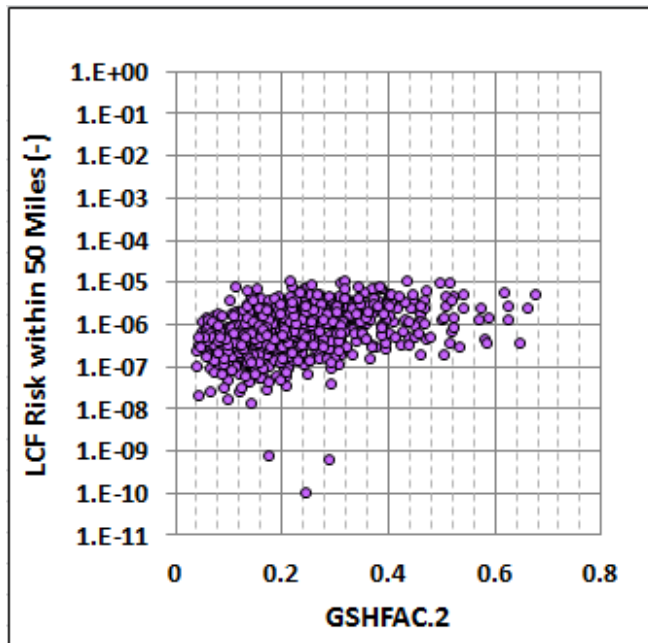


Figure 6-120 Scatter plot of mean, individual, LCF risk (based on LNT) within a 50-mile circular area for realizations that do not involve SGTR, conditional on an STSBO accident, versus groundshine shielding factor for normal activity during the emergency phase, GSHFAC.2

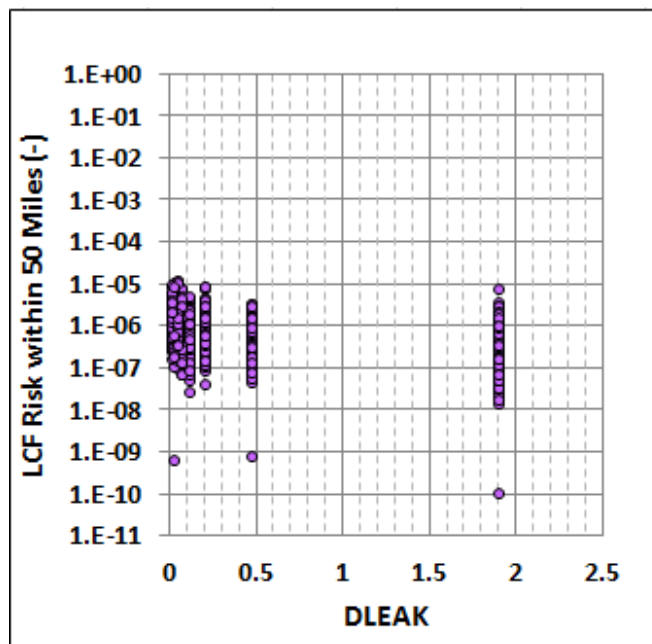
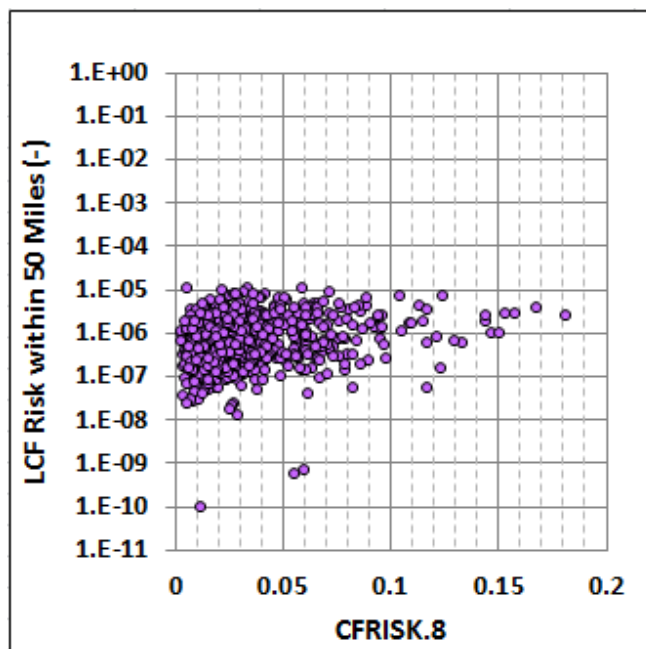


Figure 6-121 Scatter plot of mean, individual, LCF risk (based on LNT) within a 50-mile circular area for realizations that do not involve SGTR, conditional on an STSBO accident, versus containment leak path length, DLEAK



**Figure 6-122 Scatter plot of mean, individual, LCF risk (based on LNT) within a 50-mile circular area for realizations that do not involve SGTR, conditional on an STSBO accident, versus residual cancer fatality risk factor, CFRISK.8**

### 6.2.3.2 Regression Analysis of Latent Cancer Fatality Risk Using Nonlinear Dose-Response Models

This subsection discusses the regression results for three sets of realizations: (1) all of the realizations performed in this study; (2) only the realizations that resulted in an SGTR; and (3) only the realizations that resulted in no SGTR. Each set of realizations is evaluated for two linear-with-threshold dose-response models, which are referred to as US background and HPS truncation models. The two respective variations of dose threshold (truncation) are described as follows: (1) annual dose truncation based on average background plus medical radiation, which is 620 mrem/yr and (2) dose truncation based on the HPS position statement, which states that “the Health Physics Society recommends against quantitative estimation of health risks below an individual dose of 50 millisievert (mSv) in one year or a lifetime dose of 100 mSv above that received from natural sources.” These dose levels are equivalent to 5 rem/yr and 10 rem over a lifetime. The HPS position states that all doses above natural background are to be included in the evaluation of health consequences, but here only the excess doses induced by the reactor accident are evaluated. This implicitly assumes that no other excess exposures to ionizing radiation occur. Note that the HPS does not say that there are no health effects below these dose thresholds, only that they should not be evaluated.

Regression analyses for nine distance intervals were performed. Five are circular areas with an outer radius of 10, 20, 30, 40, and 50 miles; the other four are annuli (rings) from 10 to 20 miles, 20 to 30 miles, 30 to 40 miles, and 40 to 50 miles. The combination of regression techniques and distance intervals resulted in a set of 36 results for each of the two dose-response models. The discussion in this subsection focuses on three of the distance intervals. Results for the other distance intervals that were evaluated are similar to the results for the three intervals that are discussed and including them would not have added additional insights.

6.2.3.2.1 All Cases

This subsection discusses the results from applying the four regression techniques to the 1003 realizations that were evaluated in this UA for each of the two dose truncation models. The most important of the uncertain input variables are shown in Table 6-33 through Table 6-38.

Table 6-33 through Table 6-35, which are based on US background dose truncation, identify the same set of four important parameters (the highlighted parameters under the Main Contribution column), except that Table 6-34 only identifies the first two on the list. The first most important parameter is the tube thickness of the steam generator tube that potentially fails, TUBTHICK. Under some circumstances, tube failure can occur very early and this affects the predicted source term. The second most important parameter is the SV open area fraction, SVOAFRAC. These two parameters largely control whether an SGTR occurs or not, which has a dominant effect on the consequences. Both of these parameters have large conjoint contributions, implying that the two parameters have a synergistic influence on LCF risk. Conjoint contributions are shown in the last column of the table and indicate that parameters reinforce each other in their effect. The third most important parameter is the time during the fuel cycle when the accident occurs (CYCLE). This parameter directly influences inputs to MELCOR, through decay heat, and to MACCS, through radionuclide inventory. The fourth most influential parameter is the groundshine shielding factor for normal activity during the emergency phase (GSHFAC.2). This parameter is correlated with a coefficient of 1.0 with the groundshine shielding factor during the long-term phase, which has a more pronounced effect on LCF risk by virtue of the longer time period for groundshine exposure.

**Table 6-33 Mean, individual, LCF risk regression results within a 10-mile circular area for all realizations (US background dose-response model).**

Input	Rank Regression		Quadratic		Recursive Partitioning		MARS		Main Contr.*	Conjoint Contr.*
	R <sup>2</sup> contr.	SRRC	S <sub>1</sub>	T <sub>1</sub>	S <sub>1</sub>	T <sub>1</sub>	S <sub>1</sub>	T <sub>1</sub>		
Final R <sup>2</sup>	0.55		0.52		0.84		0.53			
TUBTHICK	0.04	-0.19	0.36	0.67	0.29	0.88	0.50	0.79	0.183	0.269
SVOAFRAC	0.10	-0.27	0.22	0.47	0.09	0.59	0.18	0.42	0.095	0.226
CYCLE	0.15	0.43	---	---	---	---	0.00	0.01	0.037	0.002
GSHFAC.2	0.11	0.31	---	---	0.00	0.07	---	---	0.027	0.020
DLEAK	0.06	0.21	0.01	0.01	---	---	---	---	0.015	0.001
CYSIGA.1	0.06	-0.23	---	---	0.00	0.00	---	---	0.014	0.000
TUBETEMP	---	---	0.02	0.03	0.00	0.03	0.01	0.03	0.005	0.013
PARTSHAPE	0.01	0.08	0.01	0.05	0.01	0.00	0.00	0.00	0.004	0.007
VDEPOS.1	0.01	0.11	0.00	0.02	---	---	0.00	0.05	0.004	0.012
RCPSL	0.00	-0.09	0.01	0.06	---	---	0.01	0.01	0.003	0.007
DEV_DEC_HEAT	0.01	-0.10	---	---	0.00	0.08	---	---	0.003	0.023
SV_STATUS	0.00	0.11	0.01	0.04	---	---	0.00	0.01	0.002	0.006
PROTIN_5.2	0.00	0.07	---	---	---	---	0.00	0.01	0.001	0.001
DDREFA.8	0.00	-0.06	---	---	---	---	0.00	0.01	0.001	0.001
CFC	0.01	-0.07	---	---	---	---	---	---	0.001	0.000
CWASH1.	0.00	0.06	---	---	0.00	0.02	---	---	0.001	0.007
CM.242_I.9	---	---	0.00	0.02	---	---	0.00	0.00	0.001	0.003
PROTIN_3.3	---	---	---	---	0.00	0.02	---	---	0.001	0.004
ZR.95_I.9	---	---	---	---	0.00	0.01	---	---	0.001	0.001
SC1131	---	---	---	---	---	---	0.00	0.00	0.001	0.000
DLTEVA_5.7	---	---	---	---	0.00	0.03	---	---	0.000	0.009
PROTIN_5.3	---	---	---	---	0.00	0.02	0.00	0.00	0.000	0.006

\* highlighted if main contribution larger than 0.02 or conjoint contribution larger than 0.1

**Table 6-34 Mean, individual, LCF risk regression results within a 10- to 20-mile annular area for all realizations (US background dose-response model).**

Input	Rank Regression		Quadratic		Recursive Partitioning		MARS		Main Contr.*	Conjoint Contr.*
	R <sup>2</sup> contr.	SRRC	S <sub>I</sub>	T <sub>I</sub>	S <sub>I</sub>	T <sub>I</sub>	S <sub>I</sub>	T <sub>I</sub>		
Final R <sup>2</sup>	0.31		0.60		0.84		0.72			
TUBTHICK	0.12	-0.22	0.11	0.21	0.28	0.91	0.25	0.93	0.151	0.357
SVOAFRAC	0.10	-0.22	0.08	0.05	0.05	0.58	0.04	0.08	0.055	0.158
LA.140_ICH.9	---	---	0.00	0.00	0.02	0.01	0.02	0.51	0.010	0.116
RCPSL	---	---	0.04	0.61	---	---	0.00	0.06	0.009	0.129
CFRISK.5	---	---	0.04	0.60	---	---	0.00	0.07	0.008	0.130
CYSIGA.1	0.01	-0.08	0.01	0.08	0.00	0.04	0.01	0.05	0.006	0.036
CYCLE	0.02	0.10	0.00	0.10	---	---	---	---	0.005	0.019
DLEAK	0.01	0.06	0.01	0.11	---	---	---	---	0.003	0.020
TUBETEMP	0.01	0.06	0.00	0.00	0.00	0.02	---	---	0.003	0.004
DEV_DEC_HEAT	0.01	-0.06	---	---	0.00	0.03	0.00	0.02	0.003	0.012
PROTIN_5.2	0.01	0.05	0.00	0.00	---	---	0.00	0.04	0.002	0.010
VDEPOS.1	0.01	-0.05	0.00	0.00	0.00	0.04	0.00	0.03	0.002	0.018
CWASH1.	0.01	0.05	---	---	---	---	---	---	0.001	0.000
GSHFAC.2	0.00	0.04	0.00	0.12	---	---	---	---	0.001	0.023
RU.106_ICH.9	0.00	-0.03	---	---	---	---	0.00	0.03	0.001	0.007
SV_STATUS	---	---	0.01	0.00	---	---	0.00	0.07	0.001	0.017
RDMTC	0.00	-0.04	0.00	0.10	---	---	---	---	0.001	0.020
I.135_ICH.9	0.00	0.03	---	---	---	---	0.00	0.06	0.001	0.014
DDREFA.6	---	---	---	---	0.00	0.03	---	---	0.001	0.007
DLTEVA_5.7	0.00	0.03	---	---	0.00	0.00	---	---	0.001	0.000
PROTIN_5.3	---	---	---	---	0.00	0.12	---	---	0.000	0.034
DDREFA.1	---	---	---	---	0.00	0.01	---	---	0.000	0.001

\* highlighted if main contribution larger than 0.02 or conjoint contribution larger than 0.1

**Table 6-35 Mean, individual, LCF risk regression results within a 50-mile circular area for all realizations (US background dose-response model).**

Input	Rank Regression		Quadratic		Recursive Partitioning		MARS		Main Contr.*	Conjoint Contr.*
	R <sup>2</sup> contr.	SRRC	S <sub>I</sub>	T <sub>I</sub>	S <sub>I</sub>	T <sub>I</sub>	S <sub>I</sub>	T <sub>I</sub>		
Final R <sup>2</sup>	0.56		0.54		0.84		0.53			
TUBTHICK	0.04	-0.19	0.29	0.57	0.36	0.91	0.37	0.81	0.172	0.282
SVOAFRAC	0.10	-0.27	0.19	0.36	0.06	0.28	0.15	0.32	0.083	0.122
CYCLE	0.15	0.43	---	---	---	---	---	---	0.037	0.000
GSHFAC.2	0.11	0.31	0.02	0.05	0.00	0.02	0.00	0.01	0.030	0.012
DLEAK	0.06	0.24	0.01	0.08	---	---	---	---	0.017	0.013
CYSIGA.1	0.06	-0.24	0.01	0.03	---	---	0.01	0.05	0.017	0.011
VDEPOS.1	0.01	0.11	0.01	0.01	---	---	0.01	0.10	0.005	0.017
PARTSHAPE	0.01	0.08	0.00	0.04	0.01	0.05	---	---	0.004	0.018
TUBETEMP	---	---	0.01	0.01	0.00	0.08	0.01	0.04	0.003	0.028
CM.242_ICH.9	---	---	0.01	0.03	0.01	0.27	0.00	0.02	0.003	0.081
DEV_DEC_HEAT	0.01	-0.09	0.00	0.03	---	---	---	---	0.002	0.005
CFC	0.01	-0.07	---	---	---	---	0.01	0.08	0.002	0.013
CWASH1.	0.00	0.06	---	---	0.00	0.01	---	---	0.002	0.001
SV_STATUS	0.00	0.11	0.01	0.05	---	---	---	---	0.002	0.008
PROTIN_5.3	---	---	0.00	0.02	0.00	0.01	0.00	0.01	0.002	0.005
PROTIN_5.2	0.00	0.07	---	---	---	---	0.00	0.03	0.001	0.004
RCPSL	0.00	0.06	0.01	0.06	---	---	---	---	0.001	0.009
PROTIN.2	---	---	0.01	0.02	---	---	0.00	0.02	0.001	0.006
DDREFA.8	0.00	-0.06	---	---	---	---	---	---	0.001	0.000
PROTIN_3.3	---	---	---	---	0.00	0.00	---	---	0.001	0.000
DL1131	---	---	---	---	---	---	0.00	0.02	0.000	0.003
DLTEVA_5.3	---	---	---	---	---	---	0.00	0.00	0.000	0.001

\* highlighted if main contribution larger than 0.02 or conjoint contribution larger than 0.1

**Table 6-36 Mean, individual, LCF risk regression results within a 10-mile circular area for all realizations (HPS dose-response model).**

Final R <sup>2</sup>	Rank Regression		Quadratic		Recursive Partitioning		MARS		Main Contr.*	Conjoint Contr. *
	0.50		0.71		0.71		0.64			
	R <sup>2</sup> contr.	SRRC	S <sub>i</sub>	T <sub>i</sub>	S <sub>i</sub>	T <sub>i</sub>	S <sub>i</sub>	T <sub>i</sub>		
Input										
TUBTHICK	0.04	-0.18	0.12	0.31	0.34	0.96	0.15	0.22	0.115	0.205
CYCLE	0.16	0.45	0.01	0.05	---	---	---	---	0.042	0.010
SVOAFRAC	0.08	-0.24	0.09	0.17	0.01	0.13	0.03	0.23	0.041	0.092
CFRISK.5	0.02	0.15	0.04	0.47	0.01	0.19	0.12	0.72	0.033	0.273
CYSIGA.1	0.07	-0.26	0.01	0.04	0.01	0.14	---	---	0.021	0.037
DLEAK	0.05	0.20	0.02	0.23	---	---	0.00	0.06	0.015	0.064
SV_STATUS	---	---	0.04	0.09	---	---	0.00	0.03	0.008	0.017
GSHFAC.2	0.03	0.17	---	---	---	---	---	---	0.007	0.000
CFC	0.01	-0.08	---	---	---	---	0.01	0.21	0.003	0.043
PARTSHAPE	0.01	0.10	0.00	0.07	0.00	0.00	0.00	0.03	0.003	0.021
PROTIN_6.2	0.01	0.09	---	---	0.00	0.00	---	---	0.003	0.000
CFRISK.2	0.01	0.10	---	---	0.00	0.00	---	---	0.002	0.000
PROTIN_3.3	---	---	0.01	0.02	---	---	---	---	0.002	0.003
DEV_DEC_HEAT	0.01	-0.08	0.00	0.03	---	---	---	---	0.002	0.006
DLTEVA_5.3	---	---	---	---	0.00	0.26	0.00	0.08	0.002	0.077
TUBETEMP	0.00	0.07	0.00	0.02	---	---	---	---	0.002	0.003
TE.127M_ICH.9	---	---	0.00	0.01	0.00	0.04	0.01	0.14	0.002	0.041
SGTRLOC	0.00	0.04	0.00	0.09	---	---	---	---	0.001	0.021
SV_NBCYC	0.00	0.07	0.00	0.04	0.00	0.04	---	---	0.001	0.019
GSHFAC.3	---	---	0.00	0.04	---	---	0.00	0.02	0.001	0.012
DLTEVA_5.7	---	---	---	---	---	---	0.01	0.16	0.001	0.032
ZR.95_ICH.9	---	---	---	---	---	---	0.00	0.02	0.001	0.004

\* highlighted if main contribution larger than 0.02 or conjoint contribution larger than 0.1

**Table 6-37 Mean, individual, LCF risk regression results within a 10- to 20-mile annular area for all realizations (HPS dose-response model).**

Final R <sup>2</sup>	Rank Regression		Quadratic		Recursive Partitioning		MARS		Main Contr.*	Conjoint Contr. *
	0.31		0.68		0.49		0.77			
	R <sup>2</sup> contr.	SRRC	S <sub>i</sub>	T <sub>i</sub>	S <sub>i</sub>	T <sub>i</sub>	S <sub>i</sub>	T <sub>i</sub>		
Input										
TUBTHICK	0.16	-0.22	0.05	0.20	0.52	0.64	0.14	0.75	0.138	0.210
CFRISK.5	---	---	0.09	0.47	0.33	0.33	0.04	0.32	0.083	0.158
SVOAFRAC	0.09	-0.15	0.08	0.30	0.01	0.08	0.03	0.13	0.042	0.089
CYSIGA.1	0.00	-0.03	0.02	0.10	0.00	0.03	0.03	0.25	0.009	0.082
SV_STATUS	0.00	0.05	0.04	0.17	---	---	---	---	0.007	0.030
SV_NBCYC	---	---	0.02	0.06	---	---	0.00	0.02	0.005	0.012
DLTEVA_2.6	0.00	-0.03	0.01	0.04	---	---	0.01	0.22	0.004	0.061
TUBETEMP	0.02	0.07	---	---	0.00	0.01	---	---	0.004	0.001
DDREFA.4	0.01	0.06	---	---	---	---	---	---	0.002	0.000
PU.241_ICH.9	0.01	-0.05	---	---	---	---	0.00	0.02	0.002	0.004
TE.129M_ICH.9	0.00	-0.04	0.00	0.02	0.00	0.00	---	---	0.002	0.004
RDMTC	0.01	-0.04	---	---	---	---	---	---	0.002	0.000
SC1131	0.00	-0.03	0.00	0.02	---	---	0.00	0.02	0.001	0.008
CO.58_ICH.9	0.00	0.03	0.00	0.02	---	---	0.00	0.02	0.001	0.008
ND.147_ICH.9	0.00	0.03	---	---	---	---	---	---	0.001	0.000
DDREFA.6	---	---	---	---	0.00	0.01	0.00	0.04	0.001	0.009
DLTEVA.6	---	---	---	---	---	---	0.00	0.07	0.001	0.017
RCPSL	0.00	0.05	---	---	---	---	0.00	0.01	0.001	0.003
SGTRLOC	---	---	0.00	0.08	---	---	---	---	0.001	0.018
DLTEVA_5.7	---	---	0.00	0.01	---	---	---	---	0.001	0.002
RU.106_ICH.9	0.00	-0.03	---	---	---	---	---	---	0.001	0.000
I.135_ICH.9	---	---	0.00	0.20	---	---	---	---	0.000	0.046

\* highlighted if main contribution larger than 0.02 or conjoint contribution larger than 0.1

**Table 6-38 Mean, individual, LCF risk regression results within a 50-mile circular area for all realizations (HPS dose-response model).**

	Rank Regression		Quadratic		Recursive Partitioning		MARS		Main Contr.*	Conjoint Contr.*
Final R <sup>2</sup>	0.39		0.64		0.48		0.51			
Input	R <sup>2</sup> contr.	SRRC	S <sub>i</sub>	T <sub>i</sub>	S <sub>i</sub>	T <sub>i</sub>	S <sub>i</sub>	T <sub>i</sub>		
TUBTHICK	0.04	-0.18	0.05	0.17	0.32	0.96	0.16	0.83	0.077	0.241
SVOAFRAC	0.08	-0.23	0.02	0.24	0.01	0.09	---	---	0.023	0.061
CFRISK.5	0.02	0.13	0.05	0.31	0.00	0.00	0.08	0.26	0.023	0.084
CYSIGA.1	0.06	-0.24	0.02	0.04	0.00	0.04	0.03	0.61	0.020	0.110
CYCLE	0.07	0.29	0.00	0.01	---	---	0.00	0.03	0.017	0.007
DLEAK	0.04	0.19	0.02	0.19	---	---	---	---	0.012	0.036
GSHFAC.2	0.03	0.17	---	---	---	---	---	---	0.007	0.000
SV_NBCYC	0.01	0.10	0.01	0.32	---	---	0.00	0.04	0.004	0.070
DEV_DEC_HEAT	0.01	-0.08	0.00	0.06	0.02	0.58	0.00	0.03	0.004	0.107
PROTIN_6.2	0.01	0.11	---	---	0.00	0.03	0.00	0.03	0.003	0.009
TE.127M_IJCH.9	---	---	0.01	0.12	---	---	0.00	0.03	0.003	0.028
CFRISK.2	0.01	0.10	---	---	---	---	0.00	0.02	0.003	0.004
PARTSHAPE	0.01	0.10	---	---	0.00	0.02	---	---	0.002	0.003
DLTEVA_5.3	---	---	0.01	0.02	0.00	0.01	0.00	0.03	0.002	0.008
CHEMFORMI2	---	---	0.00	0.02	0.01	0.04	---	---	0.002	0.008
CFC	0.01	-0.08	---	---	---	---	---	---	0.002	0.000
SGTRLOC	0.00	0.04	0.00	0.05	---	---	---	---	0.001	0.010
TUBETEMP	0.00	0.07	---	---	---	---	0.00	0.00	0.001	0.001
SV_STATUS	---	---	0.00	0.22	---	---	---	---	0.001	0.046
DLTEVA.8	---	---	---	---	---	---	0.00	0.05	0.000	0.009
DDREFA.1	---	---	0.00	0.03	---	---	0.00	0.04	0.000	0.012
SC1131	---	---	0.00	0.02	---	---	---	---	0.000	0.004

\* highlighted if main contribution larger than 0.02 or conjoint contribution larger than 0.1

Table 6-36 through Table 6-38, which are based on HPS dose truncation, identify these same parameters mentioned in the preceding paragraph, but additionally identify cancer fatality risk for thyroid cancer, CFRISK.5, and the crosswind dispersion parameters, denoted by CYSIGA.1, as additional parameters that significantly affect LCF risk. The risk factor for thyroid cancer is one of the smaller of the risk factors, but it can be important when emergency-phase inhalation of radioiodine is significant. The dispersion parameters are rank correlated with a coefficient of 1.0, so CYSIGA.1 represents all of the dispersion parameters.

#### 6.2.3.2.2 Cases Involving Steam Generator Tube Rupture

This subsection discusses the results from applying the four regression techniques to the subset of the realizations that involved an SGTR for the two dose truncation models. The most important of the uncertain input variables are highlighted in Table 6-39 through Table 6-44.

Table 6-39 through Table 6-41, which are based on US background dose truncation, identify four parameters as important in all three tables and two additional parameters in two of the three tables, although not necessarily in the same order.

The four parameters that appear in all three tables based on US background dose truncation are (1) steam generator tube thickness of the most damaged tube, TUBTHICK; (2) aerosol deposition velocity, VDEPOS.1; (3) cross-wind dispersion coefficient, CYSIGA.1; and (4) two of the groundshine shielding factors, GSHFAC.2 and GSHFAC.3. The two shielding factors are correlated with a coefficient of 0.8. Each of these is discussed in preceding paragraphs.

**Table 6-39 Mean, individual, LCF risk regression results within a 10-mile circular area for realizations with SGTR (US background dose-response model).**

Final R <sup>2</sup>	Rank Regression		Quadratic		Recursive Partitioning		MARS		Main Contr.*	Conjoint Contr.*
	0.68		1.00		0.74		0.40			
Input	R <sup>2</sup> contr.	SRRC	S <sub>i</sub>	T <sub>i</sub>	S <sub>i</sub>	T <sub>i</sub>	S <sub>i</sub>	T <sub>i</sub>		
TUBTHICK	0.08	-0.24	0.01	0.04	0.27	0.64	0.25	0.25	0.099	0.100
VDEPOS.1	0.13	0.17	0.02	0.06	0.00	0.03	0.36	0.36	0.074	0.018
CYSIGA.1	0.10	-0.20	0.03	0.41	---	---	0.25	0.25	0.056	0.127
GSHFAC.3	---	---	0.01	0.11	0.06	0.32	0.15	0.15	0.037	0.100
GSHFAC.2	0.09	0.28	0.03	0.12	0.00	0.03	---	---	0.031	0.035
I.134_ICH.9	0.03	0.12	0.00	0.12	0.12	0.16	0.00	0.00	0.031	0.051
CFRISK.7	0.03	0.14	0.01	0.04	0.03	0.09	---	---	0.014	0.027
ESPEED.2	0.04	-0.19	0.01	0.03	0.01	0.13	---	---	0.013	0.036
CFRISK.6	---	---	0.04	0.45	---	---	---	---	0.012	0.137
PROTIN_6.2	---	---	---	---	0.04	0.07	---	---	0.011	0.007
RU.103_ICH.9	0.03	-0.14	---	---	0.02	0.05	---	---	0.010	0.008
CYCLE	0.03	0.18	0.01	0.06	---	---	0.00	0.00	0.008	0.017
RCPSL	0.03	0.26	0.00	0.07	---	---	0.00	0.00	0.008	0.022
GSHFAC_6.2	0.02	0.18	0.01	0.08	---	---	---	---	0.007	0.023
GSHFAC_2.2	0.03	-0.17	0.00	0.03	---	---	---	---	0.007	0.011
DLTEVA_2.8	0.02	-0.16	---	---	---	---	0.00	0.00	0.006	0.000
TE.132_ICH.9	0.02	-0.21	0.00	0.09	---	---	0.00	0.01	0.005	0.032
DLTEVA.2	0.02	-0.11	---	---	---	---	0.00	0.00	0.004	0.000
DLTEVA_3.5	---	---	---	---	---	---	0.01	0.00	0.001	0.000
SR.91_ICH.9	---	---	0.00	0.08	---	---	0.00	0.00	0.001	0.027
DLTEVA_4.10	---	---	---	---	---	---	0.00	0.00	0.000	0.000
DLTEVA_2.11	---	---	---	---	---	---	0.00	0.01	0.000	0.001

\* highlighted if main contribution larger than 0.02 or conjoint contribution larger than 0.1

**Table 6-40 Mean, individual, LCF risk regression results within a 10- to 20-mile annular area for realizations with SGTR (US background dose-response model).**

Final R <sup>2</sup>	Rank Regression		Quadratic		Recursive Partitioning		MARS		Main Contr.*	Conjoint Contr.*
	0.77		1.00		0.83		0.62			
Input	R <sup>2</sup> contr.	SRRC	S <sub>i</sub>	T <sub>i</sub>	S <sub>i</sub>	T <sub>i</sub>	S <sub>i</sub>	T <sub>i</sub>		
CYSIGA.1	0.22	-0.41	0.07	0.18	0.10	0.31	0.24	0.32	0.132	0.109
VDEPOS.1	0.11	0.22	0.00	0.12	0.01	0.03	0.16	0.15	0.054	0.046
GSHFAC.3	---	---	0.00	0.11	0.05	0.33	0.14	0.15	0.044	0.114
TUBTHICK	---	---	0.00	0.15	0.15	0.56	---	---	0.042	0.164
RCPSL	0.09	0.32	---	---	---	---	0.12	0.13	0.041	0.001
CFRISK.5	---	---	0.01	0.12	---	---	0.17	0.25	0.037	0.056
PARTSHAPE	0.06	0.29	0.00	0.12	0.05	0.22	0.00	0.01	0.026	0.088
GSHFAC.2	0.09	0.36	---	---	---	---	---	---	0.023	0.000
DLTEVA.2	---	---	---	---	---	---	0.09	0.09	0.019	0.000
DLTEVA_5.8	0.05	0.15	---	---	---	---	---	---	0.013	0.000
PROTIN.2	0.04	0.18	0.01	0.05	---	---	0.00	0.00	0.013	0.011
DLTEVA_4.8	0.01	0.09	0.03	0.24	---	---	0.00	0.01	0.010	0.071
CFRISK.8	0.03	0.22	---	---	0.00	0.00	---	---	0.008	0.000
GSHFAC_6.2	0.03	0.17	---	---	0.01	0.02	---	---	0.008	0.004
CM.242_ICH.9	0.01	-0.12	0.00	0.07	0.02	0.22	---	---	0.006	0.079
CFRISK.7	0.02	0.19	---	---	0.01	0.04	0.00	0.01	0.005	0.012
DLTEVA_2.8	---	---	0.01	0.10	---	---	---	---	0.005	0.029
PROTIN_2.2	0.01	0.12	---	---	---	---	0.00	0.00	0.004	0.000
I.134_ICH.9	0.01	0.10	---	---	0.01	0.03	---	---	0.003	0.008
DLTEVA.12	0.01	0.08	0.00	0.10	0.00	0.00	0.00	0.01	0.003	0.032
PROTIN_6.2	---	---	0.01	0.08	---	---	---	---	0.002	0.025
DLTEVA_5.10	---	---	0.01	0.08	---	---	0.00	0.00	0.002	0.024

\* highlighted if main contribution larger than 0.02 or conjoint contribution larger than 0.1

**Table 6-41 Mean, individual, LCF risk regression results within a 50-mile circular area for realizations with SGTR (US background dose-response model).**

Final R <sup>2</sup>	Rank Regression		Quadratic		Recursive Partitioning		MARS		Main Contr.*	Conjoint Contr. *
	0.75		1.00		0.71		0.67			
	R <sup>2</sup> contr.	SRRC	S <sub>I</sub>	T <sub>I</sub>	S <sub>I</sub>	T <sub>I</sub>	S <sub>I</sub>	T <sub>I</sub>		
Input										
CYSIGA.1	0.22	-0.42	0.04	0.11	0.10	0.26	0.26	0.27	0.127	0.063
TUBTHICK	0.01	-0.09	0.04	0.12	0.28	0.64	0.14	0.14	0.085	0.113
VDEPOS.1	0.10	0.25	0.03	0.11	0.00	0.02	0.14	0.15	0.056	0.031
GSHFAC.3	0.01	0.13	---	---	0.00	0.01	0.25	0.25	0.045	0.003
GSHFAC.2	0.13	0.29	0.01	0.17	0.00	0.04	---	---	0.035	0.061
PARTSHAPE	0.04	0.18	0.05	0.18	0.05	0.16	---	---	0.028	0.070
DLTEVA.2	---	---	0.01	0.12	---	---	0.10	0.10	0.027	0.034
RCPSL	0.08	0.27	0.00	0.12	0.00	0.00	---	---	0.021	0.039
CFRISK.8	0.04	0.14	---	---	0.01	0.02	0.05	0.04	0.018	0.003
CFRISK.7	0.02	0.15	0.04	0.06	---	---	0.00	0.00	0.015	0.006
CM.242_ICH.9	0.01	-0.14	0.01	0.10	0.06	0.32	0.00	0.00	0.015	0.093
CFRISK.5	---	---	---	---	---	---	0.06	0.05	0.013	0.000
PROTIN.2	0.04	0.20	---	---	---	---	0.00	0.00	0.011	0.000
CO.60_ICH.9	---	---	0.02	0.06	0.02	0.08	---	---	0.011	0.026
DLTEVA_3.3	---	---	0.03	0.13	---	---	---	---	0.010	0.034
CS.136_ICH.9	0.01	0.14	0.02	0.08	---	---	---	---	0.008	0.020
DLTEVA_5.8	0.03	0.16	---	---	---	---	---	---	0.008	0.000
GSHFAC_6.2	0.02	0.16	---	---	0.00	0.01	---	---	0.005	0.001
PROTIN_5.2	---	---	0.01	0.07	---	---	---	---	0.004	0.019
DLTEVA_2.1	---	---	0.00	0.10	0.00	0.01	0.00	0.01	0.002	0.033
DLTEVA_2.4	0.01	0.09	---	---	---	---	---	---	0.001	0.000
I.131_ICH.9	---	---	---	---	---	---	0.00	0.00	0.001	0.000

\* highlighted if main contribution larger than 0.02 or conjoint contribution larger than 0.1

**Table 6-42 Mean, individual, LCF risk regression results within a 10-mile circular area for realizations with SGTR (HPS dose-response model).**

Final R <sup>2</sup>	Rank Regression		Quadratic		Recursive Partitioning		MARS		Main Contr.*	Conjoint Contr. *
	0.72		1.00		0.48		0.84			
	R <sup>2</sup> contr.	SRRC	S <sub>I</sub>	T <sub>I</sub>	S <sub>I</sub>	T <sub>I</sub>	S <sub>I</sub>	T <sub>I</sub>		
Input										
CYSIGA.1	0.32	-0.39	0.01	0.03	0.05	0.16	0.05	0.17	0.099	0.058
SVOAFRAC	---	---	0.22	0.37	0.05	0.14	---	---	0.080	0.066
CFRISK.5	0.03	0.13	0.02	0.05	0.46	0.48	0.07	0.72	0.080	0.196
ESPEED.2	0.06	-0.28	---	---	0.29	0.33	0.00	0.04	0.049	0.016
TUBTHICK	0.08	-0.21	0.00	0.02	---	---	0.10	0.17	0.040	0.029
CYCLE	0.08	0.23	0.02	0.07	---	---	---	---	0.023	0.018
SGTRLOC	0.01	0.04	0.08	0.28	---	---	0.00	0.03	0.023	0.077
TC.99M_ICH.9	---	---	0.05	0.11	---	---	0.00	0.02	0.017	0.024
DLTEVA_2.12	0.04	-0.19	---	---	---	---	0.00	0.01	0.011	0.002
DLTEVA_5.6	0.02	-0.17	---	---	---	---	0.02	0.70	0.010	0.188
PROTIN_5.2	---	---	0.03	0.15	0.00	0.00	0.00	0.02	0.009	0.048
GSHFAC_3.2	0.02	0.12	0.02	0.04	---	---	0.00	0.01	0.008	0.012
GSHFAC_3.1	0.01	-0.08	0.02	0.10	---	---	---	---	0.008	0.028
DLTEVA_2.11	0.01	0.15	0.02	0.03	0.00	0.01	---	---	0.007	0.007
Y.91M_ICH.9	---	---	0.02	0.08	---	---	0.00	0.02	0.007	0.026
CFC	0.02	-0.14	---	---	---	---	---	---	0.005	0.000
DLTEVA_2.1	0.01	-0.09	0.01	0.05	---	---	---	---	0.004	0.014
PROTIN_6.2	0.01	-0.11	---	---	0.01	0.02	---	---	0.004	0.002
DLTEVA_4.1	---	---	0.01	0.04	0.00	0.01	---	---	0.002	0.011
DLTEVA_3.5	---	---	0.00	0.04	---	---	0.00	0.02	0.001	0.017
PROTIN_6.1	0.01	-0.09	---	---	---	---	---	---	0.001	0.000
GSHFAC_6.3	---	---	---	---	0.00	0.02	0.00	0.03	0.000	0.010

\* highlighted if main contribution larger than 0.02 or conjoint contribution larger than 0.1

**Table 6-43 Mean, individual, LCF risk regression results within a 10- to 20-mile annular area for realizations with SGTR (HPS dose-response model).**

Final R <sup>2</sup>	Rank Regression		Quadratic		Recursive Partitioning		MARS		Main Contr.*	Conjoint Contr.*
	0.81		1.00		0.48		0.96			
Input	R <sup>2</sup> contr.	SRRC	S <sub>i</sub>	T <sub>i</sub>	S <sub>i</sub>	T <sub>i</sub>	S <sub>i</sub>	T <sub>i</sub>		
CYSIGA.1	0.48	-0.60	0.01	0.18	0.26	0.35	0.13	0.95	0.184	0.333
CFRISK.5	0.09	0.29	0.01	0.12	0.60	0.61	0.07	0.87	0.114	0.296
SVOAFRAC	---	---	0.18	0.76	0.05	0.11	---	---	0.067	0.204
PARTSHAPE	0.06	0.21	0.00	0.02	---	---	0.00	0.05	0.014	0.021
GSHFAC.3	0.05	0.18	---	---	---	---	0.00	0.09	0.014	0.028
SV_STATUS	---	---	0.03	0.08	---	---	---	---	0.010	0.018
PROTIN_2.2	0.03	0.14	0.00	0.04	0.00	0.00	0.00	0.12	0.009	0.049
RCPSL	0.02	0.22	---	---	---	---	0.01	0.00	0.007	0.000
DLTEVA_3.6	---	---	0.02	0.12	---	---	---	---	0.006	0.034
I.131_ICH.9	0.01	-0.09	0.02	0.18	---	---	---	---	0.006	0.054
DLTEVA_4.6	0.02	0.14	---	---	---	---	---	---	0.005	0.000
PROTIN_6.2	0.02	-0.10	0.00	0.01	---	---	---	---	0.004	0.004
PROTIN.2	0.01	0.11	0.00	0.06	0.00	0.00	0.00	0.00	0.004	0.020
AM.241_ICH.9	0.01	0.07	---	---	0.01	0.02	0.00	0.05	0.003	0.018
DLTEVA_2.12	0.01	-0.09	---	---	---	---	---	---	0.002	0.000
DLTEVA_2.1	---	---	0.01	0.03	---	---	---	---	0.002	0.007
DLTEVA_5.10	---	---	0.00	0.04	---	---	---	---	0.001	0.011
TE.129M_ICH.9	0.00	-0.09	---	---	---	---	---	---	0.001	0.000
DLTEVA.5	---	---	0.00	0.01	---	---	---	---	0.001	0.003
GSHFAC_3.1	---	---	---	---	---	---	0.00	0.03	0.001	0.010
ND.147_ICH.9	---	---	0.00	0.02	---	---	0.00	0.03	0.000	0.015
PROTIN.3	---	---	0.00	0.05	---	---	0.00	0.05	0.000	0.034

\* highlighted if main contribution larger than 0.02 or conjoint contribution larger than 0.1

**Table 6-44 Mean, individual, LCF risk regression results within a 50-mile circular area for realizations with SGTR (HPS dose-response model).**

Final R <sup>2</sup>	Rank Regression		Quadratic		Recursive Partitioning		MARS		Main Contr.*	Conjoint Contr.*
	0.77		1.00		0.44		0.95			
Input	R <sup>2</sup> contr.	SRRC	S <sub>i</sub>	T <sub>i</sub>	S <sub>i</sub>	T <sub>i</sub>	S <sub>i</sub>	T <sub>i</sub>		
CYSIGA.1	0.48	-0.64	0.03	0.29	0.36	0.47	0.16	0.96	0.203	0.356
CFRISK.5	0.09	0.25	0.02	0.16	0.47	0.48	0.05	0.85	0.092	0.299
SVOAFRAC	---	---	0.11	0.78	0.04	0.10	---	---	0.043	0.232
PARTSHAPE	0.05	0.16	---	---	0.01	0.04	---	---	0.014	0.004
GSHFAC.3	0.05	0.19	---	---	---	---	---	---	0.013	0.000
TUBTHICK	0.02	-0.16	0.02	0.09	---	---	0.00	0.02	0.010	0.029
SV_STATUS	---	---	0.03	0.07	---	---	0.00	0.03	0.010	0.022
RCPSL	0.02	0.16	---	---	---	---	---	---	0.005	0.000
DLTEVA_3.6	---	---	0.01	0.17	---	---	0.00	0.07	0.005	0.073
PROTIN_6.2	0.02	-0.13	0.00	0.02	---	---	---	---	0.004	0.007
PROTIN.2	0.01	0.11	0.00	0.00	0.00	0.00	0.00	0.00	0.003	0.000
DLTEVA_5.10	---	---	0.01	0.05	---	---	0.00	0.06	0.003	0.031
DLTEVA_2.12	0.01	-0.12	---	---	---	---	---	---	0.003	0.000
DLTEVA_3.1	0.01	0.11	0.00	0.03	0.00	0.03	0.00	0.08	0.003	0.040
PROTIN_5.3	0.01	0.09	---	---	---	---	0.00	0.03	0.002	0.008
AM.241_ICH.9	0.01	0.10	---	---	---	---	---	---	0.002	0.000
GSHFAC_3.1	---	---	0.00	0.02	---	---	0.00	0.03	0.002	0.011
RDSTC	---	---	0.00	0.03	---	---	0.00	0.09	0.001	0.036
ESPEED.2	---	---	0.00	0.00	---	---	---	---	0.001	0.000
DLTEVA_3.5	---	---	---	---	---	---	0.00	0.01	0.001	0.004
ND.147_ICH.9	---	---	0.00	0.07	---	---	---	---	0.000	0.022
CO.60_ICH.9	---	---	---	---	---	---	0.00	0.11	0.000	0.034

\* highlighted if main contribution larger than 0.02 or conjoint contribution larger than 0.1

The parameters that appear in two of the three tables for US background dose truncation are (1) the reactor coolant pump seal leakage rate, RCPSL, and (2) the aerosol dynamic shape factor, PARTSHAPE.

Table 6-42 through Table 6-44, which are based on HPS dose truncation, identify most of these same parameters, but additionally identify SV open area fraction, SVOAFRAC, and thyroid cancer fatality risk, CFRISK.5, as additional parameters of importance that are highlighted in at least two of the three tables.

### 6.2.3.2.3 Cases not Involving Steam Generator Tube Rupture

This subsection discusses the results from applying the four regression techniques to the subset of the realizations that do not involve SGTR for the two dose truncation models. The most important of the uncertain input variables are highlighted in Table 6-45 through Table 6-50.

Table 6-45 through Table 6-47, which are based on US background dose truncation, identify four parameters as important in at least two of the three tables, although not necessarily in the same order. These are (1) groundshine shielding factor, GSHFAC.2; (2) aerosol dynamic shape factor in the MELCOR model, PARTSHAPE; (3) time of the accident during the fuel cycle, CYCLE; and (4) cross-wind dispersion factors, denoted by CYSIGA.1.

**Table 6-45 Mean, individual, LCF risk regression results within a 10-mile circular area for realizations without SGTR (US background dose-response model).**

Input	Rank Regression		Quadratic		Recursive Partitioning		MARS		Main Contr.*	Conjoint Contr.*
	0.65		0.65		0.65		0.39			
	R <sup>2</sup> contr.	SRRC	S <sub>i</sub>	T <sub>i</sub>	S <sub>i</sub>	T <sub>i</sub>	S <sub>i</sub>	T <sub>i</sub>		
GSHFAC.2	0.16	0.35	0.23	0.51	0.09	0.82	0.15	0.55	0.106	0.271
CYCLE	0.22	0.50	0.03	0.13	0.01	0.51	0.04	0.05	0.066	0.130
CYSIGA.1	0.10	-0.31	0.02	0.06	0.01	0.55	0.06	0.28	0.034	0.155
PARTSHAPE	0.02	0.12	0.01	0.05	0.05	0.04	0.21	0.28	0.033	0.018
DLEAK	0.05	-0.22	0.02	0.22	0.00	0.00	---	---	0.015	0.044
CFRISK.6	---	---	0.03	0.10	0.02	0.06	0.03	0.08	0.013	0.031
VDEPOS.1	0.03	0.15	0.01	0.05	0.01	0.45	0.01	0.10	0.011	0.113
SVOAFRAC	0.04	-0.14	---	---	---	---	---	---	0.010	0.000
CFC	0.02	-0.12	---	---	---	---	0.00	0.01	0.004	0.002
GSHFAC.3	0.00	0.05	0.01	0.15	---	---	---	---	0.003	0.030
CWASH1.	0.00	0.05	0.01	0.05	---	---	---	---	0.003	0.008
DEV_DEC_HEAT	0.01	-0.09	---	---	0.00	0.07	0.00	0.01	0.003	0.015
Y.91M_IJH.9	---	---	---	---	---	---	0.02	0.08	0.002	0.009
DDREFA.8	---	---	0.00	0.06	---	---	0.01	0.05	0.002	0.017
ZR.95_IJH.9	---	---	0.01	0.07	---	---	0.00	0.01	0.002	0.015
SV_NBCYC	0.01	0.08	---	---	0.00	0.01	---	---	0.001	0.002
CE.143_IJH.9	---	---	0.00	0.04	---	---	---	---	0.001	0.008
PROTIN.3	---	---	0.00	0.02	---	---	---	---	0.001	0.004
GSHFAC_2.3	---	---	0.00	0.02	---	---	---	---	0.001	0.003
PROTIN.2	0.00	0.06	---	---	0.00	0.00	---	---	0.001	0.000
CHEMFORMCS	0.00	-0.05	---	---	---	---	---	---	0.001	0.000
SC1131	0.00	-0.06	---	---	---	---	0.00	0.05	0.001	0.006

\* highlighted if main contribution larger than 0.02 or conjoint contribution larger than 0.1

**Table 6-46 Mean, individual, LCF risk regression results within a 10- to 20-mile annular area for realizations without SGTR (US background dose-response model).**

Input	Rank Regression		Quadratic		Recursive Partitioning		MARS		Main Contr.*	Conjoint Contr.*
	0.21		0.75		0.30		0.84			
	R <sup>2</sup> contr.	SRRC	S <sub>i</sub>	T <sub>i</sub>	S <sub>i</sub>	T <sub>i</sub>	S <sub>i</sub>	T <sub>i</sub>		
PARTSHAPE	0.02	0.06	0.03	0.31	0.73	0.75	0.08	0.64	0.081	0.228
GSHFAC.2	0.02	0.06	0.02	0.11	0.08	0.07	0.03	0.34	0.019	0.112
CYSIGA.1	0.05	-0.11	0.02	0.08	0.01	0.10	0.01	0.04	0.019	0.032
CYCLE	0.04	0.10	0.03	0.13	---	---	---	---	0.015	0.025
CWASH1.	0.01	0.05	0.03	0.37	---	---	0.02	0.58	0.013	0.243
GSHFAC.3	---	---	0.00	0.04	---	---	0.04	0.19	0.011	0.050
DLTEVA.9	0.00	-0.03	0.02	0.07	0.05	0.13	---	---	0.008	0.021
DEV_DEC_HEAT	0.01	-0.05	---	---	---	---	0.02	0.10	0.007	0.023
SVOAFRAC	0.01	-0.06	---	---	---	---	0.01	0.11	0.006	0.027
LA.141_I.CH.9	0.01	-0.04	0.01	0.13	---	---	---	---	0.004	0.029
DLEAK	0.01	0.04	0.01	0.24	---	---	0.00	0.05	0.004	0.072
CE.144_I.CH.9	0.01	0.04	---	---	0.01	0.04	0.00	0.04	0.004	0.012
VDEPOS.1	0.01	-0.04	0.01	0.05	---	---	---	---	0.004	0.009
CFC	0.01	-0.04	0.01	0.03	---	---	---	---	0.003	0.007
RU.106_I.CH.9	---	---	0.01	0.04	0.00	0.08	0.00	0.02	0.002	0.020
RU.105_I.CH.9	---	---	0.01	0.04	---	---	---	---	0.001	0.009
DLTEVA_5.2	0.00	-0.03	---	---	---	---	---	---	0.001	0.000
PROTIN_4.2	0.00	0.03	---	---	---	---	0.00	0.02	0.001	0.006
DDREFA.2	---	---	---	---	---	---	0.00	0.05	0.001	0.013
CHEMFORMI2	---	---	---	---	---	---	0.00	0.01	0.001	0.003
CFRISK.8	---	---	0.00	0.03	---	---	---	---	0.000	0.008
DLTEVA_5.8	---	---	0.00	0.06	---	---	---	---	0.000	0.015

\* highlighted if main contribution larger than 0.02 or conjoint contribution larger than 0.1

**Table 6-47 Mean, individual, LCF risk regression results within a 50-mile circular area for realizations without SGTR (US background dose-response model).**

Input	Rank Regression		Quadratic		Recursive Partitioning		MARS		Main Contr.*	Conjoint Contr.*
	0.65		0.66		0.53		0.43			
	R <sup>2</sup> contr.	SRRC	S <sub>i</sub>	T <sub>i</sub>	S <sub>i</sub>	T <sub>i</sub>	S <sub>i</sub>	T <sub>i</sub>		
GSHFAC.2	0.16	0.35	0.25	0.51	0.11	0.79	0.12	0.51	0.108	0.232
CYCLE	0.22	0.50	0.03	0.11	0.01	0.46	---	---	0.060	0.098
PARTSHAPE	0.02	0.12	0.01	0.05	0.07	0.10	0.27	0.34	0.043	0.025
CYSIGA.1	0.10	-0.31	0.02	0.05	0.03	0.62	0.04	0.30	0.035	0.148
DLEAK	0.05	-0.22	0.01	0.22	0.00	0.00	0.01	0.02	0.014	0.049
VDEPOS.1	0.03	0.15	0.02	0.04	---	---	0.01	0.09	0.010	0.017
SVOAFRAC	0.04	-0.14	---	---	---	---	---	---	0.010	0.000
CFRISK.6	---	---	0.00	0.10	0.03	0.02	0.02	0.04	0.008	0.022
CFC	0.02	-0.12	---	---	0.00	0.02	0.00	0.02	0.004	0.006
CWASH1.	0.00	0.05	0.01	0.08	---	---	---	---	0.003	0.014
DEV_DEC_HEAT	0.01	-0.09	---	---	0.00	0.00	---	---	0.003	0.000
GSHFAC.3	0.00	0.05	0.01	0.15	---	---	---	---	0.002	0.031
DDREFA.8	---	---	0.01	0.07	---	---	0.01	0.09	0.002	0.024
Y.91M_I.CH.9	---	---	---	---	---	---	0.01	0.10	0.002	0.013
SV_NBCYC	0.01	0.08	0.00	0.02	0.00	0.01	0.00	0.02	0.002	0.009
ZR.95_I.CH.9	---	---	0.01	0.06	---	---	---	---	0.002	0.012
DLTEVA.5	---	---	---	---	0.01	0.11	---	---	0.001	0.018
GSHFAC_2.3	---	---	0.01	0.02	0.00	0.02	---	---	0.001	0.007
CHEMFORMI2	---	---	0.00	0.04	---	---	0.00	0.01	0.001	0.010
PROTIN.2	0.00	0.06	---	---	---	---	---	---	0.001	0.000
CHEMFORMCS	0.00	-0.05	---	---	---	---	---	---	0.001	0.000
SC1131	0.00	-0.06	0.00	0.04	---	---	---	---	0.001	0.008

\* highlighted if main contribution larger than 0.02 or conjoint contribution larger than 0.1

**Table 6-48 Mean, individual, LCF risk regression results within a 10-mile circular area for realizations without SGTR (HPS dose-response model).**

Final R <sup>2</sup>	Rank Regression		Quadratic		Recursive Partitioning		MARS		Main Contr.*	Conjoint Contr.*
	0.56		0.60		0.34		0.82			
Input	R <sup>2</sup> contr.	SRRC	S <sub>i</sub>	T <sub>i</sub>	S <sub>i</sub>	T <sub>i</sub>	S <sub>i</sub>	T <sub>i</sub>		
PARTSHAPE	0.02	0.13	0.04	0.14	0.60	0.60	0.39	0.47	0.141	0.041
CYCLE	0.24	0.52	0.01	0.03	---	---	0.01	0.02	0.063	0.008
GSHFAC.2	0.05	0.21	0.17	0.46	0.00	0.00	0.02	0.18	0.041	0.105
CYSIGA.1	0.11	-0.33	0.01	0.06	0.01	0.04	0.00	0.07	0.031	0.032
GSHFAC.3	---	---	0.08	0.32	---	---	0.00	0.16	0.017	0.090
DLEAK	0.04	0.20	0.00	0.15	---	---	---	---	0.011	0.030
DLTEVA_3.12	---	---	---	---	0.04	0.33	0.01	0.35	0.009	0.124
DLTEVA.5	---	---	0.00	0.05	0.01	0.00	0.02	0.18	0.006	0.052
CFRISK.5	0.02	0.16	---	---	0.00	0.01	---	---	0.006	0.000
DEV_DEC_HEAT	0.01	-0.10	0.00	0.06	0.01	0.02	0.01	0.05	0.005	0.023
SVOAFRAC	0.02	-0.12	---	---	---	---	0.00	0.09	0.005	0.023
CFRISK.2	0.01	0.07	0.02	0.15	---	---	---	---	0.005	0.025
CFC	0.02	-0.13	0.00	0.03	---	---	---	---	0.004	0.006
PROTIN_6.2	0.01	0.11	---	---	---	---	---	---	0.003	0.000
CHEMFORMI2	0.00	0.05	0.00	0.05	0.01	0.06	---	---	0.001	0.015
SV_NBCYC	0.01	0.08	---	---	---	---	0.00	0.03	0.001	0.009
TE.127M_ICH.9	0.01	-0.07	---	---	---	---	---	---	0.001	0.000
MO.99_ICH.9	---	---	0.01	0.03	0.00	0.28	---	---	0.001	0.036
ZR.95_ICH.9	---	---	---	---	---	---	0.00	0.02	0.001	0.005
SV_STATUS	---	---	---	---	---	---	0.00	0.08	0.001	0.020
VDEPOS.1	0.00	0.05	---	---	---	---	---	---	0.001	0.000
CM.242_ICH.9	---	---	0.00	0.02	---	---	---	---	0.000	0.004

\* highlighted if main contribution larger than 0.02 or conjoint contribution larger than 0.1

**Table 6-49 Mean, individual, LCF risk regression results within a 10- to 20-mile annular area for realizations without SGTR (HPS dose-response model).**

Final R <sup>2</sup>	Rank Regression		Quadratic		Recursive Partitioning		MARS		Main Contr.*	Conjoint Contr.*
	0.15		0.62		0.33		0.99			
Input	R <sup>2</sup> contr.	SRRC	S <sub>i</sub>	T <sub>i</sub>	S <sub>i</sub>	T <sub>i</sub>	S <sub>i</sub>	T <sub>i</sub>		
PARTSHAPE	0.02	0.03	0.00	0.00	1.00	0.99	1.00	0.99	0.335	0.000
CYSIGA.1	0.03	-0.05	0.00	0.15	---	---	0.00	0.00	0.007	0.031
CYCLE	0.02	0.03	0.00	0.41	---	---	---	---	0.006	0.084
DLTEVA_5.5	---	---	---	---	---	---	0.02	0.12	0.005	0.034
RDMTC	0.01	-0.03	---	---	---	---	---	---	0.003	0.000
GE.144_ICH.9	0.01	0.02	---	---	---	---	0.01	0.07	0.002	0.022
SGTRLOC	0.01	0.03	0.00	1.00	0.00	0.00	0.00	0.02	0.002	0.213
DDREFA.4	0.01	0.02	0.00	0.15	---	---	---	---	0.002	0.032
PROTIN_4.2	0.01	0.02	---	---	---	---	0.00	0.09	0.002	0.030
DLEAK	0.01	0.02	0.00	0.40	---	---	0.00	0.06	0.002	0.103
DEV_DEC_HEAT	0.01	-0.02	0.00	0.20	0.00	0.01	0.00	0.01	0.001	0.046
H2LFL	---	---	0.01	0.19	---	---	---	---	0.001	0.037
DLTEVA_4.6	0.01	0.02	---	---	---	---	---	---	0.001	0.000
DDREFA.5	0.01	-0.02	---	---	---	---	---	---	0.001	0.000
DLTEVA.10	0.00	0.02	---	---	---	---	0.00	0.01	0.001	0.002
GSHFAC.2	0.00	0.02	---	---	---	---	0.00	0.09	0.001	0.031
DLTEVA_3.6	0.00	-0.02	0.00	0.00	---	---	---	---	0.001	0.000
DLTEVA_4.4	---	---	0.00	0.41	---	---	0.00	0.04	0.001	0.098
SV_WTR_CYC	---	---	0.00	0.97	---	---	---	---	0.000	0.200
CS.137_ICH.9	---	---	0.00	0.16	---	---	---	---	0.000	0.033
CHEMFORMI2	---	---	0.00	0.00	---	---	---	---	0.000	0.000
GSHFAC_5.1	---	---	0.00	0.00	---	---	---	---	0.000	0.000

\* highlighted if main contribution larger than 0.02 or conjoint contribution larger than 0.1

**Table 6-50 Mean, individual, LCF risk regression results within a 50-mile circular area for realizations without SGTR (HPS dose-response model).**

	Rank Regression		Quadratic		Recursive Partitioning		MARS		Main Contr.*	Conjoint Contr.*
Final R <sup>2</sup>	0.56		0.55		0.33		0.90			
Input	R <sup>2</sup> contr.	SRRC	S <sub>i</sub>	T <sub>i</sub>	S <sub>i</sub>	T <sub>i</sub>	S <sub>i</sub>	T <sub>i</sub>		
PARTSHAPE	0.02	0.13	0.08	0.37	0.87	0.84	0.52	0.93	0.205	0.175
CYCLE	0.24	0.52	---	---	---	---	0.00	0.10	0.061	0.029
CYSIGA.1	0.11	-0.33	0.01	0.05	---	---	---	---	0.029	0.008
GSHFAC.2	0.05	0.21	0.10	0.28	---	---	0.01	0.43	0.029	0.158
GSHFAC.3	---	---	0.08	0.20	---	---	0.00	0.10	0.014	0.054
DLEAK	0.04	0.18	0.01	0.14	---	---	0.00	0.04	0.010	0.036
CFRISK.5	0.02	0.16	---	---	---	---	---	---	0.005	0.000
CFC	0.02	-0.13	0.00	0.07	---	---	---	---	0.005	0.012
SVOAFRAC	0.02	-0.12	---	---	---	---	---	---	0.005	0.000
DLTEVA_3.12	---	---	0.00	0.05	0.01	0.08	0.01	0.00	0.004	0.017
CFRISK.2	0.01	0.07	0.01	0.15	---	---	0.00	0.12	0.003	0.061
PROTIN_6.2	0.01	0.11	---	---	---	---	---	---	0.003	0.000
DEV_DEC_HEAT	0.01	-0.10	---	---	0.00	0.04	0.00	0.05	0.003	0.018
DLTEVA.5	---	---	0.01	0.04	0.00	0.00	0.00	0.25	0.002	0.081
DLTEVA_5.8	---	---	0.01	0.04	---	---	---	---	0.002	0.006
SV_NBCYC	0.01	0.08	---	---	---	---	0.00	0.08	0.001	0.023
VDEPOS.1	0.00	0.05	---	---	---	---	0.00	0.07	0.001	0.020
TE.127M_IJH.9	0.00	-0.07	---	---	---	---	0.00	0.09	0.001	0.026
CE.143_IJH.9	---	---	0.00	0.02	---	---	---	---	0.001	0.004
CHEMFORMI2	0.00	0.05	0.00	0.05	0.00	0.07	---	---	0.001	0.016
DOSHOT.	---	---	0.00	0.05	---	---	---	---	0.000	0.009
CM.242_IJH.9	---	---	0.00	0.08	---	---	---	---	0.000	0.015

\* highlighted if main contribution larger than 0.02 or conjoint contribution larger than 0.1

The aerosol shape factor (PARTSHAPE) in the MELCOR model affects the amount of deposition of aerosols in the RCS and containment and the resulting aerosol size distribution that is released into the atmosphere. A noteworthy point is that the MACCS model assumptions are disconnected from the MELCOR assumptions for this parameter in that deposition velocities are not correlated with the value of dynamic shape factor. Currently, the overall framework does not have the capability to include such a correlation. Such a capability would allow greater self-consistency in the aerosol modeling of the source term and consequence analyses.

Table 6-48 through Table 6-50, which are based on HPS dose truncation, identify the same four parameters discussed for US background dose truncation discussed in this subsection.

### 6.2.3.3 Regression Analysis of Early Fatality Risk

Only one realization had a nonzero risk for early fatalities. Within this realization, only a few of the weather trials had doses large enough to exceed the dose threshold for early fatalities and the reported risk for this realization was approximately  $7 \cdot 10^{-13}$  within a 2-mile radius of the site. This number is so small that it is essentially zero. Because of this, there was nothing to be learned by performing a regression analysis on early fatality risk for the Surry UA.

### 6.2.4 Analysis of Single Realizations

Select individual realizations from the uncertainty analysis were further investigated in greater detail to identify the influences affecting the predicted consequences.

### 6.2.4.1 MACCS Single Realizations Consequence Analysis

Three single source term realizations were evaluated for consequences. These are intended to represent small, medium, and large source terms (STs). The three realizations selected are 856 (small), 9 (medium), and 562 (large), as discussed in Section 6.1.6.

The results of these single source term realizations are shown in Figure 6-123. The results are for the linear no-threshold dose-response model and show mean, population-weighted, LCF risk at distance intervals of 0 to 10 and 10 to 20 miles. The curves labeled small, medium, and large are the results of the single source-term realizations from MELCOR but represent means over weather variability for 300 realizations based on the other uncertain inputs to the consequence analysis, as discussed in Section 4.2. The CCDFs labeled Surry UA show uncertainties from both MELCOR and MACCS inputs (source term and consequences) averaged over weather variability. They are the same as the curves for the corresponding distance intervals in Figure 6-101.

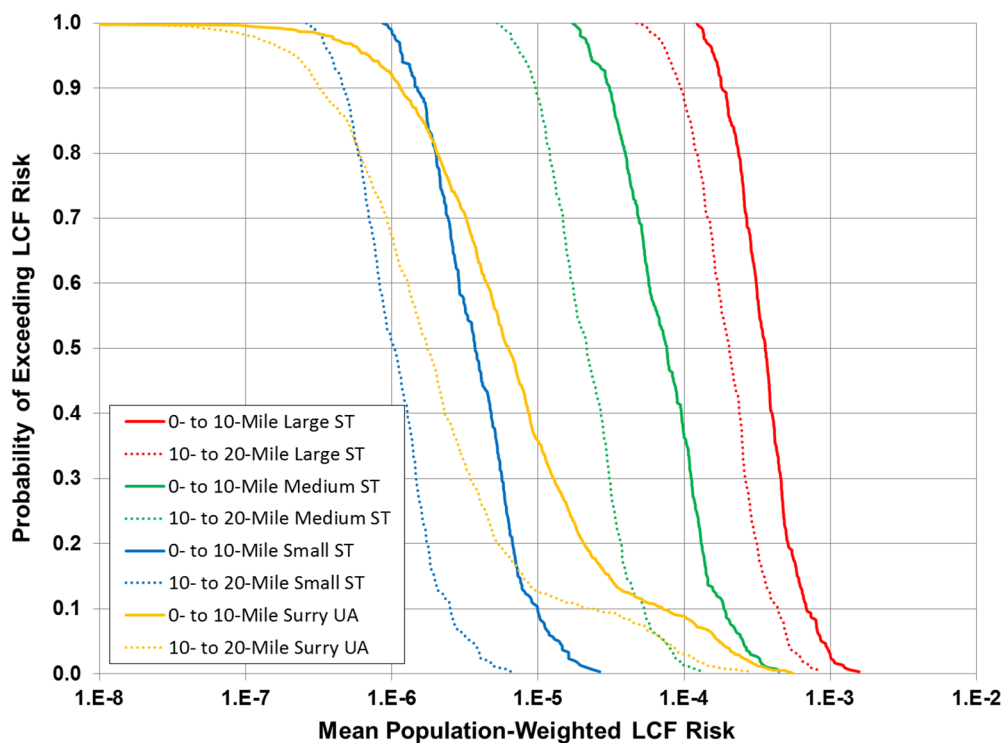


**Figure 6-123 Complementary cumulative distribution function of mean, population-weighted LCF risk (based on LNT dose response) within two annular areas centered on the Surry site for three single realizations and for the base Surry uncertainty analysis results from Figure 6-101**

The results show that the Surry UA CCDFs span the results for the single MELCOR realizations, with the exception of the upper end of the curves for the large source term (Large ST). These curves pair one of the larger source terms with a large sample set of other MACCS input parameters. This shows that there are low probability combinations of input parameters that can produce larger consequences than any of those in the set of 1003 realizations discussed earlier in this chapter. This is not surprising and shows that the tails of the distributions are the most difficult to quantify.

The results in Figure 6-123 also show that the distribution is much narrower when only uncertain consequence parameters are considered than when both source-term and consequence parameters are considered in the analysis. It appears that the results are more heavily influenced by uncertainties in source term than by uncertain consequence parameters, just as they were for the Peach Bottom uncertainty analysis. This is true when a single dose-response model (LNT) is used, but uncertainties in risks created by uncertainties in dose-response model are large and might have altered this conclusion if dose response had been included as part of the integrated uncertainty analysis.

### **6.2.5 Sensitivity Results for Phase Durations and Dose Projection Period**

Four MACCS sensitivity results were evaluated using the large source term discussed in Subsection 6.2.4.1, which corresponds to realization 562 from the Surry uncertainty analysis (cf. Subsection 6.1.6). The sensitivity cases investigated the following four combinations of input choices:

1. A case using a 15-day emergency phase; the base case uses a 7-day emergency phase.
2. A case using a 30-day emergency phase.
3. A case using a 6-month intermediate phase; the base case does not include an intermediate phase (duration set to zero).
4. A case using a 4-day dose projection period for emergency-phase relocation; the base case uses a 7-day dose projection period.

These sensitivity cases are discussed in this subsection and the results are compared with a base case.

Figure 6-124 shows the results for these sensitivity cases. The base case is the Large Source Term case discussed in the previous subsection. The base case uses the default input values for this uncertainty analysis: the emergency phase is 7 days; there is no intermediate phase (duration is zero); the dose-projection period is the entire duration of the emergency phase, 7 days. Each of the other cases shown in the figure has the same parameter values except that one of them is varied to examine the effect of this parameter on the mean, population-weighted, LCF risk.

Figure 6-124 shows that the results are all essentially the same with one exception, the risks for the 0- to 10-mile distance interval are noticeably larger for the case when the intermediate phase is 6 months than when its duration is 0 (no intermediate phase). There is no obvious reason why including an intermediate phase should increase or decrease the mean individual risk. The increase in risk for the 0- to 10-mile interval indicates that less decontamination occurs when the intermediate phase is included and that more individuals receive a larger dose when they return home than receive a smaller dose. This can occur when the 6 months of decay and weathering provided by the intermediate phase brings the dose levels below the habitability threshold without the need to decontaminate. However, these dose levels can be higher than they would have been if decontamination were performed because the modeling approach to decontamination reduces dose levels by a factor of 3 or 15. If the source term had been a

different magnitude (mainly in terms of overall cesium release) this could have gone the other way and the risk could have been reduced.

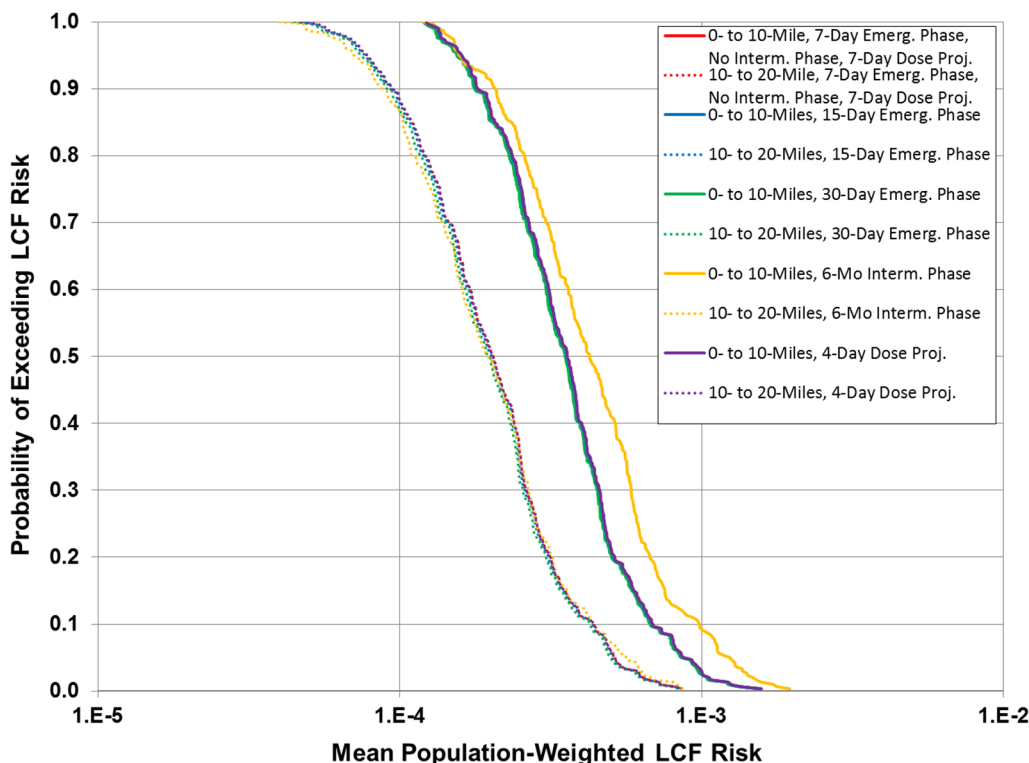


**Figure 6-124 Complementary cumulative distribution function of mean, population-weighted LCF risk (based on LNT dose response) within two annular areas centered on the Surry site for four sensitivity cases and for the Large Source Term case shown in Figure 6-123**

### 6.2.6 Evaluation of Multiple Tube Ruptures

Consequence results are presented in Figure 6-125 for the source term analysis evaluating uncertainty of the number of steam generator tubes that rupture, as discussed in the SGTR joint sensitivity analysis in Section 6.1.7.1. The points on the curves represent the mean LCF risk over variable weather for each of the realizations representing epistemic uncertainty and are conditional on the accident occurring. The results are for three spatial intervals and compare the main UA results for the Surry unmitigated STSBO (discussed in Section 6.2.1) with those from the SG tube failure joint sensitivity (called “SG Tube UA” here) described in the current section. All other sampling is performed the same way for the two sets of results; the only difference is the set of source terms that were used. The Surry UA curves are comprised of 1003 results that include cases in which no SGTR occurs (899) and cases in which a single SGT ruptures (104); the SGT UA is comprised of 388 results using the 97 source terms described in Section 6.1.8.1. Each source term is paired with four sets of sampled MACCS input parameters to create the 388 realizations that were evaluated. A single SG tube fails in 50 percent of the source terms, two tubes fail in 25 percent of the source terms, and three or more tubes fail in 25 percent of the source terms generated by MELCOR.

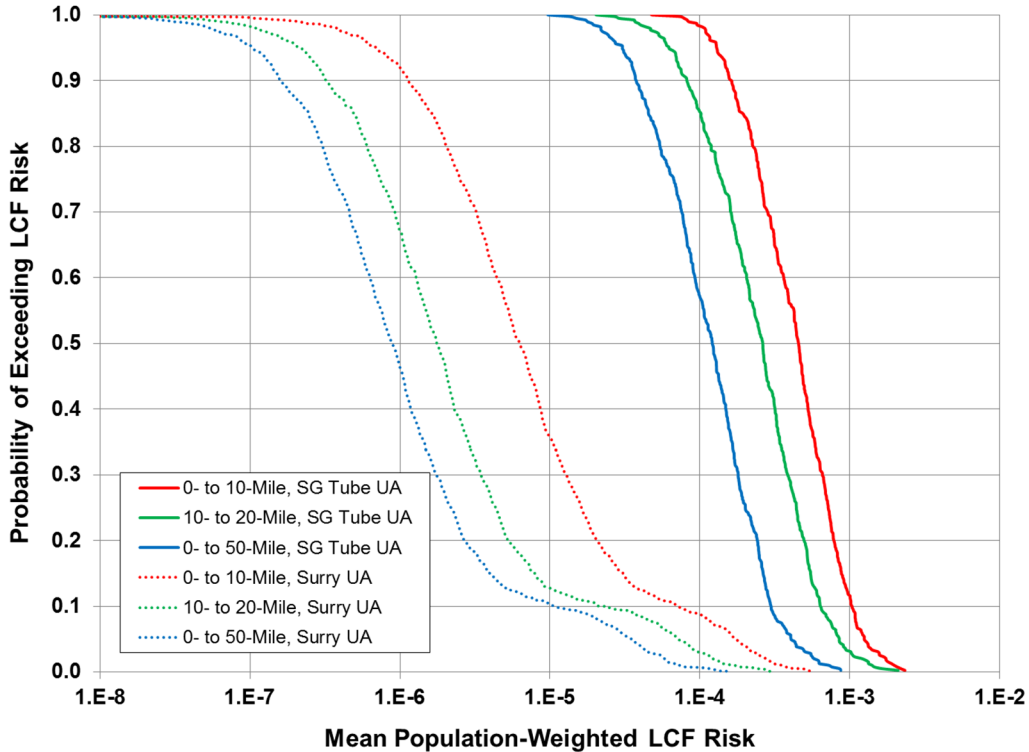


**Figure 6-125 Complementary cumulative distribution function of mean, population-weighted LCF risk (based on LNT dose response) within three distance intervals centered on the Surry site for the SGT UA and the Surry UA**

The CCDFs for the SG tube UA span the range of  $10^{-5}$  to more than  $10^{-3}$  mean, population-weighted, LCF risk per event. The CCDFs for the SG tube UA overlap the portion of the Surry UA CCDFs representing a single SGTR (probability of exceedance below 0.1), but also extend beyond them at the upper end of the range. This is because the source terms are larger when multiple SGTRs occur in a realization. The effect of up to five tube ruptures increases the consequences by less than an order of magnitude, as shown in Figure 6-125.

An extremely small risk of an early fatality results from multiple tube failures. The largest mean early fatality risk that was evaluated for any of the 388 realizations for multiple tube failure was about  $2 \times 10^{-6}$  and the mean over the set of realizations was about  $1 \times 10^{-8}$ . These are early fatality risks for the population living within 1.3 miles conditional on an STSBO that involves one or more induced SG tube ruptures; risks at longer distances are lower. The large majority (92%) of the realizations do not generate doses to an individual that exceeded the threshold for an early fatality, so the risk of an early fatality is zero for most of the realizations. Since frequency of an STSBO with induced SGTR is about  $2 \times 10^{-7}$  pry according to this study (one order-of-magnitude lower than the frequency of an STSBO), the risk of an early fatality is so low that it can be considered to be zero, even very close to the plant.

### 6.2.7 Summary of Consequence Results

Mean (over epistemic uncertainty and weather variability), individual, LCF risks assuming LNT dose response, conditional on occurrence of an accident, estimated in this uncertainty analysis of the Surry STSBO are very low, approximately  $2 \times 10^{-5}$  within 10 miles and lower at longer

distances. This is even lower than the risk evaluated in the original SOARCA study, which was  $9 \times 10^{-5}$ . The primary reason for this reduction in estimated risk is that refinements in the MELCOR model, primarily in representation of the containment, have led to smaller source terms. Most of the risks (99% within 10 miles and about 84% beyond 10 miles from the plant) are from long-term exposure following the emergency phase. Early fatality risks for this scenario are essentially zero.

Mean, individual, LCF risks are even smaller when health effects are truncated at small annual doses. Two alternate linear-with-threshold dose-response models were considered, one using the average annual dose to the population of the US (620 mrem/yr) and the other using the HPS Position Statement as a basis for truncation. The HPS position statement discourages evaluation of LCF risk below an annual dose of 5 rem, provided that the lifetime dose does not exceed 10 rem. The dose-response models are based on the assumption that the response is the same as LNT above these thresholds. Evaluation of risk using dose truncation models results in even lower LCF risks, about  $3 \times 10^{-6}$  and  $5 \times 10^{-7}$  within 10 miles of the site for the US background and HPS models, respectively (cf., Table 6-20 through Table 6-22). Mean, individual risks beyond 10 miles are zero for the large majority of the realizations using these dose-response models because the annual doses fall below the threshold values.

Regression analyses of the UA results were performed to determine the uncertain inputs that most affect the LCF risks. No regression analysis was performed for early fatality risks because only one realization displayed risks greater than zero. The regression analyses were performed for three sets of realizations: the full set, only those with SGTRs, and those without an SGTR. The regression analyses were also performed for each of the three dose-response models. This created nine sets of regression results.

When the full set of realizations was evaluated, the most important input variables identified were consistently the SG tube thickness and the safety valve area fraction assumed when a valve stuck open (representing the occurrence and timing of RCS depressurization) (cf., Table 6-18 through Table 6-20). These two parameters play a synergistic role in the occurrence of a SGTR and thus influence the size and timing of the source term. Other important uncertain inputs depend on the dose-response model. For the LNT model, additional parameters identified as important are time during the fuel cycle when the accident occurs, groundshine shielding factors, and a parameter controlling the rate of containment leakage. For the non-LNT models, the other important variables also include cancer fatality risk for thyroid cancer and the dispersion parameters (cf., Table 6-33 through Table 6-38).

When the set involving SGTR was evaluated, residual cancer fatality risk factor, aerosol deposition velocities, steam generator tube thickness, groundshine shielding factors, the inhalation dose coefficients for iodine-134, and a parameter controlling the containment leak rate are important when using the LNT dose-response model (cf., Table 6-27 through Table 6-29). For the non-LNT models, the dispersion parameters, a parameter controlling reactor coolant pump seal leakage, and the dynamic shape factor for aerosols in the MELCOR model were also important (cf., Table 6-39 through Table 6-44).

When the set excluding the occurrence of SGTR was evaluated, time during the fuel cycle when the accident occurs, groundshine shielding factors, containment leakage rate, and residual cancer fatality risk factor are important when using the LNT dose-response model (cf., Table 6-30 through Table 6-32). For the non-LNT models, the dispersion parameters are also important (cf., Table 6-45 through Table 6-50).

The sensitivity studies for the effects of the duration of the emergency and intermediate phases show that mean, individual, LCF risk is relatively insensitive to these parameters. The exception is that the LCF risk within 10 miles is increased somewhat when a 6-month intermediate phase is included in the analysis. The effect of including an intermediate phase could have gone either way and depends on the magnitude of the source term, primarily the amount of cesium release. The duration of the dose-projection period used in the emergency phase was also evaluated and found to have a minimal effect on mean, individual, LCF risk.

The consequences evaluated for the set of MELCOR source terms for single or multiple SG tube failure offer no surprises (Section 6.2.6). The cases with a single SG tube failure roughly overlap the portion of the STSBO UA curves in which a single SG tube fails. The cases with multiple SG tube ruptures exceed the Surry UA risks because the source terms are larger for multiple tube failures than for a single failure (cf., Figure 6-125). The risk of an early fatality for the population closest to the plant is essentially zero, even for multiple SG tube ruptures.

## 7. SUMMARY OF RESULTS AND CONCLUSIONS

Through the application of modern analysis tools and techniques, the SOARCA project [1] developed a body of knowledge regarding the realistic outcomes of severe reactor accidents with best estimate analyses of selected accident scenarios with specific boundary conditions for nuclear power plants at Peach Bottom and Surry. SOARCA efforts have continued with an integrated UA of the unmitigated LTSBO at Peach Bottom [2] and the UA presented herein of the Surry unmitigated STSBO. The Surry UA follows the approach developed for the Peach Bottom UA investigating the same figures of merit, which for MELCOR includes environmental release fractions of cesium and iodine, in-vessel hydrogen production, and release timing, and for MACCS includes individual LCF risk and early fatality risk at specified distances. These analyses were completed for specific accident scenarios at specific plants. Thus, the application of results must be tempered with the understanding of the reactor type, scenario for which results were produced, and site specific characteristics.

One of the original objectives of the Surry UA was to quantify the robustness of the Surry best estimate results for the unmitigated STSBO [3]. However, since the completion of the Surry SOARCA study [3], there have been many model enhancements and updates to all of the severe accident codes making a direct comparison less meaningful. This UA provides a comparison of the results of the Surry best estimate analysis [3] with the current, more advanced, severe accident modeling systems applied in an uncertain framework. Additional objectives included:

- Determining whether the Surry UA results corroborate the general conclusions and insights from the original SOARCA best estimate study.
- Developing insights into the overall sensitivity of SOARCA results to uncertainty in selected modeling inputs.
- Identifying the most influential input parameters contributing to accident progression and offsite consequences through application of an uncertainty analysis methodology.
- Informing the NRC's Site Level 3 PRA and post-Fukushima activities including Tier 3 items.

To accomplish the final objective above, the Level 3 PRA staff supported the Surry parameter development meetings and were presented with early Surry UA results. The project team interacted with Level 3 PRA staff on key issues of interest throughout the project.

This Surry UA modeled distributions for parameter values that historically were modeled with fixed values and applied multiple regression techniques to support an understanding of the results. The analysis produced substantial information that is described in detail in this document. A summary of important insights is provided below:

- SGTRs occurred in about 10 percent of the analyses, although this number may be slightly conservative considering the assumption that the most damaged tube is in the hottest region, and had release fractions one to two orders of magnitude larger than non-SGTR realizations.
- SGTRs always included both a thermal and a pressure element.

- In most of the Monte Carlo realizations, iodine and cesium environmental release fractions were higher early in the transient than the Surry SOARCA calculation [3], but all were significantly lower at 48 hours except that cesium was equal in a few realizations.
- The spread of release fractions was an order of magnitude lower for non-SGTR realizations.
- Lower release fractions were primarily the result of slower containment pressurization, caused by sampling of multiple parameters, including decay heat, nominal containment leakage, and changes to the containment failure model.
- Total in-vessel hydrogen production ranged from about 250 to 600 kg.
- The LCF risk was lower than the Surry SOARCA [3] result and is attributable to the lower source terms from the UA.
- The consequence analysis showed that the mean population-weighted LCF risk distribution is much narrower when only uncertain consequence parameters are considered than when both source-term and consequence parameters are considered in the analysis. It appears the results are more heavily influenced by uncertainties in source term than by uncertain consequence parameters, just as they were for the Peach Bottom uncertainty analysis [2]. This is true when a single dose-response model (LNT) is used, but uncertainties in risks created by uncertainties in dose-response model are large and most likely would have altered this conclusion if dose response had been included as part of the integrated uncertainty analysis.

The most influential input parameters contributing to accident progression and offsite consequences were identified with respect to the figures of merit.

- For early hydrogen production, primary system depressurization followed by time at cycle were most important. But the total magnitude of hydrogen was most influenced by the effective fuel melt temperature.
- For non-SGTR realizations (90% of all realizations), the most important parameters were time at cycle, design leakage, the containment failure curve, and the dynamic shape factor. For iodine, the amount that was gaseous was very important and determined by time at cycle and CHEMFORMI2.
- Primary SV open fraction and tube thickness were the main determinants regarding whether an SGTR occurred, and secondary SV open fraction had the highest importance in Cs and I release fractions for SGTR releases.
- For LCF risk, TUBTHICK and SVOAFRAC are the most influential parameters. These two parameters largely determine whether the accident progresses toward an SGTR. Thus, they have an important influence on magnitude and timing of the release and directly influence LCF risk.

In addition, like the Peach Bottom UA [2] did, the results of this Surry UA corroborate the conclusions from the SOARCA project [1]:

- Public health consequences from severe nuclear accident scenarios modeled are smaller than those projected in NUREG/CR-2239.
- The delay in releases calculated provides more time for emergency response actions (such as evacuating or sheltering).
- “Essentially zero” absolute early fatality risk is projected.

## **MELCOR**

The above insights were produced through implementation of a systematic project that began with an updated base case MELCOR calculation. The updated base case included model enhancements and updated parameters. Selected insights from the base calculation include:

- An over-cycling FTC of the lowest set-point SV on the pressurizer occurred.
- A hot leg nozzle rupture occurred.
- Energetic hydrogen deflagrations occurred in containment.
- Containment design pressure and the pressure associated with liner yield were both exceeded.
- Releases to the environment of iodine and cesium were small, 0.073 percent and 0.029 percent of the inventory at scram, respectively.

After the updated base case was complete, a comparison of the results from the UA base case calculation and the direct conversion of the Surry SOARCA SBO model was performed (See Appendix A). Both calculations used the identical code version.

The uncertainty runs were completed using Monte Carlo simulation and regression analyses conducted on the results. The regression results are based on metrics at the end of the 48 hour analysis time, and it should be recognized that results could be different if the metrics were evaluated at an earlier or later time. Results from each regression technique for the individual contribution of a parameter and the conjoint influence of a parameter on the result metrics are provided. Overall influence of a parameter is reported as an average of the influence suggested by the four regression techniques. A Monte Carlo simulation with 1200 MELCOR runs was initiated, of which 1003 were successful. In the 1003 successful calculations:

- An SGTR occurred in 104 realizations reflecting a small (10%) minority of the overall results;
- A hot leg nozzle rupture occurred in 930 realizations;
- In every realization that an SGTR occurred, a hot leg nozzle rupture also occurred;

- A failure of one or more RCS secondary side safety valves (SG safety valves) to close occurred in 954 realizations;
- An SV on the RCS primary side (on the pressurizer) failed to close on 686 realizations;
- Individual safety valves on the RCS primary side failed to open in 10 realizations, but as a system the 3 parallel valves never failed to open;
- The steel containment liner yielded and tore in 742 realizations;
- Containment concrete rebar yielded (and the concrete fractured) in 72 realizations; and
- In 162 realizations, the noble gas release to the environment had not accrued to 1 percent of the total inventory by 48 hours.

There were 104 SGTRs observed in the results, reflecting a tube rupture in about 10 percent of the realizations. Even though only 10 percent of realizations had SGTRs, with the exception of in-vessel hydrogen production, these SGTR realizations dominated the regression results. Therefore, regression analyses were performed on the full set of realizations, the set of realizations that experienced an SGTR, and the set of realizations that did not experience an SGTR. For the full set of realizations and the non-SGTR set, regression analyses were performed for beginning of cycle (BOC), middle of cycle (MOC), and end of cycle (EOC) to understand the extent to which time at cycle (i.e., burnup) influenced non-SGTR realizations and whether any parameters would have raised importance with time at cycle kept constant. This was accomplished by including an uncertain parameter named CYCLE, which identifies to the point during the fuel cycle (BOC, MOC, and EOC) at which the accident occurs.

This sampled CYCLE parameter directly affects the MELCOR source term calculation through decay heat, and it directly affects the MACCS consequence analysis through fission product inventory. Of all the sampled parameters, CYCLE is the only one that has such a dual status. Because fission product inventories in the fuel increase with burnup, this parameter can have a significant influence on risk. The inventories of shorter lived isotopes increase with burnup only until secular equilibrium is established; however, the inventories of longer lived isotopes, like Cs-137, can nearly double from BOC to EOC. Because the longer lived isotopes have a significant effect on LCF risk, especially in the long-term phase, this parameter is significant to the predicted results. The correlation between CYCLE and predicted risk is positive, (i.e., greater burnup relates to increased risk).

Almost all of the MELCOR realizations showed the iodine and cesium environmental release fractions were significantly lower than their respective Surry SOARCA calculation [3], (either STSBO, or induced SGTR variation of STSBO), except for a few non-SGTR realizations where cesium was equal or greater. The lower release fractions were driven primarily by slower containment pressurization, caused by a number of factors including generally lower decay heat, and a modification to the containment failure model that implemented a more realistic yield-before-rupture model.

Results showed a large split between SGTR and non-SGTR runs, where SGTR runs had one to two orders of magnitude higher release fractions. The most influential parameters contributing to cesium and iodine environmental release fractions for non-SGTR (the majority of releases) are time at cycle (e.g., burnup), nominal leakage, the containment failure curve, and dynamic shape

factor. The first three influence containment pressurization rates and determine the open area from the containment to the environment, while dynamic shape factor influences agglomeration and deposition rates for aerosols before release. The time at cycle parameter is specific to Surry and very well understood, while nominal leakage and the dynamic shape factor are based on technical specifications and well understood experimental results, respectively. There is slightly lower confidence in the containment failure curve (CFC) model, based on difficulties scaling from the 1/6<sup>th</sup> scale tests from which the model was created, but the yield-before-rupture behavior was confirmed as more realistic by structural experts. Important for iodine release fractions but not cesium was the fraction of gaseous iodine, because gaseous iodine does not deposit on structures but remains airborne. Thus, gaseous iodine is released in much higher percentages than aerosolized CsI. The two parameters that determine the amount of gaseous iodine, time at cycle and ChemformI2, are both identified as significant main contributors by the regression analyses. For BOC analyses, design leakage becomes the most important parameter contributing to iodine and cesium release because containment liner yield is never reached and leakage is the only release path to the environment.

In-vessel hydrogen production through 48 hours was similar in magnitude to the Surry SOARCA calculation [3], in that the mean and median of the distributions were close to the Surry SOARCA best estimate, and the 5<sup>th</sup> and 95<sup>th</sup> percentiles were within a factor of two of the central and best estimates. Regression results for hydrogen production uncertainty were essentially the same with and without an SGTR, because this is an in-vessel effect. The most important parameters early in hydrogen production were those related to primary system depressurization, which directly influences steam flow rates and oxidation, followed by time at cycle. The magnitude of the total hydrogen generation within 48 hours was driven by effective fuel melt temperature and the time at cycle, both of which determine the amount of time the fuel remains in place before relocation, which suppresses the oxidation process. There were no significant differences in regression results for the time at cycle independent analyses.

For release timing, the metric evaluated was release of 1 percent of noble gas to the environment. It was observed that 18 percent of non-SGTR realizations do not release 1 percent of noble gases by 48 hours. Investigation of the release timing identified a large timing difference between SGTR and non-SGTR realizations, with non-SGTR realizations meeting the environmental release timing metric about 20 to 40 hours later, if they meet the criteria at all. In the original SOARCA analysis the timing difference was about 25 hours, at the lower end of this range. Since almost all noble gases enter containment quickly after core damage, this may indicate that the flow area to the environment for SGTRs is larger than design leakage. This was tested through one-off calculations and results show that flow rates to environment through the secondary side (combination of MSIV leakage and a stuck open secondary SV) are approximately three orders of magnitude greater than nominal leakage, regardless of any uncertainty sampling. However, since only 10 percent of runs have SGTRs, and because the majority of realizations do not reach rebar failure, design leakage is the highest contributor to release timing uncertainty in regression results for all realizations and for non-SGTR realizations.

The environmental release fractions from SGTRs were 1 to 2 orders of magnitude higher than the non-SGTR realizations; therefore, even though they only consisted of about 10 percent of realizations, they were analyzed separately. The two parameters that show the highest importance in determining whether an SGTR occurs are TUBTHICK, which represents the initial tube thickness of the most damaged steam generator tube in the hottest region, and SVOAFRAC, which represents the fraction of the full open area of a primary or secondary safety relief valve at the time it fails. Both of these parameters have physical bounds. The TUBTHICK

parameter directly affects the initial damage state (and effective stress multiplier for creep) of one of the steam generator tubes. The SVOAFRAC parameter influences the depressurization of the RCS after SV failure, and thus controls the pressure differential across the damaged steam generator tube. Testing of SGTR realizations showed that there needed to be a pressure differential of 1000 psi or more during core damage to induce the SGTR. Together, these parameters largely control the likelihood of an SGTR.

The magnitude of releases for an SGTR was primarily driven by the time between the SGTR and hot leg creep rupture, because before hot leg rupture, the SGTR is the primary transport path for radionuclides released from the fuel. The timing is affected by multiple sampled parameters and thus does not appear directly in regression results. The average time difference in these realizations was 28 minutes. A secondary contributor was the secondary SV open fraction upon failure, because this can increase leakage area to the environment.

Containment pressure was generally observed to increase from 48 to 72 hours, unless the rebar yield point was reached. In the cases where rebar yield was reached, the pressure levels off (to a plateau) and then gradually begins to decrease as the leakage more than compensates for steam generation and heating of the atmosphere. There are marked increases in cesium and iodine environmental release at the point of liner yield, with some increases of an order of magnitude from 48 to 72 hours. Such increases did not occur with rebar yield only. There appear to be no realizations that could ablate through all available concrete by 72 hours, nor are there any BOC realizations that will reach liner yield by 72 hours.

## **MACCS**

The MACCS uncertainty analysis was performed with analysis input defined by (i) the previously indicated 1003 successful MELCOR realizations, and (ii) an additional set of 1003 samples from the 622 uncertain MACCS input parameters summarized in Table 4-7. The results of the consequence analyses are presented in terms of risk to the public for each of the probabilistic source terms analyzed. The reported risk metrics (figures of merit) are individual LCF and early-fatality risks to residents within circular and annular regions centered on the reactor site. The risk values are defined by the predicted number of fatalities divided by the population for each selected dose-response model. The risk values incorporated the distribution of the population within the circular or annular region, and the interplay between the population distribution and the wind rose probabilities. All consequence results are presented as conditional risks, which are the risks conditional on the accident occurring. The emergency phase used in this analysis is the first seven days following the beginning of release to the environment. The long-term phase immediately follows the emergency phase and lasts for 50 years.

Review of the MACCS figures of merit showed the early fatality risks are negligible (essentially zero risk) and the LCF risks are small compared to the Surry SOARCA analysis results [3]. Mean, individual, LCF risks obtained with LNT dose response, conditional on occurrence of the Surry STSBO accident, estimated in this uncertainty analysis are very low, approximately  $2 \times 10^{-5}$  per reactor year within 10 miles and lower at longer distances. This is lower than the risk estimated in the Surry SOARCA study [3], which is  $9 \times 10^{-5}$ . The primary reason for this reduction in estimated risk is that refinements in the MELCOR model, primarily in representation of the containment, have led to smaller source terms. Most of the risks (99% within 10 miles and about 84% beyond 10 miles from the plant) are from long-term exposure following the emergency phase. Early fatality risks in this analysis are essentially zero.

When the full set of realizations was evaluated, the most important input variables identified were consistently the SG tube thickness and the safety valve area fraction for a valve stuck open. These two parameters are synergistic in playing a significant role in the occurrence of a SGTR and thus control the size and timing of the source term. Other important uncertain inputs depend on the dose-response model. For the LNT model, additional parameters identified as important are time during the fuel cycle when the accident occurs, groundshine shielding factors, and a parameter controlling the rate of containment leakage. For the non-LNT models, where the calculated risks are much lower and the emergency phase doses become a relatively larger proportion of the total doses, other important variables include cancer fatality risk for thyroid cancer and the dispersion parameters.

Evaluation of the realizations involving SGTR showed residual cancer fatality risk factor, aerosol deposition velocities, steam generator tube thickness, groundshine shielding factors, the inhalation dose coefficients for iodine-134, and a parameter controlling the containment leak rate are important when using the LNT dose-response model. For the non-LNT models, the dispersion parameters, a parameter controlling reactor coolant pump seal leakage, and the dynamic shape factor for aerosols in the MELCOR model are also important. Evaluation of the realizations that did not involve SGTR showed time during the fuel cycle when the accident occurs, groundshine shielding factors, containment leakage rate, and residual cancer fatality risk factor are important when using the LNT dose-response model. For the non-LNT models, the dispersion parameters are also important.

In the MACCS analysis of the LNT dose response for all realizations, the top two parameters are TUBTHICK, which represents the initial tube thickness of the most damaged steam generator tube, and SVOAFRAC, which represents the fraction of the full open area of an SV at the time it fails. These parameters largely determine whether the accident progression is driven toward an SGTR. Both parameters have large values for individual and conjoint contributions. The TUBTHICK parameter directly affects the initial damage state of one of the steam generator tubes; the SVOAFRAC parameter controls the depressurization of the RCS after safety valve failure, and thus controls the pressure differential across the damaged steam generator tube. Together, these parameters largely control the likelihood of an SGTR. Thus, they have a critical influence on both the magnitude and timing of the release and through it the resulting LCF risk.

### **Single realizations**

Additional insights related to accident progression were obtained through investigation of selected single realizations to identify phenomena driving the Cs and I releases to the environment and in-vessel hydrogen production figures of merit. Key phenomena identified in the MELCOR single realization analysis include:

- Containment building rebar yielding and resulting concrete fracture,
- Timing of PRT dryout,
- The number of successful cycles experienced by the system of 3 parallel safety valves serving the primary-side of the RCS, and
- Chemisorption of Cs from CsOH into the stainless steel of the RPV internals.

### **Separate Sensitivity Analyses**

Lastly, targeted areas of interest were examined through sensitivity analyses. The following parameters were investigated in MELCOR sensitivity analyses:

- Containment concrete aggregate (limestone and basaltic) – Results of the sensitivity show the environmental release fraction for cesium and iodine from limestone concrete is greater than from basaltic concrete at the end of the 48 hour simulation. This is attributed to the increased containment pressurization in the limestone concrete analysis, which reaches liner yield (i.e., functional failure of containment) at approximately 36.5 hours as compared to basaltic concrete analysis which reaches liner yield at approximately 41 hours.
- Containment rebar - This sensitivity considered two extremes for rebar including zero percent and 30% (approximately double the 17% value used in the base case) rebar by mass within the concrete. Although zero percent would never be expected, analyzing zero percent supports quantification of the effect of the rebar. Results of the sensitivity on mass of containment rebar show the environmental release fraction from the no rebar and 30 percent rebar cases for cesium are 16 percent and 11 percent less, respectively, when compared to the base case at the end of the 48 hour simulation. Additionally the environmental release fraction from the no rebar and 30 percent rebar cases for iodine were 6 percent and 15 percent less, respectively, when compared to the base case at the end of the 48 hour simulation. The slightly higher environmental release fractions for the base case are attributed to revaporization of previously airborne material within containment near the end (40 to 44 hours) of the simulation. However, since the releases from these analyses are very low for both cesium and iodine (i.e., <0.1%), these releases can be essentially considered the same.
- Number of steam generator tubes ruptured -A distribution was created to sample failure of 1 to 5 tubes to determine the effect on environmental release fractions for cesium and iodine from having more than one SG tube fail. Sampling was performed on number of tubes, primary and secondary SV open fraction, and SGTR location. Releases for 1 tube were slightly higher than the base uncertainty SGTR realizations. There were step increases in release fractions for the failure of 2 and 3 tubes, but no significant difference from 3 to 5 tubes, indicating that when 3 or more tubes fail, flow to environment is limited by MSIV leakage and the stuck open secondary SV, and not by the flow through the SG tubes. Another key result was that releases from 1 tube increase gradually while 3 to 5 tubes have more of a quick puff release, potentially due to revaporization. A large factor in the total release fractions is the time of hot leg creep failure relative to the SGTR, which is primarily due to depressurization rate, based on the number of tubes failing and exacerbated by the primary pressurizer SV open fraction. Out of 97 Monte Carlo realizations in this joint sensitivity, one had sampled five tubes failing and had no hot leg creep leading to the highest release fractions.

MACCS sensitivity analyses were performed on the duration of the early phase and intermediate phase, and the PAG duration in the early phase. The sensitivity studies evaluated emergency phase durations of 15 and 30 days, intermediate phase duration of 6 months, and a 4-day dose projection period for the emergency phase. The results were all essentially the same with one exception, the risks for the 0- to 10-mile distance interval was noticeably larger for the case when the intermediate phase is 6 months than when there was no intermediate phase. The increase in risk for the 0- to 10-mile interval indicates that less decontamination occurs when the intermediate phase is included and that more individuals receive a larger dose when they return home than receive a smaller dose. This can occur when the 6 months of

decay and weathering provided by the intermediate phase brings the dose levels below the habitability threshold without the need to decontaminate. However, these dose levels can be higher than they would have been if decontamination were performed because the MACCS decontamination modeling reduces dose levels by pre-defined fixed factors of 3, or 15 if a reduction factor of 3 is insufficient to restore habitability.

The habitability criteria applied in these sensitivity analyses is considered to be an important uncertain parameter, but was not included with this Surry UA because a detailed sensitivity analysis was performed with the Peach Bottom UA [2]. The Peach Bottom analysis showed, as would be expected, that when the dose truncation models were used, the LCF risks within the EPZ were orders of magnitude lower when the habitability criteria was below the dose truncation level. Beyond the EPZ, the habitability criteria showed a smaller effect on the overall LCF risk when a dose truncation model was applied.



## 8. REFERENCES

- [1] NUREG/CR-1935, "State-of-the-Art Reactor Consequence Analyses (SOARCA) Report," ML12332A057, U.S. Nuclear Regulatory Commission, Washington, DC, November 2012.
- [2] NUREG-7155, "State-of-the-Art Reactor Consequence Analyses Project, Uncertainty Analysis of the Unmitigated Long-Term Station Blackout of the Peach Bottom Atomic Power Station," Draft Report. ML13189A145, U.S. Nuclear Regulatory Commission, Washington, DC, 2013.
- [3] NUREG/CR-7110 Volume 2, Rev. 1, "State-of-the-Art Reactor Consequence Analysis Project Volume 2: Surry Integrated Analysis," U.S. Nuclear Regulatory Commission, Washington, DC, August 2013.
- [4] SECY-12-0092, "State-of-the-Art Reactor Consequence Analyses – Recommendation for Limited Additional Analysis," U.S. Nuclear Regulatory Commission, Washington, DC, July 5, 2012.
- [5] NUREG/CR-2239, "Technical Guidance for Siting Criteria Development," Nuclear Regulatory Commission: Washington DC. 1982.
- [6] NUREG/CR-7009, "MACCS2 Best Practices as Applied in the State-of-the-Art Reactor Consequence Analyses (SOARCA) Project," U.S. Nuclear Regulatory Commission, Washington, DC, 2014.
- [7] Lind, T., and A. Dehbi, "The Final Summary Report of the ARTIST II Project Severe Accident Tests," TM-42-11-25; ARTIST-95-11, Paul Scherrer Institute, 2012.
- [8] NUREG/CR-6119, "MELCOR Computer Code Manuals, Vol. 2: References Manuals, Version 1.8.5." Revision 3. U.S. Nuclear Regulatory Commission, Washington, DC, 2005.
- [9] NUREG/CR-6119, "MELCOR Computer Code Manuals, Vol. 1: Primer and User's Guide, Version 1.8.5." Revision 2. U.S. Nuclear Regulatory Commission, Washington, DC, 2000.
- [10] NUREG-1150, "Severe Accident Risks: An Assessment for Five U.S. Nuclear Power Plants," U.S. Nuclear Regulatory Commission, Washington, DC, 1990.
- [11] Bixler, N.E., et al., "Software Regression Quality Assurance for MACCS2 Version 2.5.0.0 through Version 2.5.0.9," SAND2012-6333, Sandia National Laboratories, Albuquerque, NM. July 2012.
- [12] Mitchell, Jerry T., et al., "Evacuation behavior in response to the Graniteville, South Carolina, Chlorine Spill," Quick Response Research Report 178. Boulder, CO: Natural Hazards Center, University of Colorado. 2005.
- [13] Mitchell, J.T., S.L. Cutter, and A.S. Edmonds. "Improving shadow evacuation management: Case study of the Graniteville, South Carolina, chlorine spill," Journal of Emergency Management. 5(1): 28-34. 2007.

- [14] Regulatory Guide 1.174, "An Approach for Using Probabilistic Risk Assessment in Risk-Informed Decisions on Plant-Specific Changes to the Licensing Basis." U.S. Nuclear Regulatory Commission, Washington, DC, 1998.
- [15] NUREG/CR-6953 Volume 2, "Review of NUREG-0654, Supplement 3, 'Criteria for Protective Action Recommendations for Severe Accidents' Focus Groups and Telephone Survey," U.S. Nuclear Regulatory Commission, Washington, DC, October 2008.
- [16] Kaplan, S. and B.J. Garrick, "On the Quantitative Definition of Risk," *Risk Analysis*, 1(1): p. 11-27, 1981.
- [17] Sobol', I. "Sensitivity Estimates for Nonlinear Mathematical Models," *Mathematical Modeling and Computational Experiment*, 1, 407-414. 1993.
- [18] Helton, J.C., et al., "Survey of Sampling-based Methods for Uncertainty and Sensitivity Analysis," *Reliability Engineering & System Safety*, 91(10-11): p. 1175-1209, 2006.
- [19] Storlie, C.B. and J.C. Helton, "Multiple predictor smoothing methods for sensitivity analysis: Description of techniques," *Reliability Engineering & System Safety*, 93(1): p. 28-54, 2008.
- [20] Helton, J.C. "Uncertainty and Sensitivity Analysis in the Presence of Stochastic and Subjective Uncertainty," *Journal of Statistical Computation and Simulation* 1997; Volume 57: pages 3-76.
- [21] Helton, J.C. Johnson, J.D, Oberkampf W.L. Sallaberry C.J. "Representation of Analysis Results Involving Aleatory and Epistemic Uncertainty," *International Journal of General Systems*; 39(6): 605-646, 2010.
- [22] Helton JC, Sallaberry CJ. "Uncertainty and Sensitivity Analysis: From Regulatory Requirements to Conceptual Structure and Computational Implementation." *IFIP Advances in Information and Communication Technology*; 377 AICT: 60-76, 2012.
- [23] Helton JC, Johnson JD, Sallaberry CJ. "Quantification of Margins and Uncertainties: Example Analyses from Reactor Safety and Radioactive Waste Disposal Involving the Separation of Aleatory and Epistemic Uncertainty." *Reliability Engineering and System Safety*; 96(9): 1014-1033. 2011.
- [24] Storlie, C.B., et al., "Implementation and evaluation of nonparametric regression procedures for sensitivity analysis of computationally demanding models," *Reliability Engineering & System Safety*, 94(11): p. 1735-1763, 2009.
- [25] Metropolis, N. and Ulam S., "The Monte Carlo Method," *Journal of the American Statistical Association*; 44(247):335-341, 1949.
- [26] McKay, M.D., Beckman, R.J., and Conover, W.J., "A Comparison of Three Methods for Selecting Values of Input Variables in the Analysis of Output from a Computer Code," *Technometrics* 21(2): 239-245, 1979.

- [27] Sallaberry CJ, Helton JC, Hora SC. "Extension of Latin Hypercube Samples with Correlated Variables." *Reliability Engineering and System Safety*; 93: 1047-1059. 2008.
- [28] Helton J.C. and Davis F.J., "Latin hypercube sampling and the propagation of uncertainty in analyses of complex systems" *Reliability Engineering and System Safety* 81 (1) 23-69, 2003.
- [29] Efron B. and Tibshirani R.J., "An Introduction to the Bootstrap" *Monographs on Statistics and Applied Probability* 57 - Chapman & Hall/CRC – ISBN 0-412-04231-2, 1993.
- [30] NUREG/CR-7037, "Industry Performance of Relief Valves at U.S. Commercial Nuclear Power Plants through 2007," U.S. Nuclear Regulatory Commission, Washington, DC, March 2011.
- [31] NUREG-1570, "Risk Assessment of Severe Accident-Induced Steam Generator Tube Rupture," U.S. Nuclear Regulatory Commission, Washington, DC, March 1998.
- [32] NUREG/CR-6995, "SCDAP/RELAP5 Thermal-Hydraulic Evaluations of the Potential for Containment Bypass During Extended Station Blackout Severe Accident Sequences in a Westinghouse Four-Loop PWR," U.S. Nuclear Regulatory Commission, Washington, DC, March 2010.
- [33] Stewart, W.A., Pieczynski, A.T., and Srinivar, V., "Natural Circulation Experiments for PWR Degraded Core Accidents," EPRI Report NP 6324 D, 1989.
- [34] Stewart, W.A., Pieczynski, A.T., and Srinivar, V., "Natural Circulation Experiments for PWR High Pressure Accidents," EPRI Report TR 102815, 1993.
- [35] Eide, S., T. Wierman, et al., "Industry-Average Performance for Components and Initiating Events at U.S. Nuclear Power Plants," INL/EXT-01-01623, Idaho National Laboratory 2007.
- [36] Fuller, E. L., G. Hannaman, and M. Kenton. "Steam Generator Management Project Risks from Severe Accidents Involving Steam Generator Tube Leaks or Ruptures," Volume 2. EPRI Report TR-106194-V2. October 1997.
- [37] M. Zhu and A. Lu, "The Counter-intuitive Non-informative Prior for the Bernoulli Family", *Journal of Statistics Education*, 12:2, 2004.
- [38] NUREG/CR-6928, "Industry-Average Performance for Components and Initiating Events at U.S. Commercial Nuclear Power Plants," U.S. Nuclear Regulatory Commission, Washington, DC, 2007.
- [39] Ang AH-S, Tang WH. "Probability Concepts in Engineering," 2<sup>nd</sup> edition. Hoboken, NJ: Wiley; 2007.
- [40] NUREG/CR-6823, "Handbook of Parameter Estimation for Risk Assessment," U.S. Nuclear Regulatory Commission, Washington, DC, 2003.
- [41] NUREG/CR-4294, "Leak Rate Analysis of the Westinghouse Reactor Coolant Pump," U.S. Nuclear Regulatory Commission, Washington, DC, July 1985.

- [42] Westinghouse Electric Company, LLC. "WOG 2000 Reactor Coolant Pump Seal Leakage Model for Westinghouse PWRs." Revision 1. Pittsburgh, PA. May 2002.
- [43] NUREG-1953, "Confirmatory Thermal-Hydraulic Analysis to Support Specific Success Criteria in the Standardized Plant Analysis Risk Models – Surry and Peach Bottom," U.S. Nuclear Regulatory Commission, Washington, DC, September 2011.
- [44] NUREG-1781, "CFD Analysis of 1/7th Scale Steam Generator Inlet Plenum Mixing During a PWR Severe Accident," U.S. Nuclear Regulatory Commission, Washington, DC, October 2003.
- [45] NUREG-1788, "CFD Analysis of Full-Scale Steam Generator Inlet Plenum Mixing During a PWR Severe Accident," U.S. Nuclear Regulatory Commission, Washington, DC, May 2004.
- [46] NUREG-1922, "Computational Fluid Dynamics Analysis of Natural Circulation Flows in a Pressurized-Water Reactor Loop under Severe Accident Conditions," U.S. Nuclear Regulatory Commission, Washington, DC, March 2010.
- [47] NUREG/CR-6365, "Steam Generator Tube Failures," U.S. Nuclear Regulatory Commission, Washington, DC, 1996.
- [48] NUREG/CR-6575, "Failure Behavior of Internally Pressurized Flawed and Unflawed Steam Generator Tubing at High Temperature – Experiments and Comparison with Model Predictions," U.S. Nuclear Regulatory Commission, Washington, DC, 1997.
- [49] NUREG-1740, "Voltage-Based Alternative Repair Criteria," U.S. Nuclear Regulatory Commission, Washington, DC, 2001.
- [50] N. Girault, F. Payot, "Insights into iodine behavior and speciation in the Phebus Primary circuit." Institut de Radioprotection et de Surete Nucleaire, PSN-RES/SAG, Cadarache Center. St. Paul lez Durance, France. Annals of Nuclear Energy 61 143-156. 2013
- [51] R.O. Gauntt, N. Bixler, and K.C. Wagner, "An Uncertainty Analysis of the Hydrogen Source Term for a Station Blackout Accident in Sequoyah Using MELCOR 1.8.5 (Draft For Review)," Sandia National Laboratories, Albuquerque, NM, 2003.
- [52] Y. Pontillon, et al., "Lessons learnt from VERCORS tests. Study of the active role played by UO<sub>2</sub>-ZrO<sub>2</sub>-FP interactions on irradiated fuel collapse temperature," Journal of Nuclear Materials 344, pp. 265–273 (2005).
- [53] P. Hofmann et al., "ZrO<sub>2</sub> Dissolution by Molten Zircaloy and Cladding Oxide Shell Failure. New Experimental Results and Modeling," Wissenschaftliche Berechte, INV-CIT(98)-P026, December 1999.
- [54] NUREG/CR 7008, "MELCOR Best Practices as Applied in the State-of-the-Art Reactor Consequence Analyses (SOARCA) Project," U.S. Nuclear Regulatory Commission, Washington, DC, August 2014.
- [55] R. K. Kumar, "Flammability of Limits of Hydrogen-Oxygen-Diluent Mixtures," Journal of Fire Sciences, Vol. 3, July/August 1985.

- [56] ANSI/ANS-5.1-2005, "American National Standard Decay Heat Power in Light Water Reactors." American Nuclear Society, La Grange Park, Illinois. April 1, 2005.
- [57] NUREG-1493, "Performance-Based Containment Leak-Test Program," Draft Report for Comment. U.S. Nuclear Regulatory Commission, Washington, DC, January 1995.
- [58] NUREG/CR-5121, "Experimental Results from Pressure Testing a 1:6 Scale Nuclear Power Plant Containment," U.S. Nuclear Regulatory Commission, Washington, DC, January 1992.
- [59] Duhanyan N, Roustan Y. Below-Cloud Scavenging by Rain of Atmospheric Gases and Particulates," *Atmospheric Environment* 2011; 45(39): 7201-7217. 2011.
- [60] Wang X, Zhang L, Moran MD. Uncertainty Assessment of Current Size-Resolved Parameterizations for Below-Cloud Particle Scavenging by Rain," *Atmospheric Chemistry and Physics* 2010; 10(12): 5685-5705. 2010.
- [61] Sportisse B. A Review of Parameterizations for Modelling Dry Deposition and Scavenging of Radionuclides," *Atmospheric Environment* 2007; 41(13): 2683-2698. 2007.
- [62] Andronache C. "Estimated Variability of Below-Cloud Aerosol Removal by Rainfall for Observed Aerosol Size Distributions," *Atmospheric Chemistry and Physics* 2003; 3(1): 131-143. 2003.
- [63] Baklanov A, Sorensen JH. "Parameterisation of Radionuclide Deposition in Atmospheric Long-Range Transport Modelling," *Physics and Chemistry of the Earth, Part B: Hydrology, Oceans and Atmosphere* 2001; 26(10): 787-799. 2001.
- [64] NUREG/CR-6244, "Summary of Objectives, Approach, Application, and Results for the Dispersion and Deposition Uncertainty Assessment," U.S. Nuclear Regulatory Commission, Washington, DC, 1994.
- [65] Leadbetter SJ, Hort MC, Jones AR, Webster HN, Draxler RR. "Sensitivity of the Modelled Deposition of Caesium-137 from the Fukushima Dai-ichi Nuclear Power Plant to the Wet Deposition Parameterisation in NAME," *Journal of Environmental Radioactivity* 2014.
- [66] Saito K, Shimbori T, Draxler R. JMA's Regional Atmospheric Transport Model Calculations for the WMO Technical Task Team on Meteorological Analyses for Fukushima Daiichi Nuclear Power Plant Accident. *Journal of Environmental Radioactivity* 2014; In press.
- [67] Brenk HD, Vogt KJ. "The Calculation of Wet Deposition from Radioactive Plumes," *Nuclear Safety* 1981; 22(3): 362-371. 1981.
- [68] McMahon TA, Denison PJ. "Empirical Atmospheric Deposition Parameters: A Survey," *Atmospheric Environment - Part A General Topics* 1979; 13(5): 571-585. 1979.

- [69] NUREG/CR-7161, Rev. 1, "Synthesis of Distributions Representing Important Non-Site-Specific Parameters in Off-Site Consequence Analysis," U.S. Nuclear Regulatory Commission, Washington, DC, 2013.
- [70] NUREG/CR-4551, Vol. 2, Rev. 1, Part 7, "Evaluation of Severe Accident Risks: Quantification of Major Input Parameters," U.S. Nuclear Regulatory Commission, Washington, DC, 1990.
- [71] Gregory, J.J., et al., "Task 5 Letter Report: MACCS2 Uncertainty Analysis of EARLY Exposure Results," Sandia National Laboratories, Albuquerque, NM, September 2000.
- [72] Eckerman, K., "Radiation Dose and Health Risk Estimation: Technical Basis for the State-of-the-Art Reactor Consequence Analysis (SOARCA) Project," Oak Ridge National Laboratory, Oak Ridge, TN, 2011.
- [73] NUREG/CR-6526, "Probabilistic Accident Consequence Uncertainty Analysis, Uncertainty Assessment for Deposited Material and External Doses," U.S. Nuclear Regulatory Commission, Washington, DC, December 1997.
- [74] NUREG/CR-6953, Vol. 1, "Review of NUREG-0654, Supplement 3, 'Criteria for Protective Action Recommendations for Severe Accidents'," U.S. Nuclear Regulatory Commission, Washington, DC, December 2007.
- [75] D.J. Pawel, Leggett, R.W., Eckerman, K.F., and Nelson C.B., "Uncertainties in Cancer Risk Coefficients for Environmental Exposure to Radionuclides," ORNL/TM-2006/583, Oak Ridge National Laboratory, Oak Ridge, TN, 2007.
- [76] NUREG/CR-6613, "Code Manual for MACCS2: Volume 1, User's Guide," U.S. Nuclear Regulatory Commission, Washington, DC, 1997.
- [77] NUREG/CR-6853, "Comparison of Average Transport and Dispersion Among a Gaussian, a Two-Dimensional, and a Three-Dimensional Model," U.S. Nuclear Regulatory Commission, Washington, DC, October 2004.
- [78] NUREG-75/014, (WASH-1400) "Reactor Safety Study: An Assessment of Accident Risks in U.S. Commercial Nuclear Power Plants. Appendix VI," U.S. Nuclear Regulatory Commission, Washington, DC, 1975.
- [79] NUREG/CR-7003, "Background and Derivation of ANS-5.4 Standard Fission Product Release Model," U.S. Nuclear Regulatory Commission, Washington, DC, January, 2010.
- [80] International Atomic Energy Agency (IAEA). "Actions to Protect the Public in an Emergency due to Severe Conditions at a Light Water Reactor." Emergency Preparedness and Response. Vienna, Austria. May, 2013.
- [81] NUREG/CR-6864, "Identification and Analysis of Factors Affecting Emergency Evacuations," U.S. Nuclear Regulatory Commission, Washington, DC, January 2005.
- [82] Surry Power Station Development of Evacuation Time Estimates. Rev. 1. (ML13037A63) KLD, 2012.

- [83] NUREG/CR-6525, Rev. 1, "SECPOP2000: Sector Population, Land Fraction, and Economic Estimation Program," U.S. Nuclear Regulatory Commission, Washington, DC, 2003.
- [84] Wolshon, Brian, J. Jones, and F. Walton. "The Evacuation Tail and Its Effect on Evacuation Decision Making," *Journal of Emergency Management*. January/February 2010, Volume 8, Number 1. 201.
- [85] Environmental Protection Agency (EPA). "PAG Manual Protective Action Guides and Planning Guidance for Radiological Incidents." Draft for Interim Use and Public Comment. Washington, DC, March 2013.
- [86] NUREG/CR-7002, "Criteria for Development of Evacuation Time Estimate Studies." Washington, DC.: NRC. November 2011.
- [87] NUREG/CR-6863, "Development of Evacuation Time Estimate Studies for Nuclear Power Plants," U.S. Nuclear Regulatory Commission, Washington, DC, January 2005.
- [88] NUREG/CR-6981, "Assessment of Emergency Response Planning and Implementation for Large Scale Evacuations," U.S. Nuclear Regulatory Commission, Washington, DC, October 2008.
- [89] NUREG/CR-7032, "Developing an Emergency Risk Communication (ERC)/Joint Information Center (JIC) Plan for a Radiological Emergency," U.S. Nuclear Regulatory Commission, Washington, DC, February 2008.
- [90] NUREG/CR-7110 Volume 1, Rev. 1, "State-of-the-Art Reactor Consequence Analysis Project Volume 1: Peach Bottom Integrated Analysis," U.S. Nuclear Regulatory Commission, Washington, DC, March 2013.
- [91] NUREG/CR-7160, "Emergency Preparedness Significance Quantification Process: Proof of Concept," U.S. Nuclear Regulatory Commission, Washington, DC, 2012.
- [92] Regulatory Guide 1.23, Rev.1, "Meteorological Monitoring Programs for Nuclear Power Plants," U.S. Nuclear Regulatory Commission, Washington, DC, March 2007.
- [93] Cardoni, J.N., "Radionuclide Inventory and Decay Heat Quantification Methodology for Severe Accident Simulations," SAND2014-17667, Sandia National Laboratories, Albuquerque, NM 2014
- [94] Oak Ridge National Laboratory, "Scale: A Comprehensive Modeling and Simulation Suite for Nuclear Safety Analysis and Design," ORNL/TM-2005/39, Version 6.1, June 2011.
- [95] Gauntt, R.; D. Kalinich, J. Cardoni, J. Phillips, et al. "Fukushima Daiichi Accident Study Status as of April 2012," SAND2012-6173. July 2012.
- [96] Cardoni, J., R. Gauntt, D. Kalinich, J. Phillips. "MELCOR Simulations of the Severe Accident at the Fukushima 1F3 Reactor," 2012 ANS Winter Meeting and Nuclear Technology Expo. SAND2012-5866C. November, 2012.

- [97] P. Hofmann et al., "ZrO<sub>2</sub> Dissolution by Molten Zircaloy and Cladding Oxide Shell Failure. New Experimental Results and Modeling," Wissenschaftliche Berichte, INV-CIT(98)-P026, December 1999.
- [98] T.J. Haste et al., "In-Vessel Core Degradation in LWR Severe Accidents, European Commission," EUR16695EN, 1996.
- [99] Holser, J., "Relief Valve Thermal Analysis: Development of a Transient Thermal/Mechanical Model of a Crosby Relief Valve," Electric Power Research Institute (EPRI), Palo Alto, CA. EPRI-1006934. 2002.
- [100] DeGarmo, E.P., J.T. Black, and R.A. Kohser, "Materials and Processes in Manufacturing" 9th ed. New Jersey: John Wiley & Sons, Inc. 2003.
- [101] NUREG/CR-6920, "Risk-Informed Assessment of Degraded Containment Vessels," U.S. Nuclear Regulatory Commission, Washington, DC, June 2006.
- [102] NUREG/CR-6906, "Containment Integrity Research at Sandia National Laboratories, An Overview," U.S. Nuclear Regulatory Commission, Washington, DC, March 2006.
- [103] NUREG/CR-6433, "Containment Performance of Prototypical Reactor Containments Subjected to Severe Accident Conditions," U.S. Nuclear Regulatory Commission, Washington, DC, August 1996.
- [104] NUREG/CR-7149, "Effects of Degradation on the Severe Accident Consequences for a PWR Plant with a Reinforced Concrete Containment Vessel," U.S. Nuclear Regulatory Commission, Washington, DC, June 2013.
- [105] NUREG/CR-6533, "Code Manual for CONTAIN 2.0: A Computer Code for Nuclear Reactor Containment Analysis," U.S. Nuclear Regulatory Commission, Washington, DC, December 1997.
- [106] Helton JC, Iman RL, Johnson JD, Leigh CD. "Uncertainty and Sensitivity Analysis of a Model for Multicomponent Aerosol Dynamics." Nuclear Technology; 73: 320-342. 1986.
- [107] Helton JC, Iman RL, Johnson JD, Leigh CD. "Uncertainty and Sensitivity Analysis of a Dry Containment Test Problem for the MAEROS Aerosol Model." Nuclear Science and Engineering; 102: 22-42. 1989.
- [108] Nuclear Regulatory Commission (NRC). Tills, J., Notafrancesco, A., and Murata, K., "An Assessment of CONTAIN 2.0: A Focus on Containment Thermal Hydraulics (Including Hydrogen Distributions)," SMSAB-02-02, (ML022140438). July 2002.
- [109] F. Kreith and W. Z. Black, "Basic Heat Transfer," pg. 15. Harper & Row, Publishers, New York, 1980.
- [110] Kasper, G., T. Niida, and M. Yang, "Measurements of viscous drag on cylinders and chains of sphere with aspect ratios between 2 and 50," J. Aerosol Science, **16** (6), 535-556. Great Britain 1985.
- [111] Hinds, W. C., "Aerosol Technology." Wiley, 1982.

- [112] Brockmann, J. E., et al, Appendix F, "Uncertainty in Radionuclide Release Under Specific LWR Accident Conditions," in "Range of Possible Dynamic and Collision Shape Factors," Sandia National Laboratories, Albuquerque, New Mexico, SAND84-0410 Volume 2, 1985.
- [113] Kissane, M.P., "On the nature of aerosols produced during a severe accident of a water-cooled nuclear reactor", Nuclear Engineering and Design, 238, 2792-2800, 2008.
- [114] NUREG/CR-4691. Vol. 2. "MELCOR Accident Consequence Code System (MACCS) Model Description," U.S. Nuclear Regulatory Commission, Washington, DC, February, 1990.
- [115] NUREG/CR-1465. "Accident Source Terms for Light-Water Nuclear Power Plants," Final Report. U.S. Nuclear Regulatory Commission, Washington, DC, February, 1995.
- [116] Electric Power Research Institute, "Modeling of Molten Corium-Concrete Interaction," EPRI NP-5403, Palo Alto, CA, 1987.



## **APPENDIX A: MELCOR MODEL AND CODE ENHANCEMENTS**



# TABLE OF CONTENTS

<u>Section</u>	<u>Page</u>
TABLE OF CONTENTS .....	A-III
LIST OF FIGURES .....	A-V
LIST OF TABLES.....	A-VII
1. INTRODUCTION.....	A-1
2. SUMMARY OF THE MODEL UPDATES AND CORRECTIONS.....	A-3
2.1 Conversion to MELCOR 2.1 .....	A-3
2.2 New Decay Heat and Radionuclide Inventory .....	A-18
2.2.1 Generation of Problem-dependent Data Libraries for ORIGEN-S/ARP.....	A-19
2.2.2 TRITON (NEWT) Model for Surry 15x15 Fuel Assemblies.....	A-19
2.2.3 Simplifying Assumptions in TRITON Analyses for Generating ORIGEN-S/ARP Libraries.....	A-20
2.2.4 ORIGEN-S/ARP Calculation Process.....	A-20
2.2.5 Surry Plant Operating Data.....	A-20
2.2.6 Simplifying Assumptions for ORIGEN-S/ARP Analyses.....	A-21
2.2.7 Post-processing and Automated Generation of Consistent MELCOR and MACCS Inputs .....	A-22
2.2.8 Selection of Base Case Conditions for MELCOR and MACCS Models for Surry UA .....	A-23
2.2.9 MELCOR Decay Power and Inventory Inputs for Surry UA.....	A-27
2.2.10 MACCS Input for the New Base Case and for Surry UA.....	A-30
2.3 Summary of the Model Corrections and Improvements Not Included in the Uncertainty Sampling .....	A-34
2.3.1 Concrete type .....	A-35
2.3.2 Hot leg creep rupture modeling .....	A-35
2.3.3 Tin aerosol release model .....	A-37
2.3.4 Cavity heat transfer modeling.....	A-37
2.3.5 Improvements in the steam generator nodalization.....	A-38
2.3.6 Miscellaneous changes .....	A-39
2.4 Summary of the Model Enhancements Included in the Uncertainty Sampling.....	A-40
2.4.1 Hot steam generator tube failure modeling.....	A-40
2.4.2 Steam generator tube thickness.....	A-41
2.4.3 Improved valve failure modeling.....	A-41

2.4.4	Modifications to the pump seal failure .....	A-42
2.4.5	Improvements in containment condensation .....	A-43
2.4.6	Improvements in the containment overpressure and design leakage .	A-43
2.4.7	Hydrogen ignition modeling .....	A-46
2.4.8	Model modifications for the effective fuel eutectic formation .....	A-49
2.4.9	Updated iodine and cesium modeling.....	A-51
2.4.10	Improvements in the secondary side decontamination factor.....	A-53
2.4.11	Aerosol shape factor .....	A-53
3.	BASE UA CALCULATION .....	A-55
4.	REFERENCES.....	A-81

## LIST OF FIGURES

<u>Figure</u>	<u>Page</u>
Figure A-1	Comparison of the MELCOR 1.8.6 SOARCA and MELCOR 2.1 RPV pressure response ..... A-8
Figure A-2	Comparison of the MELCOR 1.8.6 SOARCA and MELCOR 2.1 RPV pressure response ..... A-8
Figure A-3	Comparison of the MELCOR 1.8.6 SOARCA and MELCOR 2.1 RPV reactor coolant pump leakage ..... A-9
Figure A-4	Comparison of the MELCOR 1.8.6 SOARCA and MELCOR 2.1 SG downcomer level response ..... A-9
Figure A-5	Comparison of the MELCOR 1.8.6 SOARCA and MELCOR 2.1 RPV downcomer level response ..... A-10
Figure A-6	Comparison of the MELCOR 1.8.6 SOARCA and MELCOR 2.1 debris mass discharged to the containment ..... A-10
Figure A-7	Comparison of the MELCOR 1.8.6 SOARCA and MELCOR 2.1 ex-vessel core-concrete radial and axial erosion depth ..... A-11
Figure A-8	Comparison of the MELCOR 1.8.6 SOARCA and MELCOR 2.1 ex-vessel core-concrete gas generation ..... A-11
Figure A-9	Comparison of the MELCOR 1.8.6 SOARCA and MELCOR 2.1 ex-vessel energy flows ..... A-12
Figure A-10	Comparison of the MELCOR 1.8.6 SOARCA and MELCOR 2.1 containment pressure response ..... A-12
Figure A-11	Comparison of the MELCOR 1.8.6 SOARCA and MELCOR 2.1 containment leak rate ..... A-13
Figure A-12	Comparison of the MELCOR 1.8.6 SOARCA and MELCOR 2.1 lower containment and reactor cavity water mass ..... A-13
Figure A-13	Comparison of the MELCOR 1.8.6 SOARCA and MELCOR 2.1 lower containment and reactor cavity temperatures ..... A-14
Figure A-14	Comparison of the MELCOR 1.8.6 SOARCA and MELCOR 2.1 containment burn energy ..... A-14
Figure A-15	Comparison of the MELCOR 1.8.6 and MELCOR 2.1 iodine distributions ... A-15
Figure A-16	Comparison of the MELCOR 1.8.6 and MELCOR 2.1 cesium distributions . A-16
Figure A-17	Comparison of the MELCOR 1.8.6 SOARCA and MELCOR 2.1 highest volatile radionuclide environmental releases ..... A-17
Figure A-18	Comparison of the MELCOR 1.8.6 SOARCA and MELCOR 2.1 volatile radionuclide environmental releases ..... A-17
Figure A-19	Comparison of the MELCOR 1.8.6 SOARCA and MELCOR 2.1 steel components in the ex-vessel debris ..... A-18
Figure A-20	TRITON/NEWT models for full 15x15 assembly (left) and quarter-assembly with multi-rod depletion (right) ..... A-19
Figure A-21	Processed Surry data (left) mapped over to MELCOR COR rings (right) ..... A-21
Figure A-22	Decay power on logarithmic time scale for several shutdown times in Cycle 20 ..... A-23
Figure A-23	Decay power on severe accident time scale for several shutdown times in Cycle 20 ..... A-24
Figure A-24	Decay power on logarithmic time scale relative to full-cycle EOC decay powerA-25

Figure A-25	Decay power on severe accident time scale relative to full-cycle EOC decay power .....	A-25
Figure A-26	BOC and MOC decay powers relative to full-cycle EOC decay power .....	A-26
Figure A-27	New base-case decay heat curve for MELCOR Surry model at MOC conditions .....	A-27
Figure A-28	BOC, MOC, and EOC decay powers for Surry UA on severe accident time scale.....	A-28
Figure A-29	BOC and MOC decay power normalized to EOC power on a logarithmic scale .....	A-28
Figure A-30	Natural circulation flow patterns in a PWR [28].....	A-36
Figure A-31	Illustration of hot leg nozzle [29].....	A-37
Figure A-32	Illustration of accentuated heat transfer .....	A-38
Figure A-33	Comparison of the SOARCA and UA steam generator nodalizations .....	A-39
Figure A-34	Representation of the hottest tube in the Surry model for creep rupture evaluations.....	A-41
Figure A-35	Surry SOARCA containment overpressure models .....	A-45
Figure A-36	Flammability limits for hydrogen for H <sub>2</sub> -O <sub>2</sub> -H <sub>2</sub> O and H <sub>2</sub> -O <sub>2</sub> -CO <sub>2</sub> systems [35].....	A-49
Figure A-37	Ignition energy for dry hydrogen mixtures [36].....	A-49
Figure A-38	Measured fission gas release to the fuel/cladding gap .....	A-52
Figure A-39	Comparison of the UA hot SG tube and SOARCA SG tube gas and tube temperature responses .....	A-65
Figure A-40	Comparison of the UA and SOARCA SG tube creep rupture index responses .....	A-65
Figure A-41	Comparison of the short-term UA and SOARCA core decay heat power responses (log-log scale).....	A-66
Figure A-42	Comparison of the short-term UA and SOARCA core decay heat power responses.....	A-66
Figure A-43	Comparison of the short-term UA and SOARCA SG levels.....	A-67
Figure A-44	Comparison of the short-term UA and SOARCA SG water masses.....	A-67
Figure A-45	Comparison of the short-term UA and SOARCA SG pressures .....	A-68
Figure A-46	Comparison of the short-term UA and SOARCA pressurizer pressures.....	A-68
Figure A-47	Comparison of UA and SOARCA RPV level responses .....	A-69
Figure A-48	Comparison of UA and SOARCA top and midplane fuel cladding temperature responses.....	A-69
Figure A-49	Comparison of the UA and SOARCA short-term total (oxidation + decay heat) and decay heat powers.....	A-70
Figure A-50	Comparison of the UA hot SG tube and SOARCA hot leg gas and piping temperature responses .....	A-70
Figure A-51	Comparison of the UA and SOARCA hot leg piping creep rupture index responses.....	A-71
Figure A-52	Comparison of the UA and SOARCA core mass ejected to the containment.....	A-71
Figure A-53	Comparison of the UA and SOARCA concrete erosion depths .....	A-72
Figure A-54	Comparison of the UA and SOARCA ex-vessel core-concrete gas generation .....	A-72
Figure A-55	Comparison of the UA and SOARCA ex-vessel energy flow .....	A-73
Figure A-56	Comparison of the UA and SOARCA containment pressure response .....	A-73
Figure A-57	Comparison of the UA and SOARCA containment leak rate .....	A-74
Figure A-58	Comparison of the UA and SOARCA lower containment and reactor cavity gas temperatures.....	A-74
Figure A-59	Comparison of the UA and SOARCA lower containment and reactor cavity water mass.....	A-75

Figure A-60	Comparison of the UA and SOARCA containment burn energy.....	A-75
Figure A-61	Comparison of the UA and SOARCA iodine distributions.....	A-76
Figure A-62	Comparison of the UA and SOARCA cesium distributions.....	A-77
Figure A-63	Comparison of the UA and SOARCA pressurizer relief tank water mass.....	A-78
Figure A-64	Comparison of the comparison of the UA and SOARCA highest volatile radionuclide environmental releases.....	A-78
Figure A-65	Comparison of the comparison of the UA and SOARCA volatile radionuclide environmental releases.....	A-79
Figure A-66	Comparison of the UA and SOARCA steel components in the ex-vessel debris.....	A-79

## LIST OF TABLES

<u>Table</u>		<u>Page</u>
Table A-1	Comparison of original and MELCOR 2.1 SOARCA STSBO calculations.....	A-7
Table A-2	Surry reactor information used for ORIGEN-S/ARP analyses. ....	A-21
Table A-3	Lumped MELCOR RN inventories for Surry. ....	A-29
Table A-4	Variations in lumped MELCOR RN inventories for Surry.....	A-30
Table A-5	MACCS nuclide inventories (in Bq) for Xe, Cs, Ba, I, and Te classes. ....	A-32
Table A-6	MACCS nuclide inventories (in Bq) for Ru, Mo, and Ce classes. ....	A-33
Table A-7	MACCS nuclide inventories (in Bq) for La class. ....	A-34
Table A-8	RCP seal leak probabilities at operating pressure. ....	A-42
Table A-9	Fuel collapse observed in the VERCORS experiments. ....	A-50
Table A-10	Values prescribed for UA uncertain parameters in the base calculation.....	A-62
Table A-11	Comparison of the key event timing in the SOARCA, converted MELCOR 2.1, and base UA calculations.....	A-64



# **Appendix A      Code and Model Enhancement to Develop the Surry UA Base Model**

## **1.            INTRODUCTION**

The intended purpose of the uncertainty analysis is to quantitatively evaluate the effects of selected key uncertain parameters on the estimation of hydrogen production as well as the release of radionuclides to the environment and downstream consequences. Validation of a computer model for a physical system involves a series of activities designed to generate and enhance confidence in the model's conceptualization and results during and after model development. The SOARCA Surry STSBO model presented in NUREG/CR-7110 Volume 2 represents a complex system of the reactor core, pressure vessel, reactor coolant system, safety systems, environmental conditions, and downstream consequences including evacuation planning. In conventional modeling practice, model validation is achieved by comparing model results with experimental measurements. However, such measurements are impossible to obtain at the temporal and spatial scales of interest at a complex integrated level for reactor safety analyses. From a strictly computational perspective, a well-designed, correctly implemented numerical model should produce results that are explainable and appropriate for its intended purpose. Validation of the SOARCA model is a process to establish confidence that the model adequately represents with sufficient accuracy the accident scenario and satisfies its intended purpose. The SOARCA Surry model presented in NUREG/CR-7110 Volume 2 included verification of the inputs and software and is considered valid for its intended use.

The results presented in this analysis were generated with an updated version of the SOARCA Surry unmitigated STSBO model. The STSBO calculations presented in NUREG/CR-7110 Volume 2 were performed in September 2007. The updated input model includes both modeling enhancements and error corrections since 2007. The Surry analysis performed in NUREG/CR-7110 Volume 2 used MELCOR 1.8.6. In 2012, the NRC released MELCOR 2.1 and stopped maintaining MELCOR 1.8.6. MELCOR 2.1 includes new models not previously available in MELCOR 1.8.6. The new Surry UA model includes a conversion to the MELCOR 2.1. Furthermore, MELCOR 2.1 includes new enhancements to support the UA that were not previously available in MELCOR 1.8.6. Consequently, it will not be possible to directly converge on the previous SOARCA results because of the model input and the major MELCOR code change. This appendix describes the model input changes and corrections to develop the MELCOR 2.1 Surry UA STBO model.



## **2. SUMMARY OF THE MODEL UPDATES AND CORRECTIONS**

The model changes and enhancements described in this section include:

- Conversion to MELCOR 2.1
- Model updates and corrections identified during the course of the project
- Model enhancements to improve functionality
- Model enhancements to support sampling of parameters

First, the differences in the calculations resulting from the code conversion from 2007 MELCOR 1.8.6 code to the 2015 MELCOR 2.1 code are discussed in Section 2.1. Second, best estimate decay heat and radionuclide inventory calculations were performed for the current study to update the conservative values used in the SOARCA study. The new decay heat and radionuclide inventory was a significant new model addition for the state of the art evaluation of the source term. The development of the new decay heat model and radionuclide inventory is described in Section 2.2. The decay heat is a sampled variable that is included in the UA. The model corrections and improvements are described in Section 2.3. Some model corrections implemented are a result of an improved understanding of the Surry plant. The model improvements in Section 2.3 are not included in the UA uncertainty sampling. The model enhancements that were added to support the uncertainty sampling are described in Section 2.4. These model enhancements fulfilled two goals, (a) improve the simulation fidelity of the phenomena and (b) include flexibility to sample uncertainty in the response.

### **2.1 Conversion to MELCOR 2.1**

The archived MELCOR 1.8.6 SOARCA Surry STSBO model from September 2007 was retrieved and converted to MELCOR 2.1 input format using the NRC SNAP Model Editor Version 2.3.1. Without making any changes to the model input, a new STSBO calculation was performed using MELCOR 2.1.6843 (2015). Table A-1 provides a comparison of the timings of key events between the NUREG/CR-7110 Volume 2 SOARCA STSBO calculation and the new MELCOR 2.1 calculation. The timings are very close until the timing of start of core collapse. In particular, the timing to RCP pump seal failure and hot leg nozzle failure are nearly identical.

The phenomena following the hot leg creep rupture failure is particularly complex, which led to differences in timing. The sharp depressurization of the primary system due to the large pipe break led to a complete and rapid discharge of the accumulator water into the hot core. Although the fuel rods were standing at the time of the hot leg failure, there was cladding failure and heavy oxidation. However, some regions remained in film boiling. The core degradation proceeded as the accumulator water boiled away.

A comparison of the primary and secondary system pressure responses is shown in Figure A-1 and Figure A-2. At the start of the accident sequence, the reactor successfully scrams in response to the loss of power. The main steam line isolation and containment isolation valves close in response due to the loss of power. The reactor coolant and main feedwater pumps also trip due to the loss of power. Once the main steam lines close, the normal mechanism of heat removal from the primary system is unavailable. Consequently, both the primary and secondary system pressures rise. The secondary system quickly pressurizes to the safety valve opening pressure, which cause the safety valves to open and then subsequently close when the closing pressure criterion is achieved. The relief flow through the steam generator (SG) safety valves is the principle primary system energy removal mechanism in the first hour.

There is also energy removal through the RCP seal leakage (see Figure A-3), but the energy flow is small relative to the SG SRV flow.

Due to the complete loss of all feedwater at the start of the calculation, the water inventory in the steam generators decreased very rapidly and was completely boiled away by 1 hr 16 min and 1 hr 14 min in MELCOR 1.8.6 and 2.1, respectively (see Table A-1 and Figure A-4). Although the steam generator relief valves continue to cycle and release steam, the associated heat removal is inadequate and the primary system sharply increases to the pressurizer safety relief valve opening pressure. The safety valves on the pressurizer begin opening and closing to remove excess energy. The pressurizer relief valve flow causes a steady decrease in the primary system coolant inventory (see Figure A-5). The fuel starts to uncover at 2 hr 19 min and 2 hr 20 min in MELCOR 1.8.6 and MELCOR 2.1, respectively (see Table A-1). The fuel cladding fails at 2 hr 57 min, which starts the release of fission products from the fuel. The fuel rods start to degrade above 2400 K as the molten zirconium breaks through the oxidized shell of the cladding on the fuel rods and eventually collapse due to a thermal mechanical weakening of the remaining oxide shell at high temperature.

An in-vessel natural circulation flow develops between the hot fuel in the core and the cooler structures in the upper plenum following the uncovering of the fuel. Hot gases rise out of the center of the core into the upper plenum and return down the cooler peripheral sections of the core. Simultaneously, a natural circulation circuit develops between the hot gases in the vessel and the steam generator. Due to its close proximity to the hot gases exiting in the vessel, the Loop C hot leg nozzle at the interface region to the stainless steel piping was predicted to fail by creep rupture at 3 hr 45 min (see Table A-1). There was good agreement between MELCOR 1.8.6 and MELCOR 2.1 on the event timings through the hot leg failure.

Upon creep failure of the hot leg nozzle, a large hole opened that rapidly depressurized the RCS (i.e., like a large break loss of coolant accident). The RCS depressurization permitted a complete accumulator injection at low pressure (water level rise at 3 hr 45 min on Figure A-5). Although the water filled above the core region, the hottest fuel regions in the core remained in film boiling and continued to heat and degrade. The lower temperature regions on the periphery of the core quenched but subsequently reheated once the water level decreased into the core.

Following the accumulator injection at 3 hr 45 minutes, the decay heat from the fuel boiled away the injected water. A large debris bed formed in the center of the core and continued to expand. The hot debris failed the core support plate at 4 hr 23 min and 4 hr 51 min and fell onto the lower core support plate, which failed at 6 hr 36 min and 7 hr 33 min for MELCOR 1.8.6 and 2.1, respectively. The differences in the two code versions increased from 28 min at core plate failure to the 57 min for lower core plate failure. Following the lower core support plate failure, the debris bed relocated onto the lower head. The small amount of remaining water in the lower head was quickly boiled away (see timings in Table A-1). The lower head weakened and failed at 7 hr 16 min and 8 h 6 min for Versions 1.8.6 and Version 2.1, respectively.

After the RPV lower head failure, the hot debris relocated from the vessel into the reactor cavity in the containment under the reactor vessel (see Figure A-6). The hot debris boiled away the water in the reactor cavity and started to ablate the concrete. The ex-vessel molten core concrete interactions (MCCI) continued for the remainder of the calculation, which ablated the concrete (see Figure A-7) and generated non-condensable gases (see Figure A-8). There were relatively large differences in the ablation depths and the integral CO and CO<sub>2</sub> gas generation between the MELCOR 1.8.6 and MELCOR 2.1 models. As will be discussed in Section 2.3.1, the Surry concrete type was incorrectly specified as limestone in the SOARCA Surry model.

The converted MELCOR 2.1 calculation also used limestone concrete to facilitate direct comparisons. There were also code and user-input improvements to the core-concrete ablation models since MELCOR 1.8.6. The MELCOR 2.1 predicted an increase in the CO<sub>2</sub> gas generation rate and a decrease in the CO gas generation rate after 40 h. The MELCOR 1.8.6 calculation was originally extended to 7 days and showed a similar change in non-condensable gas generation rates but not until 96 h.

A comparison of the ex-vessel debris heat flow in the MELCOR 2.1 and MELCOR 1.8.6 calculations provides the following insights (see Figure A-9),

- The ex-vessel decay heat power is almost identical (QDH on Figure A-9) between the two versions,
- The power due to chemical reactions is relatively small and diminishes shortly after the start of core-concrete interactions (QRea on Figure A-9), and
- The surface heat loss (Qsurf on Figure A-9) is higher in MELCOR 1.8.6 and the heat flow for concrete ablation of the concrete (QAB on Figure A-9) is higher in MELCOR 2.1.

The resultant non-condensable gas and steam generation pressurized the containment (see Figure A-10). The MELCOR 2.1 case reached the design pressure at 11 hr 16 min versus 11 hr for MELCOR 1.8.6. The containment failed due to liner tearing near the containment equipment hatch at mid-height in the cylindrical region of the containment at 25 h 32 min and 26 h 22 min, respectively for MELCOR 1.8.6 and 2.1 (i.e., containment leakage area in Figure A-11). Although the MELCOR 2.1 calculation had a higher CO and CO<sub>2</sub> generation, the higher heat loss from the debris MELCOR 1.8.6 (Figure A-9) calculation resulted in higher temperatures in cavity, slightly higher containment gas temperatures overall, and a slightly faster containment pressurization. The containment continued to pressurize until the leakage flow balanced the steam and non-condensable gas generation. All the water spilled on the floor from the reactor coolant pump seal leakage, and the pressurizer relief tank (PRT) evaporated by 44 hr 14 min in MELCOR 1.8.6 calculation. There was still water on the containment floor in the MELCOR 2.1 calculation at 48 hr. The water evaporation had slowed after 45 h 22 min in the MELCOR 2.1 calculation, which allowed the containment to start depressurizing (see Figure A-10).

The only hydrogen burns in the containment occurred following the initial discharge of hydrogen and steam at hot leg failure (Figure A-14). The magnitude of the burns was slightly higher in MELCOR 1.8.6. However, the resulting containment pressurization from the hydrogen burn and large pipe break from high reactor coolant system pressure was small compared to the long-term pressurization (Figure A-10). The steam concentration is above the minimum threshold (55%) for combustion in both calculations thereafter.

The fission product releases from the fuel started following the first thermal-mechanical failures of the fuel cladding in the hottest rods at 2 hr 57 min, or about 38 min after the uncovering of the top of the fuel rods. The in-vessel fission product release phase continued through vessel failure. Initially, the fission product releases from the fuel circulated through the primary system as well as being released to the containment through the pressurizer safety relief valves. The PRT rupture disk opened about 1 hour before the start of the fission product releases. There was good agreement on the timing of these early core progression events between the two code versions.

Figure A-15 and Figure A-16 shows a comparison of the MELCOR 1.8.6 and MELCOR 2.1 long-term distributions of the iodine and cesium radionuclides that were released from the fuel, respectively. Both codes show nearly complete in-vessel release of the iodine and cesium released from the fuel prior to vessel failure. A small (~1%) iodine and cesium ex-vessel release after vessel failure is also shown on the figures. MELCOR 2.1 had a slightly smaller ex-vessel release. However, nearly all the iodine and cesium released from the fuel occurs in the vessel prior to lower head failure. At the time of the hot leg failure, approximately 40% of these volatile radionuclides had been released. After hot leg failure at 3 hr 45 min, there are some variations in the fission product release, which are somewhat exaggerated on the semi-log scale. The radionuclide release slowed after the accumulator discharge in MELCOR 2.1. However, in the MELCOR 1.8.6 calculation, in-vessel iodine and cesium releases were not appreciably slower during the accumulator reflood of the vessel. The MELCOR 1.8.6 calculation retains slightly less iodine and cesium in the steam generator and slightly less iodine in the vessel. The MELCOR 1.8.6 calculation also shows a slightly larger long-term revaporization of iodine from the vessel and a larger ex-vessel release of cesium and iodine. These small differences led to slightly higher airborne concentrations in the containment for the MELCOR 1.8.6 calculation. As described previously, the containment pressurization and resulting leakage was also slightly higher in the MELCOR 1.8.6 calculation. Consequently, the iodine and cesium releases to the environment were slightly higher in MELCOR 1.8.6 (i.e., see Figure A-17).

As shown in Figure A-17 and Figure A-18, the volatile radionuclide releases were higher in MELCOR 1.8.6 except the long-term Molybdenum release. The change in Mo release from the ex-vessel debris occurs when the steel components in the melt have been oxidized. There is also an increase in carbon-dioxide production and a decrease in carbon-monoxide production (see Figure A-8). Although the MELCOR 1.8.6 and 2.1 calculations had similar amounts of steel in the ex-vessel debris, the steel components were oxidized more quickly in the MELCOR 1.8.6 calculation (see Figure A-19). The higher oxidation rate in the MELCOR 2.1 calculation is consistent with the higher erosion rate (see Figure A-7) and the higher gas generation rate (see Figure A-8), which was a result of the differences in the heat balance (Figure A-9). The steel component of Cr is oxidized first and followed by Fe and Ni. When the steel components in the melt (Ni, Cr, and Fe) are exhausted, the Molybdenum becomes the preferred metal in the debris for oxidation of the ablation gases, which is released to the containment atmosphere when oxidized.

In summary, a comparison of the results from the direct conversion of the MELCOR 1.8.6 model to the MELCOR 2.1 model shows very good comparison of the thermal-hydraulic response prior to the hot leg creep rupture. After the hot leg creep rupture failure, the MELCOR 2.1 accident progression proceeds more slowly than the original MELCOR 1.8.6 calculation. The timing to core plate and lower core plate is 28 and 57 minutes slower, respectively. The failure of the lower head occurs 50 minutes later. The timing differences are not unexpected, considering the number of code changes between 2007 and the current version. A slightly higher fraction of volatile radionuclides were released from the fuel to the containment following the accumulator discharge in the MELCOR 1.8.6 calculation. Following the vessel failure, the core debris relocates to the reactor cavity. More of the debris energy goes to ablating the concrete in the MELCOR 2.1 calculation, which is due to differences in the core-concrete models. As a result of higher heating from the ex-vessel debris in the MELCOR 1.8.6 calculation, the containment pressurized slightly faster and had a slightly larger leakage rate. The net effects of the lower in-vessel retention and higher containment leakage were slightly higher releases of volatile radionuclides to the environment. The only exception was the Molybdenum, which was due to differences in the ex-vessel core-concrete interaction heat balance.

**Table A-1 Comparison of original and MELCOR 2.1 SOARCA STSBO calculations.**

Event Description	MELCOR 1.8.6 Time (hh:mm)	MELCOR 2.1 Time (hh:mm)
Initiating event Station blackout – loss of all onsite and offsite AC and DC power	00:00	00:00
MSIVs close Reactor trip RCP seals initially leak at 21 gpm/pump TD-AFW starts but fails to inject due to ECST rupture	00:00+	00:00+
First SG SRV opening	00:03	00:03
SG dryout	01:16	01:14
Pressurizer SRV opens	01:27	01:26
PRT rupture disk opens	01:46	01:46
Start of fuel heatup	02:19	02:20
RCP seal failures	02:45	02:47
First fission product gap releases	02:57	02:57
Creep rupture failure of the C loop hot leg nozzle	03:45	03:45
Accumulators start discharging	03:45	03:46
Accumulators are empty	03:45	03:45
First failure of the core support plate	04:23	04:51
First failure of the lower support plate	06:36	07:33
Lower plenum dryout	06:39	07:35
Vessel lower head failure by creep rupture	07:16	08:06
Debris discharge to reactor cavity	07:16	08:06
Cavity dryout	07:27	08:35
Containment at design pressure (45 psig)	11:00	11:16
Start of increased leakage of containment ( $P/P_{\text{design}} = 2.18$ )	25:32	26:22
Containment pressure stops decreasing	44:14	45:22
End of calculation	48:00	48:00

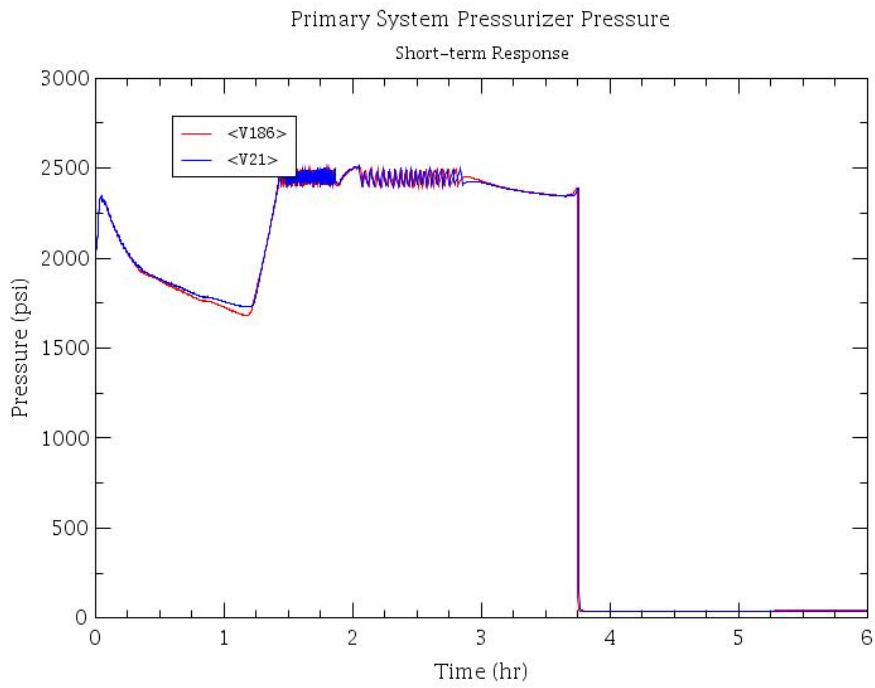


**Figure A-1 Comparison of the MELCOR 1.8.6 SOARCA and MELCOR 2.1 RPV pressure response**

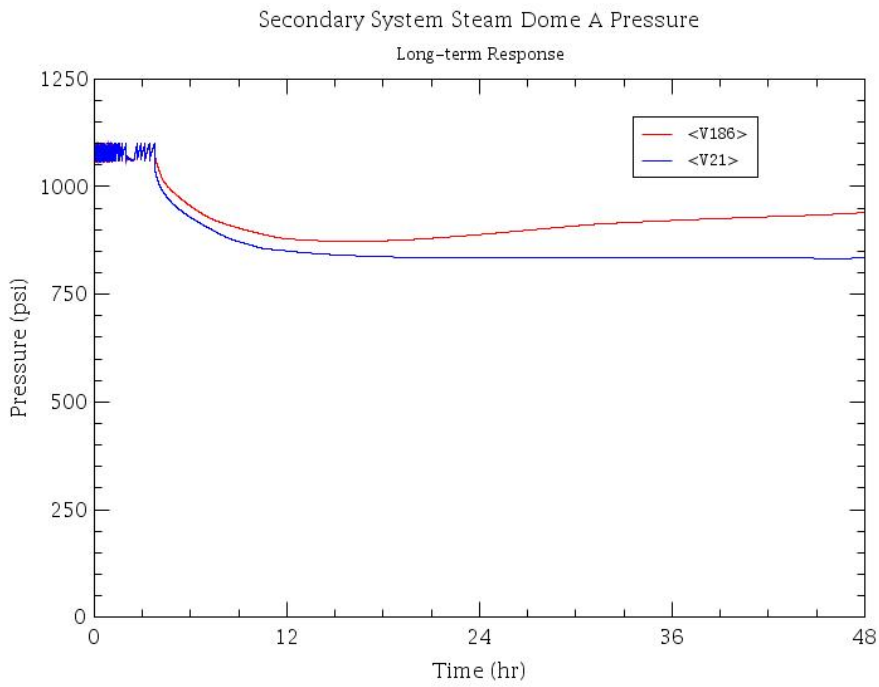


**Figure A-2 Comparison of the MELCOR 1.8.6 SOARCA and MELCOR 2.1 RPV pressure response**

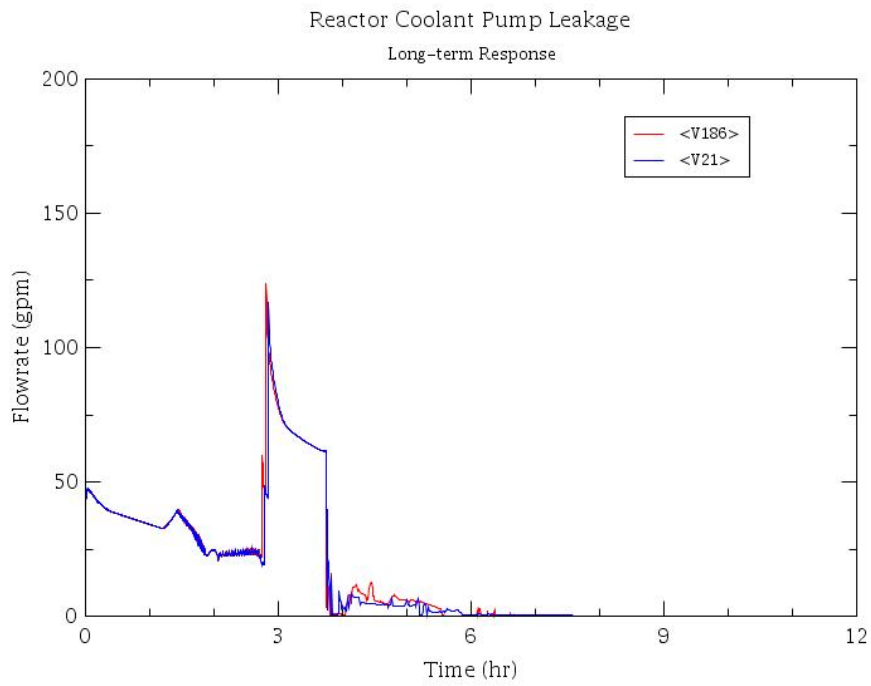


**Figure A-3 Comparison of the MELCOR 1.8.6 SOARCA and MELCOR 2.1 RPV reactor coolant pump leakage**

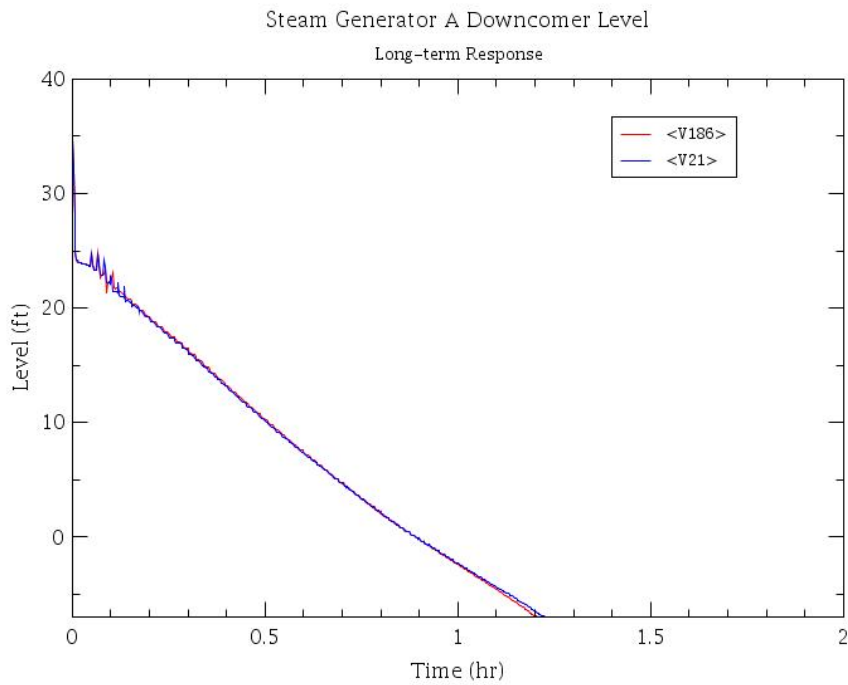


**Figure A-4 Comparison of the MELCOR 1.8.6 SOARCA and MELCOR 2.1 SG downcomer level response**

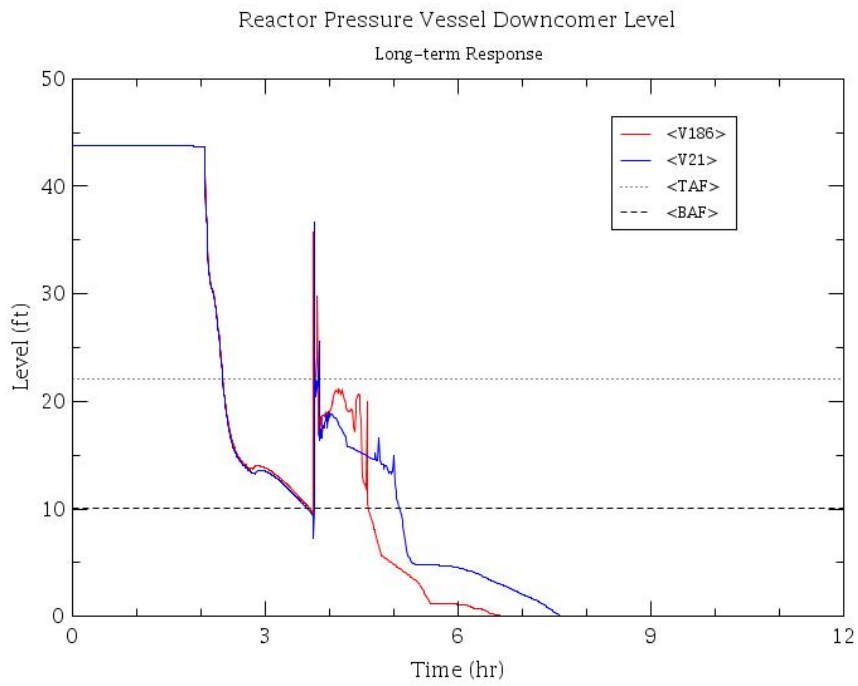


**Figure A-5 Comparison of the MELCOR 1.8.6 SOARCA and MELCOR 2.1 RPV downcomer level response**

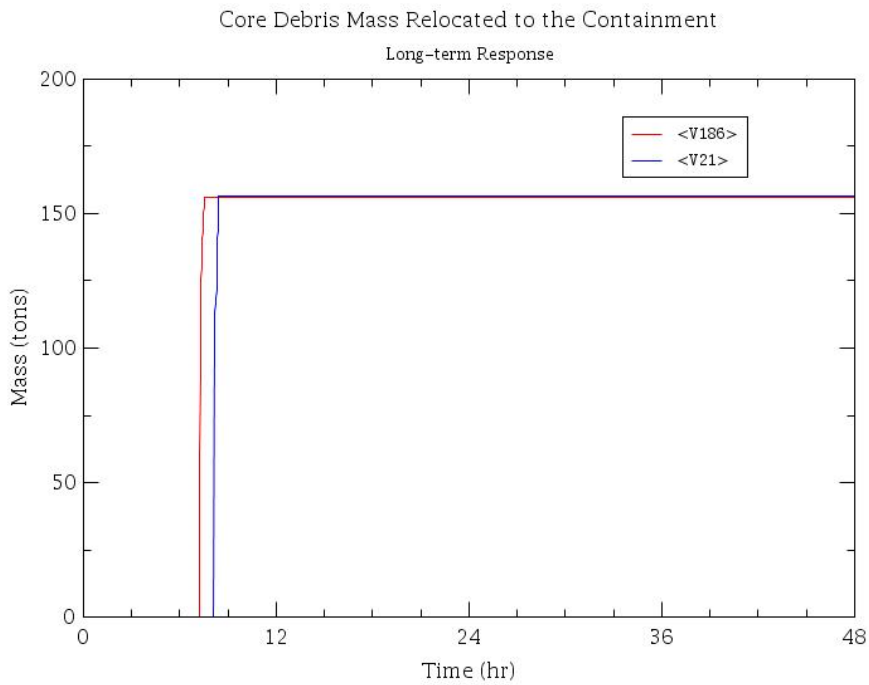


**Figure A-6 Comparison of the MELCOR 1.8.6 SOARCA and MELCOR 2.1 debris mass discharged to the containment**

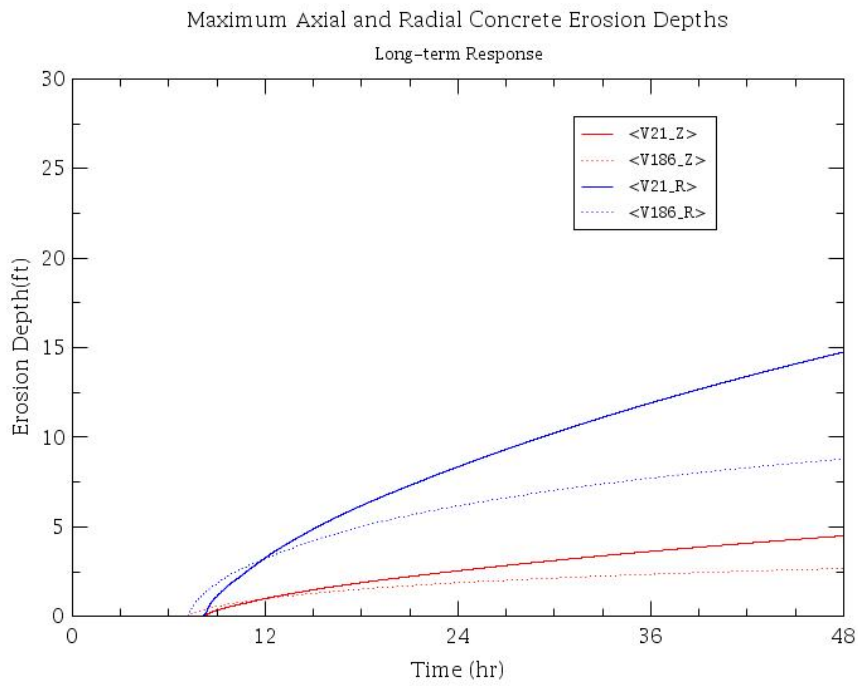


**Figure A-7 Comparison of the MELCOR 1.8.6 SOARCA and MELCOR 2.1 ex-vessel core-concrete radial and axial erosion depth**

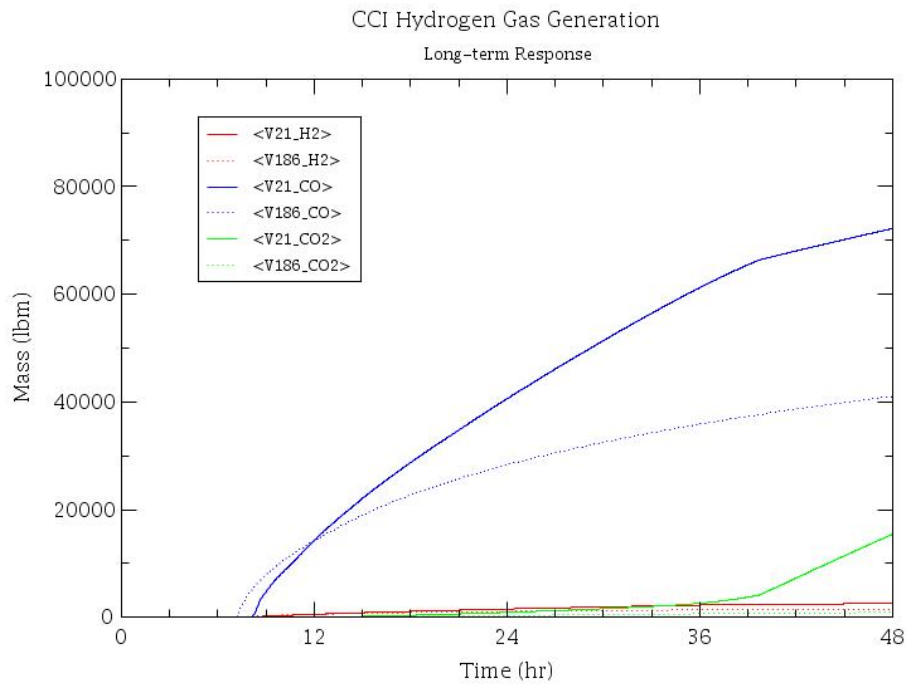


**Figure A-8 Comparison of the MELCOR 1.8.6 SOARCA and MELCOR 2.1 ex-vessel core-concrete gas generation**

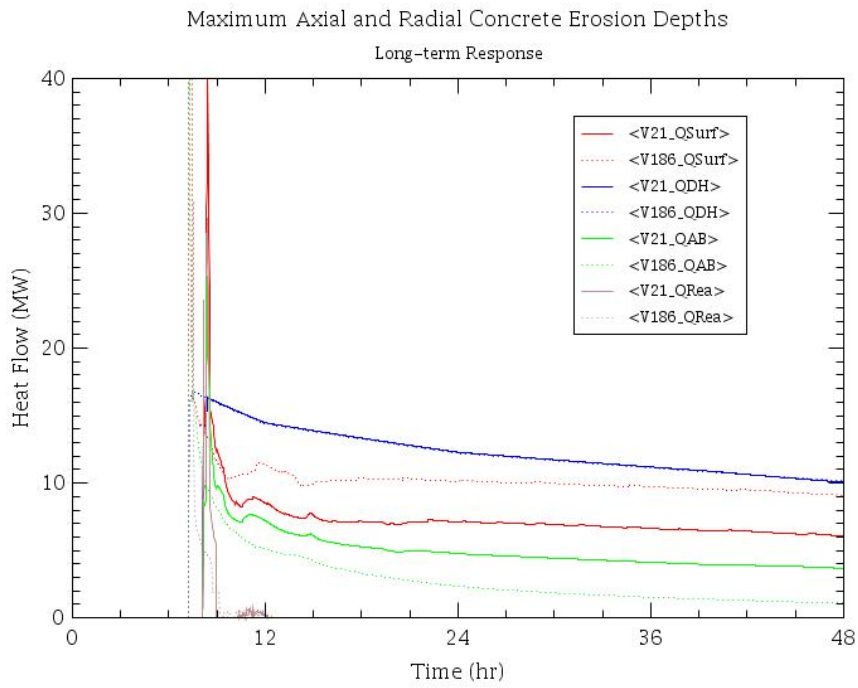


**Figure A-9 Comparison of the MELCOR 1.8.6 SOARCA and MELCOR 2.1 ex-vessel energy flows**

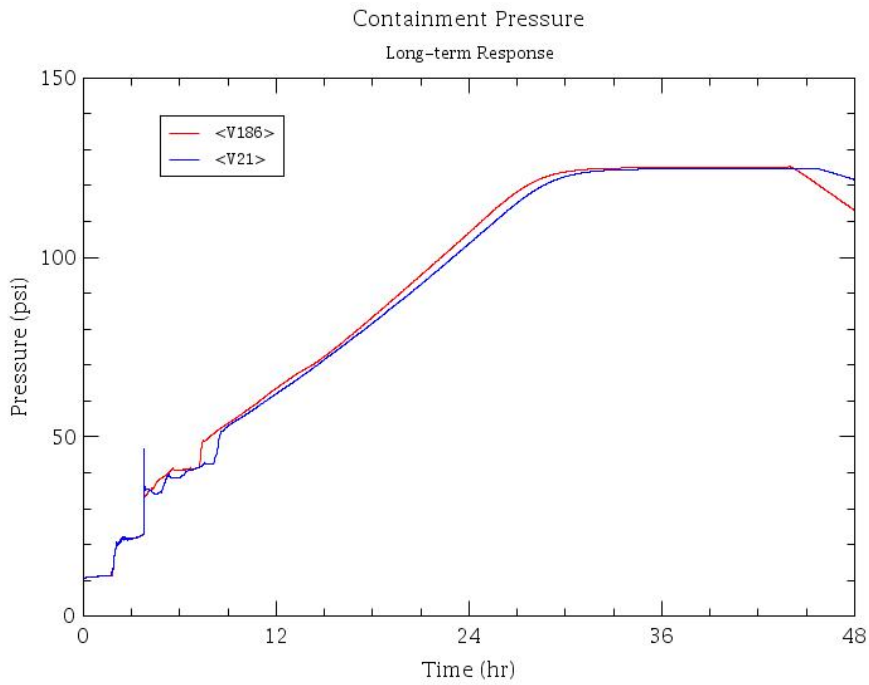


**Figure A-10 Comparison of the MELCOR 1.8.6 SOARCA and MELCOR 2.1 containment pressure response**

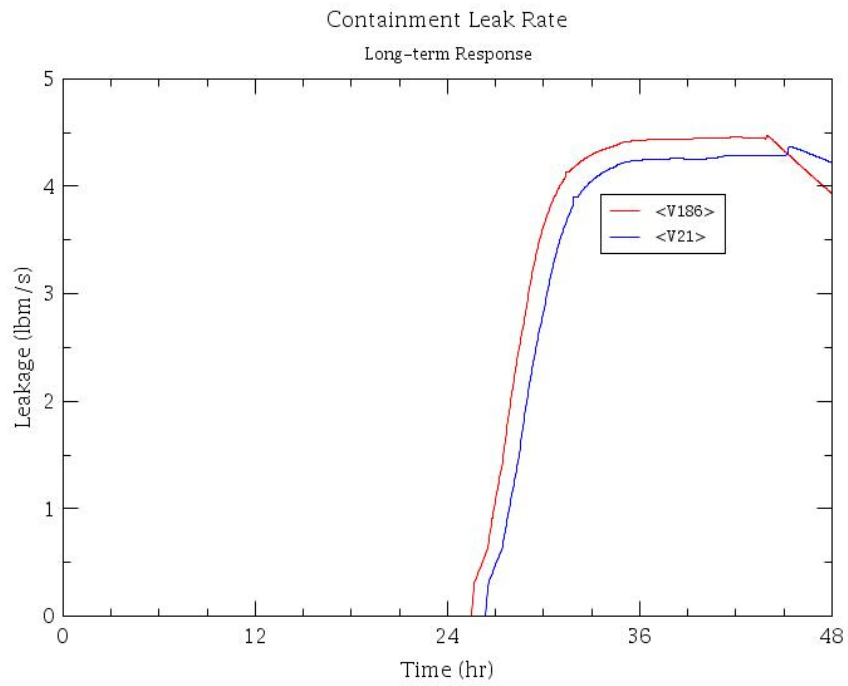


**Figure A-11 Comparison of the MELCOR 1.8.6 SOARCA and MELCOR 2.1 containment leak rate**

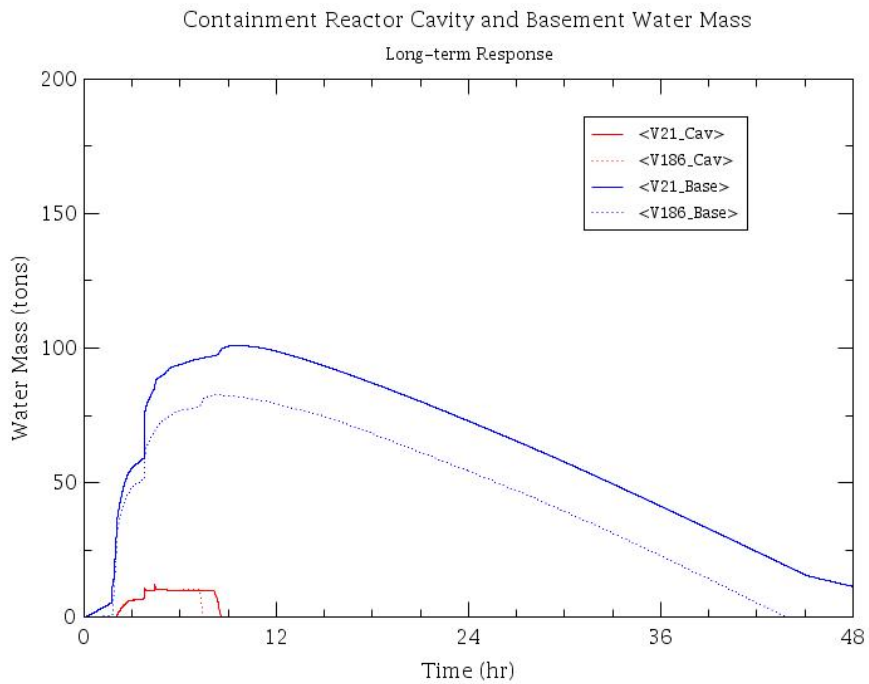


**Figure A-12 Comparison of the MELCOR 1.8.6 SOARCA and MELCOR 2.1 lower containment and reactor cavity water mass**

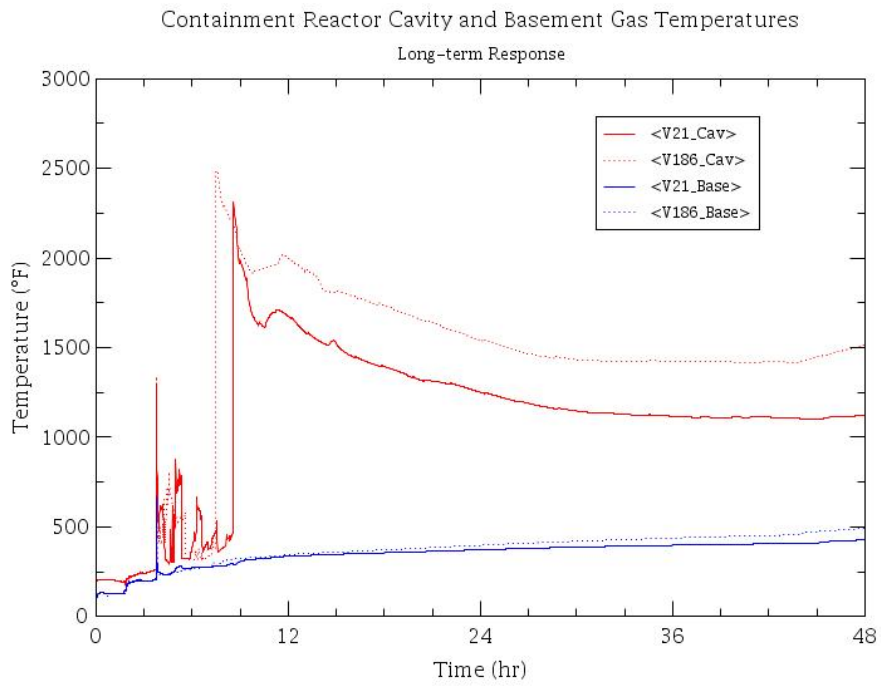


**Figure A-13 Comparison of the MELCOR 1.8.6 SOARCA and MELCOR 2.1 lower containment and reactor cavity temperatures**

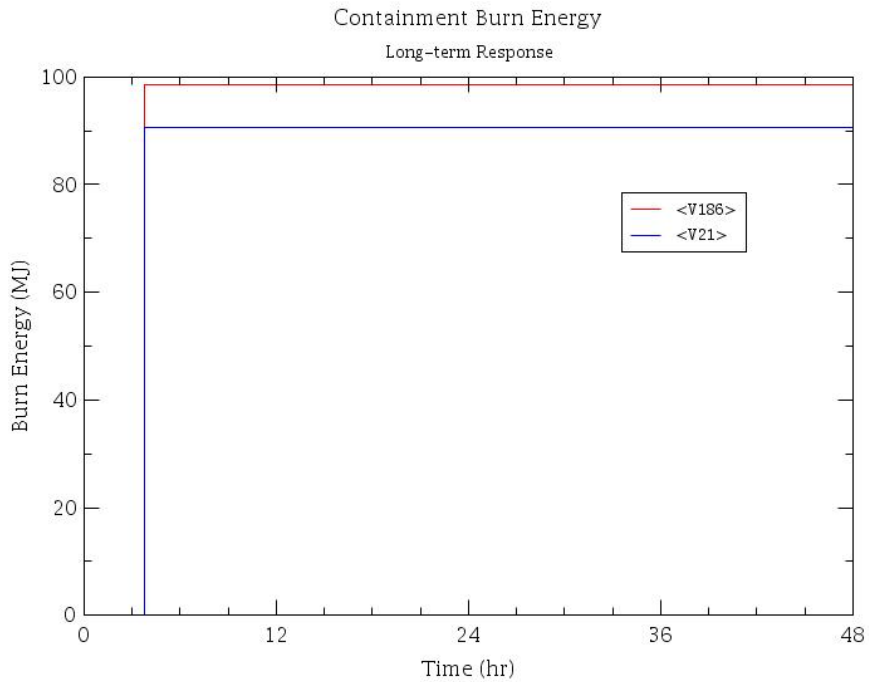


**Figure A-14 Comparison of the MELCOR 1.8.6 SOARCA and MELCOR 2.1 containment burn energy**

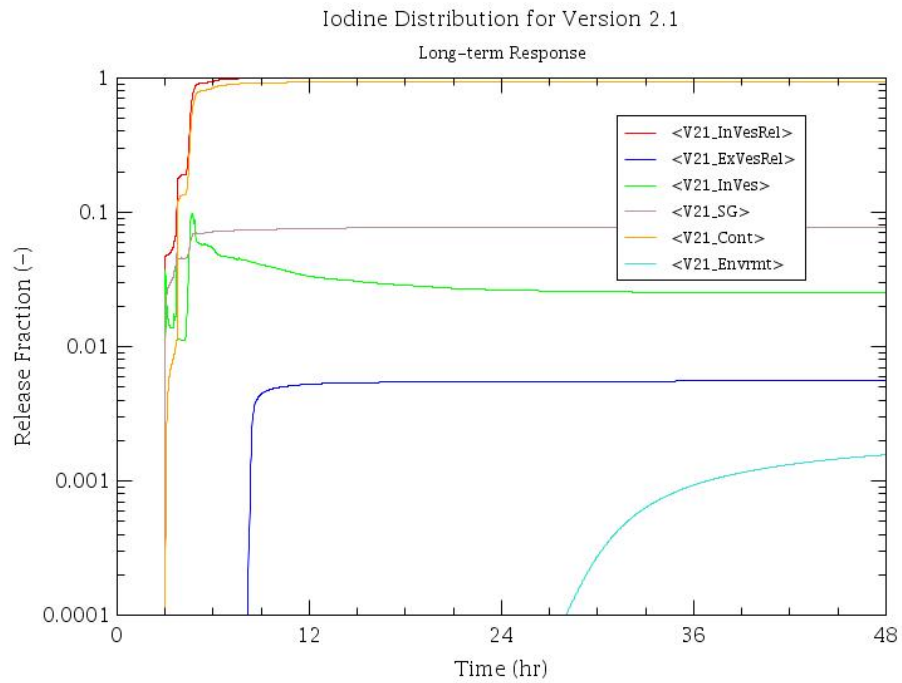
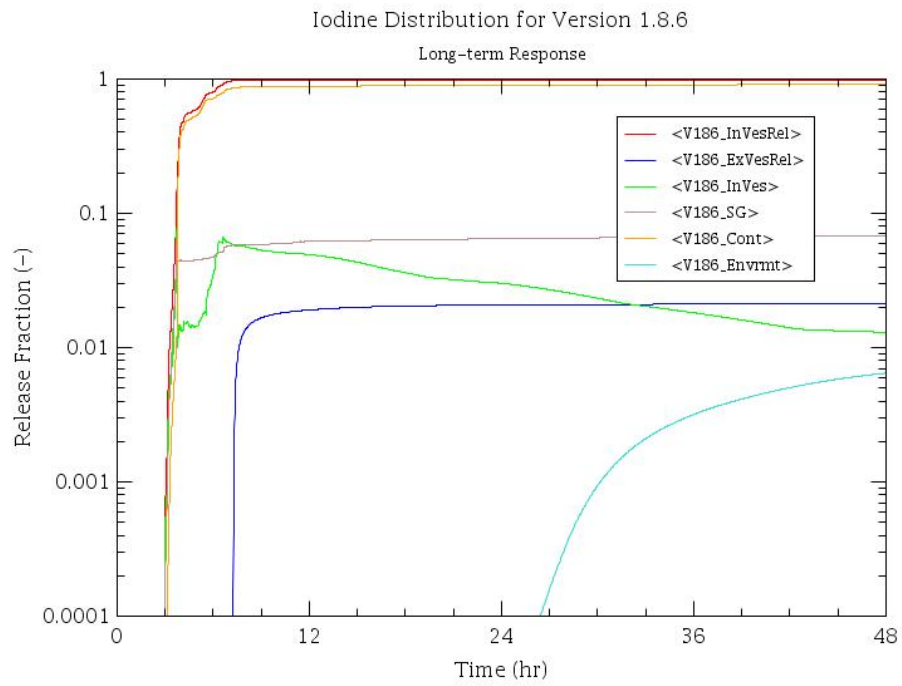


**Figure A-15 Comparison of the MELCOR 1.8.6 and MELCOR 2.1 iodine distributions**

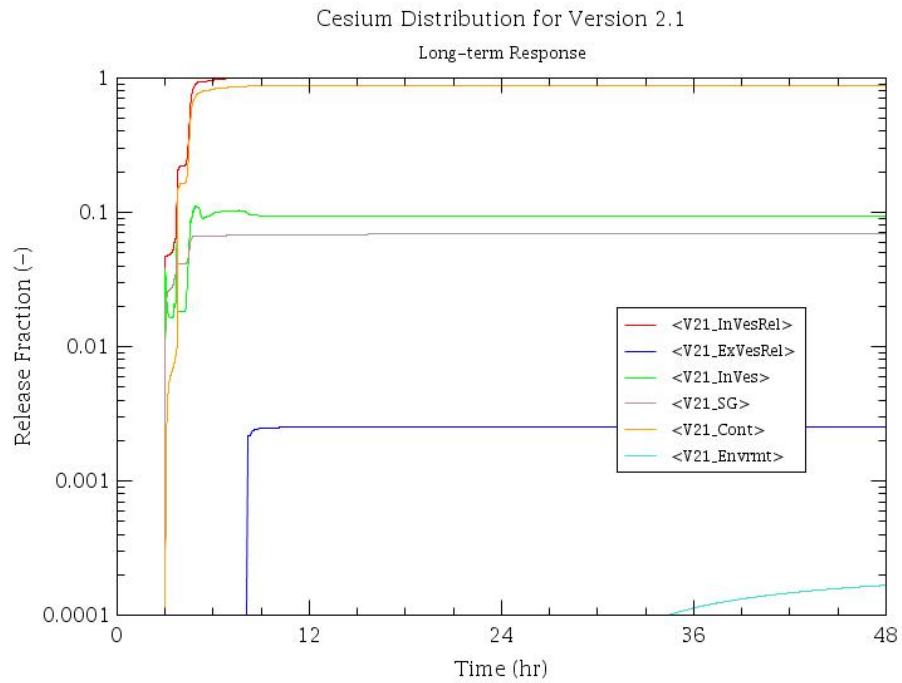
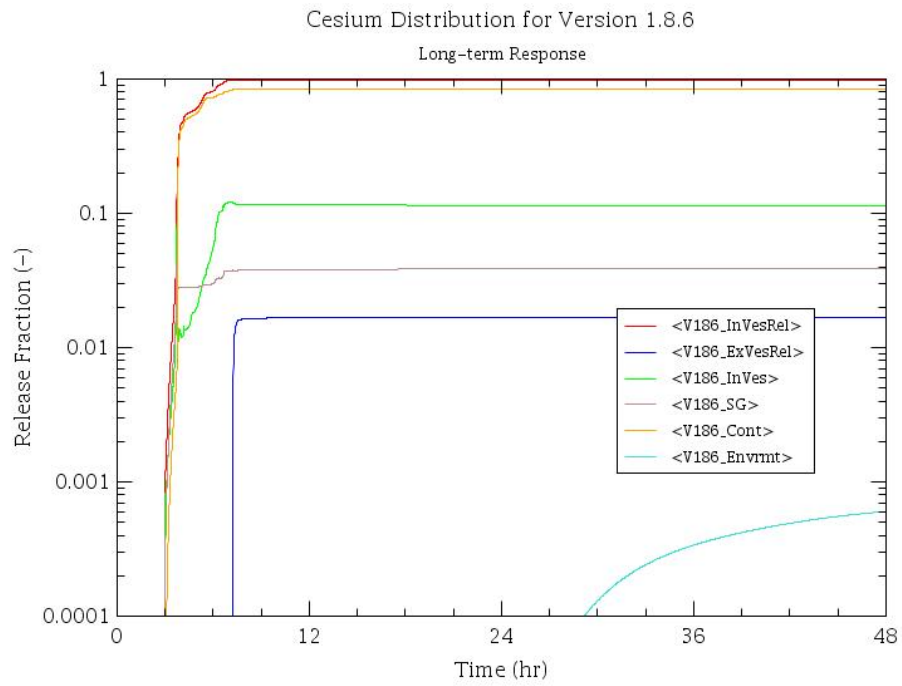


**Figure A-16 Comparison of the MELCOR 1.8.6 and MELCOR 2.1 cesium distributions**

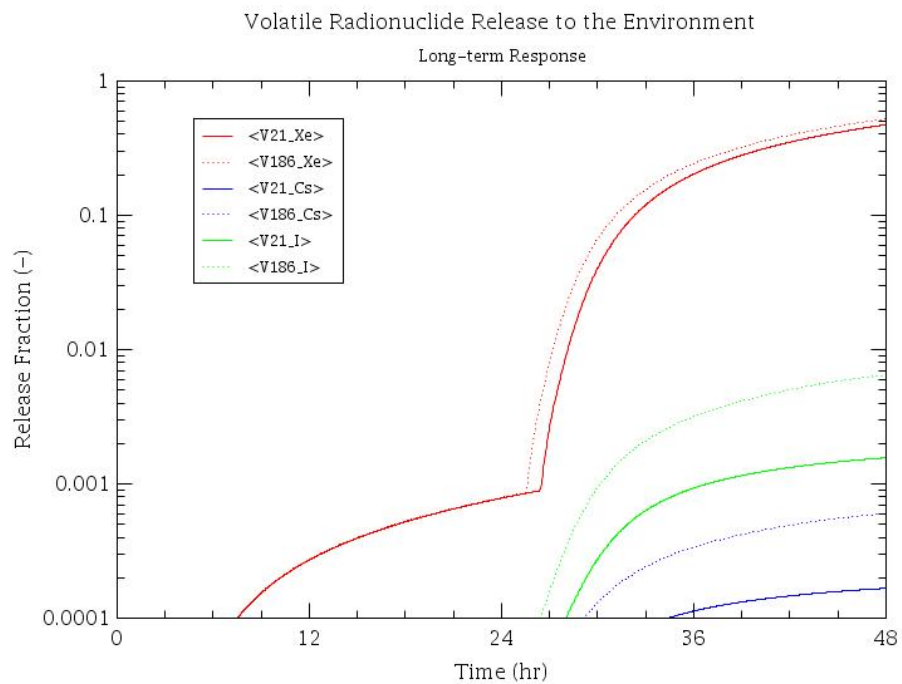


**Figure A-17 Comparison of the MELCOR 1.8.6 SOARCA and MELCOR 2.1 highest volatile radionuclide environmental releases**

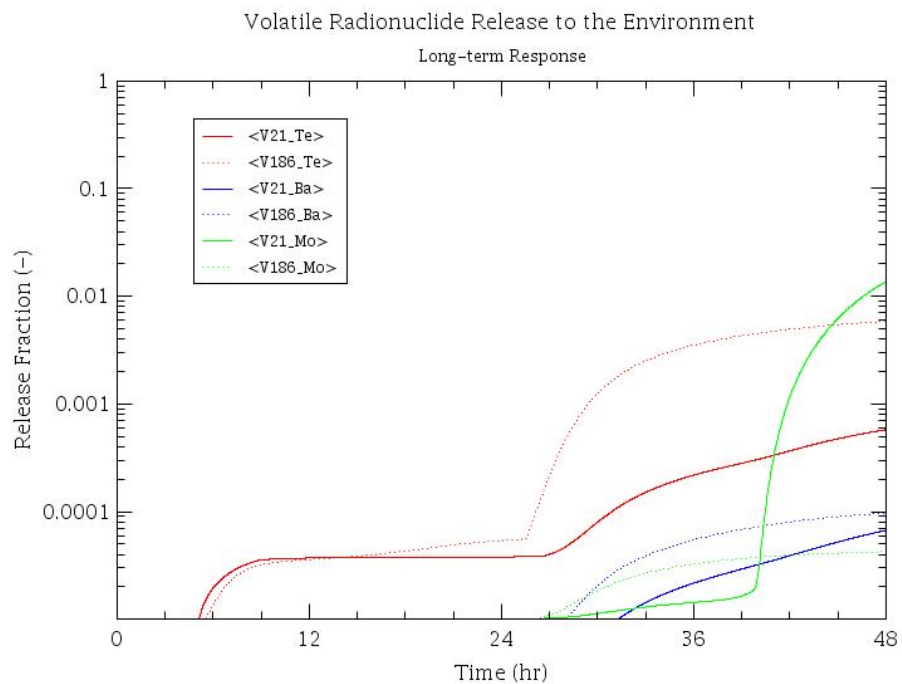


**Figure A-18 Comparison of the MELCOR 1.8.6 SOARCA and MELCOR 2.1 volatile radionuclide environmental releases**

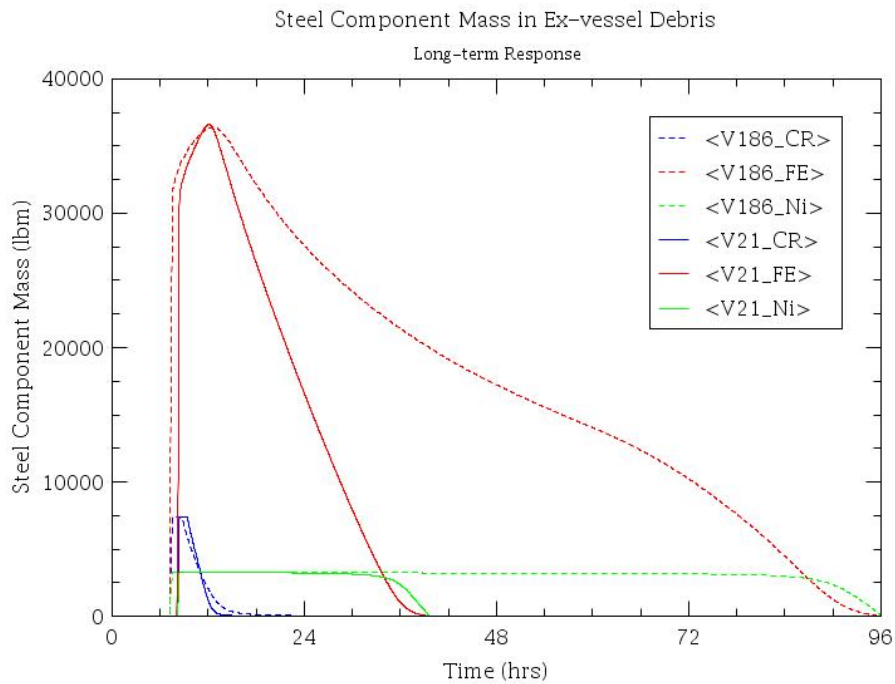


**Figure A-19 Comparison of the MELCOR 1.8.6 SOARCA and MELCOR 2.1 steel components in the ex-vessel debris**

## 2.2 New Decay Heat and Radionuclide Inventory

An updated decay power and radionuclide inventory was calculated using ORIGEN-S/ARP [13] and implemented into the Surry model in order to support the UA. Decay power and inventory are treated as an integrated uncertain parameter in the UA. It should be noted that the entirety of this discussion refers to creating baseline decay heat curves for different times at cycle. Decay heat was also varied from these base curves in the UA by sampling another uncertain parameter. Starting from a truly 'best estimate' and consistent (between MELCOR and MACCS) set of decay power and inventory input facilitates a technically rigorous treatment of the uncertain parameter. The NUREG/CR-7110, Volume 2 model used a decay heat curve from ORIGEN analyses of an extrapolated high burnup core for Surry, in conjunction with an inventory scaled from similar analyses of a Sequoyah reactor [7]. Thus, the decay heat curve used in the model is conservative. In keeping with the best estimate approach intended for the SOARCA project, consistent sets of decay power, lumped MELCOR RN inventories, and nuclide-level MACCS inventories were calculated using ORIGEN-S/ARP (in SCALE6.1.3 [13]) and more realistic Surry plant operating data.

State-of-the-art nuclear data and problem-dependent cross sections are generated using TRITON with the latest ENDF/B-VII.1 library. This provides ORIGEN-S/ARP libraries for the Westinghouse 15x15 assemblies used at Surry for Cycles 18, 19, and 20 over a range of enrichments and burnups. Using plant operating data from these cycles for each fuel assembly, ORIGEN-S/ARP calculations were performed that consider the burnup history, power fraction, and enrichment of each assembly from Cycle 20, which is the cycle chosen to undergo the severe accident initiator. Previously irradiated assemblies at BOC of Cycle 20 are modeled from

Cycles 18 and 19, as is the location of fuel assemblies in the core to ascertain the radial distributions of radionuclide inventory and decay power over MELCOR core rings.

### 2.2.1 Generation of Problem-dependent Data Libraries for ORIGEN-S/ARP

Problem-dependent cross sections and modern ENDF/B-VII.1 nuclear data are incorporated by generating ORIGEN-S/ARP data libraries using the TRITON sequence in SCALE6.1.3. SCALE has numerous pre-generated data libraries for a variety of fuel assemblies and reactor types, including Westinghouse 15x15 fuel like that used in Surry. However, these data libraries were created using older ENDF/B-V data. More modern evaluated nuclear data libraries have improved decay, fission product yield, and gamma emission data, particularly for short-lived nuclides, which supports nuclide summation codes such as ORIGEN in accurately calculating decay heat for short-term applications (e.g. severe accidents) [15]. Since the release of ENDF/B-VI, best estimate predictions of decay heat soon after shutdown are possible with ORIGEN-S and similar codes. Therefore, the TRITON calculations are performed to provide the ORIGEN-S/ARP analyses with data libraries that include the latest ENDF/B-VII.1 data.

### 2.2.2 TRITON (NEWT) Model for Surry 15x15 Fuel Assemblies

TRITON models of a Westinghouse 15x15 fuel assembly were created to support the ORIGEN-S/ARP calculations for the Surry UA. Two basic models were created, as shown in Figure A-20, a full assembly model that depletes all fuel rods uniformly and a quarter-assembly model that takes advantage of geometric symmetry and depletes each fuel rod individually. ORIGEN-S/ARP calculations were performed using the data libraries generated by both models, and the differences caused by the two different TRITON models are quite small (generally less than 1%). The data libraries generated for the quarter-assembly TRITON model with multi-rod depletion were used in the final ORIGEN-S/ARP analyses for the Surry UA.

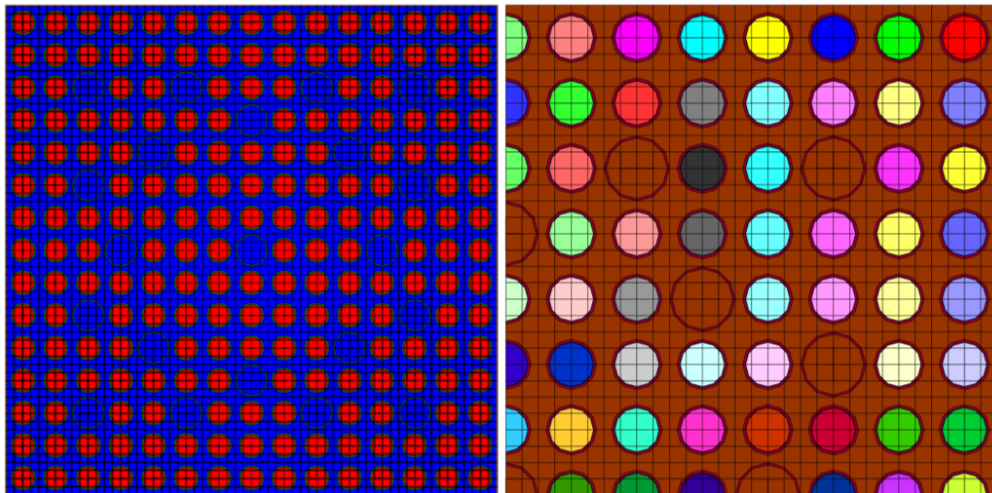


**Figure A-20 TRITON/NEWT models for full 15x15 assembly (left) and quarter-assembly with multi-rod depletion (right)**

The TRITON models burn all fuel material by constant power depletion. The ENDF/B-VII 238 group library is used (“v7-238”) along with CENTRM for cross section processing, which is the one-dimensional discrete ordinates option in SCALE for calculating point-wise energy spectra and preparing the problem-dependent, multigroup data library [13]. A constant moderator

density of 0.72 g/cm<sup>3</sup> is used, and the soluble boron concentration is also assumed constant at a value of 758 ppm, which is informed by Surry operating data. The soluble boron is not depleted in the TRITON simulations as it is assumed the boron concentration is controlled by the operators.

Using the quarter-assembly TRITON model with multi-rod depletion, data libraries for ORIGEN-S/ARP are generated for the Surry enrichment levels present in Cycle 20, which range from 3.8 w/o to 4.25 w/o. The model uses the Surry specific power level (35 MW/MTU) and depletes over a wide range of burnup values, up to about 72 GWd/t.

### **2.2.3 Simplifying Assumptions in TRITON Analyses for Generating ORIGEN-S/ARP Libraries**

The Surry core contains several different types of fuel assemblies. Some assemblies have ZrB<sub>2</sub> Integral Fuel Burnable Absorbers (IFBA), wet annular burnable absorbers (WABA, B<sub>4</sub>C/Al<sub>2</sub>O<sub>3</sub>) in the guide tubes, or flux suppression inserts. These burnable poisons likely have some effect on the flux-weighted cross sections generated for ORIGEN-S/ARP. In the TRITON and ORIGEN-S analyses for the Surry UA, however, each fuel assembly is treated as a Westinghouse 15x15 assembly in an infinite lattice with no fixed burnable poison (i.e. ZrB<sub>2</sub> and WABA assemblies are not considered). This also means that unique cross sections for assemblies adjacent to the reflector are not considered. The letdown curve for the soluble boron in the moderator is not modeled, but the letdown curve is typically not modeled for lattice physics calculations for generating ORIGEN-S/ARP data libraries [13].

### **2.2.4 ORIGEN-S/ARP Calculation Process**

ORIGEN-S/ARP is executed for each fuel assembly in the core from Cycle 20 at Surry using the pre-generated data libraries and Surry operation data from Cycles 18, 19, and 20. This includes each fuel assembly's power fraction, burnup, enrichment, and the number of times each was irradiated. The ORIGEN-S/ARP analyses are intended to have a similar level of detail as the TRITON analyses performed by ORNL for the Peach Bottom SOARCA model [8]. The ORNL analyses generated spatial distributions of inventories and decay power for several axial and radial nodes of the Peach Bottom core. Hence, the analyses for the Surry core consider each fuel assembly individually, since plant data exists on this scale, and the results are lumped over the MELCOR radial nodalization.

### **2.2.5 Surry Plant Operating Data**

The ORIGEN-S/ARP simulations use proprietary operating information from the Surry plant for Cycles 18-20. This includes fuel design details, enrichments, power/burnup distributions, and fuel shuffling schemes. The analyses take into account the numbers of fresh assemblies, once-burned, and twice-burned assemblies at the beginning of Cycle 20.

The raw plant data is pre-processed and mapped onto the COR ring nodalization in the Surry MELCOR model, as shown by Figure A-21. This facilitates later post-processing of the ORIGEN-S output to create radial distributions of decay power and/or MELCOR RN mass.

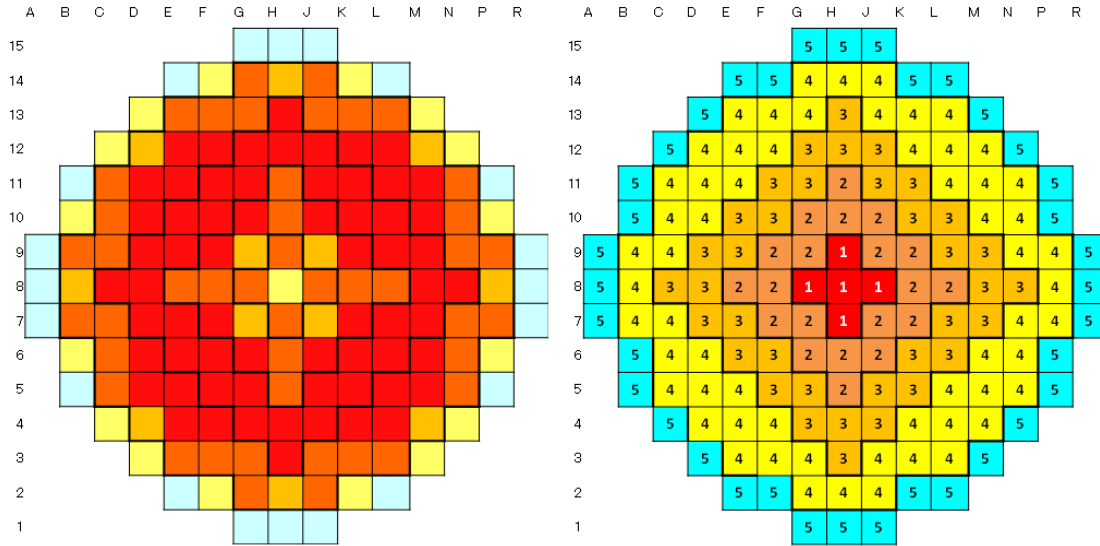


**Figure A-21 Processed Surry data (left) mapped over to MELCOR COR rings (right)**

Table A-2 lists a summary of fuel assembly and core information used for the decay power and inventory calculations for Surry. All of the previously irradiated assemblies in Cycle 20 can be traced back to Cycles 18 and 19, excluding just one assembly (probably from the SFP), which is just treated as an assembly from Cycle 18 since its burnup history is not known.

**Table A-2 Surry reactor information used for ORIGEN-S/ARP analyses.**

Quantity	Value for Surry Cycle 20
Total fuel loading (MTU)	72.58
Power rating (MWt)	2546
Specific power level (MW/MTU)	35.1
Total fuel assemblies in core	157
Number of fuel assemblies in COR Ring 1	5 (3.2% of core)
Number of fuel assemblies in COR Ring 2	20 (12.7% of core)
Number of fuel assemblies in COR Ring 3	36 (22.9% of core)
Number of fuel assemblies in COR Ring 4	60 (38.2% of core)
Number of fuel assemblies in COR Ring 5	36 (22.9 % of core)
Approximate full cycle operating time (days)	505

*\*Includes one extra fuel assembly that was not present in Cycles 18 or 19; it was likely from the SFP, but it is treated as being a twice-irradiated assembly from Cycle 18 for simplicity.*

## 2.2.6 Simplifying Assumptions for ORIGEN-S/ARP Analyses

The ORIGEN-S/ARP calculations only consider the radial variations of burnup, enrichment, and power distributions. Due to modern fuel shuffling strategies, radial distributions of burnup, radionuclide inventories, and decay power can differ greatly from each other. High burnup assemblies in the inner core are typically allocated in a checkerboard-type pattern, which would be homogenized over the inner MELCOR COR rings. In the outer core regions, however, modern fuel shuffling tends to concentrate high burnup assemblies in a ring around the periphery of the core, which acts to concentrate high burnup inventories (e.g., more Cs-137) in the outer MELCOR COR ring (ring 5). The operating and decay power distributions are generally still peaked around the inner regions of the core, indicating higher concentrations of shorter-lived fission products and actinides that drive decay power soon after shutdown. Conversely, enhanced quantities of stable and long-lived nuclides are present in the relatively higher burnup regions of the core, such as in the outer ring(s) of assemblies. The ORIGEN-S/ARP calculations provide insights into such details for MELCOR inputs.

Since there is no axial fuel shuffling, the post-processor for the ORIGEN-S outputs axially allocates radionuclide mass and power according to a time-integrated axial power distribution from nominal reactor operation. General agreement between axial power and burnup distributions permits this simple approach to axial partitioning of the decay power and inventories; i.e. the RN mass and decay power distributions are quite similar. The ORNL TRITON/ORIGEN analyses for Peach Bottom SOARCA considered axial effects, but this is more relevant for a BWR given the enhanced axial variation of moderator density/void fraction and the associated influence on local neutron spectrum and flux-weighted cross sections [8] [13][17].

The exact power histories from the two previous cycles (18 and 19) are also not currently modeled. For example, there were a few brief unplanned outages in these cycles that are neglected. However, the number of previous irradiations for each fuel assembly and the refueling outages are modeled. The BOC burnup distribution for Cycle 20 is recreated in this process. The Surry UA treats the operating time in Cycle 20 as uncertain, which affects the integrated decay heat and inventory uncertain parameter. Therefore, unplanned outages or variations in operating power in Cycle 20 are also neglected in the ORIGEN-S models.

### **2.2.7 Post-processing and Automated Generation of Consistent MELCOR and MACCS Inputs**

Varying the decay heat and inventory entails a fairly large amount of data reduction and input generation for MELCOR and MACCS. Fortunately, Sandia National Laboratories (SNL) developed a highly automated and efficient approach in support of similar efforts for Fukushima-related research [11][19][20][21][22]. A Perl script post-processes outputs from ORIGEN-S and directly generates consistent MELCOR inputs of decay heat and lumped RN-class inventories (including class specific decay heats), along with consistent nuclide-detail input for MACCS.

The Perl script reads ORIGEN-S and OPUS outputs directly for each fuel assembly. OPUS is a SCALE auxiliary tool that is used to assist with some post-processing, such as extracting element-based decay powers, which are later lumped into MELCOR RN class decay powers and an overall core decay power. The generation of ring-based and whole-core values of RN class masses and decay power is a simple matter of summation over the output files for each fuel assembly. No ambiguous scaling or normalization schemes are necessary.

## 2.2.8 Selection of Base Case Conditions for MELCOR and MACCS Models for Surry UA

The decay power and inventory calculated for reactor shutdown near MOC of Cycle 20 are taken to be the new 'base case' inputs for the MELCOR and MACCS models of Surry. A scoping study using ORIGEN-S/ARP was performed to determine how decay power varies with the final cycle operating time. This assisted in the selection of the new base inputs for MELCOR and MACCS, and helps inform the development of the distribution and bounds for the uncertain parameter treatment in the UA. The scoping study examined decay power after scram as a function of the final cycle (20) operating time on logarithmic (Figure A-22) and severe accident time scales for Surry STSBOs (Figure A-23).

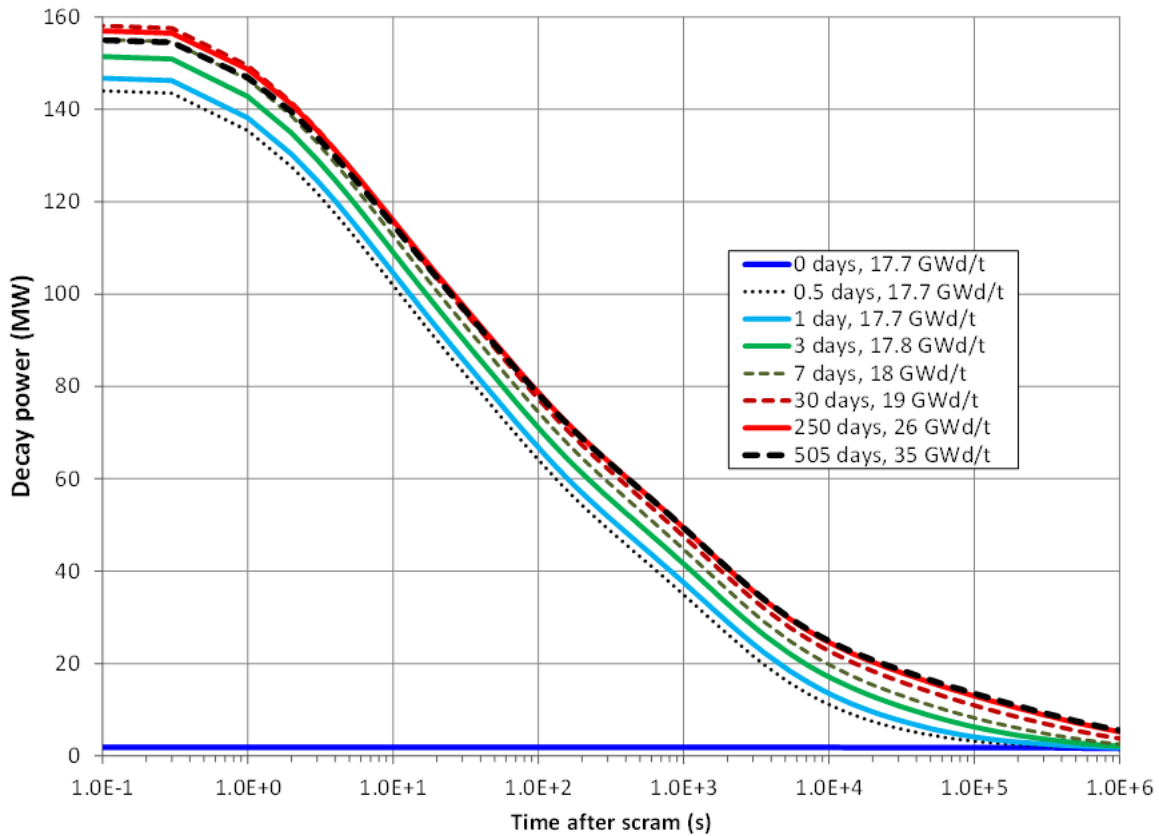
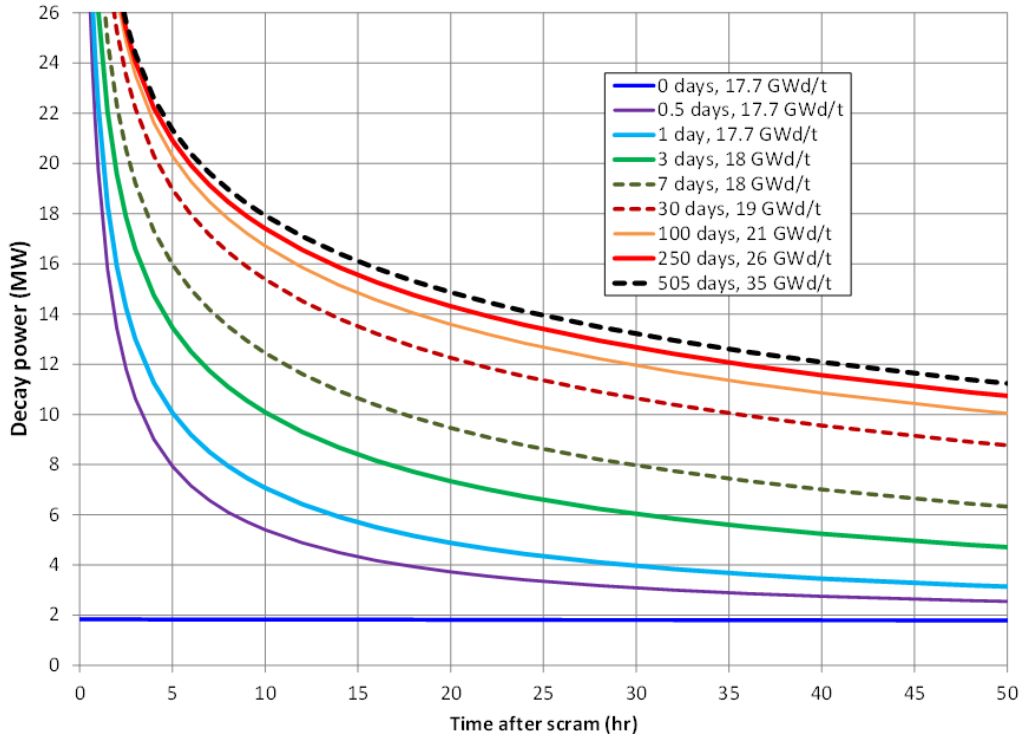
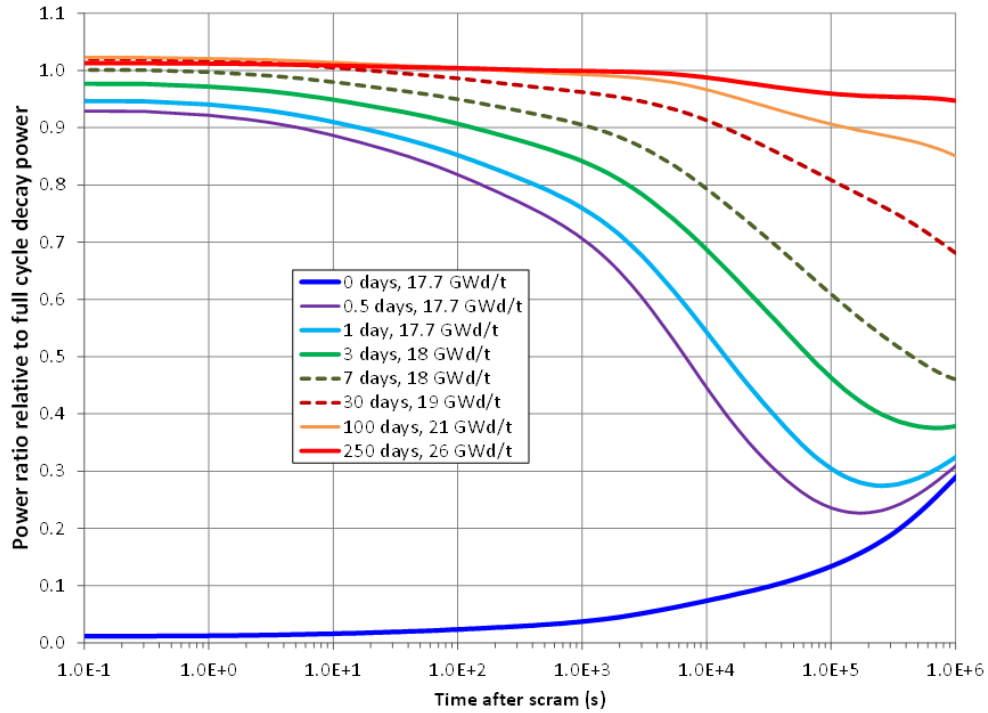


Figure A-22 Decay power on logarithmic time scale for several shutdown times in Cycle 20



**Figure A-23 Decay power on severe accident time scale for several shutdown times in Cycle 20**

Any significant reactor operation results in a decay power of 6 to 7% operating power immediately at shutdown due to quasi-equilibrium levels of short lived nuclides that drive decay power. Concentrations for these nuclides saturate rather quickly with full power operation due to short half-lives and possibly significantly large neutron absorption cross sections. Later in the cycle, the concentrations of these short lived nuclides are mainly influenced by changes in production rate, such as changes in power level, fission yields, and/or reaction rates due to evolving neutron spectrum and flux-weighted cross sections. Since these short lived nuclides drive decay heat immediately after shutdown, and considering these variations for production rate, it is possible for EOC decay power to be slightly lower than MOC for a short period after SCRAM, as seen in Figure A-22. After 10 to 1000 seconds, the decay power for BOC conditions (1 to 30 days operating time) ranges from 30% to 90% of the EOC decay power, as shown in Figure A-24 and Figure A-25. These two figures depict decay power curves for several operating times, normalized to the EOC decay power. Near-MOC conditions (100 to 250 days) exhibit decay power curves that are very similar to the EOC decay power for times near shutdown. After a few hours, MOC decay power is 90% to 95% of the EOC decay power. Differences in decay power hours after scram are indicative of different concentrations of medium and longer-lived fission products that are the result of varying burnup levels.



**Figure A-24** Decay power on logarithmic time scale relative to full-cycle EOC decay power

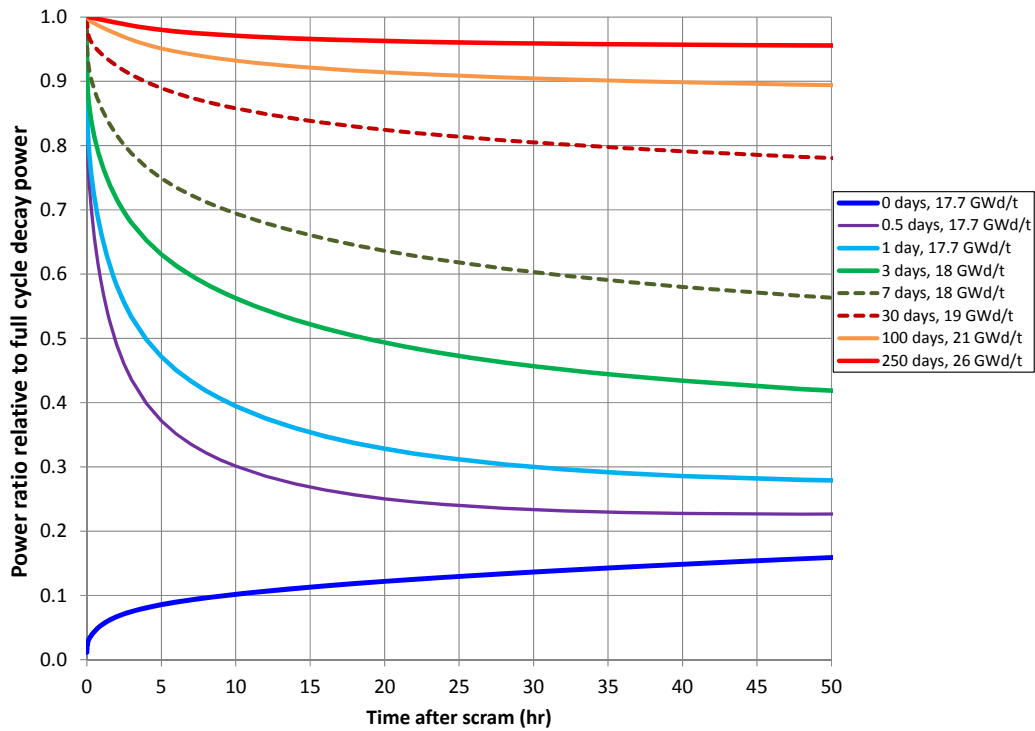


**Figure A-25** Decay power on severe accident time scale relative to full-cycle EOC decay power

The Surry UA aims to quantify the effects of shutdown time over the entire range of Cycle 20, including the effects of varied decay power later after shutdown during severe accident phenomena such as core degradation/oxidation, RPV failure, and MCCI. The differences between MOC and EOC decay power support such analyses. Therefore, an MOC operating time of 200 days is selected to provide the decay power and inventory for the new base case MELCOR model. The resulting decay power is about 95% of the EOC decay power after about 18 hours since shutdown, as depicted in Figure A-26. This MOC condition is also one of the realization values for the decay heat and inventory uncertain parameter in the UA. The new base-case decay power for the Surry MELCOR model at MOC conditions is shown on a logarithmic time scale in Figure A-27. The base MOC curve is compared to the SOARCA decay heat curve, which is conservative given that it reflects an extrapolated high burnup state. The SOARCA decay heat exhibits 'lumps' in its curve since it used a very coarse time-mesh for the tabular function in the MELCOR model, which MELCOR linearly interpolates between tabular functions entries.

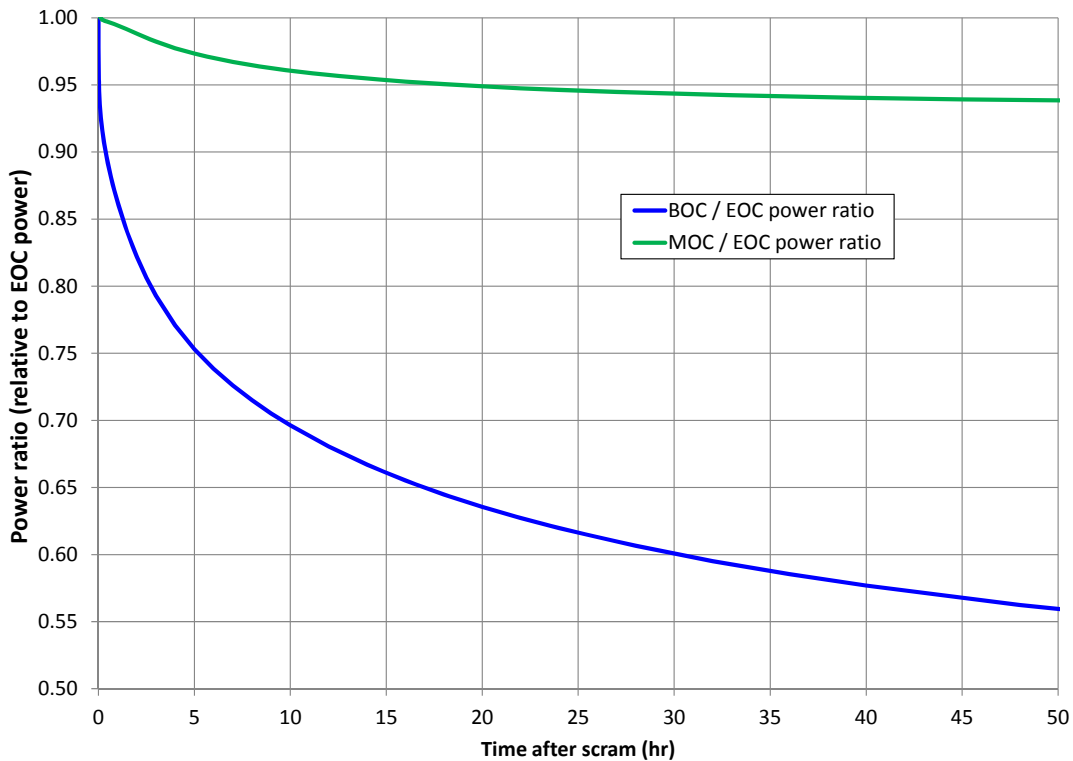


**Figure A-26 BOC and MOC decay powers relative to full-cycle EOC decay power**

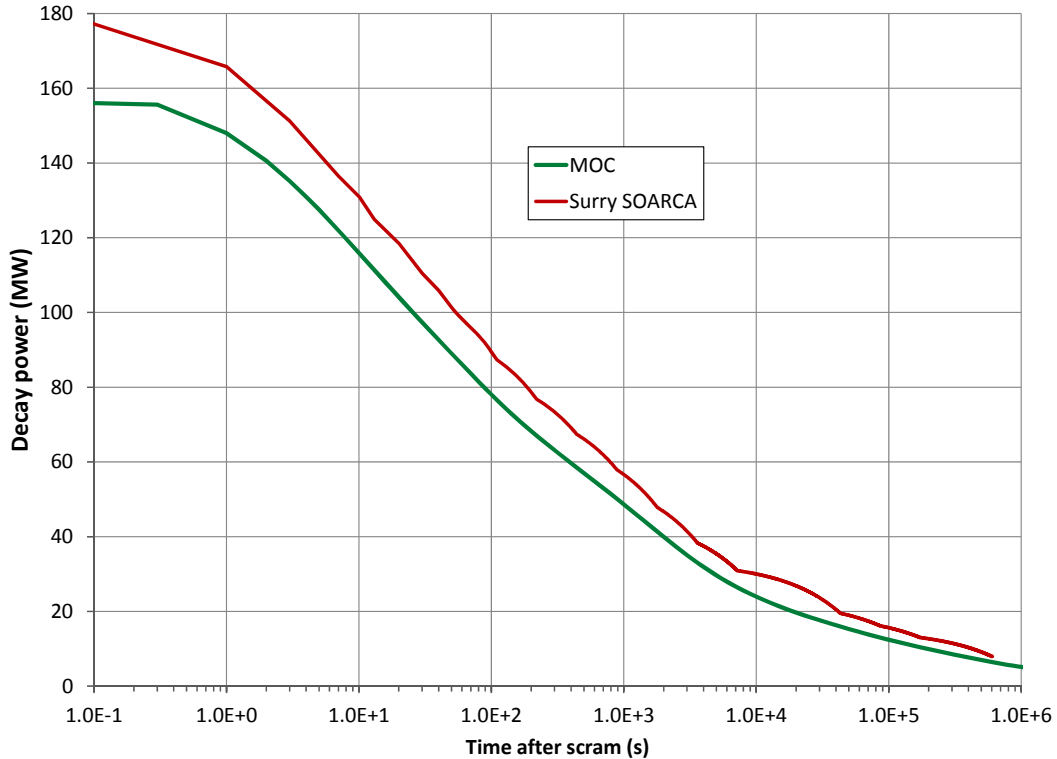


**Figure A-27 New base-case decay heat curve for MELCOR Surry model at MOC conditions**

### 2.2.9 MELCOR Decay Power and Inventory Inputs for Surry UA

The ORIGEN-S/ARP calculations and post-processing provides sets of consistent decay power and inventory information for MELCOR and MACCS to support the Surry UA. Three predetermined conditions were generated for BOC, MOC, and EOC to capture the inherent uncertainty of when the accident initiator occurs in the final cycle. It was observed in the scoping study that the decay power for 0-3 days of operation is very small compared to the EOC decay power, especially for hours after scram important for severe accident phenomena (i.e. after core uncover and damage). Thus, a BOC operating time of 7 days is selected to permit investigation of significantly reduced decay power soon after shutdown (see Figure A-28), but not such that it excessively reduces power to avoid gross core damage altogether. As discussed in the previous section, the MOC operating time of 200 days is chosen because it is relatively similar to the EOC decay power until about 18 hours after scram, and this facilitates examining the influence of varied decay power during later stages of severe accident progression. The EOC operating time is taken to be the actual operating duration of Cycle 20 (about 505 days), which therefore considers the effects of a larger inventory and higher decay heat later into the accident for the UA, while still being a realistic burnup state of the reactor (i.e., it is not a hypothetical condition extrapolated to very high burnup). The BOC, MOC, and EOC decay power curves for the Surry UA are depicted in Figure A-28 on a severe accident time frame. The same information is portrayed in Figure A-29 but normalized to the EOC decay power and on a logarithmic time scale. It better shows the quantitative details of the decay powers soon after shutdown and for longer cooling times up to  $10^6$  seconds, or about 278 hours.

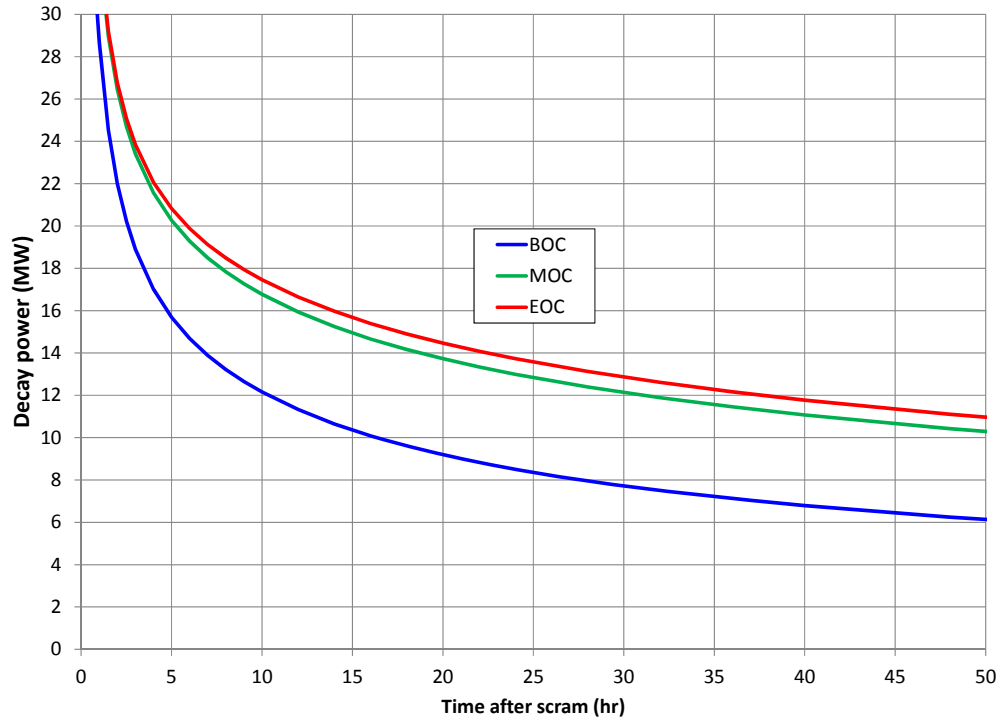


**Figure A-28 BOC, MOC, and EOC decay powers for Surry UA on severe accident time scale**

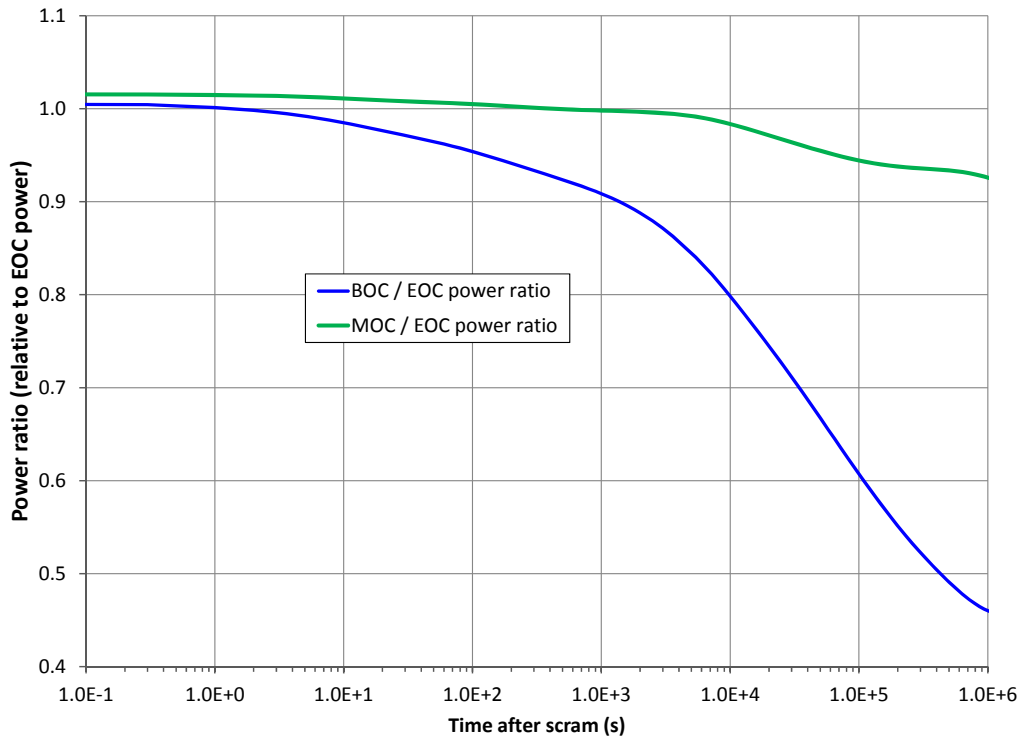


**Figure A-29 BOC and MOC decay power normalized to EOC power on a logarithmic scale**

The lumped MELCOR RN inventories calculated by ORIGEN-S/ARP for BOC, MOC, and EOC are listed in Table A-3. The SOARCA inventory is also listed for comparison. MELCOR RN class masses are dominated by long-lived and stable nuclides; thus RN class mass builds monotonically and nearly linearly with burnup, excluding the iodine and uranium class masses. Therefore the scaled inventory used in SOARCA nearly matches the EOC inventory (however, larger differences can exist in the MACCS inventories for key isotopes, as described in the following section). The inclusion of stable nuclides in RN mass is important for radionuclide transport calculations in MELCOR [9][11]. For example, overall aerosol masses affect the conglomeration and deposition of aerosols [9][24]. The selection of operating times from nearly-BOC (7 days) to the full 505 day cycle permits analyses that span the full range of potential MELCOR and MACCS inventories for a chosen cycle. The default speciation of cesium, iodine, and molybdenum classes for each point in the cycle are taken from SOARCA methodology [7][8], which are informed by experimental data from the Phebus and VERCORS programs [23]. However, these base speciations are varied by the UA Chemform parameters. The variations across the lumped MELCOR inventories (BOC vs. EOC) are summarized in Table A-4.

**Table A-3 Lumped MELCOR RN inventories for Surry.**

#	Class (representative)	BOC (kg)	MOC (kg)	EOC (kg)	SOARCA (kg)
1	Noble Gases (Xe)	224.28	310.53	444.45	448.1
2	Alkali Metals (Cs)	5.97	8.19	11.51	11.7
3	Alkaline Earths (Ba)	95.05	132.97	186.03	187.6
4	Halogens (I)	all in CsI	all in CsI	all in CsI	all in CsI
5	Chalcogens (Te)	20.87	28.78	41.42	40.9
6	Platinoids (Ru)	146.47	202.43	304.79	309.5
7	Early Transition Elements (Mo)	125.92	170.62	244.06	243.3
8	Tetravalent (Ce)	628.55	867.65	1164.17	1225.9
9	Trivalent (La)	307.71	422.00	608.30	621.2
10	Uranium (U)	73827.20	73172.91	72207.44	66771.30
11	More Volatile Main Group (Cd)	4.11	5.46	8.49	7.263
12	Less Volatile Main Group (Sn)	4.55	6.28	9.66	9.19
16	Cesium Iodide (CsI)	17.24	23.92	34.54	34.82
17	Cesium Molybdate (Cs <sub>2</sub> MoO <sub>4</sub> )	154.50	211.78	297.75	302.47
	Total cesium class mass	128.32	176.04	247.96	251.76
	Total iodine class mass	8.42	11.68	16.87	17.01
	Total molybdenum class mass	166.90	226.78	323.02	323.52

**Table A-4 Variations in lumped MELCOR RN inventories for Surry.**

#	Class (representative)	BOC to MOC % change	BOC to EOC % change	MOC to EOC % change	EOC % difference with SOARCA
1	Noble Gases (Xe)	38.5	98.2	43.1	-0.8
2	Alkali Metals (Cs)	37.1	92.7	40.6	-1.6
3	Alkaline Earths (Ba)	39.9	95.7	39.9	-0.8
4	Halogens (I)	NA	NA	NA	NA
5	Chalcogens (Te)	37.9	98.5	43.9	1.2
6	Platinoids (Ru)	38.2	108.1	50.6	-1.5
7	Early Transition Elements (Mo)	35.5	93.8	43.0	0.3
8	Tetravalent (Ce)	38.0	85.2	34.2	-5.3
9	Trivalent (La)	37.1	97.7	44.1	-2.1
10	Uranium (U)	-0.9	-2.2	-1.3	7.5
11	More Volatile Main Group (Cd)	32.8	106.5	55.5	14.4
12	Less Volatile Main Group (Sn)	37.9	112.3	54.0	4.9
16	Cesium iodide (Csl)	38.7	100.3	44.4	-0.8
17	Cesium molybdate (Cs <sub>2</sub> MoO <sub>4</sub> )	37.1	92.7	40.6	-1.6
	Total cesium class mass	37.2	93.2	40.9	-1.5
	Total iodine class mass	38.7	100.3	44.4	-0.8
	Total molybdenum class mass	35.9	93.5	42.4	-0.2

### 2.2.10 MACCS Input for the New Base Case and for Surry UA

MACCS requires isotopic breakdowns of the RN classes present in the MELCOR source term output. It accomplishes this task through a pre-processing program called MELMACCS, which takes user input masses and activities for nuclides separated by ORIGEN-S output libraries (i.e. light elements, actinides, and fission products) and reactor model type. MELMACCS requires both nuclide mass and activity because it does not contain nuclear decay data such as decay constants. The nuclide masses were historically used to linearly scale the activities for each nuclide by comparing the appropriate MELCOR class mass (in the MELCOR plot file) to the class mass in MELMACCS, which is calculated by summing the applicable user-specified nuclide masses. This process allowed for rough usage of inconsistent source terms and nuclide inventories, if desired. However, the SNL process for automatic generation of consistent MELCOR and MACCS inventories directly from ORIGEN-S output supersedes the need for the scaling algorithm. Thus for the Surry UA, class masses in MELCOR and MACCS are completely consistent.

Activities for key nuclides in Cycle 20 at Surry are calculated by ORIGEN-S/ARP and compared in Table A-5, Table A-6, and Table A-7. The SOARCA nuclide inventories are listed to highlight the important effects that different burnup levels and nuclear data (ENDF/B-VII.1) have on isotopic inventory predictions. Differences in isotope and isomer inventories are not nearly as simple and straight-forward as the lumped RN mass inventories.

**Table A-5 MACCS nuclide inventories (in Bq) for Xe, Cs, Ba, I, and Te classes.**

Isotope	BOC	MOC	EOC	SOARCA	EOC % difference with SOARCA
<b>Noble gases (Xe)</b>					
Kr-85	1.59E+16	2.17E+16	2.94E+16	2.94E+16	0.0
Kr-85m	8.56E+17	7.77E+17	6.76E+17	8.07E+17	-19.4
Kr-87	1.74E+18	1.56E+18	1.34E+18	1.60E+18	-19.7
Kr-88	2.32E+18	2.06E+18	1.76E+18	2.14E+18	-21.5
Xe-133	2.78E+18	5.31E+18	5.27E+18	6.07E+18	-15.1
Xe-135	1.51E+18	1.46E+18	1.31E+18	1.80E+18	-37.4
Xe-135m	1.04E+18	1.09E+18	1.12E+18	1.29E+18	-14.9
<b>Alkali metals (Cs)</b>					
Cs-134	1.84E+17	2.49E+17	4.16E+17	4.32E+17	-3.8
Cs-136	1.97E+16	7.13E+16	1.10E+17	1.57E+17	-43.0
Cs-137	1.53E+17	2.11E+17	3.00E+17	3.05E+17	-1.6
Rb-86	1.02E+15	3.38E+15	5.63E+15	5.36E+15	4.8
Rb-88	2.34E+18	2.09E+18	1.79E+18	2.16E+18	-20.5
<b>Alkali earths (Ba)</b>					
Ba-139	4.72E+18	4.79E+18	4.65E+18	5.54E+18	-19.1
Ba-140	1.72E+18	4.63E+18	4.48E+18	5.37E+18	-19.9
Sr-89	1.14E+18	2.77E+18	2.48E+18	2.98E+18	-20.4
Sr-90	1.19E+17	1.63E+17	2.22E+17	2.27E+17	-2.2
Sr-91	3.94E+18	3.56E+18	3.09E+18	3.75E+18	-21.2
Sr-92	4.12E+18	3.76E+18	3.34E+18	4.00E+18	-19.8
Ba-137m	1.46E+17	2.01E+17	2.86E+17	2.92E+17	-2.0
<b>Halogens (I)</b>					
I-131	1.09E+18	2.49E+18	2.55E+18	2.78E+18	-9.0
I-132	2.80E+18	3.74E+18	3.76E+18	4.08E+18	-8.5
I-133	5.31E+18	5.25E+18	5.22E+18	5.76E+18	-10.2
I-134	6.09E+18	6.01E+18	5.89E+18	6.48E+18	-10.1
I-135	5.04E+18	5.02E+18	5.00E+18	5.49E+18	-9.8
<b>Chalcogens (Te)</b>					
Te-127	1.11E+17	1.89E+17	2.23E+17	2.60E+17	-16.6
Te-127m	9.28E+15	1.60E+16	1.77E+16	4.22E+16	-138.1
Te-129	5.10E+17	6.05E+17	6.69E+17	7.79E+17	-16.4
Te-129m	3.49E+16	8.97E+16	9.82E+16	1.49E+17	-51.8
Te-131	2.14E+18	2.18E+18	2.20E+18	2.55E+18	-16.0
Te-131m	3.74E+17	4.33E+17	4.75E+17	5.71E+17	-20.3
Te-132	2.77E+18	3.60E+18	3.63E+18	4.29E+18	-18.1

**Table A-6 MACCS nuclide inventories (in Bq) for Ru, Mo, and Ce classes.**

Isotope	BOC	MOC	EOC	SOARCA	EOC % difference with SOARCA
<b>Platinoids (Ru)</b>					
Rh-105	1.52E+18	1.91E+18	2.38E+18	2.90E+18	-21.8
Ru-103	1.39E+18	3.42E+18	3.93E+18	4.61E+18	-17.4
Ru-105	1.68E+18	2.17E+18	2.72E+18	3.14E+18	-15.6
Ru-106	6.17E+17	8.34E+17	1.25E+18	1.40E+18	-11.7
Rh-103m	1.37E+18	3.38E+18	3.89E+18	4.61E+18	-18.6
Rh-106	7.19E+17	9.74E+17	1.45E+18	1.56E+18	-7.2
<b>Early transition metals (Mo)</b>					
Nb-95	2.35E+18	3.98E+18	4.33E+18	5.18E+18	-19.6
Co-58	1.37E+13	2.65E+13	2.78E+13	4.79E+13	-72.2
Co-60	1.66E+15	2.29E+15	3.26E+15	2.65E+14	91.9
Mo-99	4.03E+18	4.82E+18	4.77E+18	5.68E+18	-19.1
Tc-99m	3.47E+18	4.25E+18	4.33E+18	5.03E+18	-16.2
Nb-97	4.59E+18	4.51E+18	4.35E+18	5.24E+18	-20.3
Nb-97m	4.37E+18	4.26E+18	4.12E+18	4.95E+18	-20.2
<b>Tetravalents (Ce)</b>					
Ce-141	1.57E+18	4.31E+18	4.21E+18	4.87E+18	-15.7
Ce-143	4.26E+18	4.18E+18	3.95E+18	4.55E+18	-15.2
Ce-144	1.81E+18	2.59E+18	3.15E+18	3.42E+18	-8.5
Np-239	3.49E+19	4.26E+19	4.78E+19	5.67E+19	-18.7
Pu-238	2.83E+15	4.08E+15	7.31E+15	8.31E+15	-13.6
Pu-239	5.05E+14	7.05E+14	8.26E+14	9.56E+14	-15.7
Pu-240	5.96E+14	8.07E+14	1.18E+15	1.17E+15	0.8
Pu-241	1.61E+17	2.13E+17	3.20E+17	3.39E+17	-5.8
Zr-95	1.99E+18	4.28E+18	4.31E+18	4.96E+18	-15.0
Zr-97	4.59E+18	4.48E+18	4.33E+18	5.00E+18	-15.6

**Table A-7 MACCS nuclide inventories (in Bq) for La class.**

Isotope	BOC	MOC	EOC	SOARCA	EOC % difference with SOARCA
<b>Trivalentes (La)</b>					
Am-241	1.75E+14	2.53E+14	3.98E+14	3.43E+14	13.8
Cm-242	3.70E+16	5.43E+16	1.03E+17	1.14E+17	-11.0
Cm-244	2.33E+15	3.64E+15	8.55E+15	1.13E+16	-32.1
La-140	1.35E+18	4.71E+18	4.61E+18	5.67E+18	-23.1
La-141	4.48E+18	4.37E+18	4.23E+18	5.10E+18	-20.6
La-142	4.39E+18	4.25E+18	4.07E+18	4.92E+18	-20.9
Nd-147	6.80E+17	1.70E+18	1.66E+18	2.04E+18	-22.6
Pr-143	1.24E+18	4.19E+18	3.95E+18	4.65E+18	-17.7
Y-90	1.21E+17	1.67E+17	2.30E+17	2.39E+17	-4.1
Y-91	1.49E+18	3.49E+18	3.21E+18	3.93E+18	-22.6
Y-92	4.17E+18	3.81E+18	3.38E+18	4.11E+18	-21.7
Y-93	4.49E+18	4.18E+18	3.80E+18	4.62E+18	-21.5
Y-91m	2.32E+18	2.10E+18	1.82E+18	2.20E+18	-20.8
Pr-144	1.82E+18	2.62E+18	3.18E+18	3.63E+18	-14.2
Pr-144m	2.15E+16	4.01E+16	4.67E+16	5.06E+16	-8.3

The isotopic inventories for BOC, MOC, and EOC calculated using ORIGEN S are implemented in MeIMACCS for the consequence analyses in the Surry UA. Consequently, three MeIMACCS inventories are used in the Surry UA. The time at cycle was a simple random sample selection with a uniform distribution within the MELOCR uncertainty inputs. While time at cycle is a uniform distribution, simple random sampling resulted in an uneven amount of BOC (390), MOC (390), and EOC (420) input samples. Additionally, of the 1200 MELCOR runs initially submitted for analysis, only 1003 ran to completion (83% success rate) with the BOC and MOC MELCOR runs having a higher success rate (~84.3%) as compared to the success rate for the EOC MELCOR runs (~82.1%). Additionally, the final number of BOC (329), MOC (329), and EOC (345) MELCOR runs are random distributed throughout the set of successful MELCOR runs. This means the first set of successful MELCOR runs (e.g., realizations 1 to 390) are not a single time at cycle, but instead each time at cycle is randomly distributed.

## **2.3 Summary of the Model Corrections and Improvements Not Included in the Uncertainty Sampling**

The model corrections and improvements are described in this section and Section 2.4. Some model corrections implemented are a result of an improved understanding of the Surry plant. Those model improvements included an improved SG nodalization and improvements to the calculation of the hot leg nozzle creep rupture. The model corrections and improvements in this section are not included in the UA uncertainty sampling. The model enhancements included as sampled uncertainty variables are described in Section 2.4.

### **2.3.1 Concrete type**

There was a long-standing error in the Surry concrete type. The constituency of the aggregate in the Surry containment was corrected to be basaltic rather than limestone. The correct concrete type was confirmed from the plant documentation. Researchers at CEA Cadarache cite the following differences between limestone and silica-rich (i.e., basaltic) concrete [27]. The ablation of limestone-rich concretes is almost isotropic, whereas the ablation of silica-rich (i.e., basaltic) concretes is much faster towards the sides than towards the bottom of the cavity; limestone concretes liberate about twice as much gas, at a given ablation rate than siliceous concretes; limestone concrete has a higher liquidus temperature than siliceous concrete and the molten limestone concrete has a larger diffusion coefficient and can more easily dissolve a corium crust than siliceous melt.

The nodalization of the reactor cavity was also extended upward to increase the available height for debris to remove the potential for core-concrete debris overflowing the cavity. This extended nodalization is a more realistic representation of the Surry cavity.

### **2.3.2 Hot leg creep rupture modeling**

Several locations are monitored in the reactor system circulation (RCS) for failure rupture during the high temperature phase of the accident. Natural circulation flows from the core during the core degradation phase circulate hot steam from the core to upper reactor internals, the hot leg, and the steam generators (i.e., the natural circulation pattern on the right-hand side of Figure A-30). The resultant heating of the RCS and the steam generator piping increases the thermal stress, which can lead to pressure boundary failure and a subsequent depressurization. The MELCOR 1.8.6 SOARCA model monitored for the potential creep rupture failures at the hot leg nozzle, the RCS piping, the pressurizer surge line, and the SG tubes near the inlet of the steam generator. The hot leg nozzle (shown in Figure A-31) is a relatively complex structure that includes a large carbon steel nozzle that interfaces with the stainless steel hot leg piping. The end of the nozzle (i.e., the safe end) is field welded to the hot leg piping. The most vulnerable part of the nozzle is adjacent to the safe end, where the nozzle connects to the hot leg piping. This is seen in Figure A-31 directly to the left of the safe-end where the outer diameter is still the same as the hot leg piping. The hot leg nozzle is made from carbon steel and clad with stainless steel.

The MELCOR 1.8.6 SOARCA creep rupture model modeled the structure as carbon steel (i.e., the creep rupture correlations were only developed for a uniform material property). The approach neglected the 3/8" stainless steel cladding in the piping. However, experience from the Davis-Besse reactor pressure vessel head degradation illustrates the strength and importance of the stainless steel layer. Boric acid had degraded the vessel head at Davis-Besse such that the remaining thickness of the RPV head in the wastage area was found to be approximately 3/8 inch. This thickness consisted of the thickness of the stainless steel cladding on the inside surface of the RPV head, which is nominally 3/8 inch. The stainless steel cladding without support by the carbon steel head withstood the full reactor pressure during normal operation.

An innovative approach was implemented into the UA model that accounted for both the carbon steel nozzle and the stainless steel cladding. The new approach first determines if the thermal stress has failed the carbon steel portion of the nozzle (i.e., same as MELCOR 1.8.6 SOARCA model). If the carbon steel fails, then the stainless steel cladding is the primary pressure boundary. Next, the stainless steel cladding is monitored for creep rupture. Consequently, both

components must fail to develop a breach in the RCS. Interestingly in the UA results, it was observed that once the carbon steel fails, the stainless steel also fails almost instantaneously, and does not provide the delay in hot leg nozzle creep, expected based on observations at Davis-Besse.

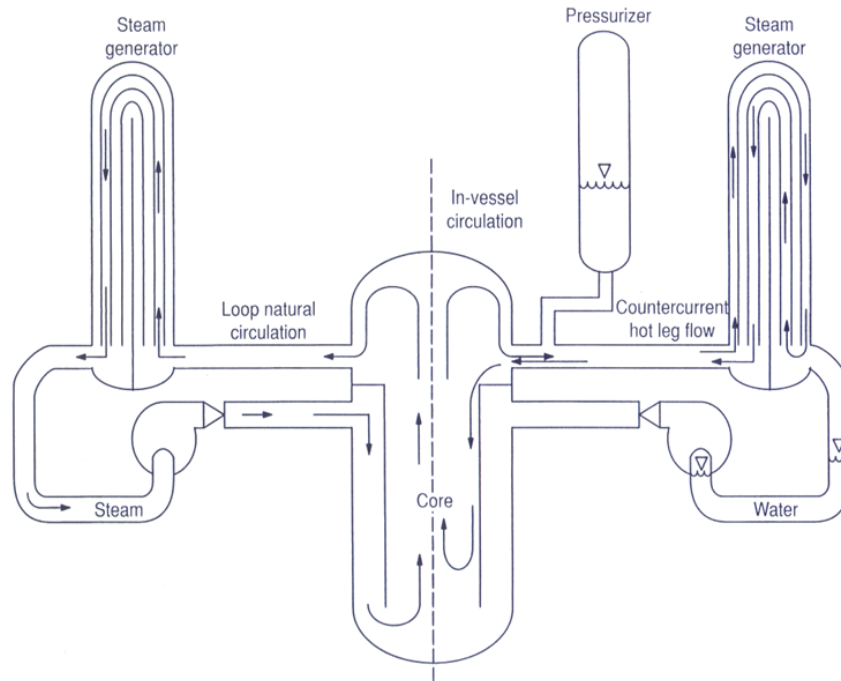
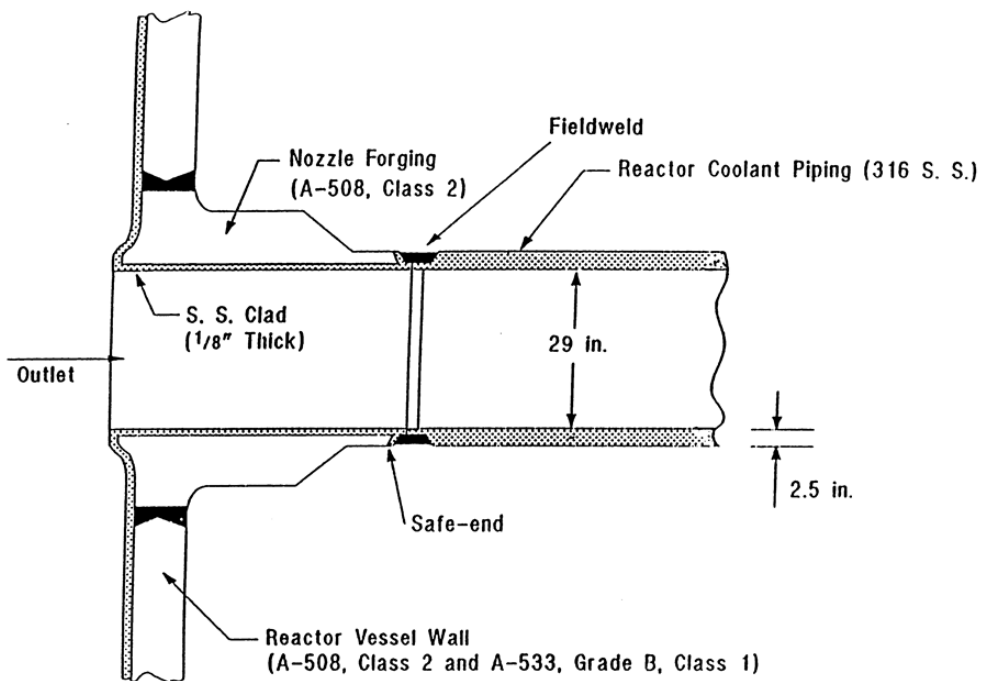


Figure A-30 Natural circulation flow patterns in a PWR [28]



## Figure A-31 Illustration of hot leg nozzle [29]

### 2.3.3 Tin aerosol release model

There is trace amount of tin (1.45 wt%) in the zircaloy cladding of the Surry fuel. The NUREG/CR-7110, Volume 2 Surry SOARCA calculations did not include tin release from the cladding. It was not believed to be important relative to the Ag-In-Cd aerosol source. In contrast, a BWR has considerably more tin from the zircaloy cladding and the canisters. Consequently, the Peach Bottom BWR SOARCA model [31] included a tin release model from the zircaloy cladding and canisters. The nonradioactive tin is released as a vapor from the cladding at high temperatures. A parametric release model is adjusted to approximate experimental observations from Phebus [23]. In Phebus posttest inspections, the tin content in unoxidized Zircaloy is significantly reduced from its normal levels but not completely depleted. In contrast, no tin is typically found in remnants of  $ZrO_2$ . The total quantity of tin measured on downstream surfaces represents roughly half of the total mass available. The tin vapor quickly aerosolizes after being released as a vapor in enough abundance to affect overall aerosol agglomeration. Based on the observations from the BWR SOARCA analyses [31], the PWR structural tin release model was assessed to also be important in PWR analysis. Consequently, a tin release model added to the UA Surry model.

### 2.3.4 Cavity heat transfer modeling

In the original SOARCA calculations, the cavity debris conductivity and heat transfer to the overlying water was enhanced to reflect observations from MACE tests. Ex-vessel core-concrete experiments, such as the MACE experiments predicted maximum heat transfer from the debris to the liquid could reach  $4 \text{ MW/m}^2$  [32]. This was over an order of magnitude higher than the rate predicted by MELCOR. It was determined that the MELCOR ex-vessel debris-to-water heat transfer models were limited by conduction through the debris. Consequently, multipliers were applied to the metallic and oxide debris conductivities to increase heat flow to the water. While this approach improved the agreement with the MACE heat fluxes, it also led to excessive concrete erosion when water was not present.

The ex-vessel debris behavior model was improved in 2012 to address deficiencies in the debris to water heat transfer modeling. The new features physically accentuate ex-vessel heat rejection from core debris to an overlying pool of water. The accentuated heat rejection, illustrated in Figure A-32, is managed via:

- A multiplier on conduction heat transfer within the debris top crust to account for the ingress of water through fissures in the crust and the associated increased area for boiling and reduced path length for conduction, and
- A multiplier on the convective heat transfer at the interface between the molten corium beneath the top crust and the crust to acknowledge the attenuation of heat transfer at the interface due to gas generation from core-concrete interaction and the mixing caused by this interaction.

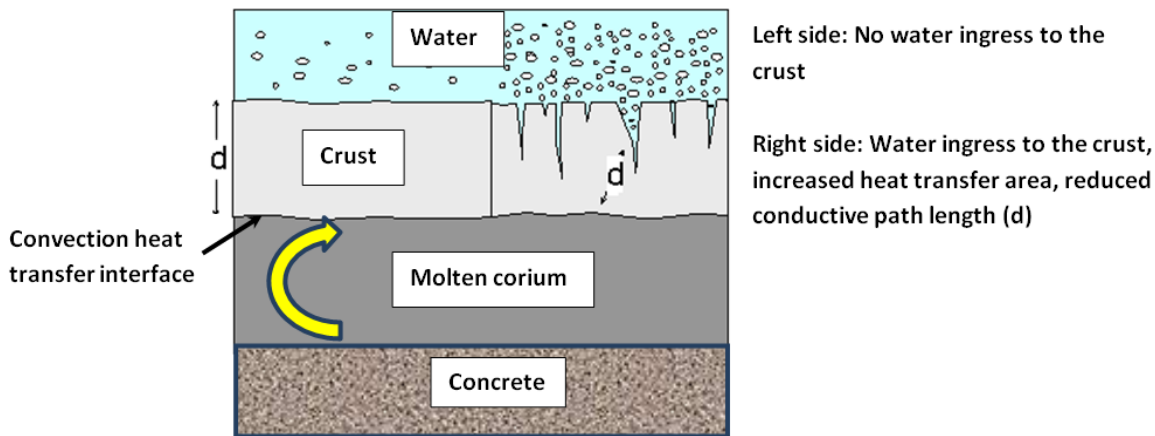


**Figure A-32 Illustration of accentuated heat transfer**

### 2.3.5 Improvements in the steam generator nodalization

In NUREG/CR-7110, Volume 2, a relatively simple steam generator nodalization was used for computing efficiency. To facilitate natural circulation modeling, the primary system tube nodalization was split to represent the hot upflow and cold downflow natural circulation pathways (see Figure A-33). Due to improvements in computer speed since 2007, it was possible to run larger model nodalizations. The steam generator model nodalization was further subdivided for the UA calculations. Each of the upflow SG tube control volumes were split into three control volumes. The primary system fluid entering the steam generator is hottest and has the highest heat transfer rate to the secondary fluid. The refined vessel side steam generator nodalization provided an improved representation of the primary system temperature and density gradient. An accurate calculation of the temperature and density gradients is important for natural circulation. During the core degradation phase, the refined upflow nodalization is also important for discretizing the temperature gradient for natural circulation flow as well as improving the spatial resolution of the aerosol deposition. The downflow SG tubes were split into 2 control volumes, which reflect the lower importance of this region for natural circulation and aerosol deposition.

The secondary boiler nodalization was increased from one control volume to three control volumes. The new boiler nodalization matched the height ranges of the new vessel-side primary system nodalization. The new SG secondary side boiler nodalization improved the representation of the secondary side inventory following the loss of injection as well as the local conditions following an SGTR.

The downcomer nodalization was split into two control volumes. The new lower downcomer control volume exactly matched the height of the boiler section, which better represented the hydrostatic heads of the two regions and shared walls for heat transfer. The upper downcomer control volume represented the region surrounding the steam separators and the location of the feedwater injection ring.

Previously the water level was controlled to 39.9 feet above the bottom of the SG downcomer. At steady state conditions, this resulted in a SG water mass of 48 tons. After a more detailed review of transient calculations in the Surry Updated Safety Analysis Report, the downcomer level was adjusted to 42.6 feet [55]. However, the more refined boiler void distribution in the

new nodalization resulted in 40 tons of water at steady state. Although there is some variability in the SG mass depending on the level and power, the information from the utility's individual plant examination (IPE) suggested 44.6 tons was appropriate, or approximately halfway between the SOARCA and UA SG masses.

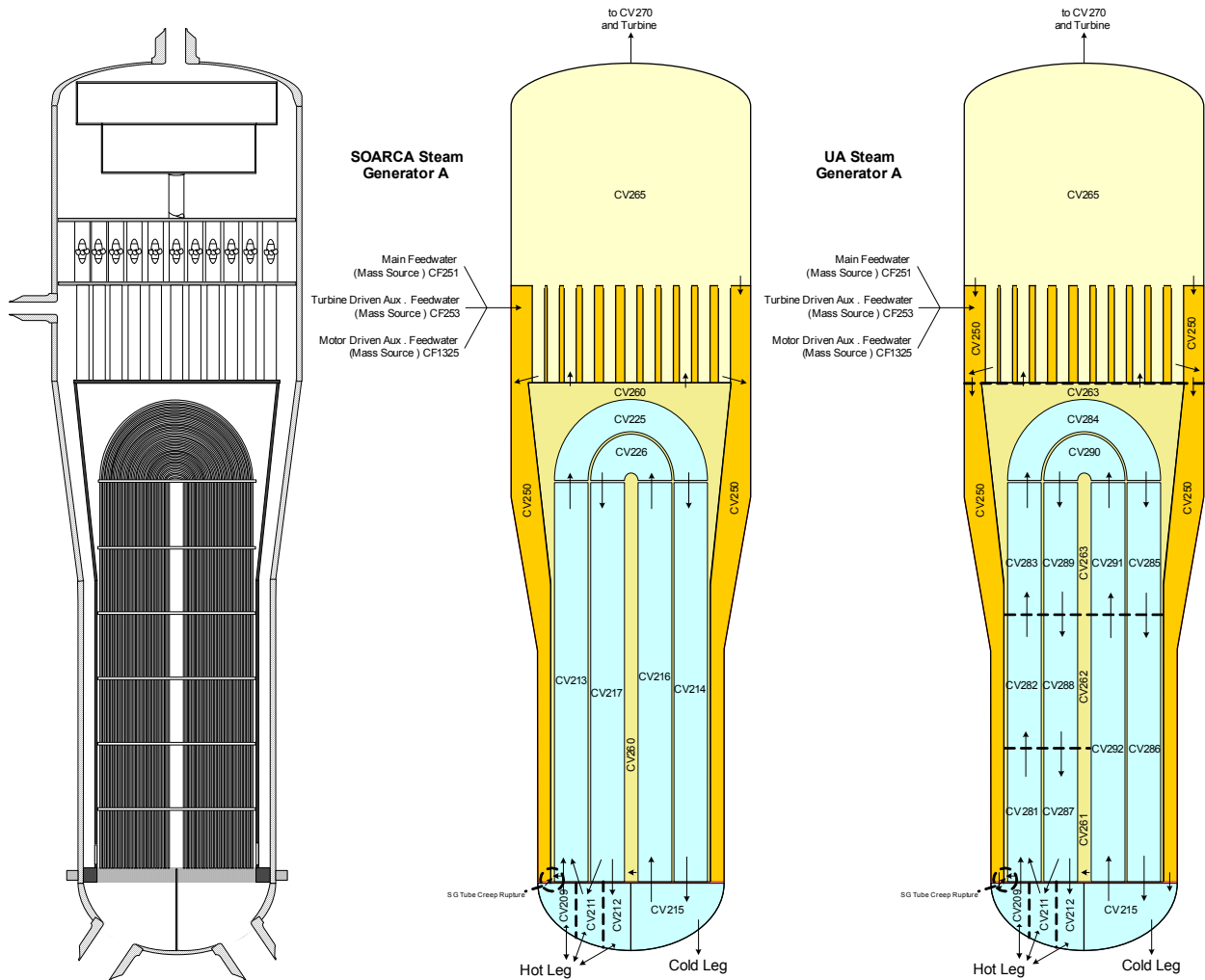


Figure A-33 Comparison of the SOARCA and UA steam generator nodalizations

### 2.3.6 Miscellaneous changes

Although there is no technical specification for MSIV leakage for a PWR, it was the consensus of the MELCOR subject matter experts that due to the lack of motivation for tight machining to prevent MSIV leakage, steam generators will depressurize during a severe accident. To accomplish this in every realization, a flow path was added for leakage after MSIV closure with a flow area of 0.5 in<sup>2</sup> for each steam generator, which provides pressurization before core damage occurs. This flow path opens at time 0 since it is assumed leakage would be based on pre-existing valve defects not those induced by severe accident conditions. Additionally, while not a correction or an enhancement, the “revised treatment of near-equilibrium thermodynamics” was disabled (using CVH sensitivity coefficient 4408) in the UA work to

alleviate related code execution complications that have proven difficult to troubleshoot historically and that persist today.

A maximum time step size was defined as 250 ms throughout the UA MELCOR calculations and the time step size being invoked within the COR package was imposed on the calculation as a whole. In NUREG/CR-7110, Volume 2, the maximum timestep was 1000 ms. Both MELCOR 1.8.6 and MELCOR 2.1 include logic to limit the timestep as necessary for convergence of the physics routines. However, smaller maximum timesteps improve the consistency of the model convergence with less reliance on the built-in code criteria.

## **2.4 Summary of the Model Enhancements Included in the Uncertainty Sampling**

The model enhancements included as sampled uncertainty variables are described in this section. These model enhancements fulfilled two goals, (a) improve the simulation fidelity of the phenomena and (b) include flexibility to sample uncertainty of the response. For example, a hot steam generator tube model was added to the model nodalization (see Section 2.4.1). The hot tube model greatly increased the thermal resolution of the hottest portion of the gas entering the steam generator that was not possible in the full system model. The new model also allowed uncertainty sampling on the peak hot plume temperature as predicted in the NRC numerical studies. The model corrections and improvements not related to the uncertainty sampling are described in Section 2.3.

### **2.4.1 Hot steam generator tube failure modeling**

The NRC and industry have been studying SG tube ruptures for decades because of their importance in maintaining the reactor coolant system pressure boundary (e.g., see [1] and [2]). In particular, a tube failure during a severe accident has the potential for radioactive release to the environment that bypasses containment. At high temperature conditions during a severe accident, natural circulation flow patterns are established where high temperature gases from the core circulate into the hot leg and SG. The effectiveness of the high temperature gases to heat the SG tubes is an important factor in determining their failure. The NRC and industry performed 1/7<sup>th</sup>-scale experimental tests to characterize the natural circulation flows between the vessel and the steam generator [3][4]. The tests were studied using computational fluid dynamics (CFD) techniques [5]. The CFD techniques were subsequently scaled to full plant geometry and severe accident conditions [6].

A representation of a single steam generator tube was included for evaluating the greatest potential stress in a steam generator tube bundle. The stress in the hottest tube, or one of the multiple tubes in the hottest bin, is also conservatively assumed to have the weakest structural condition, e.g., the most wall thinning of any tube (see Figure A-34). This is a separate MELCOR nodalization that is included with the MELCOR system model of Surry. Each timestep, the single tube model is coupled to the system calculation via specified boundary conditions for the inlet flowrate, the inlet temperature ( $T_{ht}$ ), and the fluid composition (e.g., water, steam, and hydrogen). However, the inlet temperature is adjusted higher during the natural circulation phase to represent the hottest portion of the plume as quantified by the computational fluid dynamic calculations [6]. The potential for creep rupture is evaluated using the tube wall temperature at the inlet to the hot tube model. When the hottest tube predicts a creep rupture failure, a corresponding SGTR flow path is opened in the system nodalization. The hottest tube representation is discussed in greater detail in Section 4 of the main report.

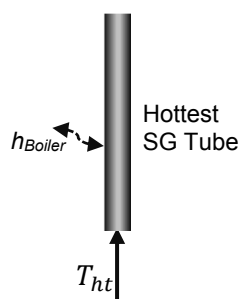


**Figure A-34 Representation of the hottest tube in the Surry model for creep rupture evaluations**

## 2.4.2 Steam generator tube thickness

An induced SGTR is a very important accident scenario for a PWR, as it creates a release path for radionuclides to bypass the containment building and be transported directly to the environment. In the NUREG/CR-7110, Volume 2 SOARCA analysis, a thermally induced SGTR due to creep rupture was only predicted after prescribing a stuck-open secondary SRV and lowering the stress criterion on the tube. New modeling done for the UA work includes implementation of a single steam generator tube model, which will be run concurrently with the full steam generator (see Section 2.4.1). The thickness of the tube, which is used in the creep stress equations, is input via a control function. The approach for this parameter is discussed in greater detail in Section 4 of the main report.

## 2.4.3 Improved valve failure modeling

The NUREG/CR-7110, Volume 2 SOARCA calculations used valve failure data provided by the utility. The various safety relief valves were configured to fail open using the following criteria.

- The pressurizer safety relief valves had a per demand failure probability of 0.0027 [33] and failure at a cumulative distribution function value of 0.5 (i.e., failure after 256 cycles) or at 10 cycles above 1,000 K.
- The secondary safety relief valves had a per demand failure probability demand failure probability of 0.0027 [33] and failure at a cumulative distribution function value of 0.5 (i.e., failure after 256 cycles), or 10 cycles above 1,000 K.

The valve sampling for the Surry UA is based on NUREG/CR-7037 [34], which only used data from real plant SCRAMs. No experimental test data included frequencies. It is believed the data from NUREG/CR-7037 is more realistic than the values provided by the utility. The median number of cycles to valve failure is considerably smaller in NUREG/CR-7037 (i.e., failure after 45 cycles). This is a substantial change from PWR SOARCA approach, which did not indicate any potential for valve failure. A new feature for the UA project is the potential for the RCS to depressurize by failing to open a pressurizer safety relief valve due to excessive cycling while passing liquid. This is based on the liquid level calculated in the pressurizer.

The failure position was assumed to be fully open in SOARCA (i.e., although no valve failures were predicted). Based on insights from the NUREG/CR-7110, Volume 1 and the Peach Bottom UA (i.e., [8] and [31], respectively), the potential to fail open at various fractional open areas was also added.

The primary SVs are modeled to only allow for one failure mode, stochastic cycling failing, liquid cycling failure, and thermal failure. The number of cycles to stochastic and liquid failure and the temperature limit for thermal failure are all sampled inputs. SV temperature is modeled to only increase when the valve is open. Once the failure mode is reached, the open fraction is determined. It is sampled for thermal and stochastic cycling failure, but set at 1.0 for liquid failure. The potential for the valve to not open was also considered. However, this failure mode was not supported by the actual plant data.

#### 2.4.4 Modifications to the pump seal failure

Under normal operating conditions, cooling water is supplied to the reactor coolant pump (RCP) seals at a higher pressure than the primary. As a result, the cooling water keeps the RCP seals cool while preventing any primary coolant to flow up the RCP shaft and contaminating areas outside the primary boundary. When a loss of AC power occurs, the RCP seal cooling system no longer supplies cooling/seal water and as a result, primary coolant begins leaking along the RCP shaft through the mechanical seals at a 21 gpm per RCP flow rate for pressures near operating pressure. As the primary system heats up, the mechanical seals begin to thermally degrade and fail resulting in a higher leak rate estimated at 76 gpm, 182 gpm, or 480 gpm per RCP as per NUREG-1935, Table 13.

In the SOARCA analysis, the RCPs started to leak at 21 gpm following the loss of power, which is the nominal intact seal flow rate. If the water at the pump inlet became saturated, then the RCP seal was assumed to fail and leak at 182 gpm. AECL performed an analysis of the second seal assuming various amounts of surface roughness. Any leakage caused by the surface roughness or the waviness of the seal faces is smaller than the critical amount required to cause it to pop open. However, the second seal may pop open if there are deep surface defects on the seal face. Consequently, the SOARCA modeling implied deep defects always existed to cause failure when saturated conditions occurred.

A better method than assuming deep defects on the seal surface is the Westinghouse Owners Group (WOG) probabilistic model [53]. The probabilistic values from the WOG RCP seal failure model are shown in Table A-8. The RCP seal leakage will begin at 21 gpm per pump for all scenarios for 13 minutes [53]. It takes 13 minutes for the RCP seal cavity to be filled. If there are flaws in the seal, then this is a likely time for seal failure. As indicated in Table A-8, the most likely outcome is the seal remains intact. There is only a 19.75% probability that the seal will fail to leak at 182 gpm. There are small probabilities of 75 gpm and 480 gpm failures. This allows for a more realistic representation on the RCP pump seal response than always failing to 182 gpm, but removed variation in timing of the failure that was calculated in the original SOARCA runs.

**Table A-8 RCP seal leak probabilities at operating pressure.**

Time = 0 min	Time ≥ 13 min	Probability
--------------	---------------	-------------

21 gpm/RCP	21 gpm/RCP	0.79
21 gpm/RCP	76 gpm/RCP	0.01
21 gpm/RCP	182 gpm/RCP	0.1975
21 gpm/RCP	480 gpm/RCP	0.0025

### 2.4.5 Improvements in containment condensation

The heat transfer coefficients at the walls in containment affect the rates of steam condensation on the walls which in turn influence the steam concentration in the containment atmosphere as well as the pressure in containment. The steam concentration and containment pressure are critical to the magnitude of containment leakage. The steam concentration also affects the potential for a hydrogen burn and the magnitude of the pressure rise. Consequently, the calculated values of the heat transfer coefficient are critical to the modeling of hydrogen burns and fission product releases to the environment.

The natural convection heat transfer coefficients (HTCs) calculated by MELCOR are typically low ( $<10 \text{ W/m}^2\text{K}$ ) for heat structures such as those representing concrete walls in containment. The calculation of HTC in MELCOR involves determining Nusselt (Nu) number as it does in the CONTAIN computer code [44]. Increasing the leading coefficient in the correlation for the Nu number from 0.10 to 0.14 in CONTAIN has historically been found to give more realistic results in comparisons with experimental data [42]. The Nu number is a multiplier in the relation for HTC, and increasing the leading coefficient in the relation for Nu from 0.1 to 0.14 increases HTC by 40%.

For implementation into MELCOR, the HTCs on just the heat structures representing containment walls are adjusted by increasing the heat and mass transfer coefficient multipliers individually associated with each heat structure. The mass and heat transfer multipliers augment the overall heat transfer and condensation and are recommended to have the same input value to prevent MELCOR code operation difficulties, effectively extending the bounds of the distribution. The magnitude of the heat transfer adjustment was implemented as a UA sampling parameter that permitted uncertainty evaluations.

### 2.4.6 Improvements in the containment overpressure and design leakage

For accident scenarios without containment bypass, containment failure due to overpressure is the dominant release path for radionuclides. In this context, containment failure does not refer to a catastrophic rupture, but to greatly increased leakage caused by overpressure. Relatively small radionuclide releases can also occur through nominal containment leakage prior to containment overpressure failure. A best estimate design leakage was used in SOARCA. However, the technical specifications allow higher leakage for a limited operation time. The containment design leakage and over-pressure leakages are described in Sections 2.4.6.1 and 2.4.6.2, respectively. The implementation as a sampling parameter for the UA is described in Section 2.4.6.3.

#### 2.4.6.1 Design Containment Leakage

Prior to containment overpressure failure, radionuclide releases through nominal leakage tends to be relatively small. The release fractions were  $<10^{-4}$  (excluding noble gases) in the

unmitigated SOARCA STSBO scenario (Fig. 5-36 in SOARCA [7]) before the containment overpressure failure near 26 hours. After containment liner yield, the release fractions can increase by several orders of magnitude. While the SOARCA STSBO exhibited relatively small early releases, uncertainty in the design leakage rate can increase radionuclide releases prior to containment failure.

From the conclusions in NUREG-1493, “The allowable leak rate can be increased by one to two orders of magnitude without significantly impacting the estimates of population dose in the event of an accident [43]. The PRA for Surry Unit 1, which was performed assuming a containment leak rate a factor of 10 times greater than the nominal 0.1 % per day established in the plant’s technical specifications, indicates that accident scenarios where containment does not fail and is not bypassed contribute only about 0.05% of the population risk from all core-melt accidents.” Additionally from NUREG-1493, “The design basis leak rate for the Surry plant is nominally 0.1% per day. However, the technical specifications for the plant allow limited time operation with up to 1% per day containment leak rate” [43].

The base value for containment design leakage was instilled in the MELCOR Surry model by defining a flow path sized such that flowrate is limited by frictional resistance as opposed to by a choked flow condition. The flow path accommodates a 0.1 percent volume per day flow of steam at  $P/P_{\text{Design}}=1$ . It has a diameter of 0.0953”, a length of 6’-3.2”, and is absent from losses. Realizing flowrate in this flow path for fixed containment conditions to be proportional to the inverse of the square root of the length of the path, the desired variation in design leakage rate is accomplished by varying path length accordingly. A uniform discrete distribution of 10 lengths varying from 6’-3.20” to 0’-0.75” was sampled where each length was associated with an even multiple of the base value of design leakage.

#### **2.4.6.2 Enhanced Leakage Due to Containment Overpressure**

The SOARCA model for containment overpressure failure is informed by over 25 years of research [10]. This research included both experimental and advanced computational efforts, such as the scaled PWR containment experiments at SNL (particularly the 1:4 for pre-stressed and 1:6 for reinforced concrete) and nonlinear finite element simulations. In general it was concluded that upon pressurization, concrete containments for PWRs exhibit significantly increased leakage before a global failure of the structure due to the physically redundant arrangement of the steel-liner enclosed in concrete [10]. This enhanced leakage can effectively preclude catastrophic containment rupture for reasonable pressurization rates. Enhanced leakage following overpressure is most likely to occur near equipment hatches and other penetrations through the containment; these are regions of material and geometric discontinuities that cause high local stresses [10].

The experimental test data was not used directly in the SOARCA model due to the reduced scale and the prototypical (i.e. idealized) nature of the experimental models. A smaller pressure vessel can inherently withstand higher internal pressures. Moreover, normalizing absolute experimental pressures to an approximate “design pressure” of the experimental mockup still yields upper-bound estimates for simplified conditions. For example, the experimental models do not possess the full complexity of geometric and material discontinuities as the actual Surry containment, and it is these details that drive localized failures and enhanced leakage upon pressurization [10].

Volatile radionuclide transport to the containment occurs about 24 hours before containment overpressure failure in the SOARCA STSBO (Figures 5-34 and 5-35 [7]), and thus

concentrations of airborne volatiles are relatively low (mostly due to gravitational settling) at the time of containment liner yield. However, uncertainty in the containment overpressure failure model can change the relative timing of these processes. In conjunction with other uncertain parameters, overpressure failure can potentially occur sooner when airborne radionuclide concentrations are still relatively high. Conversely, delayed radionuclide transport (due to other uncertain parameters) to the containment can shift airborne concentrations later into the accident and closer to the time of containment overpressure. It is therefore sensible to include the containment overpressure failure model as an uncertain parameter in the Surry UA.

The test data for normalized mass flow rate is used in the SOARCA MELCOR model, while a set of simple stress calculations provides the internal pressures at key stages of containment pressurization. This process yields tabular data of containment pressure vs. enhanced mass leak rate. Informed by the experimental observations, the hand-calculations estimate the internal containment pressures associated with the following events:

1. Liner plate yield: 82.1 psig
2. Rebar yield: 119.36 psig
3. 2% global containment strain: 126.71 psig (SNL research quantified containment failure at global free-field strains of 1.5% to 2.0% for reinforced concrete [10]).

Both the original SOARCA model and the current UA model for containment failure are based on this experimental data. Figure A-35 displays the curve for the original SOARCA run on the left, with the modified UA curve on the right. The original SOARCA model removed the liner plate yield point and fit a parabolic function to the remaining three data points, which results in the enhanced failure leakage not initiating until much higher containment pressures. With the liner plate yield point included, and a linear fit between the four points, the Surry UA model starts enhanced leakage much earlier.

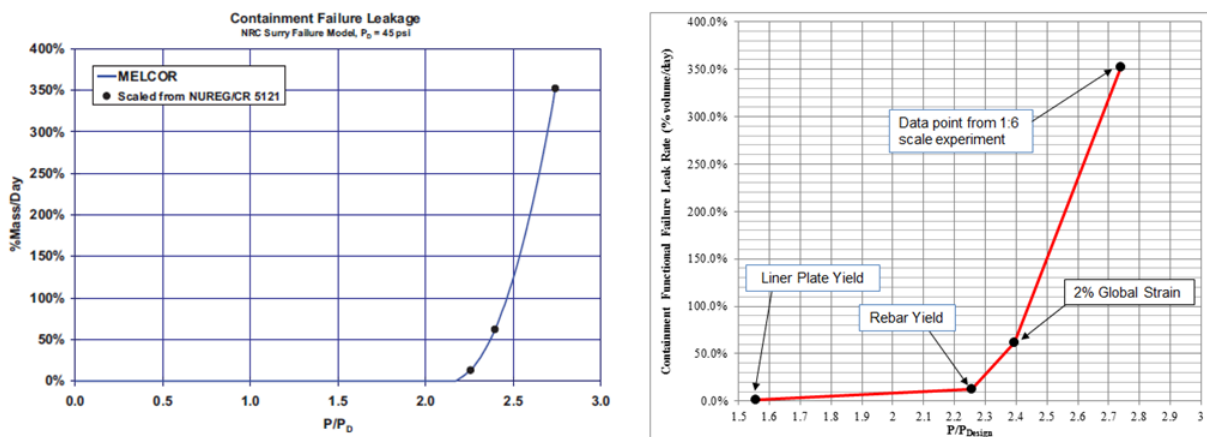


**Figure A-35 Surry SOARCA containment overpressure models**

**2.4.6.3 Containment leakage modifications to support the Surry UA**

The modifications required to support the Surry UA are minor given that the actual prediction of mechanical failure is not the responsibility of MELCOR, i.e. it does not calculate local stress fields, strain fields, and failures; MELCOR calculates time-dependent pressures in the containment while a simple curve of pressure (normalized to design pressure) vs. mass leak rate is input as a tabular function. In essence, the containment overpressure model is a dynamic boundary condition in MELCOR. The tabular function is informed by containment failure predictions using experimental data and external calculations. Consequently, the containment overpressure leak rate is only a function of the time dependent pressures predicted by MELCOR and the assumed design pressure. There is no dependence on temperature distributions in the containment other than thermodynamic feedback on pressure. The leak area for a MELCOR flow path is derived from the leak mass flow rate on the tabular function, and its growth with increasing pressure is monotonic pressure relief does not decrease the leak area. In summary, the overpressure leakage input in the MELCOR Surry deck consists of:

- a single flow path,
- the tabular function of normalized pressure vs. mass leak rate,
- supporting control functions, and
- a MELCOR valve to appropriately change the leak area according to the tabular function and current MELCOR predictions of containment pressure.

To increase the flexibility of the model for the Surry UA, the design pressure and the minimum overpressure ratio to begin enhanced leakage are made easily variable via control functions alone. The tabular function (based on the right side of Figure A-35) is dynamically shifted to start the enhanced leakage from new variable minimum overpressure ratio, sampled as the liner plate yield point. The entire curve is shifted laterally when liner yield is sampled below its best estimate value. However, the points for rebar yield and beyond are not shifted when liner yield is sampled higher since they are based on experimental data and are considered fixed within structural mechanics.

#### 2.4.7 Hydrogen ignition modeling

**Note:** In the course of reviewing the report, an issue was identified with the implementation of hydrogen ignition. The Surry UA assumes the hydrogen will burn as soon as the “lower” flammability limit (LFL) is reached allowing no possibility for buildup to higher concentrations. The sampling of the LFL was performed correctly, and thus hydrogen burns initiated at the proper limits (almost always upon hot leg creep). However, due to an internal mistake in the model, there was not a steam inerting limit and CO<sub>2</sub> and N<sub>2</sub> were not included in the inerting calculation. This can affect the likelihood of having burns later in the transient, when the containment is steam inerted. The magnitude of the mistake can be quantified when considering the gas mole fractions must add up to a 100%.

The following was done correctly:

- The UA implementation correctly satisfied that O<sub>2</sub> had to be > 5% + temperature effects
- The UA implementation correctly satisfied the minimum upward and downward H<sub>2</sub> concentrations of 4% and 8.5% + temperature effects

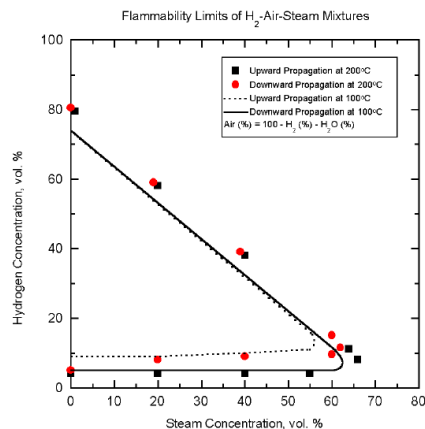
- The UA implementation correctly satisfied the increase in H<sub>2</sub> concentration needed at higher H<sub>2</sub>O concentrations (i.e., based on Kumar's data)

The following describes what was incorrect in the implementation:

- The UA implementation did not limit combustion based on high steam concentrations (all diluents should be added or Kumar Figure 7 should have been used).
- The UA implementation incorrectly used CO instead of CO<sub>2</sub> and did not correctly limit on high CO<sub>2</sub> concentration (this was not a factor because the low CO<sub>2</sub> generation and steam was the limiting diluent).

The impact on where the UA implementation would predict steam inerting is described below:

- At 69.7% steam concentration, the UA implementation predicts 5.3% H<sub>2</sub> for upward propagation. %5 O<sub>2</sub> is required. This implies 20% N<sub>2</sub>. The sum of N<sub>2</sub>+O<sub>2</sub>+H<sub>2</sub>O+H<sub>2</sub>=100%. This is ~4-7% higher the maximum steam inerting data (see fig below).
- At 65.4% steam concentration, the UA implementation predicts 9.6% H<sub>2</sub> for downward propagation. %5 O<sub>2</sub> is required. This implies 20% N<sub>2</sub>. The sum of N<sub>2</sub>+O<sub>2</sub>+H<sub>2</sub>O+H<sub>2</sub>=100%. This is 4-5% higher than maximum steam inerting (see figure below).



The hydrogen combustion model was updated for the Surry uncertainty analysis to better predict the lower limit of flammability. The updates include two parts, (1) an uncertainty parameter for the location of the ignition source and (2) a new flammability model. The implementation of the new hydrogen lower flammability limits uses the research of Kumar and can be used independent of the specification of the ignition location. Kumar's paper [35] describes the experimental determination of the flammability limits of hydrogen/oxygen mixtures with various diluents. He also presents a deduction of semi-empirical relationships based on experimental results to estimate limits on flammability for the various propagation directions based on principle energy balances.

Kumar's research shows the flammability strongly depends on the deficient reactant [35]. Consequently, the diluent may include excess oxygen or hydrogen. The flammability limit remains constant if the mixture has nearly the same thermo-physical properties. Kumar observes that the physical properties of oxygen and nitrogen are nearly identical. Replacing oxygen by nitrogen does not affect observed limits. Although steam and carbon monoxide (i.e., gases that may be possible in the containment) are both triatomic gases and have similar properties, carbon monoxide shows a stronger influence on the lean-downward limits.

Kumar notes that the inerting diluent concentration corresponding to the nose of the flammability curves is nearly the same for all diluents [35]. It is about 86% for CO<sub>2</sub> and 87% for steam. The MELCOR default uses 55% for steam inerting. However, experiments by Tamm show combustion at 59% in turbulent conditions, which Kumar suggests would extrapolate to a value of 63% in quiescent conditions. When the diluent of nitrogen is included with the minimum oxygen limit (5%), the diluent inerting limit is 87%.

The UA implementation uses the lean flammability limits from Kumar's data for H<sub>2</sub>-O<sub>2</sub>-H<sub>2</sub>O and H<sub>2</sub>-O<sub>2</sub>-CO<sub>2</sub> mixtures (see Figure A-36 and Figure A-37). The impact of N<sub>2</sub> on flammability limits is almost negligible. However, the impact of CO<sub>2</sub> and H<sub>2</sub>O is observable as their concentrations increase. Consequently, separate flammability tables are entered for hydrogen flammability as a function of steam concentration and carbon monoxide concentration for upward and downward propagation (i.e., total of four tables). Kumar estimated the criteria for horizontal flammability as approximately the average of upward and downward propagation, which is also used here in this update.

The following approach and approximations are used to update the Surry MELCOR hydrogen combustion model. For each control volume in the containment, it is determined whether there is >5% O<sub>2</sub> concentration. This quantity of oxygen was experimentally identified as a lower limit for combustion. Then it is determined whether the hydrogen concentration is high enough for flammability considering the local concentration of steam and CO<sub>2</sub> and the direction of propagation from the ignition source. Additionally, the influence of the temperature is also incorporated using Kumar's experimental findings and deduced theoretical observations. Over the temperature range of the data, the lower limits of hydrogen flammability decrease by 0.5% hydrogen/100°C for upward propagation and 1% hydrogen/100°C for downward propagation. For rich limits, the oxygen concentration decreases by 0.5% oxygen/100°C. If all these criteria are satisfied, then hydrogen ignition is allowed in the control volume. The ignition is triggered, which starts a burn in the control volume. Propagation to adjacent cells occurs using the existing MELCOR burn package model, which is consistent with the findings of Kumar. Spontaneous ignition for CO is also allowed using the default criteria.

The implementation of the new combustion logic at the lower limit of flammability was especially developed for application in the Surry UA. The current approach presumes an ignition source is always available to explore the uncertainty in the lower limits of flammability. Although previous SOARCA calculations included combustion at the default limit for spontaneous ignition (10%), the presence of steam and other diluents precluded combustion in the containment during the unmitigated short-term station blackout except upon the initial release of hydrogen-rich gas following hot leg creep rupture failure.

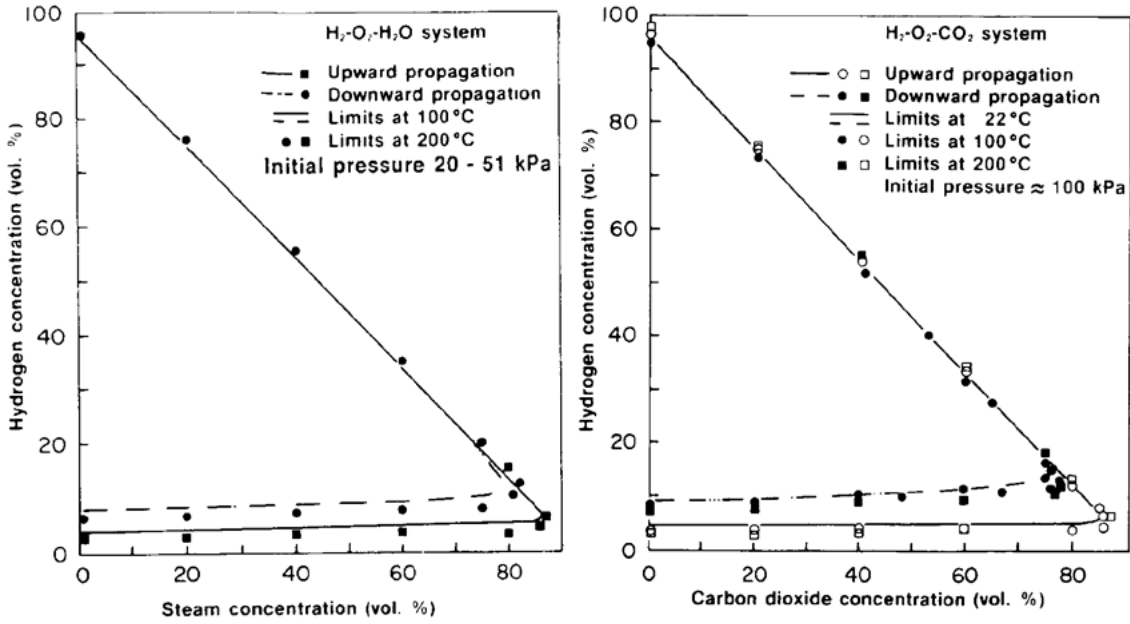


Figure A-36 Flammability limits for hydrogen for  $H_2-O_2-H_2O$  and  $H_2-O_2-CO_2$  systems [35]

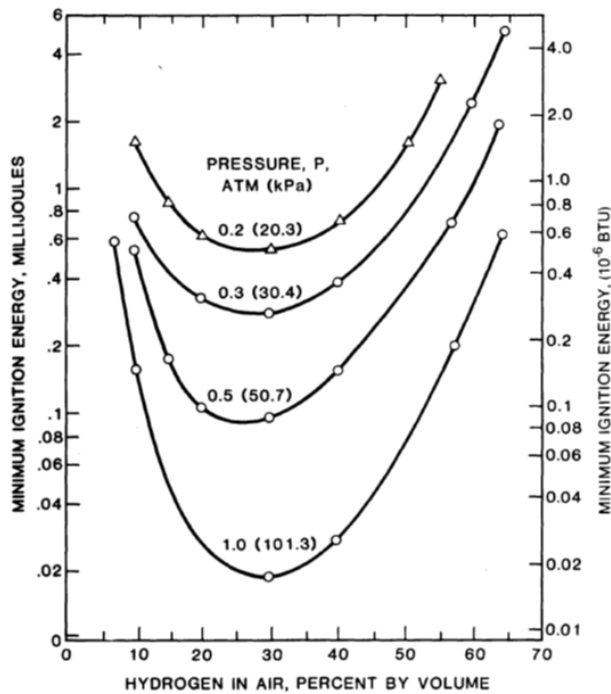


Figure A-37 Ignition energy for dry hydrogen mixtures [36]

## 2.4.8 Model modifications for the effective fuel eutectic formation

The binary phase diagram for  $ZrO_2/UO_2$  suggests eutectic liquefaction for equilibrium conditions is approximately 2800 K for a 50/50 molar mixture (i.e., the temperature used in SOARCA [7][8]). Any liquefaction below this temperature accounts for the effect of molten Zircaloy metal

or alpha-Zr(O) “wetting” the oxide surfaces. Observations of the VERCORS experiments suggest that irradiated fuel and oxidized cladding exhibit eutectic liquefaction at significantly lower temperatures [45]. Six experimental data points for eutectic induced core collapse are readily available from the VERCORS experiments to help inform the uncertainty distribution (see Table A-9 [45]).

**Table A-9 Fuel collapse observed in the VERCORS experiments.**

Test	Collapse Temperature (K)
T1	2525
HT1	2550
HT2	2400
HT3	2525
V_6	2525
RT6	2350
Mean	2479

In selecting this experimental data, the observed core slump was assumed to correspond to a eutectic reaction. This was strongly indicated by the test results but cannot be definitively confirmed due to a lack of needed instrumentation. While the VERCORS results do not provide randomly distributed evidence of eutectic formation temperatures, these tests do provide a range of temperatures over which eutectics were significant enough to cause core collapse. A normal distribution fitted to the data in the table above was used to assess uncertainty in the average core collapse temperature for higher burnup fuel. The simple parameter treatment is not intended to rigorously quantify eutectic effects on severe accidents and core degradation—such treatment is impossible when the MELCOR eutectic model is not activated. Rather, the proposed treatment roughly evaluates the influences that the physical state of the core debris has on core degradation kinetics and subsequent severe accident progression. A lower temperature for this parameter results in an increased generation of molten pools in the RPV during core disassembly. Alternatively, a higher temperature for this parameter results in a decreased generation of molten pool formation for ZrO<sub>2</sub> and UO<sub>2</sub> debris.

The fuel melt associated with this parameter is a localized effect. MELCOR evaluates the temperature independently for each core cell and allows the fuel in that specific cell to melt when it reaches a failure temperature, such as the eutectic temperature. Thus, the entire core will not fail at once when the hottest region reaches the sampled temperature. It is possible that melting of a core cell can cause the subsequent failure of fuel above in the same radial ring that was previously supported by the failed cell. However, this is a physical effect and still only affects a section of a single ring, keeping it a localized effect.

Currently, eutectic reactions are approximated by user-modification of melting and failure temperatures in model input. Thus, to effectively represent the eutectic temperature, the user must modify:

- The sensitivity coefficient in the Core package that defines the cladding temperature resulting in rods collapse without Zr-metal cladding remaining, and

- The melting temperatures of both ZrO<sub>2</sub> and UO<sub>2</sub> in the MP package.

## **2.4.9 Updated iodine and cesium modeling**

The modeling of iodine and cesium are considered together to conserve their elemental radiological inventory. The updated modeling expands the number of chemical forms and the distribution among the various compounds. The chemical form of the elements is important to the release and transport properties of the radionuclides while the elemental radionuclide content is important to the health consequences. The rationale for changing the iodine and cesium speciation is described in Sections 2.4.9.1 and 2.4.9.2, respectively.

### **2.4.9.1 Iodine modeling**

The presence of gaseous iodine remains an uncertain source term issue, especially with respect to long-term radioactive release mitigation issues after the comparatively much larger airborne aerosol radioactivity has settled from the atmosphere. Mechanistic modeling of gaseous iodine behavior is a technology still under development with important international research programs to determine the dynamic behavior of iodine chemistry with respect to paints, wetted surfaces, buffered and unbuffered water pools undergoing radiolysis, and gas phase chemistry.

Consistent with past MELCOR best practice, NUREG/CR-7110, Volume 2 assumed all released iodine combines with cesium [7]. Recent experiments at the Phebus facility show that gaseous iodine is found within containment [40]. With the different core make-ups of the various Phebus tests, gaseous iodine percentage in the containment has varied as well, from as low as 0.2% to as high as 7%. The chemical form of iodine is an important factor in the physics of the transport and release to the environment.

Since there is still a lack of understanding on the gaseous iodine behavior during the Phebus tests, the team recommends an approach where the fission gas release to the fuel/cladding gap is used as a surrogate for the gaseous iodine fraction. Figure A-38 summarizes real data from French reactors for low enriched uranium (LEU) and mixed oxide fuel. The fuel was removed from operating reactors, and the cladding was punched out to determine the gases present in the gap.

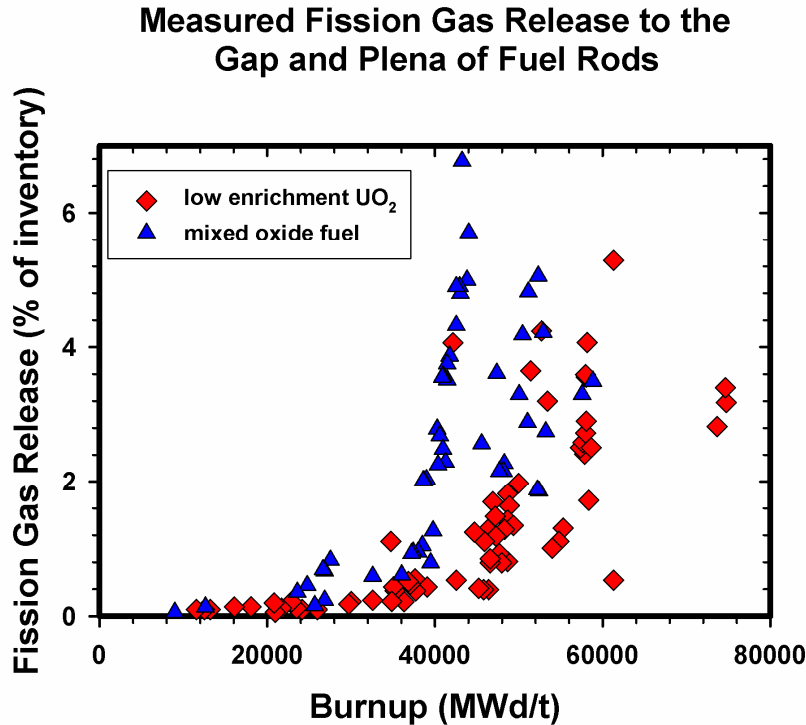


**Figure A-38 Measured fission gas release to the fuel/cladding gap**

Surry uses exclusively LEU in its fuel, so an exponential curve was fit to the red data points in the above figure. Specific plant information was provided for three different times in a single operating cycle – beginning, middle, and end of cycle (BOC, MOC, and EOC). This included specific burn-up data, in MWd/t, which was used to calculate an average burn-up for each time at cycle. The three average burn-ups were input to the curve fit to the French data, yielding base case gaseous iodine percentages of 0.1%, 0.18%, and 0.42% for each time at cycle, respectively. These values agree with the majority of Phebus tests, which showed the concentration of hydrogen in containment was generally <1%.

The uncertainty in this parameter is created from variations from the best fit to the curve. This is used to directly sample gaseous iodine fraction at the three times at cycle. These samples were used as one of the inputs to the macro that distributed decay heat and RN masses based on time at cycle.

#### **2.4.9.2 Cesium modeling**

As mentioned in the Section 2.4.9.1, the first step in the speciation of cesium is the combination with most available iodine to form CsI. Since there is generally much more cesium available than iodine, a significant amount of cesium remains to form other chemical classes by further speciation. The other predominant speciation of cesium was based on chemical analysis of the deposition and transport of the volatile fission products in the Phebus facility tests [23]. The chemical analysis revealed molybdenum combined with cesium and formed cesium molybdate. Based on the measured temperature where the cesium and molybdenum were found deposited, other likely forms of cesium (e.g., cesium hydroxide and cesium iodine) would vaporize. However, there was also evidence from the Phebus tests that cesium is revaporized at temperatures consistent with the cesium hydroxide chemical form. It is presumed that reactions

between cesium molybdate and steam cause cesium hydroxide to form after release from the fuel. Prior to NUREG/CR-7110 Volume 1 [7], the MELCOR default chemical form of cesium not bound with iodine was assumed to be cesium hydroxide. Understanding the uncertainty regarding chemical form is important because the cesium chemical behavior will determine the amount and timing of the release from containment into the environment (e.g., late phase revalorization of cesium).

The best estimate for cesium partitioning based on examination of Phebus results indicates that at the time of environmental release cesium is speciated at 80%  $\text{Cs}_2\text{MoO}_4$  and 20%  $\text{CsOH}$ . This probably does not represent the cesium distribution at the time of release from fuel, but within MELCOR there is no model for the cesium molybdate and steam reaction to form cesium hydroxide, so the environment release forms need to be initialized in the fuel.

A distribution for the speciation of cesium was created based on expert judgment. This is directly sampled and used as one of the inputs to the macro that distributed decay heat and RN masses based on time at cycle.

#### **2.4.10 Improvements in the secondary side decontamination factor**

Following a steam generator tube rupture (SGTR) in a severe accident scenario, there is some portion of the radionuclide inventory that would be transported from the primary reactor system to the system side and subsequently to the environment. However, there is a tortuous path through the steam generator that would result in a deposition of radionuclides, significantly reducing the total environmental release. The ARTIST (Aerosol Trapping in a Steam Generator) facility, built at PSI in Switzerland, hosted a series of tests, conducted to try to determine the amount of decontamination that occurs in a steam generator following a rupture under various conditions. The flow of fission products through the tube rupture into the steam generator is very complicated and beyond the current modeling capabilities in MELCOR. Several decontamination mechanisms such as: (a) impaction, vena contracta effects at the tube rupture, (b) deposition in bends, and (c) capture by the secondary side tube grid spacers are not addressed by the MELCOR aerosol deposition models. For the SOARCA SGTR calculations, it was estimated from ARTIST tests that the steam generator aerosol decontamination in a full-scale steam generator would be between 4.7 and 9 [41]. The normal aerosol capture and settling models were disabled on the secondary side in MELCOR and the secondary side decontamination factor was prescribed to be seven (i.e., approximately the average of 4.7 and 9).

The secondary side decontamination model was updated for the UA analyses. More detailed results were extracted and interpreted from the ARTIST final report. The data showed there was considerable deposition due to inertial impaction where large particles are unable to navigate the bends and obstacles while smaller particles can follow the flow stream. This is discussed in greater detail in Section 4 of the main report.

Within MELCOR a unique DF is calculated for each aerosol size bin at every time step based on current reactor conditions, and the location of the break.

#### **2.4.11 Aerosol shape factor**

The MAEROS model in MELCOR is used to determine the mass concentration evolutions of aerosols in a spatially homogenous volume, as well as deposition on surfaces and injection/removal from volumes. One of the critical assumptions of this model is that

nonspherical particle effects are adequately parameterized with the dynamic shape factor, the collision shape factor and the effective material density.

The dynamic shape factor is defined as “the ratio of the actual resistance force of the nonspherical particle to the resistance force of a sphere having the same volume and velocity” ([46], p.47). The shape factor is used to account for the stringing out of an aerosol agglomerate in a linear or complex manner as opposed to growing as a perfect sphere. A value of 1.0 is a perfect sphere and it is the lower limit for the dynamic shape factor. 1.0 is also the default value in MELCOR and as such was used in the SOARCA project [7][8].

Kasper ([47], Tables 9 &10) experimentally measured values for the dynamic shape factor for linear chains with their long axis either parallel or perpendicular to the settling direction, pictured below. As can be seen, the shape factor is reasonably linear with respect to the number of spheres. This data supports an upper bound of 2.8, with a weighting toward values under 2.0. Compiled data from Hinds ([46], pg. 48) also supports a range of 1-2.04. However, Brockmann compiled data and models to yield a range of 1-10 for the dynamic shape factor [48]. The same report includes a correlation for loosely-packed spheres which calculates a dynamic shape factor will be in the range of 1-5 for void volumes ranging from 26% to 99%.

Kissane compiled information on aerosols from a number of nuclear accident experiments, including the Phebus FPT tests [49]. The report concluded “Concerning particle shape, relatively compact particles without branching chain-like structures appear to be typical in the RCS” although a visual inspection of post-test deposition images does show slight evidence of aerosol chains. Since a compact, spherical particle has a shape factor of 1.0, the distribution should be weighted more heavily toward the lower end of the range. Additionally, most references support weighting more heavily in the 1.0-2.0 range.

The aerosol shape factor was implemented in MELCOR by modifying a single input in the RN package (CHI on record RN1\_MS00 – Miscellaneous Aerosol Dynamics Constants).

### 3. BASE UA CALCULATION

In Section 2.1, the results from the MELCOR 1.8.6 SOARCA calculation (also referred to as Surry SOARCA herein) were compared to the same model input after the conversion to the MELCOR 2.1 input. The comparison illustrated the similarities and differences between the two code versions (i.e., MELCOR 1.8.6 from 2007 and MELCOR 2.1.6843 from 2015). This section compares the results from the converted model without any changes to the UA model with the corrections and enhancements described in Section 2. Both calculations used MELCOR 2.1.6843 for the simulation. Consequently, the results in Section 2.1 evaluate the impact of the new code version on the accident progression; the results in Section 3 evaluate the impact of the new model input for the UA.

The new UA model is fully configured to perform uncertainty sampling. To facilitate comparison to the MELCOR 2.1 SOARCA results, the value of each of the uncertain parameters was specified as a fixed value determined by expert judgement to be most likely or most physically representative. Table A-10 identifies the values prescribed in this UA base calculation for the uncertain parameters sampled in the UA and discusses differences, if any, from the Surry SOARCA values. In particular, the changes related to valve failure (Items 1, 3, and 6 in Table A-10), the eutectic melting temperature (Item 11), the containment leak rate (Item 16), the hydrogen ignition criteria (Item 18), the containment condensation rate (Item 22), and the aerosol aerodynamic shape factor (Item 23) suggest significant changes.

Table A-11 shows the timing of key events for the Surry SOARCA calculation, the converted MELCOR 2.1 calculation, and the UA base calculation. As was discussed in Section 2 and documented in Table A-10, there are some significant modeling differences between the Surry SOARCA calculation and the new UA calculation. The differences in the event timings will be discussed with a comparison of responses for the selected parameters. However, the most obvious differences are (a) the timing to RCP seal failure (i.e., this does not occur in the UA calculation), (b) the timings to the stuck-open primary and secondary relief valves (i.e., this does not occur in the MELCOR 2.1 SOARCA calculation), and (c) the timing to a 0.1% release of iodine to the environment (i.e., this does not occur in the UA base calculation).

It should be noted that neither calculation predicted an STGR. Consequently, the enhanced decontamination modeling discussed in Section 2.4.10 is not illustrated. The UA calculation also included SG safety valve failures at 1 hr 11 min (see Table A-11) and wall thinning (i.e., Item 8 in Table A-10), which increases the stress in the tube and decreases tube strength, respectively. Figure A-39 shows the gas and tube temperature response in the SG inlet for the UA and Surry SOARCA calculations. The hot SG tube model in the UA calculation captures the peak plume temperature entering the SG, whereas the Surry SOARCA calculation simulates the average hot plume temperature. The UA calculation used the median hot tube plume multiplier (i.e., 0.44, see Item 11 in Table A-10). The peak gas and structure temperatures were ~400°F higher than the Surry SOARCA calculation. The corresponding creep rupture indices for the two calculations are shown in Figure A-40. A creep index of 1 is used to designate failure. The UA creep index had increased to  $<10^{-3}$ . However, the Surry SOARCA creep index showed negligible strain ( $<10^{-8}$ ). Although the UA calculation was increasing toward failure, the accumulation of damage stopped with hot leg nozzle failure at 4 hr 15 min (see Table A-11). Similarly, the Surry SOARCA creep rupture index stopped increasing at 3 hr 45 min with the hot leg nozzle failure. The UA results showed that a SGTR did not occur in this case because there was not a large enough pressure differential between the primary and secondary sides due to

the stuck open primary SV, and the base case thickness was not low enough to provide a large enough stress multiplier.

As shown in Table A-11, the timings of events calculated in the UA calculation were delayed relative to MELCOR 1.8.6 and MELCOR 2.1 SOARCA calculations until RPV lower head failure. As described in Section 2.2, new best estimate decay heat powers were developed for Surry. The Surry SOARCA model used a decay heat curve from ORIGEN analyses of an extrapolated high burnup core from Sequoyah. Due to the extrapolation to high burn-up, the SOARCA decay heat was expected to be conservative. The UA calculation also used the middle of the cycle (MOC) as the most appropriate central estimate of the decay power (i.e., see 15, Item 11 in Table A-10). The differences in the core decay heat during the in-vessel phase of the accident are shown in Figure A-41 and Figure A-42.

The boil-off of SG water inventory illustrates the decay power differences. Figure A-43 and Figure A-44 show a comparison of the UA and Surry SOARCA SG levels and water mass responses. As discussed in Section 2.3.5, the UA model had a more refined nodalization of the SG. The swollen level stayed higher in the UA downcomer level during the first 20 minutes of the boil-off until the downcomer level dropped below the top of the boiler. The new UA nodalization also resulted in a smaller SG water mass (see Section 2.3.5). Consequently, more SG water was boiled more quickly in the Surry SOARCA calculation. The net effect was similar timings to the SG dryout (1 hr 16 min for Surry SOARCA and 1 hr 22 min for the UA in Table A-11). Since the SG is the primary decay heat removal pathway when there is secondary water, the differences in the boiling rate is directly a function of the core decay power (i.e., more water boiled away in less time in the Surry SOARCA calculation).

At 11 min prior to the SGs dryout (i.e., 2 hr 11 min, Table A-11), the number of safety valve cycles reached 45 and the safety valves stuck open in each SG (see Figure A-45). In contrast, the failure of the SOARCA SG valves was not predicted until 256 cycles. The Surry SOARCA valve cycling stopped shortly after the SG water inventory was gone. Consequently, the Surry SOARCA SG safety valves did not reach 256 valve cycles. The Surry SOARCA SGs remained at relatively high pressure for the duration of calculation. As discussed previously, the depressurization of the SGs increased the stress across the SG tubes in the UA calculation.

Following the stuck-open safety valves on the SGs, the UA primary system depressurizes with the SGs until they dryout 11 min later (see Figure A-46). In contrast, the Surry SOARCA pressurizer pressure remained high because it did not include a SG depressurization by either secondary SVs sticking open or MSIV leakage. Following the SG dryout, the primary system rises in both calculations until the pressurizer safety valves open. The safety valves vent steam to control the primary system pressure, which gradually reduces the primary system water inventory (Figure A-47). Similar to the SG valve response, the pressurizer safety valve reached 45 cycles at 3 hr in the UA calculation and stuck open to 50 percent open (see Item 5 in Table A-10). Consequently, while the Surry SOARCA RPV level decrease slowed at the bottom of the active fuel until the hot leg failure at 3 hr 45 min, the UA level continued to drop as the RPV depressurized with a stuck open pressurizer valve. In summary, the drop in the UA RPV level was later and slower due to the lower decay heat and primary system depressurization following the stuck open SG valves. However, the stuck-open pressurizer safety valve in the UA calculation led to more inventory loss prior to the hot leg failure.

The hot leg failure occurred at 3 hr 45 min and 4 hr 15 min in the Surry SOARCA and UA calculations, respectively. The delayed hot leg failure in the UA is attributed to the lower decay heat power and the new hot leg creep rupture modeling. As shown in Figure A-48, the start of

the fuel heat-up was delayed by approximately 20 min in the UA calculation. However, the subsequent heatup in the UA calculation was faster than the Surry SOARCA calculation. Although the core decay power was lower in the UA calculation during the fuel heat up, the total oxidation and decay heat power was comparable (Figure A-49). The stuck-open pressurizer safety valve in the UA calculation increased the core steam flow and oxidation power. The oxidation power increased more rapidly in the UA calculation, which resulted in a faster fuel heatup (see Figure A-48).

The hot leg gas and piping temperature responses are compared in Figure A-50. Although the peak gas temperature near the hot leg nozzle is similar in the two calculations, the UA calculation remains near the peak temperature longer. As a result, the UA hot leg piping heats nearly 300°F higher than the Surry SOARCA piping before the corresponding hot leg creep rupture failure. As shown in Figure A-51, the UA hot leg creep index did not reach the failure condition until 4 hr 15 min versus 3 hr 45 min in the Surry SOARCA calculation. The delay in the UA calculation is attributable to the lower stress in hot leg (i.e.,  $\Delta P_{UA} \sim 700$  psi versus  $\Delta P_{SOARCA} \sim 1300$  psi).

Following the hot leg failure, the primary system quickly depressurized (see Figure A-46). The Surry SOARCA calculation RPV depressurized from hot leg failure whereas the UA primary system had substantially depressurized due to the stuck open pressurizer safety valve. The accumulator reflooded the core (see Figure A-47) and partially quenched the core in the Surry SOARCA calculation (see Figure A-48). Due to the delayed hot leg failure in the UA calculation, there was substantial core damage prior to the hot leg failure. As shown in Figure A-48, the cladding temperatures dropped to zero (i.e., indicating collapse of the fuel in that region) prior to the hot leg failure at 4 hr 15 min. Also, the core plate and the lower core plate failed prior to the hot leg failure in the UA calculation (see Table A-11). In contrast, the core was intact in the SOARCA calculation at the time of the hot leg failure and accumulator reflood (i.e., the UA calculation is not in the same chronological order).

The relocation of debris into the lower plenum in the UA calculation prior to hot leg failure accelerated the timing to the RPV lower plenum dryout (see Table A-11). However, the lower decay heat power delayed the lower head failure until 9 hr 3 min in the UA calculation versus 8 hr 6 min in the Surry SOARCA calculation. The subsequent debris ejection to the containment is shown in Figure A-52. The more gradual relocation of debris in the UA calculation occurred because the lowest powered fuel in the periphery of the core collapsed after RPV failure. In the Surry SOARCA calculation, the complete collapse of all the fuel occurred prior to the lower head failure.

The hot debris boiled away the water in the reactor cavity and started to ablate the concrete. The ex-vessel core concrete interactions (CCI) continued for the remainder of the calculation, which ablated the concrete (see Figure A-53) and generated non-condensable gases (see Figure A-54). There were relatively large differences in the ablation depths and the integral CO and CO<sub>2</sub> gas generation between the Surry SOARCA and UA models. As was discussed in Section 2.3.1, the concrete type was incorrectly specified as limestone in the Surry SOARCA model. The UA calculation used basaltic concrete. The ablation of limestone concrete generates significantly more (>10X) CO than basaltic concrete. The UA calculation did not predict any significant changes in the CO<sub>2</sub> gas generation rate (i.e., the Surry SOARCA gas generation rate increased after 40 h).

Figure A-55 shows a comparison of the ex-vessel debris heat flow in the UA and Surry SOARCA calculations. As discussed previously, the overall decay heat power is lower in the

UA calculation. Similarly, the ex-vessel decay heat was also correspondingly lower in the UA calculation (QDH in Figure A-55). The power due to chemical reactions is higher in the UA calculation after the start of core-concrete interactions (QRea on Figure A-55). However, the magnitude of the chemical reactions power is small relative to the other ex-vessel heat flows. As discussed in Section 2.3.4, the ex-vessel heat transfer modeling was improved in MELCOR 2.1. Although both calculations use the same physics models, the user input for the UA calculation was updated to better match the heat flow to an overlying pool (see Section 2.3.4). The MELCOR 2.1 SOARCA calculation used the conductivity and nucleate boiling multipliers from the Surry SOARCA MELCOR 1.8.6 calculation (i.e., rather than the new best estimate values described as part of the reactor cavity modeling improvements described in Section 2.3.5). The UA calculation used updated input that was optimized to match MACE heat transfer to a water pool and the dry cavity erosion rates. The recommended settings resulted in a comparable surface heat loss (Qsurf on Figure A-55) but a lower heat flow for concrete ablation of the concrete (QAB on Figure A-55) in the UA calculation. However, some of the differences in the erosion rates in the two calculations can be attributed to differences in the ablation physics for the different concrete types.

The resultant non-condensable gas and steam generation pressurized the containment (see Figure A-56). The MELCOR 2.1 case reached the design pressure at 11 hr 16 min versus 23 hr 7 min for UA calculation (see Table A-11). The much slower pressurization in the UA calculation is attributed to the lower decay heat and, to a lesser extent, the much lower non-condensable gas generation. The containment failed due to liner tearing near the containment equipment hatch at mid height in the cylindrical region of the containment at 26 h 22 min and 41 hr 5 min, respectively for Surry SOARCA and UA calculations, respectively (i.e., see the containment leakage area in Figure A-57). Although the heat loss from the debris was similar in the two calculations (Qsurf on Figure A-55), the much higher non-condensable gas generation rate in the Surry SOARCA calculation resulted in more heat flow from the reactor cavity and slightly higher overall temperatures in containment (Figure A-59). The containment continued to pressurize until the leakage flow balanced the steam and non-condensable gas generation. However, the water evaporation had slowed and the containment was depressurizing after 45 h 22 min in the SOARCA calculation (see Figure A-56).

The only hydrogen burns in the containment occurred following the initial discharge of hydrogen and steam at hot leg failure in the Surry SOARCA calculation (see Figure A-60 and at a smaller scale in Figure A-14). The magnitude of the burns was much higher in the UA calculation. Burns occurred in the UA calculation at the hot leg nozzle failure (4 hr 14 min), vessel failure (9 hr 19 min), and at 11 hr 28 min. The lower threshold for hydrogen combustion (see Table A-10 and Sections 2.4.5 and 2.4.7) led to wide-spread propagation of burn at hot leg failure. The new lean hydrogen combustion changes also permitted a late combustion in the containment basement at 11 hr 28 min. However, the resulting containment pressurization from the burns in the UA calculation did not challenge the containment integrity and were small compared to the long-term pressurization (Figure A-56).

Figure A-61 and Figure A-62 show a comparison of the UA and Surry SOARCA long-term distributions of the iodine and cesium radionuclides that were released from the fuel, respectively. The fission product releases from the fuel started following the first thermal-mechanical failures of the fuel cladding in the hottest rods at 2 hr 57 min in the SOARCA calculation and 3 hr 22 min in the UA calculation. There are several key differences in the distribution of the released radionuclides in the two calculations. Since the UA calculation was depressurizing through the stuck-open pressurizer safety valve after 3 hr (see Table A-11),

a significant portion of the radionuclides were released to the PRT. Although the PRT rupture disk opened about 1 hour before the start of the start of the fission product releases, there was a significant retention of aerosol radionuclides in the water. In contrast, the pressurizer relief valves were closed during radionuclide release in the Surry SOARCA calculation. Consequently, no radionuclides were captured in the PRT in the Surry SOARCA calculation. The decay heat from the radionuclides boiled the PRT dry at 17 hr 26 min (see Figure A-63). MELCOR conservatively resuspends the aerosols captured in the PRT water, which led to a decrease in the in-vessel inventory (i.e., the PRT is included in the in-vessel curve in Figure A-61 and Figure A-62) and an increase in containment radionuclide inventory.

A second key difference is the in-vessel radionuclide release prior to hot leg failure. Due to the delayed hot leg failure in the UA calculation, most of the volatile radionuclides were released prior to hot leg failure. This led to substantially more radionuclides in the vessel, the SG, and the PRT in the UA calculation. In contrast, the Surry SOARCA radionuclide release from the fuel was interrupted by hot leg failure with much smaller releases. The majority of the released cesium and iodine radionuclides was airborne in the RCS at hot leg failure and was discharged to containment. The majority of the radionuclide release occurred after hot leg failure and went to the containment through the hot leg failure. Consequently, the iodine and cesium containment distributions closely follow the respective release from fuel in the Surry SOARCA calculation.

Both codes show nearly complete in-vessel release of the iodine and cesium released from the fuel prior to vessel failure. A small iodine and cesium ex-vessel release after vessel failure is also shown on the figures. The ex-vessel iodine and cesium releases were approximately 10X larger and more protracted in the UA calculation but small relative to the in-vessel release.

As discussed in Section 2.1, the MELCOR 2.1 SOARCA calculation did not show any appreciable long-term re-vaporization of the iodine or cesium. Similarly, the UA calculation did not show an appreciable re-vaporization of iodine or cesium as there was no rebar failure. However, the UA calculation shows a large release of radionuclides at the PRT dryout, and there was some gradual revaporization following this event.

Finally, the release to the environment was also different between the two calculations (see Figure A-64 and Figure A-65). As discussed previously, the timing to the containment liner yield was substantially different (see Table A-11). However, the UA calculation included more nominal leakage prior to the liner failure (see Table A-10). The impact of the higher nominal containment leakage in the UA calculation is clearly observed in the xenon release to the environment. The released xenon was not retained in the PRT in the UA calculation. Consequently, the start of the xenon to the environment is evident shortly after the start of the release from the fuel. However, the xenon release to the environment was relatively small due to the small leak rate prior to the liner failure (see Figure A-57). The aerosols were initially captured in the PRT in the UA calculation, but this capture is suppressed by PRT dry-out. There are some initial signs of the iodine releases to the environment after the pressurizer tank dryout in the UA calculation. The cesium releases followed the iodine releases due to the small amount in the containment (compare the UA iodine and cesium containment distributions in Figure A-61 and Figure A-62, respectively).

Following liner failure in the Surry SOARCA calculation at 26 hr 22 min, most of the volatile radionuclide releases to the environment increase above UA values (Figure A-64 and Figure A-65). The only exception is cesium, which is slightly higher in the UA calculation. The UA calculation also shows an increase in the environmental release following the containment liner

failure at 41 hr 05 min. As discussed in Section 2.1, the MELCOR 2.1 SOARCA long-term Molybdenum release increased after the steel components in the melt were fully oxidized. There is also a decrease in carbon-dioxide production and a decrease in carbon-monoxide production following the complete oxidation of the steel components (Figure A-8). Although the Surry SOARCA and UA calculations had similar amounts of steel in the ex-vessel debris, the concrete types were different and the erosion and heat loss modeling had changed (see Section 2.3.4). The change in ablation rate and melt chemistry resulted in a much slower steel oxidation rate (see Figure A-66). Although the chromium was consumed in the UA calculation, there was ample iron and nickel available through 48 hr. Consequently, the UA calculation had a very small ex-vessel release of molybdenum. The total molybdenum release was also impacted by the new speciation of the volatile cesium with both molybdenum and steam (i.e., cesium-hydroxide, see Section 2.4.9). In contrast, essentially all the cesium was combined with molybdenum in the Surry SOARCA calculation. In both calculations, only a small portion of the molybdenum combines with the cesium (i.e., there much more molybdenum than cesium). Consequently, a vigorous ex-vessel molybdenum oxidation reaction is needed to release an appreciable amount of the molybdenum.

In summary, a comparison of the results from the UA base case calculation and the direct conversion of the Surry SOARCA SBO model show some key differences. Both calculations used the identical code version. However, the model improvements and enhancements described in Sections 2.2, 2.3, and 2.4 had important impacts on the accident progression. The initial response in the UA calculation was delayed relative to the Surry SOARCA calculation due to the new, best estimate decay heat power. The Surry SOARCA calculation used a conservative decay power from a high burn-up analysis. The following other notable differences were observed,

- The lowest set-point safety valves on each of the 3 SGs cycled 45 times and failed to close before the SGs boiled dry in the UA calculation. The SGs depressurized after the safety valves stuck open. The cycle failure limit was much higher in the Surry SOARCA calculation and the SGs remained at high pressure.
- The lowest set-point safety valve on the pressurizer stuck open after 45 cycles, which depressurized the RCS prior to a hot leg creep rupture. The cycle failure limit was much higher in the Surry SOARCA calculation and the RCS remained at higher pressure until the hot leg failure.
- The new hot leg creep rupture failure modeling and lower primary pressure delayed the failure until after substantial core damage and fuel collapse in the UA calculation. The hot leg failure occurred earlier and prior to core collapse in the Surry SOARCA calculation.
- The new lean hydrogen combustion modeling and enhanced steam condensation in containment resulted in more energetic hydrogen deflagrations in the UA calculation. Similar to the Surry SOARCA calculation, the first two burns occurred at hot leg failure and vessel failure. However, one burn took place in the UA calculation well after vessel failure when the Surry SOARCA calculation predicted steam inerting. Although the UA burns were substantially stronger than the Surry SOARCA burns, they did not challenge the containment integrity.

- Neither the UA nor the Surry SOARCA calculations were close to a thermally-induced SGTR. The UA calculation included a hot tube model that simulated the most vulnerable tube and included some wall thinning.
- The containment design pressure and the pressure associated with liner yield were exceeded in both the UA and the Surry SOARCA calculation. The UA calculation included higher containment leakage prior to the liner failure. The UA liner failure did not occur until ~15 hr after the Surry SOARCA calculation.
- The largest contributor to UA containment pressurization was the continuous heating of original RCS coolant to steam in the containment (rather than to the addition of non-condensable gasses to the atmosphere from core-concrete interaction as might have been anticipated). The containment pressurized due to both steam and non-condensable gas generation in the Surry SOARCA calculation.
- Releases to the environment of iodine and cesium were delayed and small in both calculations.

**Table A-10 Values prescribed for UA uncertain parameters in the base calculation.**

#	Variable	Best Estimate	Original SOARCA Value	Rationale (SOARCA refers to original single run)
1	Primary SV stochastic failure to close (SVLAMFTC) pri_SV_1_fail_cycl	45	256	Mean of samples, sampling is based on NUREG/CR-7037 which only used data from real plant SCRAMs, not test data, SOARCA was based on Surry point estimate, real data is more defensible.
2	Primary SV stochastic failure to open (SVLAMFTO) pri_SV_1_fail_pos	N/A	N/A	Probability of FTO is much lower than FTC based on NUREG/CR-7037 data, so it will not occur in the base case run, SOARCA did not consider this failure
3	Primary SV failure to close due to passing water (SVWTR) pri_SV_h2o	25	N/A	About 0.5 on the CDF for the mean and 50 <sup>th</sup> curves; SOARCA did not consider this failure
4	Primary SV thermal seizure criterion (SVFAILT) SV_fail_T	1000 K	1000 K	0.5 on the CDF and SOARCA value maintained
5	Primary SV open area fraction upon either stochastic or thermal failure (SVOAFRAC)	0.5	1.0	0.5 on the CDF; SOARCA assumed fully open on failing but distribution is more supported since a SV can fail in any position
6	Secondary SV stochastic failure to reclose (SVLAMFTC-S/G)	45	256	Same valve as primary, see #1 – Also of minimal importance since secondary side depressurizes from MSIV leakage
7	Reactor Coolant Pump Seal Leakage (RCPSL)	21 and 21 gpm	21 gpm with possibility to increase	Highest probability discrete bin; SOARCA allowed for increased leakage based on saturation conditions but new uncertainty logic does not support this.
8	Steam Generator Tube Thickness	1.063 mm	1.212 mm	Mode of symmetric triangular distribution and 0.5 on CDF.
9	Hot SG Tube Temperature Multiplier	0.44	N/A	0.5 on the CDF; SOARCA did not consider this
10	Zircaloy melt breakout temperature (SC1131(2))	2350 K	2400 K	0.5 on the CDF; logically supported considering new data is slightly lower than SOARCA value
11	Material Properties: Eutectic temperatures for ZRO2 and UO2 (ZRO2/UO2)	2479 K	2800 K	Mode of normal distribution; SOARCA value is melting point for a 50/50 molar mixture and wasn't modified because of the presence of time-at-temperature model; new MELCOR default is 2500 K – close to mode
12	Molten clad drainage rate (SC1141(2))	0.2	0.2	SOARCA value maintained; not at 0.5 of the CDF but justified by the CORA experiments

#	Variable	Best Estimate	Original SOARCA Value	Rationale (SOARCA refers to original single run)
13	Radial molten debris relocation time constant (RDMTC)	60 s	60 s	SOARCA value maintained, uncertainty range set to see important so there is no technical justification to modify best estimate
14	Solid radial debris relocation time constant (RDSTC)	360 s	360 s	SOARCA value maintained, uncertainty range set to see important so there is no technical justification to modify best estimate
15	Decay Heat Cycle	MOC, base decay heat	EOC, base decay heat	Assuming an accident can happen on any day of the cycle, MOC is closest to the majority of days. SOARCA used a Sequoyah EOC ORIGEN run, UA ORIGEN runs are now Surry specific. Decay heat does not have to be adjusted because the base ORIGEN decay heat is the mode of a normal distribution.
16	Containment Leakage Rate (%Volume/ay at P/P <sub>d</sub> = 1) Leak	0.55	0.1	0.5 on the CDF; SOARCA was design basis value, determined leakage would never be lower than this but limited term operation is allowable up to 1.0 so there is a strong justification to change best estimate
17	Containment Fragility Curve (CFC) Rupture	1.6 for liner yield, other points stay same	1.55	0.5 on the CDF; also approximately represents SOARCA value with 15% conservatism removed
18	Hydrogen ignition criteria (H2 LFL)	6%	10%	Median value of discrete distribution; all bins are lower than SOARCA value but are technically justified
19	Secondary side decontamination factor (ARTIST)	N=7	N/A	Highest probability discrete bin; SOARCA used a DF of 7 for any SGTR, new modeling supersedes this
20	Gaseous Iodine fraction (CHEMFORM-I)	0.00182	0.0	0.5 on MOC CDF; MOC needed since selected as inventory best estimate; SOARCA had no gaseous iodine but a small amount is technically justified
21	Cesium fraction (CHEMFORM-Cs)	0.8 Cs <sub>2</sub> MoO <sub>4</sub>	1.0 Cs <sub>2</sub> MoO <sub>4</sub>	Best estimate based on Phebus tests and mode of created PDF; SOARCA value was based on an earlier interpretation of Phebus results
22	Containment Condensation Rate – (XMTFCL)	1.4	1.0	Mode of PDF and best estimate based on comparisons to CONTAIN and experiments; parameter not considered in SOARCA so default was used
23	Radionuclide (RN) Package Reference Manual: Particle Shape Factor	1.5	1.0	0.5 on CDF, data suggests range of 1-2 is most likely, SOARCA value of 1 is for perfect spheres which is physical lower bound

**Table A-11 Comparison of the key event timing in the SOARCA, converted MELCOR 2.1, and base UA calculations.**

Event Timing	SOARCA V1.8.6	SOARCA V2.1	UA Base Model
	(hh:mm)		
STSBO – loss of all AC and DC electrical power, AFW unavailable	00:00	00:00	00:00
Reactor trips MSIVs close RCP seal leakage initiates at 21 gpm/pump	00:00	00:00	00:00
RCP seal failure (182 gpm/pump)	02:45	02:47	-
SG SV fails to close	-	-	01:11
SG dryout	01:16	01:16	01:22
First pressurizer SV opening	01:27	01:27	01:49
PRT rupture disk breaks	01:46	01:46	02:09
Start of fuel heatup	02:19	02:20	02:42
Pressurizer SV fails to close	-	-	03:00
First fission product gap release	02:57	02:57	03:22
SGTR	-	-	-
Loop A hot leg nozzle rupture	03:45	03:45	04:15
1 <sup>st</sup> hydrogen burn	03:45	03:45	04:15
Accumulators begin discharging	03:45	03:45	04:15
Accumulators empty	03:45	03:46	04:16
First failure of the core support plate	04:23	04:51	04:01 <sup>A</sup>
First failure of the lower support plate	06:36	07:33	04:08 <sup>A</sup>
RPV dry	06:39	07:35	06:15
RPV lower head breach	07:16	08:06	09:03
Reactor cavity dry	07:27	08:35	09:09
Containment pressure reaches design (45 psig)	11:00	11:16	23:07
Pressurizer surge tank dryout	-	-	17:26
Containment liner yields	25:32	26:22	41:05
Release of elemental iodine to the environment exceeds 0.1%	30:12	36:50	Max (0.07%)
Containment rebar yields	-	-	-
End of calculation	48:00	48:00	48:00

Note: A. This event is not in chronological order in the MELCOR 2.1 UA Base Model calculation.

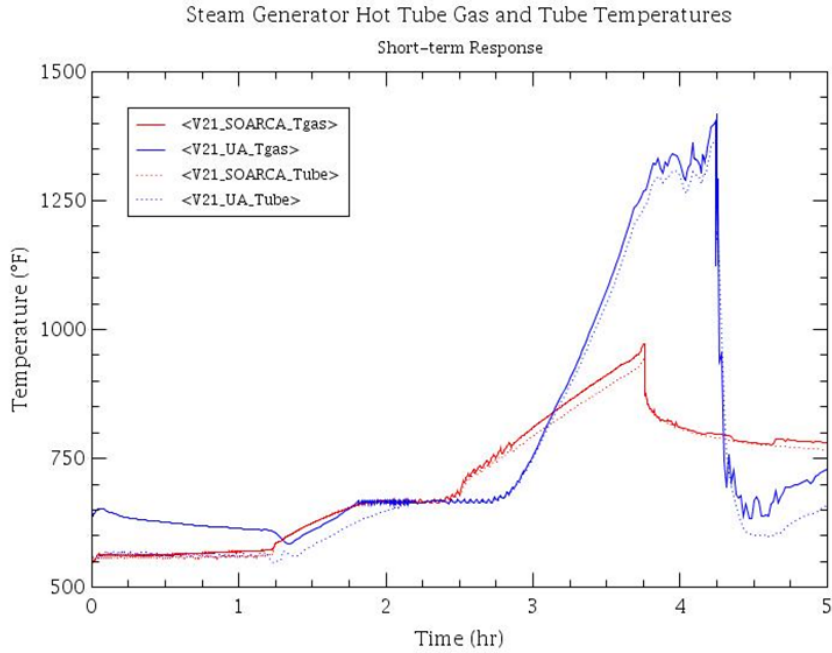


**Figure A-39 Comparison of the UA hot SG tube and SOARCA SG tube gas and tube temperature responses**

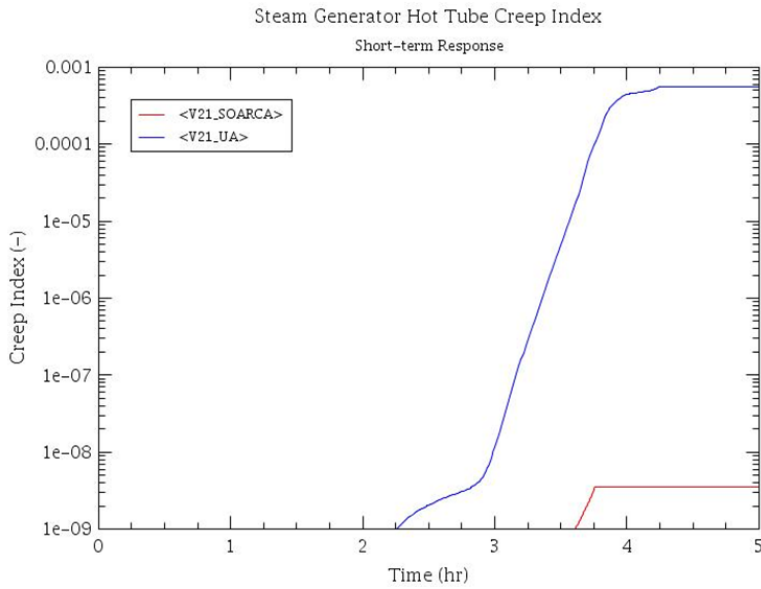


**Figure A-40 Comparison of the UA and SOARCA SG tube creep rupture index responses**

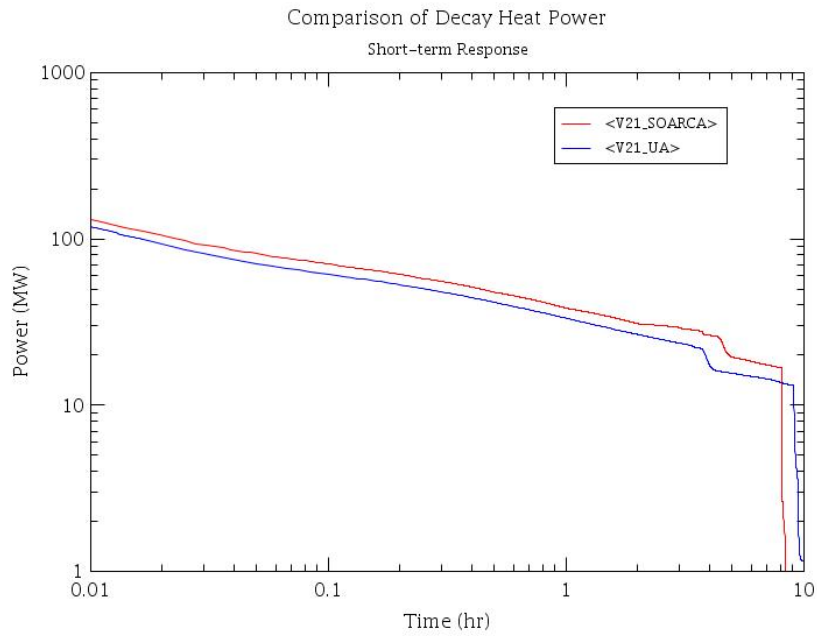


**Figure A-41 Comparison of the short-term UA and SOARCA core decay heat power responses (log-log scale)**

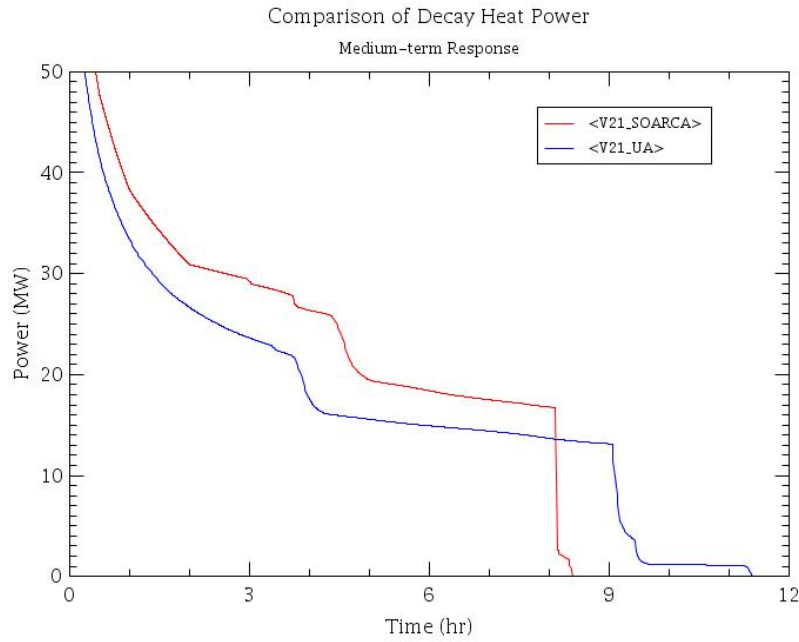


**Figure A-42 Comparison of the short-term UA and SOARCA core decay heat power responses**

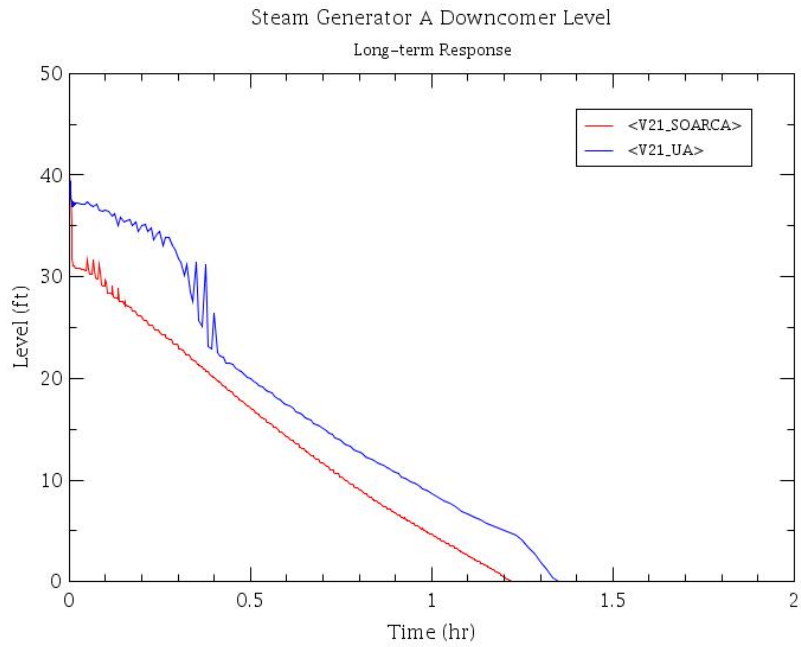


**Figure A-43 Comparison of the short-term UA and SOARCA SG levels**

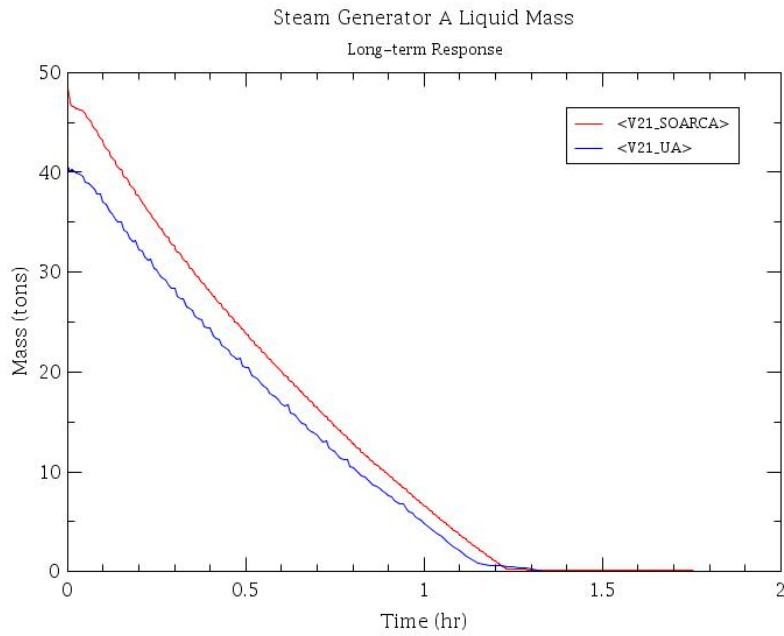


**Figure A-44 Comparison of the short-term UA and SOARCA SG water masses**

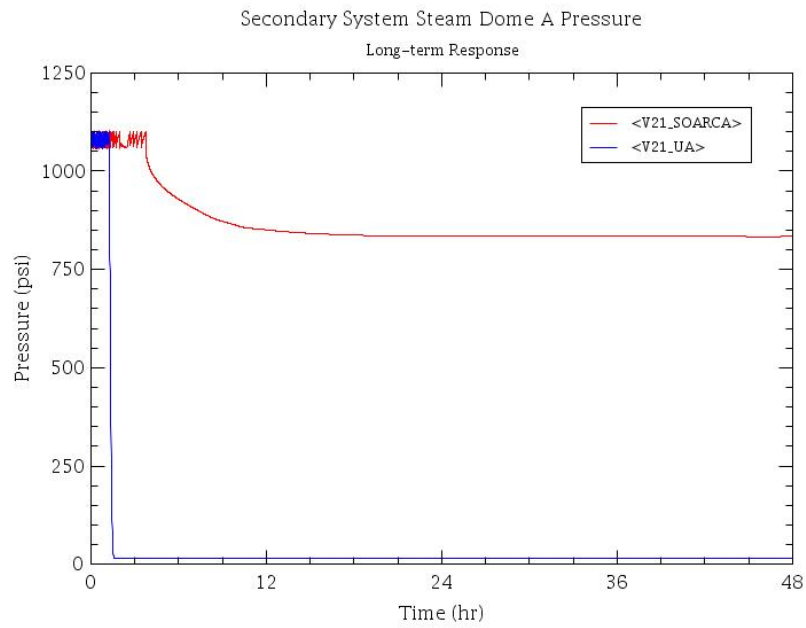


**Figure A-45 Comparison of the short-term UA and SOARCA SG pressures**

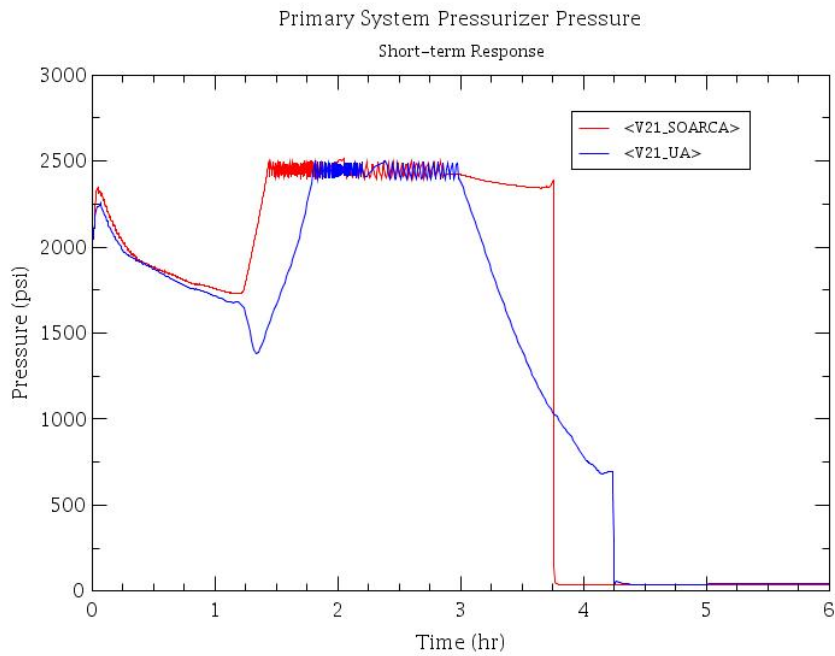


**Figure A-46 Comparison of the short-term UA and SOARCA pressurizer pressures**

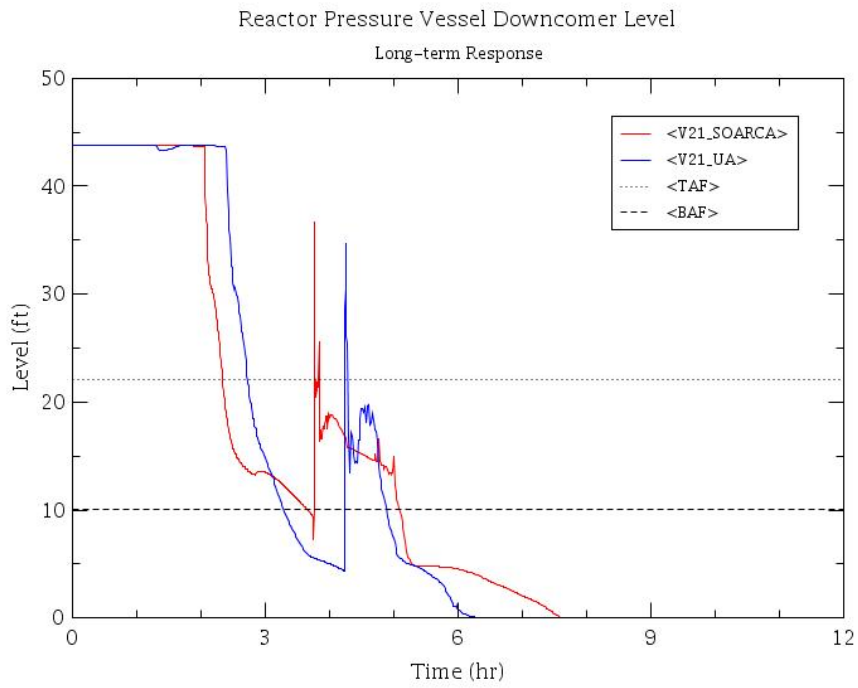


**Figure A-47 Comparison of UA and SOARCA RPV level responses**

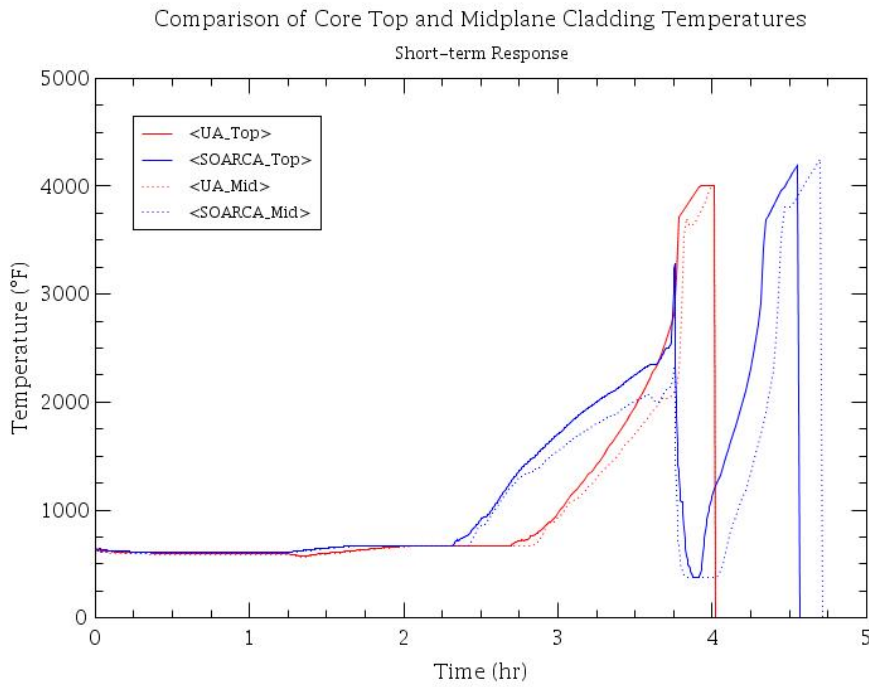


**Figure A-48 Comparison of UA and SOARCA top and midplane fuel cladding temperature responses**

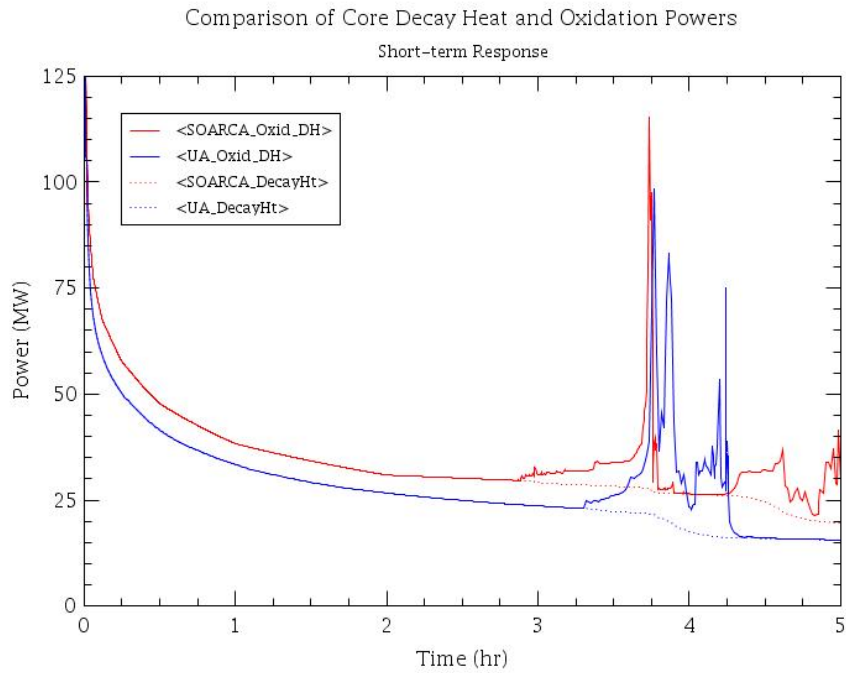


**Figure A-49 Comparison of the UA and SOARCA short-term total (oxidation + decay heat) and decay heat powers**

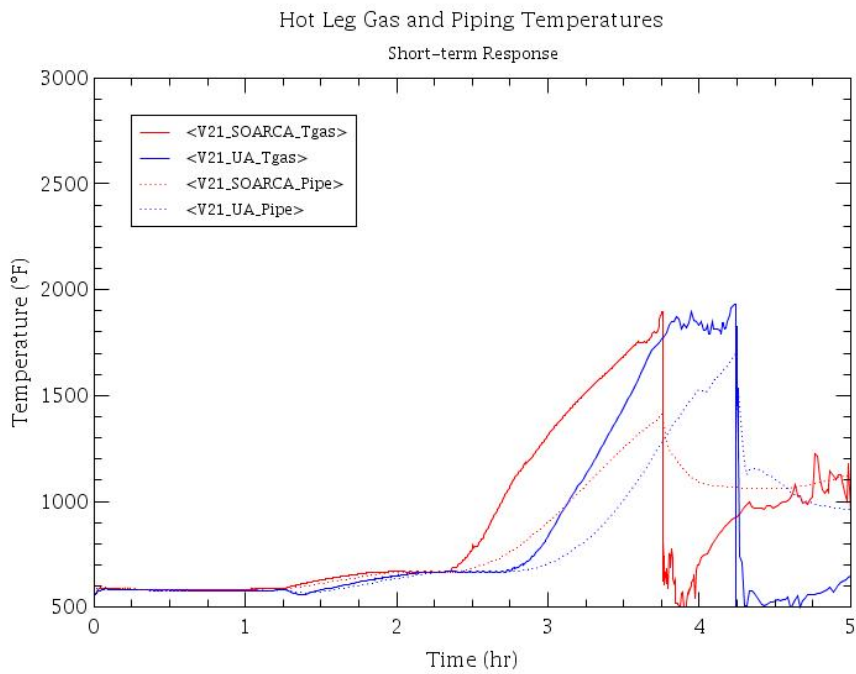


**Figure A-50 Comparison of the UA hot SG tube and SOARCA hot leg gas and piping temperature responses**

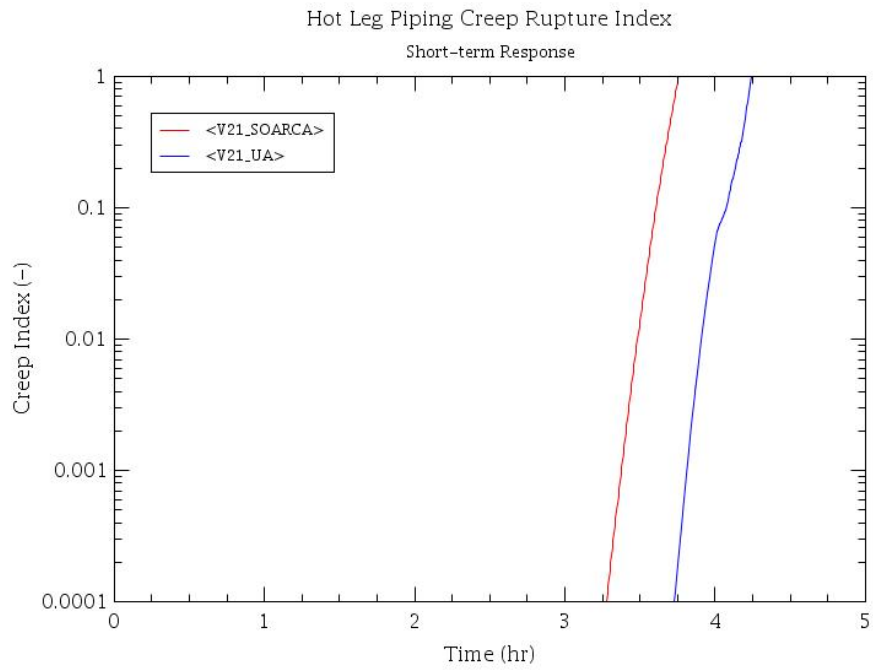


**Figure A-51 Comparison of the UA and SOARCA hot leg piping creep rupture index responses**

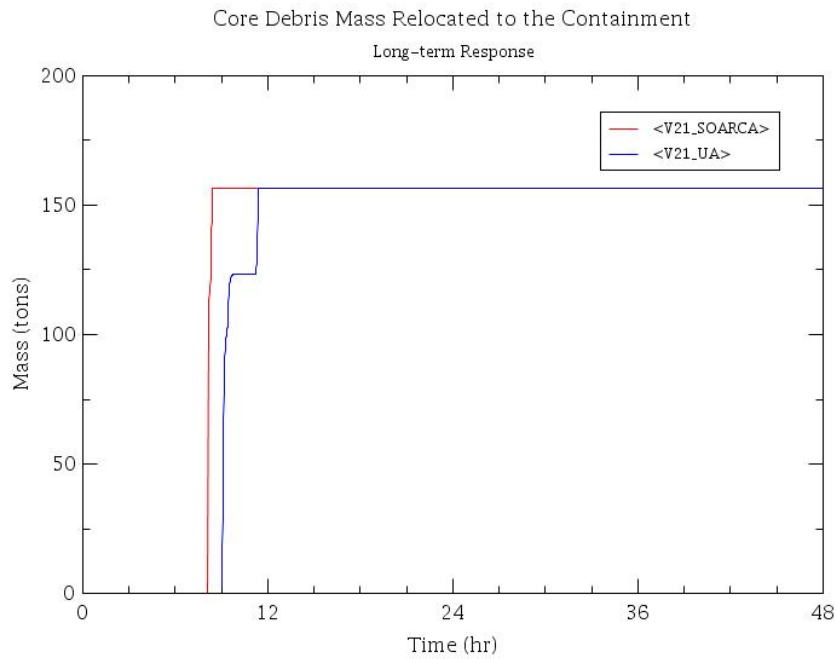


**Figure A-52 Comparison of the UA and SOARCA core mass ejected to the containment**

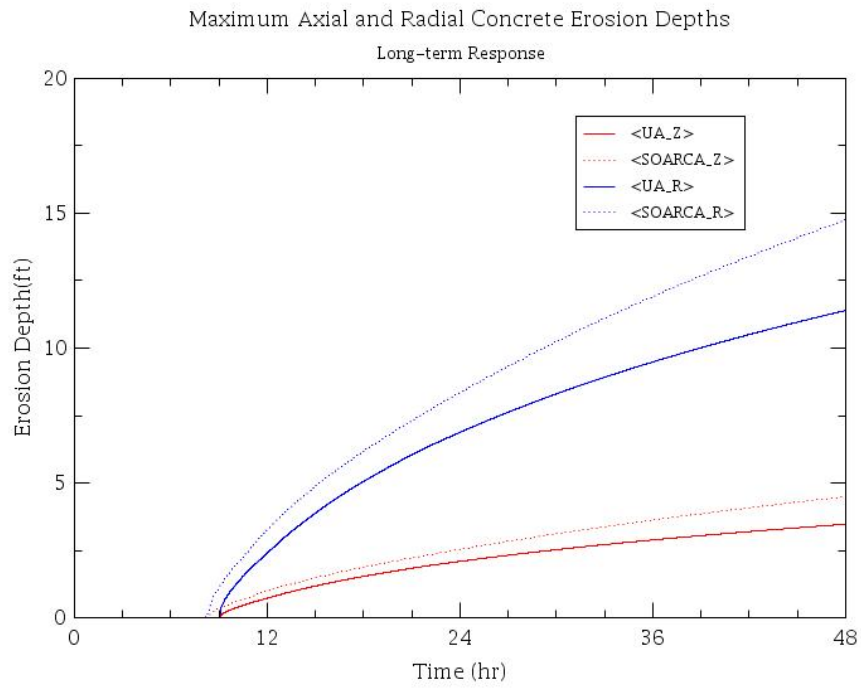


**Figure A-53 Comparison of the UA and SOARCA concrete erosion depths**

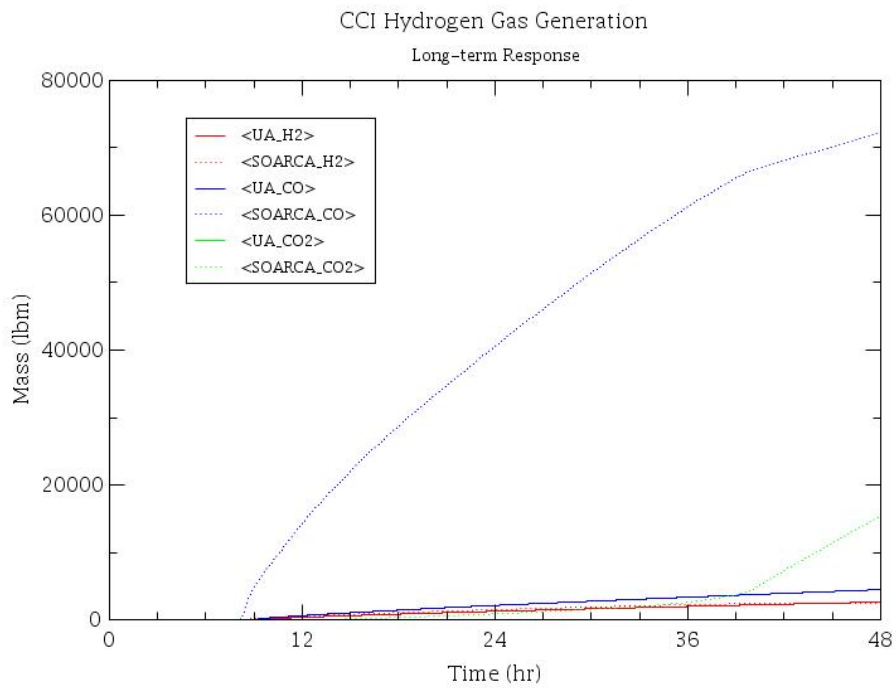


**Figure A-54 Comparison of the UA and SOARCA ex-vessel core-concrete gas generation**

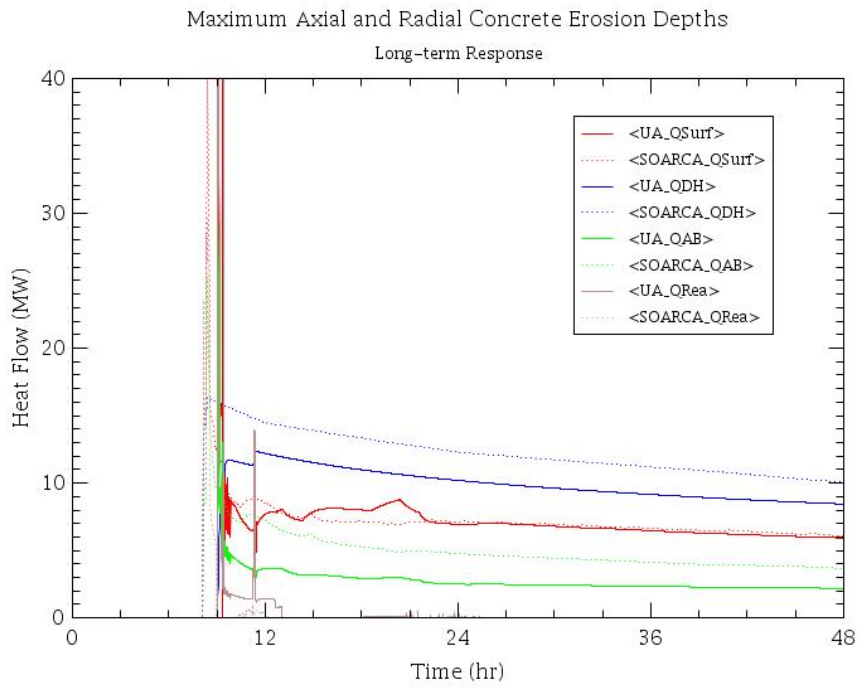


**Figure A-55 Comparison of the UA and SOARCA ex-vessel energy flow**

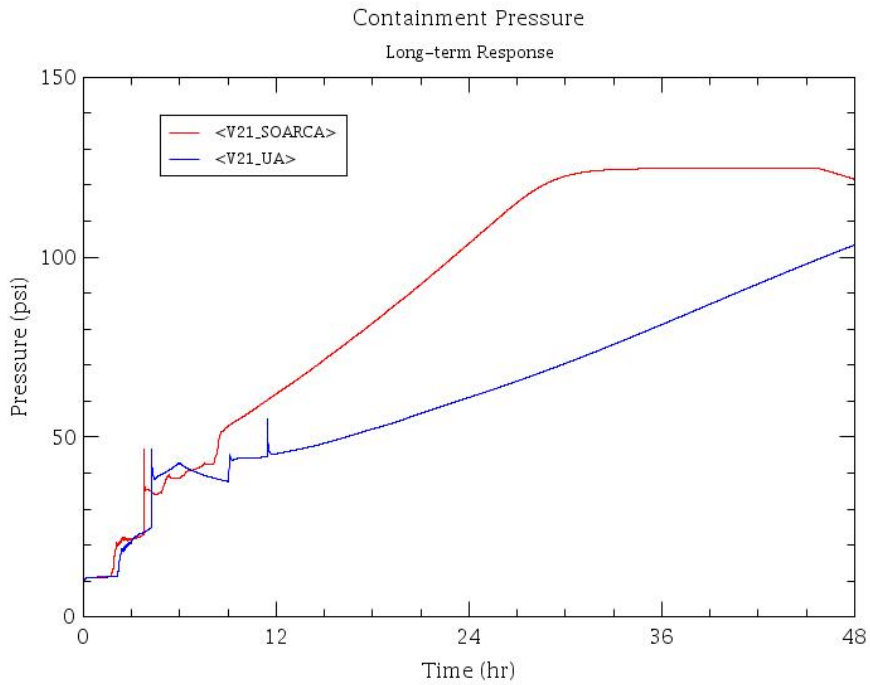


**Figure A-56 Comparison of the UA and SOARCA containment pressure response**

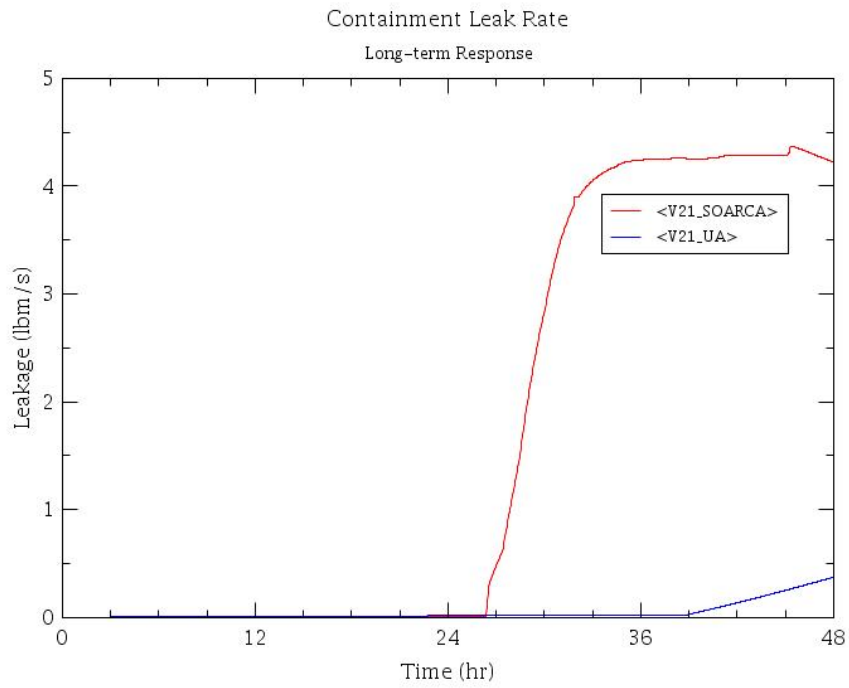


**Figure A-57 Comparison of the UA and SOARCA containment leak rate**

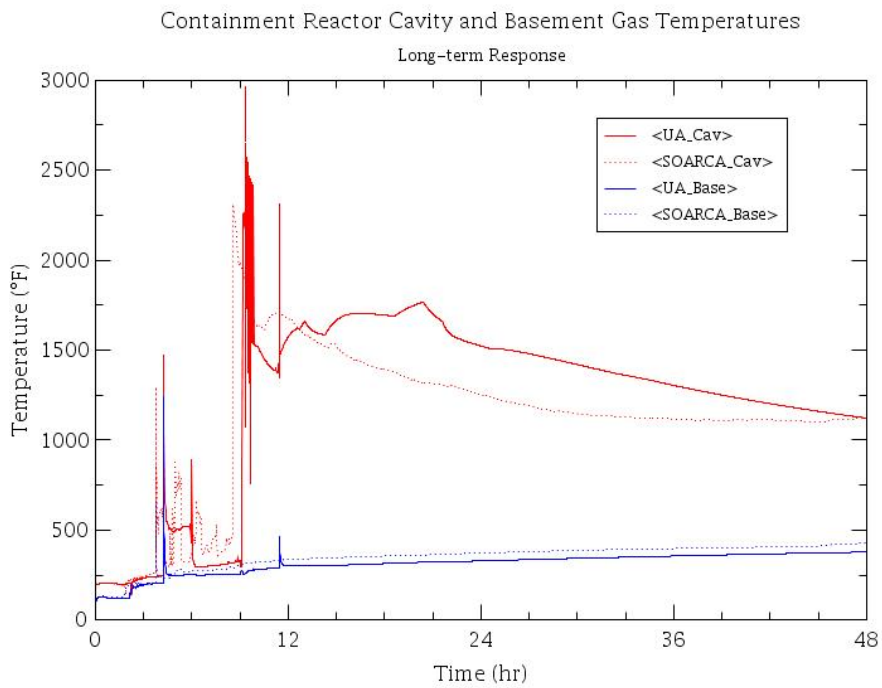


**Figure A-58 Comparison of the UA and SOARCA lower containment and reactor cavity gas temperatures**

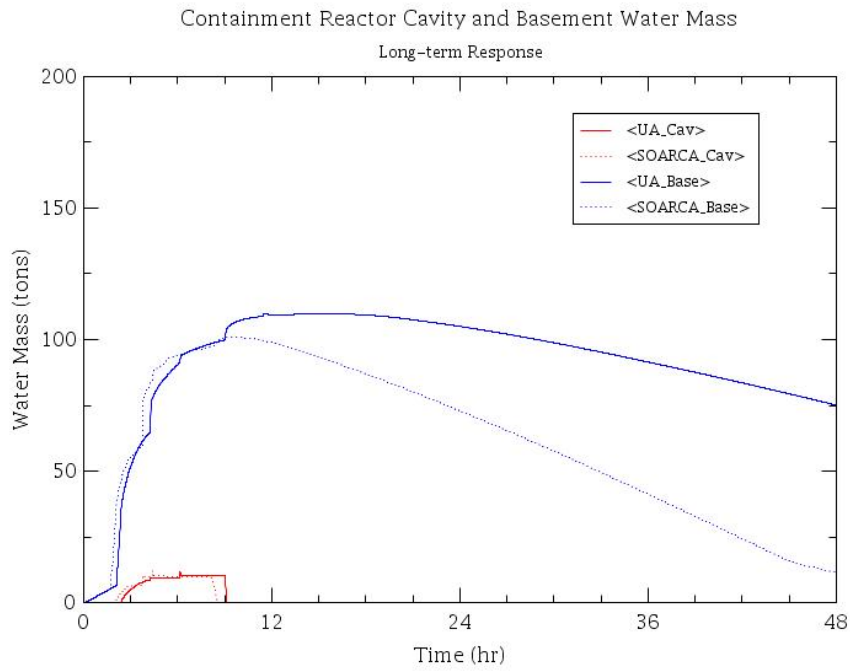


**Figure A-59 Comparison of the UA and SOARCA lower containment and reactor cavity water mass**

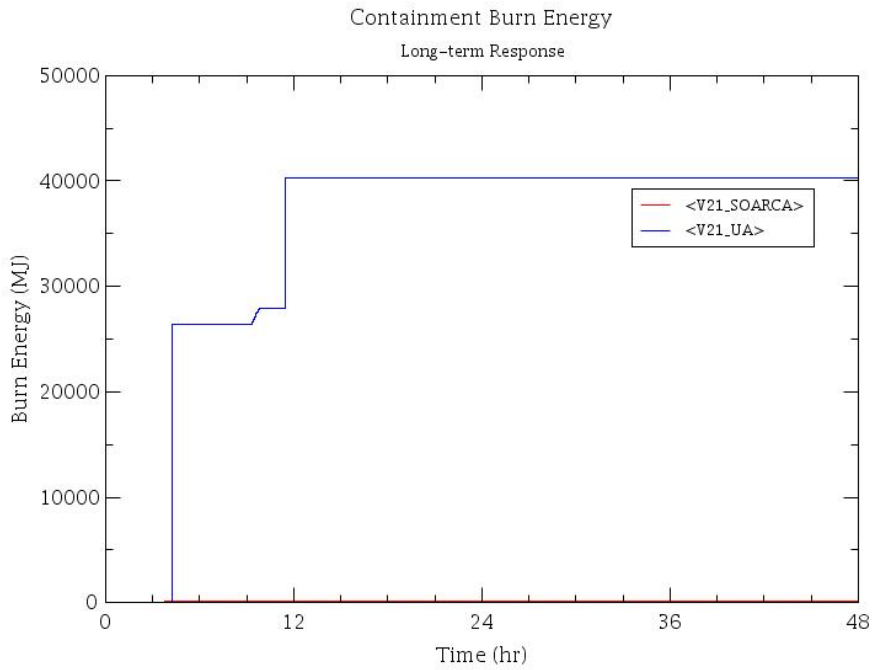


**Figure A-60 Comparison of the UA and SOARCA containment burn energy**

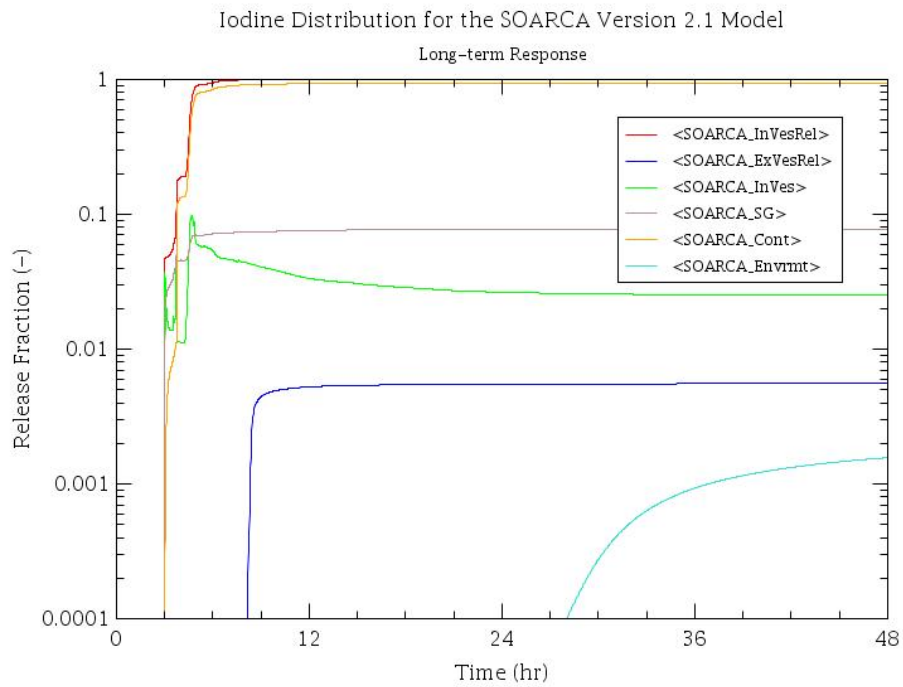
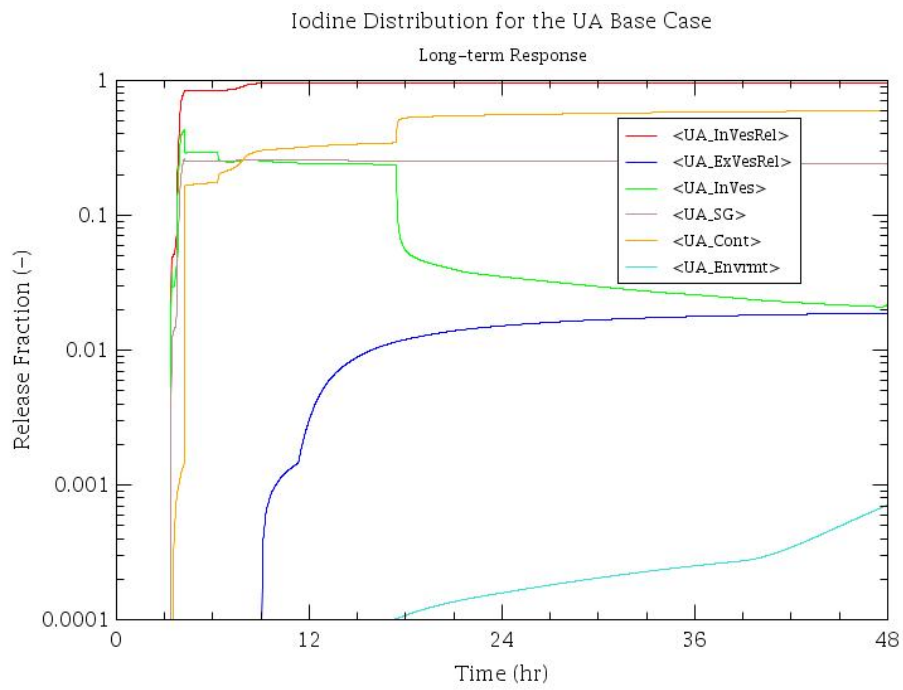


**Figure A-61 Comparison of the UA and SOARCA iodine distributions**

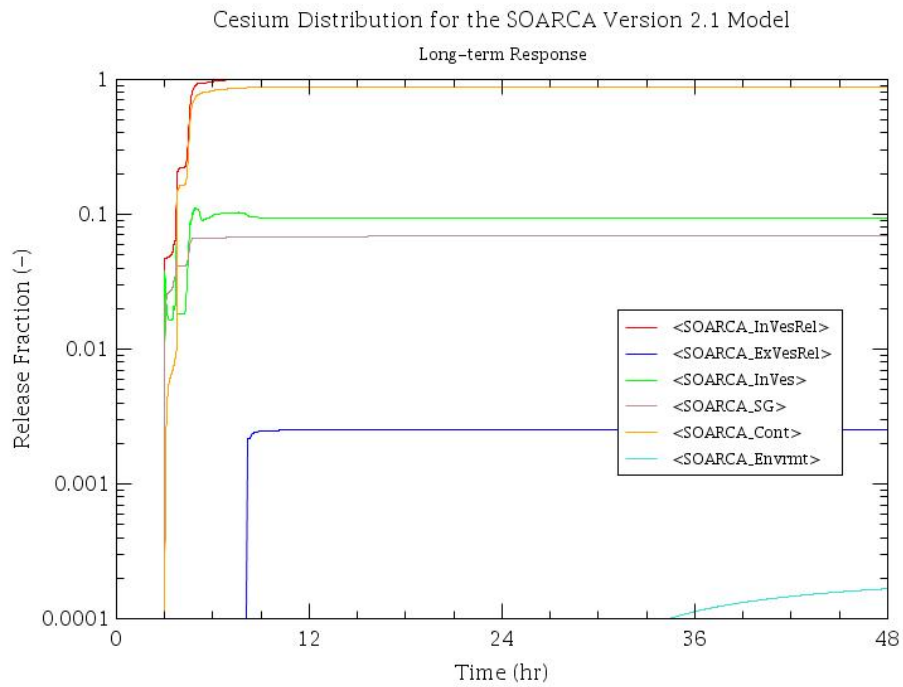
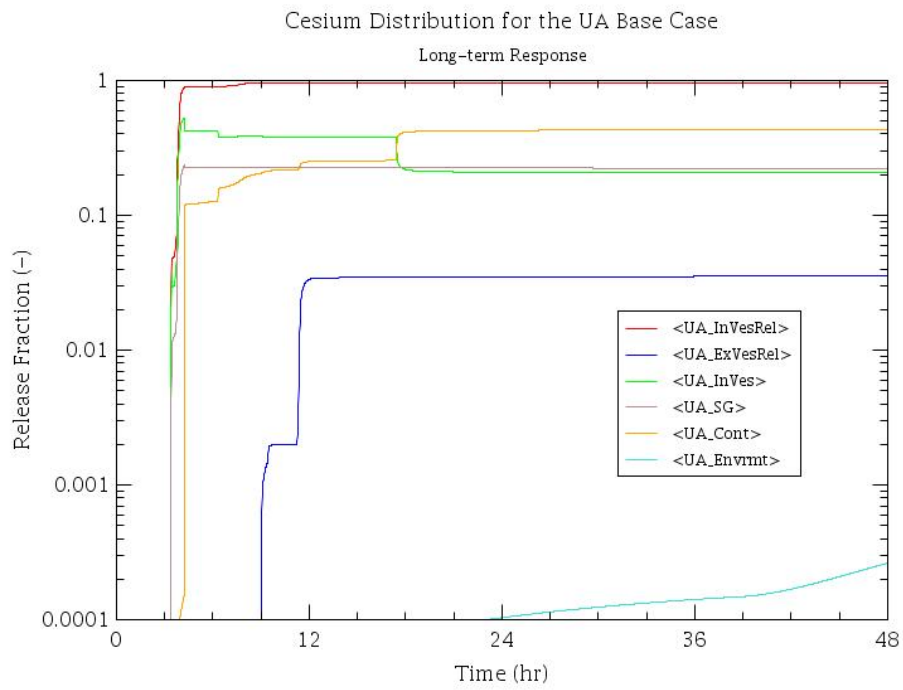


**Figure A-62 Comparison of the UA and SOARCA cesium distributions**

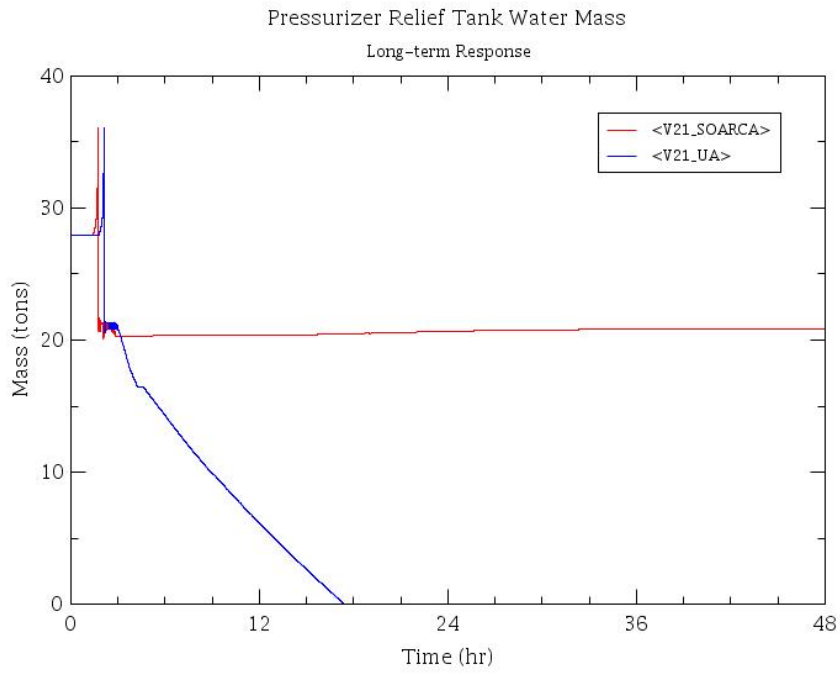


**Figure A-63 Comparison of the UA and SOARCA pressurizer relief tank water mass**

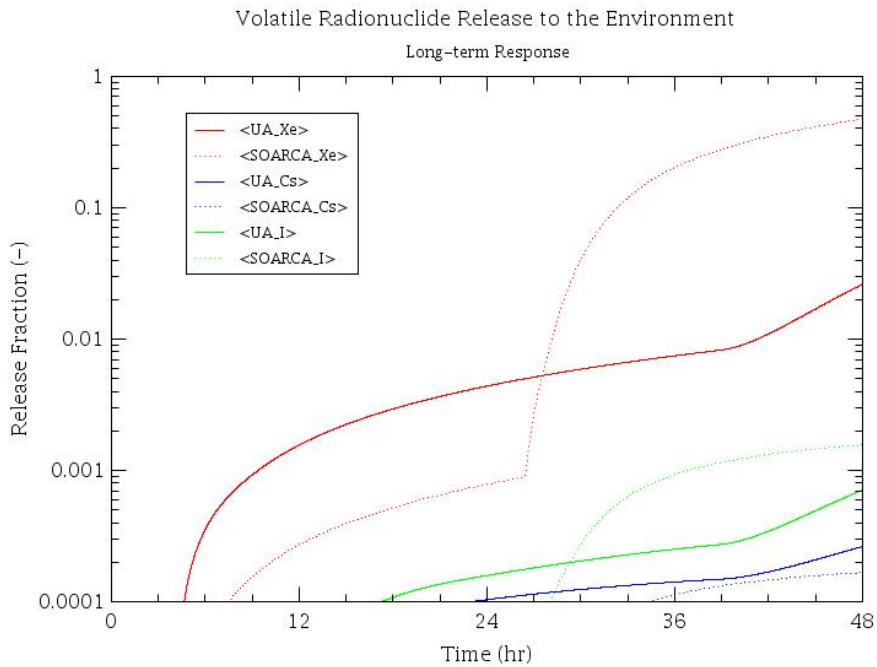


**Figure A-64 Comparison of the comparison of the UA and SOARCA highest volatile radionuclide environmental releases**

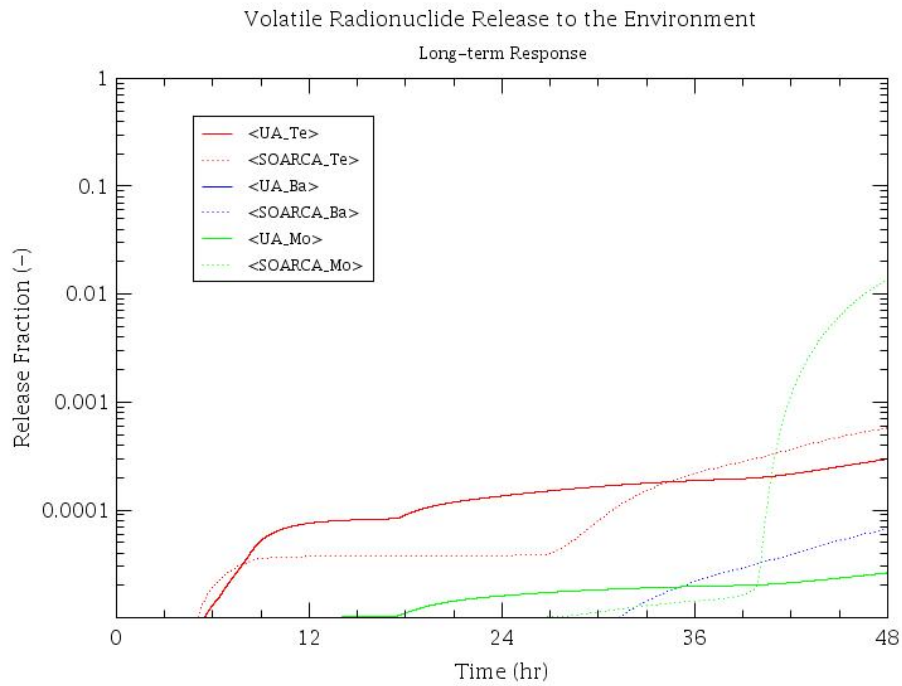


**Figure A-65 Comparison of the comparison of the UA and SOARCA volatile radionuclide environmental releases**

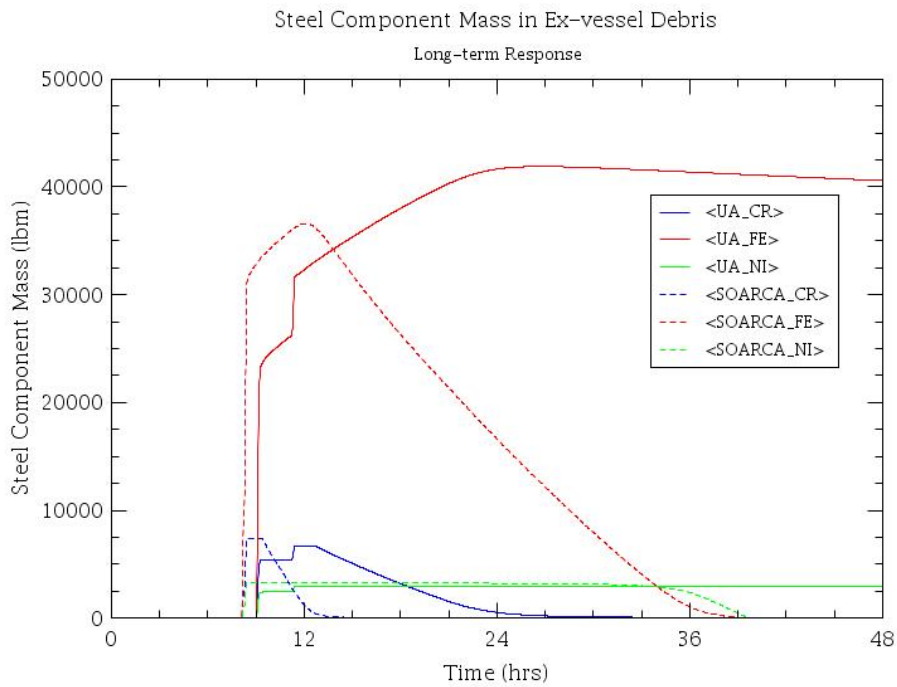


**Figure A-66 Comparison of the UA and SOARCA steel components in the ex-vessel debris**



#### 4. REFERENCES

- [1] NUREG-1570, "Risk Assessment of Severe Accident-Induced Steam Generator Tube Rupture," U.S. Nuclear Regulatory Commission, Washington DC. March 1998.
- [2] NUREG/CR-6995, "SCDAP/RELAP5 Thermal-Hydraulic Evaluations of the Potential for Containment Bypass During Extended Station Blackout Severe Accident Sequences in a Westinghouse Four-Loop PWR," U.S. Nuclear Regulatory Commission, Washington, DC, March 2010.
- [3] W. A. Stewart, A. T. Pieczynski, and V. Srinivar, "Natural Circulation Experiments for PWR Degraded Core Accidents," EPRI Report NP 6324 D, 1989.
- [4] W. A. Stewart, A. T. Pieczynski, and V. Srinivar, "Natural Circulation Experiments for PWR High Pressure Accidents," EPRI Report TR 102815, 1993.
- [5] NUREG-1781, "CFD Analysis of 1/7th Scale Steam Generator Inlet Plenum Mixing During a PWR Severe Accident," U.S. Nuclear Regulatory Commission, Washington, DC, October 2003.
- [6] NUREG-1922, "Computational Fluid Dynamics Analysis of Natural Circulation Flows in a Pressurized-Water Reactor Loop under Severe Accident Conditions," U.S. Nuclear Regulatory Commission, Washington, DC, March 2010.
- [7] NUREG/CR-7110, Rev. 1, "State-of-the-Art Reactor Consequence Analysis Project Volume 1: Peach Bottom Integrated Analysis," U.S. Nuclear Regulatory Commission, Washington, DC, March 2013.
- [8] NUREG/CR-7110, "State-of-the-Art Reactor Consequence Analyses Project Volume 1: Peach Bottom Integrated Analysis," U.S. Nuclear Regulatory Commission, Washington, DC, 2012.
- [9] NUREG/CR-6119, "MELCOR Computer Code Manuals, Vol. 2: Reference Manuals, Version 1.8.6 (Vol. 2, Rev. 3)," U.S. Nuclear Regulatory Commission, Washington, DC, 2005.
- [10] NUREG/CR-6906. "Containment Integrity Research at Sandia National Laboratories," U.S. Nuclear Regulatory Commission, Washington, DC, 2006.
- [11] NUREG/CR-5121, "Experimental Results From Pressure Testing a 1:6 – Scale Nuclear Power Plant Containment," U.S. Nuclear Regulatory Commission, Washington, DC, 1992.
- [12] NUREG/CR-6920, "Risk-Informed Assessment of Degraded Containment Vessels," U.S. Nuclear Regulatory Commission, Washington, DC, 2006.
- [13] Oak Ridge National Laboratory, "Scale: A Comprehensive Modeling and Simulation Suite for Nuclear Safety Analysis and Design," ORNL/TM-2005/39, Version 6.1, June 2011. Available from Radiation Safety Information Computational Center at Oak Ridge National Laboratory as CCC-785.

- [14] S.G. Ashbaugh, et al., "Accident Source Terms for Pressurized Water Reactors with High-Burnup Cores Calculated Using MELCOR 1.8.5," SAND2008-6664, Sandia National Laboratories, Albuquerque, NM (2008).
- [15] D. Brown, "Release of the ENDF/B-VII.1 Evaluated Nuclear Data File," Proceedings of 2012 ANS Winter Meeting & Nuclear Technology Expo, San Diego, CA, November 11-15 (2012).
- [16] I. Gauld, "Validation of ORIGEN-S Decay Heat Predictions for LOCA Analysis," Proceedings of PHYSOR-2006, ANS Topical Meeting on Reactor Physics, Vancouver, BC, Canada. September 10-14 (2006).
- [17] NUREG/CR-7041, "SCALE/TRITON Primer: A Primer for Light Water Reactor Lattice Physics Calculations," ORNL/TM-2011/21, U.S. Nuclear Regulatory Commission, Washington, DC, 2012.
- [18] J.N. Cardoni and D.A. Kalinich, "Fukushima Daiichi Unit 1 Uncertainty Analysis -- Preliminary Selection of Uncertain Parameters and Analysis Methodology," SAND2014-1170, Sandia National Laboratories: Albuquerque, NM (2014).
- [19] R.O. Gauntt, D.A. Kalinich, et al., "Fukushima Daiichi Accident Study," SAND2012-6173, Sandia National Laboratories: Albuquerque, NM (2012).
- [20] R.O. Gauntt, D.A. Kalinich, et al., "MELCOR Simulations of the Severe Accident at the Fukushima 1F1 Reactor," Proceedings of 2012 ANS Winter Meeting & Nuclear Technology Expo, San Diego, CA, November 11-15 (2012).
- [21] J. Phillips, J.N. Cardoni, et al., "MELCOR Simulations of the Severe Accident at the Fukushima 1F2 Reactor," Proceedings of 2012 ANS Winter Meeting & Nuclear Technology Expo, San Diego, CA, November 11-15 (2012).
- [22] J.N. Cardoni, R.O. Gauntt, et al., "MELCOR Simulations of the Severe Accident at the Fukushima 1F3 Reactor," Proceedings of 2012 ANS Winter Meeting & Nuclear Technology Expo, San Diego, CA, November 11-15, (2012).
- [23] R.O. Gauntt, "Synthesis of VERCORS and Phebus data in Severe Accident Codes and Applications," SAND2010-1633, Sandia National Laboratories, 2010.
- [24] NUREG/CR-4481, "Fission Product Behavior during Severe LWR Accidents: Modeling Recommendations for MELCOR Code System," Volume 1: Fission Product Release from Fuel. U.S. Nuclear Regulatory Commission, Washington, DC, 1988.
- [25] NUREG/CR-4169, "An Approach to Treating Radionuclide Decay Heating for Use in the MELCOR Code System," U.S. Nuclear Regulatory Commission, Washington, DC, 1985.
- [26] NUREG/BR-0353, "Davis-Besse Reactor Pressure Vessel Head Degradation: Overview, Lessons Learned, and NRC Actions Based on Lessons Learned (NUREG/BR-0353, Revision 1)," Revision 1, U.S. Nuclear Regulatory Commission, Washington, DC, August 2008.

- [27] C. Journeau, J. F. Haquet, P. Piluso, J. M. Bonnet, "Differences between Silica and Limestone Concretes that may Affect their Interaction with Corium," Proceedings of the 2008 International Congress on Advances in Nuclear Power Plants, ICAPP '08, Anaheim, CA USA, June 8-12, 2008, Paper 8059.
- [28] NUREG/CR 6285, "Severe Accident Natural Circulation Studies at the INEL," U.S. Nuclear Regulatory Commission, Washington, DC, February 1995.
- [29] M. Kenton, "Influence of MAAP4 Models Altered for the Purdue Code Comparison Project," EPRI, MTG-04-09-1962, May 2007.
- [30] NUREG/CR-6150, "SCDAP/RELAP5/MOD 3.3 Code Manual: MATPRO - A Library of Materials Properties for Light-Water-Reactor Accident Analysis," Idaho National Laboratory, Volume 4, Revision 2, U.S. Nuclear Regulatory Commission, Washington, DC, January 2001.
- [31] NUREG/CR-7155, "State-of-the-Art Reactor Consequence Analysis Project, Uncertainty Analysis of the Unmitigated Long-Term Station Blackout of the Peach Bottom Atomic Power Station," Draft, ML13189A145, U.S. Nuclear Regulatory Commission, Washington, DC, August 2013.
- [32] M. L. Farmer, et al., "Corium Coolability under Ex-vessel Accident Conditions for LWRs," Nuclear Engineering and technology, Vo., 41, No. 5, June 2009.
- [33] Surry response to SOARCA information request, August 9, 2007, Email from Gary Miller, Dominion to Robert Prato, NRC.
- [34] NUREG/CR-7037, "Industry Performance of Relief Valves at U.S. Commercial Nuclear Power Plants through 2007," U.S. Nuclear Regulatory Commission, Washington, DC, March 2011.
- [35] R. K. Kumar, "Flammability of Limits of Hydrogen-Oxygen-Diluent Mixtures," Journal of Fire Sciences, Vol. 3, July/August 1985.
- [36] NUREG/CR-2726, "Light Water Hydrogen Manual," U.S. Nuclear Regulatory Commission, Washington, DC, August 1983.
- [37] NUREG/CP-0027, Tamm, R. MacFarlane, D. D. S. Liu, "Ignition Effectiveness of Thermal Heating Devices in Hydrogen-Air-Steam Mixtures," in Proc. of Int. Meeting on Thermal Reactor safety, Vol. 1, U.S. Nuclear Regulatory Commission, Washington, DC, 1983.
- [38] K. Vierow, Y. Liao, J. Johnson, M. Kenton, R. Gauntt, "Severe Accident Analysis of a PWR Station Blackout with the MELCOR, MAAP4 and SCDAP/RELAP5 Codes," Nuclear Engineering and Design, Vol. 234, Issue 1-3, pp. 129-145, 2004.
- [39] NUREG/CR-6928, "Industry-Average Performance for Components and Initiating Events at U.S. Commercial Nuclear Power Plants," U.S. Nuclear Regulatory Commission, Washington, DC, February 2007.

- [40] B. Simondi-Teisseire, N. Girault, F. Payot<sup>1</sup>, B. Clément “Iodine behaviour in the containment in Phébus FP tests,” *Annals of Nuclear Energy*, Volume 61, November 2013, Pages 157–169.
- [41] “Action Item on Secondary Side Retention of Fission Products in a Steam Generator Tube Rupture Accident,” Email Memo from D. Powers, Sandia National Laboratories to US NRC, May 2008.
- [42] J. Tills, A. Notafraancesco, and K. Murata, “An Assessment of CONTAIN 2.0: A Focus on Containment Thermal Hydraulics (Including Hydrogen Distributions),” SMSAB-02-02, July 2002, Office of Nuclear Regulatory Research (ADAMS Accession Number ML022140438).
- [43] NUREG-1493, “Performance-based Containment Leak-test Program,” U.S. Nuclear Regulatory Commission, Washington, DC, January 1995.
- [44] NUREG/CR-6553, “Code Manual for the CONTAIN 2.0: A Computer Code for Nuclear Reactor Analysis,” U.S. Nuclear Regulatory Commission, Washington, DC, December 1997.
- [45] Y. Pontillon, et al., “Lessons learnt from VERCORS tests. Study of the active role played by UO<sub>2</sub>–ZrO<sub>2</sub>–FP interactions on irradiated fuel collapse temperature,” *Journal of Nuclear Materials* 344, pp. 265–273, 2005.
- [46] W. C. Hinds, *Aerosol Technology*, Wiley, 1982.
- [47] G. Kasper, T. Niida, and M. Yang, “Measurements of viscous drag on cylinders and chains of sphere with aspect ratios between 2 and 50,” *J. Aerosol Science*, 16 (6), 535-556, 1985.
- [48] J. E. Brockmann, “Range of Possible Dynamic and Collision Shape Factors,” In “Uncertainty in Radionuclide Release Under Specific LWR Accident Conditions,” Appendix F, by R. J. Lipinski, D. R. Bradley, J. E. Brockmann, J. M. Griesmeyer, C. D. Leigh, K. K. Murata, D. A. Powers, J. B. Rivard, A. R. Taig, J. Tills, and D. C. Williams, Sandia National Laboratories, Albuquerque, New Mexico, SAND84-0410 Volume 2, 1985.
- [49] M. P. Kissane, “On the nature of aerosols produced during a severe accident of a water-cooled nuclear reactor”, *Nuclear Engineering and Design*, 238, 2792-2800, 2008.
- [50] NUREG/CR-6365, “Steam Generator Tube Failures,” U.S. Nuclear Regulatory Commission, Washington, DC, 1996.
- [51] NUREG-1740, “Voltage-Based Alternative Repair Criteria,” U.S. Nuclear Regulatory Commission, Washington, DC, 2001.
- [52] M. Yetisir, “Reactor Coolant Pump Seal Leak Rate during Station Blackout,” GNP-117100-TE-001, Revision D2, Atomic Energy of Canada Limited (AECL), June 2008.

- [53] NUREG/CR-4294, "Leak Rate Analysis of Westinghouse Reactor Coolant Pump," U.S. Nuclear Regulatory Commission, Washington, DC, June 1986.
- [54] NUREG-1953, "Confirmatory Thermal-Hydraulic Analysis to Support Specific Success Criteria in the Standardized Plant Analysis Risk Models—Surry and Peach Bottom," U.S. Nuclear Regulatory Commission, Washington, DC, September 2011.
- [55] Surry Power Station Updated Final Safety Analysis Report," Revision 36, September 30, 2004.

## Appendix B Glossary of Uncertainty Analysis Terms

*Note that this glossary defines terms as they are used in this study, and the same terms may be used differently in other studies.*

**Additive Model** – A regression technique where an estimation of the regression line is formed by a summation of a collection of one-dimensional arbitrary basis functions. An additive model considers the influence of the variables themselves and does not consider any possible interaction.

**Aleatory** – Inherent randomness in the properties or behavior of the system under study. Aleatory uncertainty cannot be reduced based on increased knowledge of the system under study.

**Basis Function** – Elementary elements used in the decomposition of a function in a specific space. Every continuous function can be constructed as a linear combination of basis functions. For example, a quadratic polynomial has basis functions of  $\{1, x, x^2\}$ . Every quadratic polynomial has the form:

$$y = a * 1 + b * x + c * x^2$$

where 1,  $x$ , and  $x^2$  are the basis functions and  $a$ ,  $b$ , and  $c$  are coefficients of the basis functions that define the unique polynomial.

**Beta Distribution** – A family of continuous probability distributions defined on the interval  $[0,1]$  parameterized by two positive shape parameters ( $\alpha$  and  $\beta$ ) that control the shape of the distribution. Its probability density function is expressed as follow:

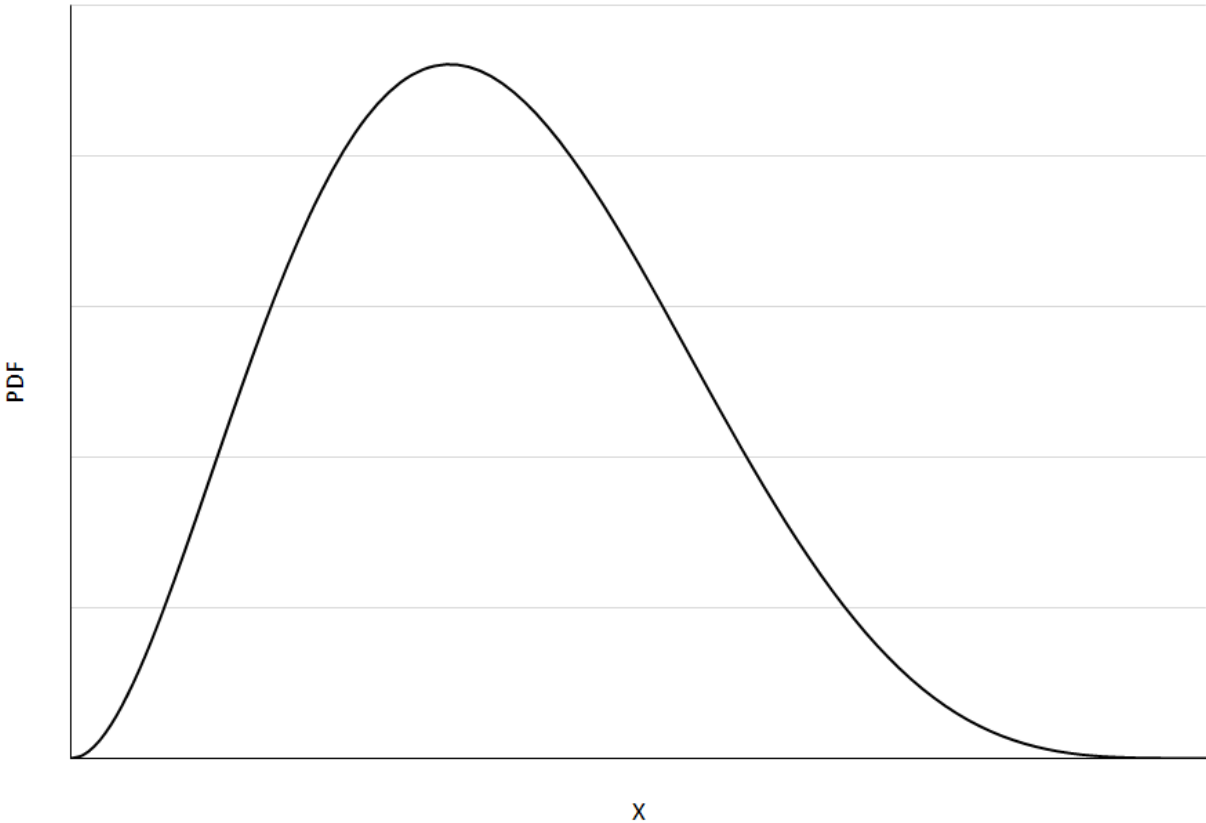
$$f(t) = \frac{\Gamma(\alpha + \beta)}{\Gamma(\alpha)\Gamma(\beta)} t^{\alpha-1}(1 - t)^{\beta-1}$$

where  $\Gamma$  represents the gamma function:

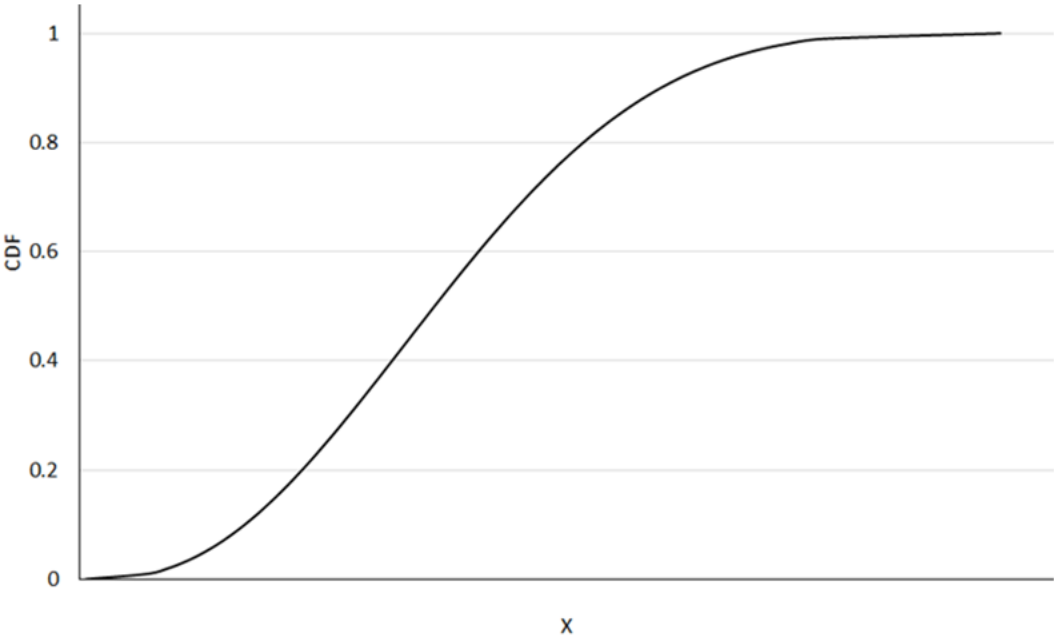
$$\Gamma(w) = \int_0^{\infty} x^{w-1} e^{-x} dx$$

Beta distributions can serve as a model for the probability that a system or component is in operation for at least  $t$  units of time. Sometimes, two parameters (min and max) are added to the beta function parameters. These parameters scale the domain of definition from  $[0,1]$  to  $[\text{min},\text{max}]$ . See illustrations below.

Beta Distribution



Beta Distribution



**Cliff-edge Effects** – An instance in which a small change in an input can lead to a large change in the response of the system.

**Coefficient of Determination** – This coefficient (noted as  $R^2$ ) estimates the proportion of the variance of the output that is explained by the regression model under consideration. Thus, this coefficient provides an indication of how well a regression model replicates the observed outcomes.

**Complementary Cumulative Distribution Function (CCDF)** – This function represents the probability for a value sampled from a probability distribution to be greater than a given quantile value. Given a real-valued random variable  $X$  and a threshold value  $x$  for a metric of interest, the complementary cumulative distribution function  $\bar{F}(x)$  is defined as:

$$\bar{F}(x) = P(X > x) = 1 - F(x)$$

where  $F(x)$  is the cumulative distribution function (CDF) defined by  $F(x) = P(X \leq x)$ .

**Conjoint Influence** – The influence of two or more input parameters acting together. This influence may have synergistic effects that would not be uncovered by studying the influence of each parameter individually.

**Correlation** – A possible dependence between two random variables. Positive correlation between two variables implies that a high value (or low value) for one variable is more likely to be associated with a respectively high value (low value) for the other. Negative correlation will reverse this relation, meaning that low values of one variable will be associated with high values of the other. Correlation does not imply causation. Correlation determines the existence of a trend but does not assess the magnitude of the change in output with respect to the change in input.

**Cumulative Distribution Function (CDF<sup>16</sup>)** - This function represents the probability for a value sampled from a probability distribution to be equal to or less than a given quantile value. For continuous variables, this function is the integral of the probability density function and is given by:

$$F(x) = \int_{-\infty}^x f(x)dx$$

where  $F(x)$  is the cumulative distribution function and  $F(x) = P(X \leq x)$ .

**Deterministic** – Describing a system in which no randomness is involved in the calculation of a given response. A set of constant inputs definitively predict the output.

**Discrete Distribution** – A probability distribution where the random variable can have a set of distinct, finite values.

**Epistemic** – Uncertainty related to the lack of knowledge or confidence about the system under analysis. This type of uncertainty is produced by a lack of knowledge regarding the inputs or models under consideration. Epistemic uncertainty is usually considered as reducible uncertainty because increased knowledge should reduce it. Also called “state-of-knowledge” uncertainty.

**Kaplan/Garrick ordered triplet representation for risk** – This representation of risk poses three questions:

- 1) What can go wrong?
- 2) How likely is it to go wrong?
- 3) What are the consequences if the event occurs?

---

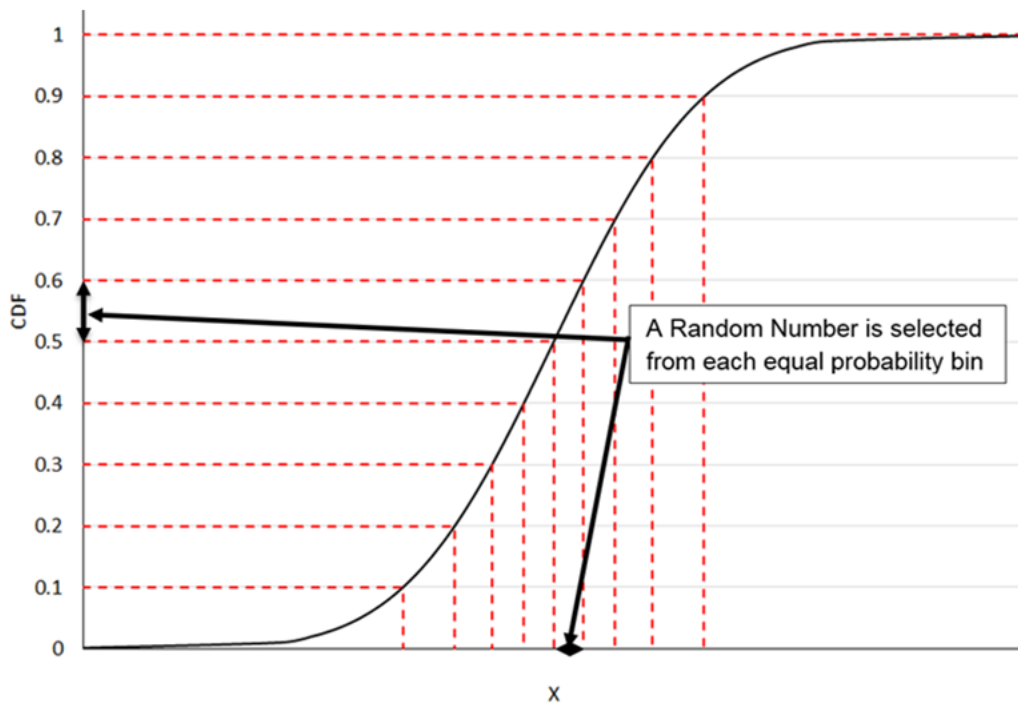
<sup>16</sup> Not to be confused with core damage frequency (CDF) from a level 1 probabilistic risk assessment.

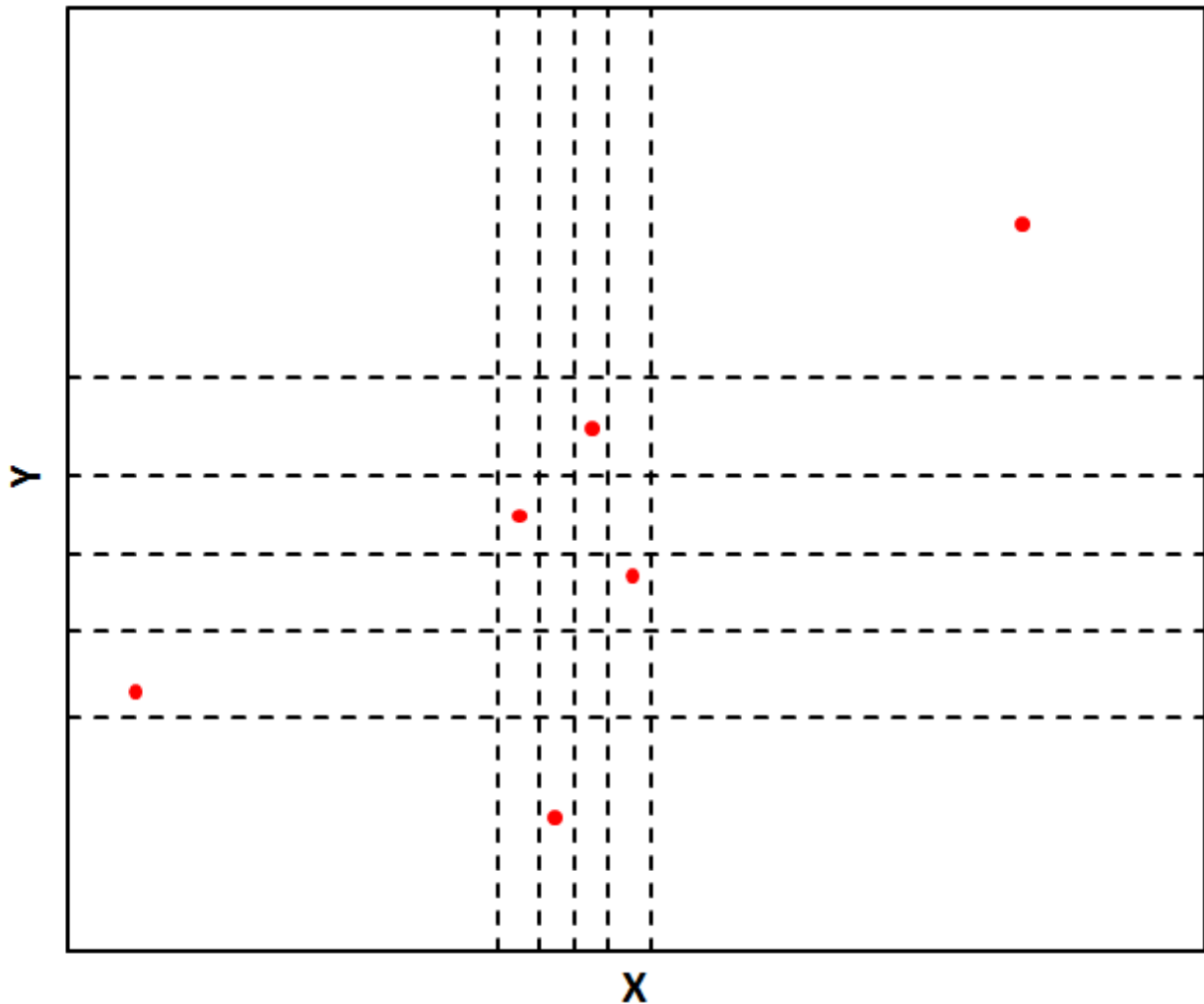
This representation is used to assess inherent randomness in the system (i.e., aleatory uncertainty). Potential lack of knowledge (i.e., epistemic uncertainty) adds a fourth question to the original triplet which is:

4) How much confidence do we have in the answers to the first three questions?

The exploration of these questions is the basis for Probabilistic Risk Assessment (PRA) (see 'Probabilistic Risk Assessment' below.) The Kaplan/Garrick ordered triplet representation is typically the NRC's definition of the term "risk."

**Latin Hypercube Sampling (LHS)** – A sampling technique in which each input variable is sampled in a stratified way in order to guarantee that all portions of the range of the variable's distribution are represented. LHS samples a probability density function (PDF) by first dividing the PDF of each variable into  $N$  bins of equal probability where  $N$  is the sample size per variable chosen ahead of time. One value is then sampled from the random variable's PDF in each of the  $N$  bins. Thus, if there are  $n$  random input variables, the input space is partitioned into  $n \times N$  hypercubes from which  $N$  will be selected such that each variable will have exactly one value sampled in each of its defined strata (PDF interval). See illustrations below for one ( $x$ ) and two ( $x, y$ ) variables, where the red marks on the 2<sup>nd</sup> illustration represent one possible Latin Hypercube Sample of size  $N = 6$ .





**Least Squares** – An optimization technique that selects the parameters of a model such that the difference between the estimation and empirical values (derived from observations or another model) is minimized according to the  $L^2$ -norm (i.e., the square root of the sum of square differences is minimized).

**Lognormal Distribution** – A normal distribution over the logarithm of the random variable.

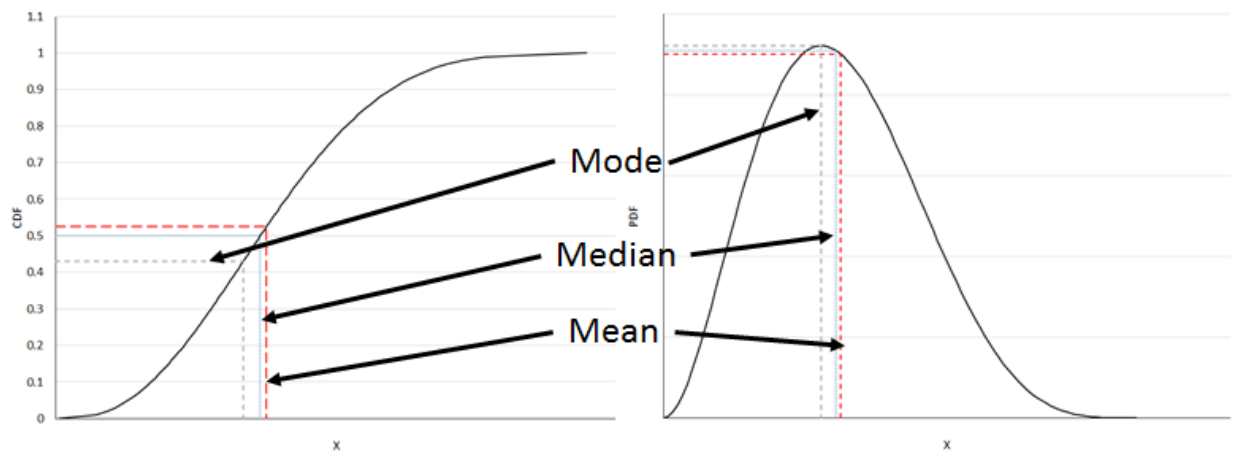
**Log Triangular Distribution** – A triangular distribution over the logarithm of the random variable. See illustrations under ‘**Triangular Distribution**’ below, where the only difference is that “ $\log(x)$ ” replaces “ $x$ ” on the x axis.

**Log Uniform Distribution** – A uniform distribution over the logarithm of the random variable. See illustrations under ‘**Uniform Distribution**’ below, where the only difference is that “ $\log(x)$ ” replaces “ $x$ ” on the x axis.

**Mean** – Estimates the expected value of a distribution of values. The mean value of a random variable is the arithmetic average of possible values as described by its probability density function. See illustration below for ‘mean,’ ‘**median,**’ and ‘**mode,**’ all of which are measures of central tendency, though they are all different.

**Median** – The median of a probability distribution corresponds to the middle value that separates a sample or a distribution into halves of equal likelihood. A random variable is equally likely to take on a value greater than the median or less than the median. In other words, the  $CDF(\text{Median value}) = CCDF(\text{Median value}) = 0.5$ . See illustration below for ‘mean,’ ‘median,’ and ‘mode,’ all of which are measures of central tendency, though they are all different.

**Mode** – The most likely value for an uncertain variable. For a discrete distribution, the mode represents the most common (most likely) value in a set of  $n$  values. For a continuous distribution, the mode represents the value at which the probability density function reaches its maximum. See illustration below for ‘mean,’ ‘median,’ and ‘mode,’ all of which are measures of central tendency, though they are all different.



**Monotonic** – A monotonic function is a function which is either solely nonincreasing or solely nondecreasing. A monotonic function cannot increase with increasing values of a dependent variable in one range and then decrease with increasing values of a dependent variable in a different range.

**Monte Carlo simulation** – A numerical technique that covers the uncertain input space (multidimensional space where each dimension represents a different random variable with its associated distribution) by sampling each probability distribution using random, or pseudo-random, numbers. This method is preferred over a direct discretization when the number of inputs is large because a regular discretization in each direction would lead to an impractically large number of simulations. The system model is then run repeatedly using a single set of values for the input variable vector at each repetition. With this process, Monte Carlo simulation produces a distribution of system model outputs (results) based on the input variable uncertainty as described by the input space.

**(Multiplicative) Interaction Term** – In regression models, interaction (or higher order) terms are basis functions that do not solely depend on one parameter. They can involve interactions amongst just two parameters up to interactions that involve all parameters under study. They can be as simple as a multiplication of two parameters or fairly complex (division, power, log, etc.). These terms are ignored by additive regression models.

**Normal distribution** – The normal distribution is one of the most common probability distributions. As demonstrated by the central limit theorem, the normal distribution can be used

to represent the distribution of the sum of random variables (if they follow the same distribution) or the distribution of the mean value. The normal distribution's probability density function is defined from  $-\infty$  to  $+\infty$  and has a bell shape:

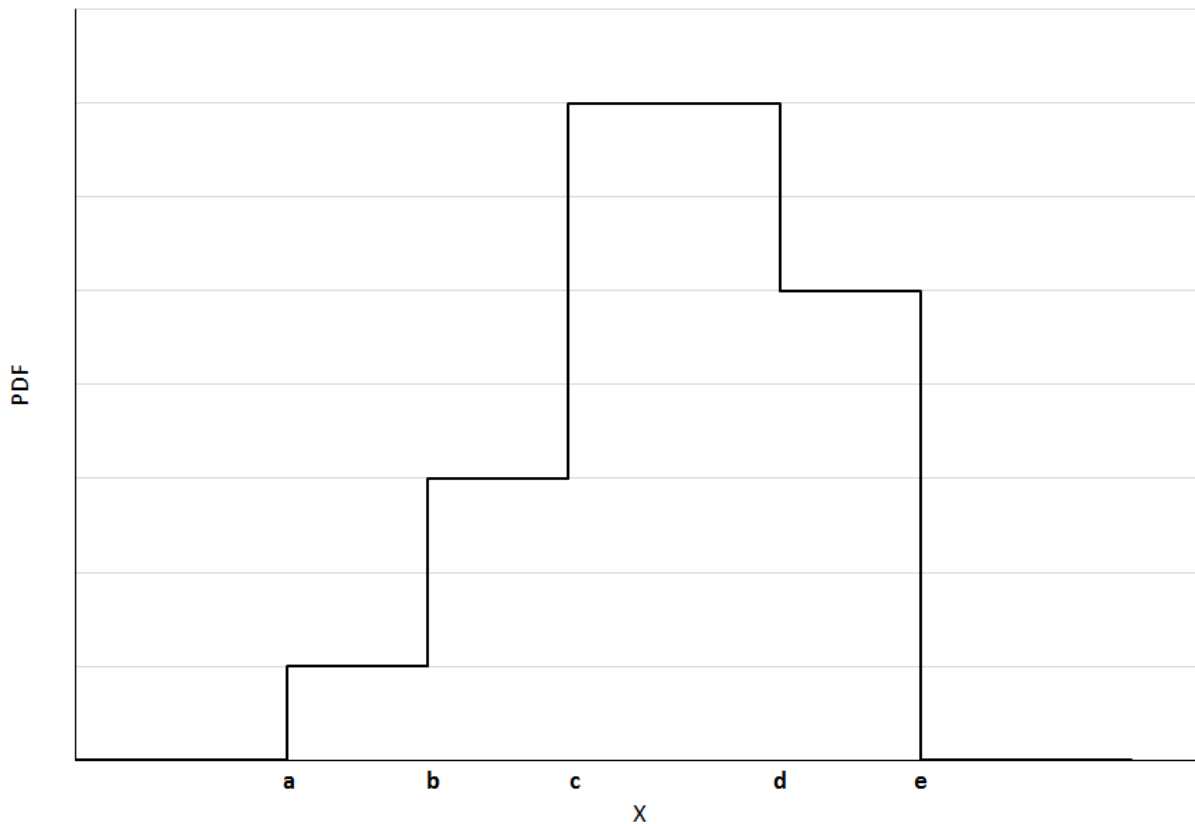
$$f(x|\mu, \sigma) = \frac{1}{\sigma\sqrt{2\pi}} e^{-\frac{(x-\mu)^2}{2\sigma^2}}$$

Where  $\mu$  and  $\sigma$  represent respectively the mean and standard distribution and are the traditional parameters used to define a normal distribution.

**Percentile** – Specific form of quantile for which the value is reported as a percentage (e.g. the 0.01 quantile is the same as the 1<sup>st</sup> percentile). See '**quantile**' for additional description.

**Piecewise Uniform Distribution** – A distribution formed by distinct uniform distributions over intervals of the range of the probability density function. See illustration below.

Piece-wise Uniform Distribution



**Probabilistic Risk Assessment (PRA)** – A systematic method for assessing three questions that the NRC uses to define "risk." These questions consider (1) what can go wrong, (2) how likely it is, and (3) what its consequences might be. (See '**Kaplan/Garrick ordered triplet representation for risk**' above.) These questions allow the NRC to understand likely outcomes, sensitivities, areas of importance, system interactions, and areas of uncertainty, which the staff can use to identify risk-significant scenarios. The NRC uses PRA to determine a numeric estimate of risk to provide insights into the strengths and weaknesses of the design and operation of a nuclear power plant.

**Probability Density Function (PDF)** – A function that describes the likelihood that a continuous random variable takes on a value in an interval. A PDF has the properties that 1) a value on the function is greater than or equal to 0 and 2) the total integral probability is 1.

$$f(t) \geq 0$$
$$\int_{-\infty}^{\infty} f(t)dt = 1$$

**Probability Distribution** – A mathematical representation of the uncertainty of a random variable in a probabilistic framework. Specification of a probability distribution can be done via probability density (or mass for discrete variable) function or a cumulative distribution function for instance.

**Probability Mass Function (PMF)** – A function that is equivalent to the probability density function for discrete variables (and for which integral is replaced with a regular sum).

**Quantile** – A quantile  $x_q$  is the value of a random variable such that there is a probability  $q$  that a sampled value will be equal or lower to  $x_q$ . Specific quantiles include the median (for which  $q = 0.5$ ), quartiles (where  $q = 0.25$  and  $0.75$  and represents the 1<sup>st</sup> and 3<sup>rd</sup> quartiles, respectively) and percentiles (in which  $q$  is expressed as a percent from 0 to 100 instead of a probability between 0 and 1).

**Rank Correlation Coefficient** – Also known as Spearman Correlation Coefficient, the rank correlation coefficient measures the degree of linearity in the relationship between two random variables after they have been rank-transformed (see ‘rank transformation’).

**Rank Regression** – Rank regression is a linear regression applied to rank values. The linear regression builds a linear function model between outputs and inputs using a least squares approach. Often, linear and rank regressions use a stepwise approach such that new parameters are added to the model only if they increase the strength of the regression model significantly enough such that the complexity of adding a parameter is overcome by the increase in variance explained. Rank Regression is solely used to estimate the influence of uncertainty in the input parameters on the output uncertainty and is not used for prediction.

**Rank Transformation** – Rank transformation consists of replacing the actual value of a random variable by its rank in the total sample. Regression methods become non-parametric when working with rank values instead of with raw data. This allows for monotonic relations to be captured instead of simple linear relations and reduces the effect of outliers.

**Realization** – An individual calculation using one sample of values for the input variable vector in Monte Carlo simulation. In other words, a Monte Carlo simulation where the system model is run N times has N realizations. Within a realization, the model is usually run deterministically and returns a unique set of output values

**Regression** – A measure of the relation between one variable (e.g., output or results of a model) and corresponding values of other variables (e.g., inputs to a model). Regression methods attempt to find a mathematical relationship between input variables and the output variable(s) of interest.

**Regression Analysis** – An analysis that determines the importance of input variables to outputs of interest by examining how sensitive an output is to a given input or set of inputs. Regression analysis in this study used the results of Monte Carlo simulation. Regression results quantify how much the uncertainty in each analysis input contributes to the variance in the output under consideration.

**Sensitivity Analysis** – A set of studies that exercise a complex system under different conditions in order to 1) validate some assumptions, 2) explore alternative conceptual models or address differences in opinion, or 3) study one particular aspect of the complex system in greater detail. These studies are different from Monte Carlo simulations in that they require changing some options that have been considered to be constants in the study of reference and may study only one variable or conceptual model in isolation. Such studies can be completed through either deterministic or probabilistic means.

**Simple Random Sampling (SRS)** – A random sampling technique where for each time sampled, the probability that a particular value of a variable is chosen is proportional to the probability density function of the variable at that particular value. No further requirements are imposed on the sampling (unlike Latin Hypercube Sampling).

**Stochastic** – A random occurrence. A stochastic simulation refers to a simulation in which randomness in uncertain input variables is used to calculate a system response.

**Stochastic Failure** – A failure that is caused by random processes.

**Sum of Square Error (SSE)** – The total sum of the squares of the differences between estimated and empirical values (i.e., observations, measurements, or an empirical model).

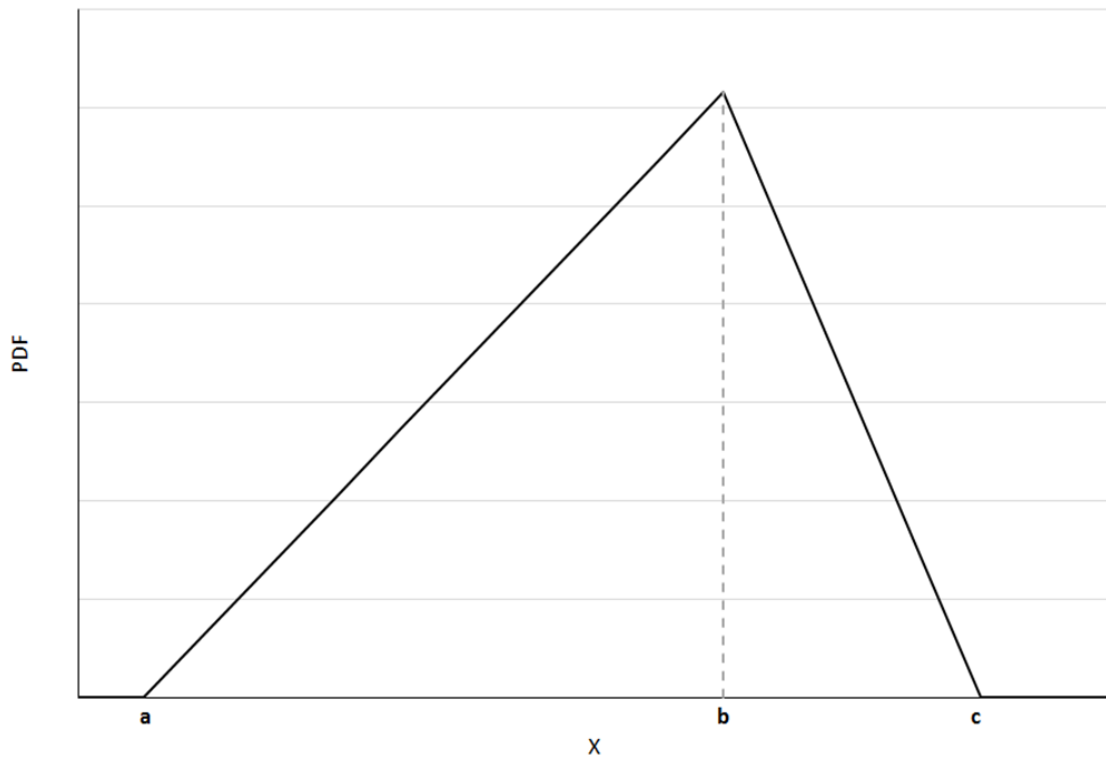
$$SSE = \sum_i (y_i - f(x_i))^2$$

A small SSE indicates a good fit between the predicted and observed values.

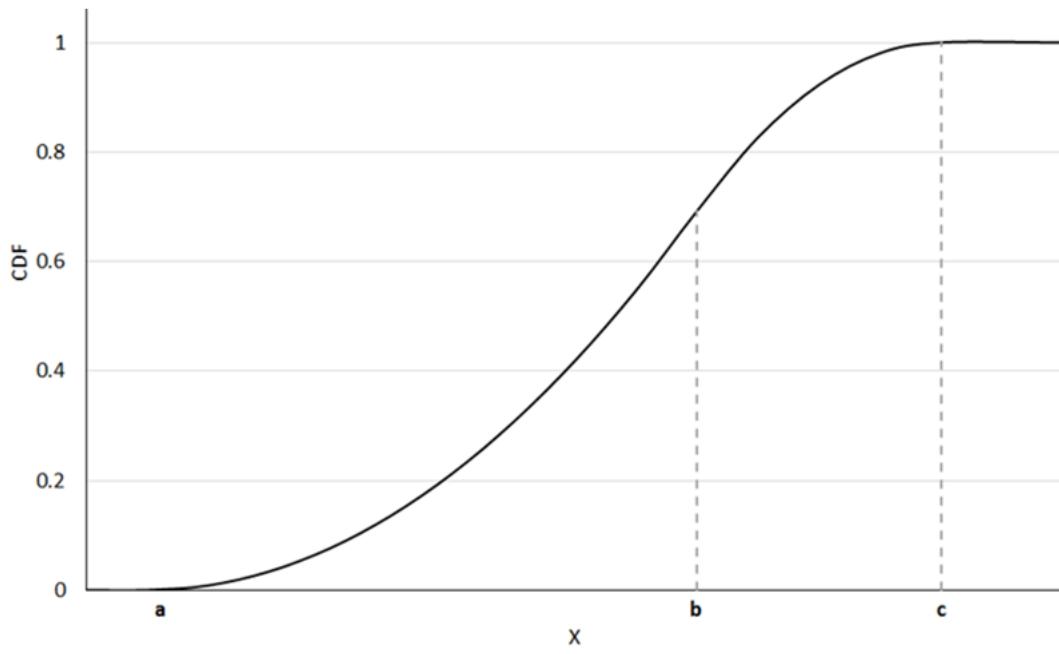
**Triangular distribution** – A continuous distribution that takes the form of a triangle. The probability density for the range  $[a,b]$  reaches its mode at the location  $c$  and form a triangular shape:

$$f(x) = \begin{cases} 0 & \text{for } x < a \\ \frac{2(x-a)}{(b-a)(c-a)} & \text{for } a \leq x < c \\ \frac{2}{b-a} & \text{for } x = c \\ \frac{2(b-x)}{(b-a)(b-c)} & \text{for } c < x \leq b \\ 0 & \text{for } x > b \end{cases}$$

Triangular Distribution



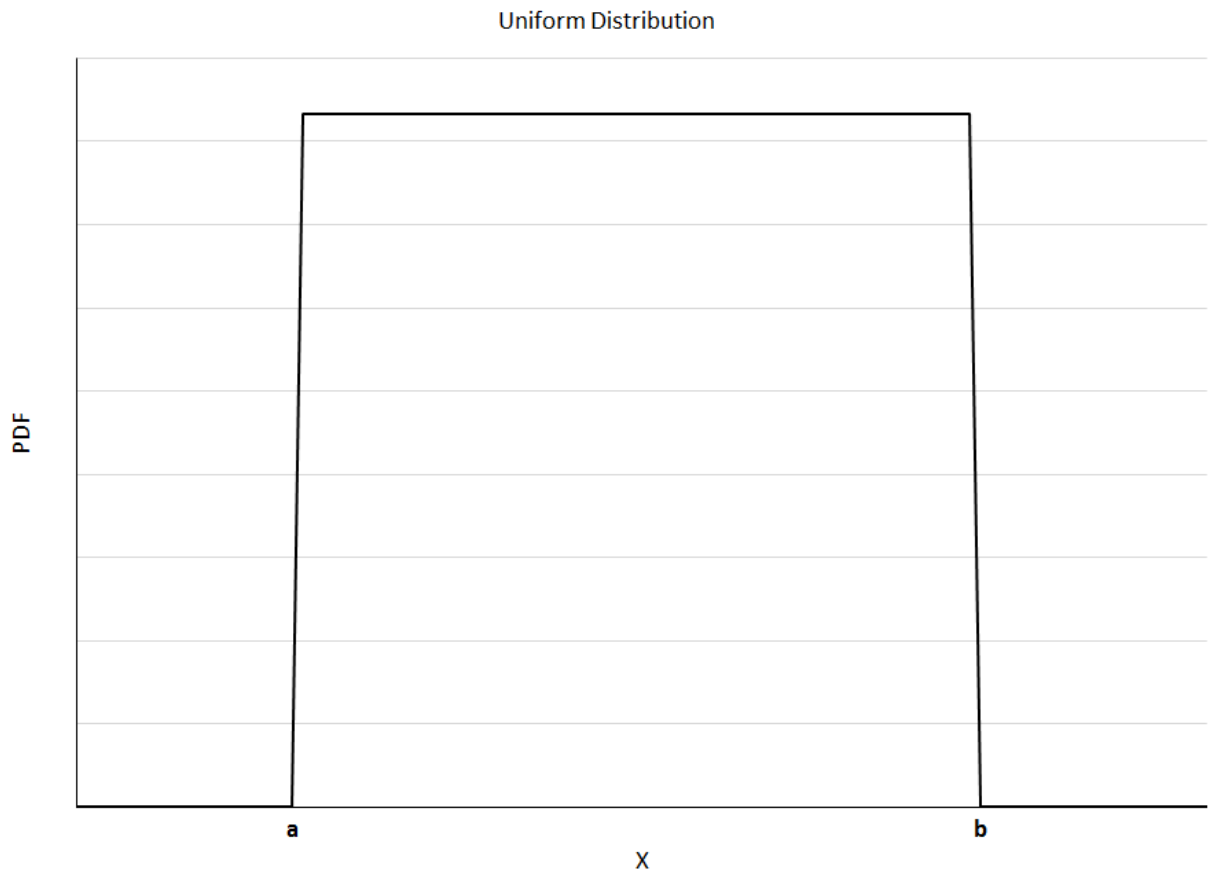
Triangular Distribution



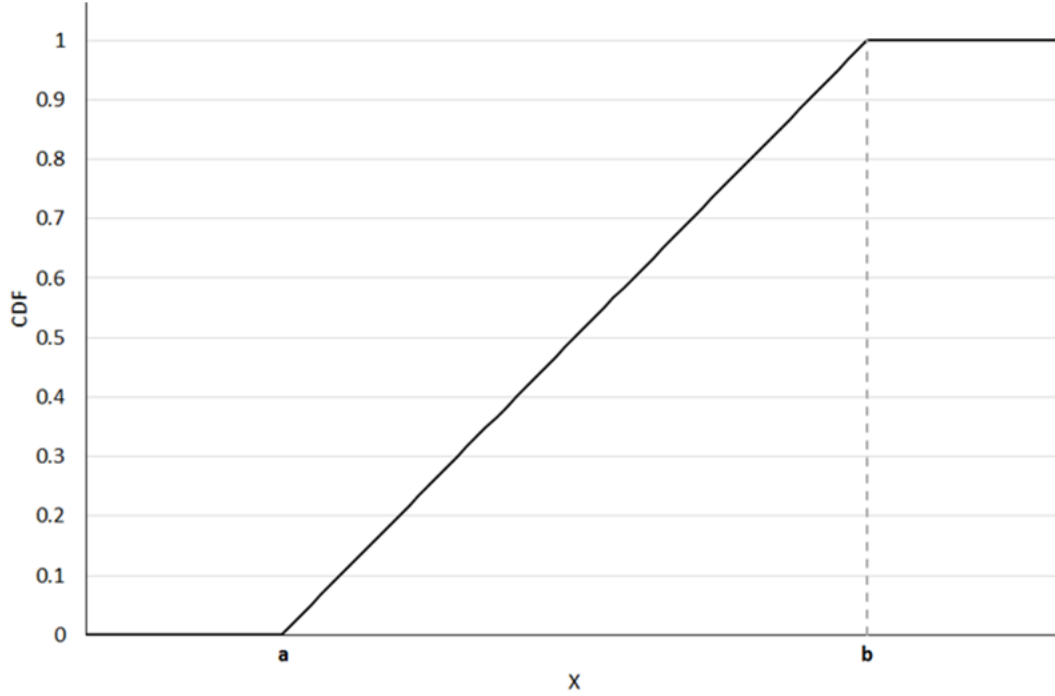
**Uncorrelated** – A situation in which no linear dependence between sampled values for two variables is observed.

**Uniform Distribution** – A distribution used when any value for a random variable defined on a range  $[a,b]$  is equally likely. The uniform probability density function forms a rectangle and is given by:

$$f(x) = \begin{cases} \frac{1}{b-a} & \text{for } x \in [a, b] \\ 0 & \text{otherwise} \end{cases}$$



### Uniform Distribution



**Variance** – A measure of the dispersion of data about a mean, given by:

$$V = \sigma^2 = \frac{\sum_{i=1}^N (Y_i - \mu)^2}{N}$$

where  $Y_i$  is a particular data point,  $\mu$  is the mean, and  $N$  is the number of data points. The variance characterizes the average spread squared of the data set.